Cover Picture

Eluvathingal D. Jemmis, Axel Schulz, Uwe Rosenthal et al.
Metallacycles from Metallocene Complexes and a Sulfurdiimide

Microreview

Maria Elena Cucciolito and Francesco Ruffo
Pt^{II}–η^1-Hydrocarbyl Complexes with cis-Coordinated Olefin or Alkyne
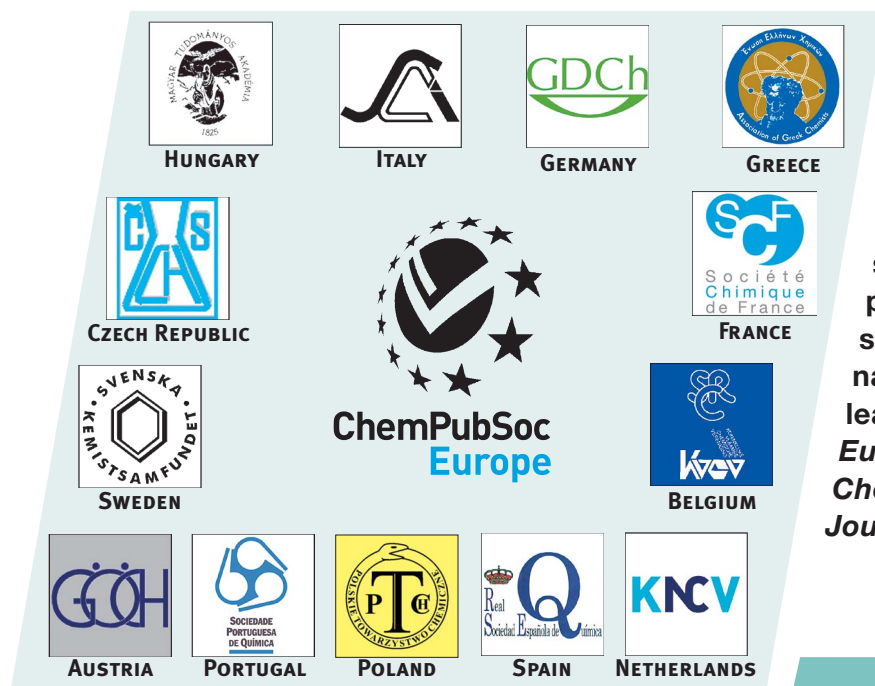
WILEY-VCH

www.eurjic.org

A Journal of

**ChemPubSoc
Europe**

HUNGARY

ITALY

GDCh
GERMANY

GREECE

CZECH REPUBLIC

ChemPubSoc Europe

SCF
Société
Chimique
de France
FRANCE

SWEDEN

KVCV
BELGIUM

AUSTRIA

PORTUGAL

POLAND
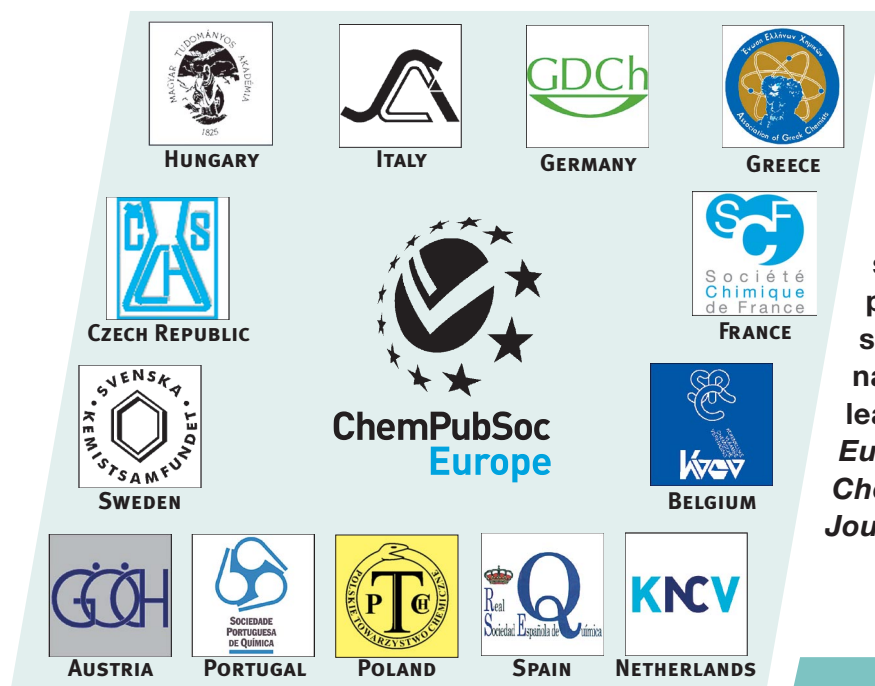
SPAIN

KNCV
NETHERLANDS

EurJIC is a journal of ChemPubSoc Europe, a union of 16 European chemical societies formed for the purpose of publishing high-quality science. All owners merged their national journals to form two leading chemistry journals, the *European Journal of Inorganic Chemistry* and the *European Journal of Organic Chemistry*.

Other ChemPubSoc Europe journals are *Chemistry – A European Journal*, *ChemBioChem*, *ChemPhysChem*, *ChemMedChem*, *ChemSusChem*, *ChemCatChem*, *ChemPlusChem* and *ChemistryOpen*.

COVER PICTURE

The cover picture shows the skyline of Rostock at night with a titanocene bis(trimethylsilyl)acetylene complex as well as the unusual metallacyclic complex $[Cp_2Ti(\eta^2-Me_3SiN=S=NSiMe_3)]$, which can readily be obtained from the former complex by reaction with the sulfurdiimide $Me_3SiN=S=N-SiMe_3$, rising brightly into the sky. The synthesis and a detailed theoretical study of the structure and bonding of this exotic organometallic compound are described in the article by E. D. Jemmis, A. Schulz, U. Rosenthal et al. on p. 611ff.

EurJIC
European Journal
of Inorganic Chemistry

HUNGARY	ITALY	GERMANY	GREECE
CZECH REPUBLIC			FRANCE
SWEDEN	ChemPubSoc Europe		BELGIUM
AUSTRIA	PORTUGAL	POLAND	SPAIN NETHERLANDS

EurJIC is a journal of ChemPubSoc Europe, a union of 16 European chemical societies formed for the purpose of publishing high-quality science. All owners merged their national journals to form two leading chemistry journals, the *European Journal of Inorganic Chemistry* and the *European Journal of Organic Chemistry*.

Other ChemPubSoc Europe journals are *Chemistry – A European Journal*, *ChemBioChem*, *ChemPhysChem*, *ChemMedChem*, *ChemSusChem*, *ChemCatChem*, *ChemPlusChem* and *ChemistryOpen*.

COVER PICTURE

The cover picture shows the skyline of Rostock at night with a titanocene bis(trimethylsilyl)acetylene complex as well as the unusual metallacyclic complex [$Cp_2Ti(\eta^2\text{-}Me_3SiN=S=NSiMe_3)$], which can readily be obtained from the former complex by reaction with the sulfurdiimide $Me_3SiN=S=N$-$SiMe_3$, rising brightly into the sky. The synthesis and a detailed theoretical study of the structure and bonding of this exotic organometallic compound are described in the article by E. D. Jemmis, A. Schulz, U. Rosenthal et al. on p. 611ff.
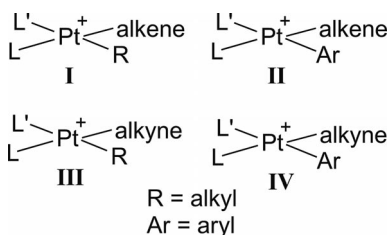
CONTENTS

MICROREVIEW

Platinum(II) Hydrocarbyl Complexes

$$R = alkyl$$
$$Ar = aryl$$

This review provides a survey of the key classes of Pt^{II} complexes containing cis-{$Pt(\eta^1$-hydrocarbyl)(η^2-unsaturated ligand)} moieties. A discussion of their main features is presented, which discloses the factors affecting their reactivity, dynamic behavior, and relative stability.

FULL PAPERS

Metallacycles

**K. Kaleta, M. Ruhmann, O. Theilmann,
S. Roy, T. Beweries, P. Arndt, A. Villinger,
E. D. Jemmis,* A. Schulz,*
U. Rosenthal*** .... 611−617
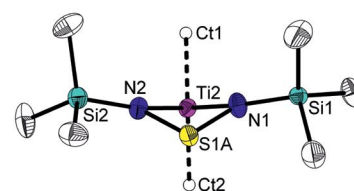
$$M = Ti, no L$$
$$M = Zr, L = py$$

Experimental and Theoretical Studies of Unusual Four-Membered Metallacycles from Reactions of Group 4 Metallocene Bis(trimethylsilyl)acetylene Complexes with the Sulfurdiimide $Me_3SiN=S=N-SiMe_3$

Keywords: Density functional calculations / Metallacycles / Titanium / X-ray diffraction / Zirconium
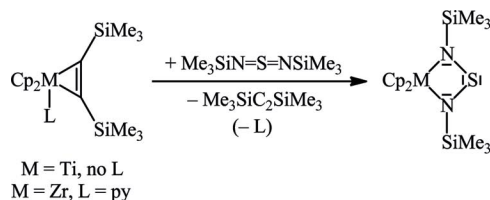
The reactions of the metallocene alkyne complexes [$Cp_2Ti(\eta^2$-$Me_3SiC_2SiMe_3$)] and [Cp_2Zr(pyridine)(η^2-$Me_3SiC_2SiMe_3$)] with the sulfurdiimide $Me_3SiN=S=NSiMe_3$ yields metallacyclic metallocene sulfurdiimide complexes. The molecular structure and DFT analysis of the titanocene product revealed the presence of a butterfly coordination of the diimide along with two Ti−N σ-bonds.
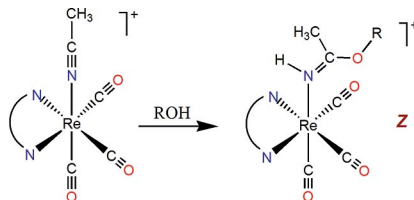
Iminoether Complexes

**T. Perera, P. Abhayawardhana,
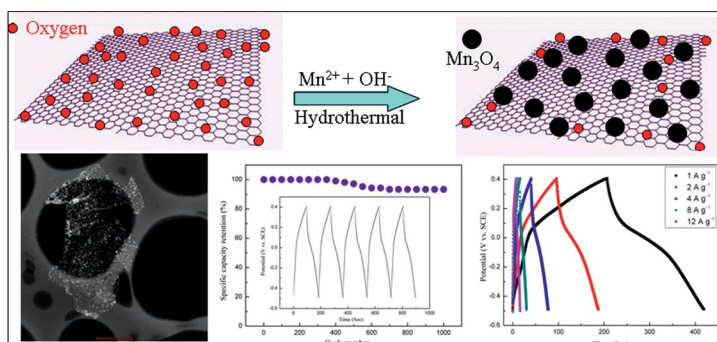F. R. Fronczek, P. A. Marzilli,
L. G. Marzilli*** .... 618−627

Iminoether Complexes of the Type, fac-[Re(CO)$_3$L{HNC(CH$_3$)OCH$_3$}]BF$_4$ (L = Bipyridine or a Substituted Bipyridine): Synthesis and Properties

Keywords: Rhenium / Carbonyl ligands / N ligands / Iminoether

fac-[Re(CO)$_3$L{HNC(CH$_3$)OCH$_3$}]BF$_4$ complexes (L = bipyridines) formed readily when fac-[Re(CO)$_3$(CH$_3$CN)$_3$]BF$_4$ in CH$_3$CN/CH$_3$OH was treated with the bipyridines. The unprecedented facile iminoether formation from the CH$_3$CN ligand bound to this low-valent Re^I center was slow compared to the amidine formation. This implies that selective bioconjugation of the amino sugars to the amine groups is feasible.

**D. Wang, Y. Li, Q. Wang,* T. Wang** .... 628−635

Facile Synthesis of Porous Mn_3O_4 Nanocrystal−Graphene Nanocomposites for Electrochemical Supercapacitors

Keywords: Manganese / Nanoparticles / Graphene / Energy conversion / Electrochemistry / Supercapacitors

Porous Mn_3O_4 nanocrystal−graphene nanocomposites have been successfully prepared by a facile solution based approach. An electrode comprising the as-prepared porous Mn_3O_4 nanocrystal−graphene nanocomposites exhibits enhanced rate capability and excellent electrochemical stability relative to electrodes comprising pure graphene or Mn_3O_4.

$(C_3H_5NH_3)_3BiBr_6$ is built up of discrete $BiBr_6^{3-}$ anions and highly disordered allyl-ammonium cations. The crystal undergoes phase transitions which were characterised by thermal, dielectric, infrared and ^1H NMR spectroscopic methods. The mechanism of the phase transitions is due to the change in the cationic dynamics.
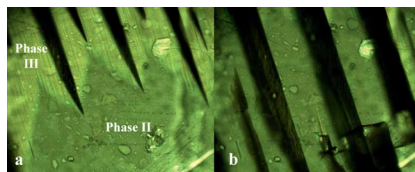
**I. Płowaś,* A. Białońska, G. Bator, R. Jakubas, W. Medycki, J. Baran** .... 636−646

Tris(allylammonium) Hexabromobismuthate(III) − Crystal Structure, Phase Transitions and Thermal, Dielectric, Vibrational and ^1H NMR Properties Over a Range of Temperatures

Keywords: Organic-inorganic hybrid composites / Materials / Ferroelasticity / Bismuth

Amongst the remarkably diverse range of structures that metallosupramolecular chemistry has generated, an important group is that of the neutral [2×2] metallogrids derived from diimine, dihydrazone and diacylhydrazone ligands. This type of neutral supramolecular inorganic architecture is, for the first time, characterized by MALDI-MS.
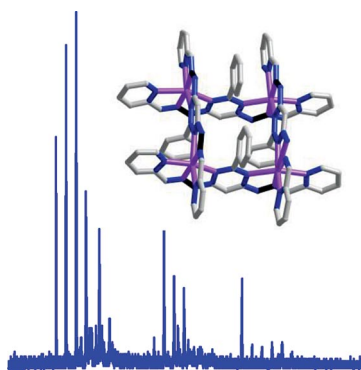
A. Même, A. R. Stefankiewicz, J. Harrowfield, X.-Y. Cao, J. Huuskonen, K. Rissanen, J.-M. Lehn, H. Nierengarten, E. Leize* .... 647−654

A Novel MALDI-MS Approach for the Analysis of Neutral Metallosupramolecular Architectures

Keywords: Supramolecular chemistry / Mass spectrometry / Noncovalent interactions / Metallogrids / Analytical methods

A family of Rh^I and Ir^I complexes based on an accepting pincer pyridine diphosphite ligand **1** has been prepared and characterized. IR studies indicate an exceedingly low ability of the metal pincer ligand fragment to back-donate. Structural characterization of complex [Rh(**1**)(C_2H_4)]-[BPh4] shows a remarkable in-plane conformation of the olefin ligand.
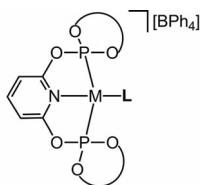
M = Rh, Ir
L = phosphanes, isonitriles, ethylene, CO

M. Rubio, A. Suárez, E. Vega, E. Álvarez, J. Díez, M. P. Gamasa,* A. Pizzano* .... 655−663

Synthesis and Structural Characterization of Pincer Pyridine Diphosphite Complexes of Rhodium and Iridium

Keywords: Hydrogenation / Rhodium / Iridium / Pincer ligands / Phosphites

CONTENTS

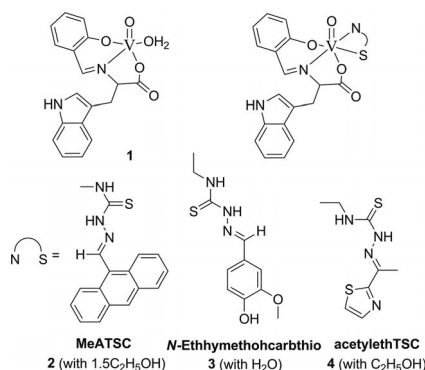## Mixed-Ligand Complexes

The synthesis, characterisation and preliminary in vitro studies of mixed-ligand vanadium(IV) complexes with a Schiff base and thiosemicarbazones are presented and discussed.

Redox Reaction Study

[Ru^{III}(hedtra)(pz)] (hedtra$^{3−}$ = N-hydroxyethylethylenediaminetriacetate; pz = pyrazine) can effectively be reduced to [Ru^{II}(hedtra)(pz)]$^{−}$ at λ_{max} = 462 nm by a biologically important reductant Red (Red = L-ascorbic acid, catechol and cysteine).

Organic-inorganic Hybrids

The organoimido derivatives NA−Mo6 and NA2−Mo6 were synthesized. LB films of covalently-linked NA−Mo6 and NA2−Mo6 and noncovalently-bonded parent hexamolybdate and neat naphthylamines were prepared and characterized. The charge transfer between the electron-donating naphthylimido and electron-accepting hexamolybdate was shown to be the cause of the luminescence quenching of the covalently-linked compound.

Electron Donors
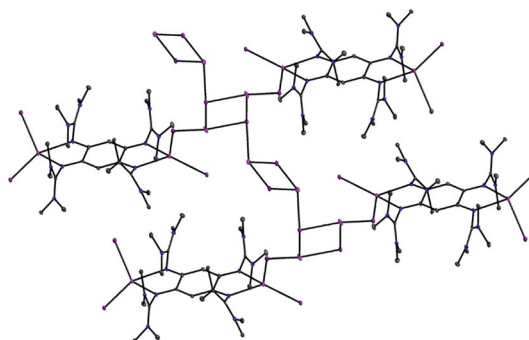
Competition between different reaction types is observed in the reaction between guanidine electron donors and silver halides. Several coordination polymers are among the products with silver halide clusters or chains connected to highly ordered arrays by guanidine spacers.

2D NLO Materials

A DFT Study on The Two-Dimensional Second-Order Nonlinear Optical (NLO) Response of Terpyridine-Substituted Hexamolybdates: Physical Insight on 2D Inorganic−Organic Hybrid Functional Materials
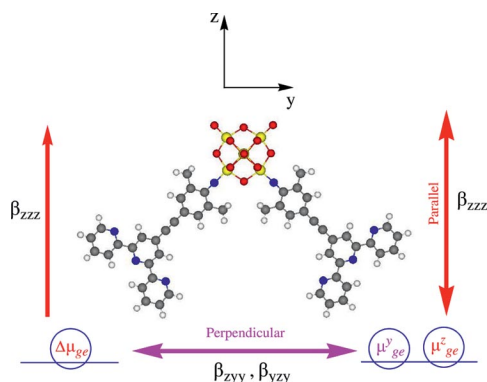
Two-dimensional second-order nonlinear optical layout in terpyridine-substituted hexamolybdates suggests that the 2D character of the charge transfer and the structure−property relationships that was revealed in this paper may provide guidelines for the rational design of further promising structures for potential applications in 2D nonlinear optics.

Keywords: Nonlinear optics / Polyoxometalates / Organic−inorganic hybrid composites / Charge transfer / Density functional calculations

Supramolecular Frameworks

The ligand (*S*)-2-(1,8-naphthalimido)propanoate (L_{ala}^-) forms a tetrameric zinc(II) complex, $[Zn_4(L_{ala})_6(OH)_2(MeOH)_4]$, in which strong $\pi\cdots\pi$ stacking interactions of the 1,8-naphthalimide groups organize the tetramers into a 3D, homochiral supramolecular framework supported exclusively by noncovalent forces. The ligand also forms the acentric dimeric cadmium(II) complex, $[Cd_2(L_{ala})_4(DMF)_3(MeOH)]$.
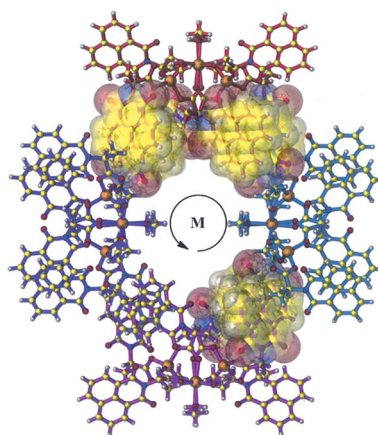
Homochiral, Supramolecular Frameworks Built from a Zinc(II) Tetramer or Cadmium(II) Dimer Containing Enantiopure Carboxylate Ligands Functionalized with a Strong $\pi\cdots\pi$ Stacking Synthon

Keywords: Homochiral structure / Carboxylate ligands / Metal−organic frameworks / Cadmium / Zinc

Coupling Reactions

C−H Bond Activation of Palladium Complexes That Feature Pendant Benzamidinate Ligands and Their Catalytic Behaviours
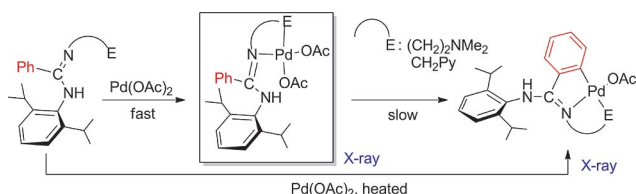
Herein we report on the blocking of the *ortho* position of the phenyl group on the nitrogen atom of the amidinate to obtain the chelate intermediate compound and then initiating the C−H activation in the *ortho* position of the phenyl group on the carbon atom of the amidinate.

Keywords: C−H Activation / Palladium / Chelates / Metalation / Benzamidinates

Superparamagnetic Nanoparticles

Superparamagnetic core-shell-type Fe_3O_4/Ru nanoparticles ($\approx$15 nm) catalyze the selective C=O hydrogenation of *trans*-4-phenyl-3-penten-2-one with 90% selectivity under mild conditions.
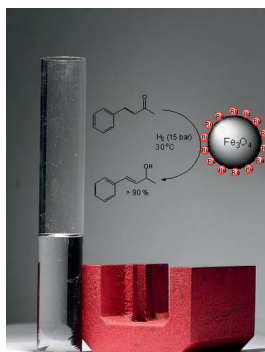
Superparamagnetic Core-Shell-Type Fe_3O_4/Ru Nanoparticles as Catalysts for the Selective Hydrogenation of an Unconstrained α,β-Unsaturated Ketone

Keywords: Nanoparticles / Ruthenium / Hydrogenation / Supported catalysts

CONTENTS
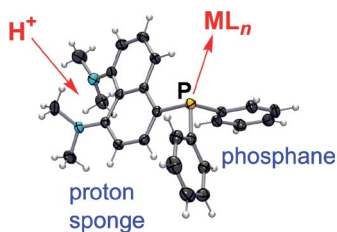
Functionalization of 1,8-bis(dimethylamino)naphthalene is better carried out at the 4- rather than the 2-position, to maximally separate the proton sponge and metal-coordinating groups and allow both to perform their roles without interference.
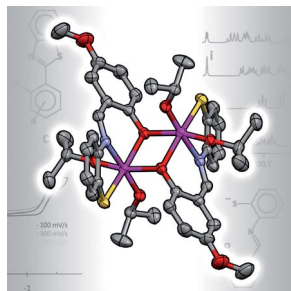
Redox-active Ti^{IV} complexes of 2-aminothiophenol−salicylaldehyde Schiff bases have been prepared and their electrochemical oxidations were assessed in view of the possible catalysis of alcohol oxidation. Five crystal structures were obtained, three of which are of solution-state products that crystallized in modified forms, which includes one example that underwent multiple redox changes.

---

* Author to whom correspondence should be addressed.

⌨ Supporting information on the WWW (see article for access details).

🔓 This article is available online free of charge (Open Access).

If not otherwise indicated in the article, papers in issue 3 were published online on January 16, 2012

SPOTLIGHTS …

On these pages, we feature a selection of the excellent work that has recently been published in our sister journals. If you are reading these pages on a computer, click on any of the items to read the full article. Otherwise please see the DOIs for easy online access through Wiley Online Library.

Biosensors

A. Duarte, M. Slutsky, G. Hanrahan,* C. M. Mello,* G. C. Bazan*

Supramolecular Electrostatic Nanoassemblies for Bacterial Forensics

Electrostatic nanoassemblies were employed to identify bacteria growth conditions. They comprise a cationic conjugated oligoelectrolyte and fluorescein-tagged ssDNA and were optimized with a hybrid, computational neural network model. The photoluminescence spectra contained the oligomer and sensitized fluorescein emission. The spectra changed depending on the growth history of the bacteria introduced (see figure).
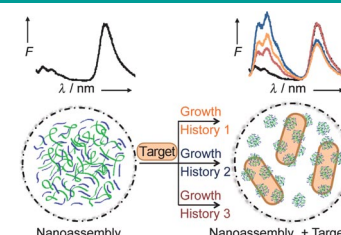
Chem. Eur. J.
DOI: **10.1002/chem.201103237**

Nanoporous Materials

H. L. Poh, M. Pumera*

Nanoporous Carbon Materials for Electrochemical Sensing

A great sense of achievement! The performance of nanoporous carbon as an electrode material was investigated and compared with that of bare glassy carbon, graphite microparticles, and carbon nanotubes. Nanoporous carbon was found to exhibit the highest heterogeneous electron transfer (HET) rate among these materials, thus sensing analytes such as NADH, DNA bases, and 2,4,6-trinitrotoluene (TNT) with an improved electrochemical response.
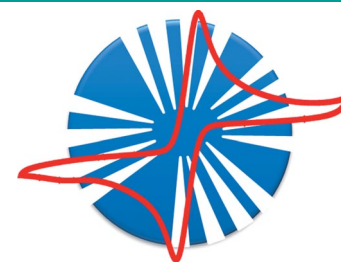
Chem. Asian J.
DOI: **10.1002/asia.201100681**
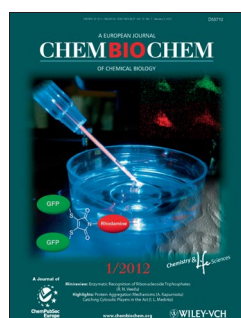
Haloalkane Dehalogenases

J. G. E. van Leeuwen, H. J. Wijma, R. J. Floor, J.-M. van der Laan, D. B. Janssen*

Directed Evolution Strategies for Enantiocomplementary Haloalkane Dehalogenases: From Chemical Waste to Enantiopure Building Blocks

Waste not, want not: A carefully optimized directed evolution strategy was used to obtain two enantiocomplementary haloalkane dehalogenase variants that convert the toxic waste compound 1,2,3-trichloropropane into either (R)- or (S)-2,3-dichloropropan-1-ol. The products can be converted into optically active epichlorohydrins that could be used for the preparation of various chiral pharmaceuticals.
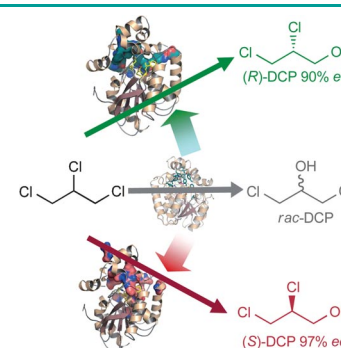
ChemBioChem
DOI: **10.1002/cbic.201100579**
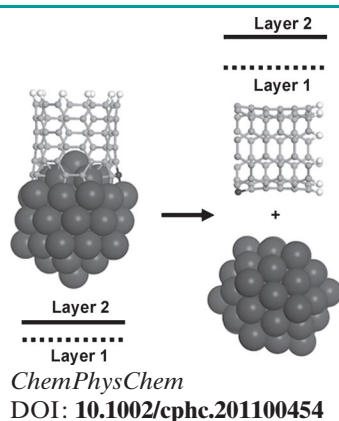
Carbon Nanotubes

J. P. O'Byrne, Z. Li, S. L. T. Jones, P. G. Fleming, J. A. Larsson, M. A. Morris, J. D. Holmes*

Nitrogen-Doped Carbon Nanotubes: Growth, Mechanism and Structure

Bamboo nanostructures: Nitrogen-doped bamboo-structured carbon nanotubes are successfully grown using a series of cobalt/molybdenum catalysts (see picture). The growth of bamboo-structured nanotubes in the presence of nitrogen, in preference to single-walled and multi-walled nanotubes, is due to the greater binding energy of nitrogen for cobalt in the catalyst compared to the binding strength of carbon to cobalt, as determined by density functional theory.

ChemPhysChem
DOI: **10.1002/cphc.201100454**
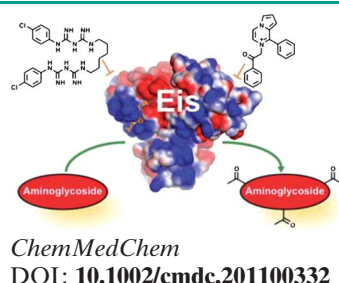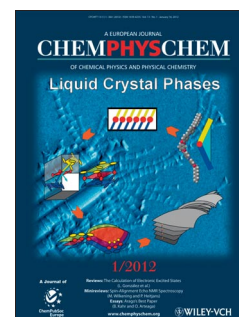
Drug resistance

K. D. Green, W. Chen, S. Garneau-Tsodikova*

Identification and Characterization of Inhibitors of the Aminoglycoside Resistance Acetyltransferase Eis from *Mycobacterium tuberculosis*

Stopping resistance in tuberculosis: The unusually regioversatile acetyltransferase Eis is a cause of resistance to kanamycin A in cases of tuberculosis. En route to new tuberculosis treatments, several inhibitors of the Eis enzyme were identified and characterized.

ChemMedChem
DOI: **10.1002/cmdc.201100332**
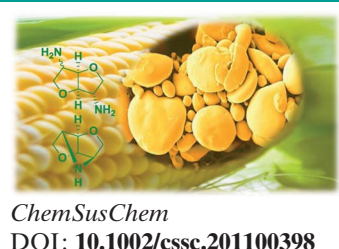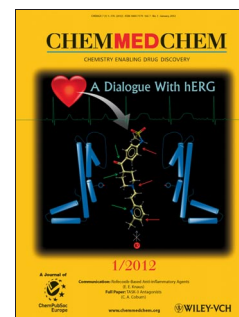
Renewable Resources

S. Thiyagarajan, L. Gootjes, W. Vogelzang, J. van Haveren, M. Lutz, D. S. van Es*

Renewable Rigid Diamines: Efficient, Stereospecific Synthesis of High Purity Isohexide Diamines

Turning up the stereo: An efficient three-step strategy for synthesizing chiral biobased dideoxy-diamino isoidide and dideoxy-diamino isosorbide in high yield with absolute stereo control is described. These highly interesting chiral building blocks are presently the subject of several investigations due to their application in high-performance biobased polymers such as polyamides and polyurethanes.

ChemSusChem
DOI: **10.1002/cssc.201100398**
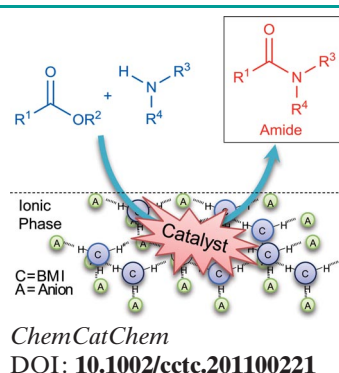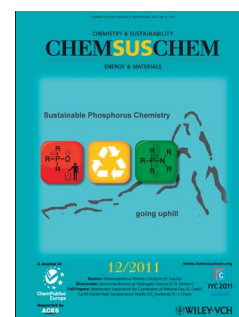
Ionic Liquids

V. M. de Oliveira, R. Silva de Jesus, A. F. Gomes, F. C. Gozzo, A. P. Umpierre, P. A. Z. Suarez, J. C. Rubim, B. A. D. Neto*

Catalytic Aminolysis (Amide Formation) from Esters and Carboxylic Acids: Mechanism, Enhanced Ionic Liquid Effect, and its Origin

Amides ride the ionic liquid cycles: A novel catalytic method to perform amide bond formation from esters and carboxylic acids in ionic liquids is described. Mechanistic studies and the ionic liquid effect are also investigated. Recycling reactions are performed successfully. NMR and electrospray ionization–quadrupole time-of-flight experiments allowed for the proposition of a catalytic cycle to explain the reaction with Brønsted acids, such as $SnCl_2$ and CdO.

ChemCatChem
DOI: **10.1002/cctc.201100221**
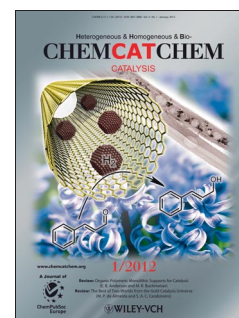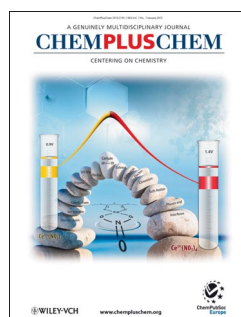
Nanoparticles

N. Ž. Knežević,* I. I. Slowing, V. S.-Y. Lin

Tuning the Release of Anticancer Drugs from Magnetic Iron Oxide/Mesoporous Silica Core/Shell Nanoparticles

A series of core/shell magnetic mesoporous silica nanoparticle (MMSN) materials were prepared comprised of iron oxide nanoparticle cores embedded in mesoporous silica shells having radial or hexagonal porous structures. The loading and release of anticancer drugs, 9-aminoacridine (9AA) and camptothecin (CPT), as well as cytotoxic activity of drug loaded materials, is influenced by the presence of phenylethyl functionalization inside the MMSN mesopores (see figure). An externally applied magnetic field accelerates the drug release from the materials.core/shell structuresdrug deliverymagnetic materialsmesoporous silicananoparticles
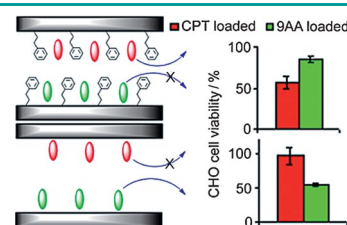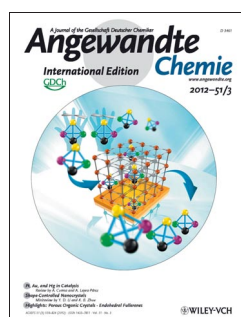
Metal Catalysis

A. Leyva-Pérez, A. Corma*

Similarities and Differences between the "Relativistic" Triad Gold, Platinum, and Mercury in Catalysis

Relatively related: Relativistic effects in the valence shell of the chemical elements reach a maximum in the triad Pt–Au–Hg and influence their catalytic activity in organic reactions. The catalytic activity for some representative reactions is examined together with other relevant properties, such as toxicity, price, and availability. For the reactions considered, gold is generally preferred to mercury or platinum catalysts.
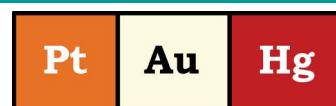
Lactam Formation

K. ó Proinsias, S. Kurcoń, D. Gryko*

Hydrophobic Vitamin B$_{12}$ Derivatives: Unprecedented Formation of a 7-Membered Lactam

Synthesis of a seven-membered lactam–cobalamin derivative was achieved through intramolecular acidic aminolysis of heptamethyl dicyanocobyrinate with the NH$_2$ group at the C10 position. Subsequent ring opening gave new C8,C10-diamides.
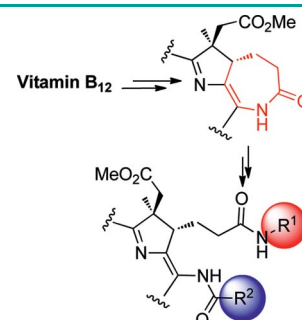
Green Carbon Dioxide – Interview with A. Quadrelli and G. Centi

Vera Köster

Green Carbon Dioxide – Interview with A. Quadrelli and G. Centi

Alessandra Quadrelli and Gabriele Centi guest edited the ChemSusChem special issue on Green Carbon Dioxide which focuses on emerging technologies for large-volume CO$_2$ recycling. They talk about how the perception of CO$_2$ has changed, the special issue, and the future of CO$_2$ recycling.

Synthesis and Reactivity of Square-Planar Pt^{II}–η^1-Hydrocarbyl Complexes Containing *cis*-Coordinated Olefin or Alkyne

Maria Elena Cucciolito[a] and Francesco Ruffo*[a]

Dedicated to Professor Augusto de Renzi on the occasion of his retirement

The review provides a survey of the key classes of Pt^{II} complexes containing *cis*-{Pt(η^1-hydrocarbyl)(η^2-unsaturated ligand)} moieties, which have been isolated or at least unequivocally characterized in solution. These compounds, which mimic reactive intermediates of fundamental catalytic processes, have been classified in four general types, which display a *cis* arrangement of an alkyl group and a monoalkene (**I**), an aryl group and a monoalkene (**II**), an alkyl group and a monoalkyne (**III**), and an aryl group and a monoalkyne (**IV**). A discussion of their main structural and chemical features, disclosing the factors affecting their reactivity, dynamic behavior, and relative stability, is presented. In some remarkable cases (**III** and **IV**), it is the *cis* arrangement of the hydrocarbyl fragments that promotes unusual reactivity.

Introduction

The presence of a hydrocarbyl group and an unsaturated ligand at the *cis* positions of a metal center (Figure 1) is a fundamental requisite for the insertion process to occur.

This reaction is a fundamental step of several catalytic processes,[1] most of them promoted by d^8 square-planar complexes of metals such as Pd^{II} or Rh^I. An arrangement of type **I** is especially invoked in the oligomerization and

[a] Dipartimento di Chimica "Paolo Corradini", Università di Napoli "Federico II",
Complesso Universitario di Monte S. Angelo, Via Cintia, 80126 Napoli, Italy
Fax: +39-081674090
E-mail: ruffo@unina.it
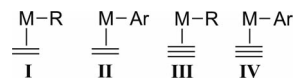
Figure 1. Arrangements of an unsaturated ligand and a hydrocarbyl group (R = alkyl, Ar = aryl) at the *cis* positions with respect to a metal center.

polymerization of alkenes.[2] An olefin and an aryl ring at the *cis* position, as in **II**, are postulated in the mechanism of the key Heck reaction,[3] and, although less common, also the remaining two moieties are relevant to catalysis.[4] However, with these metal ions, the opportunity to either isolate or detect complexes of type **I**–**IV** is quite rare, because the insertion is usually fast, and their intervention in the reaction mechanism is often only hypothesized. On the

Maria Elena Cucciolito graduated in Industrial Chemistry from the University of Napoli "Federico II" in 1987 and received her PhD in 1992 with Prof. Achille Panunzi. The activity of Dr. Cucciolito is mainly in the field of organometallic chemistry, with particular interest towards the following subfields: (1) five-coordinate olefin complexes of Pt^{II} and Pd^{II}, (2) reactivity and stereochemistry of allylic complexes of Pt^{II} and Pd^{II}, (3) reactivity of alkenes coordinated to highly electrophilic dicationic complexes of Pt^{II} and Pd^{II}.

Francesco Ruffo graduated in Industrial Chemistry from the University of Napoli "Federico II" in 1990 and received his PhD in 1994 with Prof. Achille Panunzi. He was guest at the KTH of Stockholm under the supervision of Prof. B. Åkermark (July 1992 and May–September 1997) and at the University of Göttingen (May–September 1993) under the supervision of Prof. Armin de Meijere. The activity of Prof. Ruffo is mainly in the field of organometallic chemistry, with particular interest towards the following subfields: (1) Pt and Pd complexes in low oxidation states, (2) asymmetric catalysis promoted by metal complexes containing chiral ligands derived from carbohydrates, (3) study of cationic hydrocarbyl/olefin complexes of Pt^{II} and Pd^{II}.

contrary, the corresponding Pt^{II} derivatives stand out for their superior stability and consequently lend themselves to be isolated or, at least, spectroscopically observed in non-prohibitive conditions.

These complementary behaviors offer a comprehensive scenario, for example because Pd^{II} species can be preferred for synthetic purposes, while the more versatile Pt^{II} derivatives allow a better comprehension of bonding properties and give insight into mechanistic details.

In this context, meticulous studies have been conducted in recent years to understand the behavior of stable Pt^{II} complexes containing these structural motifs. In particular, complexes containing all four possible combinations of ligands, as shown in Figure 2, have been prepared and characterized.
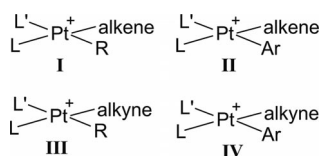
Figure 2. General formula of square-planar complexes containing an η^2-monoalkene or an η^2-monoalkyne at the *cis* position relative to an η^1-hydrocarbyl group.

As discussed in detail in the following paragraphs, this investigation allowed (1) to rationalize the steric factors that govern the intramolecular stability, (2) to elucidate the essential dynamic phenomena that involve the complexes, and (3) to disclose unprecedented reactivity, thus revealing that the overall features of the complexes are strongly dependent on the properties of the interfering hydrocarbyl ligands.

Square-Planar Pt^{II} Complexes Containing a *cis* Arrangement of an Alkyl Group and an Alkene (I)

The Pt^{II} complexes of type **I** prepared so far are reported in Tables 1, 2, 3, and 4 along with references for their synthesis and spectroscopic or structural characterization.

Table 1 lists all the cationic complexes of general formula [PtR(η^2-alkene)(L,L′-chelate)]$^+$ (L and L′ = As, N, or P), while related neutral compounds [PtR(η^2-alkene)(N,N′-chelate)] are presented in Table 2. Table 3 reports cationic cyclometallated species [Pt(N,N′,C)(η^2-alkene)]$^+$, and Table 4 completes the scenario with compounds containing solely monodentate ligands.

It is important to note that some classes were prepared with the express purpose of studying the properties of the hydrocarbyl groups, and, hence they were fundamental for clarifying the structure, general behavior and reactivity of compounds of type **I**. Some of the complexes were instead prepared as part of works focused on other aspects of related research, and, they were therefore only characterized to establish their identity.

Table 1. Cationic complexes of type **I** and their references.
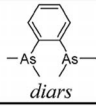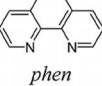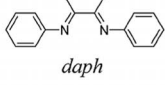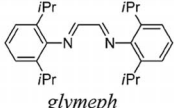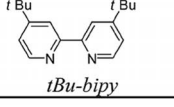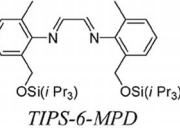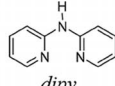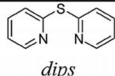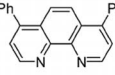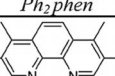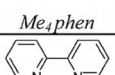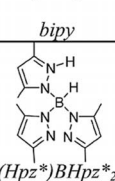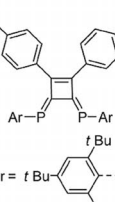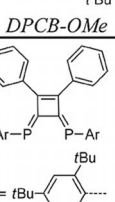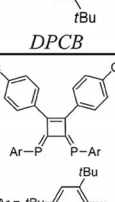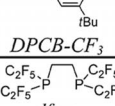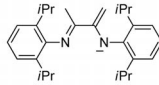
L,L′[a]	R	Alkene groups of the complexes	Refs.
diars	Me	CH$_2$=CH$_2$ (**I-1**)[b] CH$_2$=CHMe (**I-2**)[b]	[5]
phen	Me	*E*-PhCH=CHPh (**I-3**) CH$_2$=CHMe (**I-4**) CH$_2$=CHPh (**I-5**) CH$_2$=CH$_2$ (**I-6**) *E*-MeO$_2$CCH=CHCO$_2$Me (**I-7**) CH$_2$=CHCH$_2$OH (**I-8**)	[8] [8] [8] [8] [8] [8]
	Et	CH$_2$=CHMe (**I-9**) CH$_2$=CHPh (**I-10**) CH$_2$=CH$_2$ (**I-11**) *E*-MeO$_2$CCH=CHCO$_2$Me (**I-12**)	[8] [8] [8] [8]
daph	Me	*E*-PhCH=CHPh (**I-13**) CH$_2$=CHMe (**I-14**) CH$_2$=CHPh (**I-15**) CH$_2$=CH$_2$ (**I-16**)	[8] [8,10] [8] [8]
dameph	Me	CH$_2$=CHMe (**I-17**) C$_6$H$_6$ (**I-18**)[c,d]	[10] [20]
daethyph	Me	CH$_2$=CH$_2$ (**I-19**) CH$_2$=CHMe (**I-20**) CH$_2$=CHCO$_2$Me (**I-21**)	[8,10] [10] [9,10]
daproph	Me	CH$_2$=CHMe (**I-22**) CH$_2$=CH(4-MeOC$_6$H$_4$) (**I-23**) CH$_2$=CHPh (**I-24**) CH$_2$=CH(4-CF$_3$C$_6$H$_4$) (**I-25**) CH$_2$=CH$_2$ (**I-26**) CH$_2$=CHCH$_2$OH (**I-27**) CH$_2$=CHCOMe (**I-28**) CH$_2$=CHCO$_2$Me (**I-29**) CH$_2$=CHCHO (**I-30**) CH$_2$=CHC(O)NMe$_2$ (**I-31**)	[8,10] [11] [8,11] [11] [8] [8] [9] [9,10] [9] [9]
glymeph	Me	CH$_2$=CHMe (**I-32**)	[10]
tBu-bipy	Me	CH$_2$=CH$_2$ (**I-33**)[c,e]	[16]
(tBu... MeO/OMe ligand)	Me	CH$_2$=CH$_2$ (**I-34**)[f] CH$_2$=CHCN (**I-35**)[f]	[17] [17]
TIPS-6-MPD	Me	CH$_2$=CH$_2$ (**I-36**)	[18]
(acenaphthylene diimine)	Et	CH$_2$=CH$_2$ (**I-37**)	[19]

Table 1. *(Continued)*

L,L'[a]	R	Alkene groups of the complexes	Refs.
dipy	Me	CH$_2$=CH$_2$ (**I-38**)[g]	[12]
dips	Me	CH$_2$=CH$_2$ (**I-39**)[g]	[12]
Ph$_2$phen	Me	CH$_2$=CH$_2$ (**I-40**)[g,h]	[12]
Me$_4$phen	Me	CH$_2$=CH$_2$ (**I-41**)[g]	[12]
bipy	Me	CH$_2$=CH$_2$ (**I-42**)[g]	[12]
(Hpz*)BHpz*$_2$	Me	CH$_2$=CH$_2$ (**I-43**)[i]	[21]
DPCB-OMe	Me	CH$_2$=CH$_2$ (**I-44**)[h]	[22]
DPCB	Me	CH$_2$=CH$_2$ (**I-45**)[h]	[22]
DPCB-CF$_3$	Me	CH$_2$=CH$_2$ (**I-46**)[h]	[22]
dfepe	Me	CH$_2$=CH$_2$ (**I-47**)[d,i]	[23]
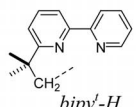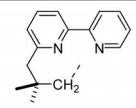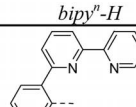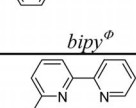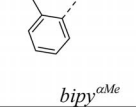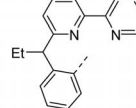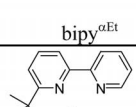
[a] The name of the ligand is given if found in the original papers. [b] The counterion is PF$_6^-$. [c] The counterion is B(OH)(C$_6$F$_5$)$_3^-$. [d] Not isolated. [e] The counterion is BMe(C$_6$F$_5$)$_3^-$. [f] Also with BMe(C$_6$F$_5$)$_3^-$ as counterion. [g] The counterion is BArF. [h] The counterion is TfO$^-$. [i] The counterion is B(C$_6$F$_5$)$_4^-$.

Table 2. Neutral complexes of type **I** and their references.

N,N'[a]	R	Alkene groups of the complexes	Refs.
depran	Me	CH$_2$=CHMe (**I-48**) CH$_2$=CHPh (**I-49**) CH$_2$=CH$_2$ (**I-50**) CH$_2$=CHCH$_2$OH (**I-51**) CH$_2$=CHCOMe (**I-52**) CH$_2$=CHCO$_2$Me (**I-53**)	[24]

[a] The name of the ligand is that given in the original paper.

Table 3. Cationic cyclometalated complexes of type **I** and their references.

L,L,R'[a]	Alkene groups of the complexes	Refs.
bipy^i-H	CH$_2$=CH$_2$ (**I-54**)[b,c,d]	[12]
bipy^n-H	CH$_2$=CH$_2$ (**I-55**)[c]	[12]
bipy^Φ	CH$_2$=CH$_2$ (**I-56**)[c]	[12]
bipy^{αMe}	CH$_2$=CH$_2$ (**I-57**)[c]	[12]
bipy^{αEt}	CH$_2$=CH$_2$ (**I-58**)[b,c]	[12]
bipy^c	CH$_2$=CH$_2$ (**I-59**)[c]	[12]

[a] The name of the ligands is that given in the original paper. [b] The counterion is TfO$^-$. [c] The counterion is BArF. [d] The counterion is PF$_6^-$.

The first reported complexes of type **I** are **I-1** and **I-2**, prepared by Clark in 1974[5] (Scheme 1), who observed that the coordinated alkene is more labile than those in related *trans*-compounds.

Table 4. Other complexes of type **I** and their references.

(**I-60**)   (**I-61**)   Ref.[6]

(**I-62**)   Ref.[6]

(**I-63**)   (**I-64**)   Ref.[6]

(**I-65**)   (**I-66**)   (**I-67**)[a]   Ref.[7]

[a] Not isolated.
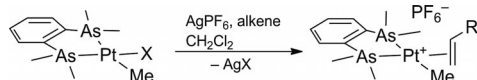
Scheme 1. Synthesis of complexes **I-1** and **I-2** (R: H or Me).

Later, dimer **I-60** and some studies on its reactivity were described by Puddephatt.[6] The complex, which was obtained by reacting Zeise's dimer with [Pt$_2$Me$_4$(SMe$_2$)$_2$] (Scheme 2), represents an important starting compound for the synthesis of methyl/ethylene–Pt^{II} species.
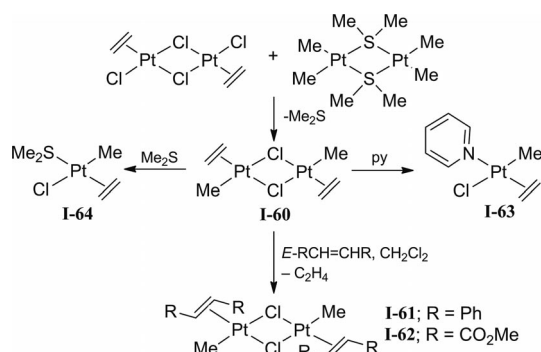
Scheme 2. Synthesis and some chemistry of complexes **I-60**.

Complex **I-65** and its derivatives **I-66** and **I-67** are related examples of type **I** species with monodentate ligands.[7] Dimer **I-65** was prepared by treating an aqueous solution of K$_2$PtCl$_4$ under ethylene pressure. Treatment of the complex with propene affords the corresponding **I-66** species, while splitting of the bridge (compound **I-67**) was observed in the presence of chloride ions (Scheme 3).

A wide class of complexes (from **I-3** to **I-32**, with exception of **I-18**) of general formula [PtR(η^2-alkene)(N,N-chelate)]$^+$ was prepared according to two procedures.[8–11]
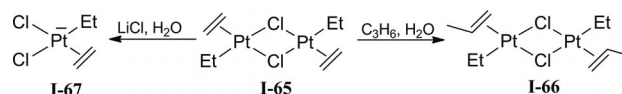
Scheme 3. Structure of complexes **I-65**, **I-66**, and **I-67**.

The first one (Scheme 4) involved oxidative addition of R$_3$OBF$_4$ (R = Me, Et) to the three-coordinate precursor [Pt(1,10-phenanthroline)(η^2-dimethyl fumarate),] which afforded the corresponding cationic complexes [PtR(1,10-phenanthroline)(η^2-dimethyl fumarate)]BF$_4$ (**I-7** and **I-12**).
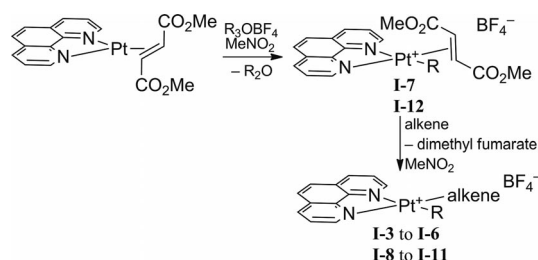
Scheme 4. Synthesis of complexes from **I-3** to **I-12** (R = Me, Et).

These species, which represent rare examples of four-co-ordinate Pt^{II} complexes bearing electron-poor alkenes, were either isolated in the solid state or transformed into other complexes of type **I** by olefin exchange.

The second procedure was carried out by substituting a halide (X = Cl or I) in the presence of a silver salt, on precursors of general formula [PtMe(X)(N,N-chelate)] (Scheme 5).
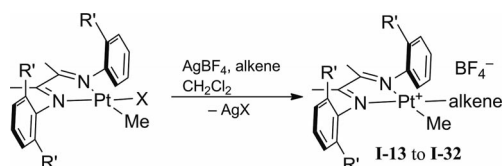
Scheme 5. Alternative synthesis of complexes of type **I** (from **I-13** to **I-32**; R′ = H, Me, Et, iPr; one R′ substituent has been omitted for the sake of clarity).

In a first study,[8] a thorough investigation was carried out on compounds containing electron-rich alkenes (trans-2-butene, propene, ethylene, styrene, allylic alcohol).

As revealed by both crystal structures of representative complexes and NMR spectroscopic shifts, the aryl rings of the diacetylarylimino ligands are oriented perpendicular to the coordination plane, projecting their R′ substituents above and below the square plane (as depicted in Scheme 5). Therefore, the N,N-chelates were selected in a way aiming to gradually increase the steric hindrance above and below the coordination plane, according to the following order: phen ≈ daph < dameph < daethyph < daproph.

Remarkably, it was observed that the dynamic phenomena involving the unsaturated ligand, that is, both rotation and exchange with free alkene, are strongly affected by this steric attribute. The following points are particularly important:

(1) Olefin rotation and exchange are fast (on the NMR time scale) with poorly demanding nitrogen chelates (*phen* and *daph*).

(2) As the steric hindrance increases (*dameph*, *daethyph*, or *daproph*), the exchange becomes strongly inhibited even at 328 K. This evidence validates the hypothesis of an associative mechanism for the process.

(3) With *dameph*, *daethyph*, and *daproph*, rotation of substituted alkenes is inhibited by steric contacts between the olefin substituents R′′ and the R′ groups on the aryl rings. As a consequence, only one stereoisomer was observed in the case of α-olefins in the temperature range 203–328 K (actually only one couple of enantiomers), namely **I^I** of Figure 3, in which the steric contacts are minimized by orienting the alkene substituent R′′ toward the Pt–Me bond.
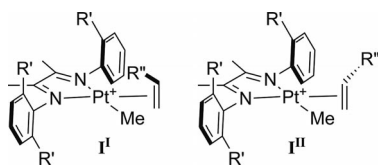
Figure 3. Possible isomers of complexes of type **I** with α-olefins (one R′ substituent has been omitted for the sake of clarity).

These qualitative studies were recently[12] confirmed and implemented by preparing other complexes of the same general type (**I-38** to **I-42**), along with related cyclometalated platinum(II) species (**I-54** to **I-59**). These compounds were analogously synthesized by substituting the halides of neutral [PtCl(*N*,*N*′,*C*)] precursors with ethylene in the presence of a silver or sodium salt. Studies on ethylene exchange by 1H NMR spectroscopic line-broadening experiments in deuterated chloroform evidenced that the mechanism takes place through an associative attack by the entering olefin, which proceeds via a trigonal bipyramidal transition state with the two ethylene molecules on the trigonal plane. The activation process is largely entropy-controlled, with activation entropies ranging between –129 and –112 J K⁻¹ mol⁻¹, as expected for associative processes.

The possibility to slow down the dynamic phenomena by using the axially hindered chelate *daproph* suggested an extension of the study[9] to the synthesis of square-planar complexes containing electron-poor alkenes, such as acrolein, methyl vinyl ketone, methyl acrylate, or *N*,*N*-dimethylacrylamide (**I-21** and from **I-28** to **I-31**). In fact, the rare examples described by previous literature were typically involved in fast dynamic processes, which prevented any accurate spectroscopic or diffractometric characterization.

As expected, the complexes were revealed to be highly inert in solution, which allowed their thorough spectroscopic characterization. For instance, coupling constants of olefin protons and carbon atoms to 195Pt nuclei were measured for the first time for electron-poor alkenes in a square-planar environment. Furthermore, the structure of **I-21** was determined by X-ray diffraction.

Unlike those with electron-rich olefins, methyl acrylate complex **I-29** was involved in a rare process of olefin insertion into a Pt–alkyl bond (path i in Scheme 6), hitherto de-

scribed only in the case of the strongly activated olefin tetrafluoroethylene.[13] The overall process leads to a 6-membered cyclometallated product **1** (Scheme 6), and all the alkyl intermediates were observed by monitoring its NMR spectrum at 333 K.
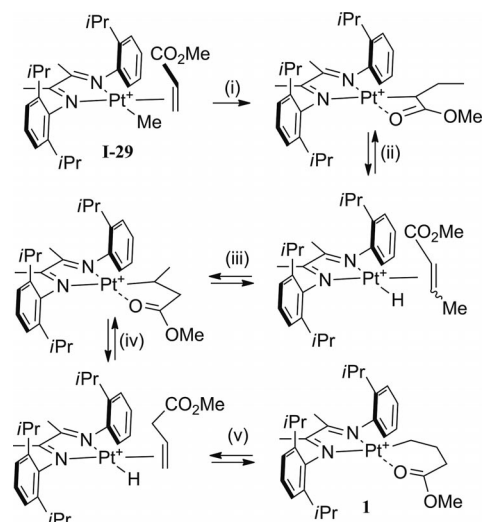
Scheme 6. The sequential insertion process leading to the cyclometallated product **1** (one *i*Pr substituent has been omitted for the sake of clarity).

Within these studies it was also possible to isolate a peculiar cationic trinuclear Pt-µ-Ag-µ-Pt species (compound **2** in Figure 4).[14]
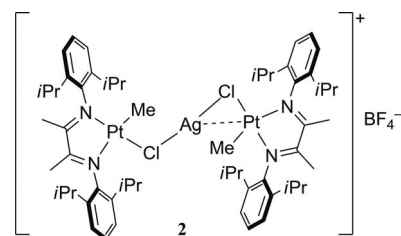
Figure 4. Trinuclear cationic Pt,Ag,Pt species **2**.

This stable molecule was isolated during the synthesis described in Scheme 5, by treating the reaction mixture prior to the precipitation of silver chloride.

It is likely that the stability of such a compound is due to the presence of the bulky *i*Pr substituents above and below the plane of coordination. In fact, the exchange of ligand, which is promoted by the silver salt, realistically involves a first Pt–Cl···Ag interaction followed by the association of the olefin with formation of the Pt–olefin bond and precipitation of AgCl. This second step is reasonably inhibited by the steric properties of the ligand to the point of allowing the isolation of the polynuclear species. This hypothesis was also corroborated by a kinetic study, which demonstrated the role of **2** as an intermediate of the reaction.

Later NMR spectroscopic studies[10] on some complexes of formula [PtMe(η²-alkene)(*N*,*N*-chelate)]BF₄ (**I-14**, **I-17**, **I-19**, **I-20**, **I-21**, **I-22**, **I-29**, and **I-32**) were aimed to assess

the relative positions of the cation and the anion in dichloromethane. This investigation was carried out by detecting specific interionic dipolar interactions in the $^{19}F\{^1H\}$-HOESY NMR spectra. It was demonstrated that the accessibility of the BF_4^- ion to the metal center was reduced as the bulkiness of the R′ substituents on the aryl rings increased. Thus, with *daph* or *dameph*, the BF_4^- ion was found to interact with several portions of the cationic complex, giving proof for an easy access to the metal center. Instead, both *daethyph* and *daproph* inhibit this approach and force the counterion to be located above or below the backside of the diimine. This finding is in-keeping with the high activity of the corresponding Pd polymerization catalysts,[15] which is reasonably enhanced by the fact that the positive charge on the metal center is not mitigated by any effective interaction with the anion.

A following study[11] gave further insight on the intimate relationship between cation and anion, revealing the existence of two equilibrating ion-pairs in the presence of styrenes as olefins (**I-23** to **I-25**). The two pairs differ because the BF_4^- anion can be above (pseudo-*cis*, **PC**) or below (pseudo-*trans*, **PT**) the coordination plane (Figure 5).
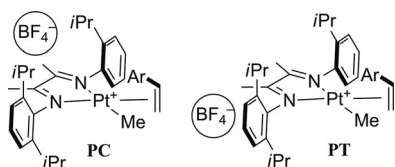
Figure 5. The equilibrating ion-pairs for **I-23** to **I-25** (Ar = Ph, 4-Me–C$_6$H$_4$, or 4-CF$_3$–C$_6$H$_4$; one *i*Pr substituent has been omitted for the sake of clarity).

The equilibrium constants were determined by a quantitative detection of H···F interionic dipolar interactions in the $^{19}F\{^1H\}$-HOESY NMR spectra. The results, corroborated also by theoretical calculations, suggest that the relative thermodynamic stabilities of the **PC** relative to the **PT** ion pairs originate from an interaction between the anion and a partial positive charge accumulated on the olefin ligand.

In another study,[16] an alternative synthesis of the related species **I-33** was proposed. The procedure involves abstraction of a Pt-bound methyl group by the Lewis acid B(C$_6$F$_5$)$_3$ in the presence of ethylene in an inert atmosphere (Scheme 7). Remarkably, if water was admitted in the reaction mixture, the counterion was B(OH)(C$_6$F$_5$)$_3^-$ instead.
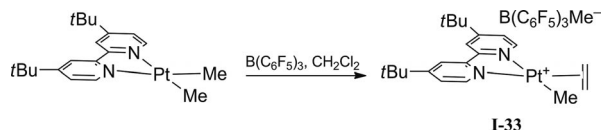
Scheme 7. The alternative synthesis of type **I** species proposed for **I-33**.

Unsymmetrical *N,N*-chelates were used to isolate ethylene and acrylonitrile complexes **I-34** to **I-36**, by using a procedure analogous to that reported in Scheme 5.[17,18] Alternatively, the same complexes were obtained by reacting the dimethyl precursor with B(C$_6$F$_5$)$_3$, giving rise to B(C$_6$F$_5$)$_3$-

Me$^-$ as counterion (as in Scheme 7). In these cases, another equilibrium was found in solution, which involved *syn/anti* isomerization of the bidentate ligand (Scheme 8).
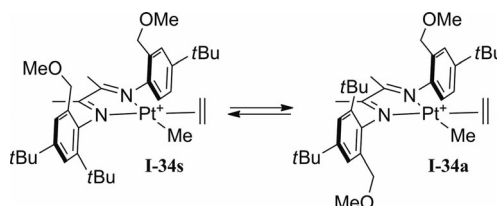
Scheme 8. The equilibrating *syn/anti* isomers of complex **I-34** (one *t*Bu substituent has been omitted for the sake of clarity).

Recently,[19] complex **I-37** was isolated as the stable resting state of a catalytic dimerization of ethylene promoted by platinum(II) (Scheme 9).
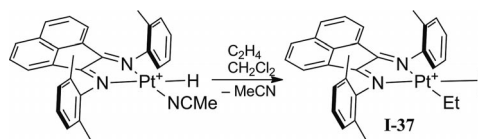
Scheme 9. Synthesis of complex **I-37**.

Remarkably, at 373 K and under ethylene pressure, **I-37** underwent insertion of the alkene into the Pt–ethyl bond to afford the corresponding butyl intermediate through a first-order process. The barrier of activation (29.6 kcal mol^{-1}) was found to be by far superior to that measured for the corresponding Pd (17–18 kcal mol^{-1}) or Ni (13–14 kcal mol^{-1}) complexes.

Within an exhaustive mechanistic study on C–H activation by "naked" platinum(II) complexes,[20] the remarkably elusive η^2-benzene adduct **I-18** was observed at 204 K by NMR spectroscopy. The compound was obtained by reacting the mixed phenyl/methyl precursor with HOTf (Scheme 10), and its structure was unequivocally assigned on the basis of the spectral pattern.
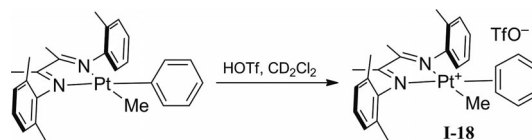
Scheme 10. Synthesis of complex **I-18** (one Me substituent has been omitted for the sake of clarity).

On raising the temperature to 233 K, formation of methane and benzene was observed, accompanied by the corresponding methyl/ and phenyl/triflate Pt^{II} compounds.

The cationic Pt^{II} complex **I-43** was synthesized by protonation of Tp′PtMe$_2$H with [H(OEt$_2$)$_2$][B(C$_6$F$_5$)$_4$], in the presence of ethylene (Scheme 11).[21] During this reaction, protonation of one pyrazole nitrogen atom occurs with concomitant generation of an open coordination site. This favors reductive elimination of methane and enables access to the incoming unsaturated ligand.
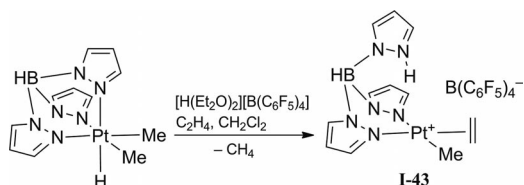
Scheme 11. Synthesis of **I-43**.

Deprotonation with a base allows the pyrazole atom to coordinate, giving rise to a five-coordinate trigonal bipyramidal compound.

Complexes **I-44** to **I-46**, containing diphosphanylidene-cyclobutene ligands, were obtained by adding ethylene to a neutral triflate precursor (Scheme 12).[22]
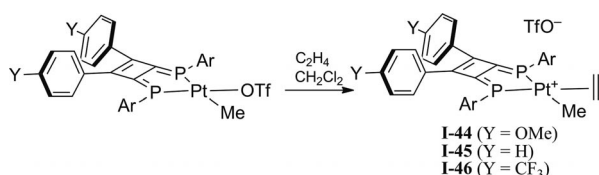
Scheme 12. Synthesis of complexes **I-44** to **I-46**.

The increasing electron-withdrawing properties of the Y substituents on the *P,P′*-ligands were correlated with a progressive augmentation of the NMR spectroscopic coordination chemical shifts of ethylene.

Treatment of complexes **I-22**, **I-24**, and **I-26** to **I-29** with KOH removes one proton from the ligand backbone, thus generating the corresponding neutral species **I** containing the anionic imino–amide ligand *depran* **I-48** to **I-53** (Scheme 13).[24]
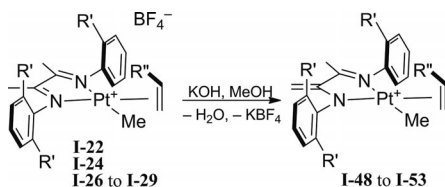
Scheme 13. Synthesis of complexes **I-48** to **I-53** (one R′ substituent has been omitted for the sake of clarity).

The NMR spectroscopic characterization disclosed high selectivity of coordination. In fact, although α-olefins can afford up to four isomers (Figure 6, each as an enantiomeric couple), only **I^I** was detected in solution. In this isomer, the alkene is *trans* to the N-amido group, and the olefin substituent R′′ is oriented towards the Pt–Me vector.
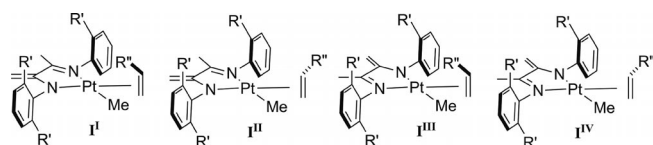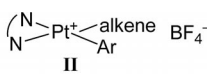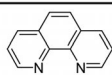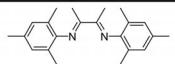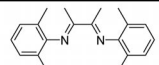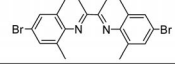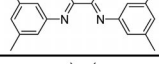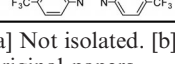
Figure 6. The four possible isomers for complexes **I-48** to **I-53** (one R′ substituent has been omitted for the sake of clarity).

It should be noted that the olefin carbon atoms undergo a significant shift of coordination at high fields (e.g., $\Delta\delta = 66$ for ethylene), whose extent is unusual for square-planar complexes of Pt^{II}. This spectral evidence suggested the presence of an unprecedented contribution of π-backbonding in the Pt–olefin interaction. A theoretical investigation showed that this contribution derives from the presence of the amide ligand, which dramatically increases the energy level of the metal orbital responsible for the back-donation, thus favoring the overlap with the olefin counterpart.

Square-Planar Pt^{II} Complexes Containing a *cis* Arrangement of an Aryl Group and an Alkene (II)

The Pt^{II} complexes of type **II** are reported in Tables 5, 6, and 7, along with references for their synthesis and spectroscopic or structural characterization.

Table 5. Cationic complexes of type **II**[a] and their references.

N,N′[b]	Ar	Alkene groups of the complexes	Refs.
phen	Ph Ph	CH$_2$=CHMe (**II-1**) CH$_2$=CH$_2$ (**II-2**)	[25] [25]
	Ph	C$_6$H$_6$ (**II-3**)	[28]
	Ph	C$_6$H$_6$ (**II-4**)	[28]
	Ph	C$_6$H$_6$ (**II-5**)	[28]
	Ph	C$_6$H$_6$ (**II-6**)	[28]
	Ph	C$_6$H$_6$ (**II-7**)	[28]

[a] Not isolated. [b] The name of the ligand is given if found in the original papers.

Table 6. Cationic cyclometalated complexes of type **II** and their references.
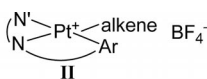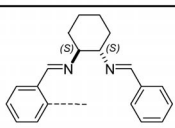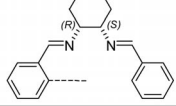
N,N′,Ar[a]	Alkene groups of the complexes	Refs.
(S),(S)	CH$_2$=CH$_2$ (**II-8**) CH$_2$=CHMe (**II-9**) CH$_2$=CHPh (**II-10**) CH$_2$=CH(4-Me-C$_6$H$_4$) (**II-11**)	[29]
(R),(S)	CH$_2$=CH$_2$ (**II-12**) CH$_2$=CHMe (**II-13**) CH$_2$=CHPh (**II-14**) CH$_2$=CH(4-Me-C$_6$H$_4$) (**II-15**)	[29]

Table 7. Other complexes of type **II**[a] and their references.

(II-16)   **(II-17)**   Ref.[27]

(II-18)   **(II-19)**   Ref.[27]
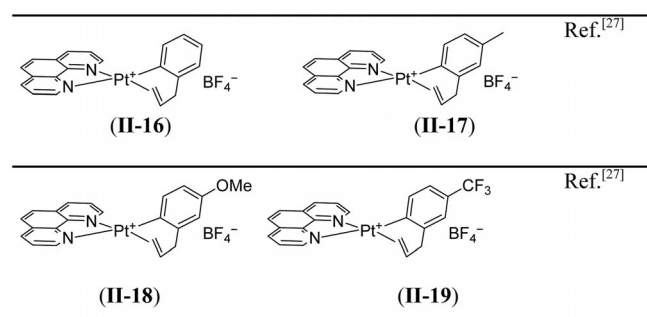
[a] Not isolated.

It should be noted that an aryl group *cis* to an alkene is by far more reactive than an alkyl fragment, and the possibility to isolate stable complexes is generally limited to particular, well-designed conditions (see below). Therefore, even the opportunity to detect simple species containing this definite requisite is particularly relevant, and it was successfully pursued in a study[25] aiming to clarify the peculiar evolution of this structural motif.[26] When complex [PtI(Ph)(phen)] was treated with AgBF$_4$ in deuterionitromethane in the presence of ethylene or propene, immediate precipitation of AgI ensued (Scheme 14). The NMR spectrum of the filtered solution revealed the presence of the sole species **II-1** or **II-2**. The signals of the coordinated alkenes were found at the expected positions, and, although not studied in detail, the dynamic behavior was in line with that of the corresponding methyl complexes **I-4** and **I-6**.
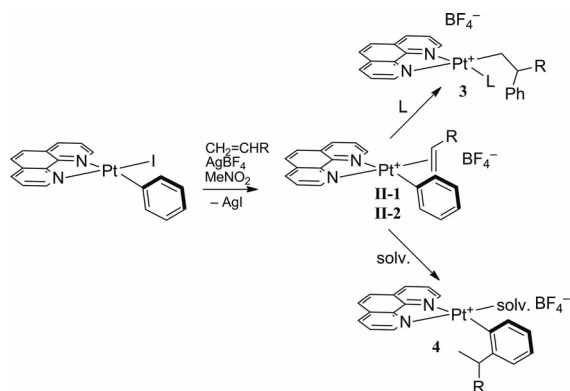
Scheme 14. Synthesis and reactivity of **II-1** (R = H) and **II-2** (R = Me).

The evolution of these elusive compounds, **II-1** and **II-2**, depended on whether a coordinating molecule L (such as the free alkene, acetonitrile, or pyridine) was present in solution.

In the first case, it was possible to isolate the corresponding Markovnikov insertion product **3** containing the β-(1-R)-phenethyl fragment σ-bound to the metal. Otherwise, when a strongly coordinating molecule was not present, final product **4** had a 2-(1-R)-ethylaryl moiety (solv.: solvent).

Mechanistic studies suggested a common intermediate in the formation of species **3** and **4**. In fact, in both cases the reaction seems to proceed through Markovnikov insertion of the alkene into the Pt–Ph bond and consequent formation of the Pt–CH$_2$CH(R)Ph fragment. In the presence of coordinating molecules, this is stabilized, and the corresponding complex **3** can be isolated. Alternatively, the "naked" metal center is able to activate an aromatic C–H bond (step i of Scheme 15), and the subsequent reductive elimination (step ii) leads to the final product of type **4**.
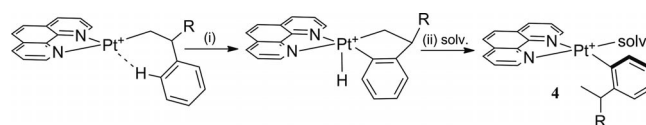
Scheme 15. Mechanism of formation of products of type **4** (R = H or Me).

An extension of this study[27] involved reaction of allylic alcohol, CH$_2$=CHCH$_2$OH, again with [PtI(Ar)(phen)] complexes in the presence of AgBF$_4$ (Scheme 16). In all cases, the prevalent products of reaction were the clearly detectable, though not isolated, **II-16** to **II-19**, which contain an η^1,η^2-(2-CH$_2$–CH=CH$_2$)–Ar moiety.
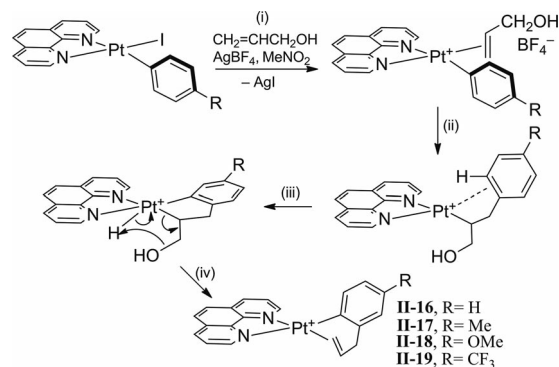
Scheme 16. Mechanism of formation of **II-16** to **II-19**.

According to a mechanistic proposal, **II-16** to **II-19** arise from an early and fast insertion process (step ii), which occurs with anti-Markovnikov stereochemistry driven by the inductive effect of the CH$_2$OH substituent. Then activation of a C–H bond takes place (step iii), with subsequent elimination of water and rearrangement (step iv). Addition of iodide to the reacting mixture allowed the isolation of the corresponding neutral five-coordinate complexes.

Recently,[28] a remarkable series of type **II** compounds (**II-3** to **II-7**) containing an η^2-coordinated benzene were thoroughly characterized by NMR spectroscopy. The complexes were obtained by reacting the diphenyl precursor with HBF$_4$ (e.g. Scheme 17) and were examined at 195 K, because of their tendency to release benzene at higher temperatures.

Notably, spin saturation transfer (SST) and exchange spectroscopy (EXSY) NMR spectra disclosed that the protons of the η^2-coordinated benzene exchange with those of
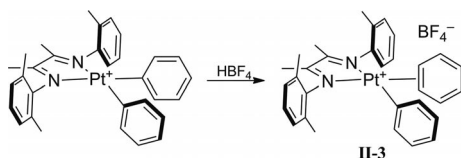
Scheme 17. Synthesis of **II-3** exemplifying that of complexes **II-3** to **II-7** (one Me substituent has been omitted for the sake of clarity).

the phenyl ring. The mechanism likely involves C–H activation and reductive elimination from a Pt^{IV}–hydride intermediate (Scheme 18).
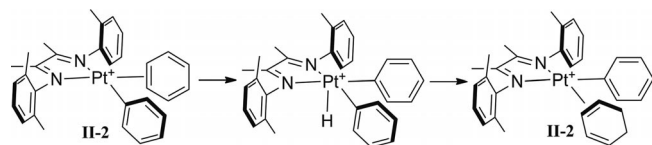
Scheme 18. Mechanism of H(benzene)/H(phenyl exchange) (one Me substituent has been omitted for the sake of clarity).

As mentioned before, the possibility to isolate type **II** complexes by proper molecular design was exploited by using *N,N′,C* cyclometalated structures (**II-8** to **II-15**), derived from *cis* and *trans*-1,2-diaminocyclohexane, respectively (Scheme 19).[29]
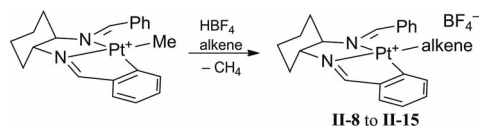
Scheme 19. Synthesis of complexes **II-8** to **II-15**.

It is plausible that the geometry imposed by chelation inhibits olefin insertion into the Pt–C bond. Notably, the chiral ligands were very effective in inducing stereoselective (90–95%) coordination of prochiral alkenes, such as propylene or styrenes. In addition, a low rate of alkene exchange was inferred from the NMR spectra of all the isolated complexes.
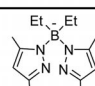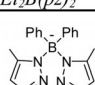
Square-Planar Pt^{II} Complexes Containing a *cis* Arrangement of an Alkyl Group and an Alkyne (III)

The Pt^{II} complexes of type **III** prepared so far are reported in Table 8 along with references for their synthesis and spectroscopic or structural characterization.

Although beyond the scope of this review, it should be noted that in the early 1970s several square-planar Pt^{II} complexes showing a *trans* arrangement of an alkyl group and an alkyne were described in the literature.[30] In other cases, compounds of type **III** were postulated as intermediates of reaction, but they were neither isolated nor observed.[31]

Instead, the first "true" examples were reported in 1974 by Clark,[32] who attributed the stable behavior of **III-1** and **III-2** to the presence of electron-donor disubstituted alk-

Table 8. Complexes of type **III** and their references.

L,L′[a]	R	Alkyne groups of the complexes	Refs.
Et$_2$B(pz)$_2$	Me	PhC≡CMe (**III-1**)[b]	[32,33]
		PhC≡CPh (**III-2**)[b]	[32]
Ph$_2$B(pz)$_2$	Me	PhC≡CMe (**III-3**)[b]	[32]
phen	Me	MeC≡CMe (**III-4**)	[34]
		PhC≡CPh (**III-5**)	[34]
		PhC≡CMe (**III-6**)	[34]
		PhC≡CH (**III-7**)[c]	[34]
		BzC≡CH (**III-8**)[c]	[34]
		MeO$_2$CC≡CCO$_2$Me (**III-9**)[c]	[34]
	Et	MeC≡CMe (**III-10**)	[34]
		PhC≡CPh (**III-11**)	[34]

[a] The name of the ligand is that given in the original paper. [b] The complex is neutral. [c] Not isolated.

ynes. The crystal structure of **III-1** confirmed the square-planar arrangement around the Pt atom, and provided evidence for a slight perturbation of the unsaturated ligand upon coordination.[33]

The study of complexes of type **III** was significantly implemented by preparing the class of compounds of general formula [PtMe(η^2-alkyne)(phen)]BF$_4$.[34] Scheme 20 summarizes the results of this investigation.
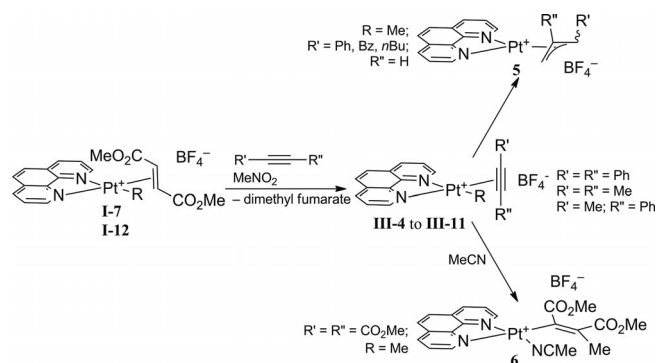
Scheme 20. Formation and reactions of type **III** species.

The complexes were prepared by replacing dimethyl fumarate from **I-7** or **I-12**. It was observed that their stability strongly depends on the properties of the alkyne, according to the following results:

(1) The complexes are stable with electron-donor disubstituted alkynes (**III-4** to **III-6**, **III-10**, and **III-11**).

(2) Complex **III-9**, which contains the electron-poor disubstituted alkyne MeO$_2$CC≡CCO$_2$Me, was spectroscopically detected at 253 K. On raising the temperature, fast insertion of the unsaturated ligand in the Pt–Me bond occurred with

attainment of the σ-vinyl product **6**. This behavior recalls that previously described for related *trans* complexes.[30]

(3) In analogy, if a terminal alkyne was used (RC≡CH), formation of complexes **III-7** and **III-8** could only be inferred by means of NMR spectroscopy. Remarkably, these transient species were found to slowly convert into π-allyl compound **5**, through an unprecedented rearrangement, which was ascribed to the reciprocal *cis* position of the reactive hydrocarbyl fragments. Use of labeled reagents revealed results that suggest a viable mechanism for the reaction (Scheme 21).
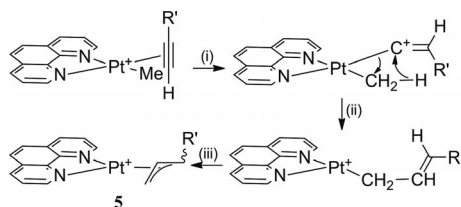
Scheme 21. Formation of π-allyl complexes from type **III** species.

It was suggested that the type **III** species undergoes a hydride shift (path i). A subsequent rearrangement (paths ii and iii) prompted by the *cis* geometry would account for the formation of the final product of type **5**.

Square-Planar Pt^{II} Complexes Containing a *cis* Arrangement of an Aryl Group and an Alkyne (IV)

Complexes of type **IV** are reported in Table 9 along with references for synthesis and spectroscopic or structural characterization.

Table 9. Complexes of type **IV** and their references.

Complexes	Refs.
cis-[Pt(C$_6$F$_5$)$_2$(EtC≡CEt)$_2$] (**IV-1**)	[35]
cis-[Pt(C$_6$F$_5$)$_2$(PhC≡CPh)$_2$] (**IV-2**)	[35]
cis-[Pt(C$_6$F$_5$)$_2$(tht)(EtC≡CEt)] (**IV-3**)	[35]
cis-[Pt(C$_6$F$_5$)$_2$(tht)(PhC≡CPh)] (**IV-4**)	[35]
cis-[Pt(C$_6$F$_5$)$_2$(py)(EtC≡CEt)] (**IV-5**)	[35]
cis-[Pt(C$_6$F$_5$)$_2$(py)(PhC≡CPh)] (**IV-6**)	[35]
cis-[Pt(C$_6$F$_5$)$_2$(PPh$_3$)(EtC≡CEt)] (**IV-7**)	[35]
cis-[Pt(C$_6$F$_5$)$_2$(SbPh$_3$)(PhC≡CPh)] (**IV-8**)	[35]
cis-[Pt(C$_6$F$_5$)$_2$(CO)(EtC≡CEt)] (**IV-9**)	[35]
cis-[Pt(C$_6$F$_5$)$_2$(CO)(PhC≡CPh)] (**IV-10**)	[35]
[Pt(C$_6$F$_5$)$_3$(PhC≡CPh)][N(PPh$_3$)$_2$] (**IV-11**)	[35]
[PtPh(MeC≡CMe)(phen)](BF$_4$) (**IV-12**)	[36]

This class of compounds is the less represented of the four types, because of the enhanced reactivity of the adjacent hydrocarbyl ligands. Thus, the only examples of stable complexes of type **IV** (**IV-1** to **IV-12**) are decorated with pentafluorophenyl rings,[35] which are quite reluctant to undergo insertion processes. Dialkyne complexes **IV-1** and **IV-2** were obtained by substituting thf from a diaryl precursor (Scheme 22), and, in turn, they were converted into monoalkyne species (**IV-3** to **IV-10**) by reaction with other donor molecules (tht, py, PPh$_3$, SbPh$_3$, CO). As expected, the complexes are stable, and could be accurately characterized.
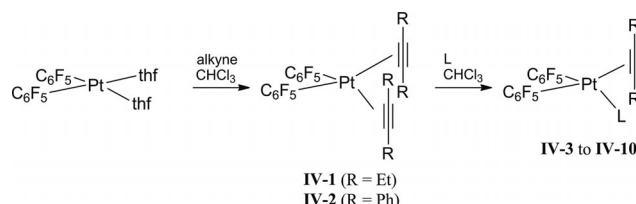
Scheme 22. Synthesis of **IV-1** to **IV-10** (L = tht, py, PPh$_3$, SbPh$_3$, CO).

Instead, when a simple phenyl ring was forced to the *cis* position relative to 2-butyne by a chelating *N,N*-ligand (*phen*), the resulting **IV-12** complex could only be observed in solution, before an unprecedented domino reaction took place (Scheme 23).[36]
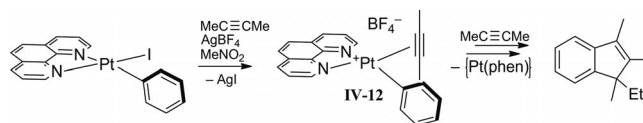
Scheme 23. Formation and rearrangement of **IV-12**.

The organic product, isolated after hydrolysis of the reaction mixture, was a substituted indene, incorporating two molecules of alkyne and the aromatic ring. By using substituted aryl ligands (C$_6$D$_5$, 4-Me–C$_6$H$_4$, or 4-CF$_3$–C$_6$H$_4$), it was also possible to propose a persuasive mechanism for the reaction.

Finally, it is worth mentioning the peculiar binuclear structures **IV-13** and **IV-14**,[37] in which a platinum atom coordinates a triple bond of a bridging phenylethynylphosphane at the *cis* position to a pentafluorophenyl ring (Figure 7).
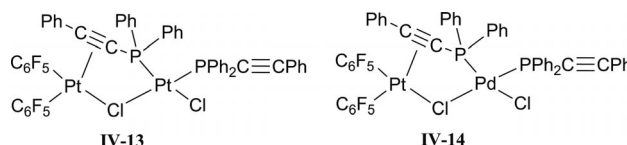
Figure 7. Structures of **IV-13** and **IV-14**.

Conclusions

This review offers a survey of the square-planar platinum(II) compounds containing a *cis* arrangement of a hydrocarbyl group and an unsaturated ligand (**I–IV**). The possibility offered by Pt to isolate or at least detect compounds with this requirement is particularly attractive, because they represent models of active intermediates in many important catalytic processes. A discussion of the factors affecting the general behavior of these compounds discloses the higher relative stability of type **I** species, which display a *cis* arrangement of an alkene and an alkyl group. More elusive are the other categories of these compounds, which, in sev-

eral cases, could be isolated only by proper structural design, or were characterized in solution. In some remarkable cases (e.g. **III** or **IV**), it is the *cis* arrangement that promotes unusual reactivity.

Acknowledgments

[1] a) R. H. Crabtree, *The Organometallic Chemistry of the Transition Metals*, Wiley Interscience, Hoboken, **2005**; b) J. F. Hartwig, *Organotransition Metal Chemistry – From Bonding to Catalysis*, University Science Books, Mill Valley, California, **2009**.

[2] a) B. Rieger, L. Saunders Baugh, S. Kacker, S. Striegler, *Late Transition Metal Polymerization Catalysts*, Wiley-VCH, Weinheim, **2003**; b) Z. Guan (Ed.), *Metal Catalysts in Olefin Polymerization*, *Topics in Organometallic Chemistry 26*, Springer, Berlin, Germany, **2009**.

[3] M. Oestreich (Ed.), *The Mizoroki-Heck Reaction*, John Wiley & Sons, Chichester, **2009**.

[4] a) C.-G. Dong, P. Yeung, Q.-S. Hu, *Org. Lett.* **2007**, *9*, 363–366; b) Y. Chen, N. A. Markina, T. Yao, R. C. Larock, *Org. Synth.* **2011**, *88*, 377; c) N. E. Schore, *Chem. Rev.* **1988**, *88*, 1081–1119.

[5] H. C. Clark, C. R. Jablonski, K. Von Werner, *J. Organomet. Chem.* **1974**, *82*, C51–C52.

[6] a) J. D. Scott, R. J. Puddephatt, *Organometallics* **1986**, *5*, 1253–1257; b) J. D. Scott, R. J. Puddephatt, *J. Chem. Soc., Chem. Commun.* **1984**, 193–195.

[7] N. Basickes, A. C. Hutson, A. Sen, G. P. A. Yap, A. L. Rheingold, *Organometallics* **1996**, *15*, 4116–4118.

[8] a) I. Orabona, A. Panunzi, F. Ruffo, *J. Organomet. Chem.* **1996**, *525*, 295–298; b) M. Fusto, F. Giordano, I. Orabona, A. Panunzi, F. Ruffo, *Organometallics* **1997**, *16*, 5981–5987.

[9] P. Ganis, I. Orabona, F. Ruffo, A. Vitagliano, *Organometallics* **1998**, *17*, 2646–2650.

[10] C. Zuccaccia, A. Macchioni, I. Orabona, F. Ruffo, *Organometallics* **1999**, *18*, 4367–4372.

[11] A. Macchioni, A. Magistrato, I. Orabona, F. Ruffo, U. Rothlisberger, C. Zuccaccia, *New J. Chem.* **2003**, *27*, 455–458.

[12] M. R. Plutino, L. Fenech, S. Stoccoro, S. Rizzato, C. Castellano, A. Albinati, *Inorg. Chem.* **2010**, *49*, 407–418.

[13] H. C. Clark, R. Puddephatt, *Inorg. Chem.* **1970**, *9*, 2670–2675.

[14] V. G. Albano, M. Di Serio, M. Monari, I. Orabona, A. Panunzi, F. Ruffo, *Inorg. Chem.* **2002**, *41*, 2672–2677.

[15] a) L. K. Johnson, C. M. Killian, M. Brookhart, *J. Am. Chem. Soc.* **1995**, *117*, 6414–6415; b) L. K. Johnson, S. Mecking, M. Brookhart, *J. Am. Chem. Soc.* **1996**, *118*, 267–268; c) S. Mecking, L. K. Johnson, L. Wang, M. Brookhart, *J. Am. Chem. Soc.* **1998**, *120*, 888–889.

[16] a) G. S. Hill, L. Manojlovic-Muir, K. W. Muir, R. J. Puddephatt, *Organometallics* **1997**, *16*, 525–530; b) G. S. Hill, L. M. Rendina, R. J. Puddephatt, *J. Chem. Soc., Dalton Trans.* **1996**, 1809–1813.

[17] K. Yang, R. J. Lachicotte, R. Eisenberg, *Organometallics* **1998**, *17*, 5102–5113.

[18] P. J. Albietz Jr., K. Yang, R. J. Lachicotte, R. Eisenberg, *Organometallics* **2000**, *19*, 3543–3555.

[19] M. Shiotsuki, P. S. White, M. Brookhart, J. L. Templeton, *J. Am. Chem. Soc.* **2007**, *129*, 4058–4067.

[20] L. Johansson, M. Tilset, J. A. Labinger, J. E. Bercaw, *J. Am. Chem. Soc.* **2000**, *122*, 10846–10855.

[21] S. Reinartz, P. S. White, M. Brookhart, J. L. Templeton, *Organometallics* **2000**, *19*, 3854–3866.

[22] F. Ozawa, S. Kawagishi, T. Ishiyama, M. Yoshifuji, *Organometallics* **2004**, *23*, 1325–1332.

[23] S. Basu, N. Arulsamy, D. M. Roddick, *Organometallics* **2008**, *27*, 3659–3665.

[24] L. Cavallo, A. Macchioni, I. Orabona, F. Ruffo, C. Zuccaccia, D. Zuccaccia, *Organometallics* **2004**, *23*, 2137–2145.

[25] M. E. Cucciolito, A. de Renzi, I. Orabona, F. Ruffo, D. Tesauro, *J. Chem. Soc., Dalton Trans.* **1998**, 1675–1678.

[26] V. De Felice, A. de Renzi, D. Tesauro, A. Vitagliano, *Organometallics* **1992**, *11*, 3665–3669.

[27] V. De Felice, A. de Renzi, N. Fraldi, G. Roviello, A. Tuzi, *J. Organomet. Chem.* **2005**, *690*, 2035–2043.

[28] B. J. Wik, M. Lersch, A. Krivokapic, M. Tilset, *J. Am. Chem. Soc.* **2006**, *128*, 2682–2696.

[29] a) C. R. Baar, H. A. Jenkins, G. P. A. Yap, R. J. Puddephatt, *Organometallics* **1998**, *17*, 4329–4331; C. R. Baar, H. A. Jenkins, M. C. Jennings, G. P. A. Yap, R. J. Puddephatt, *Organometallics* **2000**, *19*, 4870–4877.

[30] a) M. H. Chisholm, H. C. Clark, *J. Chem. Soc. C* **1970**, 763; b) M. H. Chisholm, H. C. Clark, D. H. Hunter, *J. Chem. Soc., Chem. Commun.* **1971**, 809–810; c) M. H. Chisholm, H. C. Clark, *Inorg. Chem.* **1971**, *10*, 1711–1716; d) M. H. Chisholm, H. C. Clark, *Inorg. Chem.* **1971**, *10*, 2557–2568; e) M. H. Chisholm, H. C. Clark, *J. Am. Chem. Soc.* **1972**, *94*, 1532–1539; f) M. H. Chisholm, H. C. Clark, L. E. Manzer, *Inorg. Chem.* **1972**, *11*, 1269–1275.

[31] N. Chaudhury, R. J. Puddephatt, *Inorg. Chem.* **1981**, *20*, 467–470.

[32] H. C. Clark, K. von Werner, *J. Organomet. Chem.* **1975**, *101*, 347–358.

[33] B. W. Davies, N. C. Payne, *J. Organomet. Chem.* **1975**, *102*, 245–257.

[34] M. E. Cucciolito, V. De Felice, I. Orabona, F. Ruffo, *J. Chem. Soc., Dalton Trans.* **1997**, 1351–1354.

[35] a) R. Usón, J. Forniés, M. Tomás, B. Menjón, C. Fortuño, A. J. Welch, D. E. Smith, *J. Chem. Soc., Dalton Trans.* **1993**, 275–280; b) R. Usón, J. Forniés, M. Tomás, B. Menjón, A. J. Welch, *J. Organomet. Chem.* **1986**, *304*, C24–C26.

[36] M. E. Cucciolito, A. de Renzi, G. Roviello, F. Ruffo, *Organometallics* **2008**, *27*, 1351–1353.

[37] J. Forniés, E. Lalinde, A. Martin, M. T. Moreno, A. J. Welch, *J. Chem. Soc., Dalton Trans.* **1995**, 1333–1340.

Experimental and Theoretical Studies of Unusual Four-Membered Metallacycles from Reactions of Group 4 Metallocene Bis(trimethylsilyl)-acetylene Complexes with the Sulfurdiimide $Me_3SiN=S=NSiMe_3$

Katharina Kaleta,[a] Martin Ruhmann,[a,b] Oliver Theilmann,[a,b] Subhendu Roy,[c] Torsten Beweries,[a] Perdita Arndt,[a] Alexander Villinger,[b] Eluvathingal D. Jemmis,*[c,d] Axel Schulz,*[a,b] and Uwe Rosenthal*[a]

Dedicated to Professor Bernhard Lücke on the occasion of his 75th birthday

The use of the sulfurdiimide RN=S=NR′ (R = R′ = SiMe₃, **3**) in reactions with group 4 metallocene bis(trimethylsilyl)-acetylene complexes of the type [Cp₂M(L)(η²-Me₃Si-C₂SiMe₃)] (**1**: M = Ti, no L; **2**: M = Zr, L = pyridine) has led to the formation of four-membered metallacycles **4M** containing the group 4 metal, nitrogen and sulfur. DFT calculations performed on compound **4Ti** indicate that this complex is best described as a σ-complex with cyclic delocalisation of the ring electrons. Moreover, pseudo-Jahn–Teller distortion plays a significant role in stabilising this complex.

Introduction

The role of metallacycles as an important class of organometallic compounds has been highlighted on numerous occasions.[1] One of the challenges for synthetic chemists is to explore the frontiers of stability of such cyclic compounds with respect to ring size, that is, ring strain. Promising approaches for the stabilisation of highly strained structures include the introduction of metal centres or heteroatoms into the ring system.[2] This approach was very recently demonstrated by us for four- and five-membered azametallacycles[3,4] as well as for five-membered disilametallacycles[5] along with computational studies of the structures and bonding of the complexes. Bis(trimethylsilyl)acetylene complexes of group 4 metals of the type [Cp′₂M(L)(η²-Me₃SiC₂SiMe₃)] [Cp′ = substituted or unsubstituted η⁵-cyclopentadienyl; M = Ti, no L (**1**); M = Zr, L = pyridine (**2**), thf, acetone] have shown to be excellent starting materials for these purposes, because they eliminate the alkyne spectator ligand under mild conditions to give the highly reactive 14-electron fragment [Cp₂M], which can react with unsaturated precursors to give metallacyclic structures.[6]

In previous studies, a wide range of metallacycles were obtained from the reactions of these metallocene alkyne complexes with carbodiimides, including four-membered cyclic carbenes,[3] five-membered heterometallacycloallenes and dinuclear complexes bridged by tetraaminato ligands.[4] These results prompted us to investigate substitution reactions with other heteroallene substrates such as sulfurdiimides. In principle, several coordination modes are possible for sulfurdiimides; examples are depicted in Scheme 1. Transition-metal complexes with sulfurdiimides have been described before, for example, Lorenz and co-workers reported the chromium complex [CpCr(NO)₂{η¹-κ¹-N-N(BF₃)=S=NSiMe₃}].[7] However, in the formation of this compound, one SiMe₃ group of the Me₃SiN=S=NSiMe₃ (**3**) starting material was replaced by a BF₃ group, and the product was not found to be a metallacycle. In contrast, Stufkens and co-workers published a dinuclear manganese complex [(OC)₅Mn₂(CO)₃(η²-tBu-N=S=N-tBu)][8] displaying a cyclic Mn–N–S–N unit at one of the metal centres. Moreover, Rausch, Alt and Thewalt described the formation of a titanacycle [Cp₂Ti(η²-κ²-N-Me₃SiN=S=NSiMe₃)] (**4Ti**) from the reaction of [Cp₂Ti] {generated from [Cp₂Ti(PMe₃)₂]} and the same sulfurdiimide. How-

[a] Leibniz-Institut für Katalyse e.V. an der Universität Rostock,
Albert-Einstein-Str. 29a, 18059 Rostock, Germany
Fax: +49-381-1281-51176
E-mail: uwe.rosenthal@catalysis.de
[b] Abteilung Anorganische Chemie, Institut für Chemie,
Universität Rostock,
Albert-Einstein-Str. 3a, 18059 Rostock, Germany
Fax: +49-381-498-6382
E-mail: axel.schulz@uni-rostock.de
[c] Department of Inorganic and Physical Chemistry, Indian
Institute of Science,
Bangalore 560012, India
[d] Indian Institute of Science Education and Research
Thiruvananthapuram, CET Campus,
Thiruvananthapuram 695016, India
Fax: +91-471-259-7442
E-mail: jemmis@iisertvm.ac.in
⌨ Supporting information for this article is available on the WWW under http://dx.doi.org/10.1002/ejic.201101188.

ever, the product obtained was only characterised spectroscopically.[9] In this paper we report on an alternative synthesis of this compound as well as on its X-ray crystal-structure determination and a detailed theoretical study of its structure and bonding.
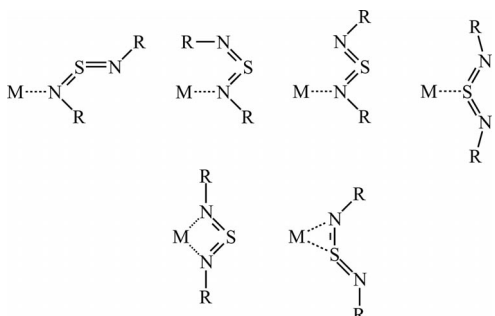
Scheme 1. Possible coordination modes for a sulfurdiimide at a metal centre.

Results and Discussion

The reaction of the titanocene alkyne complex **1** with the sulfurdiimide $Me_3SiN=S=NSiMe_3$ (**3**) in *n*-hexane at 60 °C gave a dark-violet oily residue, from which analytically pure samples of complex **4Ti** were obtained after sublimation as violet crystals with a metallic lustre in 73% yield. The reaction of the corresponding zirconocene alkyne complex **2** with **3** proceeded in *n*-hexane at room temperature to give the complex **4Zr** as an orange crystalline solid in good yield (70%; Scheme 2). Notably, in contrast to the previously described reactions with carbodiimides,[3,4] in these cases no additional coordination of metallocene to the four-membered metallacycle or dimerisation is needed for stabilisation of the system.

M = Ti, no L (**1**); *n*-hexane, 60 °C
M = Zr, L = py (**2**); *n*-hexane, r. t.
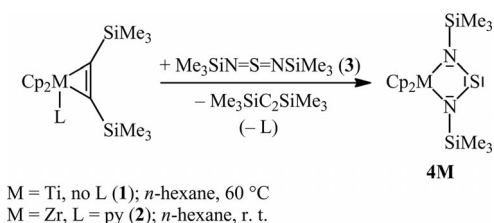
Scheme 2. Reactions of **1** and **2** with **3** to give the metallacycles **4M**.

In mass spectrometry experiments, characteristic fragments of the metallacyclic product complexes were detected at m/z = 384 [M]+ and 178 [Cp$_2$Ti]+ (**4Ti**) as well as at m/z = 426 [M]+ (**4Zr**). NMR analysis of the complexes **4Ti** and **4Zr** revealed the two species to have diamagnetic character; the resonances are slightly different to those reported in the literature.[9] In the 1H NMR spectra, two resonances were detected at δ = 5.53 and 0.17 ppm (**4Ti**) as well as at δ = 5.75 and 0.21 ppm (**4Zr**), assigned to Cp and SiMe$_3$ protons, respectively. All the observed resonances, including the single resonances in the 13C and 29Si NMR spectra, sug-

gest the formation of symmetrical, mononuclear metallocene complexes (the chemical shifts in the 13C and 29Si NMR spectra can be found in the Exp. Sect.).

This is corroborated by the molecular structure of the titanocene complex **4Ti** depicted in Figure 1. The mononuclear complex crystallises in the monoclinic space group $P2_1/c$ with eight molecules per unit cell and two formula units per asymmetric unit. In compound **4Ti**, the titanium atom adopts a strongly distorted tetrahedral geometry [N1–Ti2–N2 74.7(1)°]. The Ti–N bond lengths [av. 2.061(2) Å] are found to be slightly longer, as found before for the dinuclear titanium complex [μ-O-({*t*Bu–N=S(Ph)=N*t*Bu}-TiCl$_2$)$_2$] (av. 2.009 Å).[10]
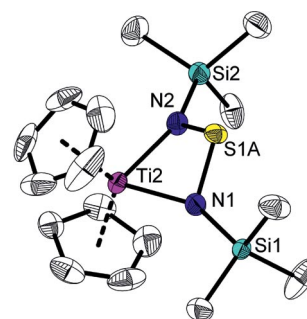
Figure 1. Molecular structure of complex **4Ti**. Thermal ellipsoids are drawn at the 30% probability level. Hydrogen atoms, the second position of the disordered part of the molecule and the second molecule of the asymmetric unit have been omitted for clarity. Selected bond lengths [Å] and angles [°]: Ti2–N1 2.057(2), Ti2–N2 2.064(2), N1–S1A 1.698(3), N2–S1A 1.673(3), N1–Si1 1.720(3), N2–Si2 1.715(2); N1–Ti2–N2 74.7(1), Ti2–N1–S1A 87.3(1), N1–S1A–N2 95.7(1), S1A–N2–Ti2 87.7(1), Ti2–N1–Si1 154.4(2), Si1–N1–S1A 117.8(2), Ti2–N2–Si2 151.2(2), Si2–N2–S1A 110.9(2).

Free trimethylsilyl-substituted sulfurdiimide **3** exhibits two S–N double bonds of similar length (S–N1 1.523(1), S–N2 1.516(1) Å];[11] when bound to a metal fragment, as in complex **4Ti**, both bonds are elongated (av. S–N bond length in **4Ti** 1.742 Å[12]) and can be referred to as S–N single bonds (Σr_{cov} = 1.74 Å[13]). This observation can be attributed to the cyclic delocalisation of the ring electrons (see below), supported by the calculated nucleus-independent chemical shift (NICS) values (Table 1). The central Ti2–N2–S1–N1 moiety displays a butterfly orientation with a deviation from planarity of 29.5° (Figure 2), the reason for which is evident from the correlation diagram shown in Figure 4. Compared with the free sulfurdiimide in which the atoms Si1–N1–S1–N2–Si2 are planar with only a small deviation of 2.5°, the effect of coordination to the titanocene centre is distinct. This butterfly orientation of the metallacycle has been observed previously for other group 4 complexes displaying M–N–S–N units.[14]

Due to the high reducing potential of titanocene(II) fragments,[15] a two-electron transfer from the metallocene unit to the sulfurdiimide ligand can be proposed that results in an expanded S–N bond and the described butterfly motif. Without any electron transfer, molecule **4Ti** may be described as a bis-π complex **A**. Stepwise electron transfer generates first a titanocene(III) sulfur diamide radical cat-

Table 1. Calculated NICS values for complex **4Ti**[a] and the ligand[b] at the BP86/BAS2 level of theory.[c]

NICS (x) [ppm]	**4Ti**		bent-[Me₃Si–HNSNH–SiMe₃]	
	Concave side	Convex side	Concave side	Convex side
NICS (0)	–19.3		–12.2	
NICS (0.5)	–14.1	–14.0	–8.1	–1.4
NICS (1.0)	–8.9	–12.7	–2.6	–0.1
NICS (1.5)	–4.9	–16.9	–0.5	–0.1

[a] Calculated at the ring centre (0 Å) and above the ring centre (0.5–1.5 Å). [b] Determined by using the same structure but without Cp₂Ti and satisfying the two dangling valencies of the bent-[Me₃SiN=S=NSiMe₃] by incorporating two H atoms. [c] BAS2: 6-311+G(d,p) for C, H, N, S and Si, and LANL2DZ for Ti.
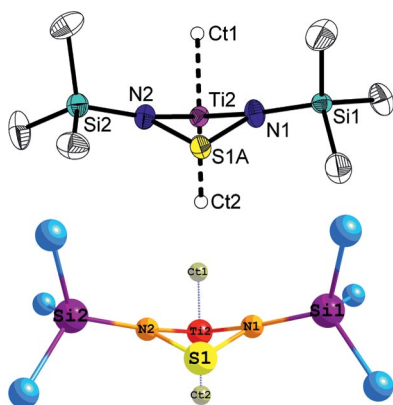
Figure 2. Top: side view of the butterfly motif of complex **4Ti**. Thermal ellipsoids are drawn at the 30% probability level. Hydrogen atoms, the second position of the disordered part of the molecule and the second molecule of the asymmetric unit have been omitted for clarity. Ct represents the centroids of the omitted Cp ligands. Bottom: computed structure of the butterfly motif of complex **4Ti**.

ion **B**. The contribution of a second electron transfer leads to a titanium(IV) species **C** (Scheme 3). Due to the diamagnetic properties, the Cp₂Ti^{II} (**A**) and Cp₂Ti^{IV} (**C**) species can be considered the main contributions to the real electronic situation. Bearing in mind that complex **4Ti** may be described by at least three resonating structures **A**–**C**, this molecule may overall be characterised by resonance struc-

ture **D**. This aspect is further addressed in a theoretical study of the structure and bonding of complex **4Ti** in the following sections.

Complex **4Ti** is found to be a minimum on the potential energy surface. Calculations show that the structural parameters computed with BAS2 (see the Exp. Sect.) match well the crystal-structure data. The results described herein are derived from calculations with the BAS2 basis set. The NICS[16] values were calculated at the geometrical centre point of the four-membered ring to judge the extent of cyclic delocalisation of electrons in complex **4Ti**. The delocalisation of electrons in the four-membered ring results from the interaction between the Ti centre and the NSN moiety. Thus, the NICS values also provide an insight into the possible interaction between the Ti centre and the NSN moiety in complex **4Ti**. The correlation diagram in Figure 4 is derived from single-point calculations of the structures. The computed structure of complex **4Ti** is in good agreement with the X-ray crystal structure (Table 2) and shows the characteristic butterfly-shaped four-membered ring of complex **4Ti** (Figure 2). The deviation from planarity (Ti2–N2–S1–N1 29.5°) matches well with the calculated value of 30.0°. The calculated average Ti–N bond length of 2.048 Å is in good agreement with the experimentally found average value of 2.057 Å and in the range of a typical Ti–N bond (between 1.885 and 2.160 Å).[17] The N–S bond length is 1.709 Å, which is longer than the calculated N–S bond in free trimethylsilyl-substituted sulfurdiimide (1.558 Å). Note also that the Ti···S contact is computed to be 2.584 Å; this
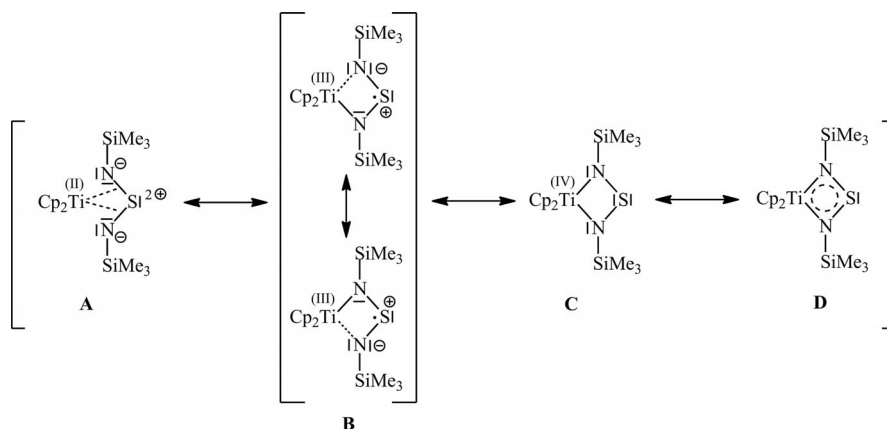
Scheme 3. Possible resonance forms for complex **4Ti**.

value is close to similar contacts in complexes with σ-bonding interactions (e.g., Ti–S 2.407 Å in the calculated complex [$Cp_2Ti(SCH_3)_2$]; Σr_{cov} = 2.36 Å[13]).

Table 2. Comparison between selected experimental and computed bond lengths [Å] and angles [°] of complex **4Ti** at the BP86/BAS2 level of theory.[a]

	BP86/BAS2	X-ray data
N1–Ti2	2.047	2.057
N2–Ti2	2.048	2.064
N1–S1	1.709	1.698
N2–S1	1.709	1.673
S1–Ti2	2.584	2.604
Ti2–Ct1	2.102	2.082
Ti2–Ct2	2.126	2.106
N2–S1–N1	96.40	95.70
S1–N1–Si1	121.02	117.77
S1–N1–Ti2	86.46	87.25
Si1–N1–Ti2	152.27	154.35
S1–N2–Si2	120.99	120.94
S1–N2–Ti2	86.45	87.69
Si2–N2–Ti2	152.43	151.24
N1–Ti2–N2	76.96	74.65
Ct1–Ti2–Ct2	130.09	130.22
Ti2–N2–S1–N1	30.00	29.45
Ti2–N1–N2–Si2	–159.57	–158.05

[a] BAS2: 6-311+G(d,p) for C, H, N, S and Si, and LANL2DZ for Ti.

We carried out a bonding analysis of complex **4Ti**. The metal atom is in the formal oxidation state of +2 in the isolated Cp_2Ti fragment with two valence (d^2) electrons. The HOMO of complex **4Ti** involves the back donation of an electron pair from the HOMO of the Cp_2Ti fragment to the vacant LUMO of the sulfurdiimide ligand, which is antibonding between the N and S atoms, resulting in an elongation of the N–S bonds. Thus, the metal atom is in the formal oxidation state of +4 in complex **4Ti**. The distortion from the planar structure in complex **4Ti** makes it possible to interact effectively between the in-plane metal orbital and out-of-plane ligand orbital, especially the in-phase interaction of the lobes of the two N atoms and the metal orbital. The nonplanarity also compensates the antibonding interaction between the N and S orbitals in the ring as the S orbital is tilted outwards with respect to the N orbitals. The HOMO, LUMO, HOMO-5, HOMO-11 and HOMO-12 of complex **4Ti** are shown in Figure 3.
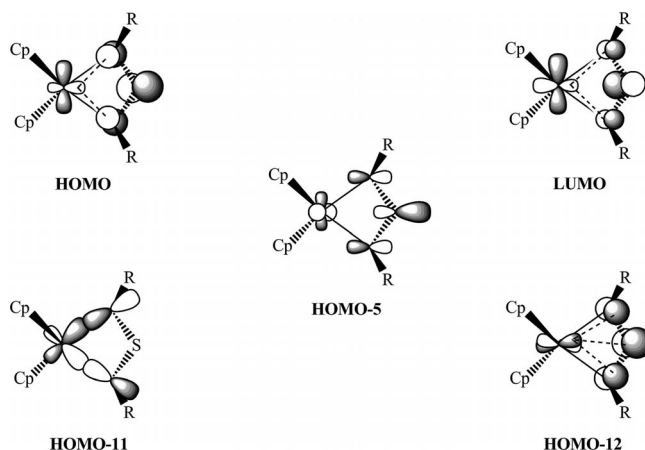
Figure 3. Selected MOs of the complex **4Ti** (R = $SiMe_3$).

HOMO-5 has substantial lone-pair character on the S atom, which is also supported by the existence of a lone pair on an $sp^{0.4}$-hybridised orbital of the S atom in the NBO analysis (Table 3).

A correlation diagram between the planar and nonplanar structures of complex **4Ti** can be drawn to provide an insight into the distorted nature of the complex (Figure 4). It is evident that the planar complex **4Ti_1** has a very small HOMO–LUMO gap (ΔE = 0.14 eV). Consequently, it undergoes structural distortion allowing mixing of the HOMO and LUMO, and thus the nonplanar complex **4Ti** is stabilised to a greater extent. The HOMO–LUMO gap of the complex, as is seen in Figure 4, increases with the extent of nonplanarity (from ΔE = 0.14 eV to ΔE = 1.7 eV). Thus, it is a pseudo- or second-order Jahn–Teller distortion.[18] Note also that a pseudo-Jahn–Teller distortion has been observed previously in five-membered metallacycloallenes.[4] Interestingly, the planar structure **4Ti-TS**[19] of complex **4Ti** turns out to be the transition state for the conformational isomerism of the complex **4Ti**, which has a barrier of 9.4 kcal/mol, the S atom moving up and down to achieve the most stable nonplanar geometry (Scheme 4).

Due to the nonplanar geometry, the Ti···S interatomic distance is shorter in complex **4Ti** than in its planar structure. As mentioned above, this distance is close to the Ti–S bonding distance. Thus, the structural distortion causes a significant interaction between the Ti and S atoms in the four-membered ring, which is also supported by the Wiberg

Table 3. NBO occupancies, polarisations and Wiberg bond indices of complex **4Ti** derived from an NBO analysis at the BP86/BAS2 level of theory.[a]

A–B	Occupancy [%]	Polarisation of Ψ_{NBO}(A–B)	Wiberg bond index
Ti2–N1	94.80	0.415 ($sd^{1.95}$) + 0.910 ($sp^{1.88}$)	0.766
Ti2–N2	96.60	0.439 ($sd^{3.78}$) + 0.899 ($sp^{1.83}$)	0.765
Ti2–S1	88.60	0.422 ($sd^{4.42}$) + 0.906 (p)	0.458
S1–N1	98.30	0.635 ($sp^{6.68}$) + 0.773 ($sp^{5.75}$)	0.981
S1–N2	98.30	0.635 ($sp^{6.66}$) + 0.772 ($sp^{5.74}$)	0.981
S1 (LP)	98.60	1.000 ($sp^{0.4}$)	

[a] BAS2: 6-311+G(d,p) for C, H, N, S and Si, and LANL2DZ for Ti.
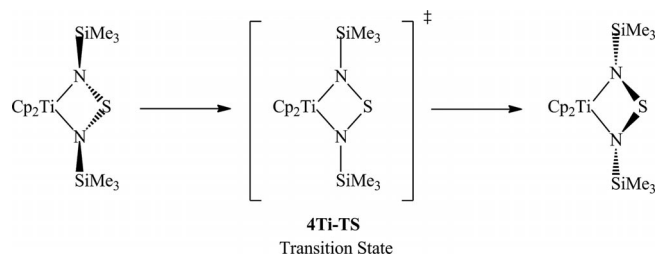
Scheme 4. Schematic representation of the transition state **4Ti-TS** of complex **4Ti**.

bond index (WBI 0.458) and the occupancy (88.6%) of the Ti···S interaction (Table 3). The HOMO-12 of complex **4Ti** accounts for this interaction (Figure 3). The NBO analysis (Table 3) suggests that there are two highly polarised Ti–N σ-bonds with occupancies of 94.8 and 96.6% and two N–S σ-bonds, each having a high occupancy of 98.3%. This, along with the Wiberg bond indices (Table 3), reveals the presence of a four-membered σ-skeleton for complex **4Ti**. The NICS values for complex **4Ti** are –19.3 at the centre and –8.9 at a distance of 1 Å above the ring centre. This implies that there is a considerable cyclic delocalisation of electrons in complex **4Ti**. The metal–ligand interaction is also shown by the increase in the negative NICS values as the isolated ligand forms the complex (Table 1). Hence, from the molecular orbitals, NBO analyses and NICS cal-

Figure 4. Correlation diagram between the planar and nonplanar structure of complex **4Ti** (R = SiMe$_3$). The variation in the HOMO and LUMO of complex **4Ti** is plotted as a function of nonplanarity of complex **4Ti_1** (on both sides). **4Ti′** refers to the other conformer of complex **4Ti**. **4Ti_2** and **4Ti_2′** are intermediate structures.[20]

culations, complex **4Ti** can be best described as a σ-complex with cyclic delocalisation of electrons (**D**, Scheme 3), as is already stated.

Conclusions

Reaction of the titanocene and zirconocene alkyne complexes **1** and **2** with N,N′-bis(trimethylsilyl)sulfurdiimide resulted in the formation of mononuclear unsaturated metallocene(IV) compounds with an N–S–N scaffold (**4M**). For complex **4Ti**, a stepwise electron transfer from the metallocene(II) fragment to the sulfurdiimide ligand is proposed, which results from the reducing properties of the titanocene(II) units. Thus, besides the Ti^{II} bis-π complex, a Cp$_2$Ti^{III} sulfurdiimide species and finally a Cp$_2$Ti^{IV} metallacycle may be formulated as a result of the transfer of one and two electrons, respectively. Theoretical calculations suggest a σ-complex with cyclic delocalisation of electrons in the four-membered ring to be the best description for complex **4Ti**. In particular, the metallacycle formed did not appear planar but a butterfly motif due to pseudo-Jahn–Teller distortion.

Experimental Section

General: All manipulations were carried out in oxygen- and moisture-free argon by using standard Schlenk and drybox techniques. Non-halogenated solvents were dried with sodium/benzophenone and freshly distilled prior to use. The metallocene alkyne complexes **1** and **2** were synthesised as previously described in the literature.[21,22] The sulfurdiimide Me$_3$SiN=S=NSiMe$_3$ (**3**) was synthesised according to a published procedure.[23] The following instruments were used. NMR spectra: Bruker AV250 and AV300, respectively. ^{1}H and ^{13}C chemical shifts are referenced to the solvent signals: [D$_6$]benzene (δ_H = 7.16 ppm, δ_C = 128.0 ppm) and CDCl$_3$ (δ_H = 7.26 ppm, δ_C = 77.2 ppm). IR: Nicolet 6700 FT-IR spectrometer with a smart endurance attenuated total reflection (ATR) device. MS: Finnigan MAT 95-XP from Thermo-Electron. Elemental analysis: Leco CHNS-932 elemental analyser. Melting points: E/Z-Melt, Standford Research Systems. The melting points were measured in sealed capillaries.

Computational Details: The structure and bonding of complex **4Ti** were analysed at the BP86 level of theory by using the Gaussian 03 and 09 program packages.[24–26] We used two types of basis sets in our calculations: (1) BAS1: LANL2DZ for all atoms; (2) BAS2: the 6-311+G(d,p) basis set for the C, H, N, S and Si atoms and the LANL2DZ basis set for the Ti atom.[27] The nature of the bonding in complex **4Ti** was studied by using NBO analysis.[28] The complex was found to be a minimum on the potential energy surface.

Synthesis of Me$_3$SiN=S=NSiMe$_3$ (3): As described in the literature,[23] the sulfurdiimide was obtained as a yellow liquid. Satisfactory pure samples were obtained after the third distillation. Yield: 65%; b.p. 75–77 °C (67 mbar). ^{1}H NMR (CDCl$_3$, 250 MHz, 300 K): δ = 0.22 (s, 18 H, SiMe$_3$) ppm. ^{13}C NMR (CDCl$_3$, 63 MHz, 300 K): δ = 5.5 (SiMe$_3$) ppm. ^{29}Si (CDCl$_3$, 60 MHz, 300 K): δ = 2.6 (SiMe$_3$) ppm.

Synthesis of [Cp$_2$Ti(η^2-Me$_3$SiN=S=NSiMe$_3$)] (4Ti): The alkyne complex **1** (0.100 g, 0.287 mmol) was dissolved in n-hexane (5 mL). After addition of sulfurdiimide **3** (0.064 mL, 0.27 mmol), the mix-

ture became deep-violet. Then the mixture was stored at 60 °C to complete the reaction. The solvent was removed in vacuo, and an oily and resinous residue was isolated. Attempts at purification by recrystallisation in common non-chlorinated solvents failed. Therefore, the crude product was sublimed at 90 °C (10^{-3} mbar). The sublimate was deep-violet with a metallic lustre. Crystals suitable for X-ray analysis were obtained from a slow sublimation at 60 °C (10^{-3} mbar) after several hours. Yield: 0.080 g (73%). M.p. 122 °C (dec. 270 °C). ^1H NMR ([D_6]benzene, 300 MHz, 300 K): δ = 5.53 (s, 10 H, Cp), 0.17 (s, 18 H, Me_3Si) ppm. ^{13}C NMR ([D_6]benzene, 75 MHz, 300 K): δ = 107.0 (Cp), 2.0 (Me_3Si) ppm. ^{29}Si INEPT NMR ([D_6]benzene, 60 MHz, 300 K): δ = 4.2 ($^2J_{Si,H}$ = 7.32 Hz, Me_3Si) ppm. IR (ATR, 16 scans): $\tilde{v}$ = 3251 (w), 3109 (w), 2951 (m), 2894 (w), 1588 (w), 1440 (m), 1401 (w), 1366 (w), 1297 (w), 1243 (s), 1151 (w), 1123 (m), 1067 (w), 1014 (m), 983 (w), 937 (s), 826 (s), 786 (m), 744 (m), 689 (m), 600 (m) cm^{-1}. MS (CI, isobutane): m/z (%) = 384 (100) [M]$^+$, 319 (7) [M – Cp]$^+$, 207 (17) [Me_3Si-N=S=NSiMe$_3$ + H]$^+$, 178 (5) [Cp$_2$Ti]$^+$. $C_{16}H_{28}N_2SSi_2Ti$ (384.54): calcd. C 49.98, H 7.34, N 7.29, S 8.34; found C 50.26, H 7.22, N 7.20, S 8.30.
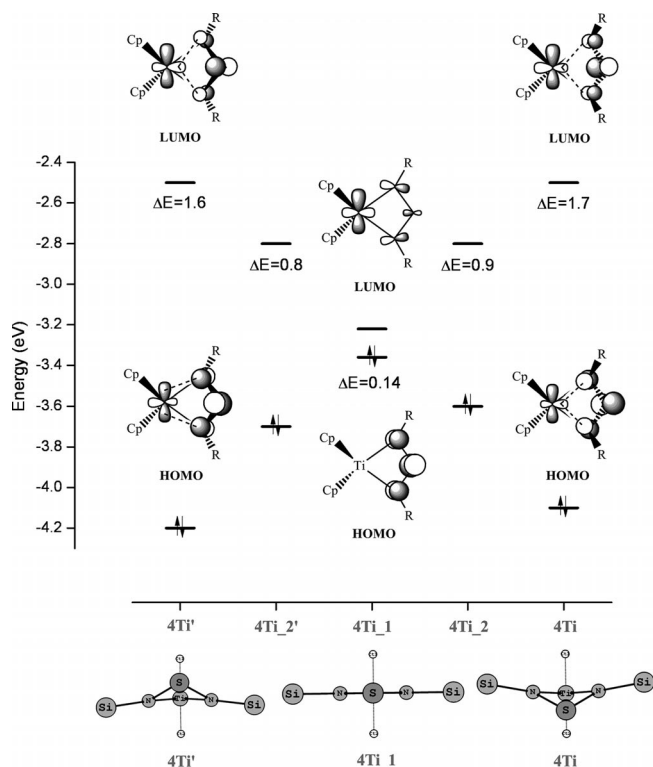
Synthesis of [Cp$_2$Zr(η^2-Me$_3$SiN=S=NSiMe$_3$)] (4Zr): The alkyne complex **2** (0.235 g, 0.500 mmol) was dissolved in *n*-hexane (5 mL). After addition of sulfurdiimide **3** (0.12 mL, 0.500 mmol), the mixture became red. The solution was filtered, all volatiles were removed in vacuo, and the residue was dissolved in *n*-hexane (1 mL). At –78 °C, orange crystals precipitated that were washed with cold *n*-hexane and dried in vacuo. Yield: 0.149 g (0.348 mmol, 70%). M.p. 57–59 °C (dec.). ^1H NMR ([D_6]benzene, 300 MHz, 297 K): δ = 5.75 (s, 10 H, Cp), 0.21 (s, 18 H, SiMe$_3$) ppm. ^{13}C NMR ([D_6]benzene, 75 MHz, 297 K): δ = 108.1 (Cp), 1.7 (SiMe$_3$) ppm. ^{29}Si INEPT NMR ([D_6]benzene, 60 MHz, 297 K): δ = 6.0 (SiMe$_3$) ppm. IR (ATR, 32 scans): $\tilde{v}$ = 2952 (w), 2896 (w), 1439 (w), 1400 (w), 1244 (m), 1094 (w), 1014 (m), 912 (m), 826 (s), 785 (vs), 745 (s), 647 (s), 596 (m) cm^{-1}. MS (EI, 70 eV): m/z (%) = 426 (100) [M]$^+$, 353 (10) [M – SiMe$_3$]$^+$, 220 (17) [Cp$_2$Zr]$^+$. $C_{16}H_{28}N_2SSi_2Zr$ (427.86): calcd. C 44.91, H 6.60, N 6.55, S 7.49; found C 44.72, H 6.84, N 5.97, S 6.91.

X-ray Structure Determination: Crystals of **4Ti** suitable for X-ray determination were selected in Fomblin YR-1800 oil (Alfa Aesar) at room temperature. The sample was cooled to 173(2) K during the measurement. The data were collected with a Bruker Apex Kappa-II CCD diffractometer. The radiation was graphite-mono-chromated Mo-K_α (λ = 0.71073 nm). The structure was solved by direct methods and refined by least-squares full-matrix methods.[29] Semiempirical absorption corrections were applied (SADABS).[30] All non-hydrogen atoms were refined anisotropically. All H atoms were positioned geometrically and refined by using a riding model. In complex **4Ti**, the positions of the sulfur atoms in molecules 1 and 2 were found to be disordered and divided into two parts. The occupancy was refined freely [molecule 1: 0.822(2)/0.178(2); molecule 2: 0.963(2)/0.037(2)]. Crystallographic details: $C_{16}H_{28}N_2SSi_2Ti$, M_r = 384.54, violet crystals, $0.28 \times 0.11 \times 0.07$ mm, monoclinic, space group $P2_1/c$, a = 16.2802(4), b = 8.7279(2), c = 29.3058(7) Å, β = 97.6070(10)°, V = 4127.47(17) Å^3, Z = 8, $\rho_{calcd.}$ = 1.238 g cm^{-3}, T = 173(2) K, μ = 0.630 mm^{-1}, numerical absorption correction (max. and min. transmission: 0.9572 and 0.8432), 31333 reflections collected, 8370 independent reflections (R_{int} = 0.0666), 4812 reflections observed [$I > 2\sigma(I)$], 429 refined parameters, final R indices [$I > 2\sigma(I)$]: R_1 = 0.0481, wR_2 = 0.1037, R indices (all data): R_1 = 0.1095, wR_2 = 0.0905. CCDC-850271 contains the supplementary crystallographic data for this paper. These data can be obtained free of charge from The Cambridge Crystallographic Data Centre via www.ccdc.cam.ac.uk/data_request/cif.

Supporting Information (see footnote on the first page of this article): Details of the DFT calculations on complex **4Ti**.

Acknowledgments

[1] For selected examples, see: a) A. K. Tomov, J. J. Chirinos, D. J. Jones, R. J. Long, V. C. Gibson, *J. Am. Chem. Soc.* **2005**, *127*, 10166–10167; b) R. D. Köhn, *Angew. Chem.* **2008**, *120*, 251–253; *Angew. Chem. Int. Ed.* **2008**, *47*, 245–247.

[2] U. Rosenthal, V. V. Burlakov, M. A. Bach, T. Beweries, *Chem. Soc. Rev.* **2007**, *36*, 719–728.

[3] O. Theilmann, M. Ruhmann, A. Villinger, A. Schulz, W. W. Seidel, K. Kaleta, T. Beweries, P. Arndt, U. Rosenthal, *Angew. Chem.* **2010**, *122*, 9469–9473; *Angew. Chem. Int. Ed.* **2010**, *49*, 9282–9285.

[4] K. Kaleta, M. Ruhmann, O. Theilmann, T. Beweries, S. Roy, P. Arndt, A. Villinger, E. D. Jemmis, A. Schulz, U. Rosenthal, *J. Am. Chem. Soc.* **2011**, *133*, 5463–5473.

[5] M. Lamac, A. Spannenberg, H. Jiao, S. Hansen, W. Baumann, P. Arndt, U. Rosenthal, *Angew. Chem.* **2010**, *122*, 2999–3002; *Angew. Chem. Int. Ed.* **2010**, *49*, 2937–2940.

[6] a) A. Ohff, S. Pulst, C. Lefeber, N. Peulecke, P. Arndt, V. V. Burlakov, U. Rosenthal, *Synlett* **1996**, 111–118; b) I. Marek, *Titanium and Zirconium in Organic Synthesis*, Wiley-VCH, Weinheim, **2002**; c) U. Rosenthal, V. V. Burlakov, P. Arndt, W. Baumann, A. Spannenberg, *Organometallics* **2003**, *22*, 884–900.

[7] M. Limmert, I.-P. Lorenz, J. Neubauer, H. Nöth, T. Habereder, *Eur. J. Inorg. Chem.* **2001**, 1593–1597.

[8] C. Mahabiersing, W. G. J. de Lange, K. Goubitz, D. J. Stufkens, *J. Organomet. Chem.* **1993**, *461*, 127–139.

[9] L. B. Kool, M. D. Rausch, H. G. Alt, M. Herberhold, B. Honold, U. Thewalt, *J. Organomet. Chem.* **1987**, *320*, 37–45.

[10] H. W. Roesky, B. Mainz, M. Noltemeyer, *Z. Naturforsch. Teil B* **1990**, *45*, 53–58.

[11] M. Herberhold, S. Gerstmann, B. Wrackmeyer, H. Borrmann, *J. Chem. Soc., Dalton Trans.* **1994**, 633–636.

[12] In complex **4Ti** the S atom is disordered over two positions in both molecules of the asymmetric unit. Therefore, the average value of four S–N distances is given here.

[13] The covalent radii were taken from: P. Pyykkö, M. Atsumi, *Chem. Eur. J.* **2009**, *15*, 12770–12779.

[14] T. Chivers, X. Gao, M. Parvez, *Inorg. Chem.* **1995**, *34*, 1681–1687.

[15] a) Y. Mugnier, C. Moise, E. Laviron, *J. Organomet. Chem.* **1981**, *204*, 61–66; b) Y. Mugnier, C. Moise, E. Laviron, *J. Organomet. Chem.* **1981**, *210*, 69–72; c) Y. Mugnier, A. Fakhr, M. Fauconet, C. Moise, E. Laviron, *Acta Chem. Scand., Ser. B* **1983**, *37*, 423–427.

[16] a) P. v. R. Schleyer, C. Maerker, A. Dransfeld, H. Jiao, N. J. R. v. E. Hommes, *J. Am. Chem. Soc.* **1996**, *118*, 6317–6318; b) P. v. R. Schleyer, H. Jiao, N. J. R. v. E. Hommes, G. V. Malkin, O. L. Malkina, *J. Am. Chem. Soc.* **1997**, *119*, 12669–12670; c) P. v. R. Schleyer, M. Manoharan, Z.-X. Wang, B. Kiran, H.

Jiao, R. Puchta, N. J. R. v. E. Hommes, *Org. Lett.* **2001**, *3*, 2465–2468.

[17] a) P. A. Seewald, G. S. White, D. W. Stephan, *Can. J. Chem.* **1988**, *66*, 1147–1152; b) V. M. Visciglio, P. E. Fanwick, I. P. Rothwell, *Acta Crystallogr., Sect. C* **1994**, *50*, 896–898; c) D. G. Dick, R. Rousseau, D. W. Stephan, *Can. J. Chem.* **1991**, *69*, 357–362; d) M. M. Olmstead, P. P. Power, M. Viggiano, *J. Am. Chem. Soc.* **1983**, *105*, 2927–2928.

[18] a) H. A. Jahn, E. Teller, *Proc. R. Soc. London, Ser. A* **1937**, *161*, 220–235; b) T. A. Albright, J. K. Burdett, M.-H. Whangbo, *Orbital Interactions in Chemistry*, part 1, Wiley, New York, **1985**, pp. 95–97.

[19] The planar structure **4Ti-TS** (which is a transition state with only one imaginary frequency) is obtained by optimisation and has small structural differences with the single-point planar complex **4Ti_1** at the BP86/BAS2 level of theory.

[20] Single-point calculations were performed for intermediate structures **4Ti_2** and **4Ti_2′**, because any effort to optimize these structures led to distorted complexes.

[21] V. V. Burlakov, U. Rosenthal, P. V. Petrovsky, V. B. Shur, M. E. Volpin, *Organomet. Chem. USSR* **1988**, *1*, 526–527.

[22] U. Rosenthal, A. Ohff, M. Michalik, H. Görls, V. V. Burlakov, V. B. Shur, *Angew. Chem.* **1993**, *105*, 1228–1230; *Angew. Chem. Int. Ed. Engl.* **1993**, *32*, 1193–1195.

[23] C. P. Warrens, J. D. Woollins, M. Witt, H. W. Roesky, "Silicon and Tin Sulfur-Nitrogen Compounds, $(Me_3Si)_2N_2S$, $(Me_3Sn)_2$-N_2S and $(Me_2Sn)S_2N_2$" in *Inorganic Syntheses*, vol. 25 (Ed.: H. R. Allcock), Wiley-Interscience, New York, **1989**, pp. 43–45.

[24] a) A. D. Becke, *J. Chem. Phys.* **1993**, *98*, 5648–5652; b) A. D. Becke, *Phys. Rev. A* **1988**, *38*, 3098–3100; c) C. Lee, W. Yang, R. G. Parr, *Phys. Rev. B* **1988**, *37*, 785–789.

[25] P. Perdew, *Phys. Rev. B* **1986**, *33*, 8822–8824.

[26] M. J. Frisch, G. W. Trucks, H. B. Schlegel, G. E. Scuseria, M. A. Robb, J. R. Cheeseman, J. A. Montgomery, Jr., T. Vreven, K. N. Kudin, J. C. Burant, J. M. Millam, S. S. Iyengar, J. Tomasi, V. Barone, B. Mennucci, M. Cossi, G. Scalmani, N. Rega, G. A. Petersson, H. Nakatsuji, M. Hada, M. Ehara, K. Toyota, R. Fukuda, J. Hasegawa, M. Ishida, T. Nakajima, Y. Honda, O. Kitao, H. Nakai, M. Klene, X. Li, J. E. Knox, H. P. Hratchian, J. B. Cross, V. Bakken, C. Adamo, J. Jaramillo, R. Gomperts, R. E. Stratmann, O. Yazyev, A. J. Austin, R. Cammi, C. Pomelli, J. W. Ochterski, P. Y. Ayala, K. Morokuma, G. A. Voth, P. Salvador, J. J. Dannenberg, V. G. Zakrzewski, S. Dapprich, A. D. Daniels, M. C. Strain, O. Farkas, D. K. Malick, A. D. Rabuck, K. Raghavachari, J. B. Foresman, J. V. Ortiz, Q. Cui, A. G. Baboul, S. Clifford, J. Cioslowski, B. B. Stefanov, G. Liu, A. Liashenko, P. Piskorz, I. Komaromi, R. L. Martin, D. J. Fox, T. Keith, M. A. Al-Laham, C. Y. Peng, A. Nanayakkara, M. Challacombe, P. M. W. Gill, B. Johnson, W. Chen, M. W. Wong, C. Gonzalez, J. A. Pople, *Gaussian 03, Revision D.01*, Gaussian, Inc., Wallingford, CT, **2004**; M. J. Frisch, G. W. Trucks, H. B. Schlegel, G. E. Scuseria, M. A. Robb, J. R. Cheeseman, G. Scalmani, V. Barone, B. Mennucci, G. A. Petersson, H. Nakatsuji, M. Caricato, X. Li, H. P. Hratchian, A. F. Izmaylov, J. Bloino, G. Zheng, J. L. Sonnenberg, M. Hada, M. Ehara, K. Toyota, R. Fukuda, J. Hasegawa, M. Ishida, T. Nakajima, Y. Honda, O. Kitao, H. Nakai, T. Vreven, J. A. Montgomery, Jr., J. E. Peralta, F. Ogliaro, M. Bearpark, J. J. Heyd, E. Brothers, K. N. Kudin, V. N. Staroverov, R. Kobayashi, J. Normand, K. Raghavachari, A. Rendell, J. C. Burant, S. S. Iyengar, J. Tomasi, M. Cossi, N. Rega, J. M. Millam, M. Klene, J. E. Knox, J. B. Cross, V. Bakken, C. Adamo, J. Jaramillo, R. Gomperts, R. E. Stratmann, O. Yazyev, A. J. Austin, R. Cammi, C. Pomelli, J. W. Ochterski, R. L. Martin, K. Morokuma, V. G. Zakrzewski, G. A. Voth, P. Salvador, J. J. Dannenberg, S. Dapprich, A. D. Daniels, Ö. Farkas, J. B. Foresman, J. V. Ortiz, J. Cioslowski, D. J. Fox, *Gaussian 09, Revision A.02*, Gaussian, Inc., Wallingford, CT, **2009**.

[27] a) P. J. Hay, W. R. Wadt, *J. Chem. Phys.* **1985**, *82*, 270–283; b) W. R. Wadt, P. J. Hay, *J. Chem. Phys.* **1985**, *82*, 284–298; c) P. J. Hay, W. R. Wadt, *J. Chem. Phys.* **1985**, *82*, 299–310.

[28] A. E. Reed, L. A. Curtiss, F. Weinhold, *Chem. Rev.* **1988**, *88*, 899–926.

[29] G. M. Sheldrick, *Acta Crystallogr., Sect. A* **2008**, *64*, 112–122.

[30] G. M. Sheldrick, *SADABS*, University of Göttingen, Göttingen, **2004**.

Iminoether Complexes of the Type, *fac*-[Re(CO)$_3$L{HNC(CH$_3$)OCH$_3$}]BF$_4$ (L = Bipyridine or a Substituted Bipyridine): Synthesis and Properties

Theshini Perera,[a] Pramuditha Abhayawardhana,[a] Frank R. Fronczek,[a] Patricia A. Marzilli,[a] and Luigi G. Marzilli*[a]

The methyl acetimidate (an iminoether) complexes, *fac*-[Re(CO)$_3$L{HNC(CH$_3$)OCH$_3$}]BF$_4$ [where L = 2,2′-bipyridine (bipy), 4,4′-Me$_2$bipy, 5,5′-Me$_2$bipy, or 6,6′-Me$_2$bipy], were formed when *fac*-[Re(CO)$_3$(CH$_3$CN)$_3$]BF$_4$ in acetonitrile/methanol was treated with 2,2′-bipyridine (bipy) or the dimethyl-2,2′-bipyridines (4,4′-Me$_2$bipy, 5,5′-Me$_2$bipy, or 6,6′-Me$_2$bipy). Structural analysis of the four *fac*-[Re(CO)$_3$-L{HNC(CH$_3$)OCH$_3$}]BF$_4$ complexes revealed that all of the complexes crystallize with the iminoether ligand in the Z configuration and that distortions in L that involved the two pyridyl rings are minor except for 6,6′-Me$_2$bipy, which is highly distorted. This distortion of the 6,6′-Me$_2$bipy ligand is reflected in the NMR-spectroscopic data. Upon complex formation, the methyl group signal in the ^{13}C NMR spectrum shifted downfield significantly for 6,6′-Me$_2$bipy, but this did not occur in the ^{13}C NMR spectrum of the 5,5′-Me$_2$bipy complex. The reaction times for forming the respective *fac*-[Re(CO)$_3$L{HNC(CH$_3$)OCH$_3$}]BF$_4$ complexes for these two ligands were comparable, which indicated that the differences in the distortion of L and the methyl substituent position have little influence on the ease of iminoether formation. However, a higher steric bulk of the alcohol (methanol, ethanol, and 2-propanol) decreases the ease of *fac*-[Re(CO)$_3$(5,5′-Me$_2$bipy){HNC(CH$_3$)OR}]BF$_4$ formation. Isopropanol did not form the iminoether complex after two days of heating the reaction mixture at reflux. The low reactivity of the alcohols tested versus the amines that were tested previously suggests that selective bioconjugation to the *fac*-{^{99m}Tc(CO)$_3$}$^+$ core through an amidine linkage is feasible for biomolecules that have both amine and hydroxy groups. Finally, a comparison of the C≡N bond lengths that were obtained for the *fac*-[Re(CO)$_3$(CH$_3$CN)$_3$]BF$_4$/PF$_6$ complexes with those values obtained for other rhenium acetonitrile complexes revealed that there is no significant difference between the C≡N bond lengths and that there is no correlation to the acetonitrile reactivity. It is possible that the *fac*-{Re(CO)$_3$}$^+$ core stabilizes the transition state for amine or alcohol addition.

Introduction

Our primary aim in the investigation of the synthesis and properties of complexes with a *fac*-{Re(CO)$_3$}$^+$ core is the development of renal imaging agents with a *fac*-{^{99m}Tc-(CO)$_3$}$^+$ core.[1–3] This approach has led to the development of *fac*-{^{99m}Tc(CO)$_3$}$^+$ renal agents that have shown promising pharmacokinetic properties in humans.[4,5] We have noted that there are some problems in utilizing water, which is the solvent that is used to prepare the common precursor, *fac*-[Re(CO)$_3$(H$_2$O)$_3$]$^+$.[1] In water, the various pH conditions lead to different linkage isomers or mixtures of isomers for the complicated ligands.[2,3] In addition, it is inconvenient to monitor the formation of the complexes by NMR-spectroscopic methods under aqueous reaction conditions. Therefore, in order to overcome the above mentioned aqueous chemistry problems, we evaluated the use

of organic solvents for the synthesis of the Re tricarbonyl compounds.[6–8] We chose 2,2′-bipyridine (bipy) and the substituted bipyridine ligands for our investigation because complexes that have the *fac*-[Re(CO)$_3$(bipy)]$^+$ fragment have been used previously by us[7,9] and by other investigators.[10–14]

Our recent work[6,7] indicates that the *fac*-[Re(CO)$_3$-(CH$_3$CN)$_3$]$^+$ complexes are useful synthons for the preparation of novel compounds where acetonitrile is used as the solvent.[6] However, acetonitrile is a coordinating solvent that inhibits the replacement of the coordinated acetonitrile by the added ligand. As a result, amidine formation occurs instead of simple ligand displacement. Although amidine formation does expand the scope of accessible chemistry, we decided to explore the use of methanol as the solvent instead. We expected that methanol would be weakly coordinating and would dissolve some of the ligands that are not so soluble in acetonitrile. Furthermore, we did not expect methanol to react with the coordinated nitriles to form iminoethers. In order for an alcohol (ROH) to react with the M–N≡CR′ group and produce an iminoether metal complex that has an M{HNC(R′)OR} group, the metal

[a] Department of Chemistry, Louisiana State University,
Baton Rouge, Louisiana 70803, USA
Fax: +1-225-578-3463
E-mail: lmarzil@lsu.edu
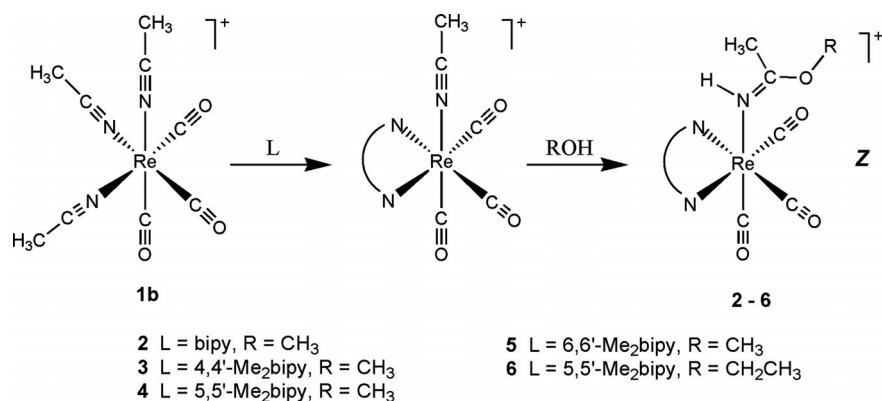
Scheme 1. Synthesis of [Re(CO)$_3$L{HNC(CH$_3$)OR}]BF$_4$ complexes (where L = bidentate bipy-type ligand and is denoted by N–N).

usually has to have at least a moderate positive oxidation state (M^{II} or M^{III}).[15] There are no reports of Re^I iminoether complexes. Thus, we explored the use of methanol as the solvent for the synthesis of the complexes with the bipy-type ligands by using *fac*-[Re(CO)$_3$(CH$_3$CN)$_3$]$^+$ as the starting material. We discovered, however, that Re^I complexes with the coordinated uncharged alkyl acetimidate iminoether ligand, HNC(CH$_3$)OR, formed readily (Scheme 1).

This discovery changed our focus from the exploration of alcohols as a solvent to assessment of the properties of the Re^I iminoether complexes. More specifically, we synthesized and characterized a series of *fac*-[Re(CO)$_3$L{HNC-(CH$_3$)OR}]BF$_4$ alkyl complexes [L = bipy or dimethyl-2,2′-bipyridine (Me$_2$bipy)] with a mixture of acetonitrile/alcohol as the solvent and where the starting complex had a coordinated acetonitrile. These complexes, the first examples of an iminoether ligand bound to a Re^I center, have provided the first evidence that the preferred configuration of the Re^I{HNC(CH$_3$)OR} group is *Z* and not *E* (Figure 1).
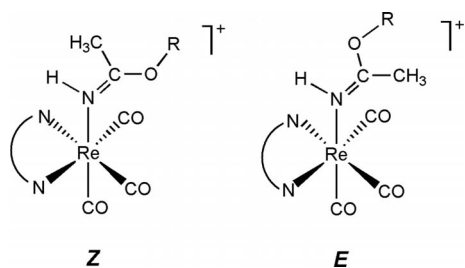
Figure 1. *Z* and *E* isomers of [Re(CO)$_3$L{HNC(CH$_3$)OR}]BF$_4$, where L is a bidentate ligand that is denoted by the N–N donor atoms.

In order to explore the possibility that steric bulk in the vicinity of the axial coordination site might influence the reaction of the coordinated acetonitrile or the properties of the coordinated alkyl acetimidate, one of the dimethyl-2,2′-bipyridine (Me$_2$bipy) ligands chosen was 6,6′-dimethyl-2,2′-bipyridine. We have not used the *fac*-designation in the rest of the paper because all of the new compounds have this geometry.

Results and Discussion

Synthesis

In a review,[15] Bokach et al. noted that the conditions required for the reaction of an alcohol with a coordinated nitrile depends substantially on the oxidation state of the metal and that basic conditions are required when the metal has a moderate oxidation state (e.g. Pt^{II},[16] Pd^{II},[17] Ni^{II},[18] Ir^{III},[19] and Cu^{II}[20]). For example, Natile and coworkers reported that the addition of alcohols to coordinated nitriles to form iminoether complexes of Pt^{II} takes place under basic conditions and that the iminoether ligand initially formed in the *Z* configuration and subsequently isomerized to the *E* configuration.[21]

Although the Re^I acetonitrile complexes we used have a low oxidation state, we discovered that, after the treatment of [Re(CO)$_3$(CH$_3$CN)$_3$]$^+$ with L to form [Re(CO)$_3$L(CH$_3$-CN)]$^+$, the Re^I iminoether complexes formed readily in methanol without the addition of base (Scheme 1). In order to assess whether or not the addition of methanol to the coordinated nitriles was facilitated by base catalysis, we investigated the synthesis of [Re(CO)$_3$(5,5′-Me$_2$bipy){HNC-(CH$_3$)OCH$_3$}]BF$_4$ by means of two reaction mixtures. One of the reactions had no base added and the other reaction had 1.34 mM KOH. These reactions were monitored by NMR spectroscopy and the results of the two reactions were compared with each other (Supporting Information). The added KOH did decrease the time required for the formation of [Re(CO)$_3$(5,5′-Me$_2$bipy){HNC(CH$_3$)OCH$_3$}]-BF$_4$, but the effect was small (the reaction was ca. two to five times faster). A similar comparison with the reactions in which no base was added for the formation of [Re(CO)$_3$-(6,6′-Me$_2$bipy){HNC(CH$_3$)OCH$_3$}]BF$_4$ and [Re(CO)$_3$(5,5′-Me$_2$bipy){HNC(CH$_3$)OCH$_3$}]BF$_4$ indicated that they formed with equal ease. Thus, neither the distortions in the coordinated 6,6′-Me$_2$bipy ligand nor the proximity of the methyl substituents in the coordinated acetonitrile affect the rate of the reaction.

Two Re^{IV} complexes that were suspected to have alkyl acetimidate ligands were reported in 1968 and were the only known Re compounds with a bound iminoether.[22] The

crystal structure of one, *cis*-[Re{HNC(CH$_3$)OCH$_3$}$_2$Cl$_4$], formed during an attempted crystallization of *cis*-[Re^{IV}(CH$_3$CN)$_2$Cl$_4$] in methanol, was reported recently.[23] This result is expected given the high oxidation state of the metal.

The ease of formation of the new iminoether complexes in this work may be attributed to π back-bonding into the carbonyl ligands with the result that Re^I behaves as if it has a higher oxidation state, which primes the nitrile towards reactions with nucleophiles. This ease of reaction may be a ground-state or a transition-state effect. The C≡N bond lengths of the acetonitrile that is bound in [Re(CO)$_3$-(CH$_3$CN)$_3$]PF$_6$ (**1a**) [1.135(5), 1.136(5), and 1.139(6) Å] and [Re(CO)$_3$L(CH$_3$CN)]BF$_4$ [1.141(4) and 1.138(3) Å for L = 5,5′-Me$_2$bipy and 6,6′-Me$_2$bipy, respectively, unpublished results][9] are similar to those of the free acetonitrile molecule (1.145 Å)[24] and of the acetonitrile that is coordinated in the *fac*-{Re(CO)$_3$} phosphane complexes.[25,26] However, these phosphane compounds have not been reported to form iminoether compounds, and such coordinated nitriles are not very reactive.[27] An alternative ground-state parameter that may be more informative is the C≡N stretching frequency. However, sufficient data are not available to assess this parameter. Thus, we cannot rule out the possibility that the transition-state energy for the formation of the activated complex that leads to the iminoether is particularly favorable for complexes that have the *fac*-{Re-(CO)$_3$} core.

Structural Results

The crystal data and details of the structural refinement of the *fac*-{Re(CO)$_3$} complexes are summarized in Table 1. The structures of the cations in [Re(CO)$_3$(CH$_3$CN)$_3$]PF$_6$ (**1a**) and [Re(CO)$_3$L{HNC(CH$_3$)OCH$_3$}]BF$_4$ (**2–5**) are shown in Figures S1 and S2 (see Supporting Information). The tetrafluoroborate salt **5** is a co-crystal with a 0.5 uncomplexed 6,6′-Me$_2$bipy ligand. The atom numbering system in Figure 2 is used to describe the solid-state data for the [Re(CO)$_3$L{HNC(CH$_3$)OCH$_3$}]BF$_4$ complexes. For the purposes of discussing the results, the coordination plane that is defined by Re, L, and the two CO *trans* to L will be called the equatorial plane. The other CO and the iminoether ligand are referred to as axial.

The methyl acetimidate ligand in the [Re(CO)$_3$L-{HNC(CH$_3$)OCH$_3$}]BF$_4$ complexes [L = bipy (**2**), 4,4′-Me$_2$-bipy (**3**), 5,5′-Me$_2$bipy (**4**), and 6,6′-Me$_2$bipy (**5**)] has a *Z* configuration in the solid state (Figures 1 and 2). The ethyl acetimidate ligand in [Re(CO)$_3$(5,5′-Me$_2$bipy){HNC-(CH$_3$)OCH$_2$CH$_3$}]BF$_4$ (Figure S2, Supporting Information) also has a *Z* configuration in the solid state.

In all of the [Re(CO)$_3$L{HNC(CH$_3$)OCH$_3$}]BF$_4$ structures (**2–5**, Figure 2), the Re–CO bond distances that are *cis* and *trans* to the methyl acetimidate ligand are not significantly different (not shown). Therefore, the methyl acetimidate ligand, which by analogy to the related amidine ligand could be considered a superbase,[7,28–30] has no *trans* influence. The Re–N (Figure 2) bond lengths of complexes **2–4** are comparable with typical Re sp^2 nitrogen bond lengths, which range from 2.14 to 2.18 Å.[1] However, the Re–N1 [2.211(3) Å] and Re–N2 [2.213(3) Å] bond lengths for **5** (L = 6,6′-Me$_2$bipy) are significantly longer than any of the other Re–N bonds in this study (Table 2). The long Re–N bond lengths to the 6,6′-Me$_2$bipy ligand can be attributed to the close proximity of the methyl substituents to the Re metal center and possibly to the highly distorted nature of the aromatic 6,6′-Me$_2$bipy ligand (see below). However, it should be noted that this distortion does not

Table 1. Crystal data and structural refinement for [Re(CO)$_3$(CH$_3$CN)$_3$]PF$_6$ and [Re(CO)$_3$L{HNC(CH$_3$)OCH$_3$}]BF$_4$.

	[Re(CO)$_3$(CH$_3$CN)$_3$]PF$_6$ (**1a**)	L = bipy (**2**)	L = 4,4′-Me$_2$bipy (**3**)	L = 5,5′-Me$_2$bipy (**4**)	L = 6,6′-Me$_2$bipy (**5**)
Empirical formula	C$_9$H$_9$N$_3$O$_3$Re·PF$_6$	C$_{16}$H$_{15}$N$_3$O$_4$Re·BF$_4$	C$_{18}$H$_{19}$N$_3$O$_4$Re·BF$_4$	C$_{18}$H$_{19}$N$_3$O$_4$Re·BF$_4$	C$_{18}$H$_{19}$N$_3$O$_4$Re·BF$_4$·0.5(C$_{12}$H$_{12}$N$_2$)
Fw	538.36	586.32	614.37	614.37	706.49
Space group	*P*2$_1$/*c*	*P*$\bar{1}$	*P*$\bar{1}$	*P*$\bar{1}$	*P*2$_1$/*c*
a [Å]	21.377(2)	7.9660(5)	8.5840(10)	8.0595(10)	8.3297(15)
b [Å]	11.7351(10)	8.8627(9)	10.7182(12)	10.4344(15)	30.840(6)
c [Å]	13.1044(13)	14.0474(10)	12.0096(12)	14.073(2)	10.857(2)
α [°]	90	74.602(4)	88.618(5)	111.599(5)	90
β [°]	95.554(5)	75.616(4)	85.671(6)	92.698(7)	111.791(8)
γ [°]	90	86.773(4)	78.227(5)	102.352(7)	90
V [Å^3]	3272.0(5)	926.13(13)	1078.6(2)	1064.5(3)	2589.7(8)
T [K]	90	90	90	90	90
Z	8	2	2	2	4
ρ_{calc} [Mg·m^{-3}]	2.186	2.103	1.892	1.917	1.812
Abs. coeff. [mm^{-1}]	7.60	6.63	5.70	5.77	4.76
$2\theta_{max}$ [°]	61.0	81.4	72.6	71.4	65.8
R indices [a]	0.033	0.023	0.025	0.023	0.035
$wR_2 = [I > 2\sigma(I)]$ [b]	0.078	0.053	0.060	0.056	0.078
Data/parameters	9942/477	11737/296	10039/288	9553/288	9081/348

[a] $R = (\Sigma||F_o| - |F_c||)/\Sigma|F_o|$. [b] $wR_2 = \{\Sigma[w(F_o^2 - F_c^2)^2]/\Sigma[w(F_o^2)^2]\}^{1/2}$ where $w = 1/[\sigma^2(F_o^2) + (dP)^2 + (eP)]$ and $P = (F_o^2 + 2F_c^2)/3$, $d = 0.0388, 0.0104, 0.0167, 0.0203$, and 0.0274 and $e = 4.4179, 2.0041, 2.412, 1.2932$, and 4.5142 for [Re(CO)$_3$(CH$_3$CN)$_3$]PF$_6$ and [Re(CO)$_3$L{HNC(CH$_3$)OCH$_3$}]BF$_4$ where L = bipy, 4,4′-Me$_2$bipy, 5,5′-Me$_2$bipy, and 6,6′-Me$_2$bipy, respectively.
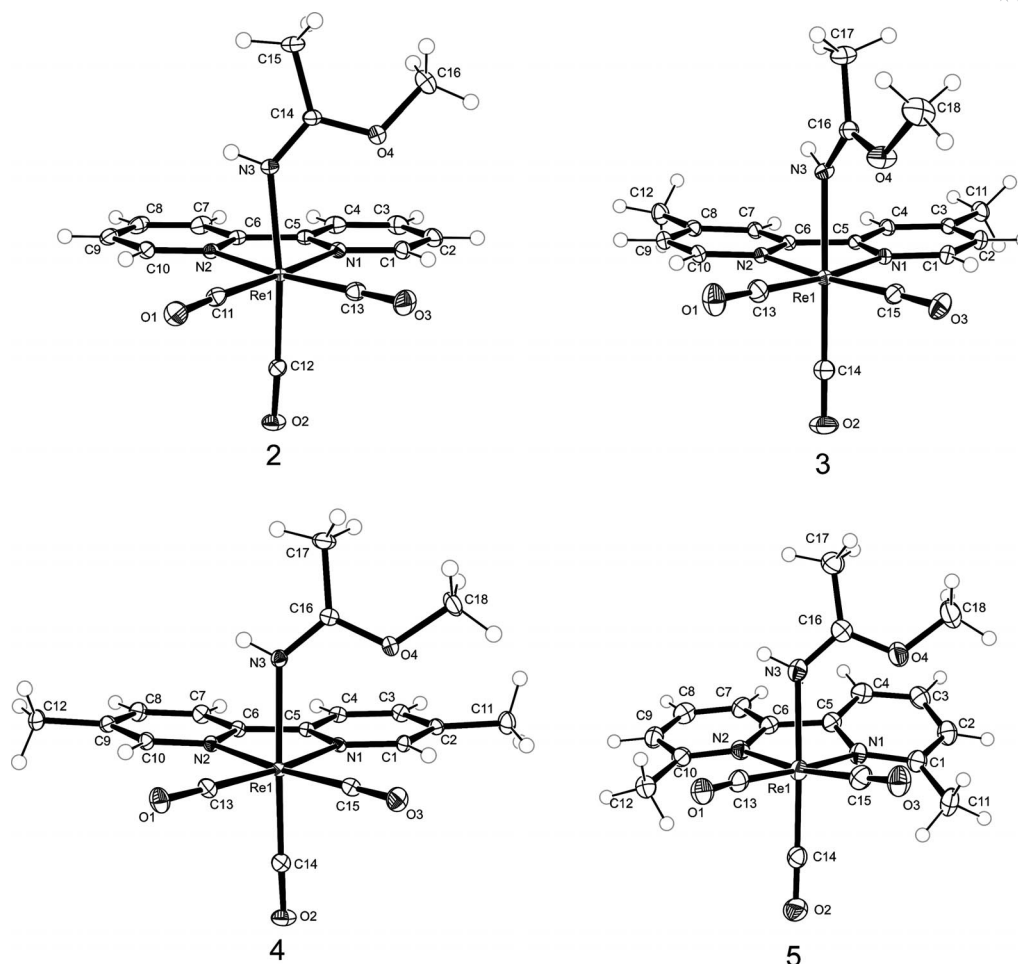
Figure 2. ORTEP plots of the cations of [Re(CO)$_3$(bipy){HNC(CH$_3$)OCH$_3$}]BF$_4$ (**2**), [Re(CO)$_3$(4,4′-Me$_2$bipy){HNC(CH$_3$)OCH$_3$}]BF$_4$ (**3**), [Re(CO)$_3$(5,5′-Me$_2$bipy){HNC(CH$_3$)OCH$_3$}]BF$_4$ (**4**), and [Re(CO)$_3$(6,6′-Me$_2$bipy){HNC(CH$_3$)OCH$_3$}]BF$_4$·0.5(6,6′-Me$_2$bipy) (**5**). The thermal ellipsoids are drawn at 50% probability.

affect the Re–N3 (methyl acetimidate) bond length, which is not significantly different in compounds **2–5**, thus, the Re–N3 (methyl acetimidate) bond length is independent of the position of the Me$_2$bipy methyl substituents. These Re–N3 (methyl acetimidate) bond lengths are not significantly different from the related Re–N3 (amidine) bond lengths in,

for example, [Re(CO)$_3$(5,5′-Me$_2$bipy){HNC(CH$_3$)NHCH-(CH$_3$)$_2$}]BF$_4$ [2.1810(18) Å] and [Re(CO)$_3$(5,5′-Me$_2$bipy)-{HNC(CH$_3$)NHCH$_2$CH(CH$_3$)$_2$}]BF$_4$ [2.174(3) Å].[7]

The Re–N bond length[23] of *cis*-[Re^{IV}{HNC(CH$_3$)-OCH$_3$}$_2$Cl$_4$], which has the methyl acetimidate ligand in the *Z* configuration and is the only previously reported molecu-

Table 2. Selected bond lengths [Å] and angles [°] for [Re(CO)$_3$L{HNC(CH$_3$)OCH$_3$}]BF$_4$.

| L | bipy | 4,4′-Me$_2$bipy | 5,5′-Me$_2$bipy | 6,6′-Me$_2$bipy |
	2	**3**	**4**	**5**
Bond lengths				
Re–N1	2.1767(14)	2.1750(18)	2.1778(16)	2.211(3)
Re–N2	2.1721(14)	2.1786(18)	2.1706(17)	2.213(3)
Re–N3	2.1705(15)	2.1771(18)	2.1860(18)	2.175(3)
N3–C16	1.288(2)[a]	1.279(3)	1.285(3)	1.294(4)
C16–O4	1.331(2)[a]	1.327(3)	1.337(3)	1.331(4)
Bond angles				
N1–Re–N2	75.21(5)	74.44(7)	75.08(6)	75.19(10)
N1–Re–N3	86.72(5)	82.55(7)	81.49(6)	83.33(11)
N2–Re–N3	80.33(5)	81.66(7)	80.72(6)	80.38(10)
C16–O4–C18	118.33(16)[a]	120.2(2)	120.21(17)	119.6(3)
N3–C16–O4–C18	171.67(18)[a]	176.2(2)	177.55(18)	174.4(3)

[a] C16 = C14; C18 = C16.

lar structure that contains a Re–N (iminoether) bond, is 2.084(5) Å. This bond is much shorter than the Re–N (iminoether) bond lengths that were found for the new complexes (Table 2), which were as expected because the bonds to Re^I are usually long.

The plane of the iminoether group that is defined by the N3, C16, and O4 atoms of the methyl and ethyl acetimidate ligands is shown for five of the structures in Figures 3 and S3 (Supporting Information). The projection of this iminoether plane into the equatorial plane bisects the two N–Re–C angles in the equatorial plane in four of the structures. However, for [Re(CO)$_3$(4,4′-Me$_2$bipy){HNC(CH$_3$)-OCH$_3$}]BF$_4$ (**3**), in which the iminoether group lies over one of the equatorial Re–CO groupings, this iminoether plane is rotated by about 45° from the position of this plane in the other complexes. Very weak hydrogen bonding (not shown) between the N3H and F1 of the BF$_4^-$ anion in **3** (L = 4,4′-Me$_2$bipy) accounts for this difference, thus, we conclude that the orientation of the methyl acetimidate ligand does not depend on the bipy bulk.
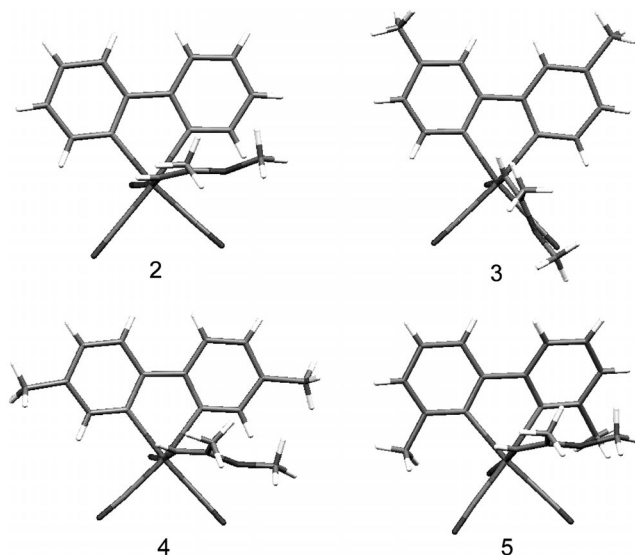
Figure 3. View of the [Re(CO)$_3$L{HNC(CH$_3$)OCH$_3$}]BF$_4$ structures oriented with the aromatic rings in the plane of the paper and the methyl acetimidate ligand projected towards the viewer. L = bipy (**2**), 4,4′-Me$_2$bipy (**3**), 5,5′-Me$_2$bipy (**4**), and 6,6′-Me$_2$bipy (**5**).

In order to further illustrate the foregoing points, the molecular structures of **2** (L = unsubstituted bipy ligand) and **5** (L = 6,6′-Me$_2$bipy) are compared in Figures 4 and S4 (Supporting Information). It is evident from these figures that the orientation of the iminoether plane in **2** is similar to that in **5**. The 6,6′-Me$_2$bipy plane in **5** must lie out of the equatorial ReC$_2$N$_2$ coordination plane so that clashes between the equatorial CO ligands and the methyl groups can be minimized. The bulk that is associated with the 6,6′-Me$_2$bipy methyl groups is projected towards the smaller axial CO ligand and away from the larger axial iminoether ligand. As a result, the steric repulsions with the

equatorial plane are decreased, as is clearly shown in Figure 4 (left view). The Re–N3 (methyl acetimidate) bond is further away from the equatorial bipy ligand in **2** than from 6,6′-Me$_2$bipy in **5**. The N1–Re–N3 angle is significantly larger the N2–Re–N3 angle in all of the compounds in Table 2 (see Figure 2 for atom numbering) and can be attributed to the clash of the methoxy group with L. More severe clashes of the methyl group with L would occur if the *E* isomer formed.
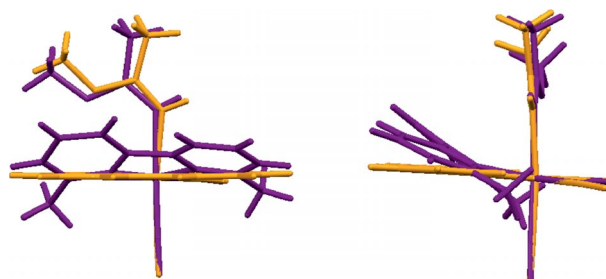
Figure 4. Overlay of Re, O1, O2, and O3 atoms of the carbonyl ligands of [Re(CO)$_3$(bipy){HNC(CH$_3$)OCH$_3$}]BF$_4$ (gold) and [Re(CO)$_3$(6,6′-Me$_2$bipy){HNC(CH$_3$)OCH$_3$}]BF$_4$ (purple). The structures are depicted with the equatorial coordination plane of the bipy complex (**2**) perpendicular to the plane of the paper (r.m.s. = 0.097).

For complexes **2**–**5** (Figure 2 and Table 2), the C16–N3 bond length in the iminoether group has a value typical of an sp^2 C=N bond with double-bond character (ca. 1.28 Å), whereas the C16–O4 bond length is close to the average sp^2 C–O single bond length (1.34 Å).[31] For example, in [Re(CO)$_3$(5,5′-Me$_2$bipy){HNC(CH$_3$)OCH$_3$}]BF$_4$ (**4**) these bond lengths are 1.285(3) Å (C16–N3) and 1.337(3) Å (C16–O4). In the related amidine complexes, for example, [Re(CO)$_3$(5,5′-Me$_2$bipy){HNC(CH$_3$)NHCH(CH$_3$)$_2$}]BF$_4$, the corresponding bond lengths are 1.308(3) Å (C16–N3, where N3 is the nitrogen atom that is bound to Re in both the amidine and iminoether compounds) and 1.339(3) Å [C16–NHCH(CH$_3$)$_2$].[7] Thus, the bond lengths alone provide sufficient support that there is electron delocalization centered at C16. In complexes **2**–**5**, extensive delocalization is not as clearly reflected in both of the bond lengths. Nevertheless, the C16–O4–C18 angle is close to 120° (Table 2). As Natile and coworkers have remarked in their study of iminoether Pt^{II} complexes,[21] an angle such as this that is close to the sp^2 value supports the presence of resonance (oxygen donates a lone pair of electrons into a delocalized O–C–N system). This argument has also been proposed for Ir^{III} complexes that bear an iminoether ligand.[19] Resonance may also explain the quasiplanarity of the iminoether group, as seen by the N–C–O–C torsion angles that range from 171.67(18)° to 177.55(18)° (Table 2).

In our study of the amidine complexes, [Re(CO)$_3$(5,5′-Me$_2$bipy){HNC(CH$_3$)NHR}]BF$_4$ (R = methyl, isopropyl, isobutyl, *tert*-butyl, and benzyl),[7] we noted that, in the delocalized N–C–N system of the monodentate amidine ligands, the C–N bond length, which involved the N bound

to Re, was only slightly shorter than the other C–N bond in the amidine ligand. These bond lengths reflect the relative ease of rotation about the N–C bonds (see below), which are necessary for the interconversion between the different configurations about the N–C bonds in the amidine complexes. However, only the E' isomer (Figure S3, Supporting Information)[7] was found in the crystals of the above amidine complexes.[7] When R = H, as in [Re(CO)$_3$-(5,5′-Me$_2$bipy){HNC(CH$_3$)NH$_2$}]BF$_4$, the Z isomer crystallized.[7] As noted above, the iminoether ligand in all of the [Re(CO)$_3$L{HNC(CH$_3$)OCH$_3$}]BF$_4$ structures in this study have the Z configuration. The Z configuration is sterically favored because the OCH$_3$ group of the methyl acetimidate ligand is less bulky than the CCH$_3$ group, but the NHR group of the amidine ligands is more bulky than the CH$_3$ group and hence the E configuration is favored.[7]

Although our studies have employed octahedral complexes, our findings parallel the results that were found for the square-planar iminoether Pt^{II} complexes that were studied by Natile and coworkers.[21] These investigators found that the large steric bulk of the alcohol-derived R group stabilized the E over the Z isomer, and that by increasing the steric bulk of the nitrile-derived R′ group the Z isomer was stabilized over the E isomer.[21] Although the configuration favored by the iminoether group differs between the square-planar Pt^{II} complexes and the octahedral Re^{I} complexes, the steric effects appear to be the controlling factor.

Although the steric effects appear to control the iminoether configuration, the partial negative charge of the iminoether oxygen, in addition to its small size, may also favor the Z configuration in the [Re(CO)$_3$L{HNC(CH$_3$)OCH$_3$}]-BF$_4$ compounds. The weak, but favorable, electrostatic attraction that exists between the partial negative charge of the oxygen atom and the partial positive charge of the hydrogen atoms of the bipyridine ligands favors the Z configuration. In most of the compounds, the separation between these atoms is ca. 3 Å. Evidence that is in favor of this attraction of the iminoether oxygen for the L hydrogen atoms has been found in the structure of an analogous methyl acetimidate complex, which has a pyridyltriazine ligand in place of the bipyridine ligand (unpublished work). This unsymmetrical aromatic bidentate L[32,33] has a pyridyl C6 H on one side, and a nitrogen that has no hydrogen atoms attached to it on the other side. The methyl acetimidate oxygen lies over the C6 H, and the iminoether adopts an orientation that is very close to that shown in this paper in Figures 2 and 3.

Our structural characterization of several closely related bipyridine complexes, in which only the position of the methyl substituent on the bipyridine moiety varied, provides an excellent opportunity to evaluate distortions in the planarity of the bipyridine ligands. The widespread usage of bipyridine ligands has provided a relatively large, almost unique database that spans numerous different metal centers and several geometries. This situation has generated much interest.[34–36] Bipyridines in metal complexes that have M–N distances within the typical range (ca. 2.0–2.2 Å) are not planar.[37,38] Re^{I} has relatively long M–N distances at the upper end of this range, which is less common, and thus the assessment of these structures can contribute to this well studied and interesting area. Earlier studies from our laboratory focused on the effects of ligand bulk in the [PtLCl$_2$] complexes where L is bipy or Me$_2$bipy.[34] These [PtLCl$_2$] complexes have typical M–N bond lengths [Pt–N bond lengths ranged from 2.017(3) to 2.032(3) Å].[34,39] For the alkyl acetimidate complexes, the Re–N bond lengths varied from 2.1706(17) to 2.1786(18) Å, with the notable exception of [Re(CO)$_3$(6,6′-Me$_2$bipy){HNCC(CH$_3$)-OCH$_3$}]BF$_4$, in which the Re–N bond lengths are about 2.21 Å (as discussed above).

The out-of-plane distortions of the bipyridine ligands in the complexes can be described by several parameters, namely, bowing (θ_B), twisting (θ_T), and S-shaped deformation (d_s).[38] Among the Re^{I} alkyl acetimidate complexes studied here (Table 3), [Re(CO)$_3$(6,6′-Me$_2$bipy){HNC-(CH$_3$)OCH$_3$}]BF$_4$ is the most distorted, with an exceptionally large twist angle (θ_T = 12.4°) and a large bow angle (θ_B = 11.0°). [Re(CO)$_3$(6,6′-Me$_2$bipy){HNC(CH$_3$)OCH$_3$}]BF$_4$ also has the largest dihedral angle (θ_{di} = 16.7°) of the acetimidate complexes that are reported in this paper. These distortions probably arise from steric repulsion between the methyl groups at the 6,6′ positions and the carbonyl ligands. Among the [PtLCl$_2$] complexes, [Pt(6,6′-Me$_2$bipy)-Cl$_2$] shows the highest θ_{di} (20.2°).[34] Thus, regardless of whether the complex is a square-planar Pt^{II} or an octahedral Re^{I} complex, the 6,6′-Me$_2$bipy complex has the highest dihedral angle.

Hazel noted that the in-plane bending (θ_P) decreased with an increase in the M–N length.[38] This relationship of a decrease in the θ_P with an increase in the M–N length is most evident (Tables 2 and 3) when the θ_P of the other complexes in this study (all of which have very similar Re–N lengths) are compared with the θ_P for [Re(CO)$_3$(6,6′-Me$_2$bipy){HNC(CH$_3$)OCH$_3$}]BF$_4$, which has slightly longer Re–N lengths and the smallest θ_P value (4.0°).

Table 3. Ligand deformation in [Re(CO)$_3$L{HNC(CH$_3$)OCH$_3$}]BF$_4$ (L = bipyridine ligand).[a]

Compound	Twist angle (θ_T)	Bow angle (θ_B)	S-shaped distortion (d_s)	In-plane distortion (θ_P)	Dihedral angle (θ_{di})
[Re(CO)$_3$(bipy){HNC(CH$_3$)OCH$_3$}]BF$_4$	0.1	1.9	0.022	6.6	1.9
[Re(CO)$_3$(4,4′-Me$_2$bipy){HNC(CH$_3$)OCH$_3$}]BF$_4$	2.0	4.3	0.014	6.8	4.7
[Re(CO)$_3$(5,5′-Me$_2$bipy){HNC(CH$_3$)OCH$_3$}]BF$_4$	0.6	5.8	0.005	8.0	5.8
[Re(CO)$_3$(6,6′-Me$_2$bipy){HNC(CH$_3$)OCH$_3$}]BF$_4$	12.4	11.0	0.087	4.0	16.7

[a] The d_s (in Å) and θ_T, θ_B, θ_P, and θ_{di} values (in degrees) were calculated by using a Fortran program that was provided by Dr. Alan Hazell. The θ_{di} values that were calculated by using SHELXL97[44] agreed with those from the Fortran program.

NMR Spectroscopy

There is no ^{1}H NMR-spectroscopic evidence of other iminoether isomers in several solvents (CDCl$_3$, [D$_6$]dmso, and [D$_3$]acetonitrile). In most cases the ^{1}H NMR spectra were recorded immediately or at least within 15 min of dissolution, and no spectral changes were observed even after several days. The more downfield position of the N3 H signal of the iminoether group for a given compound in [D$_6$]dmso (8.6–8.7 ppm) compared to that of the same signal in CDCl$_3$ or [D$_3$]acetonitrile (7.2–7.6 ppm) was attributed to the hydrogen bonding of the [D$_6$]dmso to the N3 H, which projects out towards the solvent (Figure 2). In order to assess this explanation, we conducted an experiment that we have used previously.[6,40,41] When Cl$^-$ was added to solutions of the *fac*-[Re(CO)$_3$L]$^+$ complexes, the downfield shift changes ($\Delta\delta$) for the NH signals were smaller for those NH groups that were directed towards the solvent compared to the $\Delta\delta$ for those NH groups that were directed away from the solvent.[6,40] When Cl$^-$ was added to a [D$_6$]-dmso solution of [Re(CO)$_3$(5,5′-Me$_2$bipy){HNC(CH$_3$)-OCH$_3$}]BF$_4$ (**4**), the downfield N3 H signal shifted only slightly further downfield ($\Delta\delta$ ca. 0.21 ppm), a finding that is consistent with the exposure of this proton to the solvent.[6,40,41] The half-life for the exchange reaction of the N3 H to N3 D on addition of D$_2$O (pH 6.5, 100 μL) to **4** (5 mM, 550 μL [D$_6$]dmso) was ca. 40 min. For a similar solution of **4** but one that contained 67% pH 6.5 D$_2$O, the NMR-spectroscopic data indicated that neither isomerization nor decomposition had occurred after 72 h.

For the [Re(CO)$_3$(5,5′-Me$_2$bipy){HNC(CH$_3$)NHR}]BF$_4$ complexes, three (*E*, *E*′, and *Z*, Supporting Information) of the four conceivable isomers were observed in the less polar CDCl$_3$ solvent, but only two isomers (*E*′ and *Z*) were observed in the more polar [D$_3$]acetonitrile solvent.[7] The isomer interchange follows the pathway that goes from the *Z* isomer to the *E* isomer to the *E*′ isomer. The exchange reaction between the *E* and *E*′ isomers was fast enough to give exchange spectroscopy (EXSY) cross-peaks, even though the exchange reaction between the *E*′ and *Z* isomers was slow.[7] The C16–N3 bond length (the rhenium-bound N) is shorter for the iminoether complexes (ca. 1.28 Å) than for the amidine complexes (ca. 1.31 Å). Thus, the double bond character of this bond is higher in the iminoether ligands (Table 2) than in the amidine ligands. Because the *E* to *Z* interchange, which requires rotation about the C16–N3 bond, is slow in the amidine complexes, the NMR spectrum changes slowly after the crystals of the amidine complexes are dissolved. The absence of any similar time-dependent spectral changes from the NMR spectra recorded immediately after the crystals of the iminoether complex were dissolved strongly indicates that the *E* isomer is not present in solution and that the *Z* isomer that is found in the solid state for all of the compounds dominates under all conditions.

In addition to the assignments for **4** and **5** by the 2D NMR experiments described above, the ^{1}H NMR signals for **4** were also assigned by using NOESY and COSY spectra (not shown). The ^{1}H NMR signals of **2** and **3** were assigned by using the splitting patterns and by analogy to the spectra for the Pt complexes.[34] The 1D ^{13}C NMR spectra were acquired over the course of an hour and the heteronuclear single quantum correlation (HSQC) and heteronuclear multiple bond correlation (HMBC) spectra were recorded over 8 h. The spectra that were obtained immediately upon dissolution of **4** and **5** in CDCl$_3$ are consistent with the presence of only one isomer in solution. As described in Supporting Information, the ^{1}H and ^{13}C NMR-spectroscopic signals of complexes **4** and **5** were assigned unambiguously by using the HSQC and HMBC cross-peaks (Table 4 and Experimental Section).

Table 4. ^{13}C NMR shifts [ppm] of the free Me$_2$bipy ligands and [Re(CO)$_3$L{HNC(CH$_3$)OCH$_3$}]BF$_4$ in CDCl$_3$ at 25 °C.[a]

| Carbon atom | 5,5′-Me$_2$bipy | | 6,6′-Me$_2$bipy | |
	free ligand	iminoether complex	free ligand	iminoether complex
6,6′	149.4	152.7	157.8	162.8
5,5′	132.9	138.0	122.9	127.1
4,4′	137.3	140.5	136.8	139.9
3,3′	120.1	123.6	118.0	122.5
2,2′	153.7	153.7	155.8	157.6
L-CH$_3$	18.2	18.5	24.6	30.4
Iminoether		177.3		177.6
C-CH$_3$		18.6		18.6
O-CH$_3$		57.2		57.7

[a] The free ligand values are from the 1D ^{13}C NMR spectra. The signal assignments for the free ligands were made by using values that are predicted in Supporting Information. The assignments for the complexes are discussed in Supporting Information. The carbonyl signals (observed as very weak, possibly overlapping signals at ca. 194 ppm) were not assigned.

The signals of the pyridyl *ortho* and *para* carbons are downfield compared to the signals of the pyridyl *meta* carbons in both the free and the rhenium-bound ligands, as was expected from previous NMR-spectroscopic studies.[42,43] However, all of the ^{13}C NMR-spectroscopic signals of the bipyridine rings shifted further downfield when the ligand was coordinated to Re. This was expected because the electron density in the ligand decreases upon coordination.

The downfield shift of the methyl ^{13}C NMR-spectroscopic signal with respect to that of the free Me$_2$bipy ligand is significantly greater for the 6,6′-Me$_2$bipy complex (δ =5.8 ppm) than for the 5,5′-Me$_2$bipy complex (δ =0.3 ppm). This most likely reflects the greater inductive effect of Re^I on the closer 6/6′ methyl group. However, the distortions induced in the coordinated 6,6′-Me$_2$bipy ligand may also contribute to the large shift change.

Conclusions

In contrast to the *fac*-[Re(CO)$_3$(5,5′-Me$_2$bipy)(amidine)]-BF$_4$ analogues, in which the amidine ligand favors the *E*′ configuration, the *fac*-[Re(CO)$_3$L{HNC(CH$_3$)OCH$_3$}]BF$_4$ complexes favor the *Z* configuration. We concluded that the main reason for this difference is the smaller size of the

iminoether oxygen atom compared to the larger amidine NH group. However, a second factor that influences the favored configuration is probably the attractive interactions between this iminoether oxygen atom and the bipyridine hydrogen atoms as opposed to the repulsive interactions that exist between the hydrogen atoms on the amidine and bipyridine ligands.

The iminoether is a superbase. However, there is no evidence that it has a *trans* influence. Nevertheless, we conclude that the iminoether ligand is strongly bound because, even in the *fac*-[Re(CO)$_3$(6,6′-Me$_2$bipy){HNC(CH$_3$)OCH$_3$}]BF$_4$ complex, the axial Re–N bond is not elongated.

Experimental Section

General Methods: Re(CO)$_5$Br was synthesized as described in the literature.[45] Re$_2$(CO)$_{10}$, 2,2′-bipyridine, 4,4′-dimethyl-2,2′-bipyridine (4,4′-Me$_2$bipy), 5,5′-dimethyl-2,2′-bipyridine (5,5′-Me$_2$bipy), 6,6′-dimethyl-2,2′-bipyridine (6,6′-Me$_2$bipy), AgPF$_6$, and AgBF$_4$ were obtained from Aldrich. [Re(CO)$_3$(CH$_3$CN)$_3$]PF$_6$ and [Re(CO)$_3$(CH$_3$CN)$_3$]BF$_4$ were synthesized by a slight modification of a known procedure[46] (see below). The ^{1}H and ^{13}C NMR spectra were recorded with a Bruker NMR spectrometer (400 MHz). The ^{13}C NMR-spectroscopic shifts are relative to CDCl$_3$ with TMS as the reference and were taken from the 1D NMR experiments. The ^{1}H NMR-spectroscopic peak positions are relative to TMS or the solvent residual peak (with TMS as the reference). The HSQC and HMBC 2D NMR spectra were recorded in order to assign the ^{1}H and ^{13}C NMR-spectroscopic signals. All of the NMR-spectroscopic data were processed with TopSpin and Mestre-C software.

[Re(CO)$_3$(CH$_3$CN)$_3$]PF$_6$ (1a): [Re(CO)$_3$(CH$_3$CN)$_3$]PF$_6$ was synthesized by a slight modification of a known procedure,[46] namely by using AgPF$_6$ instead of AgClO$_4$. X-ray quality crystals were obtained from an acetonitrile/isopropyl ether solution. ^{1}H NMR (400 MHz, CDCl$_3$): δ = 2.52 (s, 3 H, CH$_3$) ppm; ([D$_6$]dmso): δ = 2.65 (s, 3 H, CH$_3$) ppm; ([D$_6$]acetone): δ = 2.66 (s, 3 H, CH$_3$) ppm; ([D$_3$]acetonitrile): δ = 2.43 (s, 3 H, CH$_3$) ppm.

[Re(CO)$_3$(CH$_3$CN)$_3$]BF$_4$ (1b): [Re(CO)$_3$(CH$_3$CN)$_3$]BF$_4$ was produced by using the same procedure as **1a** but by using AgBF$_4$ instead of AgPF$_6$. The ^{1}H NMR spectrum was identical to that obtained for [Re(CO)$_3$(CH$_3$CN)$_3$]PF$_6$. Two polymorphs of [Re(CO)$_3$(CH$_3$CN)$_3$]BF$_4$ crystallized from the acetonitrile/isopropyl ether solution. One of the crystal structures, based on room temperature data, has been previously reported.[48]

Synthesis of the [Re(CO)$_3$L{HNC(CH$_3$)OCH$_3$}]BF$_4$ Complexes: In all of the experiments to form the [Re(CO)$_3$L{HNC(CH$_3$)OCH$_3$}]BF$_4$ complexes, including those that assessed the effects that changing L or adding KOH (see below) had on the reaction times, 10 mM solutions of the Re complexes in various solvents were used. Method A involved heating a benzene solution (10 mL) of [Re(CO)$_3$(CH$_3$CN)$_3$]BF$_4$ (0.1 mmol, 48 mg) and L (0.1 mmol) at reflux for 16 h. The solvent was removed by rotary evaporation and the resulting solid was dissolved in acetonitrile (ca. 1 mL). Diethyl ether (ca. 25 mL) was then added to give [Re(CO)$_3$L(CH$_3$CN)]BF$_4$ as a crystalline residue, which was washed with diethyl ether, dried, and then dissolved in an acetonitrile/methanol mixture (10 mL, 1:1). After the solution was heated at reflux for 24 h, the resulting solution was cooled to room temperature and dried by rotary evaporation. The residue was dissolved in acetonitrile and diethyl ether was

added to produce an orange precipitate, which was collected by filtration, washed with diethyl ether, and dried. Method A resulted in high yields of the [Re(CO)$_3$L{HNC(CH$_3$)OCH$_3$}]BF$_4$ complexes as a crystalline powder. In method B, which was employed to obtain X-ray quality crystals, an acetonitrile solution (10 mL) of [Re(CO)$_3$(CH$_3$CN)$_3$]BF$_4$ (0.1 mmol, 48 mg) and L (0.1 mmol) was stirred at room temperature and then heated at reflux for 2 to 3 d. The NMR spectra indicated that this time was sufficient to ensure that all of the free L was consumed. An equal volume of methanol was then added to give an ca. 5 mM solution. The resulting clear solution was heated at reflux for 1 d and on slow evaporation of the solvent yielded X-ray quality crystals of the [Re(CO)$_3$L{HNC(CH$_3$)OCH$_3$}]BF$_4$ complexes. The yields reported below are based on [Re(CO)$_3$(CH$_3$CN)$_3$]BF$_4$ (0.1 mmol, 48 mg).

[Re(CO)$_3$(bipy){HNC(CH$_3$)OCH$_3$}]BF$_4$ (2): Method A afforded **2** as an orange precipitate (39 mg, 63%). Method B afforded X-ray quality crystals (21 mg, 36%). The ^{1}H NMR spectrum of the crystals (Method B) in CDCl$_3$ was identical to that of the precipitate obtained in Method A. ^{1}H NMR (400 MHz, CDCl$_3$): δ = 8.90 (d, H6/6′), 8.37 (d, H3/3′), 8.16 (t, H4/4′), 7.62 (b, NH), 7.56 (t, H5/5′), 3.92 (s, OCH$_3$), 2.17 (s, CCH$_3$) ppm.

[Re(CO)$_3$(4,4′-Me$_2$bipy){HNC(CH$_3$)OCH$_3$}]BF$_4$ (3): Method A afforded **3** as an orange precipitate (38 mg, 62%). Method B afforded X-ray quality crystals (21 mg, 34%). ^{1}H NMR (400 MHz, CDCl$_3$): δ = 8.69 (d, H6/6′), 8.14 (s, H3/3′), 7.41 (b, NH), 7.33 (d, H5/5′), 3.90 (s, OCH$_3$), 2.59 (s, 4/4′-CH$_3$), 2.14 (s, CCH$_3$) ppm.

[Re(CO)$_3$(5,5′-Me$_2$bipy){HNC(CH$_3$)OCH$_3$}]BF$_4$ (4): Method A afforded **4** as an orange precipitate (41 mg, 67%). Method B produced X-ray quality crystals (23 mg, 37%). ^{1}H NMR (400 MHz, CDCl$_3$): δ = 8.65 (s, H6/6′), 8.17 (d, H3/3′), 7.91 (d, H4/4′), 7.51 (b, NH), 3.92 (s, OCH$_3$), 2.50 (s, 5/5′-CH$_3$), 2.17 (s, CCH$_3$) ppm.

[Re(CO)$_3$(6,6′-Me$_2$bipy){HNC(CH$_3$)OCH$_3$}]BF$_4$·0.5(6,6′-Me$_2$bipy) (5): Method A afforded **5** as an orange precipitate (39 mg, 63%). Method B produced X-ray quality crystals (20 mg, 33%), only in preparations in which the reaction had not reached completion. These crystals contained the uncomplexed ligand as was shown by the NMR spectrum. ^{1}H NMR (400 MHz, CDCl$_3$) for **5**: δ = 8.15 (d, H3/3′), 7.97 (t, H4/4′), 7.59 (b, NH), 7.49 (d, H5/5′), 3.81 (s, OCH$_3$), 3.04 (s, 6/6′-CH$_3$), 2.15 (s, CCH$_3$) ppm; ^{1}H NMR (400 MHz, CDCl$_3$) for the uncomplexed 6,6′-Me$_2$bipy: δ = 8.18 (d, H3/3′), 7.66 (t, H4/4′), 7.14 (d, H5/5′), 2.62 (s, 6/6′-CH$_3$) ppm.

[Re(CO)$_3$(5,5′-Me$_2$bipy){HNC(CH$_3$)OCH$_2$CH$_3$}]BF$_4$ (6): Ethanol was used instead of methanol in the general procedure described and afforded **6** as an orange precipitate (50 mg, 76%). Method B produced X-ray quality crystals (29 mg, 46%). ^{1}H NMR (400 MHz, CDCl$_3$): δ = 8.66 (s, H6/6′), 8.17 (d, H3/3′), 7.90 (d, H4/4′), 7.45 (b, NH), 4.18 (q, OCH$_2$), 2.49 (s, 5/5′-CH$_3$), 2.17 (s, CCH$_3$), 1.49 (t, CH$_3$) ppm.

Influence of the KOH Addition on the Formation of [Re(CO)$_3$(5,5′-Me$_2$bipy){HNC(CH$_3$)OCH$_3$}]BF$_4$: Two solutions of [Re(CO)$_3$(5,5′-Me$_2$bipy)(CH$_3$CN)]BF$_4$ (10 mM, 1:1 acetonitrile/methanol) were heated at reflux and were monitored over time by NMR spectroscopy. One of the solutions contained KOH (1.34 mM). The percentage of [Re(CO)$_3$(5,5′-Me$_2$bipy){HNC(CH$_3$)OCH$_3$}]BF$_4$ that formed was determined by taking aliquots of the solution at different time intervals. The reaction mixture aliquots (50-μL) were then dried by rotary evaporation and the residue was taken up in CDCl$_3$. The percentage of product formation was determined by integration of the H3/3′ ^{1}H NMR-spectroscopic doublet of the product and of the reactant.

Influence of the Methyl Substituent Position on the Formation of [Re(CO)$_3$(Me$_2$bipy){HNC(CH$_3$)OCH$_3$}]BF$_4$: A solution of [Re-

(CO)$_3$(6,6′-Me$_2$bipy)(CH$_3$CN)]BF$_4$ (10 mм, 1:1 acetonitrile/methanol) was heated at reflux and was monitored over time by NMR spectroscopy as in the preceding [Re(CO)$_3$(5,5′-Me$_2$bipy)(CH$_3$-CN)]BF$_4$ experiment. The percentage of [Re(CO)$_3$(6,6′-Me$_2$-bipy){HNC(CH$_3$)OCH$_3$}]BF$_4$ that formed was determined as described above.

Titration of [Re(CO)$_3$(5,5′-Me$_2$bipy){HNC(CH$_3$)OCH$_3$}]BF$_4$ with Cl⁻: A solution of [Re(CO)$_3$(5,5′-Me$_2$bipy){HNC(CH$_3$)OCH$_3$}]BF$_4$ (5 mм) in [D$_6$]dmso (600 µL) was treated with increasing amounts of Cl⁻ (1 to 150 mм), and the solution was monitored by ¹H NMR spectroscopy after each addition of Cl⁻. The complex concentration was kept constant throughout the titration by using a solution of the complex in [D$_6$]dmso (5 mм) to prepare the Cl⁻ stock solution.

X-ray Data Collection and Structure Determination: The intensity data were collected at 90 K with a Nonius KappaCCD diffractometer that was fitted with an Oxford Cryostream cooler and graphite-monochromated Mo-K_α (λ = 0.71073 Å) radiation. The data reduction included the absorption corrections by the multiscan method with the HKL SCALEPACK.[47] All of the X-ray structures were determined by direct methods and difference Fourier techniques, and were refined by full-matrix least-squares by using SHELXL97.[44] All of the non-hydrogen atoms were refined anisotropically. All of the H atoms were visible in the difference maps but were placed in idealized positions. A torsional parameter was refined for each of the methyl groups and, except for **5**, the N hydrogen atom coordinates were refined. One of the two independent PF$_6^-$ ions in **1a** was disordered into two orientations. The crystal data and refinement parameters are given in Table 1.

CCDC-829768 (for **1a**), -829770 (for **1b**), -829771 (for **1b**), -829774 (for **2**), -829769 (for **3**), -829772 (for **4**), -829773 (for **5**), and -829775 (for **6**) contain the supplementary crystallographic data for this paper. These data can be obtained free of charge from The Cambridge Crystallographic Data Centre via www.ccdc.cam.ac.uk/data_request/cif.

Supporting Information (see footnote on the first page of this article): ORTEP plots of [Re(CO)$_3$(CH$_3$CN)$_3$PF$_6$] and [Re(CO)$_3$(5,5′-Me$_2$bipy){HNC(CH$_3$)OCH$_2$CH$_3$}]BF$_4$, a table that shows the progress of several reactions with time, a figure with the predicted ¹³C NMR-spectroscopic shifts for the free 5,5′-Me$_2$bipy and 6,6′-Me$_2$bipy ligands, assignment of the ¹H and ¹³C NMR-spectroscopic signals for [Re(CO)$_3$(5,5′-Me$_2$bipy){HNC(CH$_3$)OCH$_3$}]BF$_4$ and [Re(CO)$_3$(6,6′-Me$_2$bipy){HNC(CH$_3$)OCH$_3$}]BF$_4$, and a scheme that relates the identified isomers of the [Re(CO)$_3$(5,5′-Me$_2$bipy){HNC(CH$_3$)NHR}]⁺ cations.

Acknowledgments

[1] H. He, M. Lipowska, X. Xu, A. T. Taylor, M. Carlone, L. G. Marzilli, *Inorg. Chem.* **2005**, *44*, 5437–5446.

[2] M. Lipowska, R. Cini, G. Tamasi, X. Xu, A. T. Taylor, L. G. Marzilli, *Inorg. Chem.* **2004**, *43*, 7774–7783.

[3] M. Lipowska, H. He, X. Xu, A. T. Taylor, P. A. Marzilli, L. G. Marzilli, *Inorg. Chem.* **2010**, *49*, 3141–3151.

[4] A. T. Taylor, M. Lipowska, L. G. Marzilli, *J. Nucl. Med.* **2010**, *51*, 391–396.

[5] M. Lipowska, H. He, E. Malveaux, X. Xu, L. G. Marzilli, A. T. Taylor, *J. Nucl. Med.* **2006**, *47*, 1032–1040.

[6] T. Perera, P. A. Marzilli, F. R. Fronczek, L. G. Marzilli, *Inorg. Chem.* **2010**, *49*, 2123–2131.

[7] T. Perera, F. R. Fronczek, P. A. Marzilli, L. G. Marzilli, *Inorg. Chem.* **2010**, *49*, 7035–7045.

[8] T. Perera, Ph. D. Dissertation, Louisiana State University, **2010**.

[9] T. Perera, P. Abhayawardhana, P. A. Marzilli, F. R. Fronczek, L. G. Marzilli, manuscript in preparation.

[10] A. J. Amoroso, M. P. Coogan, J. E. Dunne, V. Fernandez-Moreira, J. B. Hess, A. J. Hayes, D. Lloyd, C. Millet, S. J. A. Pope, C. Williams, *Chem. Commun.* **2007**, 3066–3068.

[11] T. J. Henly, *Coord. Chem. Rev.* **1989**, *93*, 269–295.

[12] V. Balzani, A. Juris, M. Venturi, S. Campagna, S. Serroni, *Chem. Rev.* **1996**, *96*, 759–833.

[13] R. V. Slone, D. I. Yoon, R. M. Calhoun, J. T. Hupp, *J. Am. Chem. Soc.* **1995**, *117*, 11813–11814.

[14] M. Casanova, E. Zangrando, F. Munini, E. Iengo, E. Alessio, *Dalton Trans.* **2006**, 5033–5045.

[15] N. A. Bokach, V. Y. Kukushkin, *Russ. Chem. Rev.* **2005**, *74*, 153–170.

[16] A. M. Gonzalez, R. Cini, F. P. Intini, C. Pacifico, G. Natile, *Inorg. Chem.* **2002**, *41*, 470–478.

[17] R. Ros, R. A. Michelin, T. Boschi, R. Roulet, *Inorg. Chim. Acta* **1979**, *35*, 43–48.

[18] M. Wada, T. Shimohigashi, *Inorg. Chem.* **1976**, *15*, 954–958.

[19] C. S. Chin, D. Chong, B. Lee, H. Jeong, G. Won, Y. Do, Y. J. Park, *Organometallics* **2000**, *19*, 638–648.

[20] A. M. Bianucci, F. Demartin, M. Manassero, N. Masciocchi, M. L. Ganadu, L. Naldini, A. Panzanelli, *Inorg. Chim. Acta* **1991**, *182*, 197–204.

[21] R. Cini, P. A. Caputo, F. P. Intini, G. Natile, *Inorg. Chem.* **1995**, *34*, 1130–1137.

[22] G. Rouschias, G. Wilkinson, *J. Chem. Soc. A* **1968**, 489–496.

[23] P. C. Kunz, P. Kurz, B. Spingler, R. Alberto, *Z. Anorg. Allg. Chem.* **2007**, *633*, 2753–2756.

[24] R. Enjalbert, J. Galy, *Acta Crystallogr., Sect. B* **2002**, *58*, 1005–1010.

[25] C. M. Frech, O. Blacque, H. Schmalle, H. Berke, *Chem. Eur. J.* **2006**, *12*, 5199–5209.

[26] A. Choualen, O. Blacque, H. W. Schmalle, T. Fox, T. Hiltebrand, H. Berke, *Eur. J. Inorg. Chem.* **2007**, 5246–5261.

[27] K. Rajesh, B. Dudle, O. Blacque, H. Berke, *Adv. Synth. Catal.* **2011**, *353*, 1479–1484.

[28] E. D. Raczyńska, M. Darowska, I. Dabkowska, M. Decouzon, J.-F. Gal, P.-C. Maria, C. Dubin Poliart, *J. Org. Chem.* **2004**, *69*, 4023–4030.

[29] M. Decouzon, J.-F. Gal, P.-C. Maria, E. D. Raczyńska, *Rapid Commun. Mass Spectrom.* **1993**, *7*, 599–602.

[30] I. Kaljurand, I. A. Koppel, A. Kütt, E.-I. Rõõm, T. Rodima, I. Koppel, M. Mishima, I. Leito, *J. Phys. Chem. A* **2007**, *111*, 1245–1250.

[31] F. H. Allen, O. Kennard, D. G. Watson, L. Brammer, A. G. Orpen, R. Taylor, *J. Chem. Soc. Perkin Trans. 2* **1987**, S1–S19.

[32] V. Maheshwari, D. Bhattacharyya, F. R. Fronczek, P. A. Marzilli, L. G. Marzilli, *Inorg. Chem.* **2006**, *45*, 7182–7190.

[33] V. Maheshwari, P. A. Marzilli, L. G. Marzilli, *Inorg. Chem.* **2008**, *47*, 9303–9313.

[34] V. Maheshwari, M. Carlone, F. R. Fronczek, L. G. Marzilli, *Acta Crystallogr., Sect. B* **2007**, *63*, 603–611.

[35] X. Zeng, M. Tavasli, I. F. Perepichka, A. S. Batsanov, M. R. Bryce, C.-J. Chiang, C. Rothe, A. P. Monkman, *Chem. Eur. J.* **2008**, *14*, 933–943.

[36] A. Lehleh, A. Beghidja, C. Beghidja, O. Mentre, R. Welter, *C. R. Chim.* **2011**, *14*, 462–470.

[37] A. Hazell, O. Simenson, O. Wernberg, *Acta Crystallogr., Sect. C* **1986**, *42*, 1707–1711.

[38] A. Hazell, *Polyhedron* **2004**, *23*, 2081–2083.

[39] W. B. Connick, L. M. Henling, R. E. Marsh, H. B. Gray, *Inorg. Chem.* **1996**, *35*, 6261–6265.

[40] A. M. Christoforou, P. A. Marzilli, F. R. Fronczek, L. G. Marzilli, *Inorg. Chem.* **2007**, *46*, 11173–11182.

[41] T. Perera, P. A. Marzilli, F. R. Fronczek, L. G. Marzilli, *Inorg. Chem.* **2010**, *49*, 5560–5572.

[42] X. Xiao, J. Sakamoto, M. Tanabe, S. Yamazaki, S. Yamabe, T. Matsumura-Inoue, *J. Electroanal. Chem.* **2002**, *527*, 33–40.

[43] A. G. Osbourne, *Monatsh. Chem.* **1988**, *119*, 1385–1395.

[44] G. M. Sheldrick, University of Göttingen, Germany, **1997**.

[45] S. P. Schmidt, W. C. Trogler, F. Basolo, *Inorg. Synth.* **1990**, *28*, 160–165.

[46] D. A. Edwards, J. Marshalsea, *J. Organomet. Chem.* **1977**, *131*, 73–91.

[47] Z. Otwinowski, W. Minor, *Methods in Enzymology: Macromolecular Crystallography, Part A*, New York Academic Press, New York, **1997**, vol. 276, pp. 307–326.

[48] L. Y. Y. Chan, E. E. Isaacs, W. A. G. Graham, *Can. J. Chem.* **1977**, *55*, 111–114.

FULL PAPER

Facile Synthesis of Porous Mn₃O₄ Nanocrystal–Graphene Nanocomposites for Electrochemical Supercapacitors

Dewei Wang,[a,b] Yuqi Li,[a,b] Qihua Wang,*[a] and Tingmei Wang[a]

In this work, we describe our efforts to produce Mn_3O_4–graphene nanocomposites based on a convenient and feasible solution based synthetic route under mild conditions. According to transmission electron microscopy (TEM) and high angle annular dark field scanning transmission electron microscopy (HAADF-STEM) results porous Mn_3O_4 nanocrystals (NCs), 20–40 nm in size, are uniformly deposited on both sides of the graphene nanosheet (GNS) matrix. Significantly, the as-prepared Mn_3O_4–graphene nanocomposites exhibit remarkable pseudocapacitive activity including high specific capacitance ($236.7\ F\,g^{-1}$ at $1\ A\,g^{-1}$), good rate capability ($133\ F\,g^{-1}$ at $8\ A\,g^{-1}$), and excellent cyclability (the specific capacitance only decreases by 6.32% of the initial capacitance after 1000 cycles). The excellent pseudocapacitive performance of the Mn_3O_4–graphene nanocomposites electrode is probably due to the positive synergistic effects between the Mn_3O_4 and GNS. Namely, the intimate combination of the conductive graphene network with uniformly dispersed porous Mn_3O_4 NCs not only greatly improves the electrochemical utilization of Mn_3O_4, but also increases the double-layer capacitance of the graphene sheets. These characteristics make this nanocomposite a very promising electrode material for high performance supercapacitors.

Introduction

With the rapid advancement in the development of various electronic devices such as electric vehicles and hybrid electric vehicles, the demand for a sustainable energy storage system has intensified dramatically. Supercapacitors, also called electrochemical capacitors or ultracapacitors, which can be classified simply as electric double-layer capacitors (EDLCs) and pseudocapacitors according to their charge storage mechanisms, have emerged as novel energy storage devices due to their high power density and long cycle life.[1–6] The charge storage mechanism in EDLCs involves electrostatic forces within the electrical double-layers formed along the carbon electrodes with large surface areas.[5,7–9] EDLCs comprising carbon based materials usually have high power densities but suffer from low energy densities.[10] In contrast, fast Faradaic redox reactions are responsible for the charge storage mechanism in pseudocapacitors. Some noble metal oxides (e.g. RuO_2 and IrO_2) and conducting polymers possess notable specific capacitances, however, their high cost and poor cycling stabilities arising from their low conductivities and sluggish redox kinetics have restricted the available capacitance significantly.[10–15]

Therefore, attempts have been made to find alternative inexpensive electrode materials with good capacitive properties (e.g. high power density, good specific capacitance, and excellent cyclability) in order to meet the increasing demand for a renewable energy storage system. In this context, cheap metal oxides, for example the oxides of Mn, Ni, Fe, with good pseudocapacitive behaviors are intensively investigated on account of their excellent electrochemical properties and low cost.[16–19] Among them manganese based oxides have attracted special attention because of their high specific capacitances, rich polymorphism, cost effectiveness, low environmental toxicities, structural flexibilities, redox reversibilities, wide potential windows, etc.[20,21]

Hausmannite (Mn_3O_4) has drawn particularly research attention because of its distinctive structural features combined with fascinating physicochemical properties, which are of great interest in energy, magnetic, and catalyst fields, etc.[22–25] Only a few studies, however, have been done with Mn_3O_4 as the supercapacitor electrode material, this is partly due to its extremely low electrical conductivity (about 10^{-7}–$10^{-8}\ S\,cm^{-1}$).[21] Generally, there are two ways to overcome this intrinsic drawback: one way is to design structures that can provide more electroactive sites to promote the electrochemical reaction, such as hollow structures, or those with well defined octahedra and polyhedra with enhanced capacitive behavior.[26–28] Another way is form a composite (or hybrid) of Mn_3O_4 with other components to improve the electrode conductivity. In this case structural control (shape, size, and texture) is somewhat complicated, and involves elaborately adjusting the synthetic parameters

[a] State Key Laboratory of Solid Lubrication, Lanzhou Institute of Chemical Physics, Chinese Academy of Sciences, Lanzhou 730000, People's Republic of China
[b] Graduate School of Chinese Academy of Sciences, Beijing 10039, People's Republic of China
E-mail: Wangqh@lzb.ac.cn

WILEY ONLINE LIBRARY

and reaction kinetics. Combining Mn$_3$O$_4$ with other conducting substrates such as carbon nanotubes and activated carbons has therefore been explored extensively in an effort to enhance the electrochemical performance of the resulting electrode materials. For instance, Liu and coworkers successfully synthesized Mn$_3$O$_4$–MWCNTs (MWCNT = multiwalled carbon nanotubes) composites by a simple solvothermal method with ethanol as the medium.[29] The specific capacitance of the composite electrode was 330 F g^{-1}, nearly 18 times higher than that of a pure MWCNT electrode. Yuan and coworkers developed a facile microwave method with an aqueous solution of Mn(NO$_3$)$_2$ as the precursor for the oxidant of Mn$_2$O$_3$ and mesoporous carbon (MC) as the reductant.[30] The Mn$_3$O$_4$–MC composite electrode had a specific capacitance of 266 F g^{-1} at a sweep rate of 1 mV s^{-1}. The capacitance loss of Mn$_3$O$_4$–MC is 25.8 % after 1000 cycles. Very recently, Chen and coworkers reported a novel dip-casting method with nonaqueous solutions for depositing Mn$_3$O$_4$ nanoparticles onto a highly dense millimeter long carbon nanotube array (CNTA).[31] The maximum specific capacitance of the Mn$_3$O$_4$–CNTA composite electrode was 143 F g^{-1}. The preparation of these composites, however, involves relatively complicated synthetic processes and high cost, which greatly hinders their practical use. Therefore, the development of a convenient and feasible method to prepare a Mn$_3$O$_4$ based composite with enhanced electrochemical performance is of great significance.

Graphene, a unique single layer of carbon atoms tightly packed into a two-dimensional honeycomb sp^2 carbon lattice, has attracted tremendous attention because of its novel properties and potential application in many technological fields such as supercapacitors,[7,9,32–35] lithium batteries,[36–38] sensors,[39] nanoelectronics,[40] and hydrogen storage.[41] It has been suggested that graphene is an excellent candidate as an electrode material for energy conversion/ storage systems as a result of its huge specific surface area, good chemical stability, and remarkable electrical conductivity.[42–44] Due to these features, graphene sheets (GNS) can act as matrices for hosting active nanomaterials to improve their electrochemical performance. For instance, MnO$_2$–graphene composites have been synthesized successfully and they exhibited intriguing electrochemical properties that result from the synergistic effects of their components.[45–47] However, Mn$_3$O$_4$–graphene composites have received relatively little attention. Recently, Dai and coworkers developed two step solution phase reactions for the formation of hybrid materials comprising Mn$_3$O$_4$ nanoparticles on GNS for lithium-ion battery applications.[48] They revealed for the first time that a highly insulating material such as Mn$_3$O$_4$ could approach its theoretical capacity as an anode material for lithium-ion batteries. Wang and coworkers synthesized Mn$_3$O$_4$–graphene nanocomposites by first mixing a graphene suspension in ethylene glycol with a MnO$_2$ organosol, followed by ultrasonication processing and heat treatment of the mixture.[49] As an electrode material in supercapacitors, Mn$_3$O$_4$–graphene nanocomposites exhibited a high specific capacitance of 175 F g^{-1} with 1 M

Na$_2$SO$_4$ as the electrolyte and 256 F g^{-1} with 6 M KOH as the electrolyte. However, cycle stability and high rate charge–discharge measurements were not discussed in the report of this study. Therefore, the exploration of facile synthetic methods for the synthesis of Mn$_3$O$_4$–graphene nanocomposites and the optimization of their electrochemical performance are urgently required. Herein, we report a simple and robust approach for the synthesis of Mn$_3$O$_4$–graphene nanocomposites and the systematic investigation of their supercapacitive behaviors.

Results and Discussion

In the present work, the negatively charged graphene oxide nanosheets were obtained by the initial exfoliation of graphite oxide (GO) in water (see Supporting Information, Figures S1, S2), followed by the addition of an aqueous solution of MnAc$_2$ to the graphene oxide nanosheet suspension. The numerous functional groups on the surface of the graphene oxide nanosheets will coordinate with Mn ions, a process that is driven by strong electrostatic interactions.[35,45] After continuous stirring, all of the Mn ions will adsorb onto the GO surface to form Mn ion–GO mixtures. NaOH was the precipitant that leaded to the conversion of the Mn ion–GO to Mn(OH)$_2$–GO. Because Mn(OH)$_2$ is a metastable compound that can be oxidized easily to Mn$_3$O$_4$ by oxygen,[26,28] Mn$_3$O$_4$–GO composites will form. Hydrothermal treatment of the mixture resulted in the formation of the Mn$_3$O$_4$–graphene nanocomposites in a one step reaction.[48]

The X-ray diffraction pattern obtained with the Mn$_3$O$_4$–graphene composite is shown in Figure 1, together with those of the as-prepared bare Mn$_3$O$_4$. The positions and relative intensities of the peaks associated with the Mn$_3$O$_4$–graphene composites and bare Mn$_3$O$_4$ allows them to be indexed perfectly as a pure Mn$_3$O$_4$ (hausmannite, space group: $I4_1/amd$) with lattice constants of $a = b = 5.76$ Å and $c = 9.45$ Å, which are consistent with the values given in the standard card for Mn$_3$O$_4$ (JCPDS No. 89–4837). No
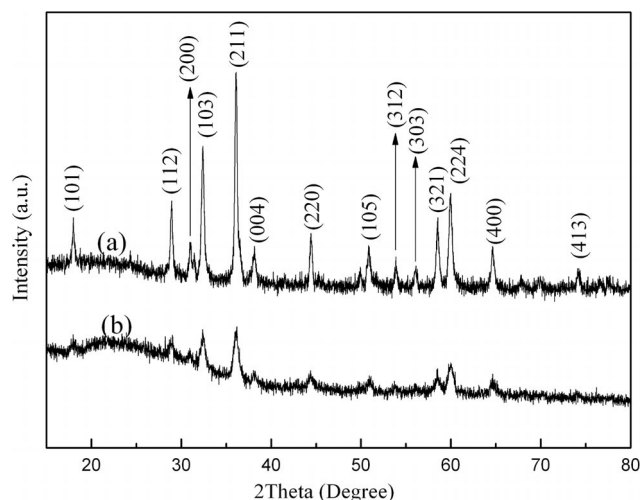
Figure 1. XRD patterns of Mn$_3$O$_4$ (a) and Mn$_3$O$_4$–graphene nanocomposites (b).

impurities were detected in the XRD pattern, confirming the high purity of the products. Moreover, the XRD diffraction peaks are relatively broad, indicating that the crystals constituting the products are small in size. Moreover, no stacking peak for the graphene sheets was detected, suggesting that the graphene sheets are stacked in a disordered manner with a low degree of graphitization. These results indicate that the as-synthesized composite consists of disorderedly stacked graphene and highly crystalline Mn_3O_4 nanoparticles. The reduction in the diffraction intensity of the Mn_3O_4–graphene composites compared with bare Mn_3O_4 probably results from the GO surface interacting strongly with the coated species, thus providing pinning forces on the small particles and hindering their diffusion and recrystallization.[52]

The composite structure was further studied by FTIR spectroscopy (Figure 2). In the FTIR spectrum of GO (Figure 2, a), the peaks around 3385, 1727, 1405, and 1057 cm^{-1} are attributed to the O–H, C–O in COOH, and C–O in C–OH/C–O–C functional moieties within the carbon frameworks, respectively.[35] Compared with the spectrum of GO, two new peaks appear in the spectrum of the Mn_3O_4–graphene composites (Figure 2, b). The new peaks at 616 and 505 cm^{-1} are assigned to the vibration of the stretching mode of the Mn–O bonds associated with Mn in tetrahedral sites and to the distorted vibration of the Mn–O bonds involving Mn ions in octahedral environments, respectively.[53] These values are shifted to higher wavenumbers compared with those for the peaks reported for the stretching vibrations of Mn–O in bulk Mn_3O_4, which are at 639 and 532 cm^{-1}. Moreover, the intensity of all of these absorption peaks related to the oxidized groups decreased significantly in the in the FTIR spectra of the Mn_3O_4–graphene composites prepared from GO relative to those in the spectrum of pure GO, indicating that reduction of GO and restoration of the conjugated aromatic system has occurred in the composite.[35] In addition, a new absorption band that appears at 1570 cm^{-1} corresponds to the C=C stretching vibration of aromatic skeleton of the graphene sheets, and its presence further confirms the reduction of GO. The chemical bonding states in the product were further analyzed by X-ray photoelectron spectroscopy (XPS) measurements, the data from which are shown in Figure 3. The binding energies obtained from the XPS analysis were corrected for specimen charging by referencing the C 1s signal to 285.0 eV. Compared to that of GO, the XPS spectrum of the Mn_3O_4–graphene composite not only exhibits O 1s and C 1s peaks, but also exhibits two peaks at 642.9 and 641.0 eV corresponding to the Mn $2p_{1/2}$ and Mn $2p_{3/2}$ states, which confirm the presence of Mn species in the composite (Figure 3, a). The Mn 2p XPS spectrum of the composite exhibits two peaks at 642.9 and 641.0 eV, corresponding to the Mn $2p_{1/2}$ and Mn $2p_{3/2}$ spin-orbit states of Mn_3O_4, respectively (Figure 3, b). It was observed that there is an energy separation of 11.9 eV between the Mn $2p_{1/2}$ and Mn $2p_{3/2}$ peaks, which is in accordance with reported data for the Mn $2p_{3/2}$ and Mn $2p_{1/2}$ signals in the spectrum of Mn_3O_4.[29] The C 1s peak locked at 284.8 eV

is related to the graphitic carbon in graphene and the O 1s peak at 532 eV in the spectrum indicates the presence of oxygen groups (Figure 3, a). The most resolved peak, located at 284.8 eV, was assigned to the C–C bonds of the graphene (Figure 3, c). Two weak peaks centered at 285.4 and 286.7 eV were attributed to C–O (epoxy and alkoxy) and COOH groups, respectively. In the deconvoluted C 1s XPS spectrum of GO four different peaks centered at 284.8, 285.6, 286.6, and 288.4 eV were observed, corresponding to the C=C/C–C bonds of the aromatic rings, C–OH, C (epoxy and alkoxy), and C=O groups, respectively (Figure 3, d). In the spectrum recorded after hydrothermal reduction of the composite, the intensities of all of the C 1s peaks of the carbon atoms bound to oxygen, especially the C–O (epoxy and alkoxy) peak, decreased dramatically, revealing that most of the epoxide and hydroxy functional groups were successfully removed. These results are in good agreement with the FTIR studies. The reduction of GO and restoration of the conjugated aromatic system guarantees good electronic conductivity, which make graphene a good channel for electronic and ionic conductivity.[35]
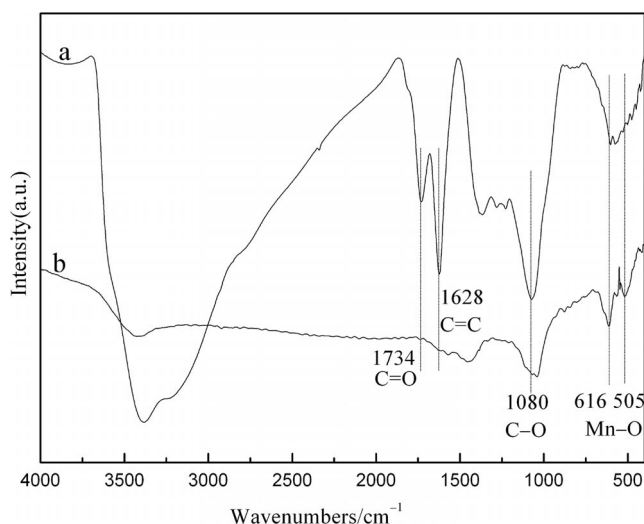
Figure 2. FTIR spectrum of GO (a) and Mn_3O_4–graphene nanocomposites (b).

The typical morphology of the Mn_3O_4–graphene composites is shown in the TEM images in Figure 4 (also see Figure S3). Figure 4 (a and b) displays the TEM images of the Mn_3O_4–graphene nanocomposites at low and high magnification, respectively. From these images it can be seen clearly that Mn_3O_4 particles with sizes of 20–40 nm are homogeneously deposited on the thin graphene layers, which was also revealed by a field emission scanning electron microscopy (FESEM) study (Figure S3). Interestingly, the Mn_3O_4 NCs are not completely dense but have some pinholes that make them porous. In addition, we found that in the image some of the Mn_3O_4 NCs are brighter than others, which seem to suggest that they are enveloped in a thin film. Since the functional groups, such as hydroxy and epoxy groups, are attached to both sides of GO sheets, the Mn_3O_4 NCs appear on both sides of the support; some NCs are located on one side of the graphene oxide sheet,
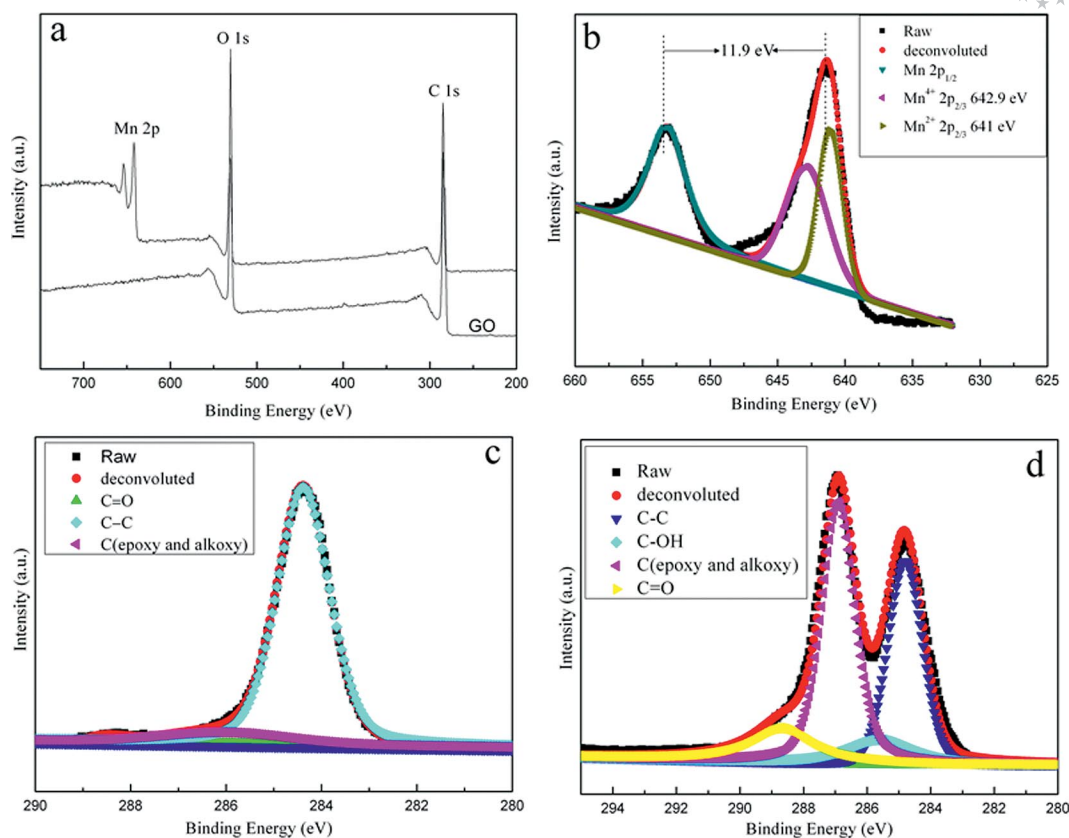
Figure 3. XPS spectra of GO and Mn₃O₄–graphene nanocomposites: (a) wide scan; (b) Mn 2p spectra of the Mn₃O₄–graphene nanocomposites; (c) C 1s spectra of the Mn₃O₄–graphene nanocomposites; (d) C 1s spectra of GO.
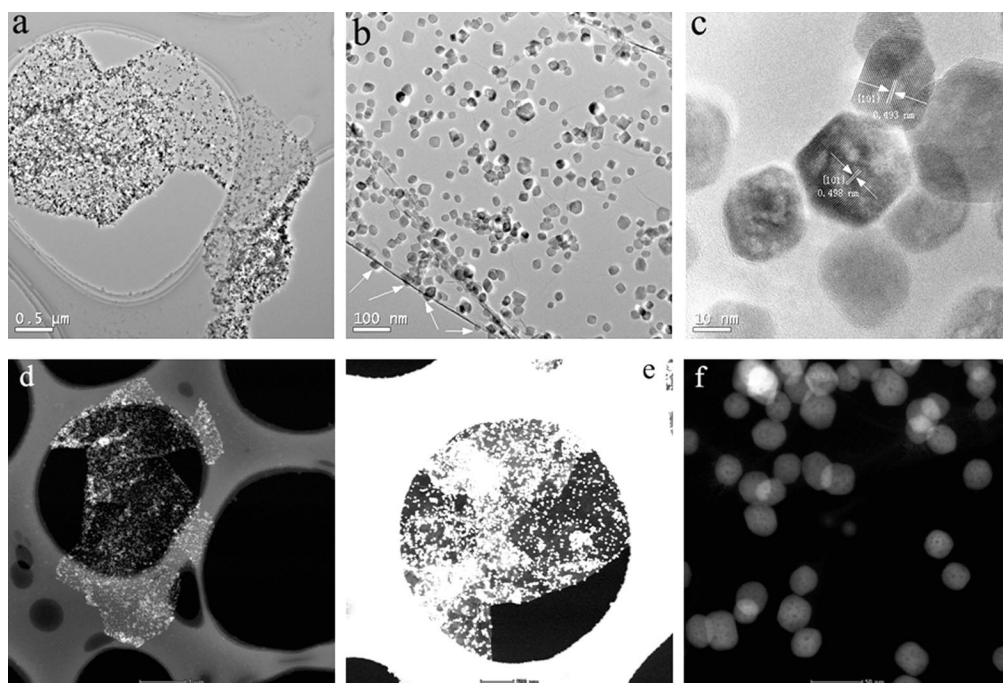
Figure 4. Typical TEM images of the as-synthesized Mn₃O₄–graphene nanocomposites: (a) low magnification; (b) high magnification; (c) HRTEM image; (d–f) HAADF–STEM images.

while others lay the other side of the sheet.[45] From the curved edge (Figure 4, b), it is easy to see that some NCs are located on the underside of the graphene surface

(marked with arrows). A high resolution transmission electron microscopy (HRTEM) measurement gave further insight into details of the morphological and structural fea-

tures of the NCs. Figure 4 (c) clearly demonstrates the well textured and single crystalline nature of the Mn_3O_4 NCs in the Mn_3O_4–graphene composite. The nanoparticles show the same lattice fringes throughout, indicating their single crystalline nature. Lattice fringes with a separation of 0.493 nm were clearly observed in the pattern shown in Figure 4 (c), and can be indexed as the {101} planes of the tetragonal Mn_3O_4 lattice. HAADF–STEM images further confirm that the Mn_3O_4 NCs (bright spots) with a diameter of 20–40 nm are homogeneously spread over the graphene surface (Figure 4, d). The presence of the thin layered GNS can be seen clearly from its edge (Figure 4, e). Some small holes scattered on the NPs surface are visible, which is in good agreement with the results of the TEM studies (Figure 4, f). It is worthwhile to note that the interactions between the NCs and graphene sheets are quite strong, and cannot be destroyed even after a long time under ultrasound irradiation. Because of the poor dispersion of the Mn_3O_4–graphene nanocomposites in ethanol, a long period of sonication is needed during the preparation of TEM specimen, however, the NCs are still strongly anchored to the surface of graphene sheets and do not become detached. The intimate contact between the Mn_3O_4 NCs and the graphene sheets enables fast electronic and ionic transport through the active materials to the charge collector, and thus improves the electrochemical performance of the mate-

rials. Moreover, the NCs on the surface of the graphene sheets can act as spacers to efficiently prevent the aggregation of the NCs as well as the restacking of graphene sheets, thus avoiding a loss of their high active surface area.[54] In addition, Mn_3O_4–graphene composites with different Mn_3O_4 loadings were prepared by simply manipulating the amount of GO sheets in the reaction mixture, while the amount of $MnAc_2$ was kept unchanged (Figure S4). FESEM images of pure Mn_3O_4 after the hydrothermal reaction are shown in Figure S5. As expected, the Mn_3O_4 nanoparticles 20–60 nm in size agglomerated severely to form particles several micrometers in size. Figure S6 shows a FESEM image of the as-synthesized graphene. It is evident that the pure graphene sheets have some wrinkles and folds but are not transparent, suggesting that serious restacking of the sheets occurs after the hydrothermal reduction of the material, which is consistent with the XRD results (Figure S6).

The electrochemical performance of the as-prepared Mn_3O_4–graphene composite was first evaluated by means of cyclic voltammetry (CV) performed with the composite in a 2 M KOH electrolyte, and over the –0.5–0.4 V range. As can be seen in Figure 5 (a), the Mn_3O_4–graphene electrode shows characteristics of pseudocapacitance caused by electrochemical reactions, which is very different from that expected for electrical double-layer capacitance in which the
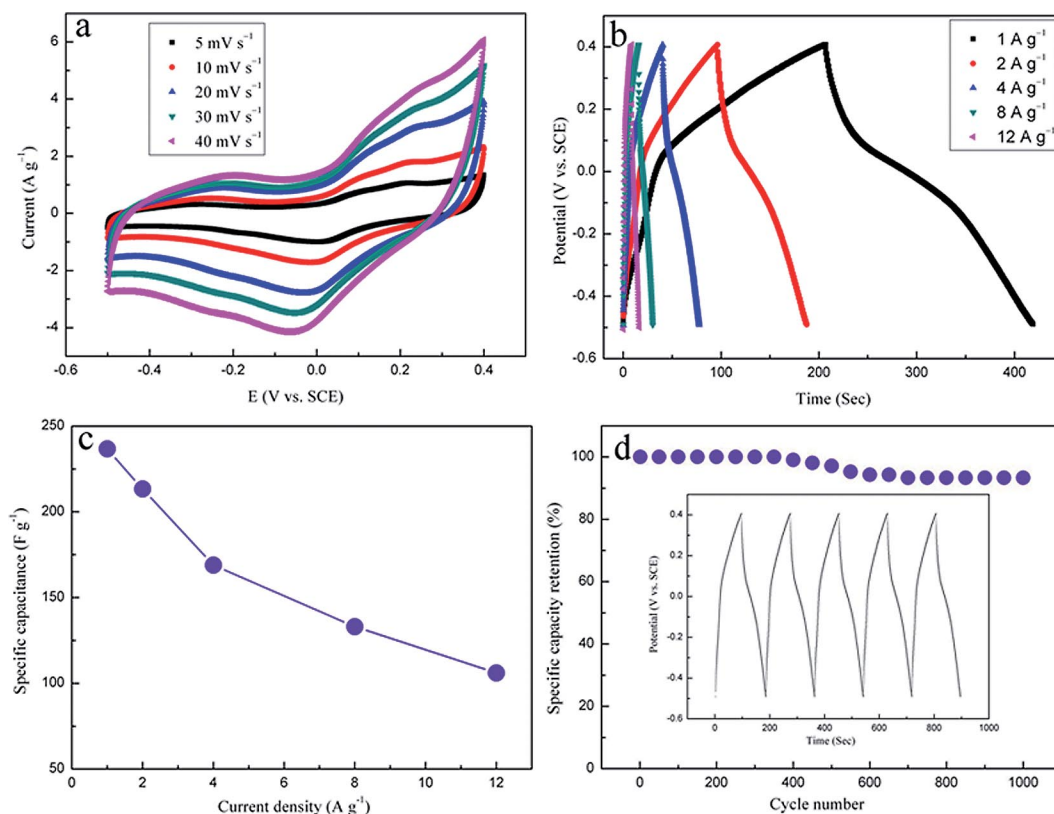
Figure 5. Cyclic voltammograms of the Mn_3O_4–graphene electrode recorded at scan rates of 5 to 40 mV s^{-1}: (a–b) charge–discharge curves for the Mn_3O_4–graphene electrode in 2 M KOH aqueous electrolyte recorded at different current densities over the potential range of –0.5 to 0.4 V; (c) plot of specific capacitance as a function of current density; (d) capacitance retention of the Mn_3O_4–graphene electrode as a function of cycle number. The inserts show the charge–discharge profiles of the first five charge–discharge cycles recorded with a current density of 2 A g^{-1} and with a voltage window of –0.5 to 0.40 V.

CV curve has close to an ideal rectangular shape.[5,10,51] Redox reaction peaks are visible in the CV curves implying that the measured capacitance is mainly associated with a redox mechanism. The pseudocapacitance arises from the reaction between the Mn^{4+} ions and the electrolyte, which is mainly governed by the intercalation and deintercalation of K$^+$ species within the manganese oxide.[10,21,45] The peak current increases when the scan rate is increased from 5 to 40 mV s^{-1}, and the shape of the CV curve changed gradually. However, the anodic peak potential and cathodic peak potential shifted only slightly indicating that a small equivalent series resistance (ESR) occurred.[55] The charge–discharge behavior of the as-prepared Mn$_3$O$_4$–graphene electrode in KOH solution (2 M) was evaluated by galvanostatic charge–discharge cycling at different current densities over the potential range of –0.5–0.4 V [vs. saturated calomel electrode (SCE)]. For comparison, pure graphene and Mn$_3$O$_4$ NCs prepared by the same procedure as the composite were also studied under the same electrochemical conditions (Figure S7). The Mn$_3$O$_4$–graphene electrode shows a longer charge–discharge time in its V/t curves than the pure graphene and Mn$_3$O$_4$ NCs, implying that it has a larger capacitance than these materials. Moreover, the charging curves are somewhat mirror-symmetrical to their discharging counterparts, indicating that the Mn$_3$O$_4$–graphene electrode has high electrochemical reversibility and excellent capacitive characteristics.[51] The specific capacitances were calculated from the galvanostatic discharge curves with the equation C = $It/(\Delta Vm)$, where I is the current applied, t is the total discharge time, ΔV is the potential drop during discharge, and m is the mass of the sample on one electrode. On the basis of this equation, the specific capacitance values for the Mn$_3$O$_4$–graphene composite, pure graphene and Mn$_3$O$_4$ NCs were calculated, from the discharge curves, to be 213.3, 57.8, and 22.2 F g^{-1}, respectively. It is worthy of note that the background capacitance of the nickel foam (including acetylene black) was negligible (Figure S7), suggesting that the capacitance measured was mainly due to the Mn$_3$O$_4$–graphene composite. Importantly, the Mn$_3$O$_4$–graphene composite exhibits much better rate capability compared to the pure Mn$_3$O$_4$ electrode. Part b of Figure 5 shows representative charge–discharge profiles for the Mn$_3$O$_4$–graphene electrode recorded at various current densities. For example, more than 71% of the specific capacitance is retained as the current density is increased to 4 A g^{-1}. The specific capacitance still has a value of 106 F g^{-1} even with a high charge and discharge current density of 12 A g^{-1} suggesting that the Mn$_3$O$_4$–graphene electrode has good rate capability (Figure 5, c). Furthermore, the electrochemical stability of the Mn$_3$O$_4$–graphene electrode in 2 M KOH aqueous solution was investigated by chronopotentiometry measurements over the range of –0.5 to +0.4 V and at 2 A g^{-1}. As shown in Figure 5 (d), the specific capacitance only decreases by 6.32% of the initial capacitance after 1000 cycles, revealing the excellent electrochemical stability of the Mn$_3$O$_4$–graphene electrode.

Figure S8 shows the Ragone plot (power density vs. energy density) of the Mn$_3$O$_4$–graphene composite electrode.

This electrode material can deliver an energy density of 12 W h kg^{-1} at a power density of 5.4 kW kg^{-1} based on the total mass of composite, which is superior to pure graphene and Mn$_3$O$_4$ NCs. Encouragingly, these values can meet the criteria (a power density of 5–10 kW kg^{-1} and energy density of approximately 5 W h kg^{-1}) for next-generation supercapacitors.[10] The excellent pseudocapacitive performance of the Mn$_3$O$_4$–graphene composite electrode is probably due to the positive synergistic effects between the Mn$_3$O$_4$ and graphene.[45,54] Firstly, the well dispersed Mn$_3$O$_4$ NCs on the GNS could effectively inhibit the stacking/agglomerating of the GNS sheets. Similarly, Mn$_3$O$_4$ NCs anchored on the GNS sheets could reduce the aggregation of the NCs making nearly every NCs accessible for electronic and ionic transport pathways, resulting in high double-layer capacitance, and importantly, enhancing the utilization of the active materials and mitigating the internal resistance of the capacitors, thus increasing the specific capacitance value and cycle stability of the composite.[56] Secondly, graphene also provides a highly conductive network for electron transport during the charge and discharge processes. Thirdly, the pores within the NCs cannot only provide more active sites for the intercalation and deintercalation of K$^+$ species, but they also improve the accessibility of the composite to the electrolyte ions and shorten the ion diffusion and migration pathways. Furthermore, the graphene in the composite can provide an elastic buffer space to accommodate the volume expansion/contraction of the Mn$_3$O$_4$ NCs during insertion/extraction processes.[48,49,54] In addition, the Faradayic charge transfer resistance for Mn$_3$O$_4$–graphene nanocomposite electrodes is very low (Figure S9), which also contributes to the enhancement of the extent of utilization of the active materials and mitigates the internal resistance of the capacitors, therefore increasing their specific capacitance values.[51] Porous Mn$_3$O$_4$–graphene nanocomposites are expected to make a significant contribution to the advancement of high performance supercapacitors because of the low cost associated with the precursor and the simplicity in the preparation of this novel structure, and they also serve as promising candidates for other applications such as catalysis and lithium-ion batteries.

Conclusions

In summary, we have succeeded in preparing porous Mn$_3$O$_4$–graphene nanocomposites by a facile solution based approach. The phase composition, morphology, and structure of the as-prepared products were studied in detail. Electrochemical studies were carried out with CV and galvanostatic charge–discharge measurements with a three-electrode system. The Mn$_3$O$_4$–graphene nanocomposite showed improved electrochemical performance relative to its individual components due to the positive synergistic effects between the Mn$_3$O$_4$ and graphene. A maximum specific capacitance of 236.7 F g^{-1} has been obtained for this nanocomposite in 2 M KOH aqueous electrolyte at a current density of 1 A g^{-1} and with a voltage window of –0.5 to

0.40 V. Furthermore, the Mn_3O_4–graphene-based supercapacitors exhibited enhanced rate capability and excellent electrochemical stability relative to electrodes comprising pure graphene or Mn_3O_4. These characteristics indicate that porous Mn_3O_4–graphene nanocomposites are promising electrode materials for supercapacitors.

Experimental Section

General: All chemical reagents (analytical grade) were used as received without further purification. Deionized water was used for all procedures.

Preparation of GO: The graphite oxide (GO) was synthesized from pristine graphite powder by a modified Hummers method (Figure S1).[50] GO (10 mg) and water (20 mL) were ultrasonicated in a beaker for 90 min in order to fully exfoliate the graphite oxide to give GO sheets (Figure S2). In this way a homogeneous GO aqueous dispersion (0.5 mg mL^{-1}) was obtained.

Preparation of Mn_3O_4–Graphene Nanocomposites: In a typical procedure, an aqueous solution (10 mL) of $MnAc_2 \cdot 4H_2O$ (0.4 mmol) was added dropwise to an aqueous suspension of GO (20 mL). After continuous stirring for 2 h, an aqueous solution of NaOH (10 mL, 0.8 mmol) was added dropwise into the mixture. Finally, the mixture was sealed in a Teflon-lined stainless steel autoclave for hydrothermal reaction at 180 °C for 12 h. The final product was washed several times with water and ethanol, and then dried at 80 °C for 12 h. For comparison studies, Mn_3O_4 particles and graphene were also prepared under the same conditions but without the presence of GO or $MnAc_2$.

Characterization: The structural phases of the products were measured by powder X-ray diffraction (XRD) experiments on a RigaKu D/max–RB diffractometer with Ni-filtered graphite-monochromatized Cu-K_α radiation (λ = 1.54056 Å). Field emission scanning electron microscopy (FESEM) studies were carried on a JEOL JSM-6701F instrument. Transmission electron microscopy (TEM), high resolution transmission electron microscopy (HRTEM), and high angle annular dark field scanning transmission electron microscopy (HAADF–STEM) studies were carried out on a FEITEC-NAIF TEM (FEI, Tecnai 30) operating with an acceleration voltage of 300 kV. Samples were prepared by first dispersing the sample powder in ethanol by ultrasonic treatment, and then the dispersion was dropped onto a carbon coated copper grid, and dried in air. Fourier transform infrared (FTIR) spectra were measured from 4000 to 400 cm^{-1}, at room temperature, on an IFS 66v/s FTIR spectrophotometer. X–ray photoelectron spectroscopy (XPS, X–ray monochromatisation, Thermon Scientific) was carried out with Al-K_α as the radiation source; the binding energies obtained in the XPS analysis were calibrated against the C 1s peak that was locked at 285.0 eV.

Preparation of Electrodes and Electrochemical Measurements: The fabrication of the working electrodes was carried out as follows: the electroactive material (80 wt.-%), acetylene black (15 wt.-%), and poly(tetrafluoroethylene) (5 wt.-%) binders were mixed in ethanol to form a homogeneous slurry, which was then pressed onto a nickel grid (about 1×1 cm^2) and dried at 60 °C overnight. The electrochemical measurements were done with a three-electrode cell with Pt foil (1×1 cm^2) as the counter electrode and a saturated calomel electrode (SCE) as the reference electrode. The electrolyte was 2 M aqueous KOH solution. CV tests were done between –0.5 and 0.4 V (vs. SCE) and at different scan rates. The long term galvanostatic charge–discharge was evaluated with a LAND CT2001A multichannel galvanostat operating in the potential range of –0.5–0.4 V (vs. SCE) and at a current density of 2 A g^{-1}. CV and chronopotentiometry (CP) tests were performed on an electrochemical workstation (CHI 660B, Chenhua, Shanghai). Before electrochemical tests, the working electrodes were aged for 12 h to ensure good soakage of the electroactive material in the electrolyte.[51]

Supporting Information (see footnote on the first page of this article): Additional TEM and FESEM images, AFM image, XRD analysis, galvanostatic charge–discharge curves, and Ragone plot.

[1] B. E. Conway, *Electrochemical Supercapacitors, Scientific Fundamental and Technological Applications*, Kluwer Academic/Plenum, New York, **1999**.
[2] M. Winter, R. J. Brodd, *Chem. Rev.* **2004**, *104*, 4245–4270.
[3] A. Burke, *J. Power Sources* **2000**, *91*, 37–50.
[4] J. R. Miller, P. Simon, *Science* **2008**, *321*, 651–652.
[5] L. L. Zhang, X. S. Zhao, *Chem. Soc. Rev.* **2009**, *38*, 2520–2531.
[6] P. Simon, Y. Gogotsi, *Nat. Mater.* **2008**, *7*, 845–854.
[7] T. Mei, T. Li, H. Y. Bi, L. B. Wang, Y. C. Zhu, Y. T. Qian, *Eur. J. Inorg. Chem.* **2010**, 4314–4320.
[8] A. S. Arico, P. Bruce, B. Scrosati, J. M. Tarascon, W. van Schalkwijk, *Nat. Mater.* **2005**, *4*, 366–377.
[9] M. Pumera, *Energy Environ. Sci.* **2011**, *4*, 668–674.
[10] X. Zhao, B. M. Sanchez, P. Dobson, P. Grant, *Nanoscale* **2011**, *3*, 839–855.
[11] B. E. Conway, *J. Electrochem. Soc.* **1991**, *138*, 1539–1548.
[12] J. P. Zheng, P. J. Cygan, T. R. Jow, *J. Electrochem. Soc.* **1995**, *142*, 2699–2703.
[13] Y. M. Chen, J. H. Cai, Y. S. Huang, K. Y. Lee, D. S. Tsai, *Nanotechnology* **2011**, *22*, 115706.
[14] D. Q. Liu, S. H. Yu, S. W. Son, S. K. Joo, *ECS Trans.* **2008**, *16*, 103–109.
[15] C. C. Hu, J. Y. Lin, *Electrochim. Acta* **2002**, *47*, 4055–4067.
[16] S. C. Pang, M. A. Anderson, T. W. Chapman, *J. Electrochem. Soc.* **2000**, *147*, 444–445.
[17] H. Y. Lee, J. B. Goodenough, *J. Solid State Chem.* **1999**, *144*, 220–223.
[18] K. C. Liu, M. A. Anderson, *J. Electrochem. Soc.* **1996**, *143*, 124–131.
[19] N. L. Wu, S. Y. Wang, C. Y. Han, D. S. Wu, L.-R. Shiue, *J. Power Sources* **2003**, *113*, 173–178.
[20] X. Wang, Y. D. Li, *J. Am. Chem. Soc.* **2002**, *124*, 2880–2881.
[21] W. F. Wei, X. W. Cui, W. X. Chen, D. G. Ivey, *Chem. Soc. Rev.* **2011**, *40*, 1697–1721.
[22] P. Li, C. Y. Nan, Z. Wei, J. Lu, Q. Peng, Y. D. Li, *Chem. Mater.* **2010**, *22*, 4232–4236.
[23] J. Gao, M. A. Lowe, H. D. Abruna, *Chem. Mater.* **2011**, *23*, 3223–3227.
[24] W. S. Seo, H. H. Jo, K. Lee, B. Kim, S. J. Oh, J. T. Park, *Angew. Chem.* **2004**, *116*, 1135; *Angew. Chem. Int. Ed.* **2004**, *43*, 1115–1117.
[25] T. Rhadfi, J. Y. Piquemal, L. Sicard, F. Herbst, E. Briot, M. Benedetti, A. Atlamsani, *Appl. Catal. A* **2010**, *386*, 132–139.
[26] M. Fang, X. L. Tan, M. Liu, S. H. Kang, X. Y. Hu, L. D. Zhang, *CrystEngComm* **2011**, *13*, 4915–4920.
[27] H. Jiang, T. Zhao, C. Y. Yan, J. Ma, C. Z. Li, *Nanoscale* **2010**, *2*, 2195–2198.

[28] C. C. Hu, Y. T. Wu, K. H. Chang, *Chem. Mater.* **2008**, *20*, 2890–2894.

[29] G. M. An, P. Yu, M. J. Xiao, Z. M. Liu, Z. J. Miao, K. L. Ding, L. Q. Mao, *Nanotechnology* **2008**, *19*, 275709.

[30] T. X. Zhou, S. S. Mo, S. L. Zhou, W. J. Zou, Y. L. Liu, D. S. Yuan, *J. Mater. Sci.* **2011**, *46*, 3337–3342.

[31] X. W. Cui, F. P. Hu, W. F. Wei, W. X. Chen, *Carbon* **2011**, *49*, 1225–1234.

[32] M. D. Stoller, S. Park, Y. Zhu, J. An, R. S. Ruoff, *Nano Lett.* **2008**, *8*, 3498–3502.

[33] J. Xia, F. Chen, J. Li, N. Tao, *Nat. Nanotechnol.* **2009**, *4*, 505–509.

[34] Y. Q. Sun, Q. Wu, G. Q. Shi, *Energy Environ. Sci.* **2011**, *4*, 1113–1132.

[35] V. Singh, D. Joung, L. Zhai, S. Das, S. Khondaker, S. Seal, *Prog. Mater. Sci.* **2011**, *56*, 1178–1271.

[36] E. J. Yoo, J. Kim, E. Hosono, H. S. Zhou, T. Kudo, I. Honma, *Nano Lett.* **2008**, *8*, 2277–2282.

[37] G. X. Wang, X. P. Shen, J. Yao, J. Park, *Carbon* **2009**, *47*, 2049–2053.

[38] P. Guo, H. H. Song, X. H. Chen, *Electrochem. Commun.* **2009**, *11*, 1320–1324.

[39] J. T. Robinson, F. K. Perkins, E. S. Snow, Z. Q. Wei, P. E. Sheehan, *Nano Lett.* **2008**, *8*, 3137–3140.

[40] R. M. Westervelt, *Science* **2008**, *320*, 324–325.

[41] C. Ataca, E. Akturk, S. Ciraci, H. Ustunel, *Appl. Phys. Lett.* **2008**, *93*, 043123.

[42] K. S. Novoselov, A. K. Geim, S. V. Morozov, D. Jiang, Y. Zhang, S. V. Dubonos, I. V. Grigorieva, A. A. Firsov, *Science* **2004**, *306*, 666–669.

[43] D. A. Dikin, S. Stankovich, E. J. Zimney, R. D. Piner, G. H. B. Dommett, G. Evmenenko, S. T. Nguyen, R. S. Ruoff, *Nature* **2007**, *448*, 457–460.

[44] A. K. Geim, K. S. Novoselov, *Nat. Mater.* **2007**, *6*, 183–191.

[45] S. Chen, J. W. Zhu, X. D. Wu, Q. F. Han, X. Wang, *ACS Nano* **2010**, *4*, 2822–2830.

[46] G. H. Yu, L. B. Hu, M. Vosgueritchian, H. L. Wang, X. Xie, J. McDonough, X. Cui, Y. Cui, Z. N. Bao, *Nano Lett.* **2011**, *11*, 2905–2910.

[47] Z. J. Fan, J. Yan, T. Wei, L. J. Zhi, G. Q. Ning, T. Y. Li, F. Wei, *Adv. Funct. Mater.* **2011**, *21*, 2366–2375.

[48] H. L. Wang, L. F. Cui, Y. A. Yang, H. S. Casalongue, J. T. Robinson, Y. Y. Liang, Y. Cui, H. J. Dai, *J. Am. Chem. Soc.* **2010**, *132*, 13978–13980.

[49] B. Wang, J. Park, C. Y. Wang, H. Ahn, G. X. Wang, *Electrochim. Acta* **2010**, *55*, 6812–6817.

[50] W. S. Hummers, R. E. Offeman, *J. Am. Chem. Soc.* **1958**, *80*, 1339–1340.

[51] D. W. Wang, Q. H. Wang, T. M. Wang, *Inorg. Chem.* **2011**, *50*, 6482–6492.

[52] H. L. Wang, J. T. Robinson, G. Diankov, H. J. Dai, *J. Am. Chem. Soc.* **2010**, *132*, 3270–3271.

[53] T. Yu, J. Moon, J. Park, Y. Il Park, H. B. Na, B. H. Kim, I. C. Song, W. K. Moon, T. Hyeon, *Chem. Mater.* **2009**, *21*, 2272–2279.

[54] Z. S. Wu, W. C. Ren, L. Wen, L. B. Gao, J. P. Zhao, Z. P. Chen, G. M. Zhou, F. Li, H. M. Cheng, *ACS Nano* **2010**, *4*, 3187–3194.

[55] Y. W. Zhu, S. Murali, M. D. Stoller, K. J. Ganesh, W. W. Cai, P. J. Ferreira, A. Pirkle, R. M. Wallace, K. A. Cychosz, M. Thommes, D. Su, E. A. Stach, R. S. Ruoff, *Science* **2011**, *332*, 1537–1541.

[56] H. L. Wang, H. S. Casalongue, Y. Y. Liang, H. J. Dai, *J. Am. Chem. Soc.* **2010**, *132*, 7472–7477.

FULL PAPER

Tris(allylammonium) Hexabromobismuthate(III) – Crystal Structure, Phase Transitions and Thermal, Dielectric, Vibrational and ^{1}H NMR Properties Over a Range of Temperatures

Iwona Płowaś,*[a] Agata Białońska,[a] Grażyna Bator,[a] Ryszard Jakubas,[a] Wojciech Medycki,[b] and Jan Baran[c]

A novel inorganic-organic hybrid compound, allylammonium hexabromobismuthate(III), $(C_3H_5NH_3)_3BiBr_6$ (ABB), was synthesised and its structure determined by means of single-crystal X-ray diffraction studies at four temperatures (280, 230, 170 and 100 K). At 100 K, the compound crystallises in the monoclinic space group, $C2/c$. Its crystal structure consists of discrete $BiBr_6^{3-}$ anions and three inequivalent allylammonium $(C_3H_5NH_3)^+$ cations. Four solid-solid structural phase transitions for ABB were detectable by means of DSC and dilatometric techniques: continuous (I↔II) at 272/272 K (upon heating/cooling), discontinuous (II↔III) at 218/215, discontinuous (III↔IV) at 205/204 K and discontinuous (IV↔V) at 146/144 K. The ferroelastic domain structure was observed over one intermediate phase (III) below 215 K. The electric properties of ABB have been measured over a wide temperature range (105–310 K). Low frequency relaxation processes with dielectric increments $\Delta\varepsilon_1 \approx 0.9$ and $\Delta\varepsilon_2 \approx 0.05$ were observed within phases II and V, respectively. Temperature-dependent vibrational properties of ABB in the frequency region 3500–500 cm^{-1} and the molecular motions of its allylammonium cations were studied by means of proton magnetic resonance. The mechanisms of the phase transitions in the title compound are discussed.

Introduction

Organic-inorganic hybrids based on the halogenoantimonates(III) and halogenobismuthates(III) of the general formula $R_aM_bX_{3b+a}$ (where R denotes the organic cation, M the Sb^{III} or Bi^{III} ion and X denotes the halogen atom: Cl, Br, I) have been studied extensively. Protonated alkylammonium or heteroaromatic amines have been incorporated into the crystal structure. Many of the organic-halogenoantimonates(III) / halogenobismuthates(III) were found to exhibit unique properties with potential applications as nonlinear polar and nonlinear optical materials (NLO).[1–5] The anionic structure can vary considerably ranging from a system based on isolated MX_6 octahedra to ones containing extended chains and up to 2- or 3D networks. Experimental studies have shown that the ferroelectric properties have some tendency to appear in the 2D anionic substructures encountered in $R_3M_2X_9$-type connections.[6–9] So far, several synthesised ferroelectrics were found to crystallise with a $R_5M_2X_{11}$ composition in which the anionic network consists of discrete bioctahedral units $Bi_2X_{11}^{5-}$.[10–15] Generally, the ferroelectricity of these subgroups of crystals is due to the dynamics of the organic cations, thus the paraelectric-ferroelectric phase transitions are characterised by an "order-disorder" mechanism. The ferroelectricity appears in the compounds comprised of different types of cations, such as small size alkylammonium (methyl-, dimethyl- and trimethylammonium) and unsubstituted heteroaromatic moieties (imidazolium and pyridinium). Recently, the ferroelectric properties were reported in R_2MX_5 and RMX_4-type compounds containing bulky organic cations (methylviologen cation and stilbazolium or 4-aminopyridinium).[16–18] In the case of the n-alkylammonium cations incorporated into the crystal structure of halogenoantimonates(III) and halogenobismuthates(III), an increase of the alkyl chain length (n-propyl-, n-butyl- and n-pentylammonium) resulted in an increase in the complexity of the phase transition sequence because of various possible reorientational motions and conformational states of the organic moieties.[19–22] Recently, three allylammonium analogues, namely $(C_3H_5NH_3)_2SbCl_5\cdot(C_3H_5NH_3)Cl,$[23] $(C_3H_5NH_3)_3BiCl_6$[24] and $(C_3H_5NH_3)_3SbBr_6$[25] were synthesised and structurally characterised. These compounds undergo structural phase transitions, mostly below room temperature and this was explained in terms of the dynamics of the allylammonium cations.

In this paper, we report the single-crystal X-ray diffraction structures at four temperatures, as well as the thermal,

[a] Faculty of Chemistry, University of Wrocław,
Joliot-Curie 14, 50-383 Wrocław, Poland
Fax: +48-71-3282348
E-mail: plowas.iwona@gmail.com
[b] Institute of Molecular Physics, PAS,
Smoluchowskiego 17, 60-179 Poznań, Poland
[c] Institute of Low Temperature and Structure Research, PAS,
Okólna 2, 50-950 Wrocław, Poland

dielectric and temperature-dependent vibrational properties of $(C_3H_5NH_3)_3BiBr_6$. The present investigation of the spin-lattice relaxation time (T_1) was undertaken to obtain information about the cationic motion. The phase transitions mechanisms in $(C_3H_5NH_3)_3BiBr_6$ are discussed.

Results and Discussion

Single-Crystal X-ray Diffraction

The crystal structure of the title compound at 280 K belongs to the monoclinic system and space group *C*2/*m*. There is half a $BiBr_6^{3-}$ [hexabromobismuthate(III)] anion and three allylammonium cations in the asymmetric unit (Figure 1a). The geometry of the anions, which form the isolated octahedral units, is presented in the Supporting Information (Table S1). The Bi atom of the anion is located in a special position (mirror plane *m*). The anion exhibits disorder in which two of the four crystallographically unrelated bromine atoms (Br3, Br4) are located in the special positions (mirror plane *m*, occupancy factors are equal to 0.21) or close to them (Br31 and Br41). Similarly, all crystallographically unrelated allylammonium cations N1–C2–C3–C4, N11–C12–C13−C14 and N21–C22–C23−C24 (marked in red, black and blue in Figure 2, respectively), which are also located close to the special positions (mirror plane *m*), reveal disorder (Figure 2a). Taking into account the orientation matrix and the magnitude of the unit cell, the *c* axis of the unit cell at 230 K is twice as large as the one at 280 K. The *a* and *b* axes, and the *β* angle change only insignificantly. At 230 K the crystal structure was determined in the monoclinic system and space group *I*2/*a*. All components are located in general positions. Similarly to what was observed in the structure at 280 K, the anion reveals the disorder at 230 K. However, at 230 K, all six crystallographically unrelated bromine atoms of the anions reveal a two-site disorder with occupancy factors 0.79 and 0.21. In the crystal at 280 K and 230 K alike, there are three crystallographically unrelated allylammonium cations (see Figures 1b and 2b), although one of them is ordered, N1–C2–C3–C4, and this shows a N1–C2–C3–C4 torsion angle equal to 107.2(12)°. At 170 K, the crystal structure was determined in the monoclinic system and space group *C*2/*c* (when the matrix of orientation at 230 and 170 K is considered the same). A decrease in temperature results in a further ordering of the ions. At 170 K, only one of the three crystallographically unrelated cations is still disordered. The hexabromobismuthate(III) anion, as well as two of the three crystallographically unrelated allylammonium cations are ordered. The N1–C2–C3–C4 and the N11–C12–C13−C14 torsion angles of the ordered cations are equal to 106.1(9) and –112.8(10)°, respectively (see Figures 1c and
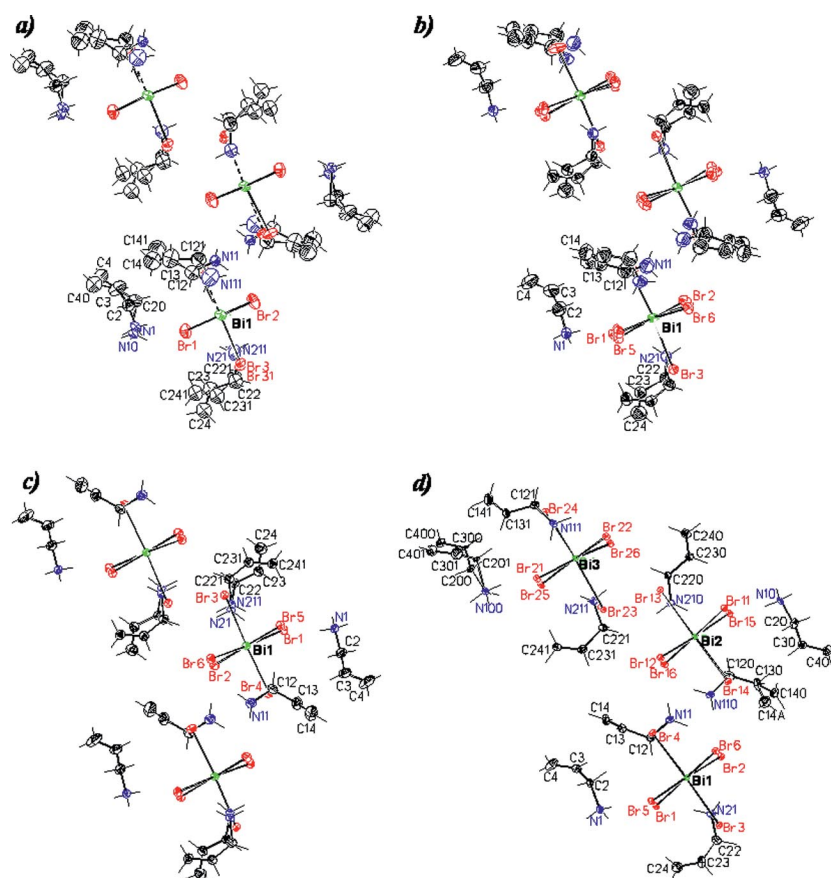
Figure 1. Crystal structure of $(C_3H_5NH_3)_3BiBr_6$ at (a) 280 K, (b) 230 K, (c) 170 K and (d) 100 K. The asymmetric unit is labelled. The thermal ellipsoids are drawn with 30% probability.
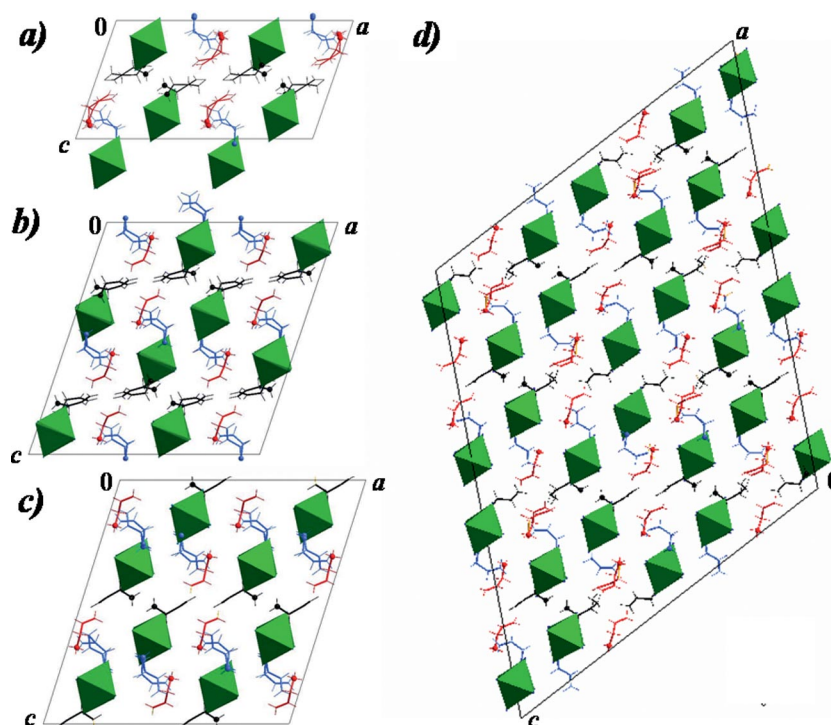
Figure 2. Packing of $(C_3H_5NH_3)_3BiBr_6$ at (a) 280 K, (b) 230 K, (c) 170 K and (d) 100 K. (The crystallographically unrelated allylammonium cations at 280 K and corresponding cations at 230, 170 and 100 K are marked in red, black and blue). The $[BiBr_6]^{3-}$ anions are shown as sold green octahedra (the disordered Br^- ions with occupancy factors smaller than 0.5 are omitted).

2c). At 100 K, the unit cell is about three times as large as the one at 170 K. Both the a and c axes are multiplied. At 100 K the crystal structure was determined in the monoclinic system and space group $C2/c$ (other than in the high temperature orientation matrix). There are three $BiBr_6^{3-}$ octahedral units and nine allylammonium cations in an asymmetric part of the unit cell (see Figures 1d and 2d). With a decrease in temperature, further ordering of the crystal structure was observed and at 100 K only two of the nine crystallographically unrelated cations exhibit disorder. The cations disordered at 170 K become ordered at 100 K. There are N21–C22–C23−C24, N210−C220−C230−C240 and N211−C221−C231−C241 cations and all of them adopt different conformations [the N21–C22–C23−C24, N210−C220−C230−C240 and N211−C221−C231−C241 torsion angles are equal to –68.9(14), –128.2(8) and –6.2(13)°, respectively]. On the other hand, two crystallographically unrelated cations ordered at 170 K become partially disordered at 100 K. The conformation of the ordered cations at 170 K does not change significantly at 100 K, except one of the two disordered cations, namely N110−C120−C130−C14A (occupancy factor equal to 0.31) for which the N110−C120−C130−C14A torsion angle is equal to –2(3)°.

Thermal Properties (TGA, DTA, DSC and Dilatometric)

Figure 3 shows the results of simultaneous TGA and DTA measurements between 300 and 700 K. The DTA thermogram clearly illustrates that the decomposition of

$(C_3H_5NH_3)_3BiBr_6$ at ca. 535 K is highly exothermic. Further heating above 620 K leads to a continuous and pronounced decomposition of the sample. The results of the calorimetric (DSC) measurements for $(C_3H_5NH_3)_3BiBr_6$ are presented in Figure 4. Four reversible anomalies were detected at: 272/272 K (I↔II), 218/215 K (II↔III), 205/204 K (III↔IV) and 146/144 K (IV↔V) (upon heating/cooling). The shape of the weak thermal anomaly observed at 272/272 K is characteristic of a continuous (second order) phase transition (PT). The sharp shape of the other thermal anomalies and the observed small temperature hysteresis suggest first order PTs. The values of the transition entropies, ΔS_{tr}, estimated to be ca. 5.4 $J\,mol^{-1}\,K^{-1}$ (II↔III),
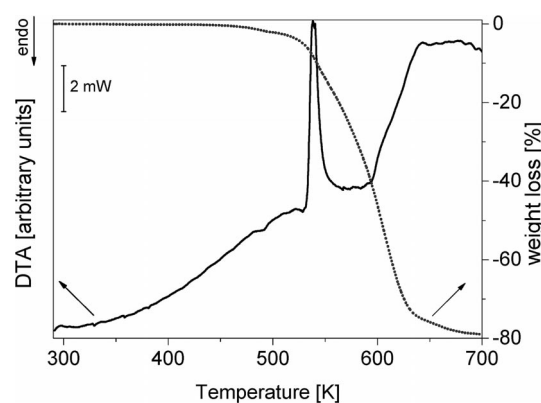
Figure 3. TGA and DTA thermograms of $(C_3H_5NH_3)_3BiBr_6$ between 300 and 700 K (m = 12.13 mg).

2.8 J mol^{-1} K^{-1} (III↔IV) and 5.5 J mol^{-1} K^{-1} (IV↔V) are characteristic of the transition with an "order-disorder" mechanism.
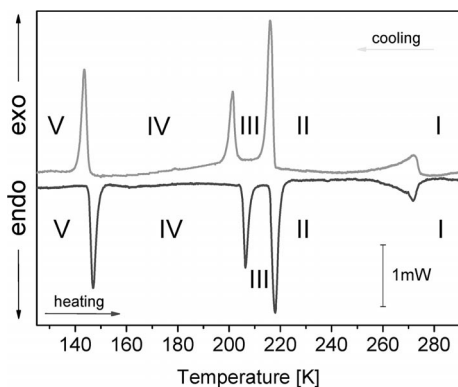
Figure 4. DSC runs of $(C_3H_5NH_3)_3BiBr_6$ (upon cooling/heating, 10 K min^{-1}, $m = 15$ mg).

Figure 5 presents the results of the linear thermal expansion, $\Delta L/L_0$, measured along three crystallographic directions for $(C_3H_5NH_3)_3BiBi_6$. The results acquired during cooling of the samples confirm the existence of four PTs. The thermal anomalies observed during the heating cycle (not presented in this paper) were reversible. The $\Delta L/L_0$ changes observed at 272 K (while cooling) along the a^* direction, perpendicular to the bc plane and the c direction are typical of a continuous (second order) transformation. This effect is not observed along the b direction. The thermal characteristics at 218/215 K, 205/204 K and 146/144 K (upon heating/cooling) confirm the first order character of the transitions. The value of $\Delta L/L_0$ at 215 K increases in the a^* and c directions and decreases in the b direction. The changes in the $\Delta L/L_0$ value at the PT are similar in the a^* and c directions and are approximately 1×10^{-2}. The value
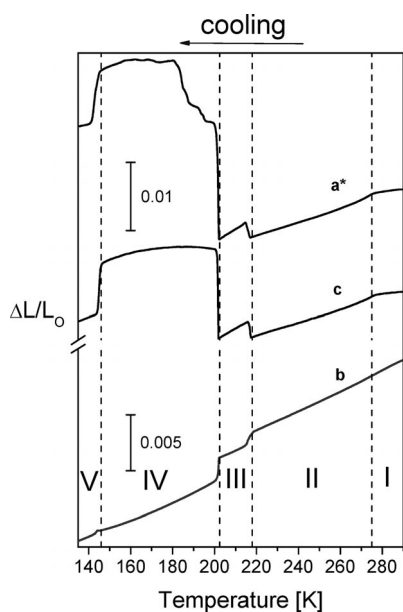
in the b direction is approximately 6×10^{-2}. The increase of the dimensionality of the sample at 204 K observed along the a^* and c directions is comparable and the $\Delta L/L_0$ value is close to 6.5×10^{-2}. Along the b axis, the $\Delta L/L_0$ value decreases by ca. 1×10^{-2}. In Figure 5, mechanical deformation over phase IV can be observed but only in the c direction. The value of $\Delta L/L_0$ at 144 K decreases along all three axes by about 3.7×10^{-2}, 3.7×10^{-2} and 2.5×10^{-4} for the a^*, c and b directions, respectively.

Dielectric Properties of $(C_3H_5NH_3)_3BiBi_6$

Dielectric measurements were performed during cooling scans in the temperature range 140–310 K at frequencies between 500 Hz and 1 MHz, in order to detect the possible relaxation processes and effects of the structural PTs on the dielectric characteristics of ABB. Figure 6a and b shows the temperature dependencies of the real part of the electric permittivity, ε', along two directions b and c. The results of the dielectric response along the c and a^* directions are quite similar thus the ε'_{a^*} (T,ω) function is presented in the Supporting Information (Figure S1). The crystal is characterised by a remarkable anisotropy of the electric permittivity. The highest values of ε' are found along the c direction and this applies to all five phases. It is worth noting that in phase II along the c direction, the permittivity increases upon cooling while along the b axis it decreases. According to expectations, at the I→II phase transition the changes within ε' are typical of the continuous phase transitions – there is no stepwise change in ε'. On the contrary, when the crystal experiences the II→III, III→IV and IV→V PTs, we observed a drop in the ε' value along the c direction by ca. 2, 1 and 0.5, respectively. Along the remaining directions, the values were adequately lower. Figure S2 (in the Supporting Information) shows, in turn, the temperature dependence of the imaginary part of the electric permittivity, ε'', measured along the a^* direction around the I→II phase transition and within phase V. A clear relaxation process can be seen at all used frequencies. Within phase V, however, it is characterised by an extremely low dielectric increment ($\Delta\varepsilon \approx 0.05$). The activation energy, E_A, was estimated on the basis of the temperature dependence of the maxima of ε''. The activation energies of the low- and high-temperature processes are less than 40 and 50 kJ mol^{-1}, respectively. The traces of these relaxation processes around the IV→V phase transition may also be observed along the b and c directions. When analysing the acquired dielectric results, it can be stated that there is a possibility of some molecular motion of dipolar groups which gradually freeze when the crystal of ABB undergoes successive phase transitions. The motion associated with the maximum change in the dielectric dipole moment is frozen in the I→II phase transition. It is interesting that the dielectric permittivity diminishes within the III, IV and V phase transitions as well. This indicates the continuous limitation of the molecular motion while cooling. The most interesting behaviour from the dielectric point of view is observed over phase II

Figure 5. Temperature dependencies of the linear thermal expansion for $(C_3H_5NH_3)_3BiBr_6$ along the a^*, b and c directions.

and within the II→III PT temperature. The increase of the dielectric increment just before reaching 215 K may be explained in terms of the strong dipole-dipole interactions and is characteristic of weak antiferroelectric materials.[26] On the other hand, the stepwise decrease in the electric permittivity below 215 K (with ε_{max} at 215 K) is encountered in crystals with antiferroelectric order.
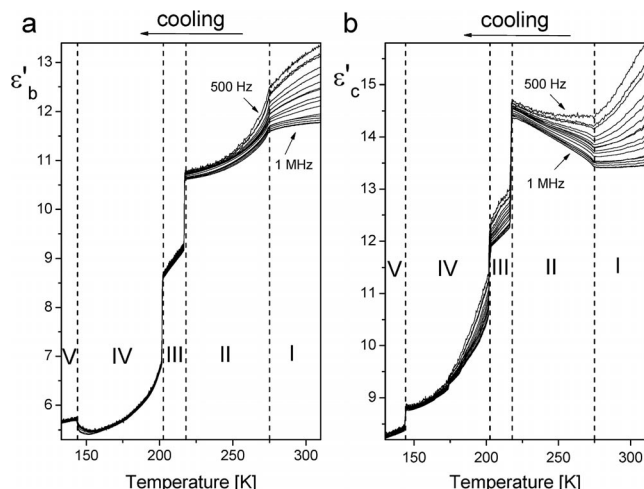
Figure 6. The temperature dependencies of the real parts of the electric permittivity at selected frequencies for $(C_3H_5NH_3)_3BiBr_6$ along the (a) b and (b) c directions.

Optical Observations

Below the transition temperature (II→III), 215 K, one can observe the plate-like ferroelastic domains in the bc plane with walls parallel to one of the monoclinic axis (b or c), see Figure 7a. The picture also shows the phase front between phases II and III. It should be emphasised that apart from the very thin domains, one can see larger in size ones (dark) which are most likely the ferroelastic needle-like domains which are straight with a sharp tip at the end. Below 204 K plate-like domains disappear whereas the traces of large needle domains, unexpectedly, are still maintained (Figure 7b). This ferroelastic domain pattern is quite complicated and requires additional studies. The presence of a domain structure over phase III suggests a change in the point group of this crystal according to the Sapriel classification – to the 2/mF1 species.[27] Below 204 K (phase IV) the compound increases its point group, once more, to the monoclinic 2/m group.
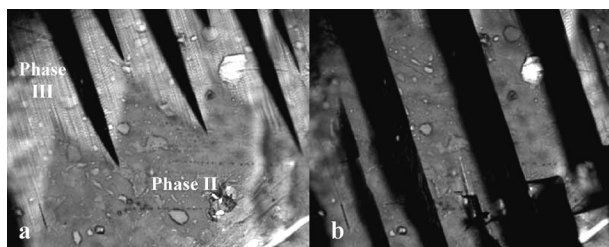
Figure 7. The microphotographs of the $(C_3H_5NH_3)_3BiBr_6$ crystal taken upon cooling during: (a) the II→III PT, (b) phase IV.

Vibrational Properties

The wavenumber regions in which the most spectacular changes are observed during heating of $(C_3H_5NH_3)_3BiBr_6$ from 10 to 300 K will be discussed in the further part of this paper. Figure 8 presents the IR spectra of $(C_3H_5NH_3)_3$-$BiBr_6$ between 3500 and 40 cm^{-1} at 10 K (in KBr) and 300 K (in KBr, Nujol and Fluorolube) as well as the Raman spectra at 300 K. The wavenumber regions between 3000 and 2800, 1530 and 1350 as well as 750 and 700 cm^{-1} are shown as dotted lines because the bands in these regions may arise both from the compound studied and the Nujol film on the KBr windows used. Additionally, the IR spectrum was recorded, in a Fluorolube suspension, covering the above-mentioned regions. The assignments of the observed bands in the IR and Raman spectra were made on the basis of the literature data for the neat allylamine[28] and allylammonium cations[25] and the internal modes of $BiBr_6^{3-}$ (Table 1).[29]
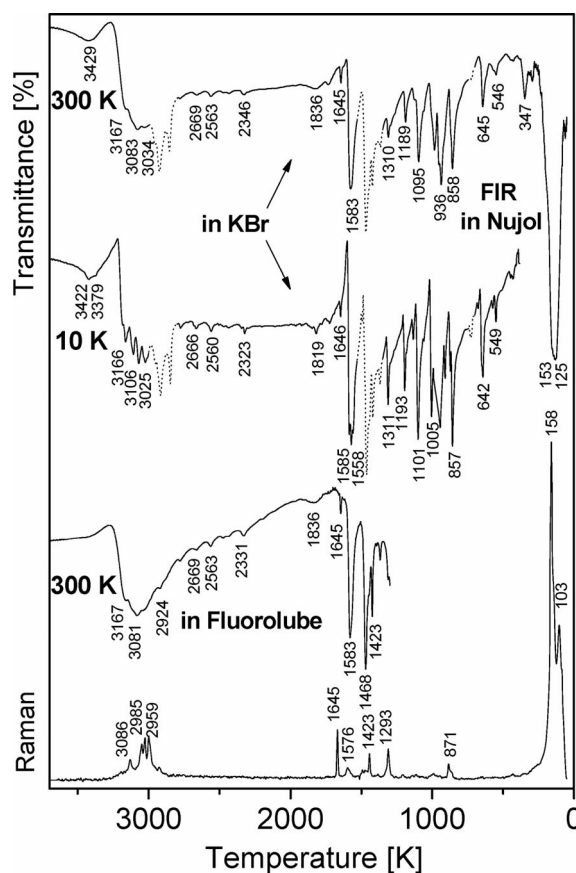
Figure 8. IR spectra of $(C_3H_5NH_3)_3BiBr_6$ in KBr mulls (10 K and 300 K), in Fluorolube mulls (300 K), FTIR spectra (in Nujol, 300 K) and the FT-Raman spectra (300 K).

The temperature evolution of the bands in the infrared spectra of $(C_3H_5NH_3)_3BiBr_6$ between 1610 and 1530 cm^{-1} assigned to the $\delta(NH_3^+)$ deformation vibrations is shown in Figure 9. There are three modes (1585, 1571 and 1558 cm^{-1}) at 10 K in this range. During the III→II phase transition, as a result of broadening of bands, the modes correspond-

Table 1. Wavenumbers [cm^{-1}], intensities and tentative assignments[a] of the bands observed in the IR and Raman spectra of $(C_3H_5NH_3)_3BiBr_6$ at 10 and 300 K.

IR 10 K	300 K	Raman 300 K	Assignments
3422 vw	3429 vw		ν(OH)
3379 vw			
3183 w			ν$_{as}$(NH$_3^+$)
3166 m	3167 m		
3117 m sh	3124 m sh		ν$_s$(NH$_3^+$)
3106 m			
3074 vs	3083 m	3086 vw	ν$_{as}$(=CH$_2$)
	3081 m*		
3039 m sh	3034 m		
3025 m		3017 vw sh	ν$_s$(=CH$_2$)
3005 m sh		3008 vw	
	2983 s*	2985 vw	
2952 m	2955 s	2959 vw	ν$_{as}$(CH$_2$)
2915 s	2924 s	2925 vw	
	2888 s*	2887 vw	
	2875 s*	2878 vw	
2847 s	2853 s		ν$_s$(CH$_2$)
		2839 vw	
2776 w	2779 w		
2666 w	2669 w		
2560 w	2563 w		
2470 w	2476 w		
2442 w	2430 w		
1819 w	1836 w		overtones
1646 w	1645 w	1645 vw	ν(C=C)
1585 vs	1583 s		
1571 vs	1568 s	1576 vw	
1558 vs		1561 vw	δ(NH$_3^+$)
		1546 vw	
1495 w			
1477 m		1472 vw	
1463 vs	1468 vs		
	1454 s*	1453 vw	δ(CH$_2$)
1444 s sh	1445 s sh	1439 vw	
1419 s	1423 s	1423 vw	δ(=CH$_2$)
	1392 w*		ω(CH$_2$)
1368 s	1365 s	1363 vw	
1311 s	1310 m		τ(NH$_3^+$)
1293 m sh	1292 m sh	1293 vw	
1264 m sh	1263 m sh		combination of
1193 s	1189 m	1189 vw	τ(CH$_2$) and
			ρ(NH$_3^+$)
1179 m sh			
1134 m	1129 w	1126 vw	
1101 vs	1095 s		ν(C–N)
1058 m	1055 m		ν(C–C)
1005 s	1009 m sh		combination of
986 s	984 s		τ(=CH$_2$) and
			ρ(NH$_3^+$)
977 s		975 vw	
961 vs			ω(NH$_3^+$)
956 vs	955 s	956 vw	

Table 1. *(Continued)*.

IR 10 K	300 K	Raman 300 K	Assignments
949 s			
944 s			
937 s sh	936 s	935 vw	
930 s sh			ρ(CH$_2$)
923 s sh			
909 m	916 m sh		
899 m sh			
873 m	871 m sh	871 vw	ρ(=CH$_2$)
857 vs	858 s	852 vw	
674 w			
653 m	645 m		γ(=CH) op
642 m		637 vw	
572 w	562 w		
549 w	546 w	549 vw	
430 vw	428 vw		
	347 w	345 vw	ν(C–C–N)
	295 vw	287 vw	
	251 vw		
	231 vw		
	153 vs	158 vs	
		140 m	
	134 vs		ν(Bi–Br)
	130 vs		
	125 vs		
		103 m	lattice vibration
81 m		82 m	
77 w			
71 w		70 vw	

[a] s: strong, w: weak, sh: shoulder, m: medium, vw: very weak, *: in Fluorolube, op: out of plane.

ing to wavenumbers 1571 and 1558 cm^{-1} overlap. Because of that, over phase II and I, only two bands can be distinguished.
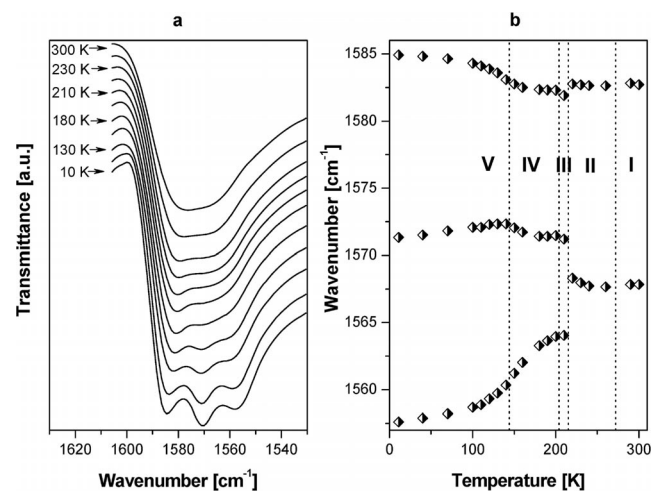
Figure 9. (a) Temperature evolution of the bands in the IR spectra of $(C_3H_5NH_3)_3BiBr_6$ between 1610 and 1530 cm^{-1}, (b) temperature dependence of their respective wavenumbers.

The other characteristic changes in the evolution of the spectra of $(C_3H_5NH_3)_3BiBr_6$ are presented in Figure 10. The modes between 1350 and 1120 cm^{-1} can be assigned to the $\tau(NH_3^+)$ twisting, $\tau(CH_2)$ twisting and $\rho(NH_3^+)$ rocking vibrations. At the lowest temperature (10 K) four bands can be detected. One of them (1179 cm^{-1} at 10 K) disappears at about 170 K (phase IV). One additional mode (1158 cm^{-1}) is found at 70 K (phase V) and disappears at about 240 K (phase II). Over phase I, three bands are observed. As we can see in Figure 10a, the three modes are rather fixed. According to expectations, the intensity of the modes decreases upon heating (Figure 10c).
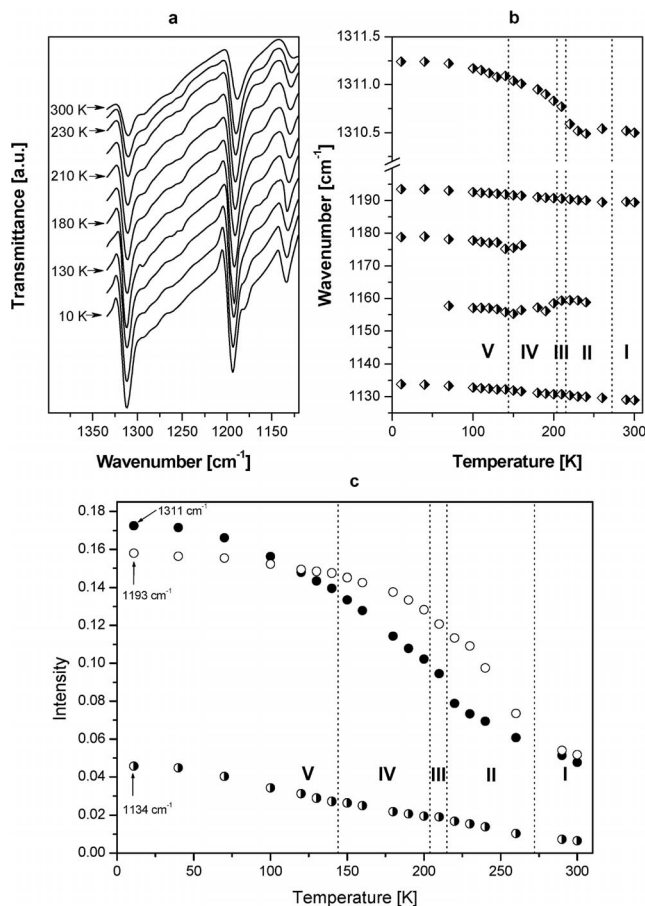
Figure 10. (a) The temperature evolution of the bands in the IR spectra of $(C_3H_5NH_3)_3BiBr_6$ between 1350 and 1120 cm^{-1}, (b) temperature dependence of their respective wavenumbers, (c) intensity of the modes (1134, 1193 and 1311 cm^{-1}).

Figure 11a presents the temperature evolution of the spectra of $(C_3H_5NH_3)_3BiBr_6$ between 970 and 830 cm^{-1} and the temperature dependence of the band wavenumbers which has been separated into two parts (Figure 11b and c). Figure 11b presents the region between 961 and 920 cm^{-1}, in which the bands are assigned to the $\omega(NH_3^+)$ wagging and $\rho(CH_2)$ rocking vibrations. Seven bands (961, 956, 950, 944, 937, 930 and 923 cm^{-1}) are observed at the lowest temperature. At $T_{c(V \rightarrow IV)}$, only three of them can still be seen. At T = 250 K (phase II) one mode (944 cm^{-1}) disappears. Over phase I, two bands can be distinguished. Figure 11c shows the temperature dependence of the band frequencies, observed in the region between 918 and 855 cm^{-1}, assigned to the $\rho(CH_2)$ and $\rho(=CH_2)$ rocking vibrations. Four bands (909, 899, 873 and 857 cm^{-1}) are seen at 10 K,
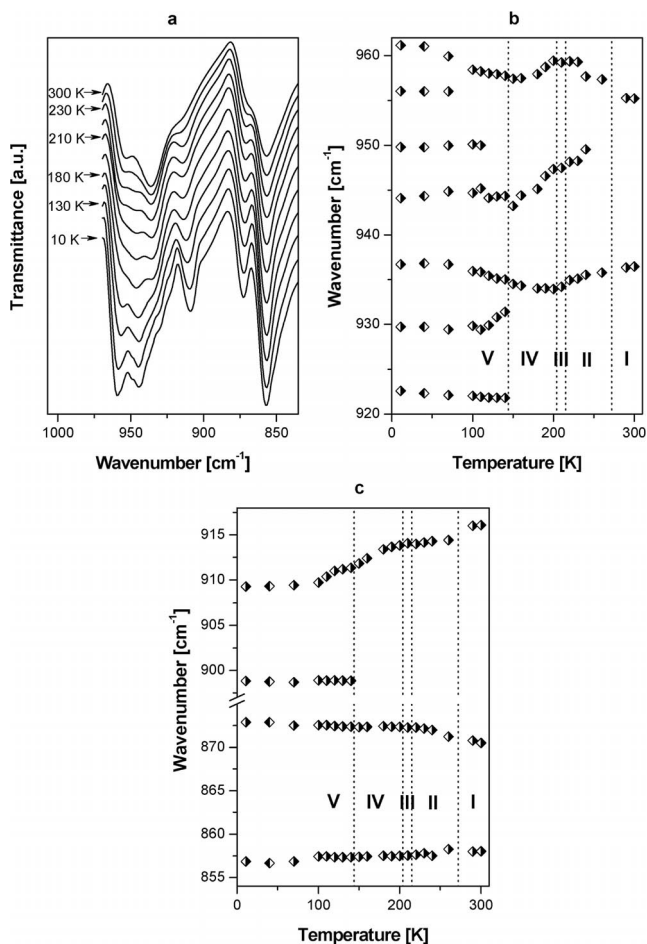
Figure 11. (a) The temperature evolution of the bands in the IR spectra of $(C_3H_5NH_3)_3BiBr_6$ between 970 and 830 cm^{-1}, (b) temperature dependencies of their respective wavenumbers between 961 and 920 cm^{-1} and (c) between 918 and 855 cm^{-1}.
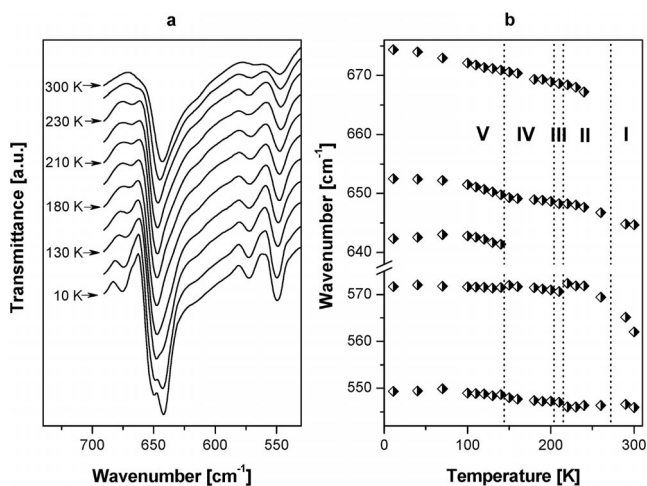
Figure 12. (a) The temperature evolution of the bands in the IR spectra of $(C_3H_5NH_3)_3BiBr_6$ between 700 and 530 cm^{-1}, (b) temperature dependence of their respective wavenumbers.

one of which (899 cm^{-1}) disappears at $T_{c(V\rightarrow IV)}$. The three remaining modes may be observed from $T_{c(V\rightarrow IV)}$ up to 310 K (Figure 11c).

The final temperature evolution of the spectra of $(C_3H_5NH_3)_3BiBr_6$ considered in this paper, is shown in Figure 12. The bands observed in the presented region between 700 and 530 cm^{-1} can be assigned to the $\gamma(=CH)$ out of plane deformation vibrations. Five bands (674, 653, 642, 572 and 549 cm^{-1}) are observed therein at 10 K, four of them are seen within phases IV and III. The mode corresponding to 674 cm^{-1} (10 K) disappears above 250 K (phase II). During phase I, only three bands are observed (Figure 12b).

Proton Magnetic Resonance (^{1}H NMR) Studies

The temperature dependence of the ^{1}H NMR spin-lattice relaxation time (T_1) for $(C_3H_5NH_3)_3BiBi_6$ is presented in Figure 13. The studied dependence has the form of a very broad minimum of the longitudinal proton relaxation times (T_1). At the temperatures of the phase transitions, the following changes can be observed: a jump of the relaxation time (272 K) and a change of slope (218, 205 K). On the other hand, at 146 K, despite the presence of a phase transition, no change in T_1 could be detected. At two temperatures, 95 and 108 K, the slope changes were found, which might indicate the presence of a phase transition not confirmed so far by other methods. For all the observed slopes in the temperature dependence of the ^{1}H NMR spin-lattice relaxation time (T_1), the activation energies were determined within the temperature range 110–196 K. In order to determine the parameters of the model, the BPP theory equation was employed:[30]

$$\frac{1}{T_1} = C\left[\frac{\tau_c}{1+\omega^2\tau_c^2} + \frac{4\tau_c}{1+4\omega^2\tau_c^2}\right]$$

where ω represents the resonance angular frequency, C is the relaxation constant and τ_c is the correlation time. The value of the observed minimum in the relaxation time T_1 within the 110–196 K temperature range equals 39 ms (at 136 K). The temperature dependence of the correlation time is described by the Arrhenius equation:

$$\tau_c = \tau_0\, exp(E_A/RT)$$

where τ_0 represents correlation time at the high temperature limit, E_A is the activation energy and R is the gas constant. The observed values of the dynamic parameters are as follows: the activation energy E_A = 6.49 kJ mol^{-1}, the correlation time $\tau_0 = 1.1\times10^{-11}$ s and the relaxation constant C = 2.66×10^9 s^{-2}. It should be added that the fitting procedure did not consider the presence of the phase transition at 146 K and we conclude that this phase transition should be associated with the dynamics of anions. The allylammonium cation consists of four components: NH$_3^+$, $-$CH, $-$CH$_2$ and $-$CH$_2$. From the NMR relaxation point of view, the C_3 reorientation of the ammonium groups $-$NH$_3^+$ should be most dominant in the allylammonium molecule.

In addition to that motion, subsequent movements of particular parts are possible due to the flexibility of the cation chain. In the room temperature phase, the beginning of axial reorientation of the entire cation may be expected.
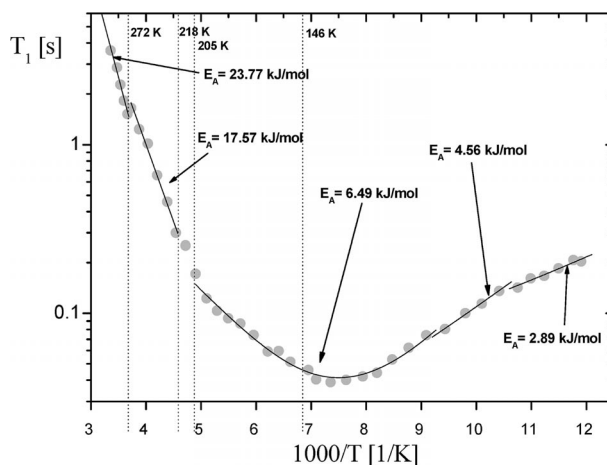
Figure 13. Temperature dependence of the relaxation time (T_1) of $(C_3H_5NH_3)_3BiBr_6$.

The activation energies (E_A) estimated over a wide temperature range reflect the sequence of relaxation processes starting progressively with increasing temperature. The E_A value obtained in the 110–196 K temperature range (ca. 6 kJ mol^{-1}) is comparable with that of the C_3 reorientation of the $-$NH$_3^+$ groups in various alkylammonium cations such as the CH$_3$NH$_3^+$ cation in (CH$_3$NH$_3$)$_5$Bi$_2$Cl$_{11}$[31] and its deuterated derivatives,[32] and the *n*-propylammonium cation of (*n*-C$_3$H$_7$NH$_3$)$_2$SbBr$_5$.[33] A rapid increase in the E_A value around 218 K coincides with the structural PT from phase II to III and may be explained by the release of cationic motion around the long axes of the molecules. A further increase in the E_A value (ca. 25%) reflects the presence of a subtle structural anomaly at about 272 K.

Discussion

The sequence of PTs in the analysed allylammonium analogues[23–25] is presented in Figure 14. According to the anionic framework, all the allylammonium compounds can be divided into two subgroups. The formal stoichiometry is R$_3$MX$_6$. For the ACA, however, the correct notation is R$_3$MX$_5$·X. The R$_3$MX$_6$-type compounds are characterised by isolated MX$_6$ octahedra while the anionic framework of ACA consists of a discrete [Bi$_2$Cl$_{10}$]$^{4-}$ bioctahedra and two isolated Cl$^-$ ions. Despite a different anionic structure, the common feature from the point of view of dynamic properties of these compounds is the presence of reorientational motions of the organic cations around their long axes. Additionally, the R$_3$MX$_6$ and R$_3$MX$_5$·X-type compounds are characterised by zero-dimensionality of the anionic substructure (0D). If the anionic network in R$_3$MX$_5$·X compound had formed polyanionic chains (1D structure), the crystal packing of cations would have been significantly different. There are some analogies between sequences of PTs

in all the R_3MX_6-type compounds. One is that they seem to be isomorphic in the monoclinic high temperature phase I ($C2/m$). The most characteristic common feature of the R_3MX_6-type analogues is the presence of an intermediate ferroelastic phase at low temperatures.
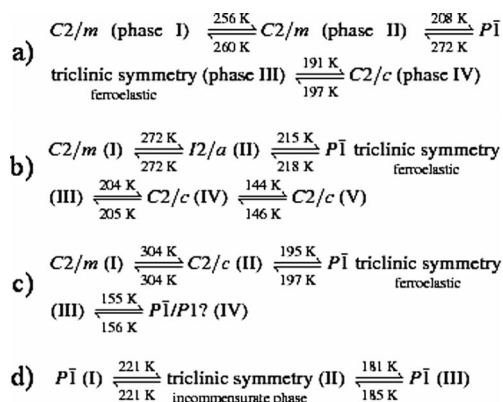
Figure 14. The sequence of PTs in (a) $(C_3H_5NH_3)_3SbBr_6$ (ABA), (b) $(C_3H_5NH_3)_3BiBr_6$ (ABB), (c) $(C_3H_5NH_3)_3BiCl_6$ (ACB), (d) $(C_3H_5NH_3)_3SbCl_5\cdot Cl$ (ACA).

The phase situation observed in ACA is less complex compared with that found in the other three allylammonium analogues. Only two phase transitions were detected in ACA. At 298 K (phase I) and 86 K (phase II) the crystal adopts the lowest point group (1). In the low-temperature phase, the volume of the unit cell is doubled. The structure in phase II is incommensurably modulated. The intermediate phase (II) of ACA is not ferroelastic as was observed in R_3MX_6-type compounds. The sequence of PTs in ABB is the most complex among the analysed allylammonium analogues. The change in the dynamic properties of ABB is related to a stepwise ordering of allylammonium cations as well as anionic octahedra (Figure 15). The I→II PT (second order) observed in ABB is accompanied by a partial ordering of the allylammonium cations (type N1), whereas the remaining ones and the $BiBr_6^{3-}$ moieties are still disordered over phase II. $\Delta S_{tr(I\to II)}$ could not be estimated based on a DSC experiment because this transition exhibits a pure continuous feature. The crystal structure of the intermediate phase (III) is still unknown. Nevertheless, the transitions from phase II to phase III and from phase III to IV are accompanied by significant changes in the dynamics of both allylammonium cations and the $BiBr_6$ octahedron. The total ΔS_{tr} for these transitions exceeds 8 J mol^{-1} K^{-1} and confirms postulated changes in the reorientational disorder of the molecules. In phase IV, except for the N21-type cations, all molecules are ordered. During the last PT, IV→V, the ordering of the N21-type cations seems to be confirmed by the calorimetric studies (ΔS_{tr} = 5.5 J mol^{-1} K^{-1}). In the lowest temperature phase (V), one of three inequivalent cations (type N1 and N11), constituting three different types (total number of cations: 9), exhibits static disorder (two-site model). All PTs in ABB, on the basis of DSC and X-ray studies, are classified as "order-disorder". The I→II PT and especially the II→III and III-

→IV PTs are dielectrically active. Two later ones are characterised by a noticeable reduction in the dielectric increment ($\Delta \varepsilon \approx 1.5$–2.5). Freezing of the motion of dipolar allylammonium cations reorienting around their long axes, leads to a significant decrease in the epsilon value. It should be emphasised that, over phase II, the electric permittivity (ε') shows a visible increase (when approaching 215 K) which may reflect weak collective motions of cations, typical of ferroelectric materials. The dynamics of these polar groups is relatively slow because the dielectric relaxation process over phase II takes place within the kilohertz frequency region. The motion of the $BiBr_6^{3-}$ moieties (embedded small dipole moment) is not expected to contribute to the electric polarisation of the system (ε). Below $T_{c(III\to IV)}$, ε' drops continuously to a relatively small value, which indicates that electric dipoles are becoming more and more ordered. The ^{1}H NMR studies at the lowest temperature (phase V), indicate merely the C_3 type motion of the $-NH_3^+$ groups. With the increase in temperature over phases II and I, release of the cationic motions around the long axis of the molecules is postulated. The cationic substructure dynamics proposed by X-ray diffraction results of ABB are fully confirmed by the present ^{1}H NMR studies of cationic motions around the long axes of the molecules.
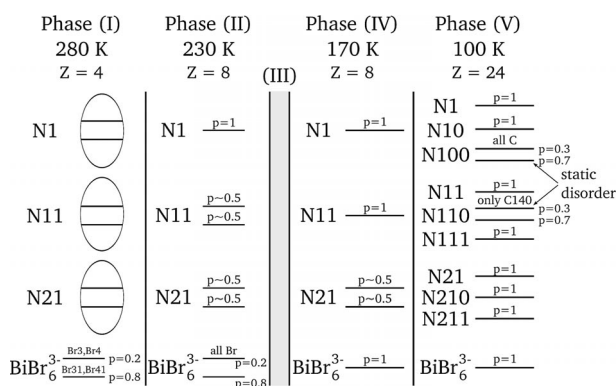
Figure 15. Schematic representation of the disorder of the allylammonium cations and BiB_6^{3-} anions in ABB (p is the probability for each position of the same ions). Ellipsoids in phase I mean that cations are characterised by multiple positions but during determination of the structure, a two-site model was assumed.

Conclusions

The complex of allylamine and bismuth(III) bromide has been discovered to crystallise in a stoichiometric ratio of 3:1 to give $(C_3H_5NH_3)_3BiBr_6$ (ABB). The anionic substructure consists of discrete $BiBr_6$ octahedral units (0D-type) and organic cations. All molecules appeared to be highly disordered in the room temperature phase (monoclinic symmetry, $C2/m$). The progressive diminishing of reorientational motions of anionic and cationic moieties with temperature leads to four solid-solid phase transitions (PTs) at 272, 215, 204 and 144 K. One intermediate phase (between 215 and 204 K) exhibits a ferroelastic domain structure. The single-crystal X-ray diffraction at four temperatures,

Table 2. Experimental data for X-ray diffraction study of $(C_3H_5NH_3)_3BiBr_6$ at 280, 230, 170 and 100 K.

Formula weight [g mol^{-1}]	862.75	862.75	862.75	2588.26
T [K]	280(2)	230(2)	170(2)	100(2)
λ [Å]			0.71073	
Crystal system			monoclinic	
Space group	$C2/m$	$I2/a$	$C2/c$	$C2/c$
a [Å]	23.725(3)	23.546(3)	23.675(3)	47.408(4)
b [Å]	8.082(2)	8.047(2)	7.987(2)	7.960(2)
c [Å]	12.497(3)	24.955(3)	24.590(3)	39.066(4)
β [°]	109.02(3)	108.65(3)	107.47(3)	116.95(3)
V [Å^3]	2265.4(8)	4480.1(14)	4435.3(14)	13141(4)
Z	4	8	8	24
ρ [g cm^{-1}]	2.530	2.558	2.584	2.616
μ [mm^{-1}]	18.359	18.567	18.754	18.989
Crystal size [mm]			$0.17 \times 0.11 \times 0.06$	
R_1/R_2 indices [$I > 2\sigma(I)$]	0.0314/0.0621	0.0276/0.0491	0.0294/0.0585	0.0314/0.0523

thermal, dielectric, vibrational (IR) and ^{1}H NMR studies confirmed the contributions of the anionic and cationic dynamics to the mechanism of successive PTs.

Experimental Section

General: The crystals of $(C_3H_5NH_3)_3BiBr_6$ were prepared by a reaction of prop-2-en-1-amine (allylamine) and $BiBr_3$ in a concentrated HBr solution (molar ratio 3:1). The crystalline products were twice recrystallised. Single crystals were grown by slow evaporation from an aqueous solution at constant room temperature.

The purity of the compound was confirmed by elemental analysis and PXRD. The mass percentages were: N 4.91 (4.90); C 12.73 (12.61); H 2.74 (2.82). The values in brackets are theoretical.

Differential scanning calorimetry (DSC) runs were recorded with a Perkin–Elmer DSC 8500 instrument in the temperature range 100–350 K with a ramp rate of 5 K min^{-1}. The TGA and DTA measurements were performed on a Setaram SETSYS 16/18 instrument between 290 and 700 K with a ramp rate of 2 K min^{-1}. The scan was performed in flowing nitrogen (flow rate: 1 dm^3 h^{-1}). The dilatometric measurements were carried out by using a Perkin–Elmer TMA-7 thermomechanical analyser in the temperature range 100–350 K with a ramp rate of 2 K min^{-1}. The dimensions of the sample were as follows $5 \times 3 \times 1$ mm.

The complex electric permittivity, $\varepsilon^* = \varepsilon' - i\varepsilon''$, was measured with Agilent 4284A and Agilent 4980A Precision LCR meters in the frequency between 100 Hz and 2 MHz and in the temperature range between 100 and 350 K. The dimensions of the single crystal sample were as follows $5 \times 3 \times 1$ mm. The plates were painted silver. The overall error in the estimation of the real and imaginary parts of the complex electric permittivity was about 5%. The pyroelectric charge was measured by using a KEITHLEY 617 electrometer with a temperature rate of 3 K min^{-1}.

The infrared spectra of the crystals [mulls in KBr and Fluorolube (at room temperature)] in the temperature range 10–300 K were recorded with a Bruker IFS-88 FTIR spectrometer over the wavenumber range 4000–40 cm^{-1} with a resolution of 1.0 cm^{-1}. Powder FT-Raman spectra were recorded with an FRA-106 attachment to the Bruker IFS-88 spectrometer over the wavenumber range 3500–80 cm^{-1} at room temperature. The program GRAMS/386 from Galactic Industries was used for numeral fitting of the experimental data.

Measurements of proton relaxation times T_1 were carried out over a wide temperature range, using a Bruker SXP pulse spectrometer

operating at a Larmor frequency of 90 MHz, by means of 180°–(τ)–90° pulse sequences for times less than 1 s and by a saturation recovery method for times longer than 1 s. For the ^{1}H NMR experiment, the sample was evacuated and sealed off.

Single-crystal X-ray diffraction measurements were performed on a Kuma KM4CCD-axis diffractometer with graphite-monochromated Mo-K_α radiation using an Oxford Cryosystem device (Table 2). The data were corrected for Lorentz and polarisation effects. An analytical absorption correction was applied. Data reduction and analysis were carried out with the Oxford Diffraction (Poland) Sp. z o.o. (formerly Kuma Diffraction Wroclaw, Poland) programs. The structures were solved by Patterson methods and refined by the full-matrix least-squares method using all F^2 data, as implemented by the SHELXL97 program.[34]

CCDC-835098, -835099, -835100, -835101 contain the supplementary crystallographic data for $(C_3H_5NH_3)_3BiBr_6$ at 280 K, 230 K, 170 K and 100 K, respectively. These data can be obtained free of charge from The Cambridge Crystallographic Data Centre via www.ccdc.cam.ac.uk/data_request/cif.

Supporting Information (see footnote on the first page of this article): Table S1. Selected bond lengths (Å) and angles (°) of $(C_3H_5NH_3)_3BiBr_6$ at 280 K, 230 K, 170 K and 100 K.

[1] R. Jakubas, L. Sobczyk, *Phase Transitions* **1990**, *20*, 163–193.
[2] L. Sobczyk, R. Jakubas, J. Zaleski, *Pol. J. Chem.* **1997**, *71*, 265–300.
[3] W. Bi, N. Louvain, N. Mercier, J. Luc, I. Rau, F. Kajzar, B. Sahraoui, *Adv. Mater.* **2008**, *20*, 1013–1017.
[4] D. B. Mitzi, P. Brock, *Inorg. Chem.* **2000**, *39*, 6107–6113.
[5] A. M. Goforth, J. R. Gardinier, M. D. Smith, L. Peterson, H. C. zur Loye, *Inorg. Chem. Commun.* **2005**, *8*, 684–688.
[6] J. Zaleski, A. Pietraszko, *Acta Crystallogr., Sect. B* **1996**, *52*, 287–295.
[7] M. Bujak, R. J. Angel, *J. Solid State Chem.* **2005**, *178*, 2237–2246.
[8] R. Jakubas, U. Krzewska, G. Bator, L. Sobczyk, *Ferroelectrics* **1988**, *77*, 129–135.
[9] J. Zaleski, C. Pawlaczyk, R. Jakubas, H. G. Unruh, *J. Phys. Condens. Matter* **2000**, *12*, 7509–7521.
[10] J. Matuszewski, R. Jakubas, L. Sobczyk, T. Głowiak, *Acta Crystallogr., Sect. C* **1990**, *46*, 1385–1388.
[11] J. Lefebvre, P. Carpentier, R. Jakubas, *Acta Crystallogr., Sect. B* **1995**, *51*, 167–174.
[12] J. Jóźków, G. Bator, R. Jakubas, A. Pietraszko, *J. Chem. Phys.* **2001**, *114*, 7239–7246.
[13] R. Jakubas, A. Piecha, A. Pietraszko, G. Bator, *Phys. Rev. B* **2005**, *72*, 104107–104108.

I. Płowaś et al.

[14] A. Piecha, G. Bator, R. Jakubas, *J. Phys. Condens. Matter* **2005**, *17*, L411–L417.

[15] A. Piecha, A. Białońska, R. Jakubas, *J. Phys. Condens. Matter* **2008**, *20*, 325224.

[16] W. Bi, N. Leblanc, N. Mercier, P. Auban-Senzier, C. Pasquier, *Chem. Mater.* **2009**, *21*, 4099–4101.

[17] G. Xu, Y. Li, W. Zhou, G. J. Wang, X. Long, L. Cai, M. Wang, G. Guo, J. Huang, G. Bator, R. Jakubas, *J. Mater. Chem.* **2009**, *19*, 2179–2183.

[18] R. Jakubas, Z. Ciunik, G. Bator, *Phys. Rev. B* **2003**, *67*, 024103–024106.

[19] P. Ciąpała, J. Zaleski, G. Bator, R. Jakubas, A. Pietraszko, *J. Phys. Condens. Matter* **1996**, *8*, 1957–1970.

[20] P. Ciąpała, R. Jakubas, G. Bator, J. Zaleski, A. Pietraszko, M. Drozd, J. Baran, *J. Phys. Condens. Matter* **1997**, *9*, 627–645.

[21] B. Zarychta, J. Zaleski, *Z. Naturforsch. B* **2006**, *61*, 1101–1109.

[22] J. Tarasiewicz, R. Jakubas, J. Zaleski, J. Baran, *J. Mol. Struct.* **2008**, *876*, 86–101.

[23] B. Zarychta, M. Bujak, J. Zaleski, *Z. Naturforsch. B* **2007**, *62*, 44–50.

[24] B. Zarychta, M. Bujak, J. Zaleski, *Z. Naturforsch. B* **2004**, *59*, 1029–1034.

[25] I. Płowaś, A. Białońska, R. Jakubas, G. Bator, B. Zarychta, J. Baran, *Chem. Phys.* **2010**, *375*, 16–25.

[26] R. Kumai, S. Horiuchi, Y. Okimoto, Y. Tokura, *J. Chem. Phys.* **2006**, *125*, 084715.

[27] J. Sapriel, *Phys. Rev. B* **1975**, *12*, 5128–5140.

[28] W. A. Herrebout, C. Zheng, B. van der Veken, J. Durig, *J. Mol. Struct.* **2003**, *645*, 109–132.

[29] J. Laane, P. W. Jagodziński, *Inorg. Chem.* **1980**, *19*, 44–49.

[30] N. Bloembergen, E. Purcell, R. Pound, *Phys. Rev.* **1948**, *73*, 679–712.

[31] W. Medycki, N. Piślewski, R. Jakubas, *Solid State Nucl. Magn. Reson.* **1993**, *2*, 197–200.

[32] W. Medycki, *Solid State Nucl. Magn. Reson.* **1999**, *13*, 213–218.

[33] N. Piślewski, J. Tritt-Goc, R. Jakubas, *Solid State Nucl. Magn. Reson.* **1994**, *3*, 293–297.

[34] G. M. Sheldrick, *Acta Crystallogr., Sect. A* **2008**, *64*, 112–122.

A Novel MALDI-MS Approach for the Analysis of Neutral Metallosupramolecular Architectures

Aurélie Même,[a] Artur R. Stefankiewicz,[b] Jack Harrowfield,[b] Xiao-Yu Cao,[b] Juhani Huuskonen,[c] Kari Rissanen,[c] Jean-Marie Lehn,[b] Hélène Nierengarten,[a] and Emmanuelle Leize*[a]

Matrix assisted laser desorption/ionisation mass spectrometry (MALDI-MS) methods have been developed for the characterisation of neutral [2×2] metallogrids derived from diimine, dihydrazone and diacylhydrazone ligands. Such grids may be protonated in solution to give cationic species but in most cases these are labile, so that rather delicate conditions are required for observation of the intact metallogrids as monoprotonated derivatives in the gas phase. As a MALDI matrix, 2,4,6-trihydroxyacetophenone (THAP) is sufficiently acidic to enable monoprotonation of the grids unaccompanied by dissociation, and if the grid sample is initially deposited by a layering technique to avoid any preliminary dissociation in solution the mass spectrum of the intact mono-

protonated grid is readily obtainable. The stoichiometry of 24 grids obtained from several different ligands and metals was confirmed with this optimized protocol. The deposition technique used means that the best signal-to-noise ratio in the spectra is obtained with only a small number of laser shots (ca. 5) to volatilise the sample. This MALDI-MS protocol can be applied to the study of grid dissociation in solution and in the case of Cu^{II} grids, in particular, has revealed the formation of various unusual clusters. The crystal structure is reported of one such cluster that was isolated and contains a nonionisable ligand that is related to that incorporated within the grids analysed by the MALDI-MS protocol.

Introduction

Metallosupramolecular chemistry has generated a variety of inorganic architectures by self-assembly processes with suitably designed ligands and specific metal ions.[1–8] Amongst the remarkably diverse range of structures now known, an important group is that of the (metallo)grids in which an essentially planar regular array of metal ions is constrained by rigid polytopic ligands.[9–15] The most abundant of these grids are those of the [2×2] type formed by relatively readily synthesised ditopic ligands, and the present work is concerned with such grids, formed with the ligands L^1H_2–$L^{10}H_2$ (Scheme 1), in their deprotonated forms i.e. as neutral $[M_4(L^n)_4]$ units, where M is a dipositive metal ion.

In regard to the possible application of these grids as receptors is solution, it is essential to know whether the grid structure, usually readily established in the solid state by single crystal X-ray diffraction measurements,[9–11,15] is in-
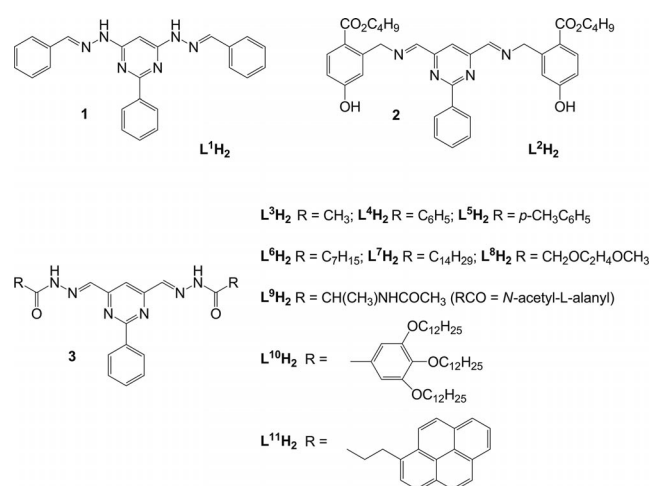
Scheme 1. Ligands that give rise to the grid complexes studied in the present work.

deed retained in solution and under what range of conditions this may be true. In some instances with diamagnetic grids, their 1D NMR spectra show characteristic splittings uniquely compatible with the grid structure,[9] but in other instances the apparent symmetry is higher than that expected for the grid, while in the spectra of most paramagnetic complexes peak broadening and the loss of coupling mean that the spectra cannot be used to establish unambiguously the grid form.[16] Diffusion ordered spectroscopy

[a] Laboratoire de Dynamique et Structure Moléculaire par Spectrométrie de Masse, Institut de Chimie – UMR7177 CNRS/UDS,
1 rue Blaise Pascal, 67008 Strasbourg Cedex, France
E-mail: leize@unistra.fr
[b] Laboratoire de Chimie Supramoléculaire, Institut de Science et d'Ingénierie Supramoléculaire,
8 allée Gaspard Monge, 67083 Strasbourg Cedex, France
[c] Department of Chemistry, Nanoscience Centre, University of Jyväskylä,
P. O. Box 35, 40014 JYU, Finland

(DOSY) measurements may prove to be suitable for this but there is uncertainty in relating diffusion coefficients to the nuclearity of nonspherical species, which is probably the state of the grid complexes in solution.[12,17] In principle, equilibrium measurements could be used to determine stability constants from which species distributions could be calculated, but the systems are extremely complicated to resolve and in practice it is nigh impossible to find a solvent suitable for all reaction components and thus enable measurements of homogeneous media. Hence, with advantages such as an insensitivity to the magnetic state of the complexes, the present study was initiated in the hope that mass spectrometry would provide a means to surmount most of these problems, at least to the extent of defining conditions under which the solid state species are retained in solution.

Over the past several years, electrospray ionization mass spectrometry (ESI-MS) has emerged as a powerful tool for the investigation of noncovalent biological complexes[18–21] as well as supramolecular assemblies,[22–25] including grid-type complexes.[26] However, ESI-MS only detects the charged species present in any solution and thus is unsuited to the characterisation of neutral species unless they are convertible to cations or anions without any other change in their composition. While certain grids do undergo reversible protonation/deprotonation reactions in solution,[26] grids derived from diacylhydrazones (Scheme 1, ligands L^3– L^{11}) are stable when the ligand is in its dianionic form but tend to dissociate when acid, sufficient to protonate the ligand, is present.[16] That MALDI-MS can provide a solution to the dilemma of how to obtain the mass spectrum of an intact neutral grid derivative was unanticipated, but in fact it appears that reaction between the neutral grids and the weakly acidic matrix materials can lead to the transfer of a single proton to each complete grid and thus to the generation of monocations that are sufficiently stable to be detectable by mass spectrometry. It is the fact that the proton transfer most certainly occurs in the MALDI-plume following laser excitation and not in solution that is the origin of the success of this method, since reaction between the matrix material and the grids in solution leads to extensive decomposition.[27] In contrast to some other metal complex systems,[28] here it appears that the special reactivity of a MALDI system can be advantageous.

It may be noted that MALDI-MS operating with adapted sample preparation and analysis conditions has been shown, since its development in 1988,[29] to be a very powerful technique for the analysis of compounds involved in noncovalent interactions, such as is commonly the case for proteins. It has been successfully used to characterise numerous multinuclear metal complexes,[30,31,32] and thus the present work defines an extension of its applicability.

Results and Discussion

Optimization of the MALDI Protocol

MALDI Matrix Selection

Three common MALDI matrices were tested in this study: α-cyano-4-hydroxy-cinnamic acid (CHCA), 1,8,9-anthracenetriol (dithranol) and 2,4,6-trihydroxyacetophenone (THAP). THAP and dithranol are often used as matrices for acid-sensitive species because of their considerably lower acidities compared to other commonly used matrices such as CHCA. For the matrix selection, two grids derived from the acylhydrazone ligands L^5H_2 and L^6H_2, that of the former having been characterised crystallographically as a grid,[16] were chosen to provide a sensitive test of the method, as it is known that grids derived from the fully protonated (or *N*-alkylated) form of the dihydrazone ligand L^1H_2 are sufficiently stable to be characterised by conventional ESI-MS methods (see ref.[34] and references cited therein). These initial experiments were conducted with the "layered sample" method (see below).

With THAP as the matrix, the mass spectrum of $[Zn_4(L^6)_4]$ showed a single peak for a mass corresponding to that of the intact protonated grid $[(L^6)_4Zn_4+H]^+$ (m/z = 2224.8) (Figure 1). With either dithranol or CHCA as the matrix additional peaks were observed in the spectra of $[Zn_4(L^6)_4]$. In the spectrum recorded with dithranol as the matrix, the peak for the free protonated ligand $[L^6H_2+H]^+$ (m/z = 493.2) was the most intense, indicating that dissociation of the complex had occurred while it was in the initial solution. In the spectrum measured with CHCA as the matrix, the free protonated ligand $[L^6H_2+H]^+$ (m/z = 493.3) provided the base peak, with additional peaks appearing for $[(L^6)_2H_2Zn+H]^+$ (39% ligand peak intensity) and for $[(L^6)_2Zn_2+H]^+$ (8% ligand peak intensity). This indicates

Figure 1. MALDI-TOF mass spectra of $[Zn_4(L^6)_4]$, prepared with the layered sample preparation technique, measured in the positive ion mode. Each spectrum is the sum of 160 shots. The y-scale is normalized to the most intense peak in each mass spectrum. (a) Matrix: THAP in THF; (b) matrix: dithranol in THF; (c) matrix: CHCA in acetone.

that at least partial dissociation of the grid had occurred, with the peak for the intact protonated grid being extremely weak (7% of the peak intensity of the protonated ligand). Similar results were obtained for $[Zn_4(L^7)_4]$ with the same matrices (data not shown).

In all spectra recorded for these two grids and with all three matrices peaks corresponding to the monoprotonated intact grids were detectable. However, with THAP as the matrix fragmentation was minimised, and according to the currently accepted classification based on proton affinity, THAP is considered as a "colder" matrix than CHCA and dithranol (proton affinity: 201.0 kcal/mol for CHCA, 211.5 kcal/mol for dithranol, 213.3 kcal/mol for THAP[34]). Qualitative experiments with peptides indicate that a "hot" matrix leads to abundant analyte fragmentation whereas a "cold" matrix results in fewer or no fragment ions.[35,36] The same result is observed in the case of the grids under study. Thus, THAP was the preferred matrix for all subsequent experimentation.

MALDI Sample Deposition Optimization

Two sample deposition techniques were assessed with the grid $[Zn_4(L^6)_4]$ and THAP as the matrix. In the "layered sample" preparation technique, 1 µL of matrix solution was applied to the stainless steel plate, dried in air, and then covered by a second layer comprising 1 µL of analyte solution, which was allowed to dry in air. In the case of the "dried droplet" method, the sample was directly mixed in a 1:1 ratio (by volume) with the matrix solution, and then 1 µL aliquot of this solution was dried on the plate.

With the layered sample preparation technique, the mass spectrum showed a single peak corresponding to the intact protonated grid $[Zn_4(L^6)_4+H]^+$ (m/z = 2224.8) (Figure 2, a). With the dried droplet method (Figure 2, b), a peak for the protonated free ligand $[L^6H_2+H]^+$ (m/z = 493.2) appeared in the spectrum corresponding to 36% of the intact grid peak intensity. In the case of the layered sample preparation technique, the contact time for the two solutions was essentially zero, whereas the contact time was at least several minutes in the case of the dried droplet method. Further experiments were therefore conducted to assess the hypothesis that the contact time determined the extent of grid dissociation, viz. that there was relatively slow acid-catalysed decomposition of the grid induced by the matrix molecules in homogeneous solution.

Thus, with the dried droplet method the solution containing both grid and matrix was allowed to stand for 5, 20 and 60 min before aliquots were withdrawn and applied to the plate. The aliquots were allowed to dry rapidly in air before the mass spectra were recorded. In the spectrum recorded after the 5 min reaction period a weak but obvious peak for the protonated free ligand was detectable along with a peak for the monoprotonated grid (Figure 2, b), indicating that significant dissociation had occurred in this time. In the spectra recorded after reaction periods of 20 or 60 min the protonated ligand peaks had become the base peaks of the spectra (Figure 2, c and d), with peaks for $[(L^6)_2H_2Zn+H]^+$ as well as for $[Zn_4(L^6)_4+H]^+$ being appar-
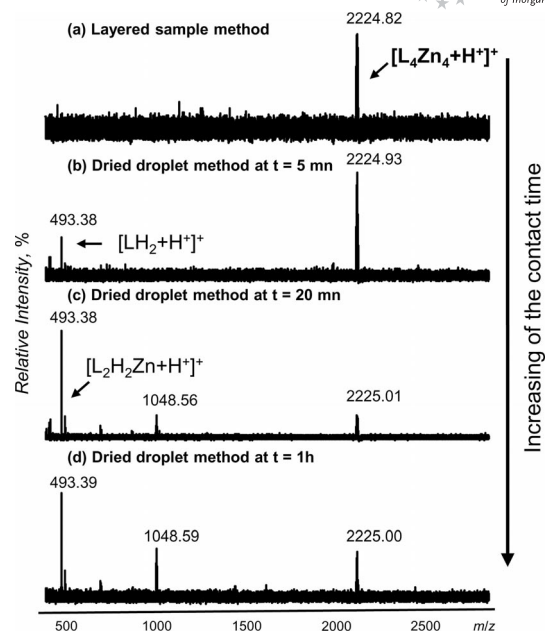
Figure 2. MALDI-TOF mass spectra of $[Zn_4(L^6)_4+H]^+$ measured in the positive ion mode with THAP as the matrix. Each spectrum is the sum of 500 shots. The y-scale is normalized to the most intense peak in each mass spectrum. (a) Sample prepared with the layered sample preparation technique; (b) sample prepared by the dried droplet method with t = 5 min; (c) sample prepared with the dried droplet method with t = 20 mn; (d) sample prepared with the dried droplet method with t = 1 h.

ent in both, consistent with a state of partial dissociation equilibrium having been reached in both cases.

Given that these observations confirmed the important influence of reaction between the matrix and the grids in solution, and given also that the layered sample technique must minimise any such reaction (it cannot be excluded that some dissolution of the pre-dried matrix in the grid solution could occur during the period required for evaporation), all subsequent measurements employed the layered sample method.

MALDI Laser Shot Optimization

For biological complexes it has been shown that some clusters formed by noncovalent interactions can be observed by MALDI-MS but only when spectra are obtained from the first or the first few laser shots directed at nonirradiated sample positions, as the signals of the dissociated species dominate the spectra arising from subsequent irradiations.[37] This has been described as the "first-shot phenomenon".[38] In this study, we investigated whether this first-shot phenomenon may also be characteristic of supramolecular chemical assemblies.

Figure 3 shows the spectra of the supramolecular grid $[(L^4)_4Co_4]$ that were obtained with the layered sample preparation method and with THAP as the matrix (see Exp. Section). A total of 400 shots were accumulated for each spectrum. To preserve the intact structure of the grid, all spectra were recorded at minimal laser intensity, which is to say slightly above the threshold for desorption. We have

found that with high laser intensities cleavage of what is presumably the weaker bonds in the ligand, the N–N bonds, may occur.
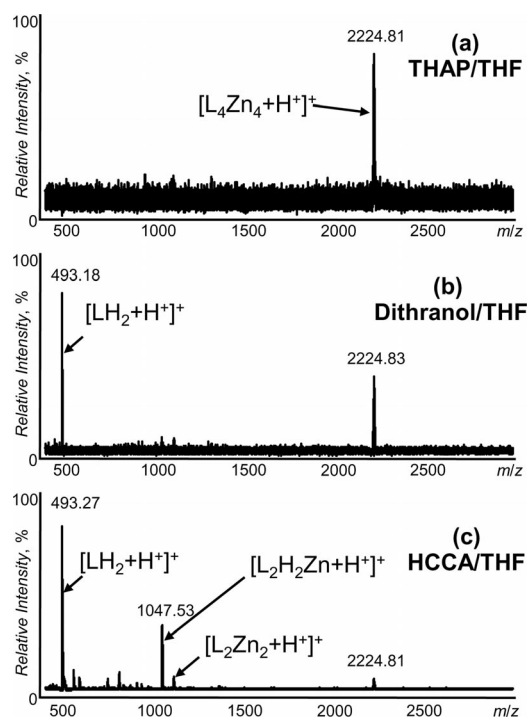

Figure 3. MALDI-TOF mass spectra of [(L^4)$_4$Co$_4$], prepared with the layered sample preparation technique, measured in the positive ion mode with THAP as the matrix. Each spectrum is the sum of 400 shots. The y-scale is normalized to the most intense peak in each mass spectrum. (a) Spectrum accumulated from data obtained only from the first shot onto a given position; (b) sum of data from the 2nd to the 11th shots onto a given position; (c) sum of data from the 11th to the 21st shots onto a given position; (d) sum of data from the 21st to the 101st shots onto a given position; (e) sum of data from the 101st to the 201st shots onto a given position.

Figure 3 (a) shows the spectrum obtained when only the first laser shot onto a new sample position is considered. In order to be able to change the laser shot position between two individual spectra, the laser pulse frequency was markedly reduced from 50 to 1 Hz. The accumulation of the 400 single spectra was performed with the instrument operating in an automatic mode so that each spectrum arose from a nonirradiated surface. Figure 3 (b to e) show the spectra obtained from the accumulation of data from the 2nd to the 11th shots onto a given position (3b), the 11th to the 20th (3c), the 21st to the 100th (3d), and the 101st to the 200th (3e). The most striking aspect of these analyses is that a prominent signal for the intact grid was observed only in the spectra generated from the first few laser shots performed at a given position; successive shots at the same position yielded only background noise. These observations were similar to those obtained with CHCA or dithranol as the matrix (data not shown).

Contrary to the expectation that this effect was due to a "first-shot" phenomenon, dissociated species were detected in deep layers with THAP as the matrix. Thus, we ascribe the effect to the deposition technique. Layering the sample produces a very thin sample sheet, which must be rapidly depleted by successive laser shots. However, since (see above) the layering technique is preferable for preservation of the grid structure, our optimised procedure with the layered sample preparation coupled with the use of only five

laser shots on nonirradiated sample positions in order to avoid background noise accumulation was selected for all subsequent experiments.

MALDI-MS Analysis of Neutral Grids

Study of the Metal Ion Dependence of the Solution Speciation of the Grids

The optimised procedure for obtaining MALDI mass spectra described above was applied to some 24 neutral grids derived from the ligands shown in Scheme 1 and various transition metal ions. The results obtained are summarised in Table 1. While in all cases a peak for a tetranuclear species corresponding to the expected grid was obtained, and in most instances this was the only peak in the spectrum, the spectrum of the Cu^{II} grid, [(L^6)$_4$Cu$_4$], provided an exception. Note that this complex, along with its Co^{II}, Ni^{II} and Zn^{II} analogues, has been shown by X-ray crystallography to have a grid form in the solid state.[16] Thus, the complexes [(L^6)$_4$Ni$_4$] and [(L^6)$_4$Zn$_4$] gave MALDI spectra in which there were essentially single peaks {[(L^6)$_4$Ni$_4$+H] (m/z = 2198.9) and [(L^6)$_4$Zn$_4$+H] (m/z = 2224.8), respectively} corresponding to the monoprotonated tetranuclear species (presumed to be the grids). The Cu^{II} complex, however, shows a far more complicated spectrum (Figure 4) with peaks corresponding to the species

Table 1. Summary of MALDI-MS results obtained for the different grids analysed.

Grid	Formula	Calcd. isotopic masses[a] [M + H]$^+$ [Da]	Measured masses [M + H]$^+$ [Da]
[(L^1)$_4$Ni$_4$]	C$_{88}$H$_{64}$N$_{32}$Ni$_4$	1801.35	1801.32
[(L^1)$_4$Zn$_4$]	C$_{88}$H$_{64}$N$_{32}$Zn$_4$	1825.32	1825.11
[(L^2)$_4$Mn$_4$]	C$_{136}$H$_{129}$N$_{16}$O$_{24}$Mn$_4$	2593.34	2593.75
[(L^2)$_4$Fe$_4$]	C$_{136}$H$_{129}$N$_{16}$O$_{24}$Fe$_4$	2594.68	2594.76[33]
[(L^2)$_4$Cu$_4$]	C$_{136}$H$_{129}$N$_{16}$O$_{24}$Cu$_4$	2629.79	2629.24
[(L^2)$_4$Zn$_4$]	C$_{136}$H$_{129}$N$_{16}$O$_{24}$Zn$_4$	2633.65	2633.52
[(L^3)$_4$Co$_4$]	C$_{64}$H$_{56}$N$_{24}$O$_8$Co$_4$	1525.21	1525.23
[(L^3)$_4$Zn$_4$]	C$_{64}$H$_{56}$N$_{24}$O$_8$Zn$_4$	1545.20	1545.02
[(L^4)$_4$Mn$_4$]	C$_{104}$H$_{72}$N$_{24}$O$_8$Mn$_4$	2005.36	2005.32
[(L^4)$_4$Co$_4$]	C$_{104}$H$_{72}$N$_{24}$O$_8$Co$_4$	2021.34	2021.18
[(L^4)$_4$Ni$_4$]	C$_{104}$H$_{72}$N$_{24}$O$_8$Ni$_4$	2017.35	2017.26
[(L^4)$_4$Cu$_4$]	C$_{104}$H$_{72}$N$_{24}$O$_8$Cu$_4$	2037.32	2037.29
[(L^4)$_4$Zn$_4$]	C$_{104}$H$_{72}$N$_{24}$O$_8$Zn$_4$	2041.32	2041.31
[(L^5)$_4$Cu$_4$]	C$_{112}$H$_{88}$N$_{24}$O$_8$Cu$_4$	2149.45	2149.46
[(L^5)$_4$Zn$_4$]	C$_{112}$H$_{88}$N$_{24}$O$_8$Zn$_4$	2153.45	2153.50
[(L^5)$_4$Co$_4$]	C$_{112}$H$_{152}$N$_{24}$O$_8$Co$_4$	2197.96	2197.87
[(L^6)$_4$Ni$_4$]	C$_{112}$H$_{152}$N$_{24}$O$_8$Ni$_4$	2193.97	2193.78
[(L^6)$_4$Cu$_4$]	C$_{112}$H$_{152}$N$_{24}$O$_8$Cu$_4$	2213.95	2213.41
[(L^6)$_4$Zn$_4$]	C$_{112}$H$_{152}$N$_{24}$O$_8$Zn$_4$	2217.95	2217.63
[(L^7)$_4$Zn$_4$]	C$_{168}$H$_{264}$N$_{24}$O$_8$Zn$_4$	3002.82	3002.76
[(L^8)$_4$Zn$_4$]	C$_{88}$H$_{104}$N$_{24}$O$_{24}$Zn$_4$	2137.49	2138.37
[(L^9)$_4$Zn$_4$]	C$_{88}$H$_{96}$N$_{32}$O$_{16}$Zn$_4$	2113.49	2113.41
[(L^{10})$_4$Zn$_4$]	C$_{392}$H$_{648}$N$_{24}$O$_{32}$Zn$_4$	6472.09[b]	6471.90[b]
[(L^{11})$_4$Zn$_4$]	C$_{208}$H$_{152}$N$_{24}$O$_8$Zn$_4$	3378.19[b]	3378.82[b]

[a] Peak assignments were verified by comparing the experimental isotopic patterns to theoretical isotopic patterns. [b] In this case, the calculated and measured masses are average masses (the observed mass of the grid is taken as the maximum of the signal formed by the overlap of the unresolved natural isotope peaks).
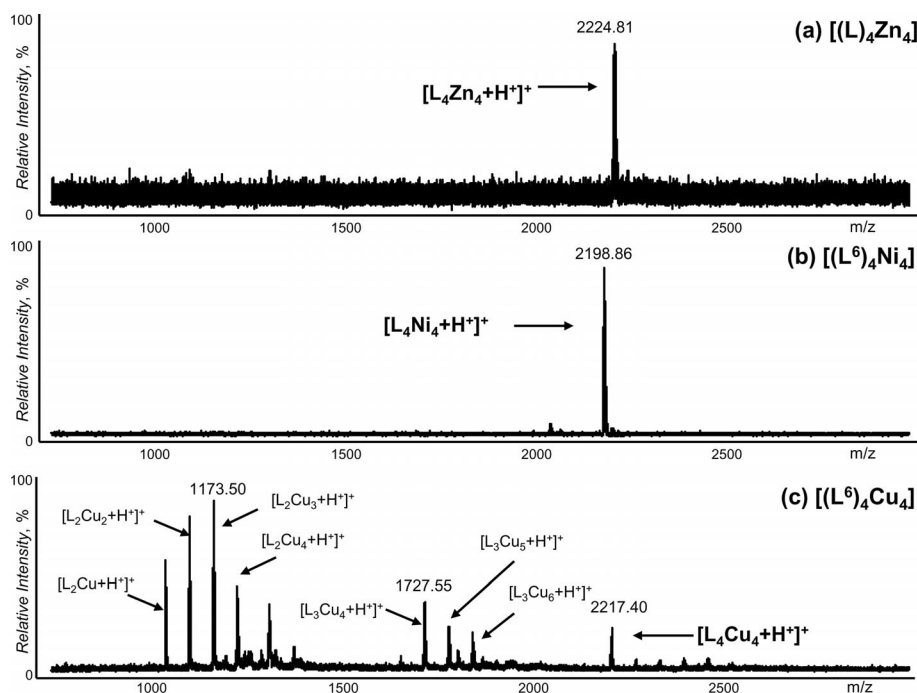
Figure 4. MALDI-TOF mass spectra of $[(\mathbf{L^6})_4Zn_4]$, $[(\mathbf{L^6})_4Ni_4]$ and $[(\mathbf{L^6})_4Cu_4]$, prepared with the layered sample preparation technique, measured in the positive ion mode with THAP as the matrix. Each spectrum is the sum of 500 shots. The y-scale is normalized to the most intense peak in each mass spectrum. (a) Metal: zinc; (b) metal: nickel; (c) metal: copper. In all cases the ligand/metal ratio equals 1.

$[(\mathbf{L^6})_4Cu_4+H]^+$, $[(\mathbf{L^6})_3Cu_6+H]^+$, $[(\mathbf{L^6})_3Cu_5+H]^+$, $[(\mathbf{L^6})_3Cu_4+H]^+$, $[(\mathbf{L^6})_2Cu_4+H]^+$, $[(\mathbf{L^6})_2Cu_3+H]^+$, $[(\mathbf{L^6})_2Cu_2+H]^+$, $[(\mathbf{L^6})_2Cu_3+H]^+$ and $[(\mathbf{L^6})_2Cu+H]^+$ being present. This is consistent with the observation of marked distortions in the solid state structure of the Cu complex when compared to its transition metal analogues,[16] and is probably a reflection of the fact that a regular octahedral coordination geometry is essentially never observed for Cu[II]. It is also possibly a reflection of the sensitivity of the Cu[II] complex to acid, since when attempting to form the Cu(CF$_3$SO$_3$)$_2$ complex of the grid forming ligand $\mathbf{L^{12}H_2}$ by condensing imidazole-2-aldehyde with 4,6-bis(*N*-methylhydrazino)-2-phenylpyrimidine the species actually isolated[39] was the complex $[Cu_2(\mathbf{L^{12}})(\mathbf{L^{12}H})_2](CF_3SO_3)_6$. The structure of the cation present in the crystal lattice of this complex[40] is shown in Scheme 2 (the structure of $\mathbf{L^{12}}$ is also shown).

Note that the grids derived from the dihydrazone ligand $\mathbf{L^1}$ and the diimine ligand $\mathbf{L^2}$ are known[27,33] to be less sensitive to acid induced dissociation in solution than the grids derived from acylhydrazones,[16] and thus it is unsurprising that peaks for monoprotonated tetranuclear species were readily observed in their MALDI mass spectra. Nonetheless, the technique remains particularly useful for their characterisation. An interesting case in the acylhydrazone series is provided by the grid $[(\mathbf{L^9})_4Zn_4]$, $\mathbf{L^9}$ being a derivative of L-alanine. Although efforts to obtain a crystal structure of this complex were unsuccessful, its ^{1}H NMR spectrum, recorded with the complex in water, is an example of one that clearly supports the assignment of a grid structure to such a complex. The twofold rotational symmetry of the free li-
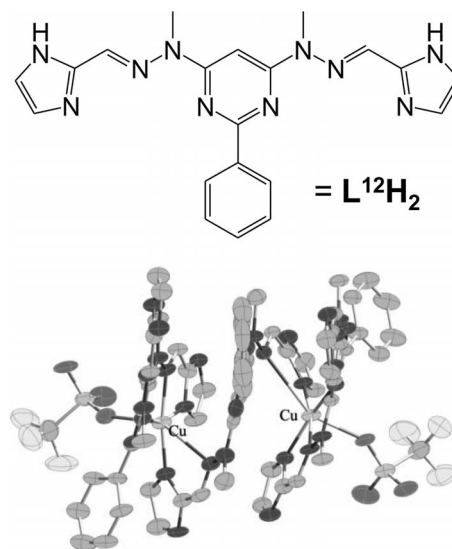
Scheme 2. A perspective view (ellipsoids drawn at the 50% probability level; H atoms not shown) of the cation present in the lattice of $[Cu_2(\mathbf{L^{12}})(\mathbf{L^{12}H})_2](CF_3SO_3)_6$. The central ligand forms a helical bridge between the two Cu[II] centres, while the terminal monoprotonated ligands each have one uncoordinated imidazole unit.

gand should be lost when it is incorporated in a grid and, consistent with this, the spectrum (Figure 5) shows two doublets for the alanine methyl groups and two hydrazone CH singlets. Hence, the NMR and mass spectra for this complex are complementary.
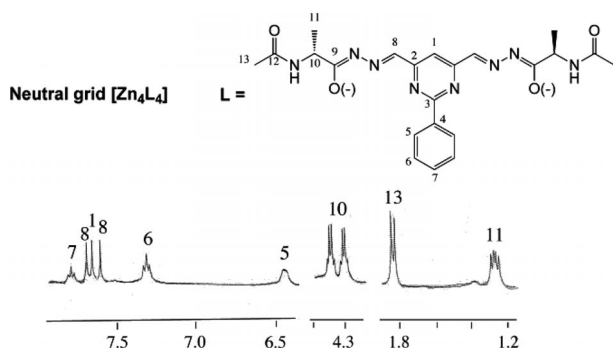
Figure 5. Structure of the ligand **L⁹** and the NMR spectrum of [(**L⁹**)$_4$Zn$_4$].

Study of the Relative Stability of the Grids

While the use of 10^{-3} M grid solutions prepared with 1:5 methanol:dichloromethane as the solvent enabled it to be shown in all cases, other than that for the Cu^{II} grids, that essentially only the intact tetranuclear grid species was present, use of more dilute solutions provided evidence that all the grids underwent dissociation in solution. Thus, when obtained under the same conditions used for collection of the data given in Figure 4, the spectrum of [(**L⁶**)$_4$Zn$_4$], for example, changed from a single peak for [(**L⁶**)$_4$Zn$_4$+H]⁺ (m/z = 2224.8) that is seen when the sample solution has an initial concentration of 10^{-3} M to one showing a peak for the free protonated ligand [**L⁶**H$_2$+H]⁺ (m/z = 493.2) that increases in intensity as the concentration of the solution was adjusted to 10^{-4} M and below (Figure 6). By determin-
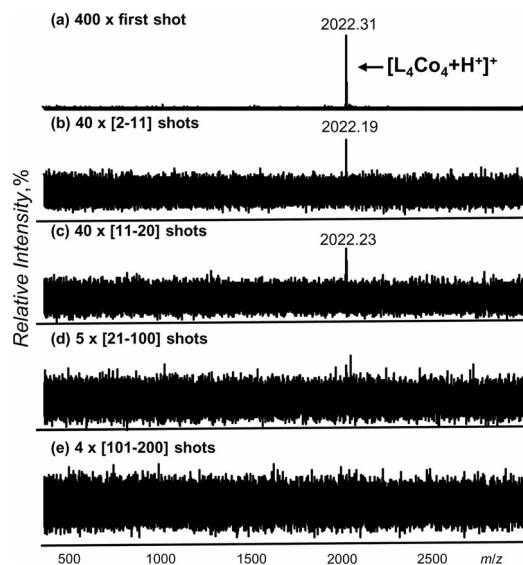

Figure 6. MALDI-TOF mass spectra of [(**L⁶**)$_4$Zn$_4$], prepared with the layered sample preparation technique, measured in positive ion mode with THAP as the matrix. Each spectrum is the sum of 500 shots. The y-scale is normalized to the most intense peak in each mass spectrum. (a) Concentration: 10^{-3} M; (b) concentration: 10^{-4} M; (c) concentration: 10^{-5} M; (d) concentration: 10^{-6} M.

ing the concentration at which the free ligand peak could be detected in the spectra, a rough order of stability was established for a selection of six grids (Table 2) involving different ligands and different metals. The order of relative stability found was: [(**L¹⁰**)$_4$Zn$_4$] > [(**L⁴**)$_4$Co$_4$] > [(**L⁶**)$_4$Co$_4$] ≈ [(**L⁶**)$_4$Ni$_4$] ≈ [(**L⁶**)$_4$Cu$_4$] ≈ [(**L⁶**)$_4$Zn$_4$], indicating that when in a relatively apolar solvent the grid stability may depend more on the nature of the ligand than that of the metal.

Table 2. Grid resistance to dissociation.[a]

Ligand	Metal ion	Dissociation concentration [M]
[**L⁴**]$^{2-}$	Co^{2+}	10^{-4}
[**L⁶**]$^{2-}$	Co^{2+}	10^{-3}
[**L⁶**]$^{2-}$	Cu^{2+}	10^{-3}
[**L⁶**]$^{2-}$	Ni^{2+}	10^{-3}
[**L⁶**]$^{2-}$	Zn^{2+}	10^{-3}
[**L¹⁰**]$^{2-}$	Zn^{2+}	10^{-5}

[a] The given concentrations correspond to those at which the free ligand peak can be detected in the mass spectrum.

Conclusions

In this study, we have successfully characterised neutral [2×2] grid complexes by MALDI-MS. This required the development of a procedure in which a matrix acidic enough to transfer a single proton to each of the grids but not so acidic as to lead to grid decomposition was used. A suitable matrix, at least for the large family of grids derived from hydrazone and acylhydrazone ligands, was found to be tri-hydroxyacetophenone (THAP). Its successful application, however, required the use of a sequential layering technique for the sample preparation so that any contact between the substrate and matrix was limited to that which occurs in the gas phase. The fact that the substrate is deposited in a very thin layer means that there is a rapid diminution of signal if the laser irradiation is concentrated on a single site.

The measurements that were possible as a result of the optimisation of this MALDI-MS technique have provided extremely valuable confirmation that the grid structure established from solid state studies is retained in solution, though they have also shown that grids derived from acylhydrazone ligands do undergo dissociation in dilute solutions ($<10^{-4}$ M). It should indeed be possible to exploit this new technique to unravel the details of grid formation and dissociation in solution, and to study in a broad sense the many factors that influence whether or not multitopic ligands form grid species in solution.[11b]

We have demonstrated for the first time the feasibility of characterising neutral supramolecular inorganic architectures by MALDI-MS under adapted sample preparation and analysis conditions. However, this is far from a routine matter: the optimal choice of matrix, preparation procedure, and instrumental parameters strongly depends on the noncovalent assembly of interest and involves optimization of these parameters for each type of noncovalent complex. A general procedure for the detection of such assemblies can therefore not yet be given.
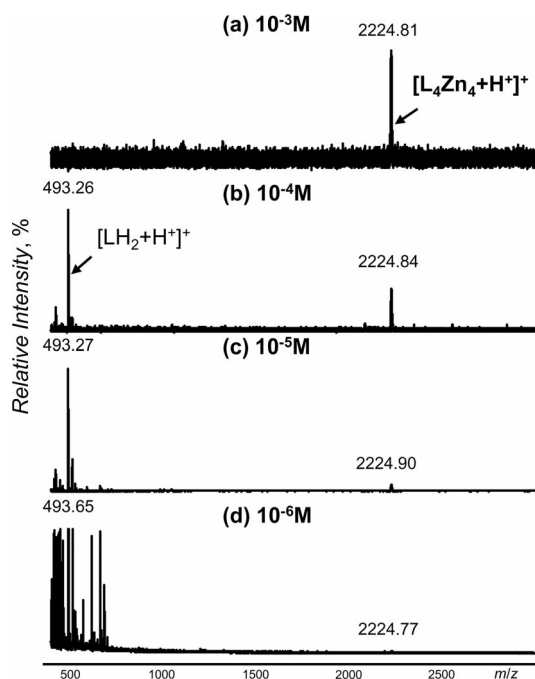
Experimental Section

Instrumentation: MALDI-MS mass spectra were acquired on a time-of-flight mass spectrometer (MALDI-TOF-TOF Autoflex II TOF-TOF, Bruker Daltonics, Bremen, Germany) equipped with a nitrogen laser ($\lambda = 337$ nm) operating at a pulse rate of 1 Hz. Full scans were acquired under the following experimental conditions: pulsed ion extraction, 90 ms; reflector, 20 kV. All the spectra shown herein were obtained in reflectron mode and positive ion mode. Scanning was performed over a m/z range of 280–3520; the low mass cut off was set in all cases to $m/z = 280$. Mass spectra were obtained by averaging over a large area, with the laser beam being scanned continuously and randomly over a spot on the sample. A total of 500 shots were accumulated for each spectrum, with a maximum of 5 shots on any one position.

The spectrometer was carefully tuned in order to preserve the non-covalent interactions within the samples and to make sure that the species detected faithfully reflected those present in solution. In particular, the laser irradiance was carefully chosen to avoid fragmentation. An increase in the laser irradiance would lead to fragmentation of any noncovalent bonds. The laser irradiance was generally slightly above the threshold for desorption.

An external multi-point calibration covering a m/z 400–3000 mass range was carried out before each measurement with the singly charged peaks of a standard peptide mixture (0.4 μM, in water acidified with 1% HCOOH).

Mass assignments were performed with unprocessed spectra to obtain optimal correlation between the observed and calculated masses. As a further check of the correctness of the mass assignments, signal attributions were verified by comparing the experimental isotopic profiles to isotopic simulations.

Scan accumulation and data processing were performed with the FlexAnalysis 3.0 software.

Materials: α-Cyano-4-hydroxycinnamic acid (CHCA) was obtained from Sigma (St Louis, MO, USA), 1,8,9-anthracenetriol (dithranol) from Alfa Aesar (Karlsruhe, Germany) and 2,4,6-trihydroxyacetophenone (THAP) from Fluka (Buchs, Switzerland).

Sample Preparation: Matrix solutions were freshly prepared before use to minimise chemical degradation, which reduces their effectiveness in the ionization process. CHCA and dithranol were dissolved in acetone to the point of saturation. THAP was used at a concentration of 100 g/L in THF.

Samples for MALDI-MS were prepared by dissolving the complex under study in an appropriate solvent (commonly a dichloromethane/methanol mixture) at a concentration of 10^{-3} M.

Two alternative sample preparation techniques were also used:

1. The Layered Sample Preparation Technique: The matrix solution (1 μL) was applied to the stainless steel plate (Bruker Daltonics, Bremen, Germany), and the rapid evaporation of the solvent resulted in a homogeneous surface comprising very small crystals. A second layer composed of the analyte solution (1 μL) was then deposited onto this matrix surface and dried in air.

2. The Dried Droplet Method: The sample was mixed in a 1:1 ratio (by volume) with the matrix solution. This solution (1 μL) was then deposited and dried on the stainless steel plate.

Acknowledgments

[1] J.-M. Lehn, *Supramolecular Chemistry – Concepts and Perspectives*, VCH, Weinheim, Germany, **1995**.

[2] D. L. Caulder, K. N. Raymond, *Acc. Chem. Res.* **1999**, *32*, 975–982.

[3] M. Albrecht, *Chem. Rev.* **2001**, *101*, 3457–3497.

[4] S. R. Seidel, P. J. Stang, *Acc. Chem. Res.* **2002**, *35*, 972–983.

[5] M. Ruben, J.-M. Lehn, P. Muller, *Chem. Soc. Rev.* **2006**, *35*, 1056–1067.

[6] B. Champin, P. Mobian, J.-P. Sauvage, *Chem. Soc. Rev.* **2007**, *36*, 358–366.

[7] J. R. Nitschke, *Acc. Chem. Res.* **2007**, *40*, 103–112.

[8] J. A. Faiz, V. Heitz, J.-P. Sauvage, *Chem. Soc. Rev.* **2009**, *38*, 422–442.

[9] M. Ruben, J. Rojo, F. J. Romero-Salguero, L. H. Uppadine, J.-M. Lehn, *Angew. Chem.* **2004**, *116*, 3728–3747; *Angew. Chem. Int. Ed.* **2004**, *43*, 3644–3662.

[10] An extensive listing of the literature relating to grid complex chemistry is given in J. Ramirez, A. M. Stadler, J. M. Harrowfield, L. Brelot, J. Huuskonen, K. Rissanen, L. Allouche, J.-M. Lehn, *Z. Anorg. Allg. Chem.* **2007**, *633*, 2435–2444; ref.[11–15] provide more recent indications of the still increasing variety of grid chemistry and its applications.

[11] a) L. N. Dawe, T. S. M. Abedin, L. K. Thompson, *Dalton Trans.* **2008**, 1661–1675; b) L. N. Dawe, K. V. Shuvaev, L. K. Thompson, *Chem. Soc. Rev.* **2009**, *38*, 2334–2359.

[12] B. R. Manzano, F. A. Jalaton, I. M. Ortiz, M. L. Soriano, F. G. De la Torre, J. Elguero, M. A. Maestro, K. Mereiter, T. D. W. Claridge, *Inorg. Chem.* **2008**, *47*, 413–428.

[13] Y. G. Zhao, D. Guo, Y. Liu, C. He, C. Y. Duan, *Chem. Commun.* **2008**, 5725–5727.

[14] D. Bhattacharya, M. Sathiyendiran, T. T. Luo, C. H. Chang, Y. H. Cheng, C. Y. Lin, G. H. Lee, S. M. Peng, K. L. Lu, *Inorg. Chem.* **2009**, *48*, 3731–3742.

[15] A. M. Stadler, *Eur. J. Inorg. Chem.* **2009**, 4751–4770.

[16] X. Y. Cao, J. Harrowfield, J. Nitschke, J. Ramirez, A. M. Stadler, N. Kyritsakas-Gruber, A. Madalan, K. Rissanen, L. Russo, G. Vaughan, J.-M. Lehn, *Eur. J. Inorg. Chem.* **2007**, 2944–2965.

[17] L. Allouche, A. Marquis, J.-M. Lehn, *Chem. Eur. J.* **2006**, *12*, 7520–7525.

[18] N. Potier, P. Barth, D. Tritsch, J.-F. Biellmann, A. Van Dorsselaer, *Eur. J. Biochem.* **1997**, *243*, 274–282.

[19] S. Sanglier, E. Leize, A. Van Dorsselaer, F. Zal, *J. Am. Soc. Mass Spectrom.* **2003**, *14*, 419–429.

[20] J. A. Loo, *Mass Spectrom. Rev.* **1997**, *16*, 1–23.

[21] A. J. R. Heck, R. H. H. van den Heuvel, *Mass Spectrom. Rev.* **2004**, *23*, 368–389.

[22] X. H. Cheng, Q. Y. Gao, R. D. Smith, E. E. Simanek, M. Mammen, G. M. Whitesides, *J. Org. Chem.* **1996**, *61*, 2204–2206.

[23] C. A. Schalley, *Int. J. Mass Spectrom.* **2000**, *194*, 11–39.

[24] N. Solladie, M. E. Walther, H. Herschbach, E. Leize, A. Van Dorsselaer, T. M. F. Duarte, J.-F. Nierengarten, *Tetrahedron* **2006**, *62*, 1979–1987.

[25] H. N. Miras, E. F. Wilson, L. Cronin, *Chem. Commun.* **2009**, 1297–1311.

[26] a) H. Nierengarten, E. Leize, E. Breuning, A. Garcia, F. Romero-Salguero, J. Rojo, J.-M. Lehn, A. Van Dorsselaer, *J. Mass Spectrom.* **2002**, *37*, 56–62; b) M. Ruben, J.-M. Lehn, G. Vaughanc, *Chem. Commun.* **2003**, 1338–1339; c) L. H. Uppadine, J. P. Gisselbrecht, J.-M. Lehn, *Chem. Commun.* **2004**, 718–719.

[27] R. Zenobi, R. Kochenmuss, *Mass Spectrom. Rev.* **1998**, *17*, 337–366.

[28] J. M. J. Nuutinen, M. Purmonen, J. Ratilainen, K. Rissanen, P. Vainiotalo, *Rapid Commun. Mass Spectrom.* **2001**, *15*, 1374–1381.

[29] M. Karas, F. Hillenkamp, *Anal. Chem.* **1988**, *60*, 2299–2301.

[30] P. Timmerman, K. A. Jolliffe, M. C. Calama, J. L. Weidmann, L. J. Prins, F. Cardullo, B. H. M. Snellink-Ruel, R. H. Fokkens, N. M. M. Nibbering, S. Shinkai, D. N. Reinhoudt, *Chem. Eur. J.* **2000**, *6*, 4104–4115.

[31] C. Jahier, S. Nlate, *J. Organomet. Chem.* **2009**, *694*, 637–642.

[32] U. S. Schubert, C. Eschbaumer, *J. Inclusion Phenom. Macrocyclic Chem.* **1999**, *35*, 101–109.

[33] A. R. Stefankiewicz, J.-M. Lehn, *Chem. Eur. J.* **2009**, *15*, 2500–2503.

[34] S. P. Mirza, N. P. Raju, M. Vairamani, *J. Am. Soc. Mass Spectrom.* **2004**, *15*, 431–435.

[35] K. F. Medzihradszky, J. M. Campbell, M. A. Baldwin, A. M. Falick, P. Juhasz, M. L. Vestal, A. L. Burlingame, *Anal. Chem.* **2000**, *72*, 552–558.

[36] C. S. Raska, C. E. Parker, C. Huang, J. Han, G. L. Glish, M. Pope, C. H. Borchers, *J. Am. Soc. Mass Spectrom.* **2002**, *13*, 1034–1041.

[37] L. R. H. Cohen, K. Strupat, F. Hillenkamp, *J. Am. Soc. Mass Spectrom.* **1997**, *8*, 1046–1052.

[38] V. Horneffer, K. Strupat, K. F. Hillenkamp, *J. Am. Soc. Mass Spectrom.* **2006**, *17*, 1599–1604.

[39] A. R. Stefankiewicz, *Ph. D. Thesis*, University of Strasbourg, France, **2009**.

[40] $[Cu_2(\mathbf{L^{12}})(\mathbf{L^{12}H})_2](CF_3SO_3)_6$: $C_{66}H_{62}Cu_2F_{18}N_{30}O_{18}S_6$, M_r 2224.9 g/mol; triclinic, space group $P\bar{1}$; $a = 18.782(4)$ Å, $b = 19.001(4)$ Å, $c = 20.477(4)$ Å, $\alpha = 107.98(3)°$, $\beta = 106.08(3)°$, $\gamma = 108.05(3)°$; $T = 123.0(1)$ K. For 12638 observed $[I > 2\sigma(I)]$ reflections, $R_1 = 0.129$, $wR_2 = 0.277$, $S = 1.057$. CCDC-7785083 contains the supplementary crystallographic data for this paper. These data can be obtained free of charge from The Cambridge Crystallographic Data Centre via www.ccdc.cam.ac.uk/data_request/cif.

Synthesis and Structural Characterization of Pincer Pyridine Diphosphite Complexes of Rhodium and Iridium

Miguel Rubio,[a] Andrés Suárez,[a] Esmeralda Vega,[b] Eleuterio Álvarez,[a] Josefina Díez,[b] M. Pilar Gamasa,*[b] and Antonio Pizzano*[a]

The synthesis of a novel pyridine diphosphite ligand **1** has been described. From this ligand, rhodium– and iridium–chlorido complexes of formula [MCl(**1**)] (M = Rh, Ir) have been prepared. Chloride abstraction by treatment with NaBPh$_4$ and a phosphane produced the corresponding cationic phosphane derivatives [M(**1**)L][BPh$_4$] [L = PPh$_3$ (Rh, Ir), PPh$_2$Me (Ir)]. The analogous reaction of [RhCl(**1**)] with CNXy (Xy = 2,6-Me$_2$-C$_6$H$_3$) and NaBPh$_4$ yielded the monosubstituted complex [Rh(**1**)(CNXy)][BPh$_4$], whereas the reaction between [IrCl(**1**)] and isonitriles led to the disubstituted complexes [Ir(**1**)(L)$_2$][BPh$_4$] (L = CNBn, CNCy). Ethylene compound [Rh(**1**)(C$_2$H$_4$)][BPh$_4$] was obtained from the reaction of [RhCl(**1**)] with NaBPh$_4$ under ethylene, whereas [Ir(**1**)-(C$_2$H$_4$)][BPh$_4$] was synthesized by a treatment of [{IrCl-(COE)$_2$}$_2$] with ethylene followed by addition of **1** and NaBPh$_4$. An IR analysis of the isocyanide complexes indicates a very poor π-donor ability of the [M(**1**)]$^+$ fragment, therefore the isocyanide metal bond is mostly due to σ donation from the isocyanide. Characterization by X-ray crystallography of [Rh(**1**)(PPh$_3$)][BPh$_4$], [Rh(**1**)(MeCN)][BPh$_4$] and [Ir(**1**)(PPh$_2$Me)][BPh$_4$] displays a square-planar structure with ligand **1** coordinated in a pincer fashion for these complexes. In addition, the ethylene derivative [Rh(**1**)(C$_2$H$_4$)][BPh$_4$] shows a near in-plane conformation of the ethylene ligand, with a short C–C distance (1.319 Å). Moreover, in all the structures, the diphosphite ligand exhibits a *meso* conformation irrespective of the size of the neutral ancillary ligand. An examination of the behaviour of some of these complexes in catalytic hydrogenation has shown that [IrCl(**1**)] is an active catalyst in the reduction of 2-methylquinoline and 2-methylquinoxaline.

Introduction

Rh and Ir complexes with phosphorus-based pincer ligands constitute a prominent class of derivatives in organometallic chemistry.[1] These complexes have exhibited a vast chemistry that includes many challenging transformations like the activation of C–H,[2] N–H,[3] C–C[4] or C–O[5] bonds among other reactions.[6] Moreover, the unique properties of pincer ligands for stabilizing transition-metal complexes have greatly helped in the detection of reaction intermediates and therefore in understanding the mechanistic aspects of some of these reactions.[1b]

Since the first examples, which correspond to cyclometalated phosphane derivatives,[7] attention has long been focused on phosphane-based donor ligands. In recent years,

however, growing attention has been given to accepting pincer ligands.[8] A comparison of the reactivity of complexes based on pincer diphosphanes with those that bear accepting pincer ligands have demonstrated the profound influence that the ligand acidity can exert on the reactivity of the metal centre. For instance, in the catalytic dehydrogenation of alkanes, it has been observed that Ir diphosphinite complexes are more reactive than their diphosphane counterparts.[9] In addition, important differences between diphosphane– and diphosphinite–rhodium complexes in C–H activation reactions have recently been revealed.[10] Moreover, computational studies support a strong ability of accepting pincer ligands to stabilize pentacoordinate complexes of d^8 metals by adopting a *fac* coordination.[8a] In connection with this, the structural characterization of a family of pentacoordinate Ir complexes based on a pincer fluorophosphane that exhibits a significant bending of the pincer ligand has been reported recently.[11]

With regards to the modulation of reactivity at the metal centre, it is pertinent to recall the difference in π-accepting ability of phosphorus ligands. Then, a decrease on acidity it is expected in the order: fluoroalkylphosphane, *N*-pyrrolylphosphane, fluoroarylphosphane, phosphite, phosphoramidite and phosphinite.[12] Notably, a wide variety of PCP-type accepting ligands that cover most of these frag-

[a] Instituto de Investigaciones Químicas (IIQ),
Consejo Superior de Investigaciones Científicas
and Universidad de Sevilla,
Avda Américo Vespucio 49, Isla de la Cartuja,
41092 Sevilla, Spain
E-mail: pizzano@iiq.csic.es
[b] Departamento de Química Orgánica e Inorgánica,
Instituto de Química Organometálica "Enrique Moles"
(Unidad Asociada al CSIC), Universidad de Oviedo,
33006 Oviedo, Spain
E-mail: pgb@uniovi.es

WILEY ONLINE LIBRARY

ments have been prepared.[13] On the contrary, for neutral PNP accepting ligands, only phosphinite[14] and phosphoramidite[15] derivatives have been reported. Therefore, the preparation of more acidic ligands is highly interesting.[16]

In a previous study, we described a family of Rh[I] complexes with pincer anionic diphosphite ligands based on resorcinol (POCOP; Scheme 1).[17] The design of these ligands allows an easy modulation of their structure and is very suitable for the introduction of chirality into the complex. Most notably, the Rh(POCOP) fragment favoured for steric reasons an unusual in-plane coordination of an olefin ligand. Alternatively, we have become interested in an analogous neutral ligand based on a pyridine backbone that can lead to more electrophilic cationic Rh[I] and Ir[I] complexes. In the present contribution we therefore report a study of the synthesis and characterization of a new pyridine diphosphite pincer ligand and its coordination in a series of Rh[I] and Ir[I] complexes. The structural characterization of some selected examples as well as an examination of π-donor strength of the metal centre has also been included. Finally, the behaviour of some of these complexes in several catalytic hydrogenations has also been examined.
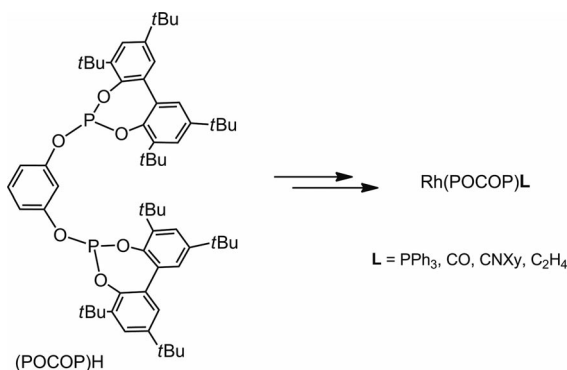
Scheme 1. Pincer complexes based on a resorcinol diphosphite.

Results and Discussion

Initially, several attempts were made to prepare the pyridine diphosphite ligand 1 by treating 2,6-dihydroxypyridinium chloride with chlorophosphite 2 in the presence of different bases. Pyridine, NEt$_3$ or KH produced unsatisfactory results, as the reactions showed the presence of significant amounts of the monophosphite 3 as a byproduct (Scheme 2). In this system, a tautomeric rearrangement of the phosphite hydroxypyridine to the corresponding lactam phosphite 3 is expected, which hinders the formation of the second phosphite functionality. Otherwise, diphosphite 1 was obtained in good yield by converting 2,6-dihydroxypyridinium chloride into the corresponding dilithium salt by treatment with three equivalents of LinBu, followed by the reaction with two equivalents of 2. Characterization of 1 by NMR spectroscopic techniques showed the expected signals for the bridged pyridine and the phosphite fragments. In

addition, the spectra are in good accord with a rapid atropisomerization of the biphenyl moieties at room temperature.
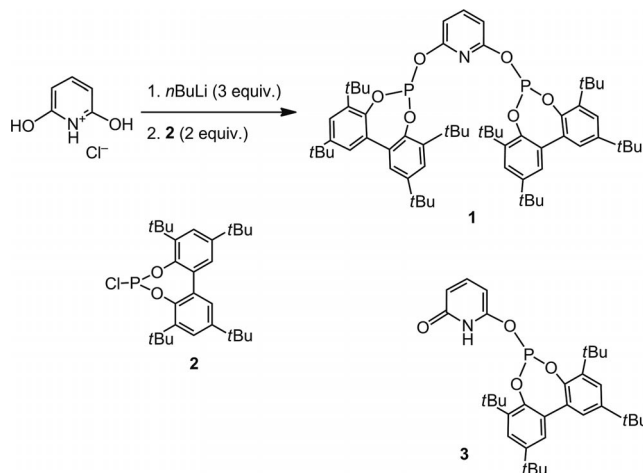
Scheme 2. Synthesis of diphosphite 1.

From ligand 1, complexes of formula [MCl(1)] [M = Rh (4), Ir (5)] were readily prepared by treatment of [{MCl(cod)}$_2$] (cod = 1,5-cyclooctadiene) with the diphosphite at a metal-to-ligand ratio of 1:1 (Scheme 3). Characterization of these compounds indicates the P,N,P-trihapto coordination of the pyridine diphosphite. For instance, for complex 4, a doublet at $\delta = 139.0$ ppm with $J_{Rh,P} = 250$ Hz is observed. Moreover, ^{1}H and ^{13}C{^{1}H} NMR spectroscopy experiments show the equivalence of the two phosphite fragments and of the two aromatic halves of each biphenyl due to a fast conformer interconversion. In addition, the IR spectrum also accounts for pyridine coordination. Two bands at 1615 and 1560 cm^{-1} are observed, the former being at higher energy than in the free ligand.[18]
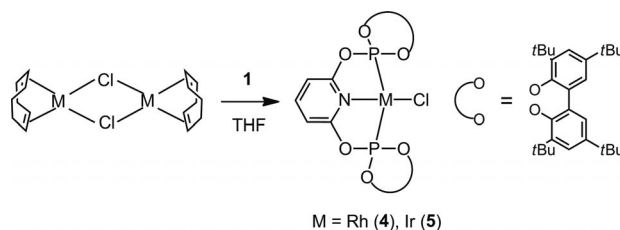
Scheme 3. Synthesis of compounds 4 and 5.

At the next stage the preparation of cationic derivatives was examined. Chloride exchange by a neutral ligand L was easily performed by reaction of 4, NaBPh$_4$ and L (Scheme 4). This reaction led to a series of complexes of formula [Rh(1)L][BPh$_4$] [L = PPh$_3$ (6), NCMe (7), C$_2$H$_4$ (8), CO (9), CNXy (Xy = 2,6-Me$_2$-C$_6$H$_3$; 10)]. Moreover, Ir derivatives [Ir(1)L][BPh$_4$] that bear a phosphane [L = PPh$_3$ (11), PMePh$_2$ (12)] were prepared from 5 by the same procedure. On the contrary, attempts to abstract the chloride with AgBF$_4$ did not provide satisfactory results.[19,20]
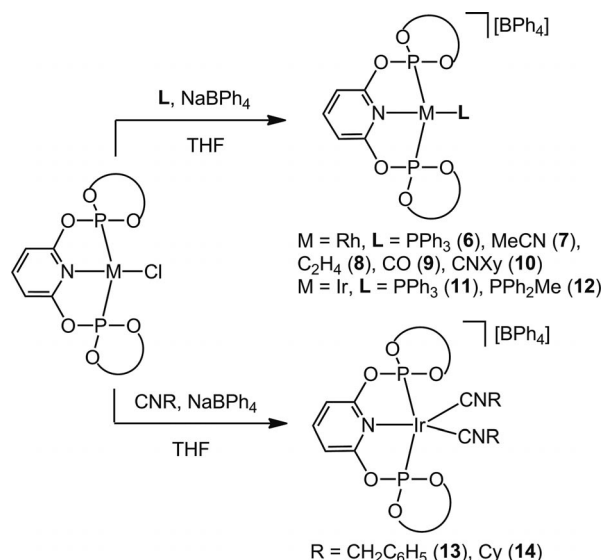
Scheme 4. Synthesis of compounds **6–14**.

Characterization data for compounds **6–12** are in good accord with square-planar structures, with the diphosphite ligand coordinated in a pincer mode and the **L** ligand occupying the remaining coordination position. For instance, complexes **6**, **11** and **12** show the typical *cis* $^2J_{P,P}$ constants (35–49 Hz) for the phosphane ligand in the $^{31}P\{^1H\}$ NMR spectra. Moreover, in the ^1H and $^{13}C\{^1H\}$ NMR spectra compound **7** shows resonances that correspond to a coordinated acetonitrile molecule. On the other hand, the olefin derivative **8** exhibits the expected signals for a coordinated ethylene. Thus, in the ^1H NMR spectroscopy experiment a broad singlet for four protons is observed at $\delta = 2.98$ ppm, whereas the corresponding resonance in the $^{13}C\{^1H\}$ NMR spectroscopic experiment appears at $\delta = 57.7$ ppm. The chemical shift of the ^{13}C resonance is very close to that observed in the related derivative of a pyridine diphosphane ligand ($\delta = 58.8$ ppm).[21] Therefore, the π-acidic nature of **1** is not reflected in a lower-field shift of this resonance. The existence of only two singlets for the *t*Bu groups in the ^1H NMR spectrum is indicative of a fast phosphite atropisomerization at room temperature. To investigate this dynamic process in more detail, we performed ^1H and $^{31}P\{^1H\}$ NMR spectroscopy at variable temperature for **8** in CD$_2$Cl$_2$. Upon cooling, the doublet observed in the $^{31}P\{^1H\}$ NMR spectrum broadens and at –50 °C appears split into two doublets centred at 158.4 ($^2J_{P,P} = 213$ Hz) and 158.1 ppm ($^2J_{P,P} = 211$ Hz) at around a 5:1 ratio. On the other hand, in the ^1H NMR spectroscopy characteristic region for coordinated ethylene, the broad singlet observed at room temperature splits into three broad singlets upon cooling. At –80 °C, these resonances appear at $\delta = 3.49$, 3.29 and 2.38 ppm in a 1.0:0.4:1.0 ratio. In addition, an ^1H COSY experiment at this temperature shows a cross-peak between the resonances at $\delta = 3.49$ and 2.38 ppm. These signals can then be assigned to the *rac* conformer. Moreover, the resonance at $\delta = 3.29$ ppm should correspond to the four ethylene protons of the *meso* isomer due to a sym-

metry plane perpendicular to the coordination one and fast olefin rotation. The *rac* conformer is therefore preferred in solution at low temperature (*rac/meso* 5:1) despite the *meso* conformer being observed in the solid state. Finally, in-plane and perpendicular rotamers could not be observed separately at the lowest temperature investigated. This solution behaviour is similar to that observed for [Rh(POCOP)(C$_2$H$_4$)].[17]

An interesting difference between complexes **4** and **5** is constituted by the reactions with isonitriles. The Ir complex shows a clear preference for the formation of pentacoordinate disubstituted complexes [Ir(**1**)(CNR)$_2$][BPh$_4$] [R = CH$_2$Ph (**13**), Cy (**14**)]. Thus, even in reactions run at an Ir/isocyanide 1:1 ratio, the presence of the disubstituted complex along with **5** was observed.

On the other hand, for the preparation of the desired Ir–ethylene derivative, chloride abstraction from **5** in an atmosphere of ethylene did not produce satisfactory results. On the contrary, treatment of [{IrCl(COE)$_2$}$_2$] under an atmosphere of ethylene followed by addition of ligand **1** and NaBPh$_4$ provided the olefin compound **15** in good yield (Scheme 5). This complex shows the expected resonances for the olefin ligand in the ^1H and $^{13}C\{^1H\}$ NMR spectra. Thus, resonances at $\delta = 2.89$ and 44.6 ppm are observed, respectively.
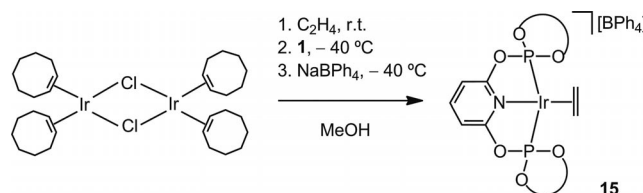
Scheme 5. Synthesis of compound **15**.

The most prominent feature of cationic complexes [M(**1**)L][BPh$_4$] is the low π basicity of the metal centre, favoured by both the formal positive charge and the strong acceptor properties of the phosphite groups. Thus, the $\tilde{v}$(CO) for **9** has a very high value of 2093 cm^{-1}. This frequency is significantly higher than the value observed for the cyclometalated diphosphite analogue [Rh(POCOP)-(CO)] (2017 cm^{-1}),[17] whereas for cationic derivatives of pincer pyridine diphosphanes the corresponding band appears around 1980 cm^{-1}.[7c,20] However, compound **9** is unstable in solution and showed decomposition after several hours at room temperature. Isocyanide compounds exhibited a higher stability and also demonstrate the low donor ability of the [M(**1**)]$^+$ fragment. Thus, the $\tilde{v}$(CN) band appears in **10** at 2153 cm^{-1}, which is significantly higher than the value observed for [Rh(POCOP)(CNXy)] (2099 cm^{-1}) [17] and even higher than that for the free isocyanide (2114 cm^{-1}). The comparison of these data indicates that in this compound the isocyanide acts very predominantly as a σ donor, whereas the π component of the bond should be minimal.[22,23] Likewise, the Ir isocyanides show results that reinforce this assumption. Thus, for **13** and **14** the values for $\tilde{v}$(CN) are around 40 cm^{-1} above the free ligand. These values are very high for late-transition metals in a low oxi-

dation state. For comparison, it can be mentioned that similar values have been reported for Ln[III] complexes {e.g., 2150 cm^{−1} for [Ce(Cp′)$_3$(CNXy)]}.[22]

To gain insight into the structure of coordinated **1** in these complexes, phosphane derivatives **6** and **12** (see Figures 1 and 2, respectively), acetonitrile adduct **7** (Figure 3) and ethylene complex **8** (Figure 4) have been characterized by X-ray crystallography.[24] As a general feature, all complexes along the series showed for the [M(**1**)] fragment similar values for the M–P bond lengths and the P–M–P bond angle, whereas the M–N bond length changes between 2.01 and 2.08 Å depending on the nature of the ancillary ligand (Table 1). The angle determined by the metal and the two P atoms of the pincer ligand, between 158 and 160°, is similar to those observed in related square-planar complexes with pincer diphosphane[21] and diphosphinite[9] ligands. Moreover, the M–P bond lengths (2.22–2.25 Å) are similar to those observed in a pyridine diphosphinite complex (2.22 and 2.28 Å),[9] yet somewhat lower than in a diphosphane

Figure 3. ORTEP diagram at 30% ellipsoid probability of complex **7**. Hydrogen atoms and the BPh$_4$ anion have been omitted for clarity.
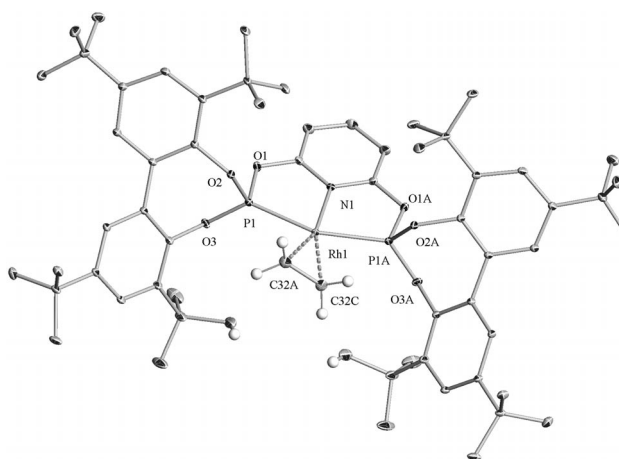
Figure 4. ORTEP diagram at 30% ellipsoid probability of complex **8**. Hydrogen atoms, except for the ethylene ligand, and the BPh$_4$ anion have been omitted for clarity.

Figure 1. ORTEP diagram at 30% ellipsoid probability of complex **6**. Hydrogen atoms and the BPh$_4$ anion have been omitted for clarity.

Figure 2. ORTEP diagram at 30% ellipsoid probability of complex **12**. Hydrogen atoms and the BPh$_4$ anion have been omitted for clarity.

complex (2.27 and 2.30 Å).[21] Noteworthy is that phosphane derivatives **6** and **12** showed a slight displacement of the phosphane ligand from the coordination plane denoted by P–M–N angles around 168°, probably caused by a steric repulsion with the phosphite groups. For these complexes, the metal phosphite bond is slightly shorter (ca. 0.05 Å) than the metal phosphane one, as observed before for complexes of the POCOP ligand.[17]

A comparison between these structures indicates that irrespective of the size of the **L** ligand, a *meso* conformation was observed in all the structures. This feature can be clearly observed by comparison of structures of phosphane complexes **6** and **12** with that of acetonitrile **7** and ethylene

Table 1. Bond lengths [Å] and angles [°] in complexes **6**–**8** and **12**.

Compound	M–N	M–P[a]	M–L	P–M–P	N–M–L
6	2.082(2)	2.2529(7)	2.3081(7)	157.78(2)	167.64(6)
7	2.013(3)	2.2251(7)	1.994(3)	160.25(3)	178.94(9)
8	2.0428(17)	2.2251(5)	2.221(6)[b]	159.21(2)	172.97[c]
12	2.075(7)	2.235(2)	2.285(2)	158.74(9)	168.4(2)

[a] Average of the two M–P(phosphite) bond lengths. [b] Average of the two Rh–C bond lengths. [c] Angle determined by the olefin centroid and Ir and N atoms.

complex **8**. Accordingly, the phosphite groups form a rather flexible cavity which accommodates the steric requirements of ligand **L**. Thus, the distances between the quaternary carbons of _endo-tert_-butyl groups below the coordination plane in **6** and **12** (i.e., 7.30 Å between C26 and C54 in **6** and 7.43 Å between C26 and C54 in **12**) are larger than the corresponding distances in complexes **7** and **8** (6.76 and 6.60 Å, respectively). This observation contrasts with the trend outlined by structures of complexes [Rh(POCOP)**L**], which showed a _meso_ conformation for sterically encumbered **L** ligands (PPh$_3$, CNXy) and a _rac_ conformation for smaller ones (CO, C$_2$H$_4$).[17]

A remarkable feature of complex **8** is a near in-plane orientation of the olefin ligand (Figure 4). Thus, the angle between the plane defined by the Rh and the olefinic carbon atoms and the best plane defined by Rh, N and P atoms amounts to 23.7°. This orientation is clearly different from the angle of 90° that is characteristic of the usual perpendicular orientation for an ethylene ligand in a square-planar complex. As discussed in detail for the resorcinol diphosphite derivatives,[17] this uncommon conformation should be favoured over the perpendicular one by steric effects, as well as by the reduction from 180° of the P–Rh–P angle.[25] The Rh–C distances in **8** are 2.121 Å which is shorter than those found in the analogue complex of the POCOP diphosphite (2.218 and 2.235 Å),[17] yet slightly shorter than the distance found in the cationic derivative of a pyridine diphosphane (2.142 and 2.157 Å).[21b] Most remarkably, the C=C bond length in the ethylene ligand is rather short (1.319 Å). This value is appreciably smaller than the distances observed in the mentioned diphosphite (1.377 Å) and in the cationic pyridine diphosphane (1.352 Å) complexes. The short C=C distance can be attributed to a very low back-donation from the metal, already mentioned above.

Finally, we were interested in exploring the ability of some complexes based on ligand **1** to perform catalytic hydrogenations. Despite [Rh(POCOP)(C$_2$H$_4$)] being active in the hydrogenation of dimethyl itaconate, no activity was shown by compound **8**. Moreover, the hydrogenation of C=N bonds of imines and heterocycles with Ir complex **5** was also examined (Scheme 6). Thus, this catalyst precursor showed full conversion in the hydrogenation of 2-methylquinoline and 2-methylquinoxaline at a substrate (S)/catalyst (C) ratio of 100 (Table 2, entries 1 and 2). Likewise, catalyst generated in situ from [{IrCl(cod)}$_2$] and **1** at an Ir/diphosphite ratio of 1 also showed conversions over 95% (entries 3 and 6). The reaction was also effected in the presence of acid additives (entries 4 and 5). A control reaction performed with [{IrCl(cod)}$_2$] also showed complete con-

version in the hydrogenation of 2-methylquinoline (entry 7), although a black deposit was observed at the end of the reaction, which points to the stabilizing role of the pincer ligand. On the contrary, no conversion was observed in the reduction of 2-methylquinoxaline (entry 8).

Table 2. Hydrogenation reactions performed with Ir complexes.[a]

Entry[a]	Substrate	Cat. precursor	Conv. [%]
1	2-methylquinoline	**5**	100
2	2-methylquinoxaline	**5**	100
3	2-methylquinoline	0.5 [{IrCl(cod)}$_2$] + **1**	98
4[b]	2-methylquinoline	0.5 [{IrCl(cod)}$_2$] + **1**	100
5[c]	2-methylquinoline	0.5 [{IrCl(cod)}$_2$] + **1**	100
6	2-methylquinoxaline	0.5 [{IrCl(cod)}$_2$] + **1**	100
7[d]	2-methylquinoline	0.5 [{IrCl(cod)}$_2$]	100
8	2-methylquinoxaline	0.5 [{IrCl(cod)}$_2$]	0
9	_N_-benzylideneaniline	0.5 [{IrCl(cod)}$_2$] + **1**	0
10	_trans_-cinnamaldehyde	0.5 [{IrCl(cod)}$_2$] + **1**	55[e]
11	methyl itaconate	0.5 [{IrCl(cod)}$_2$] + **1**	0

[a] Conditions: 30 atm H$_2$, 25 °C, toluene, S/C = 100, 24 h. [S] = 0.6 M. Conversion was determined by ^{1}H NMR spectroscopy. [b] (PhO)$_2$P(O)OH (10 equiv.) was added as additive. [c] [(_S_)-BINOL]P(O)OH (10 equiv.; BINOL = 1,1′-bi-2-naphthol) was added as additive; product obtained as a racemic mixture. [d] Heterogeneous reaction mixture. [e] Ratio allyl alcohol/saturated alcohol/aldehyde: 45:5:5.

Alternatively, no reaction was observed with methyl itaconate or (_E_)-_N_-benzylideneaniline, which do not possess the α,β-unsaturated scaffold (Table 2, entries 9, 11). Moreover, the complex is active in the hydrogenation of _trans_-cinnamaldehyde, although it does not provide a selective reaction and both reductions of the C=C and C=O bonds were observed (entry 10).

Conclusion

A family of Rh^I and Ir^I square-planar complexes based on a pyridine diphosphite ligand **1** has been prepared and characterized. The set contains both neutral chloridocomplexes [MCl(**1**)] and cationic ones of formula [M(**1**)**L**][BPh$_4$] with diverse ligands such as phosphanes, acetonitrile, isocyanides or ethylene. On the contrary, isonitriles led to pentacoordinate complexes [Ir(**1**)(CNR)$_2$][BPh$_4$] in the case of Ir. An important feature of these compounds is the very low back-donor ability of the [M(**1**)]$^+$ fragment as determined by IR spectroscopy analysis of carbonyl and isocyanide complexes. Structural characterization of complexes of the formula [M(**1**)**L**][BPh$_4$] by X-ray crystallography show the expected pincer coordination mode, with a preferred _meso_ conformation for the diphosphite. Moreover, the ethylene derivative **8** shows a near in-plane conformation of the ethylene ligand. This structure shows, in addition, a remarkably short C–C bond for the ethylene ligand, which can be attributed to a rather reduced π back-donation. A screening that explores the reactivity of these complexes in catalytic hydrogenation has shown that [IrCl(**1**)] is able to reduce the heteroaromatic ring of 2-methylquinoline and 2-methylquinoxaline, whereas it is not active in the hydrogenation of simple _N_-benzylideneaniline or dimethyl itaconate.
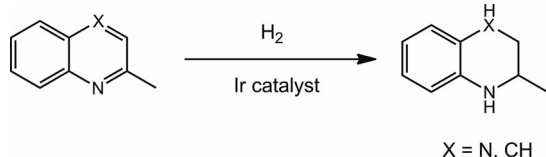
Scheme 6. Catalytic hydrogenation of nitrogen heterocycles.

Experimental Section

General Procedures: All reactions and manipulations were performed under nitrogen or argon, either in a Braun Labmaster 100 glovebox or by using standard Schlenk-type techniques. All solvents were distilled under nitrogen using the following desiccants: sodium benzophenone ketyl for diethyl ether (Et_2O) and tetrahydrofuran (THF); sodium for *n*-hexane and toluene; CaH_2 for dichloromethane (CH_2Cl_2) and NaOMe for methanol (MeOH). [{Rh(μ-Cl)(η^4-C_8H_{12})}$_2$],[26] [{Ir(μ-Cl)(η^4-C_8H_{12})}$_2$][27] and [{Ir(μ-Cl)(η^2-C_8H_{14})$_2$}$_2$][28] were prepared by reported methods. Phosphanes and isocyanides were purchased from commercial suppliers and used as received. IR spectra were recorded with a Perkin–Elmer 1720-XFT or with a Bruker Vector 22 spectrometer. NMR spectra were obtained with Bruker DPX-300, DRX-400, AV400 or DRX-500 spectrometers. $^{31}P\{^1H\}$ NMR spectroscopic shifts were referenced to external 85% H_3PO_4, whereas $^{13}C\{^1H\}$ and ^1H shifts were referenced to the residual signals of deuterated solvents. All data are reported in ppm downfield from Me_4Si. The C,H,N analyses were carried out with a LECO CHNS-TruSpec microanalyzer. HRMS data was obtained at the Instrumental Services of Universidad de Sevilla (CITIUS) with a Jeol JMS-SX 102A mass spectrometer. The following atom labels have been used for the ^1H NMR spectroscopic data of the diphosphite ligand.
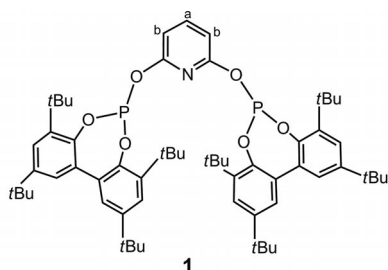
Diphosphite 1: *n*BuLi (5.0 mL, 8.0 mmol, 1.6 M in hexanes) was added dropwise to a suspension of 2,6-dihydroxypyridinium chloride (0.352 g, 2.4 mmol) in THF (10 mL). The mixture was stirred for 1 h and a solution of 3,3′,5,5′-tetra-*tert*-butylbisphen-2,2′-diyl-phosphochloridite (2.73 g, 5.7 mmol) in THF (10 mL) was added slowly to the white suspension. The reaction mixture was stirred for 12 h, volatile compounds were evaporated under vacuum and the resulting solid was washed with *n*-hexane (3 × 30 mL), dissolved in CH_2Cl_2 and the solution was filtered through Celite. Evaporation of the solvent yielded **1** as a white solid (1.15 g, 48%). IR (nujol mull): $\tilde{\nu}$ = 1600 (m, py), 1573 (m, py) cm^{-1}. ^1H NMR ($CDCl_3$, 500 MHz): δ = 7.53 (t, $^3J_{H,H}$ = 8 Hz, 1 H, H arom, H^a), 7.44 (d, $^4J_{H,H}$ = 2.5 Hz, 4 H, 4 H arom.), 7.19 (d, $^4J_{H,H}$ = 2.5 Hz, 4 H, 4 H arom.), 6.46 (d, $^3J_{H,H}$ = 8 Hz, 2 H, 2 H arom., H^b), 1.46 (s, 36 H, 4 CMe_3), 1.36 (s, 36 H, 4 CMe_3) ppm. $^{31}P\{^1H\}$ NMR ($CDCl_3$, 162 MHz): δ = 138.8 (s) ppm. $^{13}C\{^1H\}$ NMR ($CDCl_3$, 126 MHz): δ = 158.4 (d, $J_{P,C}$ = 6 Hz), 146.7, 145.5 (br.), 142.2, 140.5, 132.9, 126.5, 124.3, 106.9, 35.5, 34.7, 31.6, 31.3 ppm. HRMS (FAB): *m/z* exact mass calcd. for $C_{61}H_{84}NO_6P_2$ 988.5774; found 988.5821 [M + H]$^+$.

[RhCl(1)] (4): A solution of [{RhCl(cod)}$_2$] (0.157 g, 0.32 mmol) in THF (5 mL) was added to a solution of diphosphite **1** (0.63 g, 0.64 mmol) in THF (10 mL). The reaction mixture was stirred for 24 h, volatile compounds were removed under vacuum and the resulting residue was washed with *n*-hexane (3 × 10 mL), dissolved in CH_2Cl_2 and the resulting mixture was filtered through a pad of Celite. Evaporation of the solution obtained yielded **4** as a yellow solid (0.53 g, 75%). ^1H NMR ($CDCl_3$, 400 MHz, 298 K): δ = 7.66

(t, $^3J_{H,H}$ = 8 Hz, 1 H, H arom, H^a), 7.43 (d, $^4J_{HH}$ = 2 Hz, 4 H, 4 H arom), 7.17 (d, $^4J_{H,H}$ = 2 Hz, 4 H, 4 H arom), 6.62 (d, $^3J_{H,H}$ = 8 Hz, 2 H, 2 H arom, 2 H^b), 1.47 (s, 36 H, 4 CMe_3), 1.34 (s, 36 H, 4 CMe_3) ppm. $^{31}P\{^1H\}$ NMR ($CDCl_3$, 162 MHz, 298 K): δ = 139.0 (d, $J_{P,Rh}$ = 250 Hz) ppm. $^{13}C\{^1H\}$ NMR ($CDCl_3$, 101 MHz, 298 K): δ = 159.7 (br.), 147.6, 144.8, 140.2, 138.4, 131.1, 126.8, 124.9, 103.4 (br.), 35.6, 34.7, 31.8, 31.5 ppm. $C_{61}H_{83}ClNO_6P_2Rh$ (1126.62): calcd. C 65.03, H 7.43, N 1.24; found C 65.14, H 7.34, N 1.26.

[IrCl(1)] (5): A solution of complex [{IrCl(cod)}$_2$] (0.067 g, 0.1 mmol) in THF (10 mL) was slowly added to a solution of diphosphite **1** (0.198 g, 0.2 mmol) in THF (20 mL). The resulting solution was stirred vigorously for 24 h. Then the solvent was removed under vacuum and the residue was washed with *n*-hexane (3 × 10 mL). The orange residue was extracted with dichloromethane. Subsequently, the filtered solution was concentrated to around 2 mL and *n*-hexane (15 mL) was added. The resulting orange solid was washed with *n*-hexane (3 × 5 mL) and vacuum-dried to give **5** as an orange solid (0.186 g, 77%). ^1H NMR (400 MHz, $CDCl_3$, 298 K): δ = 7.93 (t, $^3J_{H,H}$ = 8.3 Hz, 1 H, H^a arom.), 7.48 (d, $^4J_{H,H}$ = 2.1 Hz, 4 H, H arom.), 7.22 (d, $^4J_{H,H}$ = 2.1 Hz, 4 H, H arom.), 6.56 (d, $^3J_{H,H}$ = 8.3 Hz, 2 H, H^b arom.), 1.49 (s, 36 H, 4 CMe_3), 1.36 (s, 36 H, 4 CMe_3) ppm. $^{31}P\{^1H\}$ NMR (162 MHz, $CDCl_3$, 298 K): δ = 140.0 (s) ppm. $^{13}C\{^1H\}$ NMR (101 MHz, $CDCl_3$, 298 K): δ = 155.4 (br.), 147.1, 144.8 (br.), 140.9, 137.9, 129.1, 128.1, 124.9, 102.9 (br.), 35.8, 34.9, 32.5, 31.8 ppm. $C_{61}H_{83}ClIrNO_6P_2$ (1215.93): calcd. C 60.25, H 6.88, N 1.15; found C 60.25, H 6.81, N 1.12.

[Rh(1)(PPh₃)][BPh₄] (6): PPh_3 (0.025 g, 0.095 mmol) and $NaBPh_4$ (0.031 g, 0.09 mmol) were added to a solution of **4** (0.1 g, 0.089 mmol) in THF (10 mL). The mixture was stirred for 1 h and the solvent evaporated. The resulting residue was extracted with toluene (3 × 5 mL), the obtained solution evaporated and the obtained solid was washed with *n*-hexane (3 × 5 mL) to yield **6** as a yellow-orange solid (0.09 g, 60%). ^1H NMR (C_6D_6, 500 MHz, 298 K): δ = 8.09 (br. s, 8 H, 8 arom., BPh_4), 7.55 (br. s, 4 H, 4 H arom.), 7.50 (t, $J_{H,H}$ = 9 Hz, 6 H, 6 H arom., PPh_3), 7.25 (br. s, 4 H, 4 H arom.), 7.22 (t, $J_{H,H}$ = 7 Hz, 8 H, 8 H arom., BPh_4), 7.05 (t, $J_{H,H}$ = 7 Hz, 4 H, 4 H arom., BPh_4), 6.83 (t, $J_{H,H}$ = 7 Hz, 3 H, 3 H arom., PPh_3), 6.61 (m, 6 H, 6 H arom., PPh_3), 6.33 (t, $^3J_{H,H}$ = 8 Hz, 1 H, H arom., H^a), 5.34 (d, $^3J_{H,H}$ = 8 Hz, 2 H, 2 H arom., 2 H^b), 1.31 (s, 36 H, 4 CMe_3), 1.28 (s, 36 H, 4 CMe_3) ppm. $^{31}P\{^1H\}$ NMR (C_6D_6, 162 MHz, 298 K): δ = 32.8 (dt, $J_{P,Rh}$ = 159 Hz, $J_{P,P}$ = 49 Hz, P–C), 150.3 (dd, $J_{P,Rh}$ = 243, $J_{P,P}$ = 49 Hz, P–O) ppm. $^{13}C\{^1H\}$ NMR (C_6D_6, 126 MHz, 298 K): δ = 165.2 (q, $^1J_{C,B}$ = 49 Hz), 156.3 (br.), 148.7, 147.5, 146.2 (br.), 139.8, 137.0, 133.9 (d, $J_{P,C}$ = 49 Hz), 133.4 (d, $J_{P,C}$ = 12 Hz), 130.6, 130.5 (d, $J_{P,C}$ = 10 Hz), 130.4, 128.1, 125.9 (br.), 125.5, 121.6, 104.6, 35.5, 34.5, 31.1 ppm. $C_{103}H_{118}BNO_6P_3Rh$ (1672.68): calcd. C 73.96, H 7.11, N 0.84; found C 73.52, H 7.41, N 0.78.

[Rh(1)(MeCN)][BPh₄] (7): $NaBPPh_4$ (0.02 g, 0.058 mmol) was added to a solution of complex **4** (0.06 g, 0.053 mmol) in a THF/MeCN (5:1) mixture (6 mL). The mixture was stirred for 5 h and the solvent evaporated. The resulting residue was washed with *n*-hexane (3 × 5 mL) and dissolved in toluene (10 mL). Precipitation by addition of *n*-hexane (20 mL) yielded **7** as a yellow solid (0.075 g, 95%). ^1H NMR ($CDCl_3$, 500 MHz, 298 K): δ = 7.51 (br. s, 4 H, 4 H arom.), 7.48 (t, $^3J_{H,H}$ = 8 Hz, 1 H, H arom., H^a), 7.34 (br. s, 4 H, 4 H arom.), 7.26 (br. s, 4 H, 4 H arom.), 6.87 (t, $J_{H,H}$ = 7 Hz, 8 H, 8 H arom., BPh_4), 6.70 (t, $J_{H,H}$ = 7 Hz, 4 H, 4 H arom., BPh_4), 6.60 (d, $^3J_{H,H}$ = 8 Hz, 2 H, 2 H arom., 2 H^b), 1.45 (s, 36 H, 4 CMe_3), 1.35 (s, 36 H, 4 CMe_3), 0.58 (s, 3 H, MeCN)

ppm. $^{31}P\{^1H\}$ NMR (CDCl$_3$, 162 MHz): δ = 139.5 (d, $J_{P,Rh}$ = 238 Hz) ppm. $^{13}C\{^1H\}$ NMR (CDCl$_3$, 126 MHz): δ = 164.2 (q, $^1J_{C,B}$ = 49 Hz), 159.1 (br.), 149.0, 147.6, 144.0, 140.0, 136.0 (br.), 130.8, 129.0 (br.), 127.3, 125.5 (br.), 125.4, 121.5, 104.7, 35.7, 34.9, 31.5, 31.4, 1.3 ppm. C$_{87}$H$_{106}$BN$_2$O$_6$P$_2$Rh (1451.45): calcd. C 71.92, H 7.36, N 1.93; found C 72.31, H 7.45, N 1.75.

[Rh(1)(η^2-C$_2$H$_4$)][BPh$_4$] (8): A solution of **4** (0.1 g, 0.089 mmol) in CH$_2$Cl$_2$ (10 mL) was introduced into a glass pressure reactor and NaBPh$_4$ (0.03 g, 0.09 mmol) was added. After 1 h, the vessel was charged with 1 atm of C$_2$H$_4$ and the reaction stirred for 15 h. The mixture was evaporated down to one-fourth of the volume and *n*-hexane (5 mL) was added to yield **8** as orange crystals (0.045 g, 35%). ^1H NMR (CDCl$_3$, 500 MHz, 298 K): δ = 7.53 (d, $^4J_{H,H}$ = 2 Hz, 4 H, 4 arom.), 7.44 (m, 8 H, 8 H arom., BPh$_4$), 7.29 (d, $^4J_{H,H}$ = 2 Hz, 4 H, 4 arom.), 7.17 (t, $^3J_{H,H}$ = 8 Hz, 1 H, H arom., H^a), 7.00 (t, $J_{H,H}$ = 7 Hz, 8 H, 8 H arom., BPh$_4$), 6.83 (t, $J_{H,H}$ = 7 Hz, 4 H, 4 arom., BPh$_4$), 6.56 (d, $^3J_{H,H}$ = 8 Hz, 2 H, 2 H arom., H^b), 2.98 (br. s, 4 H, C$_2$H$_4$), 1.38 (s, 36 H, 4 CMe$_3$), 1.31 (s, 36 H, 4 CMe$_3$) ppm. $^{31}P\{^1H\}$ NMR (CDCl$_3$, 162 MHz, 298 K): δ = 154.2 (d, $J_{P,Rh}$ = 211 Hz) ppm. $^{13}C\{^1H\}$ NMR (CDCl$_3$, 126 MHz, 298 K): δ = 164.3 (q, $^1J_{C,B}$ = 49 Hz), 156.9 (t, $J_{P,C}$ = 6 Hz), 149.8, 147.1, 144.2 (br.), 139.7, 136.3 (br.), 130.4, 127.6, 125.8, 125.6 (br.), 121.6, 105.6 (br.), 57.7 (br.), 35.7, 35.0, 31.4, 31.3 ppm. C$_{87}$H$_{107}$BNO$_6$P$_2$Rh (1438.45): calcd. C 72.64, H 7.50, N 0.97; found C 72.81, H 7.98, N 0.90.

[Rh(1)(CO)][BPh$_4$] (9): Obtained as yellow crystals as described for **8** using CO instead of C$_2$H$_4$ (0.05 g, 40%). IR (nujol mull): $\tilde{v}$ = 2093 (s, CO) cm^{-1}. ^1H NMR (CD$_2$Cl$_2$, 500 MHz): δ = 7.80 (t, $^3J_{H,H}$ = 8 Hz, 1 H, H arom.), 7.61 (br. s, 4 H, 4 H arom.), 7.34 (br. s, 12 H, 12 H arom.), 7.02 (t, $J_{H,H}$ = 7 Hz, 8 H, 8 H arom., BPh$_4$), 6.86 (m, 6 H, 6 H arom.), 1.46 (s, 36 H, 4 CMe$_3$), 1.40 (s, 36 H, 4 CMe$_3$) ppm. $^{31}P\{^1H\}$ NMR (CDCl$_3$, 202 MHz, 298 K): δ = 145.6 (d, $J_{P,Rh}$ = 220 Hz) ppm. $^{13}C\{^1H\}$ NMR (CD$_2$Cl$_2$, 126 MHz, 298 K): δ = 185.7 (m, $^1J_{C,Rh}$ = 72, $^2J_{C,P}$ = 16 Hz), 164.4 (q, $^1J_{C,B}$ = 49 Hz), 157.8 (br.), 150.4, 147.1, 144.1 (br.), 140.2, 136.2 (br.), 130.7, 127.9, 126.6, 126.3, 125.9, 122.0, 106.4, 36.0, 35.2, 31.6, 31.3 ppm. C$_{86}$H$_{103}$BNO$_7$P$_2$Rh (1438.40): calcd. C 71.81, H 7.22, N 0.97; found C 71.81, H 7.54, N 0.76.

[Rh(1)(CNXy)][BPh$_4$] (10): NaBPh$_4$ (0.013 g, 0.04 mmol) was added to a solution of **4** (0.043 g, 0.04 mmol) in THF (2 mL). The mixture was stirred for 1 h, and CNXy (0.005 g, 0.04 mmol) was added. The reaction was stirred overnight. Solvent was removed under reduced pressure. The resulting residue was dissolved in CH$_2$Cl$_2$ and filtered through a short pad of Celite. The solution was dried and the solid was washed with Et$_2$O (2 × 5 mL) to yield **10** as an orange solid (0.042 g, 80%). IR (CH$_2$Cl$_2$): $\tilde{v}$ = 2153 (s, CN) cm^{-1}. ^1H NMR (CD$_2$Cl$_2$, 300 MHz, 298 K): δ = 7.86 (t, $^3J_{H,H}$ = 9.0 Hz, 1 H, 1 H arom.), 7.59 (d, $^4J_{H,H}$ = 2.1 Hz, 4 H, 4 H arom.), 7.36 (m, 13 H, 13 H arom.), 7.08 (m, 8 H, 8 H arom.), 6.89 (m, 8 H, 8 H arom.), 1.58 (s, 6 H, 2 Me), 1.49 (s, 36 H, 4 CMe$_3$), 1.42 (s, 36 H, 4 CMe$_3$) ppm. $^1P\{^1H\}$ NMR (CD$_2$Cl$_2$, 121 MHz, 298 K): δ = 149.8 (d, $J_{P,Rh}$ = 235 Hz) ppm. $^{13}C\{^1H\}$ NMR (CD$_2$Cl$_2$, 75 MHz, 298 K): δ = 164.4 (q, $J_{C,B}$ = 52 Hz), 164.4 (m), 158.4 (m), 149.9, 147.1, 144.2, 140.6, 136.3, 135.6, 131.1, 129.9, 128.2, 127.8, 127.0, 126.1, 125.9, 122.0, 105.7, 36.0, 35.2, 31.8, 31.5, 18.1 ppm. C$_{94}$H$_{112}$BN$_2$O$_6$P$_2$Rh (1541.57): calcd. C 73.24, H 7.32, N 1.82; found C 72.67, H 7.33, N 1.73.

[Ir(1)(PPh$_3$)][BPh$_4$] (11): PPh$_3$ (0.010 g, 0.04 mmol) and NaBPh$_4$ (0.013 g, 0.04 mmol) was added to a solution of complex **5** (0.036 g, 0.03 mmol) in THF (10 mL). The resulting solution was stirred at room temperature for 1 h and the volatile compounds were removed under vacuum. The residue was extracted with toluene

(15 mL). Subsequently, the filtered solution was concentrated to around 2 mL and *n*-hexane (15 mL) was added. The resulting orange solid was washed with *n*-hexane (3 × 10 mL) and vacuum-dried; yield 64% (0.033 g). ^1H NMR (400 MHz, C$_6$D$_6$, 298 K): δ = 8.26 (br. s, 8 H, H arom., BPh$_4$), 7.67 (br. s, 4 H, H arom.), 7.65 (m, 6 H, H arom., PPh$_3$), 7.37 (br. s, 4 H, H arom.), 7.24 (m, 8 H, H arom., BPh$_4$), 7.14 (m, 4 H, H arom., BPh$_4$), 6.93 (m, 3 H, H arom., PPh$_3$), 6.72 (m, 6 H, H arom., PPh$_3$), 6.54 (t, $^3J_{H,H}$ = 8.1 Hz, 1 H, H^a arom.), 5.45 (d, $^3J_{H,H}$ = 8.1 Hz, 2 H, H^b arom.), 1.42 (s, 36 H, 4 CMe$_3$), 1.40 (s, 36 H, 4 CMe$_3$) ppm. $^{31}P\{^1H\}$ NMR (162 MHz, C$_6$D$_6$, 298 K): δ = 144.1 (d, $^2J_{P,P}$ = 38.9 Hz, P-O), 11.0 (t, $^2J_{P,P}$ = 38.9 Hz, PPh$_3$) ppm. $^{13}C\{^1H\}$ NMR (101 MHz, C$_6$D$_6$, 298 K): δ = 165.3 (q, $J_{C,B}$ = 47.9 Hz), 157.4 (br.), 149.6, 148.8, 146.9, 140.5, 137.0, 135.5 (br.), 134.1 (d, $J_{C,P}$ = 12 Hz), 131.2, 130.7, 129.8 (br.), 128.1, 126.9 (br.), 126.5, 122.9, 104.4 (br.), 36.1, 35.1, 31.6 ppm. C$_{103}$H$_{118}$BIrNO$_6$P$_3$ (1761.99): calcd. C 70.21, H 6.75, N 0.79; found C 70.18, H 6.68, N 0.77.

[Ir(1)(PPh$_2$Me)][BPh$_4$] (12): Prepared as described for **11** using PPh$_2$Me. Orange solid, yield 67% (0.034 g). ^1H NMR (400 MHz, C$_6$D$_6$, 298 K): δ = 8.22 (br. s, 8 H, H arom., BPh$_4$), 7.70 (br. s, 4 H, H arom.), 7.63 (m, 5 H, H arom., P*Ph$_2$*Me), 7.37 (br. s, 4 H, H arom.), 7.25 (m, 8 H, H arom., BPh$_4$), 7.12 (m, 4 H, H arom., BPh$_4$), 6.92 (m, 5 H, H arom., P*Ph$_2$*Me), 6.55 (t, $^3J_{H,H}$ = 7.8 Hz, 1 H, H^a arom.), 5.62 (d, $^3J_{H,H}$ = 7.8 Hz, 2 H, H^b arom.), 1.48 (s, 36 H, 4 CMe$_3$), 1.43 (br. s, 3 H, PPh$_2$*Me*), 1.37 (s, 36 H, 4 CMe$_3$) ppm. $^{31}P\{^1H\}$ NMR (162 MHz, C$_6$D$_6$, 298 K): δ = 146.5 (d, $^2J_{P,P}$ = 35.1 Hz, P–O), 6.2 (t, $^2J_{P,P}$ = 35.1 Hz, PPh$_2$Me) ppm. $^{13}C\{^1H\}$ NMR (101 MHz, C$_6$D$_6$, 298 K): δ = 169.3 (q, $J_{C,B}$ = 42 Hz), 153.2 (br.), 149.8, 148.6, 144.9, 140.6, 137.3, 132.7 (br.), 131.7, 131.5 (br.), 130.9 (br.), 129.7, 129.5 (br.), 126.7, 125.8, 101.4 (br.), 35.9, 35.1, 31.6, 31.1 ppm. C$_{98}$H$_{116}$BIrNO$_6$P$_3$ (1699.92): calcd. C 69.24, H 6.88, N 0.82; found C 69.21, H 6.88, N 0.75.

[Ir(1)(CNBn)$_2$][BPh$_4$] (13): Isocyanide (0.04 mmol) and NaBPh$_4$ (0.013 g, 0.04 mmol) were added to a solution of complex **5** (0.036 g, 0.03 mmol) in THF (10 mL). The resulting solution was stirred at room temperature for 1 h and the volatile compounds were removed under vacuum. The residue was extracted with toluene (15 mL). Subsequently, the filtered solution was concentrated to around 2 mL and *n*-hexane (15 mL) was added. The resulting yellow solid was washed with *n*-hexane (3 × 10 mL) and vacuum-dried; yield 71% (0.037 g). IR (KBr): $\tilde{v}$ = 2191 (br. s, CN) cm^{-1}. $^{31}P\{^1H\}$ NMR (162 MHz, C$_6$D$_6$, 298 K): δ = 145.2 (s) ppm. ^1H NMR (400 MHz, C$_6$D$_6$, 298 K): δ = 8.22 (br. s, 8 H, H arom., BPh$_4$), 7.74 (d, $J_{H,H}$ = 2.4 Hz, 4 H, H arom.), 7.49 (d, $J_{H,H}$ = 2.4 Hz, 4 H, H arom.), 7.36 (t, $J_{H,H}$ = 7.0 Hz, 8 H, H arom., BPh$_4$), 7.24 (m, 4 H, H arom., BPh$_4$), 7.15 (br. s, 4 H, 10 H, CNCH$_2$C$_6$H$_5$), 6.83 (t, $^3J_{H,H}$ = 7.8 Hz, 1 H, H^a arom.), 6.18 (d, $^3J_{H,H}$ = 7.8 Hz, 2 H, H^b arom.), 2.22 (s, 4 H, 2CNC*H$_2$*C$_6$H$_5$), 1.42 (s, 36 H, 4 CMe$_3$), 1.40 (s, 36 H, 4 CMe$_3$) ppm. $^{13}C\{^1H\}$ NMR (101 MHz, C$_6$D$_6$, 298 K): δ = 164.8 (q, $J_{C,B}$ = 52.0 Hz), 157.9 (br.), 149.5, 148.7, 146.0, 144.8 (br.), 140.8, 137.0 (br.), 136.9, 133.9, 132.8, 131.0, 128.3, 127.2 (br.), 126.2, 122.1, 104.7 (br.), 48.0, 35.5, 34.3, 31.2 ppm. C$_{101}$H$_{117}$BIrN$_3$O$_6$P$_2$ (1734.00): calcd. C 69.95, H 6.80, N 2.42; found C 69.93, H 6.88, N 2.45.

[Ir(1)(CNCy)$_2$][BPh$_4$] (14): Prepared as described for **13**. Yellow solid, yield 77% (0.034 g). IR (KBr): $\tilde{v}$ = 2178 (s, CN) cm^{-1}. $^{31}P\{^1H\}$ NMR (121 MHz, C$_6$D$_6$, 298 K): δ = 146.3 (s) ppm. ^1H NMR (400 MHz, C$_6$D$_6$, 298 K): δ = 8.13 (br. s, 8 H, H arom., BPh$_4$), 7.78 (m, 4 H, H arom.), 7.50 (br. s, 4 H, H arom), 7.43 (br. s, 8 H, H arom., BPh$_4$), 7.14 (br. s, 4 H, 4 H arom., BPh$_4$), 6.57 (m, 1 H, H^a arom.), 5.73 (d, $^3J_{H,H}$ = 9.8 Hz, 2 H, H^b arom.), 2.22 (br. s, 2 H, 2C*H*CNC$_6$H$_{11}$), 1.83 (m, 12 H, CNC$_6$H$_{11}$), 1.62 (s, 36 H, 4 CMe$_3$),

Table 3. Crystallographic data and structure refinement for **6–8** and **12**.

	6	7	8	12
Formula	$C_{107}H_{126}BNO_7PRh$	$C_{187}H_{241}B_2Cl_3N_4O_{12}P_4Rh_2$	$C_{93}H_{121}BNO_6P_2Rh$	$C_{398}H_{470}B_4Ir_4N_4O_{24}P_{12}$
M_r	1744.72	3194.51	1524.57	6877.46
T [K]	100(2)	100(2)	100(2)	293(2)
Crystal size [mm³]	$0.36 \times 0.19 \times 0.13$	$0.25 \times 0.23 \times 0.22$	$0.28 \times 0.25 \times 0.14$	$0.074 \times 0.044 \times 0.015$
Crystal system	triclinic	monoclinic	monoclinic	monoclinic
Space group	$P\bar{1}$	$C2/c$	$C2/m$	$P2_1/c$
a [Å]	17.1399(16)	34.7797(14)	25.2664(19)	12.5992(5)
b [Å]	17.544(3)	26.4707(11)	26.4744(19)	28.1831(16)
c [Å]	18.7310(17)	25.3582(18)	14.6013(11)	27.1141(10)
α [°]	101.257(4)	90	90	90
β [°]	111.742(3)	124.6180(10)	100.366(2)	99.684(4)
γ [°]	103.737(4)	90	90	90
V [Å³]	4825.5(10)	9212.6(18)	9607.6(12)	9490.6(7)
Z	2	4	4	1
$D_{calcd.}$ [g cm⁻³]	1.201	1.104	1.054	1.203
Absorption coefficient [mm⁻¹]	0.281	0.301	0.257	3.587
$F(000)$	1852	6792	3256	3586
θ range [°]	2.14 to 30.69	1.82 to 30.55	2.35 to 30.61	3.14 to 73.82
Measured reflections	90629	199998	83189	36043
Unique reflections	28363 [$R_{int} = 0.0571$]	26069 [$R(int) = 0.0355$]	14794 [$R(int) = 0.0389$]	18389 [$R(int) = 0.0887$]
Data/restraints/parameters	28363/80/1126	26069/18/982	14794/74/502	18389/ 144/1136
Goodness-of-fit on F^2	1.051	1.030	1.108	0.883
Final R indices [$I > 2\sigma(I)$]	$R_1 = 0.0498$, $wR_2 = 0.1267$	$R_1 = 0.0666$, $wR_2 = 0.2053$	$R_1 = 0.0424$, $wR_2 = 0.1236$	$R_1 = 0.0689$, $wR_2 = 0.1530$
R indices (all data)	$R_1 = 0.0903$, $wR_2 = 0.1473$	$R_1 = 0.0861$, $wR_2 = 0.2236$	$R_1 = 0.0521$, $wR_2 = 0.1291$	$R_1 = 0.1674$, $wR_2 = 0.1944$
Largest diff. peak/hole [e Å⁻³]	1.357/–1.261	4.432/–1.044	1.395/–0.638	0.788/–1.257

1.51 (m, 8 H, CH_2, CNC$_6$H$_{11}$), 1.35 (s, 36 H, 4 CMe$_3$) ppm. ¹³C{¹H} NMR (101 MHz, C$_6$D$_6$, 298 K): δ = 165.7 (q, $J_{C,B}$ = 34.0 Hz), 151.0 (br.), 148.5, 148.0, 146.7, 140.6, 137.6, 132.0, 128.2, 125.9, 125.4, 121.9, 115.7, 56.1, 35.7, 34.5, 31.3, 22.7, 21.5 ppm. C$_{99}$H$_{125}$BIrN$_3$O$_6$P$_2$ (1718.04): calcd. C 69.21, H 7.33, N 2.45; found C 69.26, H 7.40, N 2.44.

[Ir(1)(η²-C₂H₄)][BPh₄] (15): A slow flow of ethylene was bubbled into a suspension of [{Ir(μ-Cl)(η²-C$_8$H$_{14}$)$_2$}$_2$] (0.045 g, 0.05 mmol) in methanol (15 mL) at room temperature for 1 h. Then the mixture was cooled to –40 °C and a solution of diphosphite (0.099 g, 0.1 mmol) in THF (2 mL) was added. After 20 min, NaBPh$_4$ (0.032 g, 0.1 mmol) was added and the mixture was stirred at –40 °C for 30 min. Diethyl ether was added (30 mL) and the resulting pale orange solid was washed with cold diethyl ether (3 × 10 mL) and vacuum-dried; yield 62% (0.047 g). ³¹P{¹H} NMR (162 MHz, C$_6$D$_6$, 298 K): δ = 143.7 (s) ppm. ¹H NMR (C$_6$D$_6$, 400 MHz, 298 K): δ = 8.21 (br. s, 8 H, H arom., BPh$_4$), 7.75 (br. s, 4 H, H arom.), 7.51 (br. s, 4 H, H arom.), 7.37 (m, 8 H, H arom., BPh$_4$), 7.14 (m, 4 H, H arom., BPh$_4$), 6.65 (m, 1 H, H^a arom.), 5.83 (d, ³$J_{H,H}$ = 7.8 Hz, 2 H, H^b arom.), 2.89 (br. s, 4 H, C$_2$H$_4$), 1.42 (s, 36 H, 4 CMe$_3$), 1.35 (s, 36 H, 4 CMe$_3$) ppm. ¹³C{¹H} NMR (101 MHz, [D$_8$]tetrahydrofurane, 213 K): δ = 164.7 (q, $J_{C,B}$ = 48.2 Hz), 157.4 (br.), 150.0, 147.6, 144.7, 140.2, 137.0, 130.6, 128.9, 127.2 (br.), 125.9, 121.9, 105.7 (br.), 44.6, 35.7, 34.6, 31.3 ppm. C$_{87}$H$_{107}$BIrNO$_6$P$_2$ (1527.73): calcd. C 68.40, H 7.06, N 0.92; found C 68.43, H 7.08, N 0.92.

General Hydrogenation Procedure: In a glovebox, the appropriate substrate (0.3 mmol), diphosphite **1** (3.15 μmol), [{IrCl(cod)}$_2$] (1.5 μmol) and the additive (30 μmol) in toluene (0.5 mL) were added to a 2 mL glass vial. Vials were placed in a model HEL CAT18 pressure reactor that holds up to eighteen reactions. The reactor was purged three times with H$_2$ and finally pressurized.

After 24 h, the reactor was slowly depressurized, solutions were evaporated and conversions were determined by ¹H NMR spectroscopy.

X-ray Structure Determinations: Crystallographic data for complexes **6–8** were collected with a Bruker-Nonius X8Apex-II CCD diffractometer using graphite-monochromated Mo-$K_{\alpha 1}$ radiation (λ = 0.71073 Å), whereas diffraction data for **12** were recorded with an Oxford Diffraction Xcalibur Nova diffractometer using Cu-K_α radiation (λ = 1.5418 Å). The data were reduced (SAINT)[29] and corrected for Lorentz polarization and absorption effects by multiscan method (SADABS).[30] Structures were solved by direct methods (SIR-2002)[31] and refined against all F^2 data by full-matrix least-squares techniques (SHELXTL 6.12).[32] A summary of cell parameters, data collection and structure solution and refinement is given in Table 3.

Supporting Information (see footnote on the first page of this article): ¹H NMR spectra (CD$_2$Cl$_2$, 500 MHz) of compound **8** showing the ethylene signal region at several temperatures and the ³¹P{¹H} NMR spectra (CD$_2$Cl$_2$, 202 MHz) of **8** at several temperatures.

Acknowledgments

[1] a) D. Morales-Morales, C. M. Jensen, *The Chemistry of Pincer Compounds*, Elsevier, **2007**; b) M. E. van der Boom, D. Milstein, *Chem. Rev.* **2003**, *103*, 1759–1792; c) M. Albrecht, G. van Koten, *Angew. Chem.* **2001**, *113*, 3866; *Angew. Chem. Int. Ed.* **2001**, *40*, 3750–3781; d) C. M. Jensen, *Chem. Commun.* **1999**, 2443–2449.

[2] a) W. H. Bernskoetter, S. K. Hanson, S. K. Buzak, Z. Davis, P. S. White, R. Swartz, K. I. Goldberg, M. Brookhart, *J. Am. Chem. Soc.* **2009**, *131*, 8603–8613; b) M. Feller, A. Karton, G. Leitus, J. M. L. Martin, D. Milstein, *J. Am. Chem. Soc.* **2006**, *128*, 12400–12401; c) N. J. Brookes, M. T. Whited, A. Ariafard, R. Stranger, R. H. Grubbs, B. F. Yates, *Organometallics* **2010**, *29*, 4239–4250.

[3] M. Kanzelberger, X. Zhang, T. J. Emge, A. S. Goldman, J. Zhao, C. Incarvito, J. F. Hartwig, *J. Am. Chem. Soc.* **2003**, *125*, 13644–13645.

[4] a) B. Rybtchinski, D. Milstein, *Angew. Chem.* **1999**, *111*, 918; *Angew. Chem. Int. Ed.* **1999**, *38*, 870–883; b) H. Salem, Y. Ben-David, L. J. W. Shimon, D. Milstein, *Organometallics* **2006**, *25*, 2292–2300.

[5] M. E. van der Boom, S.-Y. Liou, Y. Ben-David, L. J. W. Shimon, D. Milstein, *J. Am. Chem. Soc.* **1998**, *120*, 6531–6541.

[6] a) S. Park, M. Brookhart, *Chem. Commun.* **2011**, 3643–3645; b) J. Yanga, M. Brookhart, *Adv. Synth. Catal.* **2009**, *351*, 175–187.

[7] a) C. Crocker, R. J. Errington, W. S. McDonald, K. J. Odell, B. L. Shaw, R. J. Goodfellow, *J. Chem. Soc., Chem. Commun.* **1979**, 498–499; b) C. J. Moulton, B. L. Shaw, *J. Chem. Soc., Dalton Trans.* **1976**, 1020–1024; c) G. Vasapollo, P. Giannoccaro, C. F. Nobile, A. Sacco, *Inorg. Chim. Acta* **1981**, *48*, 125–128.

[8] See for instance: a) E. Kossoy, M. A. Iron, B. Rybtchinski, Y. Ben-David, L. J. W. Shimon, L. Konstantinovski, J. M. L. Martin, D. Milstein, *Chem. Eur. J.* **2005**, *11*, 2319–2326; b) J. J. Adams, A. Lau, N. Arulsamy, D. M. Roddick, *Organometallics* **2011**, *30*, 689–696.

[9] I. Göttker-Schnetmann, P. White, M. Brookhart, *J. Am. Chem. Soc.* **2004**, *126*, 1804–1811.

[10] M. Montag, I. Efremenko, R. Cohen, L. J. W. Shimon, G. Leitus, Y. Diskin-Posner, Y. Ben-David, H. Salem, J. M. L. Martin, D. Milstein, *Chem. Eur. J.* **2010**, *16*, 328–353.

[11] J. J. Adams, N. Arulsamy, D. M. Roddick, *Organometallics* **2011**, *30*, 697–711.

[12] K. G. Moloy, J. L. Petersen, *J. Am. Chem. Soc.* **1995**, *117*, 7696–7710.

[13] a) P. A. Chase, M. Gagliardo, M. Lutz, A. L. Spek, G. P. M. van Klink, G. van Koten, *Organometallics* **2005**, *24*, 2016–2019; b) R. A. Barber, R. B. Bedford, M. Betham, M. E. Blake, S. J. Coles, M. F. Haddow, M. B. Hursthouse, A. G. Orpen, L. T. Pilarski, P. G. Pringle, R. L. Wingad, *Chem. Commun.* **2006**, 3880–3882; c) D. Benito-Garagorri, V. Bocokic, K. Mereiter, K. Kirchner, *Organometallics* **2006**, *25*, 3817–3823; d) Z. Huang, P. S. White, M. Brookhart, *Nature* **2010**, *465*, 598–601.

[14] W. H. Bernskoetter, S. K. Hanson, S. K. Buzak, Z. Davis, P. S. White, R. Swartz, K. I. Goldberg, M. Brookhart, *J. Am. Chem. Soc.* **2009**, *131*, 8603–8613.

[15] a) D. Benito-Garagorri, E. Becker, J. Wiedermann, W. Lackner, M. Pollak, K. Mereiter, J. Kisala, K. Kirchner, *Organometallics* **2006**, *25*, 1900–1913; b) D. Benito-Garagorri, K. Kirchner, *Acc. Chem. Res.* **2008**, *41*, 201–213.

[16] J. I. van der Vlugt, J. N. H. Reek, *Angew. Chem.* **2009**, *121*, 8990; *Angew. Chem. Int. Ed.* **2009**, *48*, 8832–8846.

[17] M. Rubio, A. Suárez, D. del Río, A. Galindo, E. Álvarez, A. Pizzano, *Organometallics* **2009**, *28*, 547–560.

[18] W. V. Dahlhoff, S. M. J. Nelson, *J. Chem. Soc. A* **1971**, 2184–2190.

[19] In these reactions we did not observe the desired compounds and the formation of a silver precipitate, which may indicate the formation of Rh[II] species.

[20] M. Feller, E. Ben-Ari, T. Gupta, L. J. W. Shimon, G. Leitus, Y. Diskin-Posner, L. Weiner, D. Milstein, *Inorg. Chem.* **2007**, *46*, 10479–10490.

[21] a) C. Hahn, A. Vitagliano, F. Giordano, R. Taube, *Organometallics* **1998**, *17*, 2060–2066; b) C. Hahn, J. Sieler, R. Taube, *Chem. Ber./Recueil* **1997**, *130*, 939–945.

[22] a) M. M. Conejo, J. S. Parry, E. Carmona, M. Schultz, J. G. Brennann, S. M. Beshouri, R. A. Andersen, R. D. Rogers, S. Coles, M. Hursthouse, *Chem. Eur. J.* **1999**, *5*, 3000–3009; b) M. Schultz, C. J. Burns, D. J. Schwartz, R. A. Andersen, *Organometallics* **2001**, *20*, 5690–5699.

[23] CO coordination as a σ donor in related complexes of accepting pincer ligands has previously been proposed by Milstein; see ref.[8,10]

[24] CCDC-834638 (for **6**), -834639 (for **7**), -834640 (for **8**) and -834641 (for **12**) contain the supplementary crystallographic data for this paper. These data can be obtained free of charge from The Cambridge Crystallographic Data Centre via www.ccdc.cam.ac.uk/data_request/cif.

[25] Y. Segawa, M. Yamashita, K. Nozaki, *J. Am. Chem. Soc.* **2009**, *131*, 9201–9203.

[26] G. Giordano, R. H. Crabtree, *Inorg. Synth.* **1979**, *19*, 218–220.

[27] J. L. Herde, J. C. Lambert, C. V. Senoff, *Inorg. Synth.* **1974**, *15*, 18–19.

[28] A. van der Ent, L. Onderdelinden, *Inorg. Synth.* **1973**, *14*, 92–95.

[29] *SAINT*, v. 6.02, Bruker AXS, Inc., Madison, WI 53711-5373, USA, **1997**–**1999**.

[30] *SADABS*, Bruker AXS, Inc., Madison, Wisconsin, USA, **1999**.

[31] M. C. Burla, M. Camalli, B. Carrozzini, G. L. Cascarano, C. Giacovazzo, G. Polidori, R. Spagna, *J. Appl. Crystallogr.* **2003**, *36*, 1103–1104.

[32] *SHELXTL*, v. 6.14, Bruker AXS, Inc., Madison, Wisconsin, USA, **2000**–2003.

FULL PAPER

Synthesis, Characterisation, and Preliminary In Vitro Studies of Vanadium(IV) Complexes with a Schiff Base and Thiosemicarbazones as Mixed Ligands

Nerissa A. Lewis,[a] Fange Liu,[b] Luke Seymour,[a] Anthony Magnusen,[a] Travis R. Erves,[a] Jessa Faye Arca,[a] Floyd A. Beckford,[c] Ramaiyer Venkatraman,[d] Antonio González-Sarrías,[e] Frank R. Fronczek,[f] Don G. VanDerveer,[g] Navindra P. Seeram,[e] Aimin Liu,[b] William L. Jarrett,[h] and Alvin A. Holder*[a]

[VO(sal-L-tryp)(H$_2$O)] (**1**, sal-L-tryp = N-salicylidene-L-tryptophanate) was used as a precursor to produce the new complexes [VO(sal-L-tryp)(MeATSC)]·1.5C$_2$H$_5$OH [**2**, MeATSC = 9-Anthraldehyde-N(4)-methylthiosemicarbazone], [VO(sal-L-tryp)(N-ethhymethohcarbthio)]·H$_2$O [**3**, N-ethhymethohcarbthio = (E)-N-ethyl-2-(4-hydroxy-3-methoxybenzylidene)-hydrazinecarbothioamide] and [VO(sal-L-tryp)(acetyl-ethTSC)]·C$_2$H$_5$OH {**4**, acetylethTSC = (E)-N-ethyl-2-[1-(thiazol-2-yl)ethylidene]hydrazinecarbothioamide} by reaction with the respective thiosemicarbazone. The chemical and structural properties of these ligands and complexes were characterised by elemental analysis, ESI-MS, FTIR, UV/Vis,

ESR and ^{1}H and ^{13}C NMR spectroscopy and X-ray crystallography. Dimethyl sulfoxide (DMSO) and [D$_6$]DMSO solutions of **1**–**4** were oxidised in air to produce vanadium(V) species, which were verified by ESI-MS and ^{51}V NMR spectroscopy. The anticancer properties of **2**–**4** were examined with three colon cancer cell lines, HTC-116, Caco-2 and HT-29, and noncancerous colonic myofibroblasts, CCD18-Co. Compounds **2**–**3** exhibited less inhibitory effects in the CCD-18Co cells, which indicates a possible cytotoxic selectivity towards colon cancer cells. In general, compounds that exhibit antiproliferative activity to cancer cells but do not affect noncancerous cells may have a potential in chemotherapy.

Introduction

The limited efficacy of current treatments for advanced colon cancer serves an impetus for a concerted effort to identify chemopreventive agents for treatment. This process has always involved metal complexes. Cisplatin is widely used for the treatment of many cancers[1] despite its high toxicity, undesirable side effects and problems with drug resistance in primary and metastatic cancers.[2] These limitations have spurred a growing interest in new nonplatinum metal complexes that show anticancer properties.[3] Ruthenium has been reported to possess several favourable properties suited to rational anticancer drug design,[4] and ruthenium complexes of various types are being studied as metallodrugs as they are believed to have low toxicity and good selectivity for tumors.[5] Recently, we reported the effect of ruthenium(II) complexes with new chelating thiosemicarbazones on the growth inhibition of MCF-7 and MDA-MB-231 (breast adenocarcinoma) and HCT 116 and HT-29 (colorectal carcinoma) cell lines.[6] Thiosemicarbazones and their metal complexes are used in many applications ranging from pharmacology to nuclear medicine.[7]

Here we present our efforts to expand our study of non-ruthenium systems. There have been few systematic studies of the use of vanadium compounds as potential anticancer agents, for example, there has been a report of vanadium(V) complexes with salicylaldehyde semicarbazone derivatives that featured in vitro antitumour activity towards kidney tumour cells (TK-10).[8] In addition, several vanadium(IV) compounds are known to exhibit anticancer activities.[9] Previously, bis(4,7-dimethyl-1,10-phenanthroline)sulfato-

[a] Department of Chemistry and Biochemistry, The University of Southern Mississippi,
118 College Drive, # 5043, Hattiesburg, MS 39406-0001, U.S.A.
Fax: +1-601-266-6075
E-mail: alvin.holder@usm.edu
[b] Department of Chemistry, Georgia State University,
P. O. Box 4098, Atlanta, GA 30302, U.S.A.
[c] Science Division, Lyon College,
Batesville, AR 72501, U.S.A.
[d] Department of Chemistry and Biochemistry, Jackson State University,
P. O. Box 17910, 1400 JR Lynch Street, Jackson, MS 39217, U.S.A.
[e] Bioactive Botanical Research Laboratory, Department of Biomedical and Pharmaceutical Sciences, College of Pharmacy, University of Rhode Island,
Kingston, RI 02881, U.S.A.
[f] Department of Chemistry, Louisiana State University,
Baton Rouge, LA 70803, U.S.A.
[g] Molecular Structure Centre, Chemistry Department, Clemson University
Clemson, SC 29634-0973, U.S.A.
[h] School of Polymers and High-Performance Materials, The University of Southern Mississippi,
118 College Dive, #5050, Hattiesburg, MS 39406-0076, U.S.A.
Supporting information for this article is available on the WWW under http://dx.doi.org/10.1002/ejic.201100898.

oxovanadium(IV) (metvan) was identified as the most promising multitargeted anticancer compound with apoptosis-inducing activity.[9c]
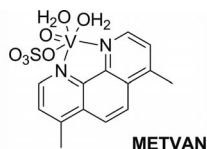
Interestingly, metvan was found to be highly effective against cisplatin-resistant ovarian and testicular cancer cell lines.[9c] Given the paucity of data regarding the use of vanadium(IV) complexes with thiosemicarbazones as ligands as potential anticancer agents, we now report the synthesis and chemical characterisation of a series of such complexes and the preliminary results of a biological study against several colorectal cancer cell lines in order to evaluate their potential as chemotherapeutic candidates.

Results and Discussion

All compounds were characterised by elemental analysis. The structural components of the ligands and complexes were confirmed by FTIR, ^1H and ^{13}C NMR spectroscopy, MS and X-ray crystallography, where appropriate.

Scheme 1. Synthesis of **1**–**4**.

Chemistry and Pharmacology

9-Anthraldehyde-*N*(4)-methylthiosemicarbazone (Me-ATSC) was synthesised as described by Beckford et al.[6] and two new thiosemithiocarbazones, (*E*)-*N*-ethyl-2-(4-hydroxy-3-methoxybenzylidene)hydrazinecarbothioamide (*N*-ethhymethohcarbthio) and (*E*)-*N*-ethyl-2-[1-(thiazol-2-yl)-ethylidene]hydrazinecarbothioamide (acetylethTSC), were also synthesised (Scheme S1, Supporting Information). 2-(2-Hydroxybenzylamino)-3-(1*H*-indol-3-yl)propanoic acid (the reduced Schiff base) was prepared using a known procedure,[10] which involved salicylaldehyde, amino acids and NaBH$_4$ with L-tryptophan (Scheme S2). [VO(sal-L-tryp)-(H$_2$O)] (**1**, sal-L-tryp = *N*-salicylidene-L-tryptophanate) was prepared as described by Pessoa et al.[11] [VO(sal-L-tryp)-(MeATSC)]·1.5C$_2$H$_5$OH (**2**), [VO(sal-L-tryp)(*N*-ethhymethohcarbthio)]·H$_2$O (**3**) and [VO(sal-L-tryp)(acetylethTSC)]·C$_2$H$_5$OH (**4**) were synthesised by the reaction of **1** with the respective thiosemicarbazones (Scheme 1). Compounds **2**–**4** were isolated in yields of 57–78%.

In this study, we investigated the cytotoxic effects of our complexes against three colon cancer cell lines, HTC-116, Caco-2 and HT-29, along with a comparative antiproliferative study of noncancerous colonic myofibroblasts, CCD-18Co, by using the standard 3-(4,5-dimethylthiazol-2-yl)-5-(3-carboxymethoxyphenyl)-2-(4-sulfenyl)-2*H*-tetrazolium, inner salt (MTS)-dye reduction assay for cell viability.
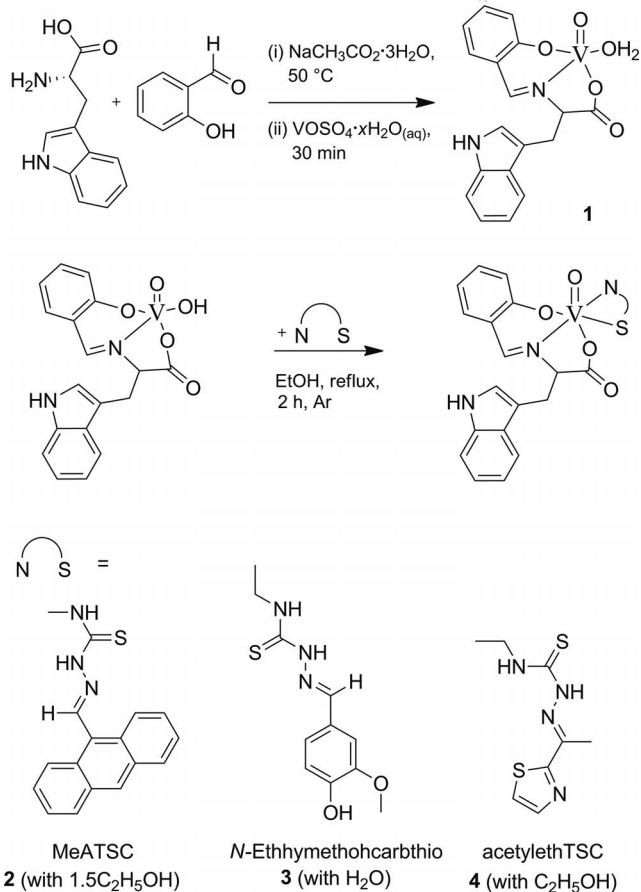
Elemental Analyses and MS

Elemental analysis was carried out on *N*-ethhymethohcarbthio and **1**–**4**. The percentage of N found in **4** was 10.91% vs. the calculated value of 12.98%. The elemental analysis data for the percentage of N is not fully consistent with the calculated value, but other spectroscopic methods confirmed the identity of **4**. Due to the fact that the discrepancy is only in the nitrogen, it is likely due to an error in the analysis process or the loss of ethanol as solvate during the analytical procedure. However, ESI-MS proved the existence of [VO(sal-L-tryp)(acetylethTSC)] without ethanol as a solvate.

ESI mass spectra were acquired for **2**–**4** and the products obtained from oxidised DMSO solutions of **1** and **3** (Figures S1–S9 and Schemes S3–S5). The results thus obtained are in agreement with a metal/ligand ratio of 1:1 in the complexes. Table 1 shows the ESI-MS data acquired for the ligands and complexes (Figures S1–S9). Overall, the suggested formulae were further confirmed by mass spectral fragmentation analysis.

Oxidovanadium(IV) complexes that contain *N*-salicylidene-L-amino acid ligands can be oxidised to form vanadium(V) compounds.[12] It was important to determine whether our vanadium(IV) complexes could be oxidised to form vanadium(V) species when dissolved in DMSO. Com-

Table 1. MS data for ligands and complexes.

A) Reduced Schiff base, K[sal-L-tryp] and **1–4**

Species	Exact mass [gmol^{-1}]	Species formed in the spectrometer	m/z	Relative int. [%]
Reduced Schiff base[a]	310.13	[M + H]$^+$	311.08	100.00
		[M – CHO$_3$ + H]$^+$	242.42	13.04
		[2M + H]$^+$	620.36	12.77
		[3M + H]$^+$	930.39	5.02
		[4M + H]$^+$	1240.92	3.92
K[(sal-L-tryp)][a]	346.07	[M + H]$^+$	344.05	39.65
		[M – OH – K + H]$^+$	300.03	100.00
		[M – OH – O – K + H]$^+$	205.20	50.43
		[M – COO – K + H]$^+$	242.62	64.65
		[M – COO – OH – K + H]$^+$	262.12	1.51
		[M – C$_7$H$_6$O – K + H]$^+$	281.14	46.08
[VO(sal-L-tryp)(MeATSC)][a]	666.14	[M + H]$^+$	666.17	100.00
		[M – C$_2$H$_5$N$_2$S + H]$^+$	577.08	33.10
		[M – C$_{17}$H$_{17}$N$_3$ + H]$^+$	405.14	31.86
		[MeATSC + H]$^+$	292.14	54.60
[VO(sal-L-tryp)(N-ethhymethohcarbthio)][b]	626.13	[M – H]$^-$	624.87	100.00
		[M – C$_{11}$H$_{10}$N$_2$O – H]$^-$	431.90	64.75
		[M – C$_{11}$H$_{15}$N$_3$O$_2$S – H]$^-$	407.85	20.99
		[[C$_{11}$H$_{15}$N$_3$O$_2$S – C$_8$H$_7$N] – H]$^-$	287.88	12.70
		[N-ethhymethohcarbthio – H]$^-$	252.00	25.74
[VO(sal-L-tryp)(acetylethTSC)][a]	601.09	[M + H]$^+$	600.25	2.71
		[M – C$_3$H$_7$NS + H]$^+$	513.57	100.00
		[M – C$_7$H$_5$NO + H]$^+$	482.38	37.11
		[M – C$_{17}$H$_{15}$N$_2$O + H]$^+$	336.06	4.13

B) Oxidised products isolated from **1** and **3**.

Species	Exact mass [gmol^{-1}]	Species formed in the spectrometer	m/z	Relative int. [%]
Proposed [VO(sal-L-tryp)(DMSO)(OH)][c,a] intermediate	468.06	[M + H]$^+$	468.60	1.67
		[M – OH – DMSO – C$_8$H$_7$N + H]$^+$	242.41	100.00
		[M – OH + H]$^+$	451.05	48.25
		[[V$_2$O$_3$(sal-L-tryp)$_2$] + H]$^+$	763.68	30.06
		[[V$_2$O$_3$(sal-L-tryp)$_2$(H$_2$O)] + H]$^+$	776.77	49.36
		[[V$_2$O$_3$(sal-L-tryp)$_2$(DMSO)$_2$] + H]$^+$	918.28	3.13
Proposed [VO(sal-L-tryp)(DMSO)(OH)][d,a] intermediate	468.06	[M + H]$^+$	470.01	0.50
		[N-ethhymethohcarbthio + H]$^+$	252.26	100.00
		[M – OH + H]$^+$	451.96	2.97
		[M – OH + N-ethhymethohcarbthio + H]$^+$	702.75	2.15
		[[V$_2$O$_3$(sal-L-tryp)$_2$] + H]$^+$	763.22	0.74
		[[V$_2$O$_3$(sal-L-tryp)$_2$(H$_2$O)] + H]$^+$	775.40	1.08
		[[V$_2$O$_3$(sal-L-tryp)$_2$(DMSO)$_2$] + H]$^+$	916.44	0.75

[a] Positive mode. [b] Negative mode. [c] Proposed vanadium(V) intermediate obtained from **1**. [d] Proposed vanadium(V) intermediate obtained from **3**.

pounds **1** and **3** were dissolved in DMSO, and the resulting solutions were allowed to evaporate to leave a solid. ESI-MS was carried out on the remaining solids and showed that **1** and **3** were oxidised to form vanadium(V) species (Table 1). Vanadium(V) species with coordinated DMSO were detected by ESI-MS. Scheme 2 shows a proposed mechanism for the formation of the oxidised compounds in DMSO.

X-ray Crystallographic Studies on acetylethTSC

A single crystal of acetylethTSC was grown by the slow evaporation of a methanol solution. The molecular structure of acetylethTSC together with the atomic numbering scheme is shown in Figure 1, and Table 2 shows the crystal data and structure refinement for acetylethTSC.

Thiosemicarbazones are known to exhibit thione–thiol tautomerism.[6] The crystal structure shows that acetylethTSC exists as a thione in the solid state. The C(1)–S(1) distance (1.6814 Å) is similar to that found in a methyl analogue of 2-acetyl-2-thiazoline thiosemicarbazone, which is in the thione form as a solid.[13] AcetylethTSC adopts a *syn* conformation about the N1–N2 bond in a similar fashion as thiosemicarbazones formed from 2-acetylthiazole.[14] The N2–H group donates an intermolecular hydrogen bond to thione S1 to form centrosymmetric hydrogen-bonded dimers with an N⋯S distance of 3.4651(15) Å. The thiazole N4 atom is not involved in hydrogen bonding as shown in Figure 2.
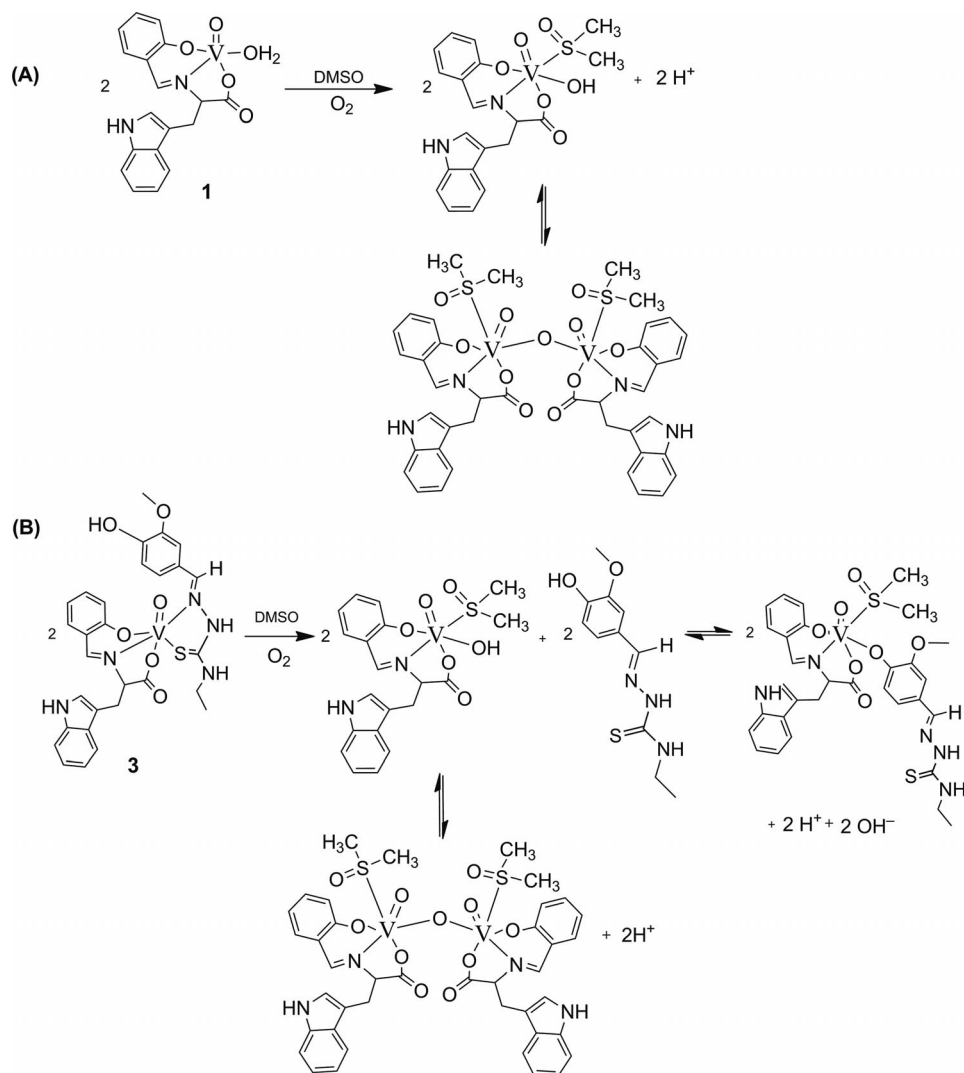
Scheme 2. Proposed mechanism for the formation of the oxidised compounds in DMSO.
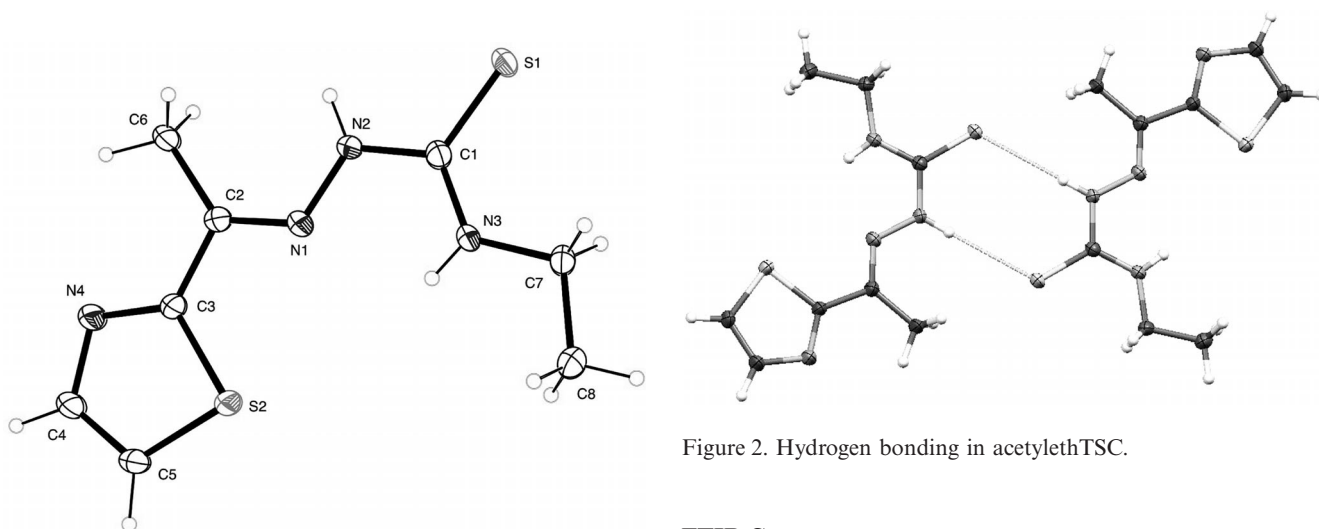
Figure 1. A thermal ellipsoid plot (50% probability envelopes) of acetylethTSC.

Figure 2. Hydrogen bonding in acetylethTSC.

FTIR Spectroscopy

Infrared spectra were acquired for the ligands and complexes (Figures S10–S18). Thiosemicarbazones exhibit char-

Table 2. Crystal data and structure refinement for acetylethTSC.

	acetylethTSC
Empirical formula	$C_8H_{12}N_4S_2$
Formula weight	228.34
Temperature	90.0(5) K
Wavelength	1.54178 Å
Crystal system, space group	monoclinic, $C2/c$
Unit cell dimensions	$a = 10.4549(10)$ Å, $\alpha = 90°$
	$b = 10.8970(10)$ Å, $\beta = 91.544(5)°$
	$c = 18.7694(15)$ Å, $\gamma = 90°$
	$V = 2137.6(3)$ Å^3
Z, calculated density	8, 1.419 Mg/m^3
Absorption coefficient	4.251 mm^{-1}
$F(000)$	960
Crystal size	$0.18 \times 0.17 \times 0.09$ mm
Theta range for data collection	5.8 to 68.1°
Limiting indices	$-12 \leq h \leq 12$, $-12 \leq k \leq 13$,
	$-22 \leq l \leq 22$
Reflections collected/unique	8017/1901 [$R_{int} = 0.026$]
Completeness to $\theta = 66.6°$	99.1 %
Absorption correction	Semi-empirical from equivalents
Max. and min. transmission	0.701 and 0.515
Refinement method	Full-matrix least squares on F^2
Data/restraints/parameters	1901/0/136
Goodness-of-fit on F^2	1.065
Final R indices [$I > 2\sigma(I)$]	$R_1 = 0.0276$, $wR_2 = 0.0691$
R indices (all data)	$R_1 = 0.0312$, $wR_2 = 0.0715$
Extinction coefficient	0.00011(3)
Largest diff. peak and hole	0.257 and -0.262 e Å^{-3}

Tautomerism in thiosemicarbazones

acteristic bands that correspond to various functional groups in different energy regions. The most significant bands in the 4000–500 cm^{-1} region are found between 3100–3500 (NH stretching vibrations), 1580–1630 (C=N and NH), and 1100–1300 and 820–900 (C=S). Thiosemicarbazones can coordinate as either a neutral (thione) or a monoanionic (thiolate) ligand.[15] The ligands (Figures S10–S12) here all seem to be in the thione form in the solid state.[16] This was inferred primarily from the absence of a ν(S–H) absorption in the 2600–2500 cm^{-1} region. There are two bands in the ν(N–H) region, and the presence of the peak due to the hydrazinic hydrogen atom confirms the thione formulation. The thiolate form was not evident in our compounds in the solid state (see Tables 3 and 4 for the respective stretching frequencies for the ligands and complexes).
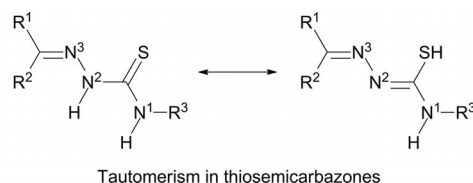
IR spectra of all the complexes (Figures S15–S18) show a band in the ν(N–H) region that may be attributed to the hydrazinic nitrogen atom and suggests that the ligands are coordinated as the thione form. Neither the hydrazinic nor the terminal (aminic) hydrogen atom shifted significantly upon coordination of the ligand. The ligands all show a medium intensity band in the 1620–1605 cm^{-1} region, which is assigned as the C=N (imine) linkage. On coordination of the ligand, this band shifts significantly for acetylethTSC (1607–1621 cm^{-1} in **4**) and *N*-ethhymethohcarbthio (1605 to 1616 cm^{-1} in **3**). The stretching frequency of MeATSC changed slightly on coordination to **1**. The shift in this band is indicative of the involvement of the iminic nitrogen atom in the ligation.[7b,17] The involvement of the thiocarbonyl group in the binding can be similarly inferred from the fact that the peaks changed frequency to lower wavenumbers on coordination to **1** (6 cm^{-1} for **2**, 11 cm^{-1} for **3** and 2 cm^{-1} for **4**). The magnitude of the shifts suggest that the ligands coordinate in their neutral bidentate form (through the iminic nitrogen and the thiocarbonyl sulfur atoms) in all the complexes.

A ν(V–S) stretching frequency is observed in the 470–400 cm^{-1} region for all complexes. The absence of a similar band in the spectra of the free thiosemicarbazone ligands confirms coordination by the thiocarbonyl sulfur atom. IR spectra of the reduced Schiff base and K[sal-L-tryp] (Figures S13 and S14) were used to assign the important stretching frequencies due to the coordination of the Schiff base moiety. A phenolate ν(C–O) stretching frequency in the 1545–1540 cm^{-1} region is observed for **1**–**4**. Broad ν(OH) stretching frequencies are observed at 3014 and 3010 cm^{-1} for **1** and **3**, respectively. The absence of the ν(O–H) stretching frequencies of the phenol in **2** and **4** confirms the coordination of the ligand to the vanadium(IV) centre by the phenolate anion.[18]

Table 3. FTIR spectroscopic data [cm^{-1}] for the ligands.

	Indolic ν(NH)	$-N^1H_2$ ν(NH)	N^2H ν(NH)	ν(N–N)	ν(C–O)	ν_s(COO)	ν_{as}(COO)	TSC ν(C=N)	sal-L-tryp ν(C=N)	ν(C=S)	ν(V–S)	ν(OH)
MeATSC	–	3399 (m)	3201 (w)	1075 (m)	–	–	–	1621 (m)	–	1255 (m), 841 (m)	–	–
N-Ethhyme-thohcarbthio	–	3304 (m)	3300 (w)	1155 (m)	–	–	–	1606 (m)	–	1267 (m), 831 (m)	–	3130 (br.)
AcetylethTSC	–	3164 (m)	3054 (w)	1059 (m)	–	–	–	1543 (m)	–	1296 (m), 813 (m)	–	–
K[(sal-L-tryp)]	3407 (m)	–	–	–	1194 (m)	1521 (m)	1604 (m)	–	1570 (m)	–	–	3169 (br.)
Reduced Schiff base ligand	3392 (m)	–	–	–	1208 (m)	1494 (m)	1592 (m)	–	–	–	–	3055 (br.)

Table 4. FTIR spectroscopic data [cm^{-1}] for the complexes.

A) Compounds **1–4**

	Indolic v(NH)	–N^{1}H$_2$ v(NH)	N^{2}H v(NH)	v(N–N)	v(C–O)	v$_s$(COO)	v$_{as}$(COO)	TSC v(C=N)	sal-L-tryp v(C=N)	v(C=S)	v(V–S)	v(V=O)	v(OH)
1	3478 (m)	–	–	–	1540 (m)	1490 (m)	1597 (s)	–	1600 (m)	–	–	997 (s)	3014 (br.)
2	3200 (m)	3340 (m)	2976 (w)	1148 (m)	1544 (m)	1491 (m)	1600 (s)	1624 (m)	1590 (m)	1225 (m), 829 (m)	455 (m)	980 (s)	–
3	3210 (m)	3306 (m)	2970 (w)	1154 (m)	1540 (m)	1480 (m)	1600 (s)	1620 (m)	1580 (m)	1270 (m), 802 (m)	454 (m)	976 (s)	3010 (br.)
4	3229 (m)	3310 (m)	2976 (w)	1149 (m)	1545 (m)	1480 (m)	1600 (s)	1624 (m)	1580 (m)	1287 (m), 819 (m)	455 (m)	982 (s)	–

B) Oxidised products isolated from compounds **1** and **3**

	Indolic v(NH)	v(C–O)	v$_s$(COO)	v$_{as}$(COO)	TSC v(C=N)	sal-L-tryp v(C=N)	v(V=O)	v(OH)	v(S=O)
A – oxidised product obtained from **1**	3185 (m)	1551 (m)	1497 (m)	1618 (s)	–	1581 (m)	949 (s)	3194 (br.)	1164 (m), 1213 (m)
B – oxidised product obtained from **3**	3201 (m)	1550 (m)	1497 (m)	1600 (s)	1666 (m)	1590 (m)	946 (s)	3193 (br.)	1133 (m), 1157 (m)

All complexes exhibited v(V=O) stretching frequencies in the 997–980 cm^{-1} region, which is the typical range for oxidovanadium(IV) complexes.[19] Upon coordination of the respective thiosemicarbazone ligands to **1**, a decrease of the V=O stretching frequency occurred, i.e. a change of 17 cm^{-1} in **2**, 21 cm^{-1} in **3** and 15 cm^{-1} in **4**.

NMR Spectroscopy

^{1}H and ^{13}C NMR Spectroscopy

^{1}H and ^{13}C NMR spectra were acquired for *N*-ethhymethohcarbthio, acetylethTSC, the reduced Schiff base, K[sal-L-tryp] and the oxidised products derived from **1** and **3** (Figures S19–S26). Figure 3 shows the ^{1}H NMR spectra of *N*-ethhymethohcarbthio and acetylethTSC.

N-Ethhymethohcarbthio and AcetylethTSC

The presence of singlets at δ = 11.42 and 10.59 ppm in the ^{1}H NMR spectra of *N*-ethhymethohcarbthio and acetylethTSC, respectively, are labelled as g in part A and as e in part B of Figure 3.[20] It is common for this signal to be used as a diagnostic test for the identification of *E* and *Z* isomers.[6] According to Afrasiabi,[21] a chemical shift at δ = 13–15 ppm proves that the ligand is in the *E* form, whereas a peak at δ = 9–12 ppm proves that the ligand is in the *Z* form. Based on this analysis and coupled with the lack of a signal at δ ≈ 4.0 ppm, which is attributed to a SH proton resonance, it can be inferred that both ligands exist as the *Z* isomer. An X-ray crystallographic study on acetylethTSC confirmed the existence of the thione moiety in the free ligand. We also believe that the chemical shift of 13.2 ppm for acetylethTSC (Figure 3, B) is due to equilibrium in solution between the hydrogen-bonded (Z-conformation) and the non-hydrogen-bonded (E-conformation) forms.

Oxidised Products Isolated from 1 and 3

It is important to determine the species that are formed when **1** and **3** are oxidised in DMSO. In order to determine

such species, ^{1}H NMR spectra were acquired of the isolated oxidised products. All ^{1}H NMR spectra exhibited broad signals (Figures S21 and S22). This is attributed to the presence of some residual paramagnetic vanadium(IV) species,

A) *N*-Ethhymethohcarbthio
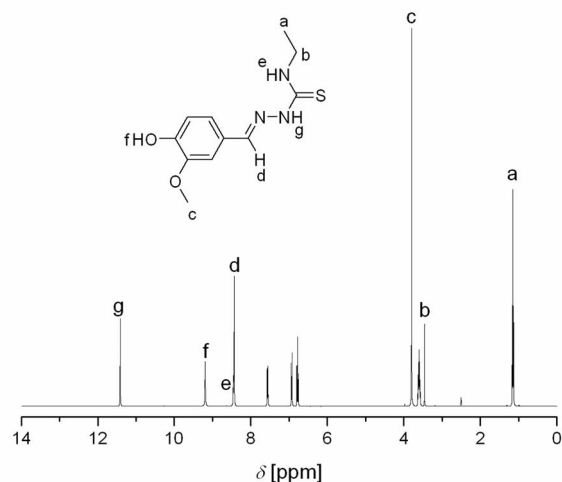
B) AcetylethTSC
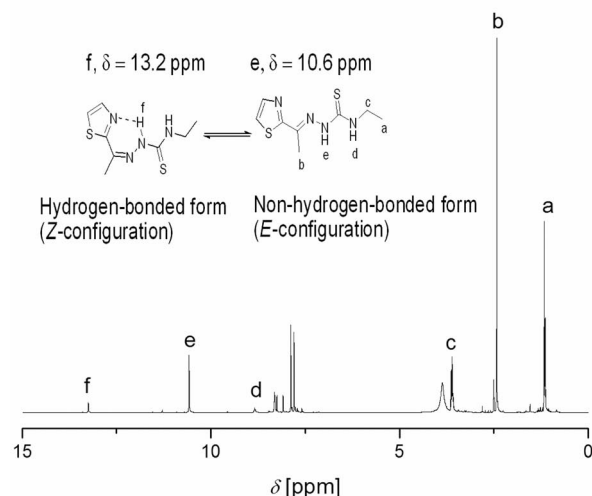
Figure 3. ^{1}H NMR spectra of *N*-ethhymethohcarbthio and acetylethTSC in [D$_6$]DMSO.

which could be due to vanadium(IV) species that are in equilibrium with vanadium(V) species that are formed upon aerial oxidation in DMSO.

The ^{1}H NMR spectrum of the oxidised product isolated from **1** exhibited resonance signals that are due to aromatic protons in the $\delta = 7.06–7.52$ ppm region. The ^{1}H NMR spectra of the oxidised products isolated from **1** and **3** exhibited resonance signals in the $\delta = 7.82–8.09$ and 7.06 to 10.43 ppm regions, respectively. These resonance signals are assigned to the proton of the azomethine group and the NH proton of the indole ring of the L-tryptophan moiety, respectively. The resonance signal that corresponds to the N2H proton of *N*-ethhymethohcarbthio in the oxidised product isolated from **3** overlaps with the resonance signal assigned to the NH proton of the indole ring of the L-tryptophan moiety. Chemical shifts are observed at $\delta = 1.17$ and 3.79 ppm for the oxidised product isolated from **3**, which are assigned to the methylene and methyl protons of the free *N*-ethhymethohcarbthio, respectively. Signals of aromatic protons are also observed as multiplets in the $\delta = 6.87–6.96$ and 7.00–7.43 ppm ranges. ESI-MS was used to prove the presence of DMSO-containing vanadium(V) complexes, but ^{1}H NMR spectroscopy proved that the chemical shifts for DMSO occur at $\delta = 2.7$ and 3.0–3.6 ppm, which proved the existence of *O*-bonded and *S*-bonded DMSO, respectively.[22] The absence of a peak at $\delta = 2.7$ ppm implies the absence of *O*-bonded DMSO.[22] The resonance due to the presence of an *S*-bonded DMSO produces singlets at $\delta = 3.36$ and 3.34 ppm for the oxidised products isolated from **1** and **3**, respectively.

^{1}H and ^{51}V NMR Spectroscopy of Oxidised Solutions of 1–4 in [D$_6$]DMSO

Over a 24 h period, [D$_6$]DMSO solutions of **1**–**4** were oxidised with the eventual formation of vanadium(V) species. ^{51}V NMR spectroscopy was used to definitively confirm the presence of vanadium(V) species. Figure 4 shows the ^{51}V NMR spectra for [D$_6$]DMSO solutions of **1**–**4** (10 mM) at room temperature, and Table 5 shows the chemical shifts and percentages of species for each vanadium(V) species. It is interesting that two species are formed on oxidation of **1**, **2** and **4**, whereas three species are formed by **3**. It is possible that a mononuclear species is formed in the range $\delta = –480.5$ to $–467.7$ ppm, based on the chemical shifts obtained for ^{51}V NMR spectra of vanadate(V) esters of monoionised and diionised aromatic 1,2-diols.[23] For example, [VO(gsal)(HL^1)], [VO(asal)(HL^1)] and [VO(vsal)-(HL^1)] (gsal, asal and vsal = diionised salicylaldimine of L-glycine, L-alanine and L-valine; HL^1 = catecholate) have chemical shifts of $\delta = –460$, $–457$ and $–455$ ppm, respectively, when [D$_6$]DMSO was used as the solvent.

Mauyra et al.[24] have reported the synthesis of new oxidovanadium(V) complexes [VOL(hq)] by the reaction of [VO(acac)$_2$] with LH$_2$ {LH$_2$ = the dibasic tridentate ONO Mannich base [(S)-H$_2$glysal, (S)-H$_2$alasal, (S)-H$_2$leusal and (S)-H$_2$ileusal; S represents the S-enantiomer] obtained by the reduction of the Schiff bases of salicylaldehyde (sal) and the amino acids: glycine (gly), D,L-alanine (ala), leucine
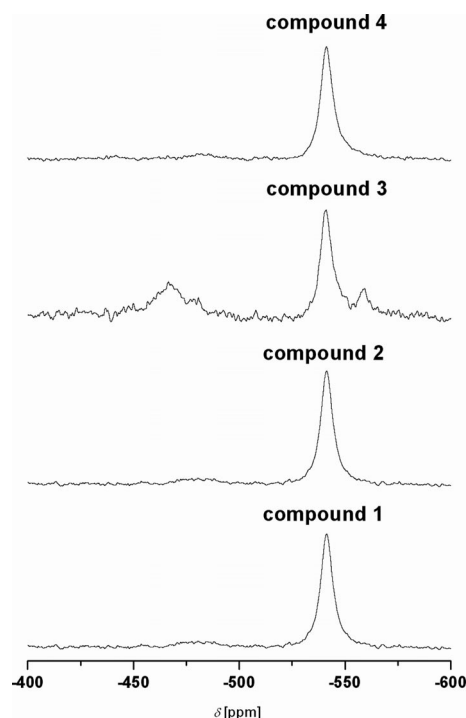
Figure 4. ^{51}V NMR spectra of **1**–**4** after oxidation in [D$_6$]DMSO for 24 h.

Table 5. ^{51}V NMR chemical shifts δ [ppm] and percentages of species of [D$_6$]DMSO solutions for **1**–**4** after being oxidised for 24 h.

	δ	Species (%)	δ	Species (%)	δ	Species (%)
1	–480.5	7.1	–541.4	92.9		
2	–481.9	9.2	–542.2	90.8		
3	–467.7	41.7	–541.0	47.9	–559.3	10.4
4	–481.9	6.9	–541.2	93.1		

(leu) and isoleucine (ileu), respectively} in the presence of 8-hydroxyquinoline (Hhq). Spectroscopic studies were used to confirm that the complexes have octahedral structures.[24] The complexes exhibited a single ^{51}V NMR signal (with [D$_6$]DMSO as solvent) in the range $\delta = –464.6$ to $–468.0$ ppm due to the existence of a single isomer in solution.[24] Due to the similar chemical shifts of the species in the $\delta = –480.46$ to $–467.69$ ppm range, we can conclude that a mononuclear vanadium(V) species is formed when the vanadium(IV) complexes are oxidised in [D$_6$]DMSO. The reason why the vanadium(V) species that is formed from **3** has a chemical shift of $\delta = –467.7$ ppm is yet to be determined.

Mauyra et al.[24] carried out a time-dependent ^{51}V NMR spectroscopic study (in [D$_7$]DMF and CD$_3$OD) in order to investigate possible isomerisation and/or further reaction in solution. Freshly prepared solutions of [VO(S-alasal)(hq)] showed a signal at $\delta = –466.7$ ppm. As time elapsed, a second, broader signal at $\delta = –516.3$ ppm formed, which had about the same integral intensity as the $\delta = –466.7$ ppm signal after three days and about twice its intensity after one week. The authors concluded that the change in chemi-

cal shift was too large to represent diastereomers based on pairs of enantiomers, and therefore, assigned the new signal to a [VO$_2$] or [(VO)$_2$μ-O] species, i.e. the oxygenated product after a slow loss of 8-hydroxyquinoline. They also concluded that, as the generation of a [(VO)$_2$μ-O] species usually dominates during oxygenation[24] in the absence of a base, the signal at δ = –516.3 ppm is most probably due to the [(VO)$_2$μ-O] species. In our case, the chemical shift at approximately δ = –541 ppm accounts for the major species formed for **1**–**4**. We believe that this due to [V$_2$O$_3$(sal-L-tryp)$_2$(DMSO)$_2$], which was also detected by ESI-MS (*m/z* = 918.3, [V$_2$O$_3$(sal-L-tryp)$_2$(DMSO)$_2$ + H]$^+$ from oxidised DMSO solutions of **1** and **3**. A similar complex with *N*-salicylidene-L-alaninate (sal-L-ala) as a ligand, [V$_2$O$_3$(sal-L-ala)$_2$]·2CH$_2$Cl$_2$, has been reported by Nakajima et al.[25]

We believe that [VO(sal-L-tryp)([D$_6$]DMSO)(OH)] was formed as an intermediate when **2** and **4** were oxidised in [D$_6$]DMSO, within experimental errors in the determination of the percentage species. We believe that the species with a chemical shift at δ = –559.3 ppm is mononuclear and propose its structure as that shown in Scheme 1 and its formula as [VO(sal-L-tryp)(DMSO)(*N*-ethhymethohcarbthio)]. Based on ^{51}V NMR spectroscopy, we propose the existence of an equilibrium between mononuclear and binuclear vanadium(V) species (Scheme 1).

Based on ^{1}H NMR spectroscopy (Figures S27–S30), it appears as if the thiosemicarbazone ligands became free when **2**–**4** were oxidised in [D$_6$]DMSO and DMSO. The ^{1}H NMR spectroscopic chemical shifts of the free ligands are similar to the values shown in Figure 3 and those obtained for MeATSC.[6] ESI-MS also proved the existence of a free thiosemicarbazone ligand for a mixture that resulted from the oxidation of **3** in DMSO. An *m/z* of 252.3 accounted for the presence of free *N*-ethhymethohcarbthio.

UV/Vis and Fluorescence Spectroscopy of 1–4

UV/Vis spectra were acquired for **1**–**4** in DMSO (Figures S31–S34), and the assignments of the absorption bands are shown in Table 6. Charge transfer bands in the 266–292 nm region, which can be assigned to π→π* transitions associated with the thioamide moiety, are observed for **2**–**4**.[18a,26] These occurred at 266 and 292 nm (shoulder) for **2**, 270 and 288 nm (both shoulders) for **3** and 276 nm for **4**. Charge transfer bands assigned to n→π* transitions of aromatic rings are observed in the 316–352 nm region[18a,19a,26–27] and are observed as a shoulder at 316 nm for **2**, at 330 nm for **3**, and 352 nm for **4**.

In the UV region, oxidovanadium(IV) complexes derived from salicylaldehyde generally possess a low-energy band at around 375 nm, which can be attributed to a π→π* transition that originates mainly from the azomethine chromophore.[11] This occurs at 388 nm for **2**, as a shoulder at 390 nm for **3** and hidden under the n→π* transitions at 352 nm for **4**. A band in the 550–558 nm region is assigned to ligand-to-metal charge transfer (LMCT) transitions of the type p→d where p and d represent the lone pair of the

Table 6. UV/Vis spectroscopic data for **1**–**4**.

	λ [nm]	ε [M^{-1} cm^{-1}]	Assignment
1	558	44	LMCT (p→d transition)
	758	27	d→d transition
2	266	74835	π→π* (thioamide moiety)
	292 (sh)	17954	π→π* (thioamide moiety)
	316 (sh)	10046	n→π* (aromatic rings)
	388	15013	π→π* (azomethine chromophore)
	550	54	LMCT (p→d transition)
	592 (sh)	45	d→d transition
	756	28	d→d transition
3	270 (sh)	10984	π→π* (thioamide moiety)
	288 (sh)	13874	π→π* (thioamide moiety)
	330	24837	n→π* (aromatic rings)
	390 (sh)	18250	π→π* (azomethine chromophore)
	620	852	d→d transition
4	276	21969	π→π* (thioamide moiety)
	352	14227	n→π* (aromatic rings)
	558	80	LMCT (p→d transition)
	590 (sh)	70	d→d transition
	756	38	d→d transition

phenolato oxygen atom and vanadium 3d orbitals, respectively.[28] This occurs at 558 nm for **1**, 550 nm for **2** and 558 nm for **4**. A similar band is absent for **3** but we believe it to be hidden under the band at 614 nm, which is assigned to d→d transitions.

Bands assigned to d→d transitions were also observed in the 756–758 nm region for **1**, **2** and **4**.[19b] This occurred at 758 nm for **1** and 756 nm for **2** and **4**. In the electronic spectra of **2** and **4**, bands at 592 nm for **2** and 590 nm for **4** are also assigned to d→d transitions and appear as shoulders of the much stronger LMCT band in the 550–558 nm region.[19b]

Fluorescence spectra were acquired for **2**–**4** in DMSO (Figures S35–S37). The excitation wavelengths for **2**, **3** and **4** were 400, 330 and 340 nm, respectively. Compound **2**, which contains an anthracene unit in MeATSC, produced the highest intensity in its fluorescence spectra, whereas **3** and **4** produced lower intensities.

ESR Spectroscopy

Compounds **1**–**4** were also characterised by low-temperature ESR spectroscopy and each complex exhibits a powder-type axial *g* = 2 signal (*S* = 1/2) with a minor rhombic distortion at 10 K. The observed hyperfine structure shows sixteen line ESR signals with partial overlap of three lines. Figure 5 shows two representative ESR spectra along with simulations for **1** and **4**. These spectra are characteristic of slowly tumbling macromolecular complexes consistent with vanadyl (VO^{2+})-containing complexes, which indicates that the vanadium centre has a +4 oxidation state in the two freshly prepared complexes. The sixteen lines seen in the anisotropic powder ESR spectra are due to the hyperfine interaction between the electron spin and the nuclear spin of ^{51}V^{IV} (*I* = 7/2, 100% natural abundance).
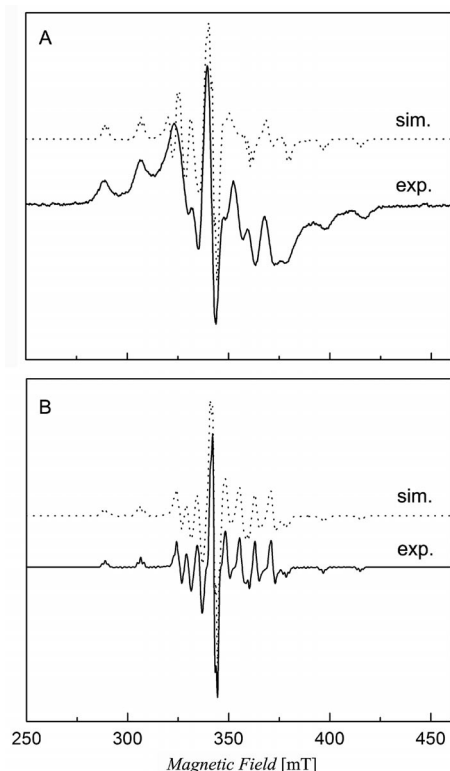
Figure 5. X-band continuous-wave ESR spectra of **1** (A, 10 mM in DMSO) and **4** (B, 10 mM in DMSO) overlaid with spectral simulations.

The powder ESR spectra of **1–4** were simulated to determine the magnitudes of the principal ^{51}V hyperfine coupling constants (A_x, A_y, and A_z) and g values using the ESR simulation program DOUBLET.EXE.[29] The ESR parameters obtained from spectral simulations are shown in Table 7. The large A values and broad linewidth are presumably due to the sulfur ligation and hexacoordinate geometry. The vanadyl cation, VO^{2+}, is known to form complexes that are pentacoordinate or square bipyramidal with a short V=O bond,[30] and few hexacoordinate vanadyl-containing complexes with mixed N,O,S ligands have been characterised to date. The ESR spectra of the complexes described here may be useful in future studies of VO^{2+} in complexes and biological systems. Nevertheless, these ESR spectroscopic results are in agreement with those of UV/Vis and FTIR spectroscopy and thus prove that each synthesised compound has a vanadium(IV) centre prior to aerial oxidation of the DMSO solution. We plan to carry out studies that involve DFT calculations to elucidate the de-

Table 7. ESR parameters of **1–4**.[a]

	g_x	g_y	g_z	A_x	A_y	A_z
1	1.958	1.988	1.953	80	68	180
2	1.98	1.98	1.968	64	65	178
3	2	1.995	1.965	63	63	175
4	1.98	1.98	1.968	64	65	178

[a] ESR parameters were obtained from spectral simulations as described in the text.

pendence of calculated ^{51}V A_z values on the orientation and geometry of the coordinated thiosemicarbazone and water ligands in **1–4**. Such a study that involves calculated and experimental A_z values for **1–4** would complement the excellent data for $V^{IV}O$ complexes that have been reported by Garriba and coworkers.[31]

Pharmacology

In Vitro Cytotoxicity

The objective of this research was to evaluate the antiproliferative activity of **2–4** against colon cancer cell lines (HTC-116, Caco-2 and HT-29) and to compare the antiproliferative activity against one noncancerous colon cell line (CCD-18Co). Compounds **2–4**, cisplatin and etoposide were evaluated for their cytotoxicity against HCT-116, Caco-2 and HT-29 by a colorimetric assay (MTS), which measures mitochondrial dehydrogenase activity as an indication of cell viability. The effects of the compounds on the viability of these cells were evaluated after continuous incubation (24, 48 and 72 h).

The growth inhibition effects of the compounds were investigated in noncancerous colonic myofibroblast CCD-18Co cells and compared to the colon cancer cell lines. The results demonstrated a great difference in the inhibition of cell proliferation between cancer lines and the noncancerous CCD-18Co cells. Compounds **2–4** have been shown to decrease the cell viability of HCT-116, Caco-2 and, more potently, HT-29 cells (Table 8). Compound **4** was the most active of the three tested, whereas **2** and **3** showed similar activities in both cancer cell lines. Figure 6 shows a plot of percentage cell viability vs. concentration of **4** against the HT-29 cancer cell line, and Table 8 shows the IC_{50} values for the inhibition of cell proliferation for **2–4**, with IC_{50} values generally around 100 μM concentration at 72 h in **2** and **3**. None of the compounds had better a efficacy against any of the cancer cell lines than etoposide. Compound **4** had a better efficacy against the HT-29 cancer cell line than cisplatin (Table 8).

Compounds **2–4** exhibited lower inhibitory effects in normal human CCD-18Co cells, which indicates a possible cytotoxic selectivity towards colon cancer cells (Table 8). IC_{50} values in CCD-18Co were around three and two times greater than those in HT-29 and Caco-2 and HCT-116, respectively. However, the cytotoxic selectivity towards cancer colon cells of cisplatin (as a positive control) was slightly lower, except with Caco-2 cells (Table 8). These results are in good agreement with those of a previous study, where it was shown that cisplatin inhibited cell proliferation by about 70% in both cell lines (cancer and normal colon cells).[32] In general, **2–4**, which have been proven to be growth suppressors of cancer cells but do not affect noncancerous cells, may have a potential in chemotherapy.

Although metal complexes are being investigated as probes and therapeutics, there have been relatively few studies on their mechanism of uptake. Metal complexes that are lipophilic cations may passively diffuse across the plasma

Table 8. Antiproliferative effects of **2**–**4**, cisplatin and etoposide on different cells lines after 24, 48 and 72 h treatment. Data are expressed as IC_{50} (μM). IC_{50} is defined as the concentration required to achieve 50% inhibition over control cells (0.5% DMSO); IC_{50} values are shown as mean standard error values taken from three independent experiments.

	HT-29 24 h IC_{50} [μM]	48 h IC_{50} [μM]	72 h IC_{50} [μM]	Caco-2 24 h IC_{50} [μM]	48 h IC_{50} [μM]	72 h IC_{50} [μM]
2	277.1 ± 10.2	239.6 ± 7.9	100.3 ± 5.1	349.1 ± 19.5	277.1 ± 16.3	147.1 ± 10.8
3	244.2 ± 8.8	169.6 ± 15.1	87.9 ± 0.5	367.0 ± 21.5	281.6 ± 14.4	152.5 ± 12.7
4	128.6 ± 10.7	82.4 ± 9.6	47.8 ± 5.5	242.1 ± 25.1	166.2 ± 15.3	85.4 ± 14.0
Cisplatin	84.7 ± 1.9	80.6 ± 1.6	69.1 ± 3.2	32.0 ± 1.6	22.8 ± 1.5	17.9 ± 1.8
Etoposide	19.2 ± 0.8	17.3 ± 1.9	15.8 ± 2.4	47.6 ± 0.8	46.2 ± 1.9	40.9 ± 1.5

	HCT-116 24 h IC_{50} [μM]	48 h IC_{50} [μM]	72 h IC_{50} [μM]	CCD-18Co 24 h IC_{50} [μM]	48 h IC_{50} [μM]	72 h IC_{50} [μM]
2	203.4 ± 7.7	181.3 ± 9.2	115.0 ± 6.5	495.6 ± 23.5	339.2 ± 16.7	208.0 ± 11.9
3	227.4 ± 6.8	192.7 ± 11.6	110.3 ± 10.1	490.6 ± 27.6	329.5 ± 15.4	203.6 ± 12.5
4	161.3 ± 4.6	134.9 ± 3.9	89.5 ± 14.5	382.7 ± 21.9	246.2 ± 11.4	152.2 ± 12.0
Cisplatin	53.8 ± 2.1	49.7 ± 1.3	41.0 ± 2.7	83.0 ± 1.1	72.0 ± 1.5	64.1 ± 1.6
Etoposide	40.8 ± 0.5	36.2 ± 2.0	38.4 ± 1.2	82.5 ± 3.1	79.2 ± 1.2	73.2 ± 1.9
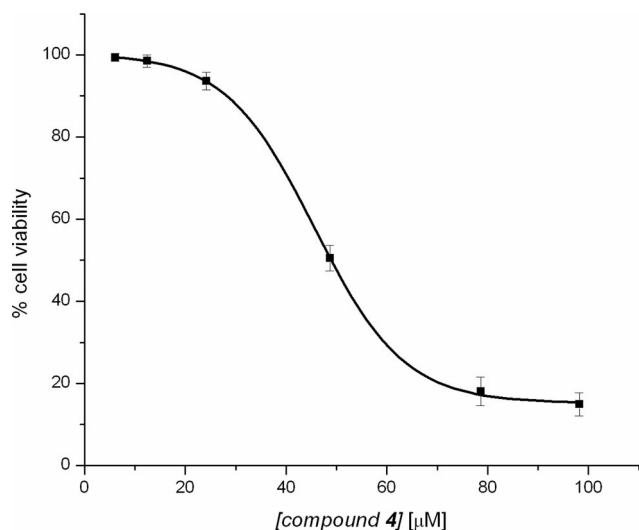
Figure 6. MTT cell proliferation assay of **4** against the HT-29 cancer cell line.

membrane in response to the membrane potential.[33] A ruthenium(II) complex that contained the lipophilic 4,7-diphenyl-1,10-phenanthroline ligand has been shown to enter the membrane by passive diffusion in a membrane-potential dependent manner.[33] It is believed that the excellent efficacy of ruthenium(II) complexes with thiosemicarbazones, which have been reported by Beckford and coworkers,[6] is likely due to the fact that the complexes are lipophilic cations. As a point of speculation, this may explain why cations such as [(bpy)$_2$Ru(TSC)]$^{2+}$ and [(phen)$_2$Ru(TSC)]$^{2+}$ (TSC = 9-anthraldehydethiosemicarbazones)[6] have better efficacies against HT-29 and HCT-116 cell lines vs. our neutral vanadium(IV) complexes. Based on ^{1}H NMR spectroscopy and ESI-MS studies where the free ligand was observed, we believe that the free ligand likely causes the cell death as opposed to the vanadium species. In order to prove this belief, we will have to carry out in vitro studies with the free ligands. A systematic study will have to be carried

out with the ruthenium(II) complexes and **2**–**4** under the same conditions. Apart from such a study, a more detailed emphasis will be placed on the methods used to examine cellular accumulations to identify the mechanism(s) of uptake, and to monitor possible efflux of **2**–**4** and their analogues.

Conclusions

Two new thiosemicarbazone and three new vanadium(IV) complexes with mixed ligands were successfully synthesised and characterised. The anticancer properties of **2**–**4** were examined with three colon cancer cell lines, HTC-116, Caco-2 and HT-29, along with a comparative antiproliferative study on noncancerous colonic myofibroblasts, CCD-18Co. Compounds **2** and **3** exhibited a less inhibitory effect in human noncancerous CCD-18Co cells, which indicates a possible cytotoxic selectivity towards colon cancer cells. In general, the compounds that exhibited antiproliferative activity on cancer cells but did not affect noncancerous colorectal cells may have a potential in chemotherapy.

Experimental Section

Materials and Methods: Analytical or reagent grade chemicals were used throughout. All the chemicals, including solvents, were obtained from Sigma–Aldrich (St. Louis, MO, USA) or other commercial vendors, and used as received. Microanalyses (C, H, N) were performed by Desert Analytics, Tucson, USA and Columbia Analytical Services 3860 S. Palo Verde Road Suite 303 Tucson, AZ 85714, USA. ^{1}H and ^{13}C NMR spectra were acquired in [D$_6$]-DMSO with JEOL ECX-300, Varian 300 MHz, Bruker 400 MHz and Varian 500 MHz spectrometers at room temperature. The residual ^{1}H and ^{13}C present in [D$_6$]DMSO (2.49 and 39.7 ppm, respectively) were used as internal references. ^{51}V NMR spectra were acquired with a Varian 500 MHz spectrometer with [D$_6$]-DMSO as solvent and VOCl$_3$ as an external reference as described for vanadium(V) compounds.[34] ESR spectra were acquired at 10 or 20 K with a Bruker ER200D spectrometer with a 4116DM reso-

nator. The sample temperature was maintained with a temperature controller (ITC503S), an ESR910 liquid helium cryostat and LLT650/13 liquid helium transfer tube (Oxford Instruments, Concord, MA, USA). Instrument conditions were as follows, modulation frequency: 100 kHz, modulation amplitude: 0.3 G, microwave frequency: 9.64 GHz and microwave power: 0.004 mW. FTIR spectra were acquired in the 4000–400 cm^{-1} range using an ATR accessory (with a diamond crystal) with a Nicolet 6700 FTIR spectrophotometer. Electronic spectra were acquired with quartz cuvettes with a HP8452 diode array spectrophotometer using DMSO as the solvent. Fluorescence spectra were acquired with a Cary Eclipse fluorescence spectrophotometer (Varian Inc.) with a slit width of 10 nm. ESI-MS were acquired with an HP Agilent 1956b single-quadrupole mass spectrometer. Samples were dissolved in an acetic acid/methanol mixture and the solution was introduced by direct injection using a syringe pump with a flow rate of 100 μL s^{-1} while sweeping the cone voltage from 0 to 200 V at a rate of 10 V min^{-1}. All *m/z* ratios and percentages were determined by using Mest-ReNova software.

X-ray Crystallography: Crystallographic data were collected at T = 90 K with a Bruker Kappa Apex-II CCD diffractometer equipped with Cu-K_α radiation and an Oxford Cryosystems Cryostream cooler. The structure of acetylethTSC was solved using SHELXS[35] and refined using the SHELX97[36] software packages. All H atoms were visible in difference maps. Coordinates of the NH hydrogen atoms were refined individually, whereas those on C were placed in idealised positions, with torsional parameters refined for the methyl groups.

Crystal data: $C_8H_{12}N_4S_2$, FW = 228.34, monoclinic, space group = $C2/c$, a = 10.4549(10), b = 10.8970(10), c = 18.7694(15) Å, β = 91.544(5)°, V = 2137.6(3) Å^3, Z = 8, T = 90.0(5)K, μ = 4.25 mm^{-1}, d_{calc} = 1.419 g cm^{-3}, colourless parallelepiped, dimensions = $0.18 \times 0.17 \times 0.09$ mm, reflections collected: 8017, unique reflections = 1901, observed reflections [$I > 2\sigma(I)$] = 1738, R_{int} = 0.026, no. of parameters: 136, R_1 = 0.028, wR_2 = 0.069, GOF(F^2) = 1.065.

CCDC-812348 contains the supplementary crystallographic data for this paper. These data can be obtained free of charge from The Cambridge Crystallographic Data Centre via www.ccdc.cam.ac.uk/data_request/cif.

Synthesis of Ligands

9-Anthraldehydethiosemicarbazone (ATSC) and 9-anthraldehyde-*N*(4)-methylthiosemicarbazone (MeATSC) were prepared according to the procedure by Beckford et al.[6]

Synthesis of *N*-Ethhymethohcarbthio: *o*-Vanillin (3.00 g, 19.7 mmol) and 4-ethyl-3-thiosemicarbazide (2.35 g, 19.7 mmol) were placed in a 250 mL round-bottomed flask followed by absolute ethanol (100 mL). Glacial acetic acid (approx. 10 drops) was added to the off-white suspension, and the reaction mixture was heated to reflux for 3 h. The reaction mixture was cooled to room temperature and filtered through a sintered glass crucible. The white residue was washed with ethanol (3 × 15 mL) and ether (3 × 10 mL) and allowed to air dry; yield 4.97 g (99%). $C_{10}H_{13}N_3O_2S$ (239.29): calcd. C 52.15, H 5.97, N 16.59; found C 52.53, H 6.16, N 17.02. FTIR: $\tilde{v}$ = 3304 (m) (N^{1}H), 3300 (m) (N^{2}H), 3130 (br.) (OH), 1155 (m) (N–N), 1606 (m) [TSC (C=N)], 1267 (m) and 831 (m) (C=S) cm^{-1}. ^{1}H NMR (400 MHz, [D$_6$]DMSO): δ = 1.15 (t, J^t = 7.10 Hz, 3 H, CH$_3$), 3.46 (s, 1 H, CH$_3$OAr), 3.60 (q, 2 H, CH$_2$), 3.80 [s, 1 H, (azomethine CH=N)], 6.79 (t, J^t = 7.95 Hz, CH$_{ar}$), 6.96 (dd, J^{dd} = 1.49 and 8.06 Hz, CH$_{ar}$), 7.55 (dd, J^{dd} = 1.51 and 7.93 Hz, CH$_{ar}$), 8.40 (s, H, aminic-NH), 11.41 (s, 1 H, ArOH), and 11.42 (s, 1 H, hydrazinic-NH) ppm. ^{13}C NMR (400 MHz, [D$_6$]DMSO): δ =

176.86 (C=S), 147.86 (CH=N), 145.88 (COCH$_{3ar}$), 139.00 (PhOH), 120.82 (CCH=N$_{ar}$), 118.91 (CH$_{ar}$), 118.10 (CH$_{ar}$), 112.66 (CH$_{ar}$), 58.85 (OCH$_3$), 38.28 (CH$_2$), 14.60 (CH$_3$) ppm.

Synthesis of AcetylethTSC: 2-Acetylthiazole (0.636 g, 0.518 mL 5.0 mmol) was placed in a 100 mL round-bottomed flask followed by anhydrous methanol (25 mL). 4-Ethyl-3-thiocarbazide (0.596 g, 5.0 mmol) in anhydrous methanol (25 mL) was slowly added to the solution followed by a few drops of concentrated hydrochloric acid. The reaction mixture was heated to reflux with stirring for 2 h and then evaporated to a minimum volume to form a yellow solid. The residue was collected by filtration, washed with diethyl ether and air-dried; yield 0.750 g (66%). A single crystal for X-ray crystallography was grown by slow evaporation of a methanol solution. FTIR: $\tilde{v}$ = 3164 (m) (N^{1}H), 3054 (m) (N^{2}H), 1059 (m) (NN), 1543 (m) [TSC (C=N)], 1296 (m) and 813 (m) (C=S) cm^{-1}. ^{1}H NMR (400 MHz, [D$_6$]DMSO): δ = 1.16 (t, J^t = 7.10 Hz, 3 H, CH$_3$), 2.42 (s, 3 H, CH$_3$CH=N), 3.61 (d, 2 H, CH$_2$), 7.79 (d, J^d = 3.21 Hz, CH$_{ar}$), 7.88 (d, J^d = 3.19 Hz, CH$_{ar}$), 8.08 (d, J^d = 3.24 Hz, CH$_{ar}$), 8.30 (s, H, aminic NH), 10.58 (s, 1 H, hydrazinic-NH), 13.2 (s, *H*-bonded hydrazinic NH) ppm.

Synthesis of the Reduced Schiff Base 2-(2-Hydroxybenzylamino)-3-(1*H*-indol-3-yl)propanoic Acid: The reduced Schiff base was prepared by a known procedure that involved salicylaldehyde, amino acids, and NaBH$_4$, but with L-tryptophan using the following procedure:[10] L-Tryptophan (2.04 g, 10.0 mmol) and potassium hydroxide (0.56 g, 10.0 mmol) were added to a 125 mL Erlenmeyer flask followed by deionised water (10 mL). Salicylaldehyde (1.029 mL, 10.0 mmol) in absolute ethanol (10 mL) was slowly added to the mixture. The yellow solution was stirred for 30 min prior to cooling in an ice bath. The intermediate Schiff base that was produced in situ was reduced with an excess of sodium borohydride (0.46 g, 12 mmol) in water (5 mL) that contained NaOH solution (10 drops, 2 M). The solution was stirred for 10 min, and the yellow colour slowly faded. The solution was acidified with concentrated HCl to pH 4.68. The resulting solid was collected by filtration, washed with ethanol (2 × 30 mL) and diethyl ether (2 × 30 mL) and dried. The white solid was recrystallised twice from water/ethanol (1:1); yield 1.08 g (35%). ESI-MS (+ve mode): *m/z* (%) = 311.08 (100.00, [M + H]$^+$), 242.42 (13.04, [M – CHO$_3$ + H]$^+$), 620.36 (12.77, [2M + H]$^+$), 930.39 (5.02, [3M + H]$^+$), 1240.92 (3.92, [4M + H]$^+$). FTIR: $\tilde{v}$ = 3392 (m) (indolic NH), 3055 (br.) (OH), 1208 (m) (C–O), 1494 (m) (COO$_s$) and 1592 (m) (CO-O$_{as}$) cm^{-1}. ^{1}H NMR (400 MHz, [D$_6$]DMSO): δ = 2.67 (d, 2 H), 3.21 (d, 2 H), 3.05 (d, 2 H), 5.91 (t, 1 H), 6.15 (d, 1 H), 6.31 (d, 1 H), 6.62 (m, 1 H), 6.62 (m, 1 H), 6.62 (m, 1 H), 6.62 (m, 1 H), 6.90 (d, 1 H) and 7.18 (d, 1 H) ppm. ^{13}C NMR (400 MHz, [D$_6$]DMSO): δ = 28.57, 46.72, 63.61, 110.66, 111.57, 113.46, 118.50, 118.69, 121.37, 123.85, 123.89, 126.95, 127.78, 128.16, 128.34, 135.97, 164.55, 182.05 ppm.

Synthesis of K[(sal-L-tryp)]: K[(sal-L-tryp)] was prepared using a method reported by Vanco et al.[37] To a mixture of L-tryptophan (3.07 g, 15.0 mmol) and potassium hydroxide (0.85 g, 15.0 mmol) dissolved in water (5 mL) was added a solution of salicylaldehyde (1.57 mL, 15.0 mmol) in ethanol (10 mL) with stirring. The resulting yellow solution was stirred at room temperature for 24 h before it was diluted by ethanol (25 mL). Upon slow evaporation of solvent, a yellow oil was formed, which was triturated with diethyl ether. The yellow powder was collected by filtration and dried under vacuum; yield 4.85 g (93%). ESI-MS (+ve mode): *m/z* (%) = 344.05 (39.65, [M + H]$^+$), 300.03 (100.00, [M – OH – K + H]$^+$), 281.14 (46.08, [M – OH – O – K + H]$^+$), 262.12 (1.51, [M – COO – K + H]$^+$), 242.62 (64.65, [M – COO – OH – K + H]$^+$), 205.20

(50.43, $[M - C_7H_6O - K + H]^+$). FTIR: $\tilde{v}$ = 3407 (m) (indolic NH), 3169 (br.) (OH), 1194 (m) (C–O), 1521 (m) (COO$_s$), 1604 (m) (COO$_{as}$), 1570 (m) [TSC (C=N)] cm^{-1}. ^{1}H NMR (400 MHz, [D$_6$]-DMSO): δ = 3.13 (dd, J^{dd} = 8.9 and 16 Hz, 2 H), 3.49 (s, 1 H), 4.07 (s, 1 H), 6.59 (s, 1 H), 6.72–7.06 (m, 1 H), 6.72–7.06 (m, 1 H), 7.20 (s, 1 H), 7.20 (m, 1 H), 7.20 (m, 1 H), 7.20 (m, 1 H), 7.35–7.58 (m, H), 7.35–7.58 (m, 1 H), 11.17 (s, 1 H) ppm. ^{13}C NMR (400 MHz, [D$_6$]DMSO): δ = 30.16, 64.82, 72.43, 111.39, 111.56, 115.74, 117.62, 117.99, 118.31, 118.33, 120.59, 123.38, 127.36, 131.77, 132.01, 163.27, 172.88 ppm.

Synthesis of [VO(sal-L-tryp)(H$_2$O)] (1): Complex **1** was prepared as described by Costa Pessoa et al.[11] L-Tryptophan (1.14 g, 5.60 mmol) and sodium acetate trihydrate (1.47 g, 10.8 mmol) were placed in a 250 mL round bottomed flask with deionised water (100 mL). The mixture was stirred and heated at 50 °C to completely dissolve the L-tryptophan. Salicylaldehyde (0.59 mL, 5.6 mmol) in absolute ethanol (14 mL) was slowly added to the mixture. The resulting yellow solution was stirred vigorously with a magnetic stirrer, and an aqueous solution of VOSO$_4\cdot x$H$_2$O (0.78 g, 4.8 mmol) in water (2 mL) was added dropwise to the solution and it was stirred for 30 min. A dark brown precipitate formed, and the resulting solution was filtered under vacuum. The grey solid collected was washed with water (30 mL) and an ethanol/water mixture (50:50, 30 mL) and air-dried; yield 1.19 g (63%). C$_{18}$H$_{16}$N$_2$O$_5$V (391.28): calcd. C 55.25, H 4.12, N 7.16; found C 55.16, H 4.31, N 6.87 (ref.[11] C$_{18}$H$_{16}$N$_2$O$_5$V: calcd. C 55.25, H 4.12, N 7.16; found C 55.2, H 4.2, N 7.1). FTIR: $\tilde{v}$ = 3478 (m) (indolic NH), 3014 (br.) (OH), 1540 (m) (C–O), 1490 (m) (COO$_s$), 1597 (m) (COO$_{as}$), 1600 (m) {[(sal-L-tryp)] C=N}, 997 (s) (V=O) cm^{-1} [ref.[11] 3480 (m) (indolic NH), 3065 (br.) (OH), 1630 (m) {[(sal-L-tryp) (C=N)}, 1600 (m) (C–O), 970 (s) (V=O) cm^{-1}]. UV/Vis (MeOH): $\lambda_{max.}$ (ε/M^{-1} cm^{-1}) = 558 (44) and 758 (27) nm [ref.[11] (DMSO) 275 (15400) and 375 (4850), 520 (45), and 730 (20) nm].

Synthesis of [VO(sal-L-tryp)(MeATSC)]·1.5C$_2$H$_5$OH (2): (E)-2-(Anthracen-9-ylmethylene)-N-methylhydrazinecarbothioamide (0.15 g, 0.51 mmol) and **1** (0.20 g, 0.51 mmol) were placed in a dry 250 mL round-bottomed flask. Absolute ethanol (100 mL) was added to the flask, and the solution was heated to reflux with stirring under argon for 2 h. The orange-blue solution was evaporated to dryness. Diethyl ether was added, the mixture was filtered under vacuum, and the green residue was collected and air-dried; yield 0.23 g (68%). C$_{38}$H$_{38}$N$_5$O$_{5.5}$SV (735.75): calcd. C 62.03, H 5.21, N 9.52; found C 62.62, H 5.25, N 9.33. ESI-MS: m/z (%) = 666.17 (100.00, $[M + H]^+$), 577.08 (33.10, $[M - C_2H_5N_2S + H]^+$), 405.14 (31.86, $[M - C_{17}H_{17}N_3 + H]^+$), 292.14 (54.60, $[MeATSC + H]^+$). FTIR: $\tilde{v}$ = 3308 (m) (indolic NH), 3340 (m) (N^{1}H), 2976 (m) (N^{2}H), 1148 (m) (N–N), 1544 (m) (C–O), 1491 (m) (COO$_s$), 1600 (s) (COO$_{as}$), 1624 (m) [TSC (C=N)], 1590 (m) {[(sal-L-tryp)] (C=N)}, (1225) (m), (829) (m) (C=S), (455) (m) (V–S), 980 (s) (V=O) cm^{-1}. UV/Vis (DMSO): $\lambda_{max.}$ (ε/M^{-1} cm^{-1}) = 226 (74835), 292 (sh) (17954), 316 (sh) (10046), 388 (15013), 550 (54), 592 (sh) (45), 756 (28) nm.

Synthesis of [VO(sal-L-tryp)(N-ethhymethohcarbthio)]·H$_2$O (3): Complex **3** was prepared in a similar manner to **2** from (E)-2-(4-hydroxy-3-methoxybenzylidene)-N-methylhydrazinecarbothioamide (0.065 g, 0.26 mmol) and **1** (0.10 g, 0.26 mmol); yield 0.12 g (78%). C$_{29}$H$_{30}$N$_4$O$_7$SV (629.58): calcd. C 53.33, H 4.64, N 11.11; found C 53.18, H 5.21, N 11.09. ESI-MS: m/z (%) = 624.87 (100.00, $[M - H]^-$), 431.90 (64.75, $[M - C_{11}H_{10}N_2O - H]^-$), 407.85 (20.99, $[M - C_{11}H_{15}N_3O_2S - H]^-$), 287.88 (12.70, $[C_{11}H_{15}N_3O_2S - C_8H_7N - H]^-$), 252.00 (25.74, $[N$-ethhymethohcarbthio $- H]^-$). FTIR: $\tilde{v}$ = 3210 (m) (indolic NH), 3306 (m) (N^{1}H), 2970 (m)

(N^{2}H), 3010 (br.) (OH), 1154 (m) (N–N), 1540 (m) (C–O), 1480 (m) (COO$_s$), 1600 (s) (COO$_{as}$), 1620 (m) [TSC (C=N)], 1580 (m) {[(sal-L-tryp)] (C=N)}, (1270) (m), (802) (m) (C=S), (454) (m) (V–S), 976 (s) (V=O) cm^{-1}. UV/Vis (DMSO): $\lambda_{max.}$ (ε/M^{-1} cm^{-1}) = 270 (sh) (10984), 288 (sh) (13874), 330 (24837), 390 (sh) (18250), 620 (852) nm.

Synthesis of [VO(sal-L-tryp)(acetylethTSC)]·C$_2$H$_5$OH (4): Complex **4** was prepared in a similar manner to **2** from 2-acetylthiazole-4,4′-dimethylthiosemicarbazone (0.12 g, 0.51 mmol) and **1** (0.20 g, 0.51 mmol); yield 0.18 g (57%). C$_{28}$H$_{32}$N$_6$O$_5$S$_2$V (647.66): calcd. C 51.93, H 4.98, N 12.98; found C 52.94, H 4.72, N 10.91. ESI-MS: m/z (%) = 600.25 (2.71, $[M + H]^+$), 513.57 (100.00, $[M - C_3H_7NS + H]^+$), 482.38 (37.11, $[M - C_7H_5NO + H]^+$), 336.06 (4.13, $[M - C_{17}H_{15}N_2O + H]^+$). FTIR: $\tilde{v}$ = 3229 (m) (indolic NH), 3310 (m) (N^{1}H), 2976 (m) (N^{2}H), 1149 (m) (N–N), 1545 (m) (C–O), 1480 (m) (COO$_s$), 1600 (s) (COO$_{as}$), 1624 (m) [TSC (C=N)], 1580 (m) {[(sal-L-tryp)] (C=N)}, (1287) (m), (819) (m) (C=S), (455) (m) (V–S), 982 (s) (V=O) cm^{-1}. UV/Vis (DMSO): $\lambda_{max.}$ (ε/M^{-1} cm^{-1}) = 276 (21969), 352 (14227), 558 (80), 590 (sh) (70), 756 (38) nm.

Oxidation of 1 and 3 in DMSO: Complex **1** (0.1 g, 0.26 mmol) was added to an evaporating dish with DMSO (10 mL), and the resulting solution was left to evaporate for 32 days to leave a solid; yield 0.09 g. ESI-MS (+ve mode): m/z (%) = 468.60 (1.67, $[M + H]^+$), 242.41 (100.00, $[M - OH - DMSO - C_8H_7N + H]^+$), 451.05 (48.25, $[M - OH + H]^+$), 763.68 (30.06, $[V_2O_3(sal$-L-$tryp)_2 + H]^+$), 776.77 (49.36, $[V_2O_3(sal$-L-$tryp)_2(H_2O) + H]^+$), 918.28 (3.13, $[V_2O_3(sal$-L-$tryp)_2(DMSO)_2 + H]^+$). FTIR: $\tilde{v}$ = 3185 (m) (indolic NH), 3194 (br.) (OH), 1551 (m) (C–O), 1497 (m) (COO$_s$), 1618 (s) (COO$_{as}$), 1667 (m) [TSC (C=N)], 1581 (m) {[(sal-L-tryp)] (C=N)}, 1164 (m), 1213 (m) (S=O), 949 (s) (V=O) cm^{-1}. ^{1}H NMR (400 MHz, [D$_6$]DMSO): δ = 2.52 (d, 3 H), 2.52 (d, 3 H), 10.89 (s, 1 H), 7.06 (s, 1 H), 7.22 (m, 1 H), 7.22 (m, 1 H), 7.52 (d, 1 H), 8.06 (d, 2 H), 3.36 (s, 1 H), 3.00 (s, 2 H), 7.22 (m, 1 H), 7.22 (m, 1 H), 7.22 (m, 1 H), 7.22 (m, 1 H), 9.93 (s, 1 H), 7.06 (s, 1 H) ppm.

Complex **3** (0.1 g, 0.16 mmol) was oxidised in an analogous manner; yield 0.09 g. ESI-MS (+ve mode): m/z (%) = 470.01 (0.50, $[M + H]^+$), 252.26 (100.00, $[N$-ethhymethohcarbthio $+ H]^+$), 451.96 (2.97, $[M - OH + H]^+$), 702.75 (2.15, $[M - OH + N$-ethhymethohcarbthio $+ H]^+$), 763.22 (0.74, $[V_2O_3(sal$-L-$tryp)_2 + H]^+$), 775.40 (1.08, $[V_2O_3(sal$-L-$tryp)_2(H_2O) + H]^+$), 916.44 (0.75, $[V_2O_3$-$(sal$-L-$tryp)_2(DMSO)_2 + H]^+$). FTIR: $\tilde{v}$ = 3193 (br.) (OH), 1666 (m) (C=N), 1600 (C=O), 1550 (m) (C–O), 1133 (m), 1157 (m) (S=O), 946 (s) (V=O) cm^{-1}. ^{1}H NMR (400 MHz, [D$_6$]DMSO): δ = 2.52 (d, 3 H), 2.52 (d, 3 H), 10.43 (s, 1 H), 6.96 (s, 1 H), 7.22 (m, 1 H), 7.22 (m, 1 H), 7.42 (d, 1 H), 8.00 (d, 2 H), 3.34 (s, 1 H), 3.00 (s, 2 H), 7.22 (m, 1 H), 7.22 (m, 1 H), 7.22 (m, 1 H), 7.22 (m, 1 H), 9.95 (s, 1 H), 6.96 (s, 1 H) ppm.

Pharmacology

Cell Culture: Three human colon cancer cells, HT-29 (human colon adenocarcinoma), HCT-116 (human colon carcinoma) and Caco-2 (human epithelial colorectal adenocarcinoma), and noncancerous human colon cells, CCD-18Co (human colon fibroblasts), were used in this study. All cell lines were obtained from the American Type Culture Collection (ATCC, Rockville, MD, USA) and maintained at the University of Rhode Island, USA. Caco-2 cells were grown in Eagle's minimal essential medium (EMEM) supplemented with 10% v/v fetal bovine serum, 1% v/v nonessential amino acids, 1% v/v L-glutamine and 1% v/v antibiotic solution (Sigma–Aldrich). HT-29 and HCT-116 cells were grown in McCoy's 5a medium supplemented with 10% v/v fetal bovine serum, 1% v/v non-essential amino acids, 2% v/v 4-(2-hydroxyethyl)-1-piperazineethanesulfonic acid and 1% v/v antibiotic solution. CCD-18Co cells were

grown in EMEM medium supplemented with 10% v/v fetal bovine serum, 1% v/v nonessential amino acids, 1% v/v L-glutamine and 1% v/v antibiotic solution and were used from PDL = 26 to PDL = 35 for all experiments. Cells were maintained at 37 °C in an incubator under a 5% CO_2/95% air atmosphere at constant humidity and maintained in the linear phase of growth. The pH of the culture medium was determined with pH indicator paper (pHydrionTM Brilliant, pH 5.5–9.0, Micro Essential Laboratory, NY, USA) inside the incubator. All test samples were dissolved in DMSO (< 0.5% in the culture medium) with sonication and filter sterilised (0.2 μm) prior to addition to the culture media. Control cells were also tested in parallel sequences and subjected to the same changes in medium with 0.5% DMSO.

Cytotoxicity Assay: This assay was carried out as described previously[38] to measure the IC_{50} values for the samples. The in vitro cytotoxicity of the samples was assessed in tumour cells by a tetrazolium-based colorimetric assay, which takes advantage of the metabolic conversion of MTS to a reduced form that absorbs light at 490 nm. Cells were counted using a hemacytometer and were plated at 2000–5000 cells per well, depending on the cell line, in a 96-well format for 24 h prior to drug addition. Test samples and a positive control, etoposide 4 mg mL^{-1} (Sigma–Aldrich), were dissolved in DMSO with sonication. All samples were diluted with media to the desired treatment concentration, and the final DMSO concentration per well did not exceed 0.5%. Control wells were also included on all plates. Following a 24, 48 or 72 h drug-incubation period at 37 °C with serially diluted test compounds, MTS and the electron coupling agent, phenazine methosulfate, were added to the wells, and the cells were incubated at 37 °C in a humidified incubator for 3 h. Absorbances at 490 nm (OD_{490}) were acquired with a spectrophotometer (SpectraMax M2, Molecular Devices Corp., operated by SoftmaxPro v.4.6 software, Sunnyvale, CA, USA) to obtain the number of surviving cells relative to control populations. The results are expressed as the median cytotoxic concentrations (IC_{50} values) and were calculated from six-point dose response curves using fourfold serial dilutions.

Statistics: Data are expressed as mean ±SE for three replications on each cell line.

Supporting Information (see footnote on the first page of this article): Mass spectra, FTIR spectra, ^{1}H and ^{13}C NMR spectra, UV/Vis and fluorescence spectra.

Acknowledgments

[1] E. Wong, C. M. Giandomenico, *Chem. Rev.* **1999**, *99*, 2451–2466.

[2] a) M. Galanski, V. B. Arion, M. A. Jakupec, B. K. Keppler, *Curr. Pharm. Des.* **2003**, *9*, 2078–2089; b) M. A. Jakupec, M. Galanski, B. K. Keppler, *Rev. Physiol. Biochem. Pharmacol.* **2003**, *146*, 1–54.

[3] I. Ott, R. Gust, *Archiv der Pharmazie – Chemistry in Life Sciences* **2007**, *340*, 117–126.

[4] a) M. J. Clarke, *Coord. Chem. Rev.* **2003**, *203*, 209–233; b) M. J. Clarke, F. Zhu, D. R. Frasca, *Chem. Rev.* **1999**, *99*, 2511–2533; c) B. Armitage, *Chem. Rev.* **1998**, *98*, 1171–1200.

[5] D. d. O. Silva, *Anti-Cancer Agents Med. Chem.* **2010**, *10*, 312–323.

[6] F. A. Beckford, M. Shaloski Jr, G. Leblanc, J. Thessing, L. C. Lewis-Alleyne, A. A. Holder, L. Li, N. P. Seeram, *Dalton Trans.* **2009**, 10757–10764.

[7] a) P. Tarasconi, S. Capacchi, G. Pelosi, M. Cornia, R. Albertini, A. Bonati, P. P. Dall'Aglio, P. Lunghi, S. Pinelli, *Bioorg. Med. Chem.* **2000**, *8*, 157–162; b) D. X. West, J. K. Swearingen, J. Valdes-Martinez, S. Hernandez-Ortega, A. K. El-Sawaf, F. Van Meurs, A. Castineiras, I. Garcia, E. Bermejo, *Polyhedron* **1999**, *18*, 2919–2929.

[8] P. Noblia, M. Vieites, B. S. Parajon-Costa, E. J. Baran, H. Cerecetto, P. Draper, M. Gonzalez, O. E. Piro, E. E. Castellano, A. Azqueta, A. Lopez de Cerain, A. Monge-Vega, D. Gambino, *J. Inorg. Biochem.* **2005**, *99*, 443–451.

[9] a) O. J. D'Cruz, Y. Dong, F. M. Uckun, *Anti-Cancer Drugs* **2000**, *11*, 849–858; b) R. K. Narla, Y. Dong, P. Ghosh, K. Thoen, F. M. Uckun, *Drugs Future* **2000**, *25*, 1053–1068; c) O. J. D'Cruz, F. M. Uckun, *Expert Opin. Invest. Drugs* **2002**, *11*, 1829–1836; d) I. Fichtner, J. Claffey, A. Deally, B. Gleeson, M. Hogan, M. R. Markelova, H. Mueller-Bunz, H. Weber, M. Tacke, *J. Organomet. Chem.* **2010**, *695*, 1175–1181; e) D. Rehder, in: *Bioinorganic Vanadium Chemistry*, John Wiley & Sons, Chichester, UK, **2008**, p. 176.

[10] L. L. Koh, J. Ranford, W. Robinson, J. O. Svensson, A. L. C. Tan, D. Wu, *Inorg. Chem.* **1996**, *35*, 6466–6472.

[11] J. C. Pessoa, M. T. Duarte, R. D. Gillard, C. Madeira, P. M. Matias, I. Tomaza, *J. Chem. Soc., Dalton Trans.* **1998**, 4015–4020.

[12] I. Cavaco, J. C. Pessoa, M. T. Duarte, R. T. Henriques, P. M. Matias, R. D. Gillard, *J. Chem. Soc., Dalton Trans.* **1996**, 1989–1996.

[13] E. Viñuelas-Zahínos, F. Luna-Giles, P. Torres-García, M. C. Fernández-Calderón, *Eur. J. Med. Chem.* **2011**, *46*, 150–159.

[14] R. Venkatraman, H. Ameera, L. Sitole, E. Ellis, F. R. Fronczek, E. J. Valente, *J. Chem. Crystallogr.* **2009**, *39*, 711–718.

[15] T. S. Lobana, R. Sharma, G. Bawa, S. Khanna, *Coord. Chem. Rev.* **2009**, *253*, 977–1055.

[16] a) M. M. Mostafa, A. El-Hammid, M. Shallaby, A. A. El-Asmay, *Trans. Met. Chem.* **1981**, *6*, 303; b) D. X. West, A. E. Liberta, S. B. Padhye, R. C. Chikate, P. B. Sonawane, A. S. Kumbher, R. G. Yerande, *Coord. Chem. Rev.* **1993**, *123*, 49.

[17] H. Beraldo, W. F. Nacif, L. R. Teixeira, J. S. Reboucas, *Trans. Met. Chem.* **2002**, *27*, 85–88.

[18] a) T. B. Demirci, Y. Koseoglu, S. Guner, B. Ulkuseven, *Cent. Eur. J. Chem.* **2006**, *4*, 149–159; b) H. Zhang, R. Thomas, D. Oupicky, F. Peng, *J. Biol. Inorg. Chem.* **2008**, *13*, 47–55.

[19] a) I. C. Mendes, L. M. Botion, A. V. M. Ferreira, E. E. Castellano, H. Beraldo, *Inorg. Chim. Acta* **2009**, *362*, 414; b) J. C. Pessoa, I. Cavaco, I. Correia, I. Tomaz, T. Duarte, P. M. Matias, *J. Inorg. Biochem.* **2000**, *80*, 35–39.

[20] M. M. M. Raposo, B. Garcia-Acosta, T. Abalos, P. Calero, R. Martinez-Manez, J. V. Ros-Lis, J. Soto, *J. Org. Chem.* **2010**, *75*, 2922–2933.

[21] Z. Afrasiabi, E. Sinn, P. P. Kulkarni, V. Ambike, S. Padhye, D. Deobagakar, M. Heron, C. Gabbutt, C. E. Anson, A. K. Powell, *Inorg. Chim. Acta* **2005**, *358*, 2023–2030.

[22] V. Mahalingam, N. Chitrapriya, F. R. Fronczek, K. Natarajan, *Polyhedron* **2008**, *27*, 2743–2750.

[23] B. Baruah, S. Das, A. Chakravorty, *Inorg. Chem.* **2002**, *41*, 4502–4508.

[24] M. R. Maurya, S. Khurana, D. Rehder, *Trans. Met. Chem.* **2003**, *28*, 511–517.

[25] K. Nakajima, M. Kojima, K. Toriumi, K. Saito, J. Fujita, *Bull. Chem. Soc. Jpn.* **1989**, *62*, 760–767.

[26] N. Kanoongo, R. Singh, J. P. Tandon, *Trans. Met. Chem.* **1987**, *12*, 271–273.

[27] a) P. K. Sasmal, A. K. Patra, M. Nethaji, A. R. Chakravarty, *Inorg. Chem.* **2007**, *46*, 11112–11121; b) K. Toshima, R. Takano, T. Ozawa, S. Matsumura, *Chem. Commun.* **2002**, 212–213.

[28] a) S. P. Rath, T. Ghosh, S. Mondal, *Polyhedron* **1997**, *16*, 4179–4186; b) J. A. Bonadies, C. J. Carrano, *J. Am. Chem. Soc.* **1986**, *108*, 4088–4095.

[29] A. Ozarowski, H. M. Lee, A. L. Balch, *J. Am. Chem. Soc.* **2003**, *125*, 12606–12614.

[30] a) M. Branca, G. Micera, A. Dessi, D. Sanna, K. N. Raymond, *Inorg. Chem.* **1990**, *29*, 1586–1589; b) N. D. Chasteen, E. M. Lord, H. J. Thompson, J. K. Grady, *Biochim. Biophys. Acta Gen. Subj.* **1986**, *884*, 84–92; c) D. C. Crans, A. R. Khan, M. Mahroof-Tahir, S. Mondal, S. M. Miller, A. la Cour, O. P. Anderson, T. Jakusch, T. Kiss, *J. Chem. Soc., Dalton Trans.* **2001**, 3337–3345; d) K. Efthimiadou Eleni, G. Psomas, Y. Sanakis, N. Katsaros, A. Karaliota, *J. Inorg. Biochem.* **2007**, *101*, 525–535; e) S. K. Ghosh, R. Patra, S. P. Rath, *Inorg. Chem.* **2008**, *47*, 9848–9856; f) M. Mahroof-Tahir, A. D. Keramidas, R. B. Goldfarb, O. P. Anderson, M. M. Miller, D. C. Crans, *Inorg. Chem.* **1997**, *36*, 1657–1668; g) T. K. Paine, T. Weyhermueller, L. D. Slep, F. Neese, E. Bill, E. Bothe, K. Wieghardt, P. Chaudhuri, *Inorg. Chem.* **2004**, *43*, 7324–7338; h) Y. Z. Xu, S. Shi, *Appl. Magn. Reson.* **1996**, *11*, 1–6.

[31] a) G. Micera, E. Garribba, *J. Comput. Chem.* **2011**, *32*, 2822–2835; b) G. Micera, V. L. Pecoraro, E. Garribba, *Inorg. Chem.* **2009**, *48*, 5790–5796; c) G. Micera, E. Garribba, *Dalton Trans.* **2009**, 1914–1918; d) E. Garribba, E. Lodyga-Chruscinska, G. Micera, A. Panzanelli, D. Sanna, *Eur. J. Inorg. Chem.* **2005**, 1369–1382.

[32] W. L. Kan, C. H. Cho, J. A. Rudd, G. Lin, *J. Ethnopharmacol.* **2008**, *120*, 36–43.

[33] C. A. Puckett, R. J. Ernst, J. K. Barton, *Dalton Trans.* **2010**, *39*, 1159–1170.

[34] D. C. Crans, A. A. Holder, T. K. Saha, G. K. Prakash, M. Yousufuddin, R. Kultyshev, R. Ismail, M. F. Goodman, J. Borden, F. Florián, *Inorg. Chem.* **2007**, *46*, 6723–6732.

[35] G. M. Sheldrick, *Acta Crystallogr., Sect. A: Foundations of Crystallography* **2008**, *64*, 112–122.

[36] a) G. M. Sheldrick, *NATO ASI Series, Series E: Applied Sciences* **1997**, *347*, 219–230; b) G. M. Sheldrick, T. R. Schneider, *Methods Enzymol.* **1997**, *277*, 319–343.

[37] J. Vanco, O. Svajlenova, J. Marek, *Acta Crystallogr., Sect. C: Cryst. Struct. Commun.* **2003**, *59*, m190–m192.

[38] A. H. Cory, T. C. Owen, J. A. Barltrop, J. G. Cory, *Cancer Commun.* **1991**, *3*, 207–212.

FULL PAPER

Redox Reactions of a [Ru^{III}(hedtra)(pz)] Complex with Biochemically Important Reductants: Kinetic, Mechanistic and Antimicrobial Studies

Debabrata Chatterjee,*[a] Sarita Ghosh,[a] Ujjwal Pal,[a] and Sudit Mukhopadhyay[b]

The kinetics of the reduction of [Ru^{III}(hedtra)(pz)] (hedtra^{3-} = N-hydroxyethylethylenediaminetriacetate; pz = pyrazine) by biologically important reducing agents, Red (Red = L-ascorbic acid, catechol and cysteine), resulting in the formation of the corresponding red-coloured ruthenium(II) complex has been studied spectrophotometrically using both conventional mixing and stopped-flow techniques. The time course of the reaction was followed as a function of [Red], pH and temperature. Alkali metal ions were found to have an insignificant effect on the reaction rate. Kinetic data and activation parameters are interpreted in terms of an outer-sphere electron-transfer mechanism, and discussed with reference to the data reported for the corresponding Ru^{III}–edta (edta^{4-} = ethylenediaminetetraacetate) complex. The antibacterial activity of the [Ru^{III}(hedtra)(pz)] complex in inhibiting the growth has been explored. Results of the biological studies have been discussed in terms of the cleavage of chromosomal DNA of the bacteria by the [Ru^{III}(hedtra)(pz)] complex in the presence of cysteine under aerobic conditions.

Introduction

While the chemistry of "edta"-type complexes of ruthenium(III) have received much attention because of their kinetic lability towards aqua-substitution, which affords a facile and straightforward synthesis to mixed-ligand complexes,[1,2] their redox ability is also documented in the literature.[3–6] Though Ru^{III} is the predominant oxidation state under physiological conditions, Ru^{II}, Ru^{IV} and Ru^{V} oxidation states are readily accessible in the presence of biological reductants[3,4] or oxidants.[5,6] The pac ligands function as pentadentate ligands (represented in Figure 1) towards ruthenium, and the lability of such complexes is governed by the nature of the pendant group R. The highest lability is induced by the pendant group when R = CH$_2$COO$^-$, with significantly decreased lability for R = CH$_2$CH$_2$OH and even further for R = CH$_3$.[1]

Notably, electrochemical studies of [Ru^{III}(pac)(H$_2$O)] complexes have shown that the electron-transfer process is rapid and reversible for the [Ru^{III}(pac)(H$_2$O)]/[Ru^{II}(pac)-(H$_2$O)] couple. The redox potential corresponding to the [Ru^{III}(pac)(H$_2$O)]/[Ru^{II}(pac)(H$_2$O)] couple for [Ru^{III}(edta)-(H$_2$O)]$^-$ (R = CH$_2$COO$^-$), [Ru^{III}(hedtra)(H$_2$O)] (R =
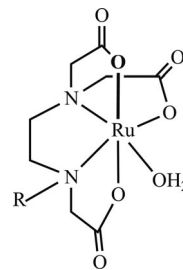
Figure 1. Structural representation of [Ru^{III}(pac)(H$_2$O)]; R = CH$_2$COO$^-$, pac = edta^{4-}; R = CH$_2$CH$_2$OH, pac = hedtra^{3-}.

CH$_2$CH$_2$OH) and [Ru^{III}(medrta)(H$_2$O)] (R = CH$_3$) complexes are –0.04, –0.07 and –0.10 V (vs. NHE), respectively.[1] In view of the above electrochemical data it appears that [Ru^{III}(edta)(H$_2$O)]$^-$ is more oxidizing than [Ru^{III}(hedtra)(H$_2$O)], and [Ru^{III}(medtra)(H$_2$O)] would be least oxidizing.

Very recently, we have reported thiol-to-disulfide conversion activity of the anionic Ru^{III}-edta complex in the oxidation of biologically significant thiols RSH (RSH = cysteine, glutathione) to RSSR.[4] It is worth noting that thiol-to-disulfide conversion is of great importance since tumor cell metabolism favours the presence of Ru^{II} relative to Ru^{III}, thus increasing the selective tumour toxicity.[7,8] We have proposed an outer-sphere electron-transfer mechanism involving the formation of an intermediate bridging two negatively-charged reactants.[4] In order to enrich our mechanistic understanding of the electron-transfer reaction of Ru–pac complexes in general, we have undertaken the present studies in which one of the reactants, the [Ru^{III}(hedtra)-

[a] Chemistry & Biomimetics Group, CSIR – Central Mechanical Engineering Research Institute,
M. G. Avenue, Durgapur 713209, India
Fax: +91-343-3546745
E-mail: dchat57@hotmail.com
[b] Department of Biotechnology, National Institute of Technology,
M. G. Avenue, Durgapur 713209, India

pz] complex, is electrically neutral. We report herein the results of the detailed kinetic and mechanistic studies of the reaction of [Ru^{III}(hedtra)pz] with the biologically significant reductant, Red (Red = L-ascorbic acid, catechol and cysteine) as a function of [Red], pH and temperature. We have extended our studies further to explore the antibacterial activity of the [Ru^{III}(hedtra)pz] complex in the presence of the celullar thioamino acid cysteine. The scope of the present work is to enrich our mechanistic understanding of the electron-transfer process of Ru^{III}–pac complexes.

Results and Discussion

Reduction of the [Ru^{III}(hedtra)pz] (**1**) complex with Red (Red = H$_2$Asc, H$_2$C and CySH) was studied spectrophotometrically by following a similar method reported for the reduction of [Ru^{III}(edta)pz]$^-$ by CySH.[4] Biologically active reductants, L-ascorbic acid, catechol and L-cysteine are abbreviated as H$_2$Asc, H$_2$C and CySH, respectively. The spectrum of the [Ru^{III}(hedtra)pz] (**1**) complex (Figure S1 in the Supporting Information), like its "edta" analogue, is featureless in the visible region, however, its Ru^{II} species exhibits a strong MLCT band in the visible region (λ_{max} = 462 nm). The [Ru^{III}(edta)pz]$^-$ complex was preformed by reacting [Ru^{III}(edta)(H$_2$O)]$^-$ with an excess of pyrazine (50 times excess over ruthenium was used in the present case). Figure 1 (a) shows the typical UV/Vis spectral changes with time that occurred upon mixing aqueous solutions of **1** and H$_2$Asc in the chamber of the stopped-flow instrument equipped with a rapid-scan spectral attachment, whereas Figure 1 (b) displays a typical kinetic trace at 462 nm generated from a number of spectra by using global kinetic analysis software (SPECFIT/32). The final spectrum of the reacting solution corresponds to the spectrum of the [Ru^{II}(hedtra)pz] species (λ_{max} = 462 nm).

Under pseudo-first-order conditions of excess H$_2$Asc (10–50 times excess over ruthenium complex concentration), the rate of the reaction was found to be first order with respect to [**1**]. The values of the observed rate constant (k_{obs}) increased linearly with increasing [H$_2$Asc]$_T$ (throughout this paper the total concentration of ascorbic acid is represented by [H$_2$Asc]$_T$ and equals the sum of [H$_2$Asc], [HAsc$^-$] and [Asc^{2-}]), and exhibited a negligible intercept (Figure 2, a).

Considering that the monoprotonated ascorbate (HAsc$^-$) species is mostly present at pH 6.0 (pK_1 and pK_2 values of H$_2$Asc are 4.1 and 11.4, respectively)[9,10] the present kinetic results are explicable in terms of the following mechanism as outlined in Scheme 1.

The rate-determining step (1) proposed in the above mechanism (Scheme 1) involves the transfer of one electron from HAsc$^-$ to the ruthenium(III) complex in an outersphere manner.[3] The HAsc$^\cdot$ radical species that was generated [Equation (1)] is highly reactive, and reduces another molecule of [Ru^{III}(hedtra)pz] to [Ru^{II}(hedtra)(pz)]$^-$ in a subsequent rapid but kinetically inconsequential step [Equation (2)]. Reduction of the Ru^{III} complex **1** by the HAsc$^\cdot$
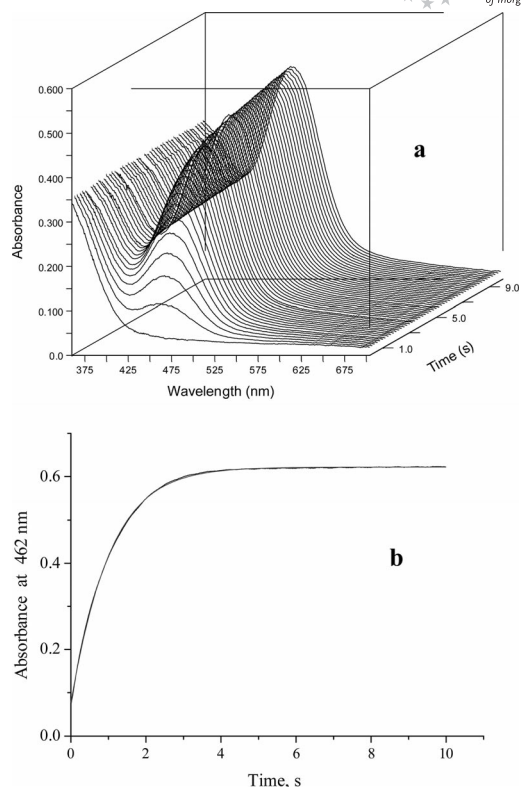
Figure 2. (a) Spectral changes that occur with the reduction of **1** (1×10^{-4} M) by H$_2$Asc (5×10^{-3} M) at 25 °C, pH 6.0. (b) Kinetic trace at 462 nm. The red line is the single exponential fit.

$$[\text{Ru}^{III}(\text{hedtra})(\text{pz})] + \text{HAsc}^- \xrightarrow{k_{\text{HAsc}^-}} [\text{Ru}^{II}(\text{hedtra})(\text{pz})]^- + \text{HAsc}^\cdot \quad (1)$$

$$[\text{Ru}^{III}(\text{hedtra})(\text{pz})] + \text{HAsc}^\cdot \xrightarrow{\text{fast}} [\text{Ru}^{II}(\text{hedtra})(\text{pz})]^- + \text{Asc}^{2-} \quad (2)$$
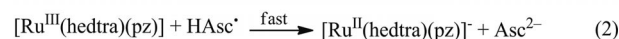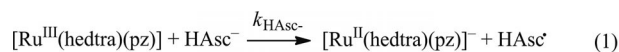
Scheme 1. Reduction of [Ru^{III}(hedtra)pz] to [Ru^{II}(hedtra)pz]$^-$ by H$_2$Asc.

radical [Equation (2)] is kinetically preferred, for which reoxidation of the Ru^{II} species by the HAsc$^\cdot$ radical becomes insignificant in step 1. This is probably the reason for the small intercept in the plot of k_{obs} vs. [H$_2$Asc] (Figure 2, a).

The rate of the reaction was found to be pH dependent (Table 1) since the reducing ability of ascorbic acid, H$_2$Asc, significantly differs from that of its conjugate bases HAsc$^-$ and Asc^{2-}. In general, reactivity decreases in the order Asc$^{2-} \gg$ HAsc$^- >$ H$_2$Asc.[9,10] The k_{obs} values at various pH values are summarized in Table 1. Considering that the pK_2 (corresponding to the second proton dissociation of H$_2$Asc) of ascorbic acid is 11.4,[9,10] it is expected that the rate of reaction would be almost pH independent in the range pH 6.0–9.0 (more than 95% of L-ascorbic acid is present as HAsc$^-$). However, the k_{obs} values are more sensitive over the pH range 6.0–9.0 (Table 1), suggesting the participation of the highly reactive species Asc^{2-}, though present in a very small concentration, in the reduction process. It is noteworthy that Elding and coworkers also reported the observance of the higher reactivity of the ascorbate anion, Asc^{2-}, in the reduction of the model octahedral plati-

num(IV) complex.[11,12] Analysis of the kinetics data revealed that the ascorbate anion Asc^{2-} is up to seven orders of magnitude more reactive than $HAsc^-$ while H_2Asc is ineffective.[14,15] Electron transfer from $HAsc^-/Asc^{2-}$ to the Pt^{IV} compounds was explained in terms of the reductive elimination mechanism involving attack by the ascorbate anion, Asc^{2-}, on the coordinated halide leading to the formation of a halide-bridged intermediate complex for the reduction of platinum(IV) compounds. The reported reactions can be visualized as a nucleophilic substitution on the halogen with the platinum moiety as the leaving group.[11,12] Facile formation of such bridged species with the ascorbate anion, Asc^{2-}, is probably the reason for the observed high reactivity as compared with that noticed for protonated $HAsc^-$ or H_2Asc.[11,12] However, reduction of $[Ru^{III}(hedtra)(pz)]$ to $[Ru^{II}(hedtra)(pz)]^-$ also occurred over a lower pH range 3.0–5.0, which normally suggests that the $HAsc^-$ species is also effective in reducing $[Ru^{III}(hedtra)(pz)]$ to $[Ru^{II}(hedtra)(pz)]^-$ through outer-sphere electron transfer. It may be noted here that the reactivity of Asc^{2-} towards some platinum(IV) compounds that undergo reduction through outer-sphere electron transfer was lower than those involving a bridged intermediate species.[11,12]

Table 1. Values of the observed rate constant (k_{obs}) as a function of pH for the reduction of $[Ru^{III}(hedrta)pz]$ by Red (Red = H_2Asc and CySH). $[Ru^{III}] = 1 \times 10^{-4}$ M, $[Red] = 5 \times 10^{-3}$ M, $T = 25$ °C.

pH	k_{obs} [s^{-1}]	
	H_2Asc	CySH
3.0	0.01 ± 0.002	$(3.55 \pm 0.03) \times 10^{-4}$
4.0	0.04 ± 0.005	$(3.61 \pm 0.03) \times 10^{-4}$
5.0	0.17 ± 0.006	$(3.59 \pm 0.03) \times 10^{-4}$
6.0	0.77 ± 0.01	$(3.65 \pm 0.01) \times 10^{-3}$
7.0	1.13 ± 0.05	$(3.77 \pm 0.01) \times 10^{-3}$
8.0	1.66 ± 0.06	$(4.81 \pm 0.03) \times 10^{-3}$
9.0	2.03 ± 0.07	$(5.37 \pm 0.05) \times 10^{-3}$

The observed rate constant (k_{obs}) values are independent of the ionic strength of the medium. The lack of ionic strength effect in the present reaction is consistent with the proposed rate-determining step with reference to the Brønsted equation[13] for a reaction between a charged and a neutral reactant. Further, as shown in Table 2, the values of the observed rate constants for this reaction were found to be insensitive to both the nature and concentration of the added metal ions (Li^+, Na^+, K^+).

Table 2. Values of the observed rate constant (k_{obs}) as a function of $[M^+]$ for the reduction of $[Ru^{III}(edta)pz]^-$ by Red (Red = H_2Asc, H_2C and CySH). $[Ru^{III}] = 5 \times 10^{-4}$ M, $[Red] = 1 \times 10^{-3}$ M, $T = 21$ °C, pH 5.0 (1 mM acetate buffer).

$[M^+]$	$[M^+]$ [M]	k_{obs} [s^{-1}]
		H_2Asc
Li^+	0.2	0.66 ± 0.03
	0.05	0.67 ± 0.02
Na^+	0.15	0.68 ± 0.03
	0.2	0.66 ± 0.02
K^+	0.2	0.68 ± 0.03

Oxidation of catechol by **1** exhibited a similar kinetic behaviour to that observed in the case of H_2Asc. The values of the pseudo-first-order rate constant increased linearly with increasing catechol concentration (Figure 3, b). The effect of pH on the k_{obs} values was found to be insignificant, which could be explicable in terms of the pK_a values of catechol (p$K_1 = 9.45$ and p$K_2 = 12.8$).[14] Catechol is not ionized in the pH range 3.0–9.0,[14] hence, its reactivity in the studied pH range is not altered enough to cause any significant change in the k_{obs} values by changing the pH.
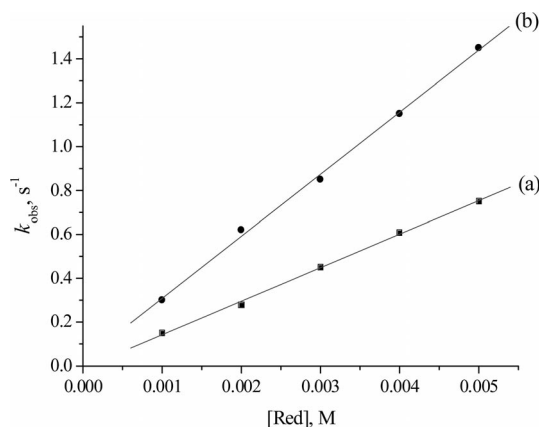
Figure 3. Plots of k_{obs} vs. [Red] for the reduction of $[Ru^{III}(hedtra)(pz)]$ (1.0×10^{-4} M) by (a) $[H_2Asc]$ and (b) H_2C at 25 °C, pH 6.0. The lines represent the linear fit.

As expected for the reaction of two uncharged molecules, the concentration of alkali metal cations $[M^+]$ and ionic strength of the reacting medium showed an appreciable effect on the values of the observed rate constant (k_{obs}) for the reduction of **1** by H_2C. On the basis of the above kinetic observations a working mechanism is proposed for the oxidation of H_2C by **1** as outlined in Scheme 2.

$$[Ru^{III}(hedtra)(pz)] + H_2C \xrightarrow{k_{H_2C}} [Ru^{II}(hedtra)(pz)]^- + BSQ \quad (3)$$

$$[Ru^{III}(hedtra)(pz)] + BSQ \longrightarrow [Ru^{II}(hedtra)(pz)]^- + BQ \quad (4)$$
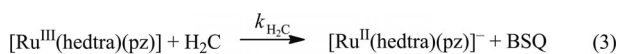
Scheme 2. Reduction of $[Ru^{III}(hedtra)pz]$ to $[Ru^{II}(hedtra)pz]^-$ by H_2C.

In Scheme 2 it is suggested that catechol reduces $[Ru^{III}(hedtra)(pz)]$ to $[Ru^{II}(hedtra)(pz)]^-$ through a rate-determining one-electron transfer step resulting in the formation of the benzosemiquinone (BSQ) intermediate, which is a one-electron oxidized product of catechol. In a subsequent rapid step BSQ reduces another molecule of **1** to produce $[Ru^{II}(hedtra)(pz)]^-$ and benzoquinone (BQ) as the ultimate reaction products.

Reduction of **1** by RSH was studied spectrophotometrically by adopting a conventional mixing technique since the reaction was found to be comparatively slower than that observed for H_2Asc or H_2C. The spectral changes and the corresponding absorbance (at 462 nm) vs. time plot associated with the formation of $[Ru^{II}(hedtra)(pz)]^-$ in the reduction of **1** by CySH in H_2O are shown in Figure S2 and Figure S3 in the Supporting Information. Under pseudo-

first-order conditions of excess RSH (10–50 times excess over the ruthenium complex concentration), the values of the observed rate constant (k_{obs}) increased linearly with increasing [CySH] and showed a negligible intercept (Figure S4 in the Supporting Information), indicative of an insignificant back reaction.

The effect of pH on the observed rate constant values for the reduction of **1** by CySH is shown in Table 1. As in the case of the reduction of [Ru^{III}(edta)pz]$^-$ by CySH,[4] no significant increase in the k_{obs} values with increasing pH in the range 3 to 7 was observed (Table 1). However, an increase in the k_{obs} values observed for the pH range 8 to 9 may be ascribed to the higher reducing ability of the deprotonated thiol (RS$^-$) as compared with RSH.[15] The reaction rate for this reaction was found to be uninfluenced by the nature and concentration of the added metal ions (Li$^+$, Na$^+$, K$^+$). The observed kinetic results could be explained in terms of the mechanism proposed in Scheme 3.

$$[Ru^{III}(hedtra)(pz)] + CySH \xrightarrow{k_{CySH}} [Ru^{II}(hedtra)(pz)]^- + CyS^· + H^+ \quad (5)$$

$$CyS^· \longrightarrow 1/2\ CySSCy \quad (6)$$
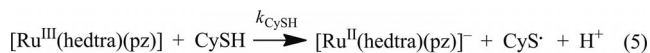
Scheme 3. Reduction of [Ru^{III}(edtra)pz] to [Ru^{II}(edtraa)pz]$^-$ by CySH.

In the proposed rate-determining step [Equation (5) in Scheme 3] the one-electron transfer from RSH to the [Ru^{III}(hedtra)(pz)] complex occurs in an outer-sphere manner. In the subsequent and kinetically inconsequential step (6), the RS$^·$ radical species rapidly transforms into RSSR (oxidized form of RSH). The production of the RSSR species in the reacting system was identified by HPLC analysis using authentic samples of RSSR.

The reduction of [Ru^{III}(hedtra)pz] with Red (Red = H$_2$Asc, H$_2$C and CySH) was followed by the formation of the corresponding Ru^{II} complex. Considering that each reductant molecule (red) produced two Ru^{II} species, the above kinetic behaviour could be expressed in terms of a general rate law as outlined in Equation (7).

$$k_{obs} = 2k_r[Red] \quad (7)$$

The values of k_r, estimated from the slope of the plots, are summarized in Table 3. The values of k_r at different temperatures were used to construct Eyring plots (Figure S5 in the Supporting Information) from which the values for $\Delta H^‡$ and $\Delta S^‡$ were determined. The rate and activation parameters for the reduction of [Ru^{III}(pac)(pz)] (pac = edta^{4-}, hedtra^{3-}) with Red are summarized in Table 4 for comparison purposes. The values of $\Delta H^‡$ (Table 4) are quite comparable to values reported for the reduction of [Ru^{III}(edta)(pz)]$^-$ with Red,[3,4] and consistent with the proposed outer-sphere electron-transfer mechanism for the presently studied system. However, the values of $\Delta S^‡$ observed in the present case are less negative than that found for the reduction of [Ru^{III}(edta)(pz)]$^-$ (Table 4). The entropy of activation ($\Delta S^‡$) for the reduction of [Ru^{III}(pac)(pz)] seems to be governed by the protonated or deprotonated forms of the reductants.

Table 3. The values of the second-order rate constant (k_r) for the reduction of [Ru^{III}(hedtra)(pz)] with biologically important reductants (Red) at pH 6.0. [Ru^{III}] = 1×10^{-4} M.

Red	T [°C]	k_r [M^{-1} s^{-1}]
H$_2$Asc	15	37 ± 1
	20	52 ± 1
	25	76 ± 2
	30	95 ± 3
	35	132 ± 4
H$_2$C	15	66 ± 2
	20	96 ± 2
	25	141 ± 3
	30	180 ± 5
	35	227 ± 6
CySH	15	0.09 ± 0.003
	20	0.14 ± 0.01
	25	0.23 ± 0.02
	30	0.34 ± 0.03
	35	0.50 ± 0.03

Table 4. Comparison of rate and activation parameters for the reduction of [Ru^{III}(pac)(pz)] by biologically important reductants (Red) at pH 6.0. [Ru^{III}] = 1×10^{-4} M.

pac	Red	k_r [M^{-1} s^{-1}] at 25 °C	$\Delta H^‡$ [kJ mol^{-1}]	$\Delta S^‡$ [J mol^{-1} deg^{-1}]
edta^{4-}	H$_2$Asc	225 ± 15	38 ± 3	–122 ± 11
	H$_2$C	285 ± 15	36 ± 4	–132 ± 12
	CySH	2.91 ± 0.1	56 ± 3	–44 ± 8
hedtra^{4-}	H$_2$Asc	76 ± 2	45 ± 1	–58 ± 3
	H$_2$C	141 ± 3	44 ± 2	–55 ± 7
	CySH	0.23 ± 0.02	62 ± 1	–47 ± 3

The [Ru^{III}(pac)(pz)] complexes are substitution inert,[1] and in the absence of any spectral evidence for the formation of an inner-sphere intermediate, the reduction of [Ru^{III}(pac)(pz)] by the biological reductants may be viewed as an outer-sphere electron-transfer process. In the present redox reaction, formation of a transient intermediate (**I**) through hydrogen bonding between the remote nitrogen of the coordinated ligand pyrazine in [Ru^{III}(hedtra)(pz)] and the reductant (Red) is postulated, which acts as a means in bringing the two reactants close enough so that electron transfer can takes place in an outer-sphere manner.

I
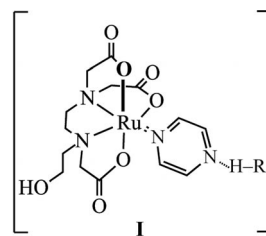
Since, no bond cleavage or bond formation take place in the activation process of the outer-sphere electron transfer, the reduction of the Ru^{III}–pac complexes by the reductants (H$_2$Asc, H$_2$C, CySH) seems to be thermodynamically controlled. This is supported by the fact that the rate of re-

D. Chatterjee, S. Ghosh, U. Pal, S. Mukhopadhyay

duction of [Ru^{III}(hedtra)(pz)] is slower in comparison with that of the reduction of its "edta" analogue[3,4] as the Ru^{III}–edta species is more oxidizing than Ru^{III}–hedtra.[1]

The antimicrobial activity of the [Ru^{III}(hedtra)(pz)] complex was tested on gram-negative bacteria (*E. coli* DH5α). The inhibition of *E. coli* growth was determined spectrophotometrically on the basis of the optical density (at 600 nm) of the cultured broth. As shown in Figure 4, inhibition of bacterial growth was not observed with an increasing amount of [Ru^{III}(hedtra)(pz)], however, a significant amount of inhibition of bacterial growth was found when the compound was added along with the cysteine. It is noteworthy that cysteine itself did not show any growth inhibition activity under the specified conditions.
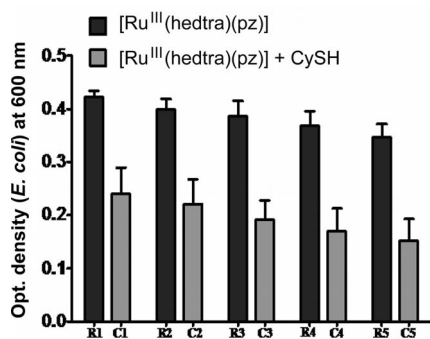
Figure 4. Comparison of the antimicrobial activity of [Ru^{III}(pac)(pz)] in the presence and absence of cysteine (CySH). The concentrations of the Ru compound at R1, R2, R3, R4 and R5 are 0.005 mM, 0.010 mM, 0.015 mM, 0.020 mM and 0.025 mM, respectively. The concentrations of cysteine at C1, C2, C3, C4 and C5 are 0.05 mM, 0.10 mM, 0.15 mM, 0.20 mM and 0.25 mM, respectively.

Considering the [Ru^{III}(pac)(pz)] complexes are substitution inert[1] towards binding DNA, the observed antimicrobial activity of the [Ru^{III}(hedtra)(pz)] complex is plausibly effected by the cleavage of the chromosomal DNA of the bacteria catalyzed by the [Ru^{III}(hedtra)(pz)] complex in the presence of CySH under an aerobic environment. In order to support the above argument we performed DNA cleavage studies independently using the [Ru^{III}(hedtra)(pz)] complex. The cleavage of supercoiled (SC; Form I) plasmid DNA (cDNA3) to its nicked circular form (NC; Form II) in the presence of the [Ru^{III}(hedtra)(pz)] complex, cysteine and oxygen was followed by gel electrophoresis studies. Control experiments using only [Ru^{III}(hedtra)(pz)] or only cysteine did not show any appreciable cleavage of DNA (Figure S6, lanes 2 and 3 in the Supporting Information). The cleavage efficiency increased with increasing cysteine concentration (Figure S6, lanes 4–6). On the basis of the above findings and considering the results of electron transfer of [Ru^{III}(hedtra)(pz)] with cysteine, the following working mechanism is proposed (Scheme 4) for the cleavage of the supercoiled plasmid by the [Ru^{III}(hedtra)(pz)]/cysteine/O$_2$ system at pH 7.2.

The oxidation potential of Ru–pac complexes lies in the range –0.29 to –0.15 V (vs. SCE).[1] Therefore, oxidation of the Ru^{II} species by molecular oxygen (O$_2$) is thermodynami-

$$2[Ru^{III}(hedtra)(pz)] + 2CyS^- \longrightarrow 2[Ru^{II}(hedtra)(pz)]^- + RSSR \quad (8)$$

$$[Ru^{II}(hedtra)(pz)]^- + O_2 \longrightarrow [Ru^{III}(edta)(pz)] + O_2^{\cdot-} \quad (9)$$

$$\begin{array}{c} Plasmid\ DNA + O_2^{\cdot-} \\ (Form\ I) \end{array} \longrightarrow \begin{array}{c} Plasmid\ DNA \\ (Form\ II) \end{array} \quad (10)$$
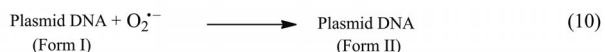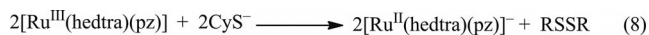
Scheme 4. Mechanism for DNA cleavage by the [Ru^{III}(hedtra)(pz)]/CySH/O$_2$ system.

cally favourable, and perhaps proceeds similar to Fenton's chemistry as proposed in Scheme 4 [Equation (9)] involving an outer-sphere oxidation of the metal ion leading to the formation of the corresponding Ru^{III} complex and superoxide radical. The superoxide radical (O$_2^{\cdot-}$), though indiscriminate in oxidative attack, presumably causes single-strand scission by attacking the deoxyribose unit leading to sugar fragmentation, followed by base release and then DNA cleavage.[16,17]

Conclusions

In conclusion, the results of the present study clearly demonstrate that the [Ru^{III}(hedtra)(pz)] complex, a neutral analogue of the Ru^{III}–pac family, can effectively be reduced by the biologically active reductants, L-ascorbic acid, catechol and cysteine to produce the corresponding Ru^{II} species, but at a slower rate as compared with that observed in the case of the negatively charged [Ru^{III}(edta)(pz)]$^-$ complex. The [Ru^{III}(hedtra)(pz)] complex demonstrates its antimicrobial activity by inhibiting the growth of *Escherichia coli* DH5α bacteria. The observed antimicrobial activity is presumably effected by the cleavage of the chromosomal DNA of the bacteria. The kinetic results obtained in the present investigation provide a mechanistic insight for better understanding the observed biological activity of the Ru–pac complexes in terms of the electron-transfer reaction.

Experimental Section

Materials: K[Ru^{III}(hedtra)Cl] was prepared by following the published procedure.[18] The micro-analysis and spectroscopic data are in good agreement with those reported in the literature.[18]. C$_{10}$H$_{15}$ClKN$_2$O$_7$Ru (450.86): calcd. C 26.6, H 3.4, N 6.2; found C 26.5, H 3.2, N 6.1. IR: $\tilde{\nu}$ = 1637 (coordinated –COO$^-$) cm^{-1}. UV/Vis in H$_2$O: λ_{max} (ε_{max}/M^{-1} cm^{-1}) = 285 (1250 ± 12) nm. The K[Ru^{III}(hedtra)Cl] complex rapidly converts into the [Ru^{III}(hedtra)(H$_2$O)] complex when dissolved in water.[18] The pK_a value related to the proton-dissociation equilibrium of the coordinated water molecule is 4.9 at 25 °C.[18] All other chemicals used were of A. R. grade. Doubly distilled H$_2$O was used throughout the experiments.

Instrumentation: The UV/Vis spectra were recorded with a Varian Model Cary 100 Bio. A Perkin–Elmer Model Lambda 783 spectrophotometer was used for obtaining IR spectra (using KBr pellets). A Perkin–Elmer 240C elemental analyzer was used to collect microanalytical (C, H, N) data. Fast kinetic measurements were performed with a stopped-flow spectrophotometer (TgK Scientific, SF-61SX2) coupled to a (KinetaScan) rapid-scan spectral attach-

ment. The slow reactions were followed spectrophotometrically adopting a conventional mixing technique using the Varian Model Cary 100 Bio spectrophotometer. A tandem cuvette was used for this purpose. The instrument was thermostatted at the desired temperature (±0.1 °C) using a Cary Single Peltier accessory. Acetate, phosphate and borate buffers were used to adjust the pH of the experimental solutions. A Mettler Delta 350 pH meter was used for pH measurements. Observed rate constants (k_{obs}) are presented as an average of several kinetic runs (at least 5–8) and were reproducible within ±4%.

Biological Studies: The bacterial strain used in this study is *Escherichia coli* DH5α. Strains were maintained on Luria–Bertani (LB) broth (Himedia). The bacterial count was also calculated spectrophotometrically by determining the optical density (OD) of the bacterial culture at 600 nm. The sterile LB broth was used as a blank reference. The serially diluted bacterial culture (1 mL) was collected in the cuvette and the optical density was read at 600 nm against the blank. The number of cells mL^{-1} in the culture was calculated by the standard population vs. absorbance relation of *E. coli* DH5α. (1 OD of the culture = 1×10^9 cells mL^{-1}). The antimicrobial activity of the [Ru^{III}(hedtra)(pz)] complex was tested on gram-negative bacteria (*E. coli* DH5α) by adopting a procedure reported by Bolhuis et al.[19]

DNA Cleavage Studies: The cleavage of the supercoiled plasmid cDNA3 by the [Ru^{III}(hedtra)(pz)] complex was carried out at pH 7.2 by adopting a related procedure reported earlier.[20] The buffer, DNA, [Ru^{III}(hedtra)(pz)] complex and sufficient water were premixed in an Eppendorf vial, then cysteine was added and the reaction was allowed to proceed for 30 min at 37 °C before being loaded onto agarose gel. The conversion of super coiled (Form-I) to open circular (Form-II) was followed by agarose gel electrophoresis of plasmid DNA performed at 50 V on 1% slab gels containing 0.5 µg mL^{-1} ethidium bromide. The DNA was visualized by photographing the fluorescence of the intercalated ethidium bromide under UV illumination.

Supporting Information (see footnote on the first page of this article): See Figure S1 for a plot of k_{obs} vs. [pz] concentration, Figure S2 for spectral changes, Figure S3 for the kinetic trace, Figure S4 for a plot of k_{obs} vs. [CySH], Figure S5 for an Eyring plot and Figure S6 for DNA cleavage.

Acknowledgments

[1] D. Chatterjee, *Coord. Chem. Rev.* **1998**, *168*, 273–293, and references cited therein.

[2] D. Chatterjee, A. Mitra, G. S. De, *Platinum Met. Rev.* **2006**, *50*, 2–12.

[3] D. Chatterjee, *J. Chem. Soc., Dalton Trans.* **1996**, 4389–4392.

[4] D. Chatterjee, U. Pal, S. Ghosh, R. van Eldik, *Dalton Trans.* **2011**, *40*, 1302–1306.

[5] D. Chatterjee, A. Mitra, R. van Eldik, *Dalton Trans.* **2007**, 943–948.

[6] D. Chatterjee, A. Sikdar, V. R. Patnam, A. Thedoridis, R. van Eldik, *Dalton Trans.* **2008**, 3851–3856.

[7] F. Wang, H. Chen, J. A. Parkinson, P. S. Murdoch, P. J. Sadler, *Chem. Rev.* **1999**, *99*, 2511–2533.

[8] R. E. Morris, R. E. Aird, P. d. S. Murdoch, H. Chen, J. Cummings, N. D. Hughes, S. Parsons, A. Parkin, G. Boyd, D. I. Jodrell, P. J. Sadler, *J. Med.* **2001**, *44*, 3616–3621.

[9] M. Kimura, M. Yamamoto, S. Yamabe, *J. Chem. Soc., Dalton Trans.* **1982**, 423–427.

[10] D. H. Macartney, N. Sutin, *Inorg. Chim. Acta* **1983**, *74*, 221–228.

[11] K. Lemma, M. Sargeson, L. I. Elding, *J. Chem. Soc., Dalton Trans.* **2000**, 1167–1172.

[12] K. Lemma, D. A. House, N. Retta, L. I. Elding, *Inorg. Chim. Acta* **2002**, *331*, 98–108.

[13] J. H. Espenson in *Chemical Kinetics and Reaction Mechanism*, McGraw-Hill, New York, **1981**, pp. 172–176.

[14] C. Timberlake, *J. Chem. Soc.* **1957**, 997, 4987–4993.

[15] D. E. Green, *Biochem. J.* **1933**, *27*, 678–689.

[16] R. P. Hertzberg, P. B. Dervan, *J. Am. Chem. Soc.* **1982**, *104*, 313–315.

[17] R. P. Hertzberg, P. B. Dervan, *Biochemistry* **1984**, *23*, 3934–3945.

[18] H. C. Bajaj, R. van Eldik, *Inorg. Chem.* **1989**, *28*, 1980–1983.

[19] A. Bolhuis, L. Hand, J. E. Marshall, A. D. Richards, A. Rodger, J. Aldrich-Wright, *Eur. J. Pharma. Sci.* **2011**, *42*, 313–317.

[20] M. G. Clarke, B. Jansen, K. A. Marx, R. Kruger, *Inorg. Chim. Acta* **1986**, *124*, 13–28.

Langmuir–Blodgett Films of Hexamolybdate and Naphthylamine Prepared by Two Different Approaches: Synthesis, Characterization, and Materials Properties

Qian Liu,[a,b] Lei Hu,[a] Hui Fu,[a] Jun Yang,[a] Qiao-Min Fu,[a] Li Liu,*[a] Shi-Zhong Liu,[a] Zu-Liang Du,[c] Cheuk-Lam Ho,[b] Feng-Rong Dai,[b] and Wai-Yeung Wong*[b]

Two novel covalently-linked organic-inorganic hybrid compounds [(n-C$_4$H$_9$)$_4$N]$_2$[Mo$_6$O$_{18}${≡N–(2-Np)}] (NA–Mo6) and [(n-C$_4$H$_9$)$_4$N]$_2$[Mo$_6$O$_{17}${≡N–(1-Np)}$_2$] (NA2–Mo6) (2-Np = 2-naphthyl; 1-Np = 1-naphthyl) have been prepared by the reaction of 2-naphthylamine (2-NpNH$_2$) or 1-naphthylamine (1-NpNH$_2$) with [(n-C$_4$H$_9$)$_4$N]$_2$[Mo$_6$O$_{19}$] (Mo6) in the presence of N,N'-dicyclohexylcarbodiimide (DCC) in anhydrous acetonitrile, and have been characterized by ^{1}H NMR, IR, UV/Vis, and fluorescence spectra as well as X-ray crystallography. Structural analyses reveal the formation of self-assembled infinite 1-D and 3-D supramolecular frameworks. The UV/Vis spectra of NA–Mo6 and NA2–Mo6 show that the lowest energy electronic transfers occur at 362 and 394 nm, respectively, which are dramatically red-shifted when compared to that of Mo6. The luminescence studies show that Mo6 can notably quench the emission of naphthylamine. Monolayer and multilayer films of NA–Mo6 and NA2–Mo6

were fabricated on different substrates by the Langmuir–Blodgett (LB) technique using H$_2$O as the subphase. For comparison, another two types of organic-inorganic hybrid films composed of noncovalently-linked 1-NpNH$_2$/Mo6 and 2-NpNH$_2$/Mo6 systems were also deposited onto the same substrates under the same conditions by the LB technique using an aqueous solution of Mo6 as the subphase. The as-prepared organic-inorganic hybrid films were characterized by π-A isotherms, UV/Vis absorption spectra, photoluminescence spectra, and scanning tunneling microscopy. The results indicate that stable monolayers can be formed at the air–water interface for NA–Mo6 and NA2–Mo6, and at the air–Mo6 solution interface for 1-NpNH$_2$ and 2-NpNH$_2$. The four LB films containing NA–Mo6, NA2–Mo6, 1-NpNH$_2$/Mo6, and 2-NpNH$_2$/Mo6 display interesting electrical conductivity.

Introduction

The design, synthesis, and structural characterization of new hybrid materials through the assembly of organic and inorganic building blocks, for which many applications can be predicted, is an important research area in materials science.[1] The construction of such organic-inorganic hybrids is useful for obtaining multifunctional materials with new electrical and/or optical properties.[2] A key aim for the design of new hybrid materials is the tuning of the nature, extent, and accessibility of the inner interfaces. The nature of the interface or of the links and interactions exchanged

by the organic and inorganic components has been used to categorize these hybrids into two main classes.[3–5] Class I corresponds to systems where no covalent or iono-covalent bonds are present between the organic and inorganic components. In such materials, the various components exchange only weak interactions (at least in terms of orbital overlap) such as hydrogen bonding, van der Waals attractions, or electrostatic forces. In contrast, in class II materials, at least a fraction of the organic and inorganic components are linked through strong chemical bonds (covalent, iono-covalent, or Lewis acid-base bonds). The chemical strategy for the construction of class II hybrid networks depends, of course, on the relative stability of the chemical links that are associated with the different components.

The Langmuir–Blodgett (LB) film processing offers the opportunity to create film materials with well-defined structure and thickness, controlled at a molecular level.[6,7] The LB method has been widely applied to make ultrathin films with specific architectures, which can be exploited as chemosensors or biosensors, modified electrodes, optical logic gates, or molecular electronic devices.[8,9]

Thanks to their topological and electronic versatilities, polyoxometalate (POM) anions represent a class of inor-

[a] Ministry of Education Key Laboratory for the Synthesis and Application of Organic Functional Molecules and School of Chemistry and Chemical Engineering, Hubei University, Wuhan 430062, People's Republic of China
Fax: +86-27-88663043
E-mail: liulihubei@gmail.com
[b] Institute of Molecular Functional Materials and Department of Chemistry and Centre for Advanced Luminescence Materials, Hong Kong Baptist University, Waterloo Road, Hong Kong, People's Republic of China
Fax: +852-34117348
E-mail: rwywong@hkbu.edu.hk
[c] Key Laboratory of Special Functional Materials, Henan University, Kaifeng 475001, People's Republic of China

ganic compounds that have found wide applications in catalysis, biology, medicine, and materials science.[10,11] Remarkably, they can act as electron reservoirs and are reversibly reduced by the addition of various numbers of electrons to give mixed-valence species. On the other hand, conjugated organic molecules and polymers are electrically and optically active materials and their molecular structures and photo-electric properties are easily modified. Therefore, the molecular nature of these two types of materials offers the opportunity to form covalently-bonded molecular hybrids where the interplay between cluster d electrons and organic delocalized π electrons can be explored at the molecular level.[12] Specifically, the surface modification of POMs with organic species can provide a platform to conveniently and effectively construct novel organic-inorganic hybrid materials with the so-called "value-added properties"[13] and possible synergistic effects.[14]

Over the past few years, a number of organoimido derivatives of Lindqvist-type polyoxometalates such as the hexamolybdate ion $[Mo_6O_{19}]^{2-}$ and hexatungstate ion $[W_6O_{19}]^{2-}$ have been directly or indirectly synthesized by three remarkable synthetic strategies towards organic and organometallic modified POMs, which include reactions with phosphinimines, isocyanates, and aromatic amines.[15]

Recently, an efficient and convenient reaction protocol has been developed to prepare the monofunctionalized arylimido derivatives of hexamolybdate and pentatungstenmolybdate with N,N′-dicyclohexylcarbodiimide (DCC) as the dehydrating agent.[16] To date, there are a number of organic derivatives of POMs synthesized by Wei and coworkers from the DCC dehydrating protocol of the reaction of POMs and aromatic amines.[17] A naphthylimide monosubstituted hexamolybdate has been prepared by the reaction of 1-amino-2-methylnaphthalene hydrochloride with an octamolybdate in the presence of DCC.[18] Here, we have prepared two new naphthylimide-monosubstituted (NA–Mo6) and -disubstituted hexamolybdate complexes in a trans configuration (NA2–Mo6) using (1- or 2-)naphthylamine and Lindqvist hexamolybdate (Scheme 1). While the latter disubstituted complex was generally difficult to prepare, only a few examples of trans-disubstituted hexamolybdates have been reported to date.[19] The structures of these two new compounds were characterized by ^{1}H NMR, IR, UV/Vis, and fluorescence spectroscopy as well as X-ray crystallography. We have also used two different strategies to construct LB films for the first time in order to compare the differences in structure and properties between these two sets of films. The as-prepared LB films were characterized by surface pressure-area (π-A) isotherm measurements, UV/Vis spectra, low-angle X-ray diffraction (LAXRD), photoluminescence spectra, and scanning tunneling microscopy. The results indicate that these LB films display similar structural features and electrical conductivity.

Results and Discussion

Synthesis and Characterization of Organoimido Compounds NA–Mo6 and NA2–Mo6

Scheme 1 outlines the synthesis of NA–Mo6 and NA2–Mo6. When a mixture of 2-NpNH₂, Mo6, and DCC is refluxed in anhydrous acetonitrile, the monofunctionalized 2-naphthylimido derivative of NA–Mo6 is formed, while the trans-coordinated bis(1-naphthylimido) derivative of NA2–Mo6 is obtained from a mixture of 1-NpNH₂, Mo6, and DCC in anhydrous acetonitrile under reflux. These metathesis reactions are usually completed in about 12 h. The key role of DCC here is to act as a dehydrating agent and activate the carboxyl group in the synthesis of an amide or peptide.[17a] In our tests, the amount of DCC is equivalent to or just slightly higher than that of the water that must be removed from the reaction system. Excess DCC usually results in unexpected side reactions and reduces the yield of the products.[17a]
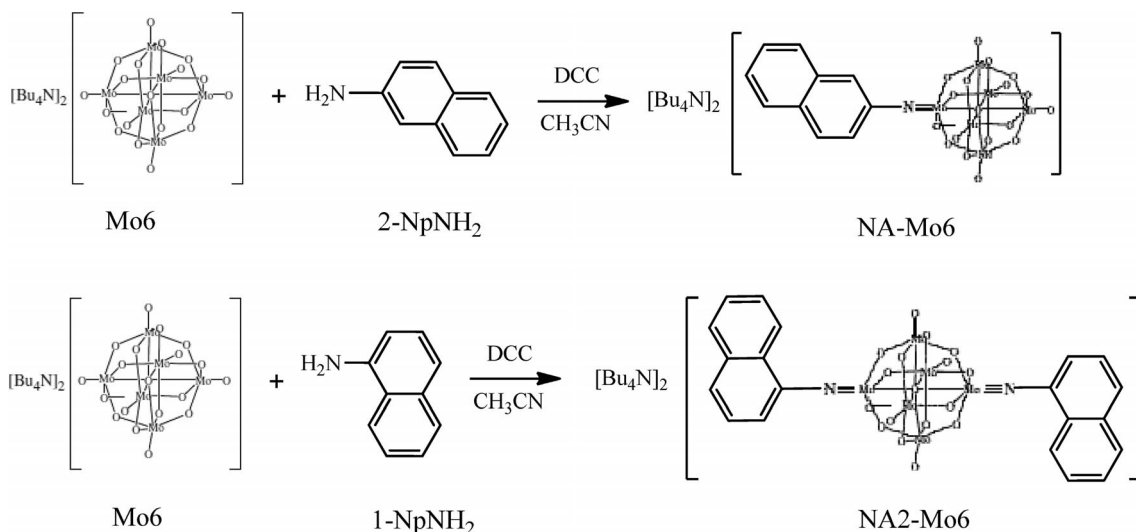
Scheme 1. Synthesis of NA–Mo6 and NA2–Mo6.

X-ray Structural Analysis

A summary of the pertinent crystallographic data for NA–Mo6 and NA2–Mo6 is provided in Table 1. Selected bond lengths and angles are listed in Tables 2, 3, and 4. Crystals of the two compounds suitable for X-ray crystal structure determination were obtained from recrystallization in acetone. Perspective views of their molecular structures together with their crystal packing diagrams are depicted in Figures 1 and 2. The compound NA–Mo6 crystallizes in the monoclinic space group $P2_1/n$ showing no π–π stacking interactions between naphthyl rings in the cell

packing. Single-crystal structural analysis shows that the arylimido ligand is covalently bonded to a terminal position of the hexamolybdate metal core in NA–Mo6. The short Mo(1)–N(1) bond length of 1.735(4) Å and the C(1)–N(1)–Mo(1) bond angle of 165.6(4)° are typical of organoimido groups bonded at an octahedral d⁰ metal center and are consistent with a substantial degree of Mo≡N triple-bond character.[20] It is apparent that intermolecular hydrogen-bonding interactions [C(9)–H(9A)⋯O(13), 2.62 Å; C(5)–H(5A)⋯O(5), 2.60 Å] exist among the molecules resulting in the Mo–N–C bond bending and deviating from 180° (part b of Figure 1 and Table 3). Notable short contact interactions for C–H⋯O (2.30–2.65 Å) between the C–H bond of Bu₄N⁺ and oxygen atom of the Mo₆ cluster anion were observed as well. Also, the Mo(1)–O(18) bond distance between the Mo atom with the imido group and the central oxygen atom within the cluster anion cage is remarkably shorter than the other five Mo–O(18) bond distances. A similar contraction has also been observed in the other imido derivatives of Lindqvist hexametalates.[21–24] Close examination of the crystal packing in NA–Mo6 shows that solid-phase dimerization of the cluster core through hydrogen-bonding interactions leads to an infinite 3-D supramolecular framework (Figure 1, c). For the disubstituted derivative NA2–Mo6, similar structural features were noted for the Mo₆ cluster core. There are also intermolecular hydrogen bonds between adjacent anions [C(4)–H(4A)⋯O(2), 2.65 Å] as well as C–H⋯O interactions (2.33–2.71 Å) for the Bu₄N⁺ and Mo₆O₁₇ groups in the unit cell (Figure 2, b and Table 4). Interestingly, an infinite 1-D sup-

Table 1. Crystal data and structural refinement for NA–Mo6 and NA2–Mo6.

	NA–Mo6	NA2–Mo6·2(CH₃)₂CO
Empirical formula	C₄₂H₇₉Mo₆N₃O₁₈	C₅₈H₉₈Mo₆N₄O₁₉
M_r [gmol⁻¹]	1489.72	1731.04
Crystal system	monoclinic	monoclinic
Space group	$P2_1/n$	$P2_1/c$
a [Å]	18.02(1)	12.792(2)
b [Å]	15.62(1)	16.431(3)
c [Å]	20.75(2)	17.780(3)
α [°]	90.00	90.00
β [°]	104.65(1)	105.198(3)
γ [°]	90.00	90.00
V [Å³]	5648(7)	3606(1)
$F(000)$	2992	1756
Z	4	2
ρ_{calcd} [gcm⁻³]	1.752	1.594
μ [mm⁻¹]	1.358	1.077
θ range [°]	2.41–25.00	2.48–28.25
Total reflections	26647	22343
Unique reflections	9657	8682
R_{int}	0.0344	0.0305
Observed reflections [$I > 2\sigma(I)$]	6403	6419
Final R indices [$I > 2\sigma(I)$][a]	$R_1 = 0.0366$	$R_1 = 0.0300$
	$wR_2 = 0.0862$	$wR_2 = 0.0526$
Final R indices [all data]	$R_1 = 0.0711$	$R_1 = 0.0674$
	$wR_2 = 0.1046$	$wR_2 = 0.0768$

[a] $R_1 = \Sigma(|F_o|-|F_c|) / \Sigma|F_o|$, $wR_2 = \{\Sigma[w(F_o^2 - F_c^2)^2] / \Sigma[w(F_o^2)^2]\}^{1/2}$.

Table 2. Selected bond lengths [Å] and angles [°] for NA–Mo6 and NA2–Mo6.

	NA–Mo6		NA2–Mo6
Mo(1)–N(1)	1.735(4)	Mo(1)–N(1)	1.737(2)
C(1)–N(1)	1.415(6)	C(1)–N(1)	1.386(3)
Mo(1)–O(1)	1.902(4)	Mo(1)–O(1)	1.941(2)
Mo(1)–O(4)	1.960(4)	Mo(1)–O(4)	1.953(2)
Mo(1)–O(9)	1.912(4)	Mo(1)–O(9)	2.2511(4)
Mo(1)–O(18)	2.232(3)	Mo(1)–O(2)	1.944(2)
Mo(2)–O(13)	1.675(4)	Mo(2)–O(5)	1.683(2)
Mo(2)–O(18)	2.318(3)	Mo(2)–O(6)	1.875(2)
Mo(3)–O(14)	1.685(4)	Mo(2)–O(8)	2.025(2)
Mo(3)–O(18)	2.364(3)	Mo(2)–O(9)	2.3596(5)
Mo(4)–O(15)	1.677(4)	Mo(3)–O(6)	2.026(2)
Mo(4)–O(18)	2.309(3)	Mo(3)–O(8)	1.873(2)
Mo(5)–O(16)	1.684(4)	Mo(3)–O(9)	2.3574(5)
Mo(5)–O(18)	2.338(3)	Mo(3)–O(7)	1.690(2)
Mo(6)–O(17)	1.679(4)	Mo(3)–O(3)	1.914(2)
Mo(6)–O(18)	2.323(3)	Mo(3)–O(1)	1.908(2)
C(1)–N(1)–Mo(1)	165.6(4)	C(1)–N(1)–Mo(1)	174.7(2)
N(1)–Mo(1)–O(1)	104.3(2)	N(1)–Mo(1)–O(1)	100.7(1)

Table 3. Hydrogen-bonding geometry [Å] of NA–Mo6.

D–H⋯A	D–H	H⋯A	D⋯A	D–H⋯A
C5–H5A⋯O5A[a]	0.93	2.60	3.525(8)	175.9
C9–H9A⋯O13A[b]	0.93	2.62	3.282(7)	129.0
C15–H15B⋯O1	0.97	2.30	3.259(6)	168.9
C18–H18B⋯O8A[c]	0.96	2.56	3.390(9)	145.2
C19–H19B⋯O17A[d]	0.97	2.50	3.386(7)	152.0
C21-H21A⋯O17A[d]	0.97	2.65	3.523(11)	149.9
C25–H25B⋯O14A[d]	0.97	2.50	3.399(7)	154.3
C27–H27A⋯O4A[e]	0.97	2.48	3.130(8)	124.4
C29–H29B⋯O15A[f]	0.97	2.63	3.543(11)	157.5
C35–H35A⋯O15A[g]	0.97	2.34	3.184(9)	144.9
C15–H15B⋯O1	0.97	2.30	3.259(6)	168.9

[a] Symmetry codes: 2 − x, −y, 1 − z. [b] 1.5 − x, −0.5 + y, 1.5 − z. [c] −x + 1.5, y − 0.5, −z + 1.5. [d] x − 0.5, −y + 0.5, z − 0.5. [e] −x + 1.5, y + 0.5, −z + 1.5. [f] 1.5 − x, 0.5 + y, 1.5 − z. [g] x − 1, y, z.

Table 4. Hydrogen-bonding geometry [Å] of NA2–Mo6.

D–H⋯A	D–H	H⋯A	D⋯A	D–H⋯A
C11–H11B⋯O4A[a]	0.97	2.33	3.261(4)	160.1
C4–H4A⋯O2A[b]	0.93	2.65	3.280(4)	125.5
C15–H15A⋯O6A[c]	0.97	2.46	3.201(4)	133.4
C16–H16A⋯O8A[d]	0.97	2.59	3.384(4)	138.7
C19–H19A⋯O3A[d]	0.97	2.50	3.325(4)	142.3
C23–H23A⋯O6A[c]	0.97	2.56	3.321(3)	135.6
C23–H23B⋯O7A[e]	0.97	2.71	3.486(4)	137.5

[a] Symmetry codes: x + 1, y, z. [b] 1 − x, 1 − y, 1 − z. [c] x + 1, −y + 0.5, z + 0.5. [d] 1 − x, 1 − y, 1 − z. [e] 1 + x, 0.5 − y, 0.5 + z.

ramolecular chain was formed through π–π stacking (ca. 3.694 Å) between the naphthyl rings attached to Mo(1) and Mo(1A) atoms on two neighboring anions (see Figure 2, c).

(a)

(b)

(c)
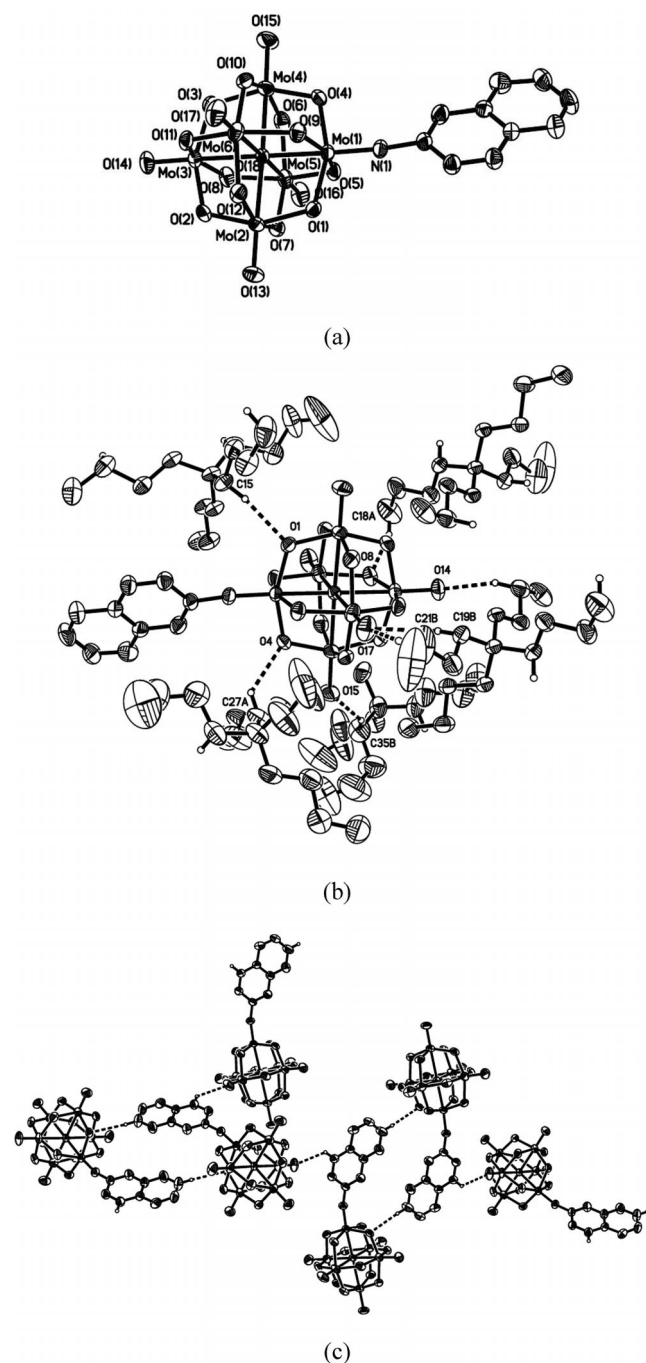
Figure 1. (a) A perspective view and atomic labeling scheme for the anion in NA–Mo6, (b) the C–H···O hydrogen-bonding interactions, and (c) the formation of an infinite 3-D supramolecular framework in the crystal packing.

Spectroscopic Characterization

The ¹H NMR spectra (in CD₃COCD₃) of NA–Mo6 and NA2–Mo6 show clearly resolved signals, all of which can be unambiguously assigned. As shown in Figure 3 and Fig-

(a)

(b)

(c)
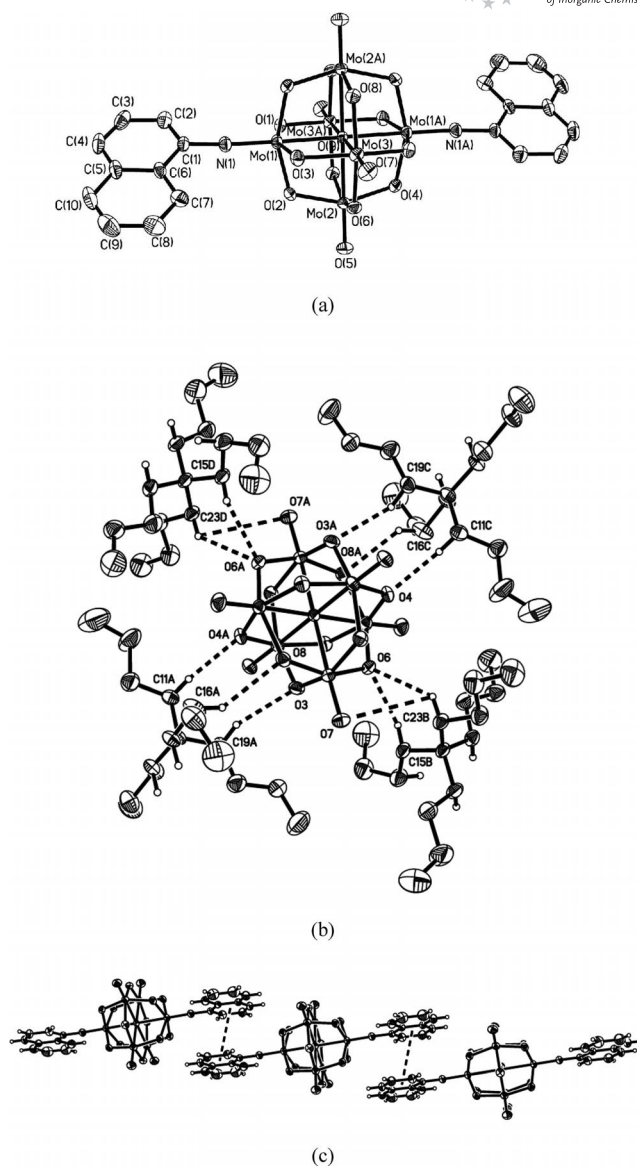
Figure 2. (a) A perspective view and atomic labeling scheme for the anion in NA2–Mo6, (b) the C–H···O hydrogen-bonding interactions, and (c) the formation of an infinite 1-D supramolecular chain in the crystal packing.

ure 4, the integral peak intensities match well with the proposed structure. Compared to the ¹H NMR spectra of the starting naphthylamines 2-NpNH₂ and 1-NpNH₂, all the protons of NA–Mo6 and NA2–Mo6, except for those in the tetrabutylammonium cation, exhibit significantly downfield chemical shifts, which are consistent with the electron-withdrawing nature of the metal core in Mo6.

The IR spectra of compounds NA–Mo6 and NA2–Mo6 (see Figure 5) resemble that of the parent species Mo6. In the low wavenumber region (<1000 cm⁻¹), both NA–Mo6 and NA2–Mo6 display a pattern characteristic of the Lindqvist structure: two very strong bands of the Mo–O$_t$ and Mo–O$_b$–Mo asymmetric stretching vibrations at ca. 953 and 796 cm⁻¹, respectively, for NA–Mo6 and 946 and 790 cm⁻¹, respectively, for NA2–Mo6. Compared with the
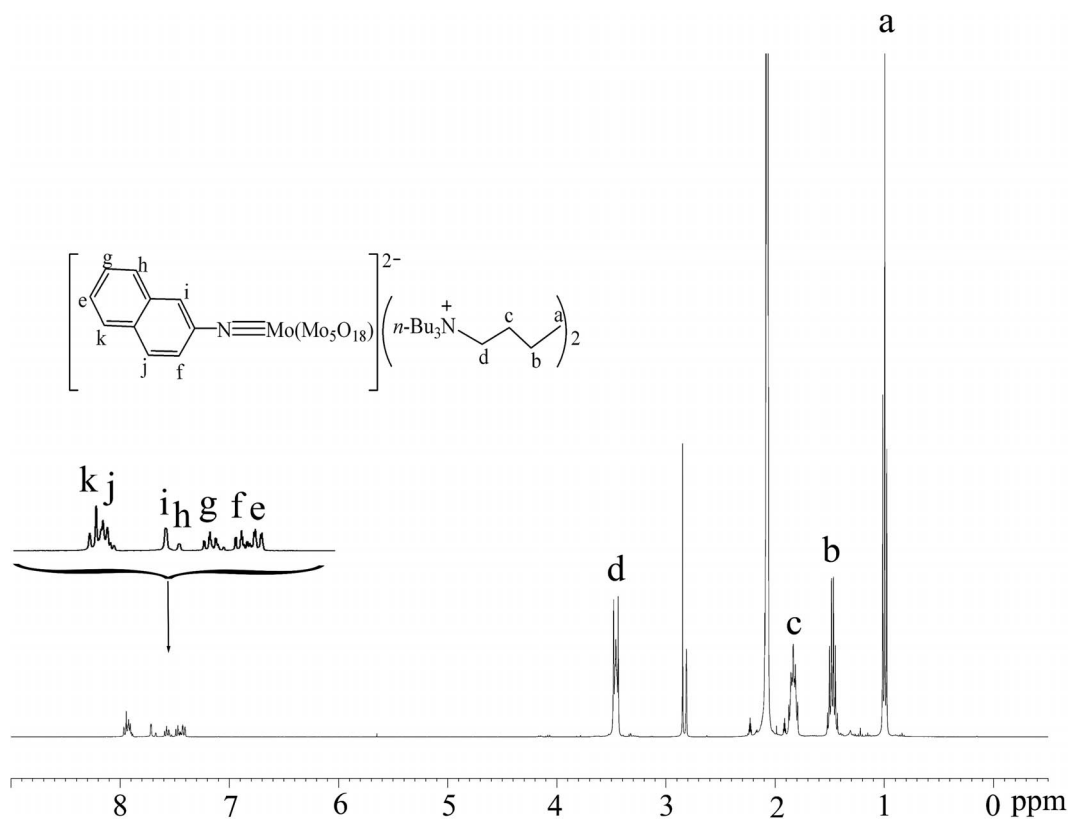
Figure 3. ^{1}H NMR spectrum of NA–Mo6 in CD_3COCD_3.
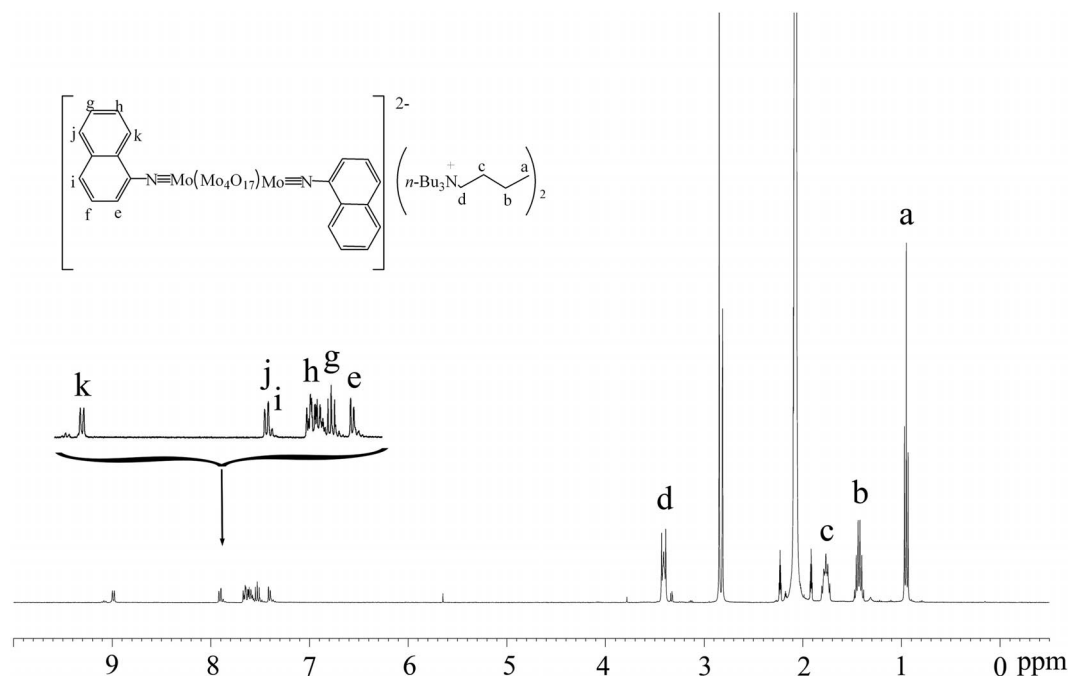
Figure 4. ^{1}H NMR spectrum of NA2–Mo6 in CD_3COCD_3.

Mo–O_t stretching (957 cm^{-1}) and Mo–O_b–Mo asymmetric stretching vibrations (799 cm^{-1}) for Mo6, a bathochromic shift can be observed in NA–Mo6 and NA2–Mo6, which implies that these bonds are weakened to some extent due to the stronger Mo≡N bonding interaction than that in Mo=O, when the terminal oxygen atom is replaced by the organoimido ligand. The band near 976 cm^{-1} usually appears as a strong shoulder peak for the Mo–O_t stretching,

which is diagnostic for the monosubstituted and disubstituted organoimido hexamolybdates derived from the Mo–N bond stretching vibration. However, the IR bands of the naphthylamine ligand in this region [mostly γ(C–C and C–H)] are of low intensity with respect to those of the polyoxometalate framework. In the high-frequency region, the aromatic γ(Ar–H) bands (>3000 cm^{-1}) are hardly visible because of their low intensity, and the complex pattern around 2900 cm^{-1} corresponds to the aliphatic γ(C–H) bands of the tetrabutylammonium cation. In the medium-frequency region (1650–1000 cm^{-1}) there are characteristic peaks from γ(C–N), the bands at 1585 and 1482 cm^{-1} that were shown to be associated with γ(C=C) of the naphthalene mode, the 1380 and 1393 cm^{-1} peaks that were assigned to δ(C–H) of the NBu$_4$ cation; and the 1321 cm^{-1} band from the γ(C–N) of the naphthyl group.
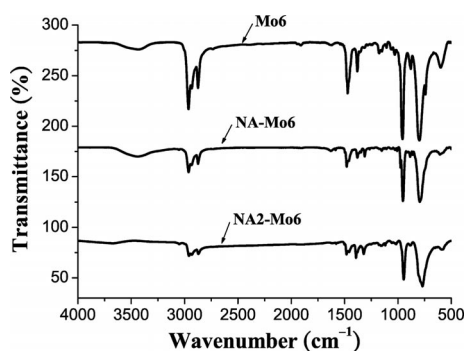
Figure 5. IR spectra of NA–Mo6 and NA2–Mo6 as compared to the parent compound Mo6.

The solution UV/Vis absorption spectra of NA–Mo6, Mo6, and 2-NpNH$_2$ are shown in Figure 6, and that of NA2–Mo6 and the corresponding starting materials are shown in Figure 7. The lowest-energy electronic transition at 325 nm in [Mo$_6$O$_{19}$]$^{2-}$ of Mo6 was assigned to a charge-transfer transition from the oxygen π-type highest occupied molecular orbital (HOMO) to the molybdenum π-type lowest unoccupied molecular orbital (LUMO). This band is bathochromically shifted by 37 and 69 nm for NA–Mo6 and NA2–Mo6, respectively, and becomes considerably more intense in NA–Mo6 (362 nm) and NA2–Mo6 (394 nm) due to the charge-transfer transition from the coordinated N atom to the molybdenum atom (LMCT). This indicates that the Mo–N π bond is formed and the delocalization of organic conjugated π electrons has extended from the naphthalene ring to the hexamolybdate skeleton. In other words, there is a strong electronic interaction between the metal–oxygen cluster and the conjugated organic segment(s) in the hybrid compounds. The band near 254 nm in [Mo$_6$O$_{19}$]$^{2-}$, originating from the n–π transition from the oxygen π-type nonbonding orbitals to the molybdenum π-type LUMO, shows no obvious variation from that in the hybrid compounds, which implies that the incorporated naphthylimido ligands have little effect on the skeleton of the hexamolybdate and the energy levels of the oxygen π-type nonbonding orbitals in these cluster anions are almost identical.
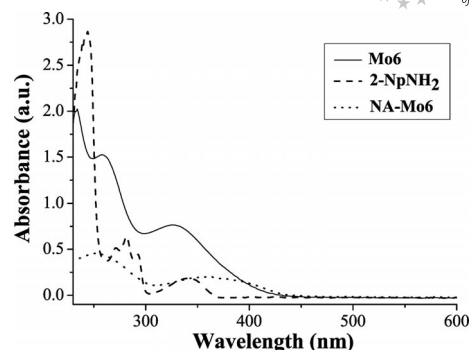
Figure 6. UV/Vis absorption spectra of NA–Mo6, Mo6, and 2-NpNH$_2$ in CH$_2$Cl$_2$.
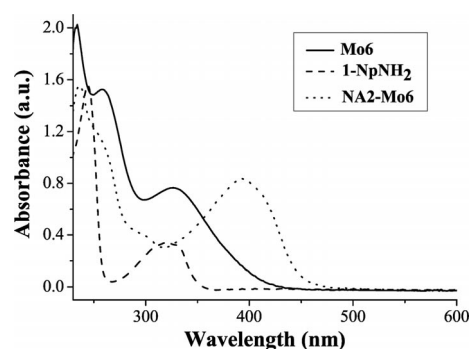
Figure 7. UV/Vis absorption spectra of NA2–Mo6, Mo6, and 1-NpNH$_2$ in CH$_2$Cl$_2$.

The fluorescence spectra of NA–Mo6, Mo6, and 2-NpNH$_2$ with the excitation wavelength at 334 nm are shown in Figure 8, and that of NA2–Mo6, Mo6, and 1-NpNH$_2$ with the excitation wavelength at 330 nm are shown in Figure 9. Compared with the luminescence of the tetrabutylammonium salt of [Mo$_6$O$_{19}$]$^{2-}$ (359 nm) and naphthylamines, the hybrid compounds are much less fluorescent than free naphthylamines. Presumably, the nonemissive LMCT excited state quenches most of the π–π* transition states.
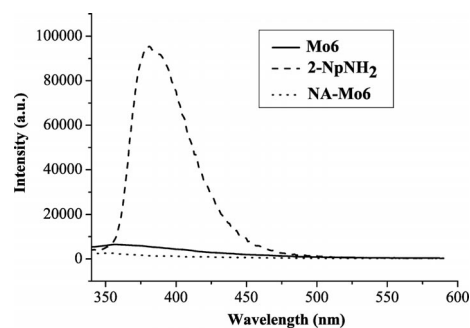
Figure 8. Fluorescence spectra of NA–Mo6, Mo6, and 2-NpNH$_2$ in CH$_2$Cl$_2$.
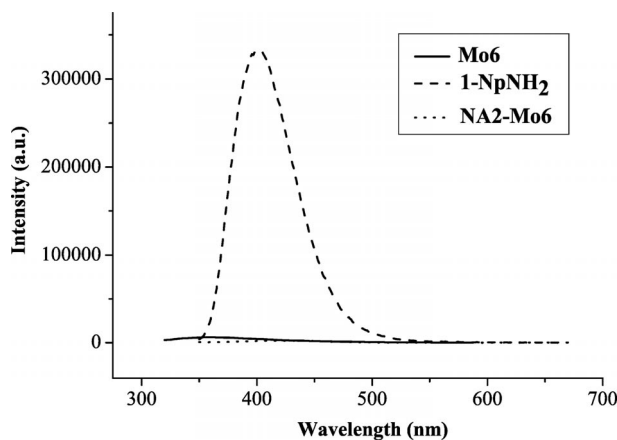
Figure 9. Fluorescence spectra of NA2–Mo6, Mo6, and 1-NpNH$_2$ in CH$_2$Cl$_2$.

π-A Isotherm of Two LB Films Containing NA–Mo6 and 2-NpNH$_2$/Mo6 Monolayers

Figure 10 depicts the surface pressure-area (π-A) isotherms of NA–Mo6 on a pure-water subphase corresponding to the NA–Mo6 monolayer as well as 2-NpNH$_2$ on a Mo6 aqueous subphase corresponding to the 2-NpNH$_2$/Mo6 monolayer at room temperature. The results show that they can form stable monolayer Langmuir films at the air–liquid interface. The molecular area of NA–Mo6 and 2-NpNH$_2$/Mo6 films can be estimated by extrapolating the line part of the π-A isotherm to the abscissa in each case. The relevant data are collected in Table 5. For the NA–Mo6 film, the limiting area per molecule is 0.17 nm^2, whereas that of 2-NpNH$_2$/Mo6 is 0.14 nm^2. The collapse pressure of NA–Mo6 is 26.4 mN m^{-1}, larger than that of 2-NpNH$_2$/

Mo6 (22.4 mN m^{-1}), which implies that the stability of the LB films of the covalently linked hybrid is better than that of the noncovalently-linked analogue. A similar situation was noted for the other pair (1-NpNH$_2$/Mo6 vs. NA2–Mo6, see Figure 11).
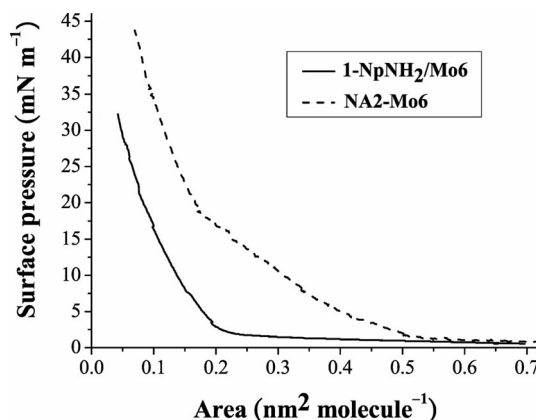
Figure 11. Surface pressure-area (π-A) isotherms of monolayer films of 1-NpNH$_2$/Mo6 and NA2–Mo6.

UV/Vis Spectroscopy

The 13-layer 2-NpNH$_2$/Mo6 and 13-layer NA–Mo6 LB films of high morphological stability were successfully deposited onto quartz substrates by the vertical method. The transfer ratio was almost unity in both the dipping and lifting processes, indicating the formation of Y-type LB films. As shown in Figure 12 and Table 6, 2-NpNH$_2$/Mo6 and

Figure 10. Surface pressure-area (π-A) isotherms of monolayer films of 2-NpNH$_2$/Mo6 and NA–Mo6.
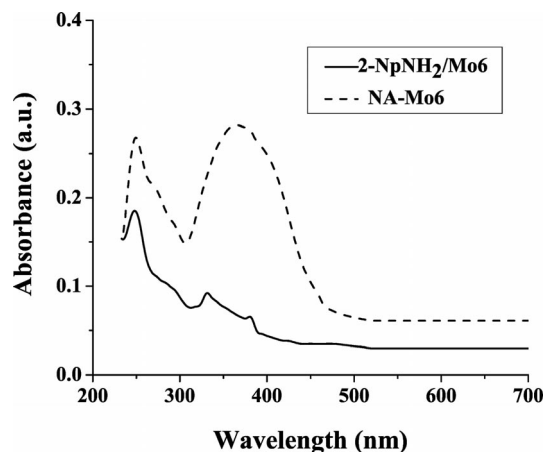
Figure 12. UV/Vis spectra of LB films (13-layer) of 2-NpNH$_2$/Mo6 and NA–Mo6.

Table 5. Surface pressure-area isotherms of the LB films.

Film	Cross section [nm^2 molecule^{-1}]	Collapse pressure [mN m^{-1}]
2-NpNH$_2$/Mo6	0.14	22.4
NA–Mo6	0.17	26.4
1-NpNH$_2$/Mo6	0.22	32.2
NA2–Mo6	0.28	43.7

Table 6. Absorption data for the LB films.

LB film	λ_{max} [nm]
2-NpNH$_2$/Mo6	248, 331, 380
NA–Mo6	249, 364, 379[a]
1-NpNH$_2$/Mo6	247, 332, 385
NA2–Mo6	248, 340, 394[a]

[a] Shoulder peak.

NA–Mo6 LB films display strong absorption bands in the near-UV region. Compared with the UV/Vis absorption band of NA–Mo6 in CH_2Cl_2 at ca. 362 nm, which is derived from the charge-transfer transition of the coordinated N atom to the Mo atom, the absorption bands of the LB films of 2-NpNH$_2$/Mo6 and NA–Mo6 both exhibit a slight red-shift (from 362 to 380 nm for the 2-NpNH$_2$/Mo6 LB film and from 362 to 379 nm for the NA–Mo6 LB film) and peak broadening, which are likely to be a result of the formation of J-aggregates.[25] This indicates similar electronic structures of the hexamolybdate core in the two types of LB films. Similar red-shifts for the NA2–Mo6 and 1-NpNH$_2$/Mo6 LB films were observed (Figure 13). It is also clear that NA2–Mo6 shows a better conjugation than NA–Mo6, leading to longer absorption wavelengths in NA2–Mo6.
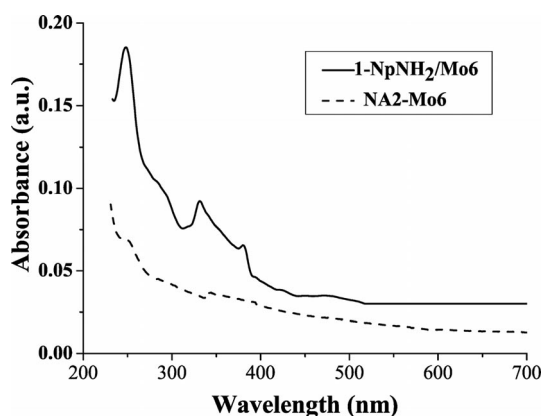
Figure 13. UV/Vis spectra of LB films (13-layer) of 1-NpNH$_2$/Mo6 and NA2–Mo6.

Low-Angle X-ray Diffraction

The lamellar structure of the hybrid LB films is clearly demonstrated by the low-angle X-ray diffraction measurement. As shown in Figure 14, two strong Bragg peaks at
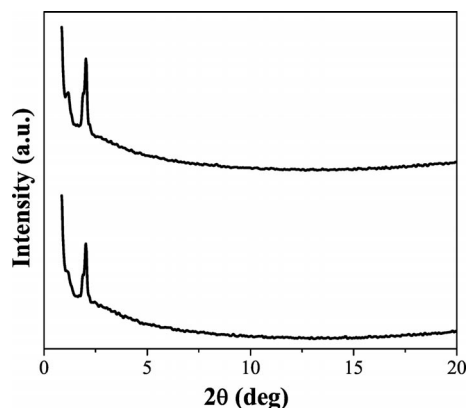
Figure 14. Low-angle X-ray diffraction patterns of the as-prepared films of 2-NpNH$_2$/Mo6 (top) and NA–Mo6 (bottom) with 13 layers deposited on the glass.

2.03° (2θ) for the 13-layer of 2-NpNH$_2$/Mo6 and 2.04° (2θ) for the 13-layer NA–Mo6, assigned to the (001) diffraction peaks, are clearly identified in the X-ray diffractogram, indicating that the layer structure of the two LB films are well organized. According to the Bragg diffraction formula, $n\lambda = 2d\sin\theta$, we can calculate the monolayer average thickness $d/2$ for 2-NpNH$_2$/Mo6 and NA–Mo6 to be 2.18 nm and 2.17 nm, respectively. On the basis of the unit-cell dimension of NA–Mo6, the height of 2-NpNH$_2$/Mo6 is estimated to be 2.07 nm, and it is likely that the NA–Mo6 molecules lie flat on the substrate. A similar case exists for the 2-NpNH$_2$/Mo6 LB film.

Study of Electrical Conductivity

The electrical conductivity behavior of the 3-layer LB films of NA–Mo6 and 2-NpNH$_2$/Mo6 on an ITO wafer was examined using scanning tunneling microscopy (STM). Saliently, they both show good electrical conductivity and representative I–V plots are shown in Figure 15 for the devices. The tunneling current for the 2-NpNH$_2$/Mo6 and NA–Mo6 LB films amounts to approximately –100 to 100 pA when the voltage is set within approximately –1.5 to 2 and –1.5 to 2.5 V, respectively. The corresponding data of 3-layer LB films of NA2–Mo6 and 1-NpNH$_2$/Mo6 on an ITO wafer are also given for the devices (Figure 15). The tunneling current for the 1-NpNH$_2$/Mo6 and NA2–Mo6 LB films amounts to approximately –100 to 100 pA when the voltage is set within approximately –2.5 to 0.5 and –2.2
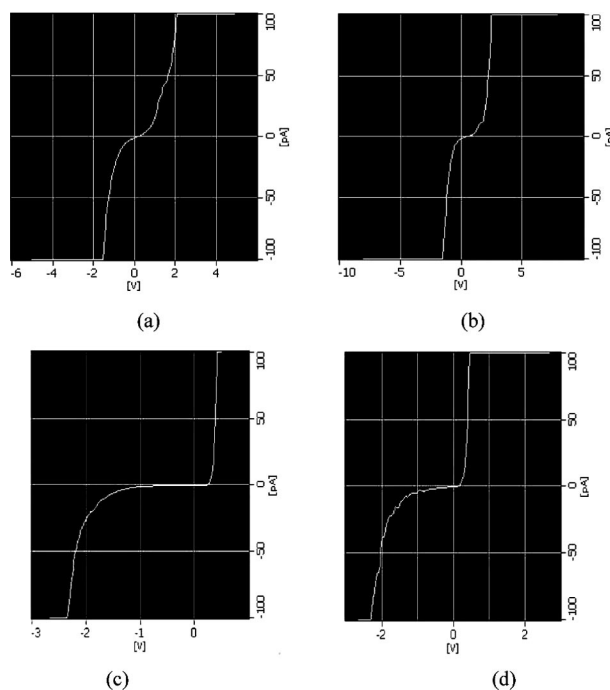
Figure 15. The I–V curve of the 3-layer LB film on the ITO wafer for (a) 2-NpNH$_2$/Mo6, (b) NA–Mo6, (c) 1-NpNH$_2$/Mo6, and (d) NA2–Mo6.

to 0.5 V, respectively. The I–V curves reveal that the noncovalently-bonded compound 2-NpNH$_2$/Mo6 and the covalently-bonded hybrid species NA–Mo6 have similar conductivities. This is also the case for 1-NpNH$_2$/Mo6 and NA2–Mo6. Compared with the voltage of the LB films of NA–Mo6 (2.5 V), the LB films derived from NA2–Mo6 have a lower voltage (0.5 V) when the tunneling current reaches 100 pA, therefore the conductivity of covalently-bonded hybrid NA2–Mo6 is better than that of NA–Mo6, presumably due to the better conjugation in the disubstituted organoimido complex. Pure naphthylamine is generally a very poor conductor in the intrinsic state; our hybrid LB composites in the device can be made to be semiconducting, which is likely attributed to the existence of electron transfer.

Conclusions

Two new organoimido derivatives [(n-C$_4$H$_9$)$_4$N]$_2$-[Mo$_6$O$_{18}$\{≡N–(2-Np)\}] and [(n-C$_4$H$_9$)$_4$N]$_2$[Mo$_6$O$_{17}$\{≡N–(1-Np)\}$_2$] have been prepared by the metathesis of the hexamolybdate ion and naphthylamines with DCC as a dehydrating agent in dry acetonitrile. These compounds belong to a family of Linqvist-type polyoxometalates. Compared to the parent hexamolybdate, they show significant redshifts of the lowest energy band, indicating that there is a stronger electronic interaction between the metal–oxygen cluster and the naphthalene ring in the hybrid compounds. The charge transfer between the electron-donating naphthylimido and electron-accepting hexamolybdate was believed to be the cause of the luminescence quenching of the covalently-linked hybrid compound.

In addition, the LB films of the covalently-bonded NA–Mo6 and NA2–Mo6 were prepared and characterized in order to make comparisons with 2-NpNH$_2$/Mo6 and 1-NpNH$_2$/Mo6. The four LB films 1-NpNH$_2$/Mo6, 2-NpNH$_2$/Mo6, NA–Mo6, and NA2–Mo6, constructed by using two different deposition strategies, were successfully fabricated onto the substrates. The results show stable monolayers of naphthylamine molecules at the air/Mo6 solution interface and stable monolayers of NA–Mo6 and NA2–Mo6 at the air/H$_2$O interface. The two LB films possess well-ordered lamellar structures and display semiconducting properties resulting from electron transfer in the two hybrid systems. In the near future, efforts on exploring the electrical, optical, and photophysical properties of polyoxometalate-based organic-inorganic hybrid molecular materials in electronic devices will be made.

Experimental Section

Materials and Reagents: [(n-C$_4$H$_9$)$_4$N]$_2$[Mo$_6$O$_{19}$] (Mo6) was obtained according to the published procedure.[26] Other starting materials are commercial products of chemical or analytical grade purity and dried using standard procedures. Analytical grade chloro-

form was redistilled before use. Ultrapure water (18 MΩ cm) delivered from a MilliPore system was employed in all of the LB film experiments.

Instrumentation: ^{1}H NMR spectra were measured in CD$_3$COCD$_3$ with a Varian Inova 600 MHz FT-NMR spectrometer, with the ^{1}H NMR chemical shifts quoted relative to SiMe$_4$. Infrared spectra were recorded with a Perkin–Elmer Spectrum One FTIR spectrometer in CH$_2$Cl$_2$ solutions or KBr pellets. Ultraviolet/visible (UV/Vis) spectra were measured with a UNICAM Heλios α spectrometer. Low angle X-ray diffraction measurements were carried out with a Philips X′pert Pro instrument, operating with a monochromated Cu-K_α radiation source at 40 kV and 50 mA. Photoluminescence spectra were recorded with a SPEX F212 fluorescence spectrometer. The I–V curves were collected within a 2×2 μm^2 image in a tapping mode, at a spot where a few molecules of LB film were located.

Monolayer and LB Film Fabrication: Monolayer formation and deposition were carried out with a Flench LB 105 slot under room temperature conditions at 20 ± 1 °C. The surface pressure was measured by the Wilhelmy method. Triple-distilled deionized water (pH = 6) was used as the subphase.

(i) Monolayer of NA–Mo6 and NA2–Mo6: The NA–Mo6 monolayer was prepared by spreading a definite quantity of a chloroform solution of NA–Mo6 (1×10^{-4} mol L^{-1}) onto an ultrapure water subphase at room temperature. After evaporation of the solvent for 15 min, the monolayer was compressed at a constant barrier rate of 3 cm^2 min^{-1} and the curve was recorded. The method of preparation of a monolayer of NA2–Mo6 was similar to that of the NA–Mo6 monolayer.

(ii) Monolayer of 1-NpNH$_2$/Mo6 and 2-NpNH$_2$/Mo6: The 1-NpNH$_2$/Mo6 and 2-NpNH$_2$/Mo6 hybrid monolayer was prepared in each case by spreading a definite quantity of 1-NpNH$_2$ and 2-NpNH$_2$ in chloroform (1×10^{-4} mol L^{-1}) onto a 1×10^{-4} mol L^{-1} aqueous solution subphase of Mo6 at room temperature. After evaporation of the solvent for 15 min, the monolayer was compressed at a constant barrier rate of 3 cm^2 min^{-1} and the curve was recorded.

The above two groups of monolayers were then allowed to stabilize for 15 min at the target pressure of 20 mN m^{-1}. The condensed monolayers were finally transferred by the vertical dipping method onto the ITO substrates for I–V measurements, onto the quartz substrates for UV and PL spectra, and onto the glass substrate for low-angle X-ray diffraction. In all cases, the dipping rate of the transfer for LB films was set at 3 mm min^{-1}, resulting in a fairly good deposition of a typical Y-mode film. The number of layers of LB film prepared here is equal to the number of dipping or lifting processes, on each of which a floating Langmuir monolayer was transferred onto the substrate with a good transfer ratio of ca. 1.

Synthesis of NA–Mo6: A mixture of 2-NpNH$_2$ (0.19 g, 1.0 mmol), [(n-C$_4$H$_9$)$_4$N]$_2$[Mo$_6$O$_{19}$] (1.37 g, 1.3 mmol), and DCC (0.41 g, 2.0 mmol) was refluxed in anhydrous acetonitrile (50 mL) for about 12 h. Then, a large amount of white precipitate was formed, which was confirmed to be N,N'-dicyclohexylurea, and a dark-red solution was obtained. After cooling the suspension to room temperature, the white precipitate was removed by filtration. While most of the acetonitrile was allowed to slowly evaporate, the product was found to deposit from the filtrate as a dark-red solid, which was washed successively with dichloromethane and acetone several times, and recrystallized from acetone to obtain red plate crystals with a moderate yield of ca. 42%. C$_{42}$H$_{79}$Mo$_6$N$_3$O$_{18}$: C 33.86, H 5.35, N 2.82; found C 33.89, H 5.37, N 2.84. ^{1}H NMR (600 MHz,

CD$_3$OCD$_3$): δ = 0.97 (t, J = 11.4 Hz, 24 H, –CH$_3$, [Bu$_4$N]$^+$), 1.47 (m, 16 H, –CH$_2$–, [Bu$_4$N]$^+$), 1.83 (m, 16 H, –CH$_2$–, [Bu$_4$N]$^+$), 3.44 (t, J = 8.4 Hz, 16 H, NCH$_2$–, [Bu$_4$N]$^+$), 7.40 (d, J = 10.2 Hz, 1 H, aromatic), 7.44 (d, J = 7.2 Hz, 1 H, aromatic), 7.56 (t, J = 7.2 Hz, 1 H, aromatic), 7.65 (d, J = 3.0 Hz, 1 H, aromatic), 7.70 (s, 1 H, aromatic), 7.90 (d, J = 7.2 Hz, 1 H, aromatic) and 7.94 (d, J = 11.4 Hz, 1 H, aromatic) ppm. IR (KBr pellet): $\tilde{v}$ = 774.48 (v_{asym}, Mo–O–Mo), 955 (v, Mo=O), 976 (v, Mo≡N) cm^{-1}. UV/Vis (CH$_3$CN): λ_{max} = 254, 362 nm.

Synthesis of NA2–Mo6: A mixture of 1-NpNH$_2$ (0.47 g, 2.5 mmol), [(n-C$_4$H$_9$)$_4$N]$_2$[Mo$_6$O$_{19}$] (1.05 g, 1.0 mmol), and DCC (0.52 g, 2.5 mmol) was refluxed in anhydrous acetonitrile (50 mL) for about 12 h. A dark-red solution was obtained, and a large amount of white N,N'-dicyclohexylurea was formed. After cooling the solution to room temperature, the white precipitate was removed by filtration. The filtrate was evaporated to give a dark-red solid, which was washed successively with dichloromethane and acetone. The product was obtained as red plate crystals in ca. 45% yield. C$_{52}$H$_{86}$Mo$_6$N$_4$O$_{17}$ (1614.91): calcd. C 38.67, H 5.37, N 3.47; found C 38.85, H 5.24, N 3.54. ^{1}H NMR (600 MHz, CD$_3$OCD$_3$): δ = 0.94 (t, J = 6.0 Hz, 24 H, –CH$_3$, [Bu$_4$N]$^+$), 1.42 (m, 16 H, –CH$_2$–, [Bu$_4$N]$^+$), 1.79 (m, 16 H, –CH$_2$–, [Bu$_4$N]$^+$), 3.40 (t, J = 6.0 Hz, 16 H, –NCH$_2$–, [Bu$_4$N]$^+$), 7.38–7.90 (m, 14 H, aromatic) ppm. IR (KBr pellet): $\tilde{v}$ = 769.93 (v_{asym}, Mo–O–Mo), 945.99 (v, Mo=O), 1017.36 (v, Mo≡N) cm^{-1}. UV/Vis (CH$_3$CN): λ_{max} = 236, 394 nm.

X-ray Crystallography: Single crystals of NA–Mo6 and NA2–Mo6 suitable for X-ray crystallographic analysis were grown by slow evaporation of its solution in acetone at room temperature. The crystal was chosen and mounted on a glass fiber using epoxy resin. The diffraction experiment was carried out at 293 K with a Bruker Axs SMART 1000 CCD area-detector diffractometer using graphite-monochromated Mo-K_α radiation (λ = 0.71073 Å). The collected frames were processed using the software SAINT[27] and an absorption correction was applied (SADABS)[28] to the collected reflections. The structure was solved by direct methods (SHELXTL)[29] in conjunction with standard difference Fourier techniques and subsequently refined by full-matrix least-squares analyses on F^2. Hydrogen atoms were generated in their idealized positions and all non-hydrogen atoms were refined anisotropically.

CCDC-843751 (for NA–Mo6) and -843752 (for NA2–Mo6) contain the supplementary crystallographic data for this paper. These data can be obtained free of charge from The Cambridge Crystallographic Data Centre via www.ccdc.cam.ac.uk/data_request/cif.

Acknowledgments

[1] J. P. Hargmann, D. Hargmann, J. Zubieta, *Angew. Chem.* **1999**, *111*, 2798–2848; *Angew. Chem. Int. Ed.* **1999**, *38*, 2638–2684.

[2] a) K. Awaga, E. Coronado, M. Drillon, *MRS Bull.* **2000**, 52–57; b) A. E. Clave, E. Coronado, C. J. Galán-Mascarós, C. J. Gómez-García, V. Laukkhin, *Nature* **2000**, *408*, 447–449; c) E. Coronado, P. Day, *Chem. Rev.* **2004**, *11*, 5419–5448; d) E. Coronado, C. J. Galán-Mascarós, *J. Mater. Chem.* **2005**, *15*, 66–74; e) L. Liu, W.-H. Ai, M.-J. Li, S.-Z. Liu, C.-M. Zhang, H.-X. Yan, Z.-L. Du, W.-Y. Wong, *Chem. Mater.* **2007**, *19*, 1704–1711.

[3] C. Sanchez, F. Ribot, *New J. Chem.* **1994**, *18*, 1007–1047.

[4] P. Judeinstein, C. Sanchez, *J. Mater. Chem.* **1996**, *6*, 511–525.

[5] *Matériaux Hybrides*; Masson: Paris, **1996**; Série Arago 17.

[6] J. A. Zasadzinski, R. Viswanathan, L. Madsen, J. Garnaes, D. K. Schwartz, *Science* **1994**, *263*, 1726–1733.

[7] G. G. Roberts, *Adv. Phys.* **1985**, *34*, 475–512.

[8] a) A. Ulman, *An Introduction to Ultrathin Organic Films: From Langmuir-Blodgett to Self-Assembly*, Academic Press, Boston, **1991**; b) D. R. Talham, *Chem. Rev.* **2004**, *104*, 5479–5501; c) H. Kuhn, D. Möbius, H. Bücher, *Physical Methods of Chemistry*, Part IIIB, Wiley-Interscience, New York, **1972**, chapter VII ; d) G. L. Gaines Jr., *Insoluble Monolayers at Liquid-Gas Interface*, Wiley-Interscience, New York, **1966**.

[9] a) M. Ide, A. Mitamura, T. Miyashita, *Bull. Chem. Soc. Jpn.* **2001**, *74*, 1355–1359; b) Y. Kado, A. Aoki, T. Miyashita, *Int. J. Nanosci.* **2002**, *5–6*, 637–640; c) B. W.-K. Chu, V. W.-W. Yam, *Langmuir* **2006**, *22*, 7437–7443; d) Y. Amao, K. Asai, T. Miyashita, I. Okumura, *Polym. J.* **1999**, *31*, 1267–1269; e) Y. Amao, K. Asai, T. Miyashita, I. Okumura, *Polym. Adv. Technol.* **2000**, *11*, 705–709; f) A. Aoki, T. Miyashita, *Macromolecules* **1996**, *29*, 4662–4667; g) N. Fukuda, M. Mitsuishi, T. Miyashita, *J. Phys. Chem. B* **2002**, *106*, 7048–7052; h) J. Matsui, M. Mitsuishi, A. Aoki, T. Miyashita, *Angew. Chem.* **2003**, *115*, 2374–2377; *Angew. Chem. Int. Ed.* **2003**, *42*, 2272–2275; i) J. Matsui, M. Mitsuishi, A. Aoki, T. Miyashita, *J. Am. Chem. Soc.* **2004**, *126*, 3708–3709.

[10] M. T. Pope, A. Müller, *Angew. Chem.* **1991**, *103*, 56–70; *Angew. Chem. Int. Ed. Engl.* **1991**, *30*, 34–38.

[11] M. T. Pope, A. Müller, *Polyoxometalates: From Platonic Solids to Anti-Retroviral Activity*, vol. 10, Kluwer Academic Publishers, Dordrecht, The Netherlands, **1994**.

[12] Z. H. Peng, *Angew. Chem.* **2004**, *116*, 948–953; *Angew. Chem. Int. Ed.* **2004**, *43*, 930–935.

[13] D. E. Katsouli, *Chem. Rev.* **1998**, *98*, 359–387.

[14] J. L. Stark Jr., V. G. Young, E. A. Maatta, *Angew. Chem.* **1995**, *107*, 2741–2753; *Angew. Chem. Int. Ed. Engl.* **1995**, *34*, 2545–2547.

[15] R. J. Errington, *Polyoxometalates Chemistry: From Topology via Self-Assembly to Applications* (Eds.: M. T. Pope, A. Müller), Kluwer Academic Publisher, Dordrecht, Boston, **2001**, pp. 7–22.

[16] L. Xu, M. Lu, B. B. Xu, Y.-G. Wei, Z.-H. Peng, D. R. Powell, *Angew. Chem.* **2002**, *114*, 4303–4306; *Angew. Chem. Int. Ed.* **2002**, *41*, 4129–4132.

[17] a) Y.-G. Wei, B. B. Xu, C. L. Barnes, Z.-H. Peng, *J. Am. Chem. Soc.* **2001**, *123*, 4083–4084; b) Y.-G. Wei, L. Meng, C. F. C. Cheung, C. L. Barnes, Z.-H. Peng, *Inorg. Chem.* **2001**, *40*, 5489–5490.

[18] J. Hao, L. Ruhlmann, Y.-L. Zhu, Q. Li, Y.-G. Wei, *Inorg. Chem.* **2007**, *46*, 4960–4967.

[19] a) W. Clegg, R. J. Errington, K. A. Fraser, S. A. Holmes, A. Schäfer, *J. Chem. Soc., Chem. Commun.* **1995**, 455–456; b) C. Qin, X.-L. Wang, L. Xu, Y.-G. Wei, *Inorg. Chem. Commun.* **2005**, *8*, 751–754; c) Y. Xia, Y.-G. Wei, Y. Wang, H.-Y. Guo, *Inorg. Chem.* **2005**, *44*, 9823–9828.

[20] D. E. Wigley, *Prog. Inorg. Chem.* **1992**, *42*, 239–245.

[21] Y. Du, A. L. Rheingold, E. A. Maatta, *J. Am. Chem. Soc.* **1992**, *114*, 345–346.

[22] A. Proust, R. Thouvenot, M. Chaussade, F. Robert, P. Gouzerh, *Inorg. Chim. Acta* **1994**, *224*, 81–95.

[23] P. F. Wu, Q. Li, N. Ge, Y. G. Wei, Y. Wang, P. Wang, H. Y. Guo, *Eur. J. Inorg. Chem.* **2004**, 2819–2825.

[24] M. Lu, Y. G. Wei, B. Xu, C. F. C. Cheung, Z. Peng, D. R. Powell, *Angew. Chem.* **2002**, *114*, 1636–1638; *Angew. Chem. Int. Ed.* **2002**, *41*, 1566–1568.

[25] C. H. Huang, F. Y. Li, Y. Y. Huang, *Ultrathin Films for Optics and Electronics*, Peking University Press, Beijing, **2001**.

[26] N. H. Hur, W. G. Klemperer, R. C. Wang, *Inorg. Synth.* **1990**, *27*, 77–85.

[27] *SAINT*, reference manual, Siemens Energy and Automation, Madison, WI, **1994**–**1996**.

[28] G. M. Sheldrick, *SADABS, Empirical Absorption Correction Program*, University of Göttingen, Germany, **1997**.

[29] G. M. Sheldrick, *SHELXTL*, reference manual, ver. 5.1, Madison, WI, **1997**.

Guanidine Electron Donors and Silver Halides: Interplay and Competition between Redox, Coordination and Polymerization Reactions

Dimitri Emeljanenko,[a] Julian Horn,[a] Elisabeth Kaifer,[a] Hubert Wadepohl,[a] and Hans-Jörg Himmel*[a]

Redox reactions compete with coordination and polymerization reactions when the organic electron donor and ligand, 1,2,4,5-tetrakis(tetramethylguanidino)benzene (**1**), is dissolved together with silver halides AgX (X = Cl, Br or I) in solvents of different polarity. The complex results obtained for the relatively simple system **1**/AgX highlight the importance of solvent effects. A variety of chain polymers have been synthesized in which the guanidine electron-donor building blocks are connected by silver halide clusters of different sizes.

Introduction

Aromatic compounds with amino substituents in a *para* position to each other are well-known organic electron donors. Examples include 1,4-bis(dimethylamino)benzene and 1,2,4,5-tetrakis(dimethylamino)benzene.[1] Oxidation of 1,4-bis(dimethylamino)benzene leads to "Wurster's blue", which was described as early as the end of the 19th century.[2] Recently, aromatic compounds functionalized by several guanidino groups in a *para* position to each other (GFA-*n*, whereby *n* denotes the number of guanidino substituents) were introduced as a new class of strong organic electron donors.[3–9] Two examples for GFA-4 compounds are 1,2,4,5-tetrakis(tetramethylguanidino)benzene[3] (**1**) and 1,2,4,5-tetrakis(*N*,*N*′-dimethyl-*N*,*N*′-ethyleneguanidino)benzene[9] (**2**) (see Scheme 1). In comparison to the corresponding amines, **1** and **2** are much stronger Brønsted bases and exhibit a higher reduction capacity. For example, the oxidation potential $E_{1/2}(CH_2Cl_2) = 0.063$ V for 1,2,4,5-tetrakis(dimethylamino)benzene[10] but –0.32 V for **1**[3] with respect to SCE. In addition, as shown in a massive body of work, guanidines are versatile ligands that have been used extensively for the synthesis of molecular compounds for manifold applications (e.g., catalysis or deposition of materials from precursors).[11–15]

GFA-4 compounds such as **1** could be engaged in different reaction types like redox reactions, Brønsted acid–base reactions and reactions to give coordination compounds. In some cases, they compete with each other, and in others they are coupled. Of course, N ligands generally
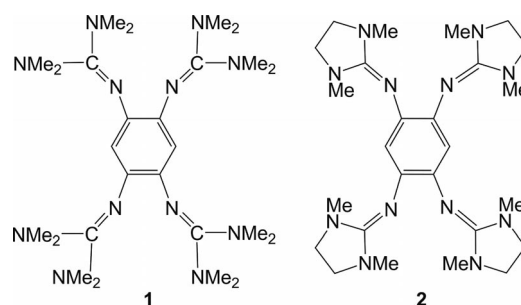
Scheme 1.

represent Brønsted bases, and in fact protonation can be considered the simplest model for complex formation. However, compounds such as **1** or **2** represent superior organic Brønsted bases, much stronger than amines, for example, and therefore readily deprotonate weak proton acids and solvents such as CH_3CN if supporting conditions {e.g., the presence of [Au(PPh$_3$)Cl]} are fulfilled.[9] In the past we reported several examples of the chemistry of **1**, in which oxidation and coordination are coupled.[4,5] This is possible because **1** could act as a ligand even after two-electron oxidation, thereby underlining its extremely strong Lewis base character. For example, treatment of a solution of **1** with Cu(BF$_4$)$_2$ in CH_3CN yielded a dinuclear complex of the guanidine dication, [**1**{Cu(NCCH$_3$)$_4$}$_2$](BF$_4$)$_6$.[4] In this case, a redox reaction is coupled with coordination. On the other hand, Brønsted acid–base reactions compete with coordination reactions and usually also with redox reactions. One example is provided by the treatment of a solution of **2** with [AuCl(PPh$_3$)] and PhCCH in CH_3CN.[16] In this case, the redox channel that leads to the salt **2**[Au(CCPh)$_2$]$_2$ and the Brønsted acid–base channel that leads to the neutral Au complex [Au(PPh$_3$)CCPh] exhibit similar kinetics in CH_3CN. Consequently, a roughly equimolar mixture of

[a] Anorganisch-Chemisches Institut, Ruprecht-Karls-Universität Heidelberg,
Im Neuenheimer Feld 270, 69120 Heidelberg, Germany
Fax: +49-6221-545707
E-mail: hans-joerg.himmel@aci.uni-heidelberg.de

both product types results. Of course, the solvent is of great importance, and highly polar solvents favour the redox channel.

Herein we present examples of the chemistry of **1** in which coordination, redox and polymerization reactions interplay and/or compete with each other. Variations in the experimental conditions, especially the polarity of the solvent, favour one channel over the other. Oxidation of the guanidine is accompanied by an intense green colouring of the solution. The reaction between a silver halide and a guanidine, which at first glance appears to be very simple, will be shown to be a complex story. Chain polymers that contain ordered arrays of silver halide clusters connected through guanidine electron-donor units are among the structurally characterized products.

Figure 1. UV/Vis spectrum of (**1**)Br$_2$ dissolved in CH$_3$CN.

Results and Discussion

In the following we discuss the reactions of **1** with silver halides in solvents of different polarities. In the reaction equations we took care to ensure that the stoichiometry of the reactants is correct; they generally are not balanced. The yields refer to the isolated crystalline material and are therefore generally lower bounds for the actual yield. Due to the manifold possible reaction pathways, most reaction products cannot be foretold; however, it will be shown that the reactions could be directed in one direction by optimization of the reaction conditions.

Reactions in MeOH

When **1** was treated with AgCl or AgBr at room temp. in MeOH, the solution turned, after a few minutes, a deep green that is characteristic of oxidized **1**. The analytical data (see the Experimental Section) show the products to be the salts (**1**)X$_2$ [X = Cl or Br, formed according to Equation (1)]. Hence the ^{1}H NMR spectra of a solution of (**1**)Br$_2$ in CD$_3$CN displays signals of the dication **1**$^{2+}$ (methyl groups and aromatic C–H) at δ = 2.88 and 5.16 ppm.

Figure 2. Structures of the salts (**1**)Cl$_2$ and (**1**)Br$_2$. Thermal ellipsoids drawn at the 50% probability level. Selected structural parameters {(bond lengths [pm], bond angles [°]) for (**1**)Cl$_2$: N1–C1 129.9(2), N1–C7 137.0(2), N2–C7 133.4(3), N3–C7 134.0(3), N4–C2 133.8(2), N4–C12 134.8(2), N5–C12 133.9(2), N6–C12 134.9(2), N7–C4 130.3(2), N7–C17 136.4(2), N8–C17 135.0(2), N9–C17 132.9(2), N10–C5 134.7(2), N10–C22 134.6(2), N11–C22 135.1(2), N12–C22 134.2(2), C1–C2 150.2(2), C1–C6 141.6(2), C2–C3 137.6(2), C3–C4 142.2(2), C4–C5 150.6(2), C5–C6 137.2(2); C1–N1–C7 129.44(15), C2–N4–C12 122.79(14), C4–N7–C17 125.48(15), C5–N10–C22 122.59(14), N2–C7–N3 121.09(17), N5–C12–N6 118.74(16), N8–C17–N9 121.17(15), N11–C22–N12 118.68(15). Selected structural parameters (bond lengths [pm], bond angles [°]) for (**1**)Br$_2$: N1–C1 135.17(19), N1–C4 133.97(19), N2–C4 135.26(19), N3–C4 134.75(19), N4–C2 130.64(19), N4–C9 136.94(19), N5–C9 134.30(19), N6–C9 132.65(19), C1–C2 149.9(2), C1–C3 137.3(2), C2–C3′ 141.8(2); C1–N1–C4 122.58(13), N2–C4–N3 117.96(13), C2–N4–C9 125.54(13), N5–C9–N6 121.13(13).

$$1 \ + \ 5 \ AgX \ \xrightarrow[\text{r.t.}]{\text{CH}_3\text{OH}} \ (1)X_2 \ + \ Ag$$

X = Cl or Br   X = Cl: 70%
                     X = Br: 68%   (1)

For comparison, the ^{1}H NMR spectroscopic signals of the neutral guanidine **1**, also dissolved in CD$_3$CN, occur at δ = 2.63 and 5.54 ppm, and that of the dication in **1**(I$_3$)$_2$ at δ = 2.88 and 5.17 ppm.[3] The UV/Vis spectrum of (**1**)Br$_2$ dissolved in CH$_3$CN (see Figure 1) contains three strong absorptions centered at λ = 218, 293 and 416 nm. In addition, a weak and broad feature occurs at 589 (614) nm (see inset in Figure 1). Single crystals of (**1**)Cl$_2$ and (**1**)Br$_2$·4MeOH suitable for XRD were obtained from CH$_3$CN/Et$_2$O and MeOH/Et$_2$O solutions, respectively. Figure 2 illustrates the structures. As known from other salts,

the guanidine dication can be described as a pair of bisguanidino-allyl monocations that are connected by two C–C single bonds [distances of 150.2(2) and 150.6(2) pm for C1–C2 and C4–C5 in (**1**)Cl$_2$, and of 149.9(2) pm for C1–C2 in (**1**)Br$_2$]. Treatment of **1** with AgI yielded a product mixture from which we isolated in a crystalline yield of 51% a brown-red chain polymer of the formula [**1**(Ag$_6$I$_8$)]$_n$; see Equation (2). The polymer is insoluble in CH$_3$CN, but to some degree soluble in DMF. Crystals of this polymer were obtained with and without cocrystallized DMF solvate molecules. Fractions of the obtained structures are visualized in Figure 3. It can be seen directly that the structures are significantly different. In the case of [**1**(Ag$_6$I$_8$)·2DMF]$_n$, the chain can formally be regarded to consist of [**1**(AgI$_2$)$_2$] units fused together by neutral chair-type-structured Ag$_4$I$_4$ clusters. The organic building blocks are directly incorporated into the main chain of the polymer. In the case of solvate-free crystals of [**1**(Ag$_6$I$_8$)]$_n$, chains of rhombic Ag$_2$I$_2$ units connected through the corners can be identified. Every second rhombic unit is bound through the Ag atoms to two [**1**(AgI$_2$)$_2$] units. Hence in this case the organic building blocks are not incorporated into the polymer main chain.

was observed. Instead, the guanidine acted as a chelating ligand and pale yellow coordination polymers [**1**(AgX)$_2$]$_n$ (X = Br or I) were formed; see Equation (3). Crystals of the chain polymer [**1**(AgBr)$_2$]$_n$ suitable for single-crystal X-ray diffraction (XRD) were grown from concentrated CH$_3$CN solutions. The structure is illustrated in Figure 4. Each Ag^I is tetrahedrally coordinated by two N and two Br atoms. The dihedral angle between the N–Ag–N and Br–Ag–Br planes is close to the ideal value of 90° for tetrahedral coordination. All polymer chains run into the same direction (see Figure 4). The Ag–N bond lengths measure 236.0(2) and 233.8(2) pm. With 72.6(1)°, the N–Ag–N bond angles are relatively small. The Br–Ag–Br angles [100.3(3)°] are close to the ideal value for tetrahedral coordination. The polymer [**1**(AgI)$_2$]$_n$ was obtained in a similar way by reaction between **1** and two equivalents of AgI in CH$_3$CN solutions. Crystals of [**1**(AgI)$_2$·4DMF]$_n$ were obtained after sev-

$$1 + 2\,AgX \xrightarrow[\text{90 °C}]{CH_3CN} 1/n\,[1(AgX)_2]_n$$

X = Br or I

X = Br: 91%
X = I: 84%

(3)

a)

$$1 + 5\,AgI \xrightarrow[\text{r.t.}]{CH_3OH} [(1)Ag_6I_8]_n$$

51%

(2)

a)

b)

Figure 3. Fractions of the crystal structures of the coordination polymers (a) [(**1**)Ag$_6$I$_8$·2DMF]$_n$ and (b) [(**1**)Ag$_6$I$_8$]$_n$ (hydrogen atoms omitted). Thermal ellipsoids drawn at the 50% probability level.

b)
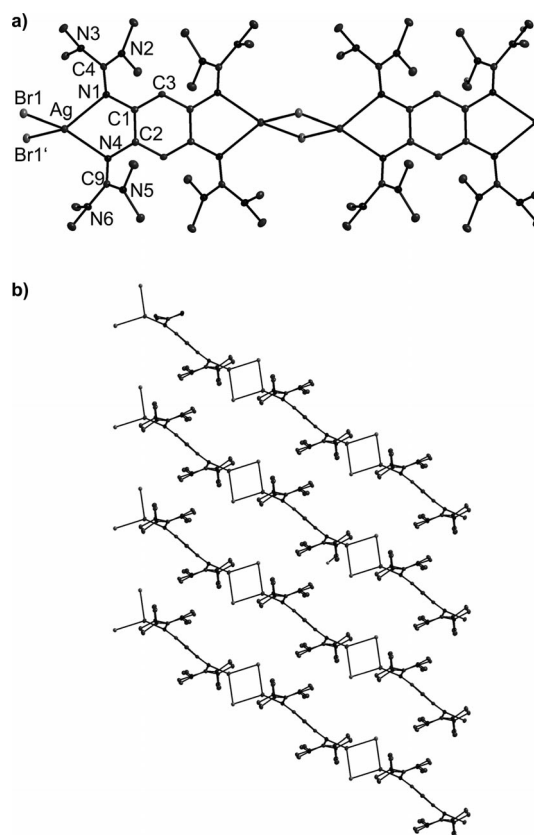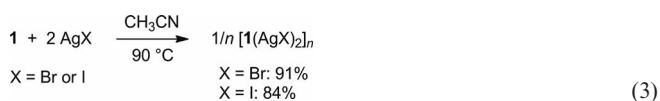
Figure 4. A part of the structure of the coordination polymer [**1**(AgBr)$_2$]$_n$ (hydrogen atoms omitted). The alignment of the one-dimensional polymers is shown below. Thermal ellipsoids drawn at the 50% probability level. Selected structural parameters (bond lengths [pm], bond angles [°]): Ag–Br1 273.23(7), Ag–Br1′ 268.47(8), Ag–N1 236.0(2), Ag–N4 233.8(2), N1–C1 140.9(3), N1–C4 130.9(3), N2–C4 138.3(3), N3–C4 136.5(3), N4–C2 141.0(3), N4–C9 131.5(3), N5–C9 138.0(3), N6–C9 135.4(3), C1–C2 140.7(3), C1–C3 139.3(3), C2–C3′ 140.0(3); N1–Ag–N4 72.63(7), Br1–Ag–Br1′ 100.25(3).

Reactions in CH$_3$CN

Reactions in CH$_3$CN proceeded very differently. Hence in the case of AgBr and AgI, no oxidation of guanidine **1**

eral weeks from concentrated DMF solutions. The structure is visualized in Figure 5. The polymer chains are structurally similar to those in [**1**(AgBr)$_2$]$_n$. The cocrystallized DMF molecules separate two adjacent polymer chains. Unlike [**1**(AgBr)$_2$]$_n$, every second chain in [**1**(AgI)$_2$·4DMF]$_n$ is tilted by approximately 90° around the chain axis (see Figure 5).
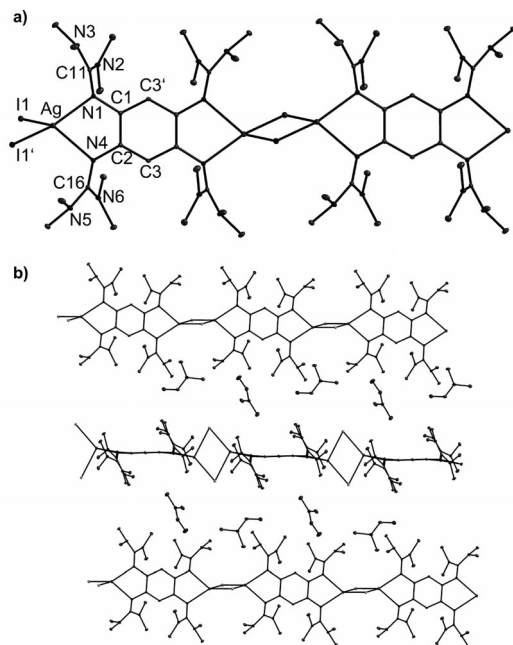
Figure 5. A part of the structure of the coordination polymer [**1**(AgI)$_2$]$_n$ (hydrogen atoms omitted). The alignment of the one-dimensional polymers is shown below. Thermal ellipsoids drawn at the 50% probability level. Selected structural parameters (bond lengths [pm], bond angles [°]): Ag–I1 276.49(7), Ag–I1′ 291.83(8), Ag–N1 234.31(18), Ag–N4 237.17(18), N1–C1 141.1(2), N1–C11 131.8(3), N2–C11 136.7(2), N3–C11 136.4(3), N4–C2 141.4(2), N4–C16 130.4(3), N5–C16 137.5(2), N6–C16 137.9(3), C1–C2 140.9(3), C1–C3′ 139.6(3), C2–C3 139.3(3); I1–Ag–I1′ 110.74(3), N1–Ag–N4 73.92(6).

For treatment of AgCl with **1**, a product mixture was obtained. In a crystalline yield of 23%, compound [**1**(AgCl)$_2$] was isolated, which is a dinuclear coordination compound, unlike the polymers of similar overall formula obtained in the reactions with AgBr or AgI. Its structure is illustrated in Figure 6. The molecular units are arranged in stacks. In addition, the salt (**1**)Cl$_2$ (11% yield) and the chain polymer [**1**(Ag$_4$Cl$_6$)]$_n$ (21% yield) were formed; see Equation (4). The latter was crystallized either from CHCl$_3$ as [**1**(Ag$_4$Cl$_6$)·4CHCl$_3$]$_n$ or from CH$_2$Cl$_2$ as [**1**(Ag$_4$Cl$_6$)·2CH$_2$Cl$_2$]$_n$. The structures of the polymers with CHCl$_3$ and CH$_2$Cl$_2$ solvate molecules are compared in Figure 7. The chains found in both compounds could be considered to consist of a cationic polymer {[**1**(AgCl)$_2$]$^{2+}$}$_n$ in which the building blocks are connected by halide bridges. The silver and halide atoms of each [**1**(AgCl)$_2$]$^{2+}$ unit interact with two [AgCl$_2$]$^-$ anions. However, the conformation of the chains differs significantly. Hence the dihedral angle between the central Ag$_2$Cl$_2$ ring plane and the N–Ag–N planes amounts to 72° in [**1**(Ag$_4$Cl$_6$)·4CHCl$_3$]$_n$, and 34° in

[**1**(Ag$_4$Cl$_6$)·2CH$_2$Cl$_2$]$_n$. Both compounds decompose in MeOH solutions. The analytical data indicate formation of AgCl and (**1**)Cl$_2$ as decomposition products.

$$\mathbf{1} + 2\,\text{AgCl} \xrightarrow[\text{r.t.}]{\text{CH}_3\text{CN}} \begin{array}{c} \text{product mixture} \\ [\mathbf{1}(\text{AgCl})_2] + (\mathbf{1})\text{Cl}_2 + [\mathbf{1}(\text{Ag}_4\text{Cl}_6)]_n \\ 23\% \qquad\quad 11\% \qquad\quad 21\% \end{array} \qquad (4)$$
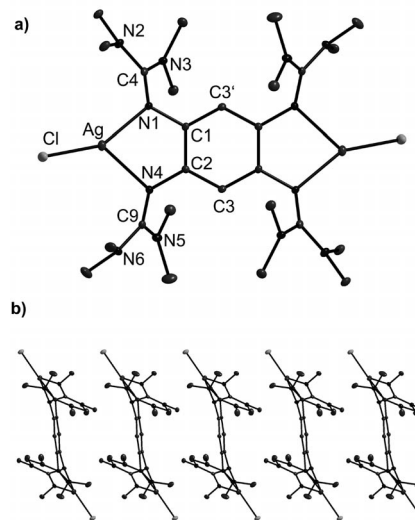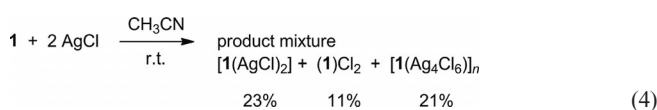
Figure 6. (a) Molecular structure of [**1**(AgCl)$_2$] (hydrogen atoms omitted). Thermal ellipsoids drawn at the 50% probability level. Selected structural parameters (bond lengths [pm], bond angles [°]): Ag–Cl 237.12(11), Ag–N1 226.3(2), Ag–N4 232.9(2), N1–C1 142.4(3), N1–C4 131.6(4), N2–C4 136.4(3), N3–C4 137.0(4), N4–C2 141.4(3), N4–C9 130.9(4), N5–C9 137.3(4), N6–C9 136.1(4), C1–C2 141.6(4), C1–C3′ 139.2(4), C2–C3 139.5(4); N1–Ag–N4 75.07(8), Cl–Ag–N1 153.81(6), Cl–Ag–N4 131.01(6).
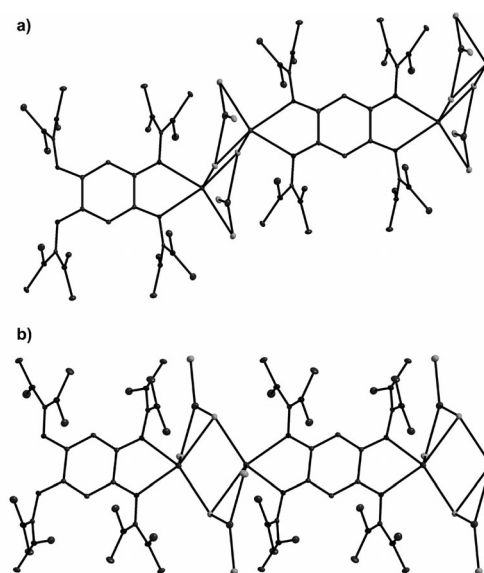
Figure 7. Parts of the crystal structures of the coordination polymers (a) [**1**(Ag$_4$Cl$_6$)·4CHCl$_3$]$_n$ and (b) [**1**(Ag$_4$Cl$_6$)·2CH$_2$Cl$_2$]$_n$ (hydrogen atoms omitted). Thermal ellipsoids drawn at the 50% probability level.

Reactions in Toluene

If the reaction between **1** and AgCl was carried out in toluene, only the coordination compound [**1**(AgCl)$_2$] with a neutral guanidine ligand was formed in 77% crystalline yield; see Equation (5). The same compound was already obtained as one of the products of the reaction between **1** and AgCl in CH$_3$CN. Further experiments with this complex showed it to be stable only in apolar solvents. When it was dissolved under heat in CH$_2$Cl$_2$, a redox reaction was initiated to yield the coordination polymer [**1**(Ag$_4$Cl$_6$)]$_n$ – see Equation (6) – which was already shown to be one of the products of reaction between **1** and AgCl in CH$_3$CN.

$$\mathbf{1} + 2\ \text{AgCl} \xrightarrow{\text{C}_7\text{H}_8} [\mathbf{1}(\text{AgCl})_2] \qquad (5)$$
$$77\%$$

$$3/n\ [\mathbf{1}(\text{AgCl})_2] \xrightarrow[\Delta]{\text{CH}_2\text{Cl}_2} 1/n\ [\mathbf{1}(\text{Ag}_4\text{Cl}_6)]_n + 2\ \text{Ag} \qquad (6)$$
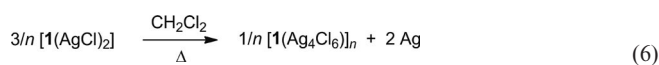
Properties of the One-Dimensional Polymers [**1**(AgX)$_2$]$_n$ (X = Br or I)

The experiments described above showed that coordination compounds of the neutral guanidines could be obtained by careful choice of the solvent. Whereas [**1**(AgCl)$_2$] is a dinuclear compound, [**1**(AgBr)$_2$]$_n$ and [**1**(AgI)$_2$]$_n$ represent chain polymers. Furthermore, [**1**(AgCl)$_2$] is highly amenable to redox reactions when brought into contact with solvents of moderate to strong polarity. In further experiments described in this section, we analyzed the properties and redox chemistry of the polymers [**1**(AgBr)$_2$]$_n$ and [**1**(AgI)$_2$]$_n$. Thermogravimetric (TG) and differential scanning calorimetric (DSC) measurements (see curves in Figure 8) indicate that both compounds are stable up to temperatures of 250 °C. Their remission spectra (see the Supporting Information) contain broad absorptions below 500 nm. When the compounds were heated to a temperature of 650 °C, gas evolution was monitored and the materials changed their optical properties dramatically. The initially yellow colour of the intact polymer turned to black with a metal-like gleam after the heat treatment (see photos provided in the Supporting Information). Up to now we have been unable to characterize the structures of these products of pyrolysis. The elemental analysis showed them to contain substantial amounts of carbon and nitrogen. Further work, which is outside the scope of this article, is necessary to study the composition and properties of these materials.

In our oxidation experiments, [**1**(AgBr)$_2$]$_n$ and [**1**(AgI)$_2$]$_n$ were treated with I$_2$ as well as organic electron acceptors [2,3-dichloro-5,6-dicyano-1,4-benzoquinone (DDQ), tetrachlorobenzoquinone (TCQ) and tetracyanoquinodimethane (TCNQ)]. The results will be briefly summarized in the fol-
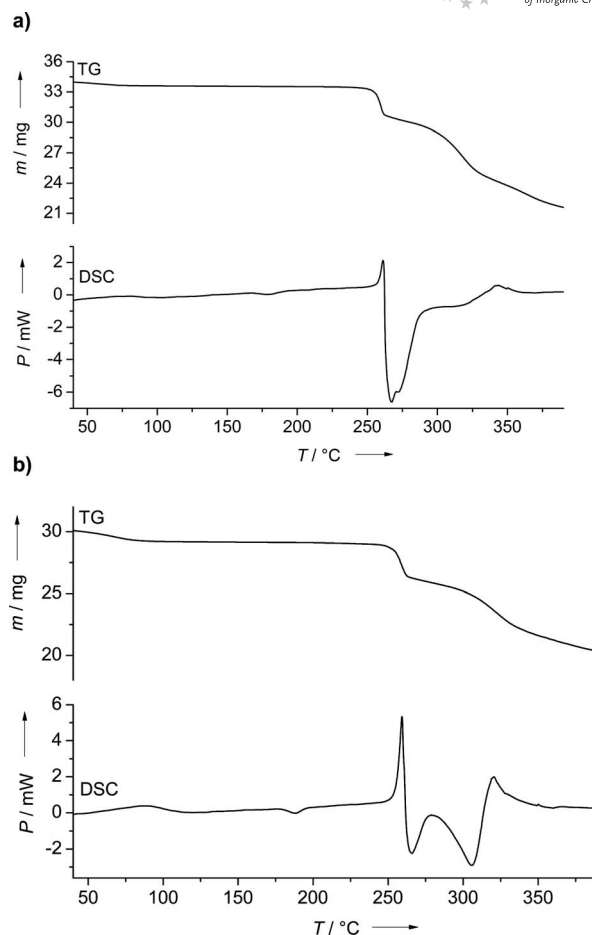
Figure 8. TG and DSC curves (at a heating rate of 10 °C min^{-1} under an N$_2$ atmosphere) for (a) [**1**(AgBr)$_2$]$_n$ and (b) [**1**(AgI)$_2$]$_n$.

lowing; see Equations (7), (8) and (9). In the case of reaction of an equimolar mixture of [**1**(AgBr)$_2$]$_n$ and I$_2$ at room temp. in CH$_3$CN, the coordination polymer [**1**(Ag$_6$I$_{8-x}$Br$_x$)]$_n$ with x = 0.7 was isolated in a crystal yield of 26%. Its structure is depicted in Figure 9 (a). It resembles that of [**1**(Ag$_6$I$_8$)]$_n$. In the case of a 2:1 molar ratio of the two reactants (but otherwise unchanged reaction conditions), a different product was isolated in extremely small but reproducible yield. This product was unambiguously identified as the coordination polymer [**1**(Ag$_5$Br$_4$I$_3$)]$_n$ (see Figure 9, b). The guanidine building blocks are incorporated into the polymer main chain. The small yield is at

$$1/n\ [\mathbf{1}(\text{AgBr})_2]_n + \text{I}_2 \xrightarrow[\text{r.t.}]{\text{CH}_3\text{CN}} [\mathbf{1}(\text{Ag}_6\text{I}_{8-x}\text{Br}_x)]_n \qquad (7)$$
$$26\%,\ x = 0.7$$

$$1/n\ [\mathbf{1}(\text{AgBr})_2]_n + 0.5\ \text{I}_2 \xrightarrow[\text{r.t.}]{\text{CH}_3\text{CN}} [\mathbf{1}(\text{Ag}_5\text{Br}_4\text{I}_3)]_n \qquad (8)$$
$$1\%$$

$$1/n\ [\mathbf{1}(\text{AgI})_2]_n + 0.5\ \text{I}_2 \xrightarrow[\text{r.t.}]{\text{CH}_3\text{CN}} \mathbf{1}(\text{AgI}_3) \qquad (9)$$
$$11\%$$
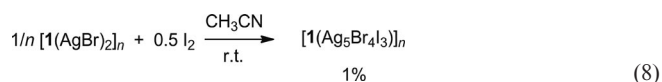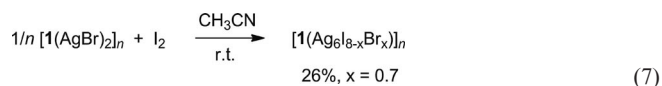
least partially caused by the low solubility of the starting reagents. On the other hand, reaction between $[1(AgI)_2]_n$ and I_2 (0.5 equiv.) yielded not a polymer but the salt $1(AgI_3)$ with separated guanidine dicationic and AgI_3 dianionic units (see Figure 10).
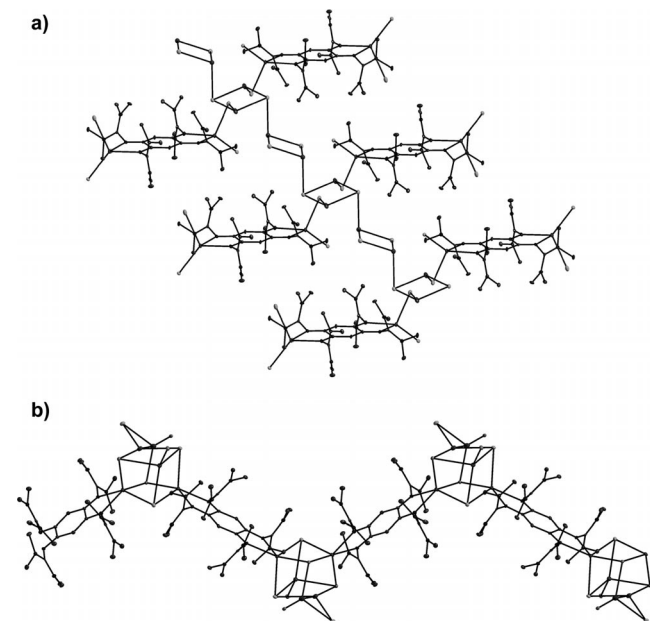
Figure 9. Fractions of the crystal structures of the coordination polymers (a) $[1(Ag_6I_{8-x}Br_x)]_n$ with $x = 0.7$ and (b) $[1(Ag_5Br_4I_3)]_n$.
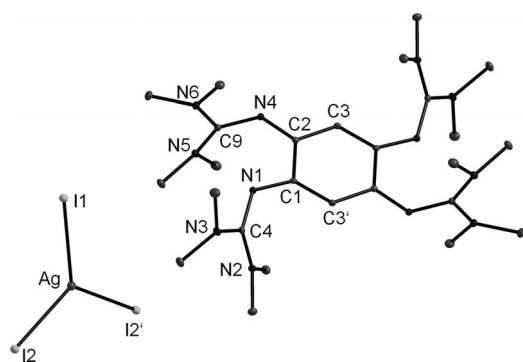
Figure 10. Structure of the salt $1(AgI_3)$. Selected bond lengths [pm]: Ag–I1 278.48(6), Ag–I2 275.88(6), N1–C1 134.6(2), N1–C4 134.6(2), N2–C4 135.1(3), N3–C4 135.0(2), N4–C2 130.8(2), N4–C9 136.9(2), N5–C9 134.6(3), N6–C9 133.1(3), C1–C2 150.1(3), C1–C3′ 137.5(3), C2–C3 142.2(3).

Treatment of $[1(AgBr)_2]_n$ or $[1(AgBr)_2]_n$ with the organic electron acceptor DDQ (2 equiv.) gave a black product, which was identified as the donor–acceptor couple $1(DDQ)_2$; see Equation (10). The crystal structure is provided in Figure 11. Clearly, this compound can be prepared more directly by reaction between 1 and DDQ. The donor and acceptor units are arranged in stacks. The packing as well as the black appearance of the material make it attractive for a future analysis of the electronic properties. Reaction between $[1(AgI)_2]_n$ and TCQ or TCNQ yielded the polymer $[1(Ag_6I_8)]_n$ – see Equations (11) and (12) – a prod-

uct that also could be obtained more directly by reaction between 1 and AgI in MeOH. This compound seems to be of especial stability, as it is obtained under various conditions.

$$1/n\ [1(AgX)_2]_n\ +\ 2\ DDQ \xrightarrow[\text{r.t.}]{\text{CHCl}_3} 1(DDQ)_2\ +\ 2\ AgX$$
$$X = Br\ or\ I \qquad\qquad 67\%\ (X = Br)$$
$$64\%\ (X = I) \qquad (10)$$

$$1/n\ [1(AgI)_2]_n\ +\ TCQ \xrightarrow{\text{CH}_3\text{CN}} [1(Ag_6I_8)]_n$$
$$30\% \qquad (11)$$

$$1/n\ [1(AgI)_2]_n\ +\ 2\ TCNQ \xrightarrow{\text{CH}_3\text{CN}} [1(Ag_6I_8)]_n$$
$$16\% \qquad (12)$$
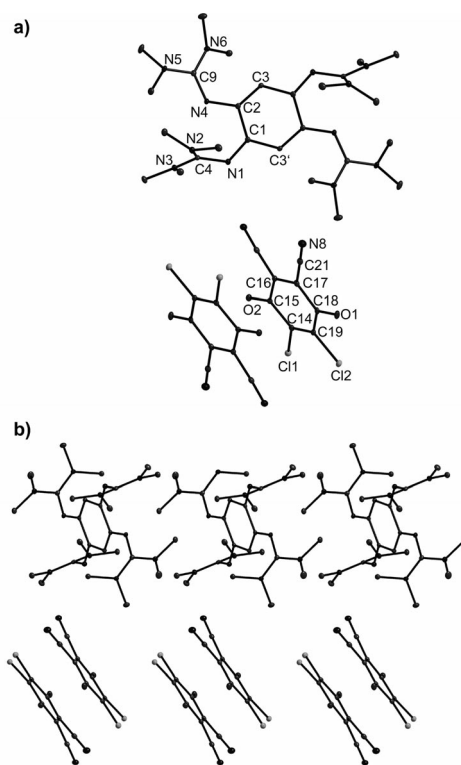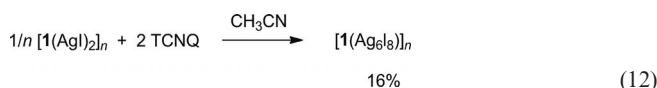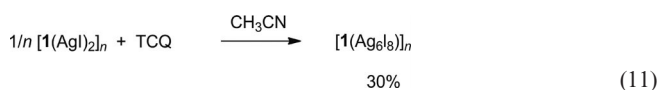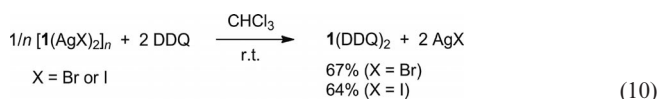
Figure 11. Structure of the salt $1(DDQ)_2$. Selected bond lengths [pm]: cationic guanidine units: N1–C1 130.4(2), N1–C4 137.4(2), N2–C4 134.1(2), N3–C4 133.7(2), N4–C2 135.9(2), N4–C9 133.7(2), N5–C9 135.3(2), N6–C9 135.3(2), C1–C2 150.0(3), C1–C3′ 143.2(3), C2–C3 136.6(3); anionic DDQ units: O1–C18 124.4(2), O2–C15 124.7(2), Cl1–C14 172.3(2), Cl2–C19 172.5(2), N8–C21 114.3(3), C17–C21 143.3(3), C14–C15 147.6(3), C14–C19 135.3(3), C15–C16 144.4(3), C16–C17 139.1(3), C17–C18 145.0(3), C18–C19 146.6(3).

Conclusion

Coordination, redox and polymerization reactions are either coupled or in competition with each other when the guanidine electron donor 1,2,4,5-tetrakis(tetramethylguanidino)benzene (1) reacts with silver halides in solvents of different polarities. By choice of solvent, the reaction could

be directed into the desired channel. The results of this work are of special importance for the use of guanidine electron donors as building blocks in coordination polymers. In these polymers, the guanidine units are generally highly oxidized and coloured, thus making them attractive for optical and/or electronic applications. This article shows how halide clusters of different sizes could be incorporated into the chain polymers, thereby opening an access route to well-defined arrays of photoactive silver halide clusters. As shown for the pairs of compounds $[1(Ag_6I_8)\cdot 2DMF]_n$ and $[1(Ag_6I_8)]_n$ as well as $[1(Ag_4Cl_6)\cdot 4CHCl_3]_n$ and $[1(Ag_4Cl_6)\cdot 2CH_2Cl_2]_n$, the incorporation of solvent molecules leads to significant changes in the polymer structures.

Experimental Section

General: The synthetic work was carried out under an inert-gas atmosphere by using standard Schlenk techniques. All solvents were dried rigorously prior to their use. UV/Vis spectra were recorded with a Varian Cary 5000 spectrometer. NMR spectra were measured with a Bruker Avance II 400 NMR machine. Elemental analyses were carried out at the Microanalytical Laboratory of the University of Heidelberg. IR spectra were recorded with a Biorad Excalibur FTS3000 spectrometer. Thermogravimetric (TG) and calorimetric (DSC) measurements were carried out with a Mettler TC15 and DSC30 apparatus under a N_2 atmosphere in a temperature range of 30–600 °C. The heating rate was varied between 2 and 10 °C min^{-1}.

Compound (1)Cl$_2$: AgCl (135 mg, 0.934 mmol) was added to a solution of **1** (100 mg, 0.188 mmol) in CH$_3$OH (10 mL). The solution was stirred at room temp. for a period of 2 h, during which time the solution quickly adopted a deep green colour. After filtration, 4/5 of the solvent volume was removed, and the initial amount of solvent was restored by the addition of Et$_2$O. A dark crystalline powder of (**1**)Cl$_2$ precipitated; yield 80 mg (0.133 mmol, 70%). Single crystals suitable for XRD were obtained from CH$_3$CN/Et$_2$O. C$_{28}$H$_{58}$Cl$_2$N$_{12}$O$_2$ [M + 2MeOH] (665.75): calcd. C 50.51, H 8.78, N 25.25; found C 49.73, H 8.71, N 25.85. ^{1}H NMR (400 MHz, CD$_2$Cl$_2$): δ = 2.76 (48 H, CH$_3$), 5.44 (2 H, Ar$_H$) ppm. ^{13}C NMR (100 MHz, CD$_2$Cl$_2$): δ = 40.2 (CH$_3$), 111.6, 135.5, 162.7 ppm. IR (CsI): $\tilde{\nu}$ = 2947, 1608, 1564, 1508, 1467, 1421, 1395, 1304, 1256, 1226, 1187, 1165, 1139, 1057, 1018, 896, 840, 806, 749, 688, 623, 532, 458 cm^{-1}. UV/Vis (CH$_3$CN, c = 3.4 × 10^{-5} mol L^{-1}): λ (ε in L mol^{-1} cm^{-1}) = 218 (42148), 293 (16240), 425 (24148) nm. MS-ESI$^+$ (MeOH): m/z (%) = 265.3 (100) [**1**]$^{2+}$, 530.3 (56) [**1**]$^+$, 565.6 (25) [**1** + Cl]$^+$. Crystal data for (**1**)Cl$_2$, C$_{26}$H$_{50}$Cl$_2$N$_{12}$: M_r = 601.68, 0.30 × 0.11 × 0.05 mm^3, orthorhombic, space group $Pca2(1)$, a = 19.210(4) Å, b = 7.5353(15) Å, c = 21.463(4) Å, V = 3106.8(11) Å^3, Z = 4, $d_{calcd.}$ = 1.286 Mg m^{-3}, Mo-K_α radiation (graphite-monochromated, λ = 0.71073 Å), T = 100 K, θ_{range} 1.90 to 30.58°. Reflections measd. 75068, indep. 9521, R_{int} = 0.0644. Final R indices [$I > 2\sigma(I)$]: R_1 = 0.0430, wR_2 = 0.0985.

Compound (1)Br$_2$: AgBr (142 mg, 0.755 mmol) was added to a solution of **1** (80 mg, 0.151 mmol) in MeOH (10 mL). The solution was stirred at room temp. for a period of 2 h, during which time the solution quickly turned deep green. Then the solution was filtered and the solvent was partially removed to around 2 mL. A dark, crystalline solid precipitated after the addition of Et$_2$O (restoring the initial 10 mL volume); yield 71 mg (0.103 mmol, 68%). Crystals suitable for XRD were grown from MeOH/Et$_2$O. C$_{26}$H$_{50}$Br$_2$N$_{12}$ (690.56): calcd. C 45.22, H 7.30, N 24.34; found C 44.79, H 7.29,

N 23.65. ^{1}H NMR (400 MHz, CD$_3$CN): δ = 2.88 (48 H, CH$_3$), 5.16 (2 H, Ar$_H$) ppm. ^{13}C NMR (100 MHz, CD$_3$CN): δ = 41.48 (CH$_3$), 103.90, 157.75, 168.07 ppm. IR (CsI): $\tilde{\nu}$ = 2946, 1608, 1583, 1564, 1505, 1468, 1420, 1390, 1301, 1253, 1227, 1190, 1164, 1142, 1057, 1016, 898, 879, 838, 749, 683, 620, 538 cm^{-1}. UV/Vis (CH$_3$CN, c = 6.2 × 10^{-5} mol L^{-1}): λ (ε in L mol^{-1} cm^{-1}) = 218 (59431), 293 (16179), 426 (27073), 589 (614) nm. MS-ESI$^+$: m/z (%) = 265.3 (100) [**1**]$^{2+}$, 530.3 (7) [**1**]$^+$, 611.0 (7) [**1** + Br]$^+$. Crystal data for (**1**)Br$_2$·4MeOH: C$_{30}$H$_{66}$Br$_2$N$_{12}$O$_4$, M_r = 818.76, 0.30 × 0.20 × 0.20 mm^3, monoclinic, space group $P2_1/n$, a = 9.4670(19) Å, b = 15.321(3) Å, c = 14.612(3) Å, β = 104.29(3), V = 2053.8(7) Å^3, Z = 2, $d_{calcd.}$ = 1.324 Mg m^{-3}, Mo-K_α radiation (graphite-monochromated, λ = 0.71073 Å), T = 100 K, θ_{range} 2.33 to 32.05°. Reflections measd. 14235, indep. 7130, R_{int} = 0.0366. Final R indices [$I > 2\sigma(I)$]: R_1 = 0.0374, wR_2 = 0.0803.

Compound [1(Ag$_6$I$_8$)]$_n$: AgI (221 mg, 0.942 mmol) was added to a solution of **1** (100 mg, 0.188 mmol) in MeOH (12 mL). The solution was stirred for a period of 16 h at room temp., during which time the formation of brown-red solid was observed. Then the reaction mixture was filtered and the product dried under vacuum; yield 212 mg (0.097 mmol, 51%). Crystals suitable for XRD were grown from concentrated DMF solutions. Compound [**1**(Ag$_6$I$_8$)]· 2DMF: C$_{32}$H$_{64}$Ag$_6$I$_8$N$_{14}$O$_2$ (2339.39): calcd. C 16.43, H 2.76, N 8.38; found C 16.78, H 2.60, N 8.22. ^{1}H NMR (400 MHz, [D$_6$]DMF): δ = 3.01 (48 H, CH$_3$), 5.35 (2 H, Ar$_H$) ppm. Low solubility hampered the ^{13}C NMR spectra. IR (CsI): $\tilde{\nu}$ = 2921, 1677, 1661, 1609, 1577, 1561, 1508, 1492, 1460, 1400, 1384, 1320, 1263, 1231, 1167, 1090, 1022, 897, 813, 785, 737, 701 cm^{-1}. UV/Vis (CH$_3$CN, c = 7.9 × 10^{-6} mol L^{-1}): λ (ε in L mol^{-1} cm^{-1}) = 245 (6827), 285 (1827), 426 (2431) nm. MS-FAB$^+$: m/z (%) = 531.7 (20) [**1** + H]$^+$, 746.5 (1) [**1** + 2Ag]$^+$, 784 (2) [**1** + 2I]$^+$, 871.0 (7) [**1** + 2Ag$^+$I]$^+$, 891.8 (5) [**1** + Ag + 2I]$^+$, 978.6 (3) [**1** + 3Ag$^+$I]$^+$, 1063.3 (1) [**1** + 5Ag − H]$^+$. Crystal data for [**1**(Ag$_6$I$_8$)]·2DMF: C$_{16}$H$_{32}$Ag$_3$I$_4$N$_7$O, M_r = 1169.70, 0.10 × 0.10 × 0.10 mm^3, monoclinic, space group $P2_1/n$, a = 11.727(2) Å, b = 19.456(4) Å, c = 12.991(3) Å, β = 94.21(3)°, V = 2956.0(10) Å^3, Z = 4, $d_{calcd.}$ = 2.628 Mg m^{-3}, Mo-K_α radiation (graphite-monochromated, λ = 0.71073 Å), T = 100 K, θ_{range} 2.09 to 30.02°. Reflections measd. 16815, indep. 8624, R_{int} = 0.0600. Final R indices [$I > 2\sigma(I)$]: R_1 = 0.0442, wR_2 = 0.0781. Crystal data for [**1**(Ag$_6$I$_8$)]: C$_{13}$H$_{25}$Ag$_3$I$_4$N$_6$, M_r = 1096.6, 0.15 × 0.10 × 0.10 mm^3, monoclinic, space group $C2/c$, a = 13.795(3) Å, b = 14.615(3) Å, c = 25.803(5) Å, β = 104.82(3)°, V = 5029.2(19) Å^3, Z = 8, $d_{calcd.}$ = 2.897 Mg m^{-3}, Mo-K_α radiation (graphite-monochromated, λ = 0.71073 Å), T = 100 K, θ_{range} 2.36 to 28.03°. Reflections measd. 24142, indep. 5969, R_{int} = 0.0516. Final R indices [$I > 2\sigma(I)$]: R_1 = 0.0397, wR_2 = 0.0972.

Compound [1(AgBr)$_2$]$_n$: Compound **1** (500 mg, 0.942 mmol) was dissolved in CH$_3$CN (10 mL). Subsequently, AgBr (354 mg, 1.884 mmol) was added, and the reaction mixture was heated at 90 °C to reflux for a period of 4 h. Then half of the solvent was removed under vacuum from the reaction mixture. The reaction mixture was filtered and washed with a small portion of CH$_3$CN. The pale yellow product was dried under vacuum to yield 779 mg (0.860 mmol, 91%) [**1**(AgBr)$_2$]$_n$. Crystals suitable for an XRD analysis were obtained from concentrated CH$_3$CN solutions. C$_{26}$H$_{50}$Ag$_2$Br$_2$N$_{12}$ (906.30): calcd. C 34.46, H 5.56, N 18.55; found C 34.31, H 5.56, N 18.36. ^{1}H NMR (199.92 MHz, CDCl$_3$): δ = 2.79 (s, 48 H, CH$_3$), 5.38 (s, 2 H, Ar$_H$) ppm. ^{13}C NMR (100.55 MHz, CDCl$_3$): δ = 39.94 (CH$_3$), 110.92, 134.94, 162.10 ppm. IR (CsI): $\tilde{\nu}$ = 2929 (m), 1515 (s, C=N), 1382 (s), 1265 (m), 1180 (s), 1063 (m), 1020 (vs), 948 (w), 925 (w), 890 (vs), 867 (s), 776 (m), 712 (m), 573 (m), 426 (w) cm^{-1}. MS-FAB$^+$: m/z (%) = 486.1 (34) [**1** − NMe$_2$]$^+$, 531.2 (100) [**1** + H]$^+$, 611.2 (2) [**1** + Br]$^+$,

719.3 (0.4) [**1** + Ag + Br + H]$^+$. UV/Vis (CH$_3$CN, c = 7.37×10^{-5} mol L^{-1}): λ_{max} (ε in L mol^{-1} cm^{-1}) = 218 (5970), 274 (4828), 427 (2460) nm. Crystal data for C$_{13}$H$_{25}$AgBrN$_6$·2CH$_3$CN: M_r = 535.28, 0.30×0.30×0.27 mm^3, triclinic, space group $P\bar{1}$, a = 9.7380(19) Å, b = 11.180(2) Å, c = 12.081(2) Å, α = 92.93(3)°, β = 109.48(3)°, γ = 109.87(3)°, V = 1145.9(4) Å^3, Z = 2, $d_{calcd.}$ = 1.551 Mg m^{-3}, Mo-K_α radiation (graphite-monochromated, λ = 0.71073 Å), T = 100 K, θ_{range} 1.97 to 30.05°. Reflections measd. 11697, indep. 6626, R_{int} = 0.0292. Final R indices [$I > 2\sigma(I)$]: R_1 = 0.0345, wR_2 = 0.0838.

Compound [1(AgI)$_2$]$_n$: AgI (442 mg, 1.884 mmol) was added to **1** (500 mg, 0.942 mmol) in CH$_3$CN (10 mL). The pale green reaction mixture was heated at 90 °C to reflux for a period of 4 h. Then half of the solvent was removed under vacuum. Subsequently, the hot reaction mixture was filtered, and the solid residue was washed with a small quantity of CH$_3$CN. Finally, the pale yellow product was dried under vacuum to obtain 791 mg of [**1**(AgI)$_2$]$_n$ (0.791 mmol, 84% yield). Crystals suitable for an XRD analysis were grown over a period of several weeks from concentrated DMF solutions. C$_{26}$H$_{50}$Ag$_2$I$_2$N$_{12}$ (1000.30): calcd. C 31.22, H 5.04, N 16.80; found C 31.05, H 4.89, N 16.57. ^{1}H NMR (199.92 MHz, CDCl$_3$): δ = 2.76 (s, 48 H, CH$_3$), 5.37 (s, 2 H, Ar$_H$) ppm. ^{13}C NMR (100.55 MHz, CDCl$_3$): δ = 40.06 (CH$_3$), 111.41, 136.16, 162.30 ppm. IR (CsI): $\tilde{\nu}$ = 2927 (m), 1536 (s, C=N) , 1420 (s), 1383 (s), 1263 (m), 1178 (m), 1064 (m), 1021 (vs), 922 (w), 888 (s), 866 (m), 774 (m), 711 (m), 572 (m), 474 (w), 428 (w) cm^{-1}. MS-FAB$^+$: m/z (%): 486.4 (25) [**1** − NMe$_2$]$^+$, 531.5 (100) [**1** + H]$^+$, 637.4 (0.3) [**1** + Ag]$^+$, 659.4 (0.6) [**1** + I]$^+$, 765.2 (0.2) [**1** + Ag + I]$^+$. UV/Vis (CH$_3$CN, c = 2.62×10^{-5} mol L^{-1}): λ_{max} (ε in L mol^{-1} cm^{-1}) = 225 (28738), 273 (17499), 329 (11595), 378 (9384), 421 (7606) nm. Crystal data for C$_{13}$H$_{25}$AgIN$_6$·2DMF: M_r = 646.35, 0.11×0.07×0.03 mm^3, monoclinic, space group $P2_1/c$, a = 11.754(5) Å, b = 22.070(9) Å, c = 10.787(5) Å, β = 110.644(6)°, V = 2618.5(19) Å^3, Z = 4, $d_{calcd.}$ = 1.640 Mg m^{-3}, Mo-K_α radiation (graphite-monochromated, λ = 0.71073 Å), T = 100 K, θ_{range} 2.07 to 32.21°. Reflections measd. 66037, indep. 8826, R_{int} = 0.0508. Final R indices [$I > 2\sigma(I)$]: R_1 = 0.0283, wR_2 = 0.0556.

Compound [1(Ag$_4$Cl$_6$)]$_n$: AgCl (270 mg, 1.88 mmol) was added to a solution of **1** (200 mg, 0.377 mmol) in CH$_3$CN (12 mL). The deep green solution was stirred at room temp. for a period of 3 h. Subsequently, the solvent was removed under vacuum and the residue was redissolved in CHCl$_3$ (<M;>30 mL). The dinuclear coordination compound [**1**(AgCl)$_2$] precipitated after approximately 1 h at 4 °C and was separated by filtration; yield 70 mg (0.086 mmol, 23%). The filtrate was kept at room temp. for several days until complete evaporation of the CHCl$_3$ solvent, during which time brown-red crystals of [**1**(Ag$_4$Cl$_6$)]$_n$ were formed. This product was washed several times with CH$_2$Cl$_2$; yield 133 mg (0.08 mmol, 21%). The third product, (**1**)Cl$_2$, dissolved in the CH$_2$Cl$_2$ phases. The solution was stored for 24 h at a temperature of 4 °C. Dark green crystals of (**1**)Cl$_2$ formed (25 mg, 0.042 mmol, 11%). Analysis for [**1**(Ag$_4$Cl$_6$)]$_n$: C$_{30}$H$_{54}$Ag$_4$Cl$_{18}$N$_{12}$ (1652.45): calcd. C 21.81, H 3.29, N 10.17; found C 21.99, H 3.32, N 10.26. ^{1}H NMR (400 MHz, CDCl$_3$): δ = 3.18 (s, 48 H, CH$_3$), 5.00 (s, 2 H, Ar$_H$) ppm. Due to low solubility in CDCl$_3$ and decomposition in other solvents (see discussion), it proved impossible to obtain reliable ^{13}C NMR spectroscopic data for this product. IR (CsI): $\tilde{\nu}$ = 2929, 1609, 1524, 1494, 1468, 1395, 1324, 1307, 1263, 1227, 1170, 1139, 1062, 1022, 898, 780, 738, 694, 595 cm^{-1}. UV/Vis (CH$_3$CN, c = 3.2×10^{-5} mol L^{-1}): λ_{max} (ε in L mol^{-1} cm^{-1}): 217 (47535), 293 (18150), 425 (28900) nm. MS-ESI$^+$ (MeOH): m/z: 265.3 (100) [**1**]$^{2+}$, 319.0 (2) [**1** + Ag]$^{2+}$, 408.2 (1) [**1** + 2Ag + 2Cl]$^{2+}$, 530.3 (30) [**1**]$^+$. MS-FAB$^+$: m/z (%) 531.7 (100) [**1** + H]$^+$, 638.1 (8) [**1** + Ag]$^+$.

Crystal data for [**1**(Ag$_4$Cl$_6$)]·4CHCl$_3$: C$_{15}$H$_{27}$Ag$_2$Cl$_9$N$_6$, M_r = 826.22, 0.35×0.25×0.25 mm^3, monoclinic, space group $P2_1/c$, a = 20.956(4) Å, b = 11.688(2) Å, c = 23.445(5) Å, β = 92.82(3)°, V = 5735.5(19) Å^3, Z = 8, $d_{calcd.}$ = 1.914 Mg m^{-3}, Mo-K_α radiation (graphite-monochromated, λ = 0.71073 Å), T = 100 K, θ_{range} 1.95 to 33.11°. Reflections measd. 42828, indep. 21709, R_{int} = 0.0707. Final R indices [$I > 2\sigma(I)$]: R_1 = 0.0523, wR_2 = 0.1190. Crystal data for [**1**(Ag$_4$Cl$_6$)]·2CH$_2$Cl$_2$: C$_{14}$H$_{27}$Ag$_2$Cl$_5$N$_6$, M_r = 672.41, 0.30×0.20×0.20 mm^3, monoclinic, space group $P2_1/n$, a = 13.058(3) Å, b = 11.688(2) Å, c = 15.697(3) Å, β = 107.03(3)°, V = 2290.7(8) Å^3, Z = 4, $d_{calcd.}$ = 1.950 Mg m^{-3}, Mo-K_α radiation (graphite-monochromated, λ = 0.71073 Å), T = 100 K, θ_{range} 2.50 to 31.14°. Reflections measd. 14081, indep. 7282, R_{int} = 0.0346. Final R indices [$I > 2\sigma(I)$]: R_1 = 0.0399, wR_2 = 0.0987.

Decomposition of [1(Ag$_4$Cl$_6$)]$_n$: Compound [**1**(Ag$_4$Cl$_6$)]$_n$ (43.8 mg) was dissolved in MeOH (3 mL). Formation of a white precipitate was observed over a period of several days. The solution was filtered and the pale yellow powder dried under vacuum. It was dissolved in aqueous NH$_3$, precipitated upon addition of aqueous HNO$_3$, and was identified as AgCl. The green filtrate contained (**1**)Cl$_2$ (15.9 mg).

Compound [1(AgCl)$_2$]: AgCl (54 mg, 0.377 mmol) was added to a solution of **1** (100 mg, 0.188 mmol) in toluene (10 mL). The reaction mixture was stirred for 3 h at a temperature of 90 °C, leading to a white precipitate of [**1**(AgCl)$_2$]. This precipitate was filtered, washed with small quantities of toluene and dried; yield 120 mg (0.147 mmol, 78%). C$_{33}$H$_{58}$Ag$_2$Cl$_2$N$_{12}$ [M + C$_7$H$_8$] (909.54): calcd. C 43.58, H 6.43, N 18.48; found C 42.96, H 6.38, N 18.31. ^{1}H NMR (400 MHz, CD$_2$Cl$_2$): δ = 2.76 (48 H, CH$_3$), 5.44 (2 H, Ar$_H$) ppm. ^{13}C NMR (100 MHz, CD$_2$Cl$_2$): δ = 40.2 (CH$_3$), 111.6, 135.5, 162.7 ppm. IR (CsI): $\tilde{\nu}$ = 2927, 1546, 1483, 1420, 1386, 1264, 1234, 1179, 1144, 1060, 1023, 890, 827, 790, 709, 572 cm^{-1}. UV/Vis (CH$_3$CN, c = 9.90×10^{-5} mol L^{-1}): λ_{max} (ε in L mol^{-1} cm^{-1}) = 218 (18908), 290 (9207), 426 (13793) nm. MS-FAB$^+$: m/z (%) = 531.5 (100) [**1** + H]$^+$, 637.3 (12) [**1** + Ag]$^+$, 675.3 (5) [**1** + Ag + Cl + H]$^+$, 781.3 (0.6) [**1** + 2Ag + Cl]$^+$, 816.2 (0.5) [M]$^+$. Crystal data for [**1**(AgCl)$_2$]·C$_7$H$_8$: C$_{33}$H$_{57}$Ag$_2$Cl$_2$N$_{12}$, M_r = 908.55, 0.25×0.20×0.10 mm^3, monoclinic, space group $P2_1/c$, a = 13.428(3) Å, b = 7.3260(15) Å, c = 21.555(4) Å, β = 107.64(3)°, V = 2020.7(7) Å^3, Z = 2, $d_{calcd.}$ = 1.493 Mg m^{-3}, Mo-K_α radiation (graphite-monochromated, λ = 0.71073 Å), T = 100 K, θ_{range} 2.13 to 27.92°. Reflections measd. 9491, indep. 4811, R_{int} = 0.0334. Final R indices [$I > 2\sigma(I)$]: R_1 = 0.0351, wR_2 = 0.0793.

Compound [1(AgCl)$_2$] Dissolved in CH$_2$Cl$_2$: Compound [**1**(AgCl)$_2$] (60 mg) was dissolved in CH$_2$Cl$_2$ (10 mL) and heated to 40 °C for several minutes. The solution turned green and formation of precipitate was observed. The solution was filtered and concentrated. Crystals of [**1**(Ag$_4$Cl$_6$)]$_n$ formed over a period of several days. For analytical data, see above.

Oxidation Experiments with [1(AgBr)$_2$]$_n$ and [1(AgI)$_2$]$_n$

[1(Ag$_6$I$_{8-x}$Br$_x$)]$_n$ (x = 0.7): I$_2$ (28 mg, 0.110 mmol) was added to a solution of [**1**(AgBr)$_2$]$_n$ (100 mg, 0.110 mmol) in CH$_3$CN (12 mL). The dark yellow reaction mixture was stirred at room temp. for a period of 2 h. The product precipitated over the course of the reaction as a black powder. The reaction mixture was filtered, the product washed twice with CH$_3$CN and dried under vacuum to yield 62 mg (0.027 mmol, 26%). Crystals of the polymer [**1**(Ag$_6$I$_{8-x}$Br$_x$)]$_n$ (x = 0.7) suitable for an XRD analysis were obtained from CH$_3$CN/Et$_2$O or concentrated DMF solutions. C$_{29}$H$_{57}$Ag$_6$Br$_{0.7}$I$_{7.3}$N$_{13}$O$_1$ [M + DMF] (2233.4): calcd. C 15.60, H 2.57, N 8.15; found C 15.85, H 2.44, N 8.30. ^{1}H NMR (400 MHz, [D$_6$]DMSO): δ = 3.08 (48 H, CH$_3$), 5.17 (2 H, Ar$_H$) ppm. Low

solubility hampered the ^{13}C NMR spectra. IR (CsI): ṽ = 2963, 1669, 1615, 1528, 1492, 1465, 1393, 1324, 1303, 1263, 1169, 1095, 1025, 801, 696, 602 cm^{-1}. MS-FAB$^+$: m/z (%) = 530.4 (100) [**1**]$^+$, 609.2 (42) [**1** + Br]$^+$, 970.1 (5) [**1** + Ag + Br + 2I]$^+$. UV/Vis (CH$_3$CN, c = 2.30 × 10^{-6} mol L^{-1}): λ$_{max}$ (ε in L mol^{-1} cm^{-1}) = 220 (27142), 245 (13434), 286 (13434), 427 (5277) nm. Crystal data for C$_{26}$H$_{50}$Ag$_6$Br$_{0.7}$I$_{7.3}$N$_{12}$: M_r = 2160.31, 0.30 × 0.20 × 0.20 mm^3, monoclinic, space group C2/c, a = 13.695(3) Å, b = 14.591(3) Å, c = 25.807(5) Å, β = 104.85(3)°, V = 4984.6(17) Å^3, Z = 4, $d_{calcd.}$ = 2.879 Mg m^{-3}, Mo-K_α radiation (graphite-monochromated, λ = 0.71073 Å), T = 100 K, θ$_{range}$ 2.08 to 30.09°. Reflections measd. 35968, indep. 7226, R_{int} = 0.0582. Final R indices [I > 2σ(I)]: R_1 = 0.0571, wR_2 = 0.1654.

Compound [1(Ag$_5$Br$_4$I$_3$)]$_n$: I$_2$ (14 mg, 0.055 mmol) was added to a suspension of [**1**(AgBr)$_2$]$_n$ (100 mg, 0.110 mmol) in CH$_3$CN (12 mL). The reaction mixture was stirred at room temp. for a period of 2 h. The product (1.2 mg, 0.6 µmol, 1%) was crystallized from the reaction mixture. The white precipitate in the suspension was identified as starting reagent. C$_{32}$H$_{64}$Ag$_5$Br$_4$I$_3$N$_{14}$O$_2$ [M + 2DMF] (1916.61): calcd. C 20.05, H 3.37, N 10.23; found C 21.03, H 3.33, N 10.08. ^{1}H NMR (400 MHz, [D$_6$]DMSO): δ = 2.86 (s, 48 H, CH$_3$), 5.13 (s, 2 H, Ar$_H$) ppm. Low solubility hampered the ^{13}C NMR spectroscopic studies. IR (CsI): ṽ = 2927, 1611, 1528, 1492, 1460, 1395, 1324, 1303, 1229, 1172, 1144, 1066, 1025, 896, 805, 782, 741, 696 cm^{-1}. UV/Vis (CH$_3$CN, c = 9.03 × 10^{-6} mol L^{-1}): λ$_{max}$ (ε in L mol^{-1} cm^{-1}) = 213 (7453), 293 (1432), 425 (2169) nm. MS-ESI$^+$ (MeOH/CH$_3$CN): m/z (%) = 265.3 (100) [**1**]$^{2+}$, 530.3 (45) [**1**]$^+$, 610.1 (6.9) [**1** + H + Br]$^+$, 689.1 (2) [**1** + H + 2Br]$^+$, 1398.7 (1) [**1** + H + 5Ag + Br + 2I]$^+$, MS-ESI$^-$ (MeOH/CH$_3$CN): m/z (%) = 156.1 (32) [Ag + Br + I]$^-$, 863.2 (7) [**1** + 2I + Br]$^-$. Crystal data for C$_{28}$H$_{53}$Ag$_5$Br$_4$I$_3$N$_{13}$: M_r = 1811.49, 0.25 × 0.18 × 0.18 mm^3, triclinic, space group P1̄, a = 10.154(2) Å, b = 12.962(3) Å, c = 20.173(4) Å, α = 91.13(3)°, β = 101.84(3)°, γ = 109.83(3)°, V = 2433.0(11) Å^3, Z = 2, $d_{calcd.}$ = 2.473 Mg m^{-3}, Mo-K_α radiation (graphite-monochromated, λ = 0.71073 Å), T = 100 K, θ$_{range}$ 2.06 to 29.99°. Reflections measd. 25403, indep. 13998, R_{int} = 0.0429. Final R indices [I > 2σ(I)]: R_1 = 0.0525, wR_2 = 0.1264.

Compound 1(AgI$_3$): I$_2$ (26.6 mg, 0.105 mmol) was added to a suspension of [**1**(AgI)$_2$]$_n$ (210 mg, 0.21 mmol) in CH$_3$CN (12 mL). The reaction mixture was stirred at room temp. for a period of 2 h. Then the reaction mixture was filtered, the solvent removed under vacuum, and the residue redissolved in CHCl$_3$ (<M;>10 mL) and filtered. The concentrated solution was kept at 4 °C overnight, while brown crystals of **1**(AgI$_3$)·2CHCl$_3$ formed; yield 29 mg (0.023 mmol, 11%). Crystals suitable for an XRD analysis were obtained from concentrated CH$_3$CN solution. C$_{28}$H$_{52}$AgCl$_6$I$_3$N$_{12}$ (1258.09): calcd. C 26.73, H 4.17, N 13.36; found C 26.98, H 4.27, N 14.40. ^{1}H NMR (400 MHz, CD$_3$CN): δ = 2.88 (48 H, CH$_3$), 5.16 (2 H, Ar$_H$) ppm. ^{13}C NMR (100 MHz, CD$_3$CN): δ = 41.46, 103.97, 157.66, 168.04 ppm. IR (CsI): ṽ = 2933, 1602, 1529, 1496, 1465, 1424, 1396, 1380, 1307, 1263, 1231, 1159, 1070, 1018, 898, 882, 845, 813, 781, 757, 737, 685, 620, 584, 540, 516, 452 cm^{-1}. UV/Vis (CH$_3$CN, c = 1.2 × 10^{-5} mol L^{-1}): λ$_{max}$ (ε in L mol^{-1} cm^{-1}) = 209 (25981), 245 (18053), 293 (6127), 426 (10216) nm. MS-ESI$^+$ (CH$_3$CN): m/z (%) = 265.3 (100) [**1**]$^{2+}$, 328.2 (13) [**1** + I]$^{2+}$, 530.3 (16.9) [**1**]$^+$, 657.2 (3) [**1** + I]$^+$, 891.1 (5) [**1** + AgI$_2$]$^+$, 1018.8 (1) [**1** + AgI$_3$]$^+$. MS-ESI$^-$ (CH$_3$CN): m/z (%) = 361.7 (100) [Ag + 2I]$^-$, 489.0 (1) [Ag + 3I + H]$^-$. Crystal data for C$_{26}$H$_{50}$AgI$_3$N$_{12}$: M_r = 1019.35, 0.45 × 0.40 × 0.40 mm^3, monoclinic, space group C2/c, a = 13.729(3) Å, b = 14.841(3) Å, c = 17.986(4) Å, β = 94.13(3)°, V = 3655.2(13) Å^3, Z = 4, $d_{calcd.}$ = 1.852 Mg m^{-3}, Mo-K_α radiation (graphite-monochromated, λ = 0.71073 Å), T = 100 K, θ$_{range}$ 2.27

to 33.12°. Reflections measd. 13682, indep. 6934, R_{int} = 0.0239. Final R indices [I > 2σ(I)]: R_1 = 0.0278, wR_2 = 0.0590.

Compound 1(DDQ)$_2$: From treatment of [**1**(AgBr)$_2$]$_n$ with 2 equiv. DDQ: DDQ (50 mg, 0.220 mmol) was added to a solution of [**1**(AgBr)$_2$] (100 mg, 0.110 mmol) in CHCl$_3$ (12 mL). The brown-red reaction mixture was stirred at room temp. for a period of 2 h. Then the solvent was removed under vacuum and the crude product redissolved in acetone (20 mL). By cooling the acetone solution to 4 °C, **1**(DDQ)$_2$ (73 mg) was obtained the next day as black crystalline solid (0.074 mmol, 67%). Crystals suitable for an XRD analysis were obtained from CH$_3$CN/Et$_2$O. C$_{42}$H$_{50}$Cl$_4$N$_{16}$O$_4$ (984.76): calcd. C 51.23, H 5.12, N 22.76; found C 51.02, H 5.12, N 22.08. ^{1}H NMR (400 MHz, CD$_2$Cl$_2$): δ = 3.07 (48 H, CH$_3$), 5.17 (2 H, Ar$_H$) ppm. ^{13}C NMR (100 MHz, CD$_3$CN): δ = 41.75, 104.69, 157.61, 168.03 ppm. IR (CsI): ṽ = 2943, 2214, 1653, 1625, 1559, 1512, 1468, 1402, 1316, 1287, 1230, 1191, 1170, 1143, 1066, 1018, 886, 787, 753, 713, 516, 476 cm^{-1}. UV/Vis (CH$_3$CN, c = 4.69 × 10^{-5} mol L^{-1}): λ$_{max}$ (ε in L mol^{-1} cm^{-1}) = 222 (21411), 301 (8228), 415 (4524) nm. MS-FAB$^+$: m/z (%) 530.5 (100) [**1**]$^+$, 758.6 (8) [**1** + DDQ]$^+$. MS-FAB$^-$: m/z (%) 228.1 (100) [DDQ]$^-$. Crystal data for **1**(DDQ)$_2$·2CH$_3$CN: C$_{46}$N$_{56}$Cl$_4$N$_{18}$O$_4$, M_r = 1066.89, 0.40 × 0.40 × 0.35 mm^3, triclinic, space group P1̄, a = 7.7080(15) Å, b = 12.654(3) Å, c = 13.100(3) Å, α = 94.95(3)°, β = 97.28(3)°, γ = 92.23(3)°, V = 1261.1(5) Å^3, Z = 1, $d_{calcd.}$ = 1.405 Mg m^{-3}, Mo-K_α radiation (graphite-monochromated, λ = 0.71073 Å), T = 100 K, θ$_{range}$ 2.36 to 30.00°. Reflections measd. 13426, indep. 7291, R_{int} = 0.0549. Final R indices [I > 2σ(I)]: R_1 = 0.0504, wR_2 = 0.1077.

Compound 1(DDQ)$_2$: From treatment of [**1**(AgI)$_2$]$_n$ with 2 equiv. DDQ: The procedure was similar to the one described above. Compound [**1**(AgI)$_2$]$_n$ (100 mg, 0.100 mmol) and DDQ (45 mg, 0.200 mmol) were used; yield 63 mg (0.064 mmol; 64%). For analysis, see above.

Compound [1(Ag$_6$I$_8$)]$_n$: From treatment of [**1**(AgI)$_2$]$_n$ with 1 equiv. TCQ: TCQ (24.5 mg, 0.100 mmol) was added to a suspension of [**1**(AgI)$_2$]$_n$ (100 mg, 0.100 mmol) in CH$_3$CN (12 mL). Then the reaction mixture was stirred at room temp. for a period of 2 h. After filtration the precipitate was washed twice with CH$_3$CN and dried under vacuum to yield 65 mg of product (0.030 mmol, 30%). Crystals were grown from the reaction mixture or concentrated DMF solutions. C$_{26}$H$_{50}$Ag$_6$I$_8$N$_{12}$ (2193.20): calcd. C 14.24, H 2.30, N 7.66; found C 14.79, H 2.42, N 7.81. Further analysis see above.

Compound [1(Ag$_6$I$_8$)]$_n$: From treatment of [**1**(AgI)$_2$]$_n$ with 2 equiv. TCNQ: TCNQ (16.3 mg, 0.80 mmol) was added to a suspension of [**1**(AgI)$_2$]$_n$ (40 mg, 0.040 mmol) in CH$_3$CN (12 mL). Then the reaction mixture was stirred at room temp. for a period of 2 h. After filtration the precipitate was washed twice with CH$_3$CN and dried under vacuum to yield 14 mg of product (0.06 mmol, 16%). Crystals were grown from reaction mixture or concentrated DMF solution. For analysis, see above.

X-ray Crystallographic Study: Suitable crystals were taken directly out of the mother liquor, immersed in perfluorinated polyether oil and fixed on top of a glass capillary. Measurements were made with a Nonius-Kappa CCD diffractometer with low-temperature unit using graphite-monochromated Mo-K_α radiation. The temperature was set to 100 K. The data collected were processed with the standard Nonius software.[17] All calculations were performed with the SHELXT-PLUS software package. Structures were solved by direct methods with the SHELXS-97 program and refined with the SHELXL-97 program.[18,19] Graphical handling of the structural data during solution and refinement was performed with XPMA.[20] Atomic coordinates and anisotropic thermal parameters

of non-hydrogen atoms were refined by full-matrix least-squares calculations.

Supporting Information (see footnote on the first page of this article): Remission spectra of [**1**(AgBr)$_2$]$_n$ and [**1**(AgI)$_2$]$_n$ and photos of [**1**(AgBr)$_2$]$_n$ before and after heating to a temperature of 650 °C.

Acknowledgments

[1] K. Elbl, C. Krieger, H. A. Staab, *Angew. Chem.* **1986**, *98*, 1024–1026; *Angew. Chem. Int. Ed. Engl.* **1986**, *25*, 1023–1024.

[2] a) C. Wurster, *Ber. Dtsch. Chem. Ges.* **1879**, *12*, 2071–2073; b) C. Wurster, E. Schobig, *Ber. Dtsch. Chem. Ges.* **1879**, *12*, 1807–1813; c) R. Kuhn, H. Katz, *Z. Angew. Chem.* **1933**, *46*, 478–479.

[3] A. Peters, E. Kaifer, H.-J. Himmel, *Eur. J. Org. Chem.* **2008**, 5907–5914.

[4] A. Peters, C. Trumm, M. Reinmuth, D. Emeljanenko, E. Kaifer, H.-J. Himmel, *Eur. J. Inorg. Chem.* **2009**, 3791–3800.

[5] D. Emeljanenko, A. Peters, N. Wagner, J. Beck, E. Kaifer, H.-J. Himmel, *Eur. J. Inorg. Chem.* **2010**, 1839–1846.

[6] V. Vitske, C. König, E. Kaifer, O. Hübner, H.-J. Himmel, *Eur. J. Inorg. Chem.* **2010**, 115–126.

[7] C. Trumm, O. Hübner, E. Kaifer, H.-J. Himmel, *Eur. J. Inorg. Chem.* **2010**, 3102–3108.

[8] A. Maronna, E. Bindewald, E. Kaifer, H. Wadepohl, H.-J. Himmel, *Eur. J. Inorg. Chem.* **2011**, 1302–1314.

[9] D. Emeljanenko, A. Peters, V. Vitske, E. Kaifer, H.-J. Himmel, *Eur. J. Inorg. Chem.* **2010**, 4783–4789.

[10] C. J. Adams, R. C. da Costa, R. Edge, D. H. Evans, M. F. Hood, *J. Org. Chem.* **2010**, *75*, 1168–1178.

[11] a) F. T. Edelmann, *Adv. Organomet. Chem.* **2008**, *57*, 183–352; b) F. T. Edelmann, *Coord. Chem. Rev.* **1994**, *137*, 403–481.

[12] a) J. Barker, M. Kilner, *Coord. Chem. Rev.* **1994**, *133*, 219–300; b) P. J. Bailey, S. Price, *Coord. Chem. Rev.* **2001**, *214*, 91–141.

[13] S. Herres-Pawlis, *Nachr. Chem.* **2009**, *57*, 20–23.

[14] a) M. P. Coles, *Dalton Trans.* **2006**, 985–1001; b) M. P. Coles, *Chem. Commun.* **2009**, 3659–3676.

[15] For some representative recent studies, see: a) J. Boerner, U. Floerke, K. Huber, A. Doering, D. Kuckling, S. Herres-Pawlis, *Chem. Eur. J.* **2009**, *15*, 2362–2376; b) F. A. Cotton, G. M. Chiarella, N. S. Dalal, C. A. Murillo, Z. Wang, M. D. Young, *Inorg. Chem.* **2010**, *49*, 319–324; c) J. Börner, U. Flörke, T. Glöger, T. Bannenberg, M. Tamm, M. D. Jones, A. Döring, D. Kuckling, S. Herres-Pawlis, *J. Mol. Catal. A* **2010**, *316*, 139–145; d) G. M. Chiarella, D. Y. Melgarejo, A. Rozanski, P. Hempte, L. M. Perez, C. Reber, J. P. Fackler Jr, *Chem. Commun.* **2010**, *46*, 136–138; e) A. Neuba, U. Floerke, W. Meyer-Klaucke, M. Salomone-Stagni, E. Bill, E. Bothe, P. Hoefer, G. Henkel, *Angew. Chem.* **2011**, *123*, 4596–4600; *Angew. Chem. Int. Ed.* **2011**, *50*, 4503–4507.

[16] D. Emeljanenko, E. Kaifer, H.-J. Himmel, *Eur. J. Inorg. Chem.* **2011**, 2975–2983.

[17] DENZO-SMN, data processing software, Nonius, **1998**; http://www.nonius.com.

[18] a) G. M. Sheldrick, *SHELXS-97, Program for Crystal Structure Solution*, University of Göttingen, **1997**; http://shelx.uni-ac.gwdg.de/SHELX/index.html; b) G. M. Sheldrick, *SHELXL-97, Program for Crystal Structure Refinement*, University of Göttingen, Germany, **1997**; http://shelx.uni-ac.gwdg.de/SHELX/index.html.

[19] *International Tables for X-ray Crystallography*, vol. 4, Kynoch Press, Birmingham, U.K., **1974**.

[20] L. Zsolnai, G. Huttner, *XPMA*, University of Heidelberg, Germany, **1994**; http://www.uni-heidelberg.de/institute/fak12/AC/huttner/software/software.html.

A DFT Study on The Two-Dimensional Second-Order Nonlinear Optical (NLO) Response of Terpyridine-Substituted Hexamolybdates: Physical Insight on 2D Inorganic–Organic Hybrid Functional Materials

Muhammad Ramzan Saeed Ashraf Janjua,*[a,b,c] Muhammad Amin,[a] Muhammad Ali,[a] Beenish Bashir,[a] Muhammad Usman Khan,[a] Muhammad Awais Iqbal,[a] Wei Guan,[c] Likai Yan,[c] and Zhong-Min Su*[c]

DFT calculations were carried out in order to study the second-order nonlinear optical (NLO) response of a series of proposed 2D polyoxometalate-based terpyridine-substituted compounds. These compounds can be formulated as $[Mo_6O_{17}\{N_4C_{25}H_{16}(X)_2\}\{N_4C_{25}H_{16}(X)_2\}]^{2-}$ (X = H, F, Cl, Br, I, CF_3, or CN), which has a wedge Λ-shaped acceptor—π-conjugated bridge—donor—π-conjugated bridge—acceptor (A-π-D-π-A) configuration. The calculations showed that these compounds possess significantly large molecular second-order polarizabilities that range from approximately 1000×10^{-30} to 4300×10^{-30} esu. The combination of trifluoromethyl (CF_3) and cyanide (CN) groups at the end of the terpyridine ligand strengthens the bridge conjugation, which is useful for the enhancement of the NLO response.

In addition, the greatest contributions to the β_{vec} values are derived from the charge transfer (CT) from the Mo≡N bond and the organoimido ligand to the terpyridine-substituted segments. This report demonstrates that various combinations of the acceptor(s) remarkably affect the second-order NLO response. The electronic transitions to the crucial excited states indicated that the y polarized transition contributed to the off-diagonal second-order polarizabiliy tensor (β_{zyy}) and that the z polarized transition accounted for the diagonal second-order polarizabiliy tensor (β_{zzz}). Thus, it steered towards in-plane nonlinear anisotropy ($u = \beta_{zyy}/\beta_{zzz}$) along with a good 2D second-order NLO response. These compounds can be used as good 2D second-order NLO materials from the point of view of their large β values.

1. Introduction

The design and synthesis of second-order nonlinear optical (NLO) materials has been getting more consideration because of their potential applications in the area of optoelectronic technology.[1] On the basis of theoretical and experimental investigations, several principles have been suggested in order to improve the second-order NLO response. These principles include planar donor—π-conjugated bridge—acceptor (D-π-A) type,[2] bond length alternation (BLA) theory,[3] auxiliary donor and acceptor representation of heterocycles,[4] and twisted π-electron systems.[5] The large second-order NLO response can be attained by optimizing the D/A strength and/or by extending the conjugated bridge.[6]

Substantial effort has been devoted previously to the investigation of 1D NLO materials. However, there are several problems with using the 1D NLO molecules to make the large bulk NLO materials, which includes the dipole–dipole interactions.[7] The 1D push–pull molecules always have a large permanent dipole moment, which favors the centro-symmetric arrangement in the crystal. This explains why no bulk NLO responses were observed in the 1D push–pull molecules. Another setback arose from the phase-matching orientations of 1D molecules in the crystal.[8] For example, for the typical *p*-nitrotoluene (PNA) molecule, the 1, 2, *m*, and *mm*2 crystal point groups are in better agreement with the optical phase-matching conditions. The angle between the molecular charge transfer (CT) axis and the principal dielectric axis of the crystal was calculated as 54.7° (or 125.3°). Therefore, only one β tensor component was assumed to be nonnegligible. It is well known that the macroscopic NLO polarizabilities are equal to the summation of the individual molecules. Obviously, the phase-matching orientations of 1D compounds are allowed to recover fewer macroscopic NLO responses in crystal materials. Recently, Wurthner et al.[9,10] and Koleva et al.[11] characterized a series of 1D organic compounds that showed an excellent NLO response because of strong self-aggregation.

[a] Deparment of Chemistry, University of Sargodha, Sargodha 40100, Islamic Republic of Pakistan
E-mail: Janjua@uos.edu.pk
mJanjua@qui.uc.pt
Dr_Janjua2010@yahoo.com
[b] Departamento de Química, Universidade de Coimbra, 3004-535 Coimbra, Portugal
[c] Institute of Functional Material Chemistry and Key Laboratory of Polyoxometalate Science of Ministry of Education, Faculty of Chemistry, Northeast Normal University, Changchun 130024, P. R. China
E-mail: zmsu@nenu.edu.cn

Thus, the multidimensional compounds that have large off-diagonal β tensor components are highly desirable to investigate by using experimental and theoretical methods. The reports explain that a range of organic multidimensional compounds can be used as excellent candidates for the second-order NLO applications.[12] The benefits of these compounds compared to those of the 1D compounds include, (1) the multidimensional NLO compounds display large off-diagonal β tensor components because of the high oscillator strength, low-lying energy excited states with the electron transition dipole moment between two states that are perpendicular to the dipolar axis,[12g,12b] (2) the multidimensional NLO molecules demonstrate an increased stability in the polar order in poled polymers and Langmuir–Blodgett (LB) films,[12e] (3) the multidimensional NLO compounds can enhance the second-order NLO response without loss of transparency in the visible region, which may have an advantage of better nonlinearity/transparency trade-off,[12a,12f] and (4) the multidimensional NLO compounds under the phase-matching orientations can offer a larger macroscopic NLO response because of the large off-diagonal β tensor component as compared to that of the 1D compounds.[12d]

Very few examples of the systematic optimization and determination of the off-diagonal β tensor components have been found in the literature. Most of the literature is based on benzene derivatives,[12d] ruthenium(II) or iron(II) complexes,[13] and dipolar D–A-substituted Schiff base complexes.[1,12] Recently, an investigation of 2D carbazole-cored chromophores explained that the introduction of a heterocycle auxiliary donor can significantly increase the off-diagonal β tensor component due to strong, low-lying energy and a perpendicular CT transition.[14] In addition, the Wurthner group[15] and the Koleva group[16] characterized three kinds of 2D organic compounds, which could become potential NLO materials because of the strong noncovalent interactions.

The polyoxometalates (POMs) are a rich class of inorganic clusters and show interesting chemical and physical properties, which have been applied to a variety of fields, such as catalysis, medicine, biology, and materials science.[17] Among the several types of POMs, the organically derived POMs have been mainly studied. The charge transfer covalently bonded organoimido derived hexamolybdate clusters have attracted particular significance because the organic π-electrons can extend their conjugation to the inorganic framework, which would produce the strong d-π interactions.[18–21] A series of organoimido derivatives that contain various delocalized π-organic ligands have been synthesized,[19] and efficient CT between the organic ligands and the hexamolybdate clusters has been reported. According to the electronic spectroscopic studies, the Mo–N π bond of the organoimido derived hexamolybdate cluster is delocalized on the organic conjugated π system. Generally, an excellent charge transfer is the basis of a large NLO response. Previous investigations on the NLO properties of organoimido derivatives of the hexamolybdates exhibited remarkably large second or third-order NLO re-

sponses. The CT from organoimido to POM was responsible for the NLO response.[22] The substitution of the terminal oxygen of the hexamolybdate clusters with organoimido ligands provided an effective move for the synthesis of difunctionalized hexamolybdates that have C_{2v} symmetry,[19] which can be used to build 2D wedge Λ-shaped structures. The introduction of various heteroatoms in the conjugated polymer is a well-known approach used to change their electronic and optical properties, increase their chemical stabilities, and introduce flexibilities for further molecular engineering.[4,23] In addition, aromatic heterocycles can modulate the NLO response through the different aromatic delocalization energy, the different charge density, the various orientations of the dipole moment of the heterocycle, and even the variable longitudinal charge transfer interaction due to the auxiliary electron donor/acceptor nature of the heterocycles.

All of these factors can be chosen properly in order to design good 2D NLO materials. For the terpyridine-substituted organoimido derivatives of the hexamolybdates, the tuning of these factors to get the maximum charge transfer between the terpyridine-substituted organoimido and the hexamolybdate (POM), and the enhancement of the second-order NLO response have not been fully studied. As a result, we designed a variety of 2D compounds **1**–**8** to probe into these NLO materials from the point of view of the large β values. In this report, we used time-dependent density functional theory (TDDFT) method in order to calculate the second-order polarizabilities of $[Mo_6O_{17}\text{-}\{N_4C_{25}H_{16}(X)_2\}\{N_4C_{25}H_{16}(X)_2\}]^{2-}$ and its constituent molecular components, where X = H, F, Cl, Br, I, CF_3, or CN. The results may open a new way to provide a useful means for designing high-performance NLO materials based on organic–inorganic composites.

2. Methodology

The DFT calculations were performed by using the ADF2008.01 suite of programs.[24] The zero-order regular approximation (ZORA) was adopted in all of the calculations to account for the scalar relativistic effects.[25] The generalized-gradient approximation (GGA) was employed in the geometry optimizations by using the Beck[26] and Perdew[27] (BP86) exchange-correlation (XC) functional. We made use of the standard ADF TZP basis set, which is triple-ζ plus polarization STO basis set. Triple-ζ plus polarization basis sets were used to describe the valence electrons of all of the atoms, while for the transition metal molybdenum atom, a frozen core composed of 1s to 3spd shells was described by means of single Slater functions. The cores (C, N, O, F: 1s; Cl: 2p; Br: 3p; I: 4p) were kept frozen. In the calculations of the polarizability, second-order polarizability, and the excitation property, the RESPONSE and EXCITATION modules[28] implemented in the ADF program were used based on the optimized geometries. The van Leeuwen–Baerends XC potential (LB94) was chosen for the calculation of all of the response properties.[29] The

reliability of the LB94 potential to calculate polarizabilites and hyperpolarizabilities has already been proven and well documented.[30–32] The adiabatic local density approximation (ALDA) was applied for the evaluation of the first and second functional derivatives of the XC potential. Moreover, the value of the numerical integration parameter that was used to determine the precision of the numerical integrals was 6.0. The functional and basis set choices for our studied inorganic–organic hybrid compounds were based on research work that has already been reported.[33,35–39]

3. Molecular Structures

We have quantum chemically designed different kinds of systems by substituting various electron acceptors at the endmost terminal and lateral terminal positions of the terpyridine ligand (positions R^1 and R, Figure 1), which are the most suitable to increase the nonlinearity in the terpyridine-substituted hexamolybdates. On the basis of system 1, we designed systems 2 to 8, which show a large second-order NLO response compared to that of system 1. The geometrical optimization of all of the systems 1–8 was carried out under the symmetry constraint C_{2v}, while the initial

geometric parameters were taken from the crystal data.[34] In order to reduce the computational cost, the torsion in the actual symmetry of the compound crystal was removed by using the C_{2v} symmetry constraint as it had already been reported[39] that it does not influence the results. Their structures are sketched in Figure 1 and the optimized bond lengths are enlisted in Table 1, which are in reasonable agreement with the reported experimental data. Experimentally, the parent compound 1, formulated as $[Mo_6O_{17}$-$(N_4C_{25}H_{18})_2]^{2-}$, crystallizes in the noncentrosymmetric triclinic space group $P\bar{1}$.[34] In our theoretical prediction, it exhibits distinct NLO properties that correspond to various previous reports.[40–42] The quantitative agreement between the experimental and calculated metrical parameters of system 1 persuaded us that the present study is consequential for this research work. Scheme 1 shows the hypothetical calculation model with a sketch map of the 2D wedge Λ-shaped Acceptor—π-conjugated bridge—Donor—π-conjugated bridge—Acceptor (A-π-D-π-A) pattern of the studied systems.
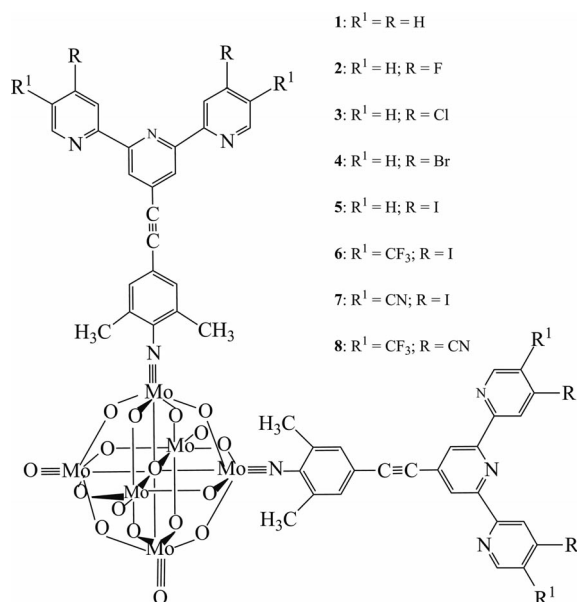
Figure 1. The calculation model for systems 1–8.

1: R^1 = R = H

2: R^1 = H; R = F

3: R^1 = H; R = Cl

4: R^1 = H; R = Br

5: R^1 = H; R = I

6: R^1 = CF$_3$; R = I

7: R^1 = CN; R = I

8: R^1 = CF$_3$; R = CN
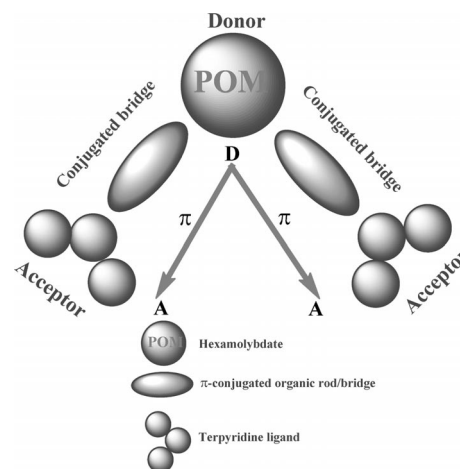
Scheme 1. Hypothetical wedge Λ-shaped 2D (A-π-D-π-A) model for the studied systems 1 to 8.

4. Results and Discussion

In order to make 2D NLO materials, the two terpyridine ligands were introduced with an angle of approximately 90° relative to each other experimentally.[34] The various electron acceptors were chosen at the end of terpyridine-substi-

Table 1. Bond lengths [Å] and angles [°] calculated by DFT for systems 1 to 8.

Metrical parameters	1	2	3	4	5	6	7	8
Mo1–N1	1.816 (1.738)[a]	1.813	1.813	1.813	1.813	1.819	1.815	1.818
C1–N1	1.342 (1.40)	1.346	1.346	1.346	1.343	1.340	1.344	1.342
Mo1–O1	2.243 (2.234)	2.241	2.241	2.241	2.238	2.237	2.239	2.239
C1–N1–Mo1	179.572 (176.5)	179.733	179.733	179.733	179.585	179.775	179.771	179.853

[a] The experimental results are given in parentheses and are taken from reference.[34]

tuted hexamolybdates because our previous studies[35–39] have shown that replacement of a hydrogen atom with other electron acceptor(s) at the end of the organic ring can remarkably increase the second-order NLO response. This is attributed to a large amount of charge transfer from POM to the end of the organic ligand. Inspired by that work, this report shows the charge transfer from POM to the end of the terpyridine ligand that leads to a 2D nonlinear optical response. The orbital features associated with intense perpendicular transitions are shown in Figures 2 and 3, which offer some interesting results. The TDDFT results show that the electronic transitions of systems **1** to **7** mainly arise from POM (HOMO and HOMO–1) to terpyridine ligand (LUMO and LUMO+1) along the *yz* direction. This ten-

dency of the charge transfer also occurs on system **8** but the transition is long range starting from HOMO and HOMO–1 to LUMO+4 and LUMO+5, which leads to the highest β_{vec} value calculated (4320.17×10^{-30} esu) among all of the compounds. The frontier molecular orbitals involved in the dominant electron transitions in systems **1** to **8** are shown in Figures 2 and 3. From these calculations, the frontier molecular orbitals of systems **1** to **8** (Figures 2 and 3), which are involved in the dominant electron transitions, imply strong electronic interactions between the organoimido-substituted hexamolybdate anions and the π electron conjugated bridges. The p-π electron of the Mo≡N bond extends the π electron conjugated bridge. The conjugation is extended and the delocalization is further improved by the introduction of various electron acceptors at the end of the terpyridine segment. The lengthened conjugated bridge, along with different electron acceptors, increase the degree of CT. It is responsible for the enhancement of the second-order polarizibility. The delocalized π bond, which comes from the carbon atoms of arylimido, and the d-p π bond from the d_{xz} orbital on the molybdenum atom, which links
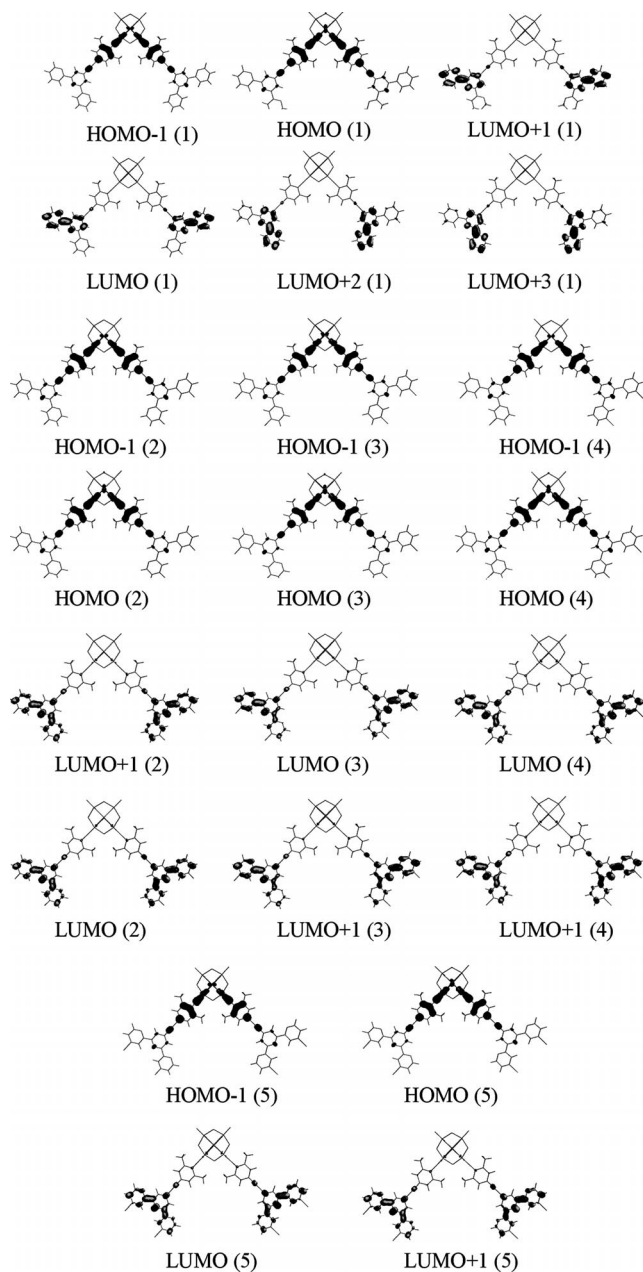
Figure 2. The frontier molecular orbitals of systems **1** to **5** that are involved in the dominant electron transitions.
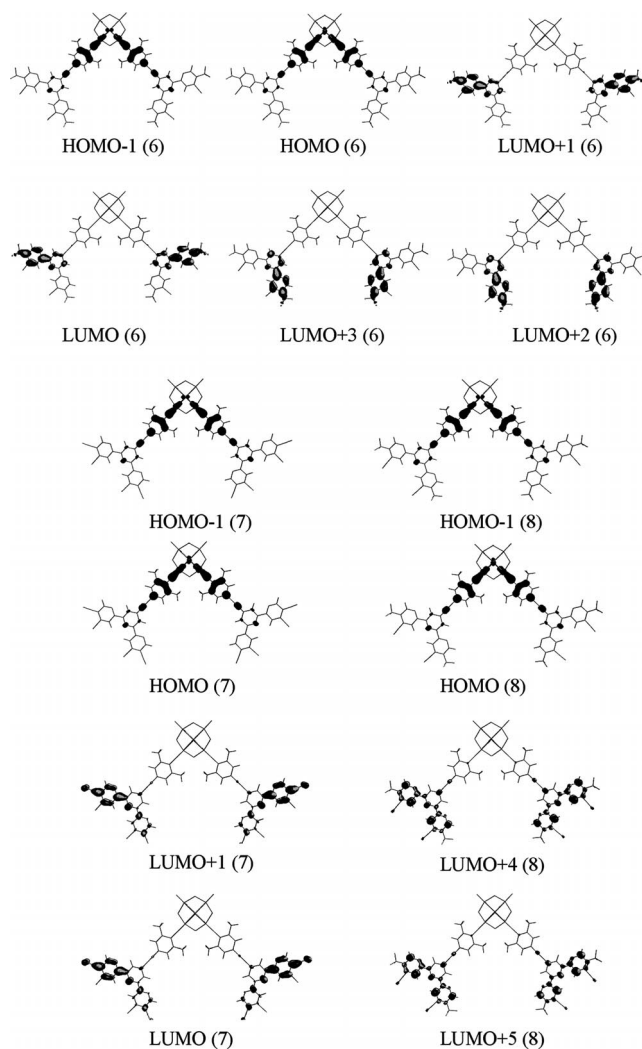
Figure 3. The frontier molecular orbitals of systems **6–8** that are involved in the dominant electron transitions.

the nitrogen atom and the p_x orbital on nitrogen, largely contribute to the highest occupied molecular orbital (HOMO). The lowest unoccupied molecular orbital (LUMO) is mainly localized at the end of the terpyridine rings. According to the TDDFT calculations, the crucial transition state that dominates the optical nonlinearity is generated from Mo≡N and the organoimido segments at the end of the terpyridine-substituted hexamolybdates. This behavior further indicates that the organoimido hexamolybdate acts as a donor and the terpyridine ligand acts as an acceptor. This kind of A-π-D-π-A 2D structure (Scheme 1) generates a strong electronic communication, which results in a large intramolecular CT and a high-performance NLO response.

The computed β_{vec} values of the studied systems show that the NLO response is in the following order: systems **8** > **7** > **6** > **5** ≈ **4** ≈ **3** ≈ **2** > **1**. However, in our studied systems the accepting ability of the terpyridine ligand was enhanced by the incorporation of various electron withdrawing groups that are helpful to increase the optical nonlinearity in this type of inorganic–organic hybrid compounds. In system **8**, two CF_3 groups at the lateral terminal position and two CN groups at the terminals of terpyridine enhance the withdrawing ability of the terpyridine segment and as a result the β_{vec} value increased from 1048.90×10^{-30} esu (system **1**) to 4320.17×10^{-30} esu (system **8**). System **8** offers maximal NLO response among all of the studied systems and it also indicates that POM is acting as a donor in all of the studied systems. The degree of charge transfer and synergistic effects between POM (D) and the terpyridine segment were strongly enhanced by the introduction of different electron acceptors by different ways, particularly through the increased strength of electron acceptors. Most importantly, for the studied 2D inorganic–organic hybrid materials, nonlinearity was significantly improved through the simultaneous introduction of CF_3 and CN. It is helpful to enhance the degree of charge transfer by decreasing the excited energy that leads to a remarkable increase in the first hyperpolarizability.

In these systems (**1**–**8**), a significant increase in the off-diagonal components, β_{zyy}, was observed (Table 2). The off-diagonal components of all of the compounds are larger than the diagonal components, β_{zzz}. For a molecule with C_{2v} symmetry in the yz plane (see Scheme 2), two β tensor

components (β_{zzz} and β_{zyy}) should display significant values while $\beta_{zyy} > \beta_{zzz}$. Hence, the β_{vec} of our studied systems can be described by the equation $\beta_{vec} \approx \beta_{zyy}$.
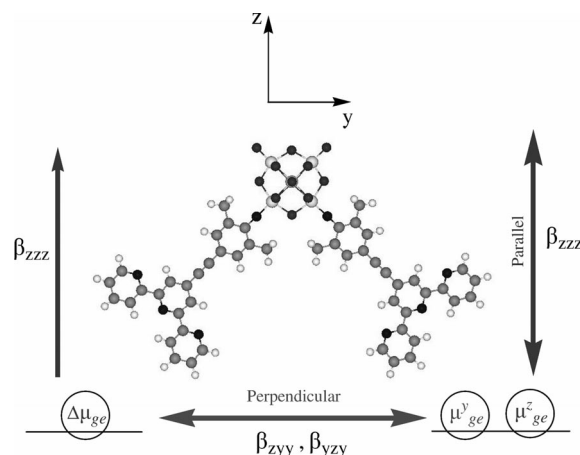
Scheme 2. The two-dimensional second-order NLO character in systems **1** to **8**.

In order to investigate the 2D character of these systems, we have also introduced the "in-plane nonlinear anisotropy" concept (u), which depends on the ratio $u = \beta_{zyy}/\beta_{zzz}$.[43] The u values of the systems are listed in Table 2 and the results show that all of the systems display significant u values (1.35 to 1.69). It demonstrates that all of these systems possess a good 2D NLO response. On the basis of the large second-order NLO response of these compounds (**1**–**8**), the transition features to crucial excited states were also studied. These largely contribute to the second-order NLO properties. For molecules with C_{2v} symmetry, only the "in-plane" y polarized and z polarized transitions are allowed. The z polarized transition dipole moment elements contribute to the diagonal second-order polarizability tensor and the y polarized transition dipole moment elements account for the off-diagonal tensor (see Scheme 2). The value of the β_{zyy} tensor is highest for system **8**, which corresponds to its highest β_{vec} value among all of the studied systems (Table 2). From these results, it can be concluded that incorporation of electron acceptors at the end of the terpyridine ligand is helpful for the enhancement of 2D nonlinearity. Therefore, the larger β_{vec} values are generated as the electron transition originates from the POM-cluster to the terpyridine segment along the yz axis.

5. Conclusions

In this article, we have studied the electronic structures and the 2D second-order NLO response of a series of charge transfer covalently bonded terpyridine-substituted hexamolybdates and clarified the structure–property relationship by using DFT calculations. The results can be summarized as follows: (1) the introduction of electron acceptors at the end of terpyridine-substituted hexamolybdates can remarkably enhance the second-order NLO response because the charge transfer between terpyridine and

Table 2. Calculated static second-order polarizabilities [1×10^{-30} esu], tensors (β_{zzz}, β_{zyy}), anisotropy ($u = \beta_{zyy}/\beta_{zzz}$), excitation energy ($\Delta E_{ge}$) [eV], transition moments (M_z^{gm}, M_y^{gm}), and oscillator strength (f_{os}) for systems **1** to **8**.

System	β_{zzz}	β_{zyy}	u	β_{vec}	ΔE_{ge}	f_{os}	M_z^{gm}	M_y^{gm}
1	654.40	1091.60	1.66	1048.90	1.46	0.55	2.62	3.90
2	813.80	1363.20	1.68	1307.40	1.33	0.58	2.99	4.20
3	841.47	1419.50	1.69	1357.60	1.33	0.55	2.79	4.11
4	866.57	1467.90	1.69	1402.10	1.33	0.58	2.89	4.22
5	872.77	1473.90	1.69	1409.18	1.36	0.62	2.96	4.31
6	1666.70	2686.90	1.61	2613.68	0.95	0.39	2.85	4.08
7	2232.20	3317.70	1.48	3331.58	0.84	0.38	3.09	4.32
8	3061.80	4135.70	1.35	4320.17	1.08	0.56	3.17	4.62

hexamolybdate is increased. (2) The simultaneous introduction of CF_3 and CN at the end of terpyridine-substituted hexamolybdates lead to a large second-order nonlinear optical response (approximately 4300×10^{-30} esu). (3) The second-order polarizabilities of compounds that contain CF_3 and CN are larger than those that have F and Cl,. (4) According to electronic transitions to crucial excited states, these compounds can become excellent 2D NLO candidates as the y polarized transition contributes to the off-diagonal second-order polarizability tensor (β_{zyy}). (5) All of the acceptors strengthen the bridge conjugation and it is advantageous to the NLO response. (6) The 2D systems, particularly systems **7** and **8** that have amazingly large second-order polarizibility, might be promising candidates for NLO materials based on the large β values. (7) The second-order NLO response of the studied compounds are sensitive to the selection of the acceptors at the end of the bonded terpyridine-substituted hexamolybdates. (8) The greatest contributions for the NLO properties of these systems derive from the Mo≡N bond as well as the organoimido ligand to the terpyridine segments. In summary, all of the systems **1**–**8** can be used as excellent 2D second-order NLO candidates from the stance of large β values. The present calculations give a theoretical framework in which the CT and NLO properties may be understood and provide new ways for experimentalists to design high-performance NLO materials. In the conceptual design of possible high-performance NLO materials, the proposed compounds should be targeted for further synthetic investigations.

Acknowledgments

[1] a) P. G. Lacroix, *Eur. J. Inorg. Chem.* **2001**, 339–348; b) D. R. Kanis, M. A. Ratner, T. J. Marks, *Chem. Rev.* **1994**, *94*, 195–242; c) S. Di Bella, *Chem. Soc. Rev.* **2001**, *30*, 355–366.

[2] J. Zyss, I. Ledoux, *Chem. Rev.* **1994**, *94*, 77–105.

[3] F. Meyers, S. R. Marder, B. M. Pierce, J. L. Bredas, *J. Am. Chem. Soc.* **1994**, *116*, 10703–10714.

[4] a) P. R. Varanasi, A. K.-Y. Jen, J. Chandrasekhar, I. N. N. Namboothiri, A. Rathna, *J. Am. Chem. Soc.* **1996**, *118*, 12443–12448; b) E. M. Breitung, C. F. Shu, R. J. McMahon, *J. Am. Chem. Soc.* **2000**, *122*, 1154; c) I. D. Albert, T. J. Marks, M. A. Ratner, *J. Am. Chem. Soc.* **1997**, *119*, 6575–6582.

[5] a) J. S. Yang, K. L. Liau, C. Y. Li, M. Y. Chen, *J. Am. Chem. Soc.* **2007**, *129*, 13183–13192; b) H. Kang, A. Facchetti, H. Jiang, E. Cariati, S. Righetto, R. Ugo, C. Zuccaccia, A. Macchioni, C. L. Stern, Z. Liu, S. T. Ho, E. C. Brown, M. A. Ratner, T. J. Marks, *J. Am. Chem. Soc.* **2007**, *129*, 3267–3286; c) H. Kang, A. Facchetti, P. Zhu, H. Jiang, Y. Yang, E. Cariati, S. Righetto, R. Ugo, C. Zuccaccia, A. Macchioni, C. L. Stern, Z. Liu, S. T. Ho, T. J. Marks, *Angew. Chem.* **2005**, *117*, 8136; *Angew. Chem. Int. Ed.* **2005**, *44*, 7922–7925.

[6] Y. Q. Shi, C. Zhang, H. Zhang, J. H. Bechtel, L. R. Dalton, B. H. Robinson, W. H. Steier, *Science* **2000**, *288*, 119–122.

[7] Y. Liao, S. Bhattacharjee, K. A. Firestone, B. E. Eichinger, R. Paranji, C. A. Anderson, B. H. Robinson, P. J. Reid, L. R. Dalton, *J. Am. Chem. Soc.* **2006**, *128*, 6847–6853.

[8] M. Yang, B. Champagne, *J. Phys. Chem. A* **2003**, *107*, 3942–3951.

[9] F. Würthner, S. Yao, B. Heise, C. Tschierske, *Chem. Commun.* **2001**, 2260–2263.

[10] U. Rusch, S. Yao, R. Wortmann, F. Wurthner, *Angew. Chem.* **2006**, *118*, 7184–7186.

[11] a) T. Kolev, B. B. Koleva, M. Spiteller, W. S. Sheldrick, H. Mayer-Figge, *J. Phys. Chem. A* **2007**, *111*, 10084–10089; b) T. Kolev, B. B. Koleva, M. Spiteller, H. Mayer-Figge, W. S. Sheldrick, *Dyes Pigments* **2008**, *79*, 7–13; c) T. Kolev, B. B. Koleva, S. Stoyanov, M. Spiteller, I. Petkov, *Spectrochim. Acta Part A* **2008**, *70*, 1087–1096; d) B. B. Koleva, T. Kolev, R. W. Seidel, H. Mayer-Figge, M. Spiteller, W. S. Sheldrick, *J. Phys. Chem. A* **2008**, *112*, 2899–2905.

[12] a) C. R. Moylan, S. Ermer, S. M. Lovejoy, I.-H. McComb, D. S. Leung, R. Wortmann, P. Krämer, R. J. Twieg, *J. Am. Chem. Soc.* **1996**, *118*, 12950–12955; b) J. Zyss, *J. Chem. Phys.* **1993**, *98*, 6583–6599; c) Y. J. Liu, Y. Liu, D. J. Zhang, H. Q. Hu, C. B. Liu, *J. Mol. Struct.* **2001**, *570*, 43–51; d) J. J. Wolff, D. Langle, D. Hillenbrand, R. Wortmann, R. Matschiner, C. Glania, P. Krämer, *Adv. Mater.* **1997**, *9*, 138–143; e) M. Tomonari, N. Ookubo, T. Takada, *Chem. Phys. Lett.* **1997**, *266*, 488–498; f) R. Wortmann, C. Glania, P. Kramer, R. Matschiner, J. J. Wolff, S. Kraft, B. Treptow, E. Barbu, D. Langle, G. Gorlitz, *Chem. Eur. J.* **1997**, *3*, 1765–1773; g) S. Di Bella, I. Fargala, I. Ledoux, J. Zyss, *Chem. Eur. J.* **2001**, *7*, 3738–3743; h) H. S. Nalwa, T. Watanabe, S. Miyata, *Adv. Mater.* **1995**, *7*, 754.

[13] a) B. J. Coe, *Acc. Chem. Res.* **2006**, *39*, 383–393; b) B. J. Coe, J. A. Harris, B. S. Brunschwig, I. Asselberghs, K. Clays, J. Garin, J. Orduna, *J. Am. Chem. Soc.* **2005**, *127*, 13399–13410; c) B. J. Coe, J. A. Harris, L. A. Jones, B. S. Brunschwig, K. Song, K. Clays, J. Garin, J. Orduna, S. J. Coles, M. B. Hursthouse, *J. Am. Chem. Soc.* **2005**, *127*, 4845–4859.

[14] C. G. Liu, Y. Q. Qiu, Z. M. Su, G. C. Yang, S. L. Sun, *J. Phys. Chem. C* **2008**, *112*, 7021–7028.

[15] a) F. Würthner, S. Yao, U. Beginn, *Angew. Chem.* **2003**, *115*, 3368; *Angew. Chem. Int. Ed.* **2003**, *42*, 3247–3250; b) A. Lohr, M. Lysetska, F. Würthner, *Angew. Chem.* **2005**, *117*, 5199; *Angew. Chem. Int. Ed.* **2005**, *44*, 5071–5074.

[16] B. B. Koleva, S. Stoyanov, T. Kolev, I. Petkov, M. Spiteller, *Spectrochim. Acta Part A* **2008**, *71*, 847–853.

[17] C. L. Hill, G. C. White, *Chem. Rev.* **1998**, *98*, 1–387.

[18] J. L. Stark, V. G. Young Jr., E. A. Maatta, *Angew. Chem.* **1995**, *107*, 2751; *Angew. Chem. Int. Ed. Engl.* **1995**, *34*, 2547.

[19] Z. H. Peng, *Angew. Chem.* **2004**, *116*, 948; *Angew. Chem. Int. Ed.* **2004**, *43*, 930–935.

[20] B. B. Xu, Z. H. Peng, Y. G. Wei, D. R. Powell, *Chem. Commun.* **2003**, 2562.

[21] B. B. Xu, M. Lu, J. H. Kang, D. G. Wang, J. Brown, Z. H. Peng, *Chem. Mater.* **2005**, *17*, 2841–2851.

[22] a) G. C. Yang, W. Guan, L. K. Yan, Z. M. Su, L. Xu, E. B. Wang, *J. Phys. Chem. B* **2006**, *110*, 23092–23098; b) L. K. Yan, M. S. Jin, J. Zhuang, C. G. Liu, Z. M. Su, C. C. Sun, *J. Phys. Chem. A* **2008**, *112*, 9919–9923; c) L. K. Yan, G. C. Yang, W. Guan, Z. M. Su, R. S. Wang, *J. Phys. Chem. B* **2005**, *109*, 22332–22336.

[23] P. K. Nandi, N. Panja, T. K. Ghanty, *J. Phys. Chem. A* **2008**, *112*, 4844–4852.

[24] a) For articles on *Chemistry with ADF*, see: G. te Velde, F. M. Bickelhaupt, E. J. Baerends, C. Fonseca Guerra, S. J. A. van Gisbergen, J. G. Snijders, T. Ziegler, *J. Comput. Chem.* **2001**, *22*, 931–967; b) C. Fonseca Guerra, J. G. Snijders, G. Te Velde, E. J. Baerends, *Theor. Chem. Acc.* **1998**, *99*, 391–403; c) ADF2008.01, SCM, Theoretical Chemistry, Vrije Universiteit, Amsterdam, The Netherlands, http://www.scm.com.

[25] E. van Lenthe, E. J. Baerends, J. G. Snijders, *J. Chem. Phys.* **1993**, *99*, 4597–4610.

[26] A. D. Becke, *Phys. Rev. A* **1988**, *38*, 3098–3100.

[27] J. P. Perdew, *Phys. Rev. B* **1986**, *33*, 8822–8824.

[28] S. J. A. van Gisbergen, J. G. Snijders, E. J. Baerends, *Comput. Phys. Commun.* **1999**, *118*, 119–138.

[29] R. van Leeuwen, E. J. Baerends, *Phys. Rev. A* **1994**, *49*, 2421–2431.

[30] a) S. J. A. van Gisbergen, V. P. Osinga, O. V. Gritsenko, R. van Leeuwen, J. G. Snijders, E. J. Baerends, *J. Chem. Phys.* **1996**, *105*, 3142–3151; b) S. J. A. van Gisbergen, J. G. Snijders, E. J. Baerends, *J. Chem. Phys.* **1998**, *109*, 10644–10656.

[31] S. J. A. van Gisbergen, J. G. Snijders, E. J. Baerends, *Phys. Rev. Lett.* **1997**, *78*, 3097–3100.

[32] S. J. A. van Gisbergen, J. G. Snijders, E. J. Baerends, *J. Chem. Phys.* **1998**, *109*, 10657–10668.

[33] a) J. Zhuang, L. K. Yan, C. G. Liu, Z. M. Su, *Eur. J. Inorg. Chem.* **2009**, 2529–2535; b) M. R. S. A. Janjua, C. G. Liu, W. Guan, S. Muhammad, Z. M. Su, *Eur. J. Inorg. Chem.* **2009**, *34*, 5181–5188; c) Y. L. Si, C. G. Liu, E. B. Wang, Z. M. Su, *Theor. Chem. Acc.* **2009**, *122*, 217–226; d) L. K. Yan, Z. Dou, W. Guan, S. Q. Shi, Z. M. Su, *Eur. J. Inorg. Chem.* **2006**, 5126–5129; e) W. Guan, G. C. Yang, L. K. Yan, Z. M. Su, *Eur. J. Inorg. Chem.* **2006**, *20*, 4179–4183.

[34] a) J. Kang, B. Xu, Z. Peng, X. Zhu, Y. Wei, D. R. Powell, *Angew. Chem.* **2005**, *117*, 7062; *Angew. Chem. Int. Ed.* **2005**, *44*, 6902–6905; b) B. Xu, Z. Peng, Y. Wei, D. R. Powell, *Chem. Commun.* **2003**, *20*, 2562–2563.

[35] M. R. S. A. Janjua, Z. M. Su, W. Guan, C. G. Liu, L. K. Yan, P. Song, G. Maheen, *Aust. J. Chem.* **2010**, *63*, 836–844.

[36] M. R. S. A. Janjua, C. G. Liu, W. Guan, J. Zhuang, S. Muhammad, L. K. Yan, Z. M. Su, *J. Phys. Chem. A* **2009**, *113*, 3576–3587.

[37] M. R. S. A. Janjua, W. Guan, L. K. Yan, Z. M. Su, *Curr. Phys. Chem.* **2011**, *1*, 99–105.

[38] M. R. S. A. Janjua, W. Guan, L. K. Yan, Z. M. Su, M. Ali, I. H. Bukhari, *J. Mol. Graph. Model.* **2010**, *28*, 735–745.

[39] M. R. S. A. Janjua, W. Guan, L. K. Yan, Z. M. Su, A. Karim, J. Akbar, *Eur. J. Inorg. Chem.* **2010**, 3466–3472.

[40] S. Pan, J. P. Smit, B. Watkins, M. R. Marvel, C. L. Stern, K. R. Poeppelmeier, *J. Am. Chem. Soc.* **2006**, *128*, 11631–11634.

[41] B. Ruiz, Z. Yang, V. Gramlich, M. Jazbinsek, P. Gunter, *J. Mater. Chem.* **2006**, *16*, 2839–2842.

[42] S. Pan, J. P. Smit, M. R. Marvel, E. S. Stampler, J. M. Haag, J. Baek, P. S. Halasyamani, K. R. Poeppelmeier, *J. Solid State Chem.* **2008**, *181*, 2087–2091.

[43] S. Di Bella, I. Fragala, *New J. Chem.* **2002**, *26*, 285–290.

FULL PAPER

Homochiral, Supramolecular Frameworks Built from a Zinc(II) Tetramer or Cadmium(II) Dimer Containing Enantiopure Carboxylate Ligands Functionalized with a Strong π···π Stacking Synthon

Daniel L. Reger,*[a] Agota Debreczeni,[a] and Mark D. Smith[a]

The enantiopure ligand (S)-2-(1,8-naphthalimido)propanoate (L_{ala}^-) forms a tetrameric zinc(II) complex $[Zn_4(L_{ala})_6(OH)_2(MeOH)_4]\cdot3(CH_2Cl_2)\cdot2(MeOH)$ (**1**) and a dimeric cadmium(II) complex $[Cd_2(L_{ala})_4(DMF)_3(MeOH)]$ (**2**). Bridging κ^2-carboxylate and hydroxide ligands link the four zinc centers in **1**. The strong π···π-stacking 1,8-naphthalimide supramolecular synthons organize the tetramers into a 3D architecture that contains linked, homochiral helical chains. In the structure, each chain is connected to four other chains by the π···π-stacking interactions of the naphthalimide rings. The structure is open with two types of channels filled with ordered and disordered solvent molecules. The two cadmium centers in **2** are linked by two κ^2-carboxylate ligands. The π···π-stacking interactions of the naphthalimide rings organize the structure into 2D sheets, which lack complex chiral features. The naphthalimide rings in these d^{10} metal complexes promote blue (**1**) and green (**2**) emission in the solid state.

Introduction

Metal–organic frameworks (MOFs) assembled from metal clusters and organic linkers have attracted the attention of the scientific community for their potential application in catalysis,[1] energy storage,[2] sensing,[3] and separation.[4] They can be considered as multifunctional materials with excellent physical properties such as luminescence,[5] magnetism,[6] nonlinear optics, and optoelectronics.[7] The interest in MOFs has led to extensive research into the rational design of a wide variety of architectures with high structural stability. Such features can be achieved by connecting robust nodes that contain multiple transition metals, referred to as secondary building units (SBUs), with organic linkers by strong covalent bonds. Transition-metal carboxylate complexes are favored SBUs in the assembly of MOFs because of their ability to serve as large rigid vertices that can be joined by multicarboxylate linkers to form very stable, porous crystalline materials.[8]

Less rigid, but still highly organized architectures that possess interesting properties can be assembled by noncovalent forces. Described as the "masterkey interaction in supramolecular chemistry", hydrogen bonding is the most widely used synthon in the crystal engineering of supramolecular network solids due to its clearly defined, reproducible and transferable directional properties.[9] Another noncovalent interaction that has received considerable attention in the self-assembly of crystalline architectures is π···π stacking between aromatic rings. This interaction is not as directional as hydrogen bonding, because variable orientations of the moieties involved often occur in order to maximize the electrostatic attraction between the σ framework and the π-electron density of the stacked groups.[10] Despite the less predictable directional properties of the π-stacked aromatic rings, an order of stability in the interaction of two π systems has been well established: π-deficient–π-deficient > π-deficient–π-rich > π-rich–π-rich, where the π-deficient–π-deficient interaction approaches the importance of hydrogen bonding in a properly chosen aromatic system.[10]

Over the past few years, our group has extensively studied the chemistry of bifunctional ligands that contain the π-deficient 1,8-naphthalimide group (Scheme 1).[11] We have shown that ligands that combine the 1,8-naphthalimide π-stacking synthon with a bis(pyrazolyl)methane or a 2,2′-bipyridine unit formed complexes that associated into dimers (structure retained in solution) and polymers by unusually strong π···π-stacking interactions.[11a–11c] Most recently, we have designed molecules in which the 1,8-naphthalimide moiety was linked to a carboxylic acid group.[11d–11j] The goal of these studies was to utilize these molecules, after deprotonation of the acid, as ligands in the construction of solids with MOF-type architectures that combine the robustness of transition metal carboxylate cores with the supramolecular organization given by the 1,8-naphthalimide rings – solids we term supramolecular metal-organic frameworks (SMOFs). In our first publication, we showed that the carboxylate ligands L_{C2}^- and L_{C3}^- (Scheme 1) form cop-

[a] Department of Chemistry and Biochemistry, University of South Carolina, Columbia, South Carolina 29208, USA Fax: +1-803-777-9521 E-mail: Reger@chem.sc.edu

per(II) complexes that contain a paddlewheel $Cu_2(O_2CR)_4$-type SBU core. Highly organized supramolecular structures were produced, which were dominated by the π···π stacking of the 1,8-naphthalimide rings.[11d]
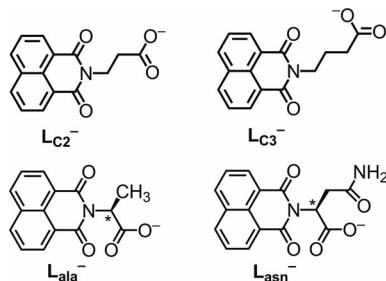
Scheme 1. Carboxylate ligands functionalized with a 1,8-naphthalimide group.

In order to explore this chemistry further for the syntheses of chiral SMOFs, we have introduced an enantiopure chiral center from an amino acid into these types of ligands to generate tri- and tetrafunctional (where the fourth functionality is the amide group from L-asparagine) molecules (Scheme 1). Although considerable effort has recently been dedicated to the syntheses of chiral framework structures because of a multitude of potential applications,[12–14] the use of simple amino acids coupled to the strong π···π-stacking naphthalimide group is a unique methodology aimed at the syntheses of homochiral SMOFs. In our earlier work, we have shown that trifunctional L_{ala}^- and tetrafunctional L_{asn}^- ligands (Scheme 1), when incorporated into the paddlewheel $Cu_2(O_2CR)_4$-type SBU core, led to homochiral solids with unique structures and interesting properties.[11f,11i] In an effort to elaborate the molecular and supramolecular chemistry of these interesting ligands with d^{10} group 12 metals, we report here the structural analysis and luminescent properties of zinc(II) and cadmium(II) complexes of the trifunctional L_{ala}^- ligand.

Results and Discussion

Results

The reaction of enantiopure KL_{ala} (generated in situ) with $Zn(O_2CCH_3)_2(H_2O)_2$ in the presence of pyridine yielded a white solid, which was insoluble in water. The subsequent crystallization by vapor diffusion of Et_2O into a CH_2Cl_2/MeOH (9:1) solution of this solid produced $[Zn_4(L_{ala})_6(OH)_2(MeOH)_4]\cdot3(CH_2Cl_2)\cdot2(MeOH)$ (**1**). The reaction of KL_{ala} with $CdCl_2$ under the same conditions resulted in a white precipitate that yielded $[Cd_2(L_{ala})_4(DMF)_3(MeOH)]$ (**2**) when the solid was crystallized from an *N,N*-dimethylformamide (DMF)/MeOH (6:1) mixture by vapor diffusion of Et_2O into the solution.

Structural Analysis

Single crystals of **1** and **2** were characterized by X-ray diffraction at 100 K. Selected bond lengths and angles for

both compounds are gathered in Table S1 (Supporting Information).

Figure 1 shows the molecular structure of **1**. The compound has a tetranuclear homochiral structure [all chiral stereocenters were determined to be (*S*)-configured] with two zinc centers that have octahedral and two that have tetrahedral coordination spheres, each related by a twofold symmetry axis. The equatorial sites of the two equivalent, six-coordinate Zn1 centers are occupied by an oxygen atom of a bridging κ^2-carboxylate ligand, two triply bridging oxygen atoms from the hydroxide groups, and the oxygen atom of a methanol molecule. The axial sites are occupied by the oxygen atom of a second bridging κ^2-carboxylate ligand and the oxygen atom of another methanol molecule. The coordination environment of the two four-coordinate Zn2 atoms is generated by a triply bridging oxygen atom from the hydroxide groups, one oxygen atom from each of the two bridging κ^2-carboxylate ligands, and the oxygen atom of a κ^1-carboxylate ligand.
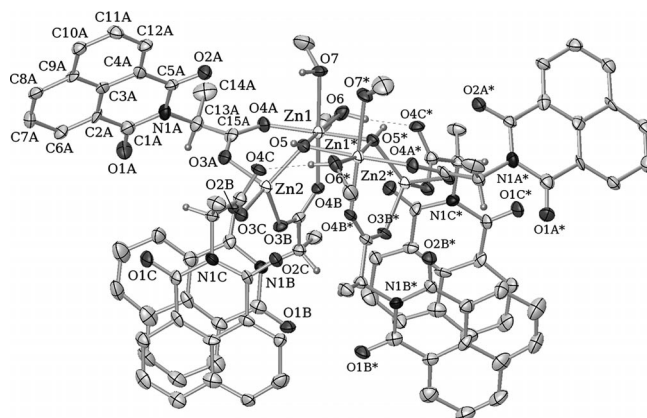
Figure 1. Ellipsoid plot for **1**. Displacement ellipsoids drawn at the 40% probability level. Some atom labels and most hydrogen atoms are omitted for clarity. All chiral carbon atoms (C13 A/B/C) were determined to be (*S*)-configured.

Intramolecular hydrogen bonds are formed between the equatorially coordinated methanol molecules and the noncoordinating oxygen atoms of the κ^1-carboxylate ligands with an OH···O distance of 1.86 Å (O···O 2.68 Å) and an O–H–O angle of 160°. The axial methanol molecules are also involved in hydrogen bonding with the two noncoordinated methanol molecules. In this case the OH···O distance is 1.86 Å (O···O 2.73 Å), and the O–H–O angle is 177°. Additionally, the OH group of the noncoordinated methanol molecules hydrogen-bond with the carbonyl oxygen atom of the naphthalimide rings situated on the bridging κ^2-carboxylate ligands. In this interaction the OH···O distance is 1.90 Å (O···O 2.74 Å), and the O–H–O angle is 176°.

Strong π···π stacking of the electron-deficient 1,8-naphthalimide groups organize the tetranuclear zinc clusters into a 3D architecture that contains linked, homochiral helical chains. The naphthalimide rings on each tetranuclear unit are involved in π···π-stacking interactions with six other naphthalimide moieties on four separate tetrazinc units. Each of the two naphthalimide rings situated on the left

side of the central blue zinc cluster in Figure 2 (containing the N1A and N1A* atoms) π···π-stacks with two other naphthalimide moieties ("clamped"), one by the red and one by the magenta tetranuclear units. These three units, when combined with the purple unit that, like the blue unit, has two of its naphthalimide rings clamped by two rings each of the red and magenta tetranuclear units, generate an (M)-helical chain.
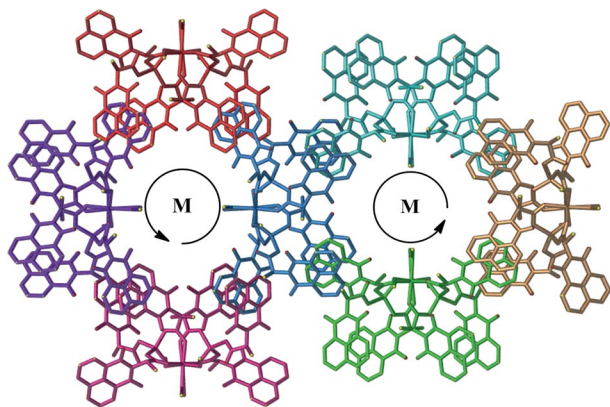
Figure 2. The π···π-stacking interactions in **1** that organize the tetranuclear SBU units into homochiral helical chains.

Figure 3 shows five color-coded units of this helical chain structure oriented perpendicular to those in Figure 2. Only the naphthalimide rings that assemble this chain are illustrated. The naphthalimide π···π-stacking interactions are represented by green dashes, which show how two sets of two rings on the red and magenta units clamp one ring on each side of the blue and purple units to form a strong interaction between the three naphthalimide rings in each case. The distance between the coils of the helical chain (the pitch) is 14.2 Å (the length of the crystallographic *c* axis).
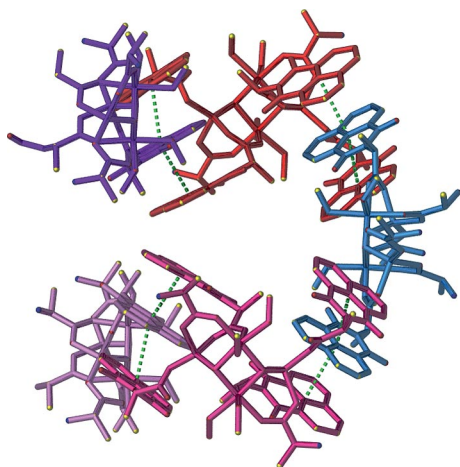
Figure 3. The (M)-helical chain in the structure of **1**. Five tetranuclear clusters are pictured with the naphthalimide rings that generate the helical structure (the other rings are omitted for clarity). Two shades of purple are used to indicate the unit that is repeated, which exactly overlap in the perpendicular orientation of Figure 2. The green dashes show the naphthalimide π···π-stacking interactions.

Two of the other four naphthalimide rings on the right side of the central blue unit pictured in Figure 2 (containing the N1B and N1C atoms) π···π-stack with one naphthalimide ring situated on the adjacent light blue SBU unit; i.e. the light blue ring is clamped by the two dark blue naphthalimide moieties. The same interactions are formed between the other two dark blue rings (containing the N1B* and N1C* atoms) and the light green naphthalimide moiety on the neighboring SBU unit. When combined with the brown unit, these π···π-stacking interactions on the right side of the central blue zinc cluster generate a second helical chain of the same (M)-helicity as the first. The central dark blue SBU unit connects the two homochiral helical chains into a 3D architecture. Figure 2 shows two helical chains connected by the dark blue unit in such a way that two of its naphthalimide rings belong to the chain on the left and the other four belong to the chain on the right. Each chain adopts a left-handed (M) conformation (Figure 2).

Figure 4 illustrates the complex 3D architecture of **1**. Five color-coded helical chains are pictured. Each chain adopts a left-handed (M) conformation and is connected to four other chains by the π···π-stacking interactions of the naphthalimide rings. There are channels through the unit cell origin (approximately 15 × 20 Å) and center (9.9 × 9.9 Å) that are filled with ordered and disordered solvent molecules.
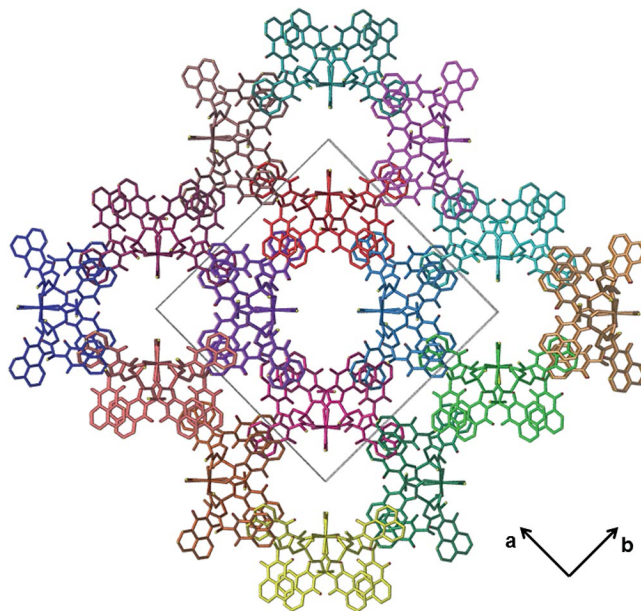
Figure 4. 3D architecture of **1** viewed along the *c* axis.

In the structure of **1** there are two types of π···π-stacking interactions between the color-coded naphthalimide rings of the neighboring units (A and B) that have similar interaction parameters (Table 1). Both of the π···π-stacking interactions are strong; the naphthalimide rings are 3.42 (A) and 3.38 Å (B) apart, and the rings are nearly parallel. The dipole vectors (which run through the central-ring carbon atoms and point towards the nitrogen atom) of the naphthalimide units involved in the π···π stacking are oriented at

Table 1. The π···π-stacking interaction parameters.

Compound	Interaction type	Central carbon atoms distance [Å]	Dipole angle [°]	Plane angle [°]	Avg. perpendicular distance [Å]	Avg. χ [Å]
1	A	3.69	139	3.2	3.42	1.33
	B	3.72	155	6.4	3.38	1.56
2	A	3.68	173	8.2	3.42	1.36
	B	3.82	167	2.5	3.62	1.22
	C	3.63	161	5.4	3.47	1.07
	D	3.67	140	5.8	3.49	1.12

139 and 155°, respectively. An additional parameter of interest in these systems is χ, which measures the amount of slippage one ring involved in the π···π stack has with respect to the other. The parameter is the third side of the triangle formed with the average perpendicular distance between the rings and the line joining the central carbon atoms of the two rings. In the structure of **1**, the slippage values for the naphthalimide rings in the two interactions are 1.33 (A) and 1.56 Å (B), which are in the range of strong interactions (0.43 to 2.4 Å).[11h]

Figure 5 illustrates the molecular structure of **2**. The compound is an asymmetric homochiral CdII dimer, in which the cadmium centers are bridged by two κ²-carboxylate ligands. Additionally, a nonbridging κ²-carboxylate ligand is coordinated to each cadmium center; two DMF molecules are bound to Cd1 and one DMF molecule and one methanol molecule to the Cd2 center. Thus, both cadmium atoms are six-coordinate with a distorted octahedral geometry. The equatorial sites on both cadmium atoms are occupied by oxygen atoms of the two separate bridging κ²-carboxylate ligands and both of the oxygen atoms of a non-bridging κ²-carboxylate ligand. The axial sites of Cd1 are populated by the oxygen atoms of the two DMF molecules, whereas the axial positions of Cd2 are occupied by the oxygen atoms of a DMF and one methanol molecule. Two of the $\mathbf{L_{ala}}^-$ ligands (B and D), one DMF (N6/O6, C19–C21), and the methanol molecule (O8–C25) are disordered over two closely separated positions (the minor disorder components were omitted for clarity).
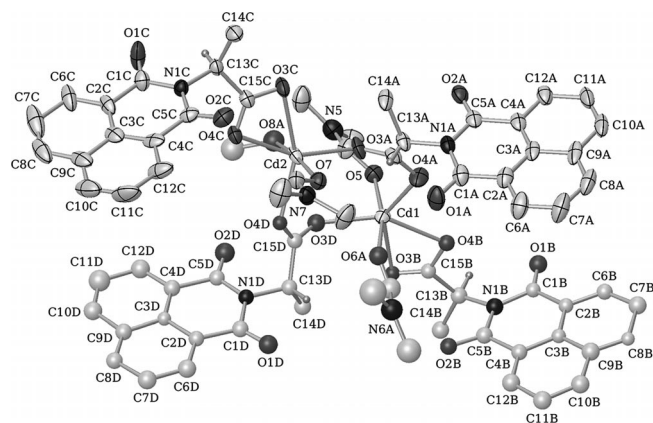
Figure 5. Molecular structure of **2**. Displacement ellipsoids drawn at the 40% probability level. Minor disorder components, most hydrogen atoms, and some atom labels are omitted. All stereocenters (C13) were determined to be (*S*)-configured.

All four naphthalimide rings of the dimeric SBU units are involved in π···π-stacking interactions with naphthalimide rings of neighboring dimeric units. As shown in Figure 6, four rings from two adjacent dimeric units form an extended π···π stack with three slightly different interaction parameters, type B between two "inner" rings and types A and C between an "inner" ring and "outer" ring that lead to the formation of 1D ribbons. The remaining interaction, D, takes place between two adjacent ribbons generating a 2D sheet structure. All four types of π···π-stacking interactions have parameters that fall in the range of strong interactions (Table 1).
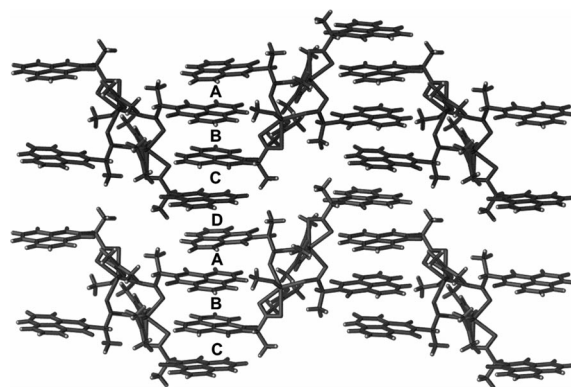
Figure 6. 2D sheet structure of **2**.

Weaker C–H···O interactions are formed between sheets, but there are no other substantial supramolecular forces in the structure of **2**. These C–H···O interactions are formed between the carbonyl oxygen atoms of the naphthalimide rings and C–H groups on the naphthalimide rings of the second sheet. In these interactions, the CH···O distance is 2.54 Å (C···O 3.08 Å) with a C–H–O angle of 118°.

Thermogravimetric Analysis

To examine the framework integrity, thermogravimetric analysis (TGA) of **1** (Figure 7) was performed on a microcrystalline solid sample. Based on the analysis, it is assumed that the disordered solvent and two dichloromethane molecules of crystallization are lost upon collection and air-drying of the crystals. Upon heating, the weight loss of 5.2% (calcd. 6.8%) in the first step corresponds to the loss of the remaining dichloromethane and the two methanol molecules of crystallization. In the next step, between 152 and

D. L. Reger, A. Debreczeni, M. D. Smith

245 °C, the loss of the four coordinated methanol molecules and the bridging OH groups occur (7.6%, calcd. 7.4%). The weight change in the last step corresponds to the loss of the six carboxylate ligands (74.0%, calcd. 73.8%). The final residual weight is 13.2%, which corresponds to ZnO (calcd. 14.9%).
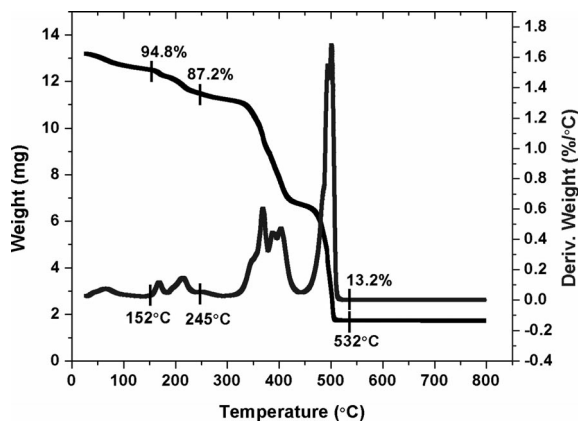
Figure 7. TGA/differential thermal analysis (DTA) curves for **1**.

UV/Vis and Fluorescence Spectroscopic Properties

The diffuse reflectance (UV/Vis) spectra show sharp maxima, $\lambda_{max,UV}$, at 365 nm for HL_{ala}, 364 nm for **1**, and 378 nm for **2**. The fluorescence emission spectra of the compounds were recorded in the solid state at room temperature (Figure 8). HL_{ala} has a blue fluorescence with $\lambda_{max,Fl}$ at 449 nm. For **1**, $\lambda_{max,Fl}$ was at 476 nm, and for **2**, $\lambda_{max,Fl}$ was at 470 nm, which are redshifted compared to the free ligand.
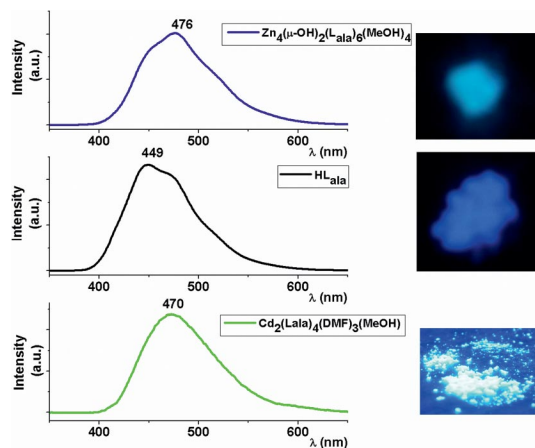
Figure 8. Fluorescence emission spectra of HL_{ala}, **1**, and **2** in the solid state with excitation at 263 nm for HL_{ala} and **1**, and 284 nm for **2**.

Discussion

Two homochiral SMOF structures that contain the enantiopure amino acid based trifunctional L_{ala}^{-} ligand

were prepared and structurally analyzed. As expected from the design of the system, in **1** the strong π⋯π-stacking interactions of the naphthalimide rings of the enantiopure L_{ala}^{-} ligands organize the $[Zn_4(L_{ala})_6(OH)_2(MeOH)_4]$ tetrameric units into a helical chain structure. Additional π⋯π-stacking interactions of the naphthalimide moieties connect these helical chains into a 3D architecture. Importantly, the central tetrameric SBU units are organized into this homochiral, helical 3D structure by noncovalent π⋯π-stacking interactions to form a homochiral SMOF structure. Although the importance of the π⋯π-stacking interactions and the lack of other important interactions such as intermolecular hydrogen bonding is evident from the structure, the exact contribution of π⋯π stacking to the overall packing forces is difficult to determine. We have previously calculated the interaction energy between the naphthalimide rings using the MP2/6-31G* level of theory to be in the range of 15–16.5 kcal/mol.[11b] Although the actual value for this interaction taking place in solution or in the solid phase will be lower than this gas-phase-calculated number, clearly the interaction is substantial. TGA demonstrated that the framework is fairly robust after the partial removal of solvents of crystallization. We have previously shown that similar ligands, with a longer connecting group between the amino acid and the naphthalimide supramolecular synthon, form homochiral, helical framework complexes with first-row transition metals. These structures are also supported in two dimensions by the covalent linkages of 4,4′-bipyridine ligands.[11g,11h] Given that the supramolecular structures of these previously reported complexes are organized by both covalent and noncovalent forces, **1** represents the first homochiral SMOF solid that we have been able to prepare from ligands that couple carboxylate groups from enantiopure amino acids with the 1,8-naphthalimide supramolecular synthon in which π⋯π-stacking interactions of the naphthalimide rings are the main organizing force of the supramolecular helical framework.

Surprisingly, in the homochiral structure of **2**, no helical chains are formed. Instead, the acentric dimeric units are assembled into a simple 2D sheet by the π⋯π-stacking interactions of the naphthalimide rings. There is no indication of a helical-type structure or any 3D structure as observed for **1**.

Despite the lack of helicity in the structure of **2**, both new complexes clearly demonstrate the importance of the naphthalimide group in the organization of highly ordered structures. This structural study, coupled with our earlier work,[11] demonstrates that the naphthalimide group forms a reliable supramolecular synthon that can be incorporated into several multicarboxylate SBU cores to generate high-dimensional materials, in the case of **1**, a homochiral SMOF.

In addition, the presence of the naphthalimide rings in these d^{10} metal complexes supports interesting luminescent properties. In this case, **1** shows blue and **2** shows green emission in the solid state that can likely be assigned to a charge-transfer transition.

Conclusions

An enantiopure ligand built from L-alanine and the 1,8-naphthalimide group formed a tetrameric zinc(II) complex, which was linked into a 3D homochiral supramolecular MOF structure exclusively by π···π-stacking interactions of the naphthalimide rings. The same ligand formed a dimeric cadmium complex with a 2D sheet structure, which lacks complex chiral features. Both complexes show luminescent properties.

Experimental Section

General Considerations: All reactants were used as purchased from Aldrich. The ^{1}H NMR spectra were recorded with Varian Mercury VX 300 and Varian Mercury VX 400 spectrometers; the chemical shifts are reported in ppm and are referenced to the protonated solvent residual. The ^{13}C NMR spectra were recorded with a Bruker Avance DRX 400 spectrometer, and the chemical shifts are referenced to the residual deuterated solvent signal. The gradient heteronuclear single quantum correlation (HSQC) experiment was performed with the same Bruker Avance DRX 400 spectrometer. TGA was performed with a Thermal Analysis (TA) SDT-Q600 simultaneous DTA/TGA system. The sample was heated in air to 800 °C with a heating rate of 10 °C/min. The fluorescence spectra were recorded with a Perkin–Elmer LS 55 fluorescence spectrometer. Ground solid samples were used in a 4 mm cell. The protonated form of the ligand, (S)-2-(1,8-naphthalimido)propanoic acid (HL$_{ala}$), was synthesized as previously reported.[11i] Elemental analyses were performed by Robertson Microlit Laboratories (Ledgewood, NJ).

Synthesis of Zn$_4$(L$_{ala}$)$_6$(OH)$_2$(MeOH)$_4$·3(CH$_2$Cl$_2$)·2(MeOH) (1): Powdered HL$_{ala}$ (0.540 g, 2.0 mmol) was suspended in water (30 mL), and a methanolic KOH solution (2 mL, 1 M) was added. The suspension was stirred until it had completely cleared. To this solution was added an aqueous solution (10 mL) of Zn$_2$(O$_2$CCH$_3$)$_2$-(H$_2$O)$_2$ (0.220 g, 1.0 mmol) that contained pyridine (0.16 mL). A white precipitate formed immediately. The mixture was stirred for 2 h, and the solid was collected by filtration, washed with water and diethyl ether (20 mL of each), and dried under vacuum. Yield: 0.512 g of Zn$_2$(L$_{ala}$)$_4$(py)$_2$. The analytical sample was dried to constant weight. C$_{70}$H$_{50}$N$_6$O$_{16}$Zn$_2$ (1361.95): calcd. C 61.73, H 3.70, N 6.17; found C 61.53, H 3.32, N 6.47. ^{1}H NMR (300 MHz, CD$_2$Cl$_2$/CD$_3$OD): δ = 8.68 (d, J = 4.5 Hz, 4 H, py) 8.26 (d, J = 7.2 Hz, 8 H, naphth), 8.04 (d, J = 8.1 Hz, 8 H, naphth), 7.84 (t, J = 7.5 Hz, 2 H, py), 7.52 (t, J = 7.6 Hz, 8 H naphth), 7.39 (t, J = 7.5 Hz, 4 H, py), 5.62 (q, J = 6.9 Hz, 4 H, CH), 1.60 (d, J = 6.9 Hz, 12 H, CH$_3$) ppm. Single crystals of **1** were grown by vapor diffusion of Et$_2$O into a CH$_2$Cl$_2$/MeOH (9:1) solution of Zn$_2$(L$_{ala}$)$_4$(py)$_2$. C$_{97}$H$_{88}$Cl$_2$N$_6$O$_{32}$Zn$_4$ (crystals lost disordered solvent and 2 equiv. of dichloromethane of crystallization upon collection and air-drying) (2182.20): calcd. C 53.39, H 4.06, N 3.85; found C 53.76, H 3.57, N 4.07. ^{1}H NMR (400 MHz, CD$_2$Cl$_2$/CD$_3$OD/[D$_7$]DMF): δ = 8.52 (d, J = 4.5 Hz, 4 H, py) 8.36 (d, J = 7.2 Hz, 8 H, naphth), 8.15 (d, J = 8.0 Hz, 8 H, naphth), 7.71 (t, J = 7.4 Hz, 2 H, py), 7.62 (t, J = 7.8 Hz, 8 H naphth), 7.28 (t, J = 6.8 Hz, 4 H, py), 5.54 (q, J = 7.1 Hz, 4 H, CH), 1.53 (d, J = 6.8 Hz, 12 H, CH$_3$) ppm. ^{13}C NMR (100.6 MHz, CD$_2$Cl$_2$/CD$_3$OD/[D$_7$]DMF): δ = 164.0 (C=O), 149.7 (CHCHN py), 137.8 (CHCHCHN py), 134.3 (CHCC=O naphth), 131.9 (CCHCH naphth), 131.1 (CHCHCH naphth), 128.3 (CCC=O), 127.2 (CHCHCH naphth), 124.6 (CHCHN py), 123.0 (CC=O naphth), 50.5 (CH), 15.5 (CH$_3$) ppm. The pyridine reso-

nances in these spectra presumably arise from its presence in the disordered solvent that was eliminated by SQUEEZE in the structural determination.

Synthesis of Cd$_2$(L$_{ala}$)$_4$(DMF)$_3$(MeOH) (2): Powdered HL$_{ala}$ (0.540 g, 2.0 mmol) was suspended in water (30 mL), and a methanolic KOH solution (2.0 mL, 1.0 M) was added. The suspension was stirred until it had completely cleared. To this solution was added an aqueous solution (10 mL) of CdCl$_2$ (0.183 g, 1.0 mmol) that contained pyridine (0.16 mL). A white precipitate formed immediately. The mixture was stirred for 2 h, and the solid was collected by filtration, washed with water and diethyl ether (20 mL of each), and air-dried. Yield: 0.456 g. ^{1}H NMR (300 MHz, CD$_2$Cl$_2$/CD$_3$OD): δ = 8.53 (d, J = 4.2 Hz, 4 H, py) 8.47 (d, J = 7.5 Hz, 8 H, naphth), 8.22 (d, J = 8.1 Hz, 8 H, naphth), 7.77 (t, J = 7.9 Hz, 2 H py), 7.71 (t, J = 7.8 Hz, 8 H naphth), 7.34 (dd, J = 7.5 Hz J = 5.7, Hz 4 H, py), 5.64 (q, J = 6.9 Hz, 4 H, CH), 1.63 (d, J = 7.2 Hz, 12 H, CH$_3$) ppm. Single crystals of **2** were grown by vapor diffusion of Et$_2$O into a DMF/MeOH (6:1) solution of the white solid. The analytical sample was dried to constant weight. C$_{70}$H$_{65}$Cd$_2$N$_7$O$_{20}$ (1549.11): calcd. C 54.27, H 4.23, N 6.33; found C 54.00, H 3.79, N 6.34. ^{1}H NMR (400 MHz, CD$_3$OD/[D$_7$]DMF): δ = 8.51 (d, J = 7.2 Hz, 8 H, naphth), 8.38 (d, J = 8.4 Hz, 8 H, naphth), 7.82 (t, J = 7.8 Hz, 8 H, naphth), 5.64 (q, J = 6.8 Hz, 4 H, CH), 1.63 (d, J = 7.2 Hz, 12 H, CH$_3$) ppm. ^{13}C NMR (100.6 MHz, CD$_3$OD/[D$_7$]DMF): δ = 164.0 (C=O), 134.0 (CHCC=O naphth), 131.7 (CCHCH naphth), 130.6 (CHCHCH naphth), 127.9 (CCC=O), 126.9 (CHCHCH naphth), 122.7 (CC=O naphth), 15.1 (CH$_3$) ppm. The chiral-center CH resonance was identified by a gradient HSQC experiment at δ = 50.4 ppm.

Crystallographic Studies: X-ray intensity data from colorless crystals of **1** and **2** were measured at 100(2) K by using a Bruker SMART APEX diffractometer (Mo-K_α radiation, λ = 0.71073 Å).[15] The raw area detector data frames were reduced and corrected for absorption effects with the SAINT+ and SADABS programs.[15] Structure solution by direct methods and subsequent difference Fourier calculations and full-matrix least-squares refinement against F^2 were performed with the SHELXTL software package.[16] X-ray crystallographic data are given in Table 2. Crystals of **1** were removed from the mother liquor and quickly mounted in the cold stream of the diffractometer with no indication of crystal degradation. Final unit-cell parameters were determined by least-squares refinement of 9174 reflections from the data set. The compound crystallized in the tetragonal system. The pattern of systematic absences in the intensity data was consistent with the enantiomorphous space group pair $P4_12_12$ and $P4_32_12$. The latter was confirmed by obtaining an absolute structure (Flack) parameter of 0.039(12) after the final refinement cycle. The crystallographically identifiable contents of the asymmetric unit consists of two zinc atoms, three independent L$_{ala}^-$ ligands, two methanol ligands coordinated to Zn1, one hydroxy group bridging Zn1 and Zn2, one noncoordinated methanol molecule, and 1.5 independent dichloromethane molecules. The "half"-CH$_2$Cl$_2$ is located on a twofold axis of rotation. The entire tetrazinc complex is generated by the operation of a twofold axis of rotation running through the complex along the crystallographic [110] and equivalent directions. There is also a large region that contains an essentially featureless distribution of disordered solvent molecules. The volume of this region was calculated to be 3393 Å^3, 26.8% of the total unit cell volume. No sensible disorder model to describe these diffusely scattering species was obtained. Their contribution to the structure factors was therefore removed by using the SQUEEZE program from PLATON.[17] The reported formula mass, calculated density, and F(000) values reflect known atoms only. Non-hydrogen

atoms were refined with anisotropic displacement parameters. Hydrogen atoms bonded to carbon atoms were placed in geometrically idealized positions and included as riding atoms. Hydrogen atoms bonded to oxygen atoms were located in difference maps, and their coordinates were refined subject to distance restraints of $d(O–H) = 0.85(2)$ Å and $U_{iso,H} = 1.5U_{eq,O}$. Final unit-cell parameters for **2** were determined by least-squares refinement of 8628 reflections from the data set. The pattern of systematic absences in the intensity data indicated the space groups $P2_1$ and $P2_1/m$. The acentric group $P2_1$ was confirmed by obtaining a stable and sensible solution and refinement of the structure and by the fixed chirality of the ligand used. The program ADDSYM implemented from PLATON found no missed symmetry elements.[17] The asymmetric unit consists of two cadmium atoms, four $\mathbf{L_{ala}}^-$ ligands, three DMF molecules, and one methanol molecule, i.e. one complete complex. The four $\mathbf{L_{ala}}^-$ ligands followed the same labeling scheme except for the suffixes A–F. Two of the $\mathbf{L_{ala}}^-$ ligands (B and D), one DMF (N6/O6, C19–C21) and the methanol molecule (O8–C25) are disordered over two closely separated positions. The minor component of the disordered $\mathbf{L_{ala}}^-$ ligands B and D were labeled with suffixes E and F, respectively. Total site occupancies were constrained to sum to unity and the atoms of these groups were refined isotropically. The occupancies for each group refined to near 50%. Geometries of the disordered ligands were restrained to be similar to those of an ordered ligand ($\mathbf{L_{ala}}$ ligand A and DMF ligand N5/O5, C16–C18), and the methanol atoms were refined with a $d(C–O) = 1.45(2)$ Å distance restraint. The methanol OH proton could not be located in difference maps and was not calculated. All other non-hydrogen atoms were refined with anisotropic displacement parameters. Hydrogen atoms were placed in geometrically idealized positions and included as riding atoms. The absolute structure (Flack) parameter refined to 0.010(18). The stereocenters C13 (A–F) were determined to have the (S) configuration. CCDC-846932 (**1**) and CCDC -846933 (**2**) contain the supplementary crystallographic data for this paper. These data can be obtained free of charge from The Cambridge Crystallographic Data Centre via www.ccdc.cam.ac.uk/data_request/cif.

Table 2. Selected crystallographic data for **1** and **2**.

	1	**2**
Empirical formula	$C_{99}H_{92}Cl_6N_6O_3Zn_4$	$C_{70}H_{65}Cd_2N_7O_{20}$
Formula mass [g mol^{-1}]	2351.97	1549.09
Crystal System	tetragonal	monoclinic
Space group	$P4_32_12$ (No. 96)	$P2_1$
T [K]	100(2)	100(2)
a [Å]	29.8242(9)	10.4417(4)
b [Å]	29.8242(9)	27.7151(11)
c [Å]	14.2147(8)	11.4934(5)
α [°]	90	90
β [°]	90	99.3670(10)
γ [°]	90	90
V [Å^3]	12643.7(9)	3281.8(2)
Z	4	2
R_1 [$I > 2\sigma(I)$]	0.0463	0.0398
wR_2 [$I > 2\sigma(I)$]	0.1223	0.0992

Supporting Information (see footnote on the first page of this article): Selected bond lengths and angles for **1** and **2**.

Acknowledgments

[1] a) A. Phan, A. U. Czaja, F. Gandara, C. B. Knobler, O. M. Yaghi, *Inorg. Chem.* **2011**, *50*, 7388; b) A. Dhakshinamoorthy, M. Alvaro, A. Corma, H. García, *Dalton Trans.* **2011**, *40*, 6344; c) P. Song, Y. Li, W. Li, B. He, J. Yang, X. Li, *Int. J. Hydrogen Energy* **2011**, *36*, 10468; d) A. Corma, H. García, F. X. Llabrés i Xamena, *Chem. Rev.* **2010**, *110*, 4606 and references cited thereine) ; D. Farrusseng, S. Aguado, C. Pinel, *Angew. Chem.* **2009**, *121*, 7638; *Angew. Chem. Int. Ed.* **2009**, *48*, 7502; f) K. K. Tanabe, S. M. Cohen, *Inorg. Chem.* **2010**, *49*, 6766; g) W. Lin, *Top. Catal.* **2010**, *53*, 869; h) C.-D. Wu, A. Hu, L. Zhang, W. Lin, *J. Am. Chem. Soc.* **2005**, *127*, 8941; i) S. Qiu, G. Zhu, *Coord. Chem. Rev.* **2009**, *253*, 2891.

[2] a) D. Zhao, D. J. Timmons, D. Yuan, H.-C. Zhou, *Acc. Chem. Res.* **2011**, *44*, 123; b) L. J. Murray, M. Dinca, J. R. Long, *Chem. Soc. Rev.* **2009**, *38*, 1294; c) A. U. Czaja, N. Trukhan, U. Muller, *Chem. Soc. Rev.* **2009**, *38*, 1284; d) U. Muller, M. Schubert, F. Teich, H. Puetter, K. Schierle-Arndt, J. Pastre, *J. Mater. Chem.* **2006**, *38*, 626; e) J. C. L. Rowsell, E. C. Spencer, J. Eckert, J. K. Howard, O. M. Yaghi, *Science* **2005**, *309*, 1350; f) R. E. Morris, P. S. Wheatley, *Angew. Chem.* **2008**, *120*, 5044; *Angew. Chem. Int. Ed.* **2008**, *47*, 4966; g) J. L. C. Rowsell, O. M. Yaghi, *Angew. Chem.* **2005**, *117*, 4748; *Angew. Chem. Int. Ed.* **2005**, *44*, 4670; h) R. Matsuda, R. Kitaura, S. Kitagawa, Y. Kubota, R. V. Belosludov, T. C. Kobayashi, H. Sakamoto, T. Chiba, M. Takata, Y. Kawazoe, Y. Mita, *Nature* **2005**, *436*, 238; i) A. R. Millward, O. M. Yaghi, *J. Am. Chem. Soc.* **2005**, *127*, 17998; j) J. C. Ro, J. Eckert, O. M. Yaghi, *J. Am. Chem. Soc.* **2005**, *127*, 14904; k) Y. Li, R. T. Yang, *Langmuir* **2007**, *23*, 12937.

[3] a) D. M. D'Alessandro, J. R. R. Kanga, J. S. Caddy, *Aust. J. Chem.* **2011**, *64*, 718; b) B. Chen, S. Xiang, G. Qian, *Acc. Chem. Res.* **2010**, *43*, 1115; c) S. Liu, J. Li, F. Luo, *Inorg. Chem. Commun.* **2010**, *13*, 870; d) M. A. Green, *Nat. Mater.* **2010**, *9*, 539; e) A. Lan, K. Li, H. Wu, D. Olson, T. Emge, W. Ki, M. Hong, J. Li, *Angew. Chem.* **2009**, *121*, 2370; *Angew. Chem. Int. Ed.* **2009**, *48*, 2334; f) B. Chen, Y. Yang, F. Zapata, G. Lin, G. Qian, E. B. Lobkovsky, *Adv. Mater.* **2007**, *19*, 1693.

[4] a) A. Centrone, E. E. Santiso, T. A. Hatton, *Small* **2011**, *7*, 2356; b) S. Basu, A. Cano-Odena, I. F. J. Vankelecom, *Sep. Purif. Technol.* **2011**, *81*, 31; c) A. U. Czaja, N. Trukhan, U. Muller, *Chem. Soc. Rev.* **2009**, *38*, 1284 and references cited thereind) ; S. Qiu, G. Zhu, *Coord. Chem. Rev.* **2009**, *253*, 2891; e) M. J. Manos, R. G. Iyer, E. Quarez, J. H. Liao, M. G. Kanatzidis, *Angew. Chem.* **2005**, *117*, 3618; *Angew. Chem. Int. Ed.* **2005**, *44*, 3552; f) H. Lee, S. I. Zones, M. E. Davis, *Nature* **2003**, *425*, 385; g) A. Corma, *Chem. Rev.* **1997**, *97*, 2373 and references cited therein.

[5] a) Q.-K. Liu, J.-P. Ma, Y.-B. Dong, *Chem. Commun.* **2011**, *47*, 7185; b) K.-L. Hou, F.-Y. Bai, Y.-H. Xing, J.-L. Wang, Z. Shi, *CrystEngComm* **2011**, *13*, 3884; c) J. D. Furman, R. P. Burwood, M. Tang, A. A. Mikhailovsky, A. K. Cheetham, *J. Mater. Chem.* **2011**, *21*, 6595; d) M. D. Allendorf, C. A. Bauer, R. K. Bhakta, R. J. T. Houka, *Chem. Soc. Rev.* **2009**, *38*, 1330 and references cited thereine) ; A.-L. Cheng, Y. Ma, Q. Sun, E.-Q. Gao, *CrystEngComm* **2011**, *13*, 2721; f) J. Crassous, *Chem. Soc. Rev.* **2009**, *38*, 830; g) C. Janiak, *Dalton Trans.* **2003**, 2781.

[6] a) M. R. Lohe, K. Gedrich, T. Freudenberg, E. Kockrick, T. Dellmann, S. Kaskel, *Chem. Commun.* **2011**, *47*, 3075; b) D. W. Ryu, W. R. Lee, J. W. Lee, J. H. Yoon, H. C. Kim, E. K. Koh, C. S. Hong, *Chem. Commun.* **2010**, *46*, 8779; c) M. Kurmoo, *Chem. Soc. Rev.* **2009**, *38*, 1353 and references cited therein; d) D. Maspoch, D. Ruiz-Molina, J. Veciana, *J. Mater. Chem.* **2004**, *14*, 2713.

[7] a) H. Khajavi, J. Gascon, J. M. Schins, L. D. A. Siebbeles, F. Kapteijn, *J. Phys. Chem. C* **2011**, *115*, 12487; b) Q.-R. Fang, G.-S. Zhu, Z. Jin, M. Xue, X. Wei, D.-J. Wang, S.-L. Qiu, *Cryst. Growth Des.* **2007**, *7*, 1035; c) O. R. Evans, W. Lin, *Acc. Chem. Res.* **2002**, *35*, 511 and references cited therein.

[8] a) L.-M. Zhao, Z.-J. Zhang, S.-Y. Zhang, P. Cui, W. Shi, B. Zhao, P. Cheng, D.-Z. Liao, S.-P. Yan, *CrystEngComm* **2011**, *13*, 907; b) D. J. Tranchemontagne, J. L. Mendoza-Cortes, M. O'Keeffe, O. M. Yaghi, *Chem. Soc. Rev.* **2009**, *38*, 1257; c) C. N. R. Rao, S. Natarajan, R. Vaidhyanathan, *Angew. Chem.* **2004**, *116*, 1490; *Angew. Chem. Int. Ed.* **2004**, *43*, 1466; d) O. M. Yaghi, M. O'Keeffe, N. W. Ockwig, H. K. Chae, M. Eddaoudi, J. Kim, *Nature* **2003**, *423*, 705; e) M. Eddaoudi, D. B. Moler, H. Li, B. Chen, T. M. Reineke, M. O'Keeffe, O. M. Yaghi, *Acc. Chem. Res.* **2001**, *34*, 319.

[9] a) J. W. Steed, J. L. Atwood, *Supramolecular Chemistry*, 2nd ed., John Wiley & Sons, Ltd, UK, **2009**, p. 28–32; b) D. Braga, L. Brammer, N. R. Champness, *CrystEngComm* **2005**, *7*, 1; c) B. Moulton, M. J. Zaworotko, *Chem. Rev.* **2001**, *101*, 1629.

[10] a) C. Janiak, *J. Chem. Soc., Dalton Trans.* **2000**, 3885; b) C. A. Hunter, J. K. M. Sanders, *J. Am. Chem. Soc.* **1990**, *112*, 5525; c) J. W. Steed, J. L. Atwood, *Supramolecular Chemistry*, 2nd ed., John Wiley & Sons, Ltd, UK, **2009**, p. 33–35.

[11] a) D. L. Reger, J. D. Elgin, R. F. Semeniuc, P. J. Pellechia, M. D. Smith, *Chem. Commun.* **2005**, 4068; b) D. L. Reger, R. F. Semeniuc, J. D. Elgin, V. Rassolov, M. D. Smith, *Cryst. Growth Des.* **2006**, *6*, 2758; c) D. L. Reger, J. D. Elgin, M. D. Smith, B. K. Simpson, *Polyhedron* **2009**, *28*, 1469; d) D. L. Reger, A. Debreczeni, B. Reinecke, V. Rassolov, M. D. Smith, R. F. Semeniuc, *Inorg. Chem.* **2009**, *48*, 8911; e) D. L. Reger, A. Debreczeni, M. D. Smith, *Inorg. Chim. Acta* **2010**, *364*, 10; f) D. L. Reger, J. Horger, M. D. Smith, *Chem. Commun.* **2011**, *47*, 2805; g) D. L. Reger, J. Horger, M. D. Smith, G. J. Long, *Chem. Commun.* **2009**, 6219; h) D. L. Reger, J. J. Horger, M. D. Smith, G. J. Long, G. Fernande, *Inorg. Chem.* **2011**, *50*, 686; i) D. L. Reger, J. J. Horger, A. Debreczeni, M. D. Smith, *Inorg. Chem.* **2011**, *50*, 10225; j) D. L. Reger, A. Debreczeni, J. J. Horger, M. D. Smith, *Cryst. Growth Des.* **2011**, *11*, 4068.

[12] a) C. Wang, M. Zheng, W. Lin, *J. Phys. Chem. Lett.* **2011**, *2*, 1701; b) W. Lin, *J. Solid State Chem.* **2005**, *178*, 2486; c) J. S. Seo, D. Whang, H. Lee, S. I. Jun, J. Oh, Y. J. Jeon, K. Kim, *Nature* **2000**, *404*, 982; d) D. Bradshaw, T. J. Prior, E. J. Cussen, J. B. Claridge, M. J. Rosseinsky, *J. Am. Chem. Soc.* **2004**, *126*, 6106; e) R. Xiong, X. You, B. F. Abrahams, Z. Xue, C. Che, *Angew. Chem.* **2001**, *113*, 4554; *Angew. Chem. Int. Ed.* **2001**, *40*, 4422; f) B. Kesanli, W. Lin, *Coord. Chem. Rev.* **2003**, *246*, 305.

[13] a) M. Kurmoo, H. Kumagai, M. Akita-Tanaka, K. Inoue, S. Takagi, *Inorg. Chem.* **2006**, *45*, 1627; b) M. Zeng, B. Wang, X. Wang, W. Zhang, X. Chen, S. Gao, *Inorg. Chem.* **2006**, *45*, 7069; c) Z. Gu, X. Zhou, Y. Jin, R. Xiong, J. Zuo, X. You, *Inorg. Chem.* **2007**, *46*, 5462; d) K. O. Ashiry, Y. Zhao, K. Shao, Z. Su, Y. Fu, X. Hao, *Inorg. Chem. Commun.* **2008**, *11*, 1181; e) G. L. Rikken, E. Raupach, *Nature* **2000**, *405*, 932; f) R. Andrés, M. Brissard, M. Gruselle, C. Train, J. Vaissermann, B. Malézieux, J. Jamet, M. Verdaguer, *Inorg. Chem.* **2001**, *40*, 4633.

[14] a) J. J. Bodwin, A. D. Cutland, R. G. Malkani, V. L. Pecoraro, *Coord. Chem. Rev.* **2001**, *216–217*, 489; b) G. Yuan, K. Shao, X. Wang, Y. Lan, D. Du, Z. Su, *CrystEngComm* **2010**, *12*, 1147; c) J. Yu, R. Xu, *J. Mater. Chem.* **2008**, *18*, 4021; d) P. D. Frischmann, G. A. Facey, P. Y. Ghi, A. J. Gallant, D. L. Bryce, F. Lelj, M. MacLachlan, *J. Am. Chem. Soc.* **2010**, *132*, 3893; e) T. Liu, Y. Liu, W. Xuan, Y. Cui, *Angew. Chem. Int. Ed.* **2010**, *49*, 4121; f) S. Sahoo, M. Ray, *Chem. Eur. J.* **2010**, *16*, 5004; g) H. Hao, W. Liu, W. Tan, Z. Lin, M. Tong, *Cryst. Growth Des.* **2009**, *9*, 457; h) G. Yuan, C. Zhu, W. Xuan, Y. Cui, *Chem. Eur. J.* **2009**, *15*, 6428.

[15] *SMART* (version 5.630), *SAINT+* (version 6.45) and *SADABS* (version 2.10), Bruker Analytical X-ray Systems, Inc., Madison, Wisconsin, USA, **2003**.

[16] G. M. Sheldrick, *Acta Crystallogr., Sect. A* **2008**, *64*, 112.

[17] MISSYM (ADDSYM) algorithm: a) Y. LePage, *J. Appl. Crystallogr.* **1987**, *20*, 264; b) *PLATON/PLUTON*: A. L. Spek, *J. Appl. Crystallogr.* **1988**, *21*, 578; c) A. L. Spek, *Acta Crystallogr., Sect. A* **1990**, *46*, C34; d) A. L. Spek, *PLATON, A Multipurpose Crystallographic Tool*, Utrecht University, Utrecht, The Netherlands, **1998**.

C–H Bond Activation of Palladium Complexes That Feature Pendant Benzamidinate Ligands and Their Catalytic Behaviours

Ming-Tsz Chen,[a] Kai-Min Wu,[a] and Chi-Tien Chen*[a]

The pendant benzamidines {Ph–C[=N–(2,6-di-iPr-C$_6$H$_3$)]-(NH^E)} [^E = (CH$_2$)$_2$NMe$_2$, CH$_2$Py] and their palladium complexes [(Ph–C{=N^E}{NH–(2,6-di-iPr-C$_6$H$_3$)})Pd(OAc)$_2$] [^E = (CH$_2$)$_2$NMe$_2$ (**1**), CH$_2$Py (**2**)] have been prepared. Upon heating, the corresponding palladacyclic complexes, [({η^1-C$_6$H$_4$}–C(=N^E){NH–(2,6-di-iPr-C$_6$H$_3$)})PdOAc] [^E = (CH$_2$)$_2$-NMe$_2$ (**3**), CH$_2$Py (**4**)], were obtained. Due to the substituent groups on the *ortho* positions of the phenyl ring attached to

the nitrogen atom of the amidinate group, the C–H bond activation process was observed on the *ortho* position of the phenyl ring attached to the carbon atom of the amidinate group. This process can be proved by X-ray structural determination. The molecular structures are reported for compounds **1** and **4**. Catalytic application of cyclopalladated derivatives **3** and **4** toward the Suzuki reaction was also investigated.

Introduction

C–H bond activation is a well-known process by means of oxidative addition or electrophilic substitution reactions to afford cyclometalated complexes. Cyclometalated complexes play important roles in modern organometallic chemistry, such as organic synthesis, asymmetric synthesis and photochemistry.[1,2] These processes predominantly focus on the second- and third-row transition metals with N-donor ligands.[1,2] The mechanistic investigations of these reactions have been studied with respect to ligand precursors precoordinated to the metal centre followed by arrangement of the ligand precursors to allow for C–H bond activation.[3] Although cyclometalation reactions on palladium(II) complexes have been thoroughly studied by a number of research groups, not many of these processes are known to result in isolation of the corresponding organometallic complexes.[4–7]

In our previous report,[8] we used molecular structures to demonstrate that the cyclometalation reaction happened at the *ortho* position of the phenyl ring attached to the nitrogen atom rather than at the *ortho* position of the phenyl ring attached to the carbon atom of the amidine function. A plausible mechanism for this process has been reported by us. However, the palladium chelate complexes that could be precursors for cyclometalation reactions cannot be isolated easily due to the quick cyclometalation process. To prove this plausible mechanism, the *ortho*-hydrogen atoms of the phenyl ring attached to the nitrogen atom of the amidine function were substituted with *i*Pr groups to prevent the *ortho*-metalation of the palladium chelate complex.

Thus the isolation of precursors for the cyclometalation reaction might be achieved. In this paper, we present benzamidinate ligand precursors with bulkier substituents to study how the cyclometalation steps take place. The application of palladacyclic complexes to a Suzuki reaction is also examined.

Results and Discussion

Synthesis of Benzamidinates Ligand Precursors and Pd Complexes

The desired *N*,*N*′-disubstituted benzamidines were prepared according to a method similar to our previous report.[8] Treatment of *N*-(2,6-diisopropylphenyl)benzimidoyl chloride[9a] with the corresponding amines (1 molar equiv.) in the presence of triethylamine affords benzamidines {Ph–C[=N–(2,6-di-*i*Pr-C$_6$H$_3$)](NH^E)} (^E = (CH$_2$)$_2$NMe$_2$, CH$_2$Py) in moderate yield. *N*-(2,6-Diisopropylphenyl)-*N*′-(2-dimethylaminoethyl)benzamidine has already been reported.[9b,9c] *N*-(2,6-Diisopropylphenyl)-*N*′-(2-methylpyridine)benzamidine was characterized by NMR spectroscopy as well as elemental analyses. Due to the tautomeric rotation of amidine, complex and broad signals were found in the ^{1}H NMR spectrum. Therefore high-temperature NMR spectroscopic data are reported in the Exp. Section for *N*-(2,6-diisopropylphenyl)-*N*′-(2-methylpyridine)benzamidine. Treatment of benzamidines with Pd(OAc)$_2$ (1 molar equiv.) in dichloromethane afforded palladium chelate complexes **1** or **2**. The gradual formation of the corresponding cyclometalated compound **3** was observed upon standing compound **1** in a solution of [D]chloroform at room temperature for a couple of days with an upfield shift of the N*H* peak and the loss of one –OAc peak in the ^{1}H NMR spectrum. The

[a] Department of Chemistry, National Chung Hsing University, Taichung 402, Taiwan, Republic of China
E-mail: ctchen@dragon.nchu.edu.tw

syntheses of palladacyclic complexes **3** and **4** were achieved by heating **1** in toluene or **2** in THF at 80 °C. Complexes **3** and **4** can also be prepared by an alternative route by means of direct reactions of benzamidines with Pd(OAc)$_2$ in toluene at 80 °C. Complexes **1**–**4** were characterized by NMR spectroscopy as well as elemental analyses. A summary of the syntheses and proposed structures of palladium complexes is shown in Scheme 1.
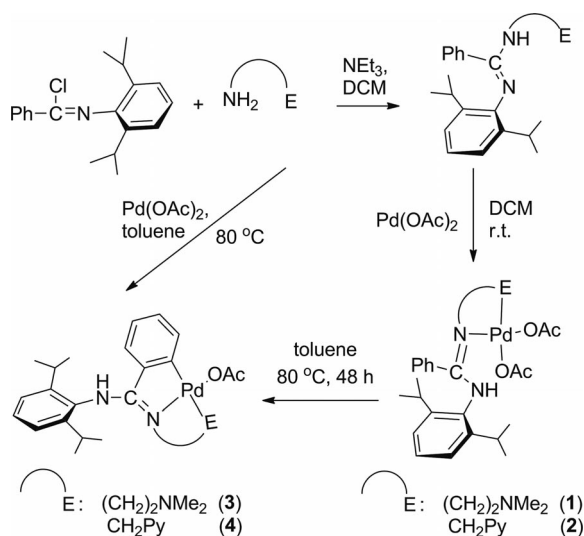
Scheme 1. Preparation of palladium complexes **1**–**4**.

In each palladium chelate complex, one N*H* singlet around δ = 10 ppm (δ = 9.99 ppm for **1**; 10.20 ppm for **2**) and two peaks that correspond to –OAc groups were found in the ^{1}H NMR spectrum. For each palladacyclic complex, the N*H* singlet moved upfield (δ = 6.67 ppm for **3**; 6.83 ppm for **4**) and only one peak that corresponded to the –OAc group appeared around δ = 2 ppm (δ = 2.11 ppm for **3**; 2.21 ppm for **4**) in the ^{1}H NMR spectra, which indicates that the carbon metalation of the phenyl group might happen instead of N*H* deprotonation with the release of one molar equivalent of HOAc, as shown in Figures 1 and 2.

Suitable crystals of **1** for X-ray refinement were grown from a solution of dichloromethane/hexane. The molecular structure is depicted in Figure 3. The bond angles [from 84.02(10) to 96.86(9)°] around the palladium metal centre can be described as a slightly distorted square planar with two *cis*-oriented nitrogen atoms from the benzamidinate ligand and two oxygen atoms from two –OAc groups. The chelate ring of complex **1** is nearly coplanar with the torsion angle O(1)–O(3)–N(3)–N(2) = 1.3°. The bond lengths of Pd–N$_{amine}$ [2.042(3) Å] and Pd–N$_{imine}$ [2.042(3) Å] are within those [2.044(4)–2.0683(19) Å for Pd–N$_{amine}$; 1.991(2)–2.050(2) Å for Pd–N$_{imine}$] found in palladium N,N′-chelate complexes.[7b] The bond lengths of Pd–O$_{OAc}$ [2.021(2) and 2.032(2) Å] are close to those [1.983(4)–2.029(2) Å] found in palladium acetate complexes.[7b,10f] The C–N bond lengths of the NCN moiety are not equal with 1.337(4) and 1.308(4) Å, respectively, thus indicating
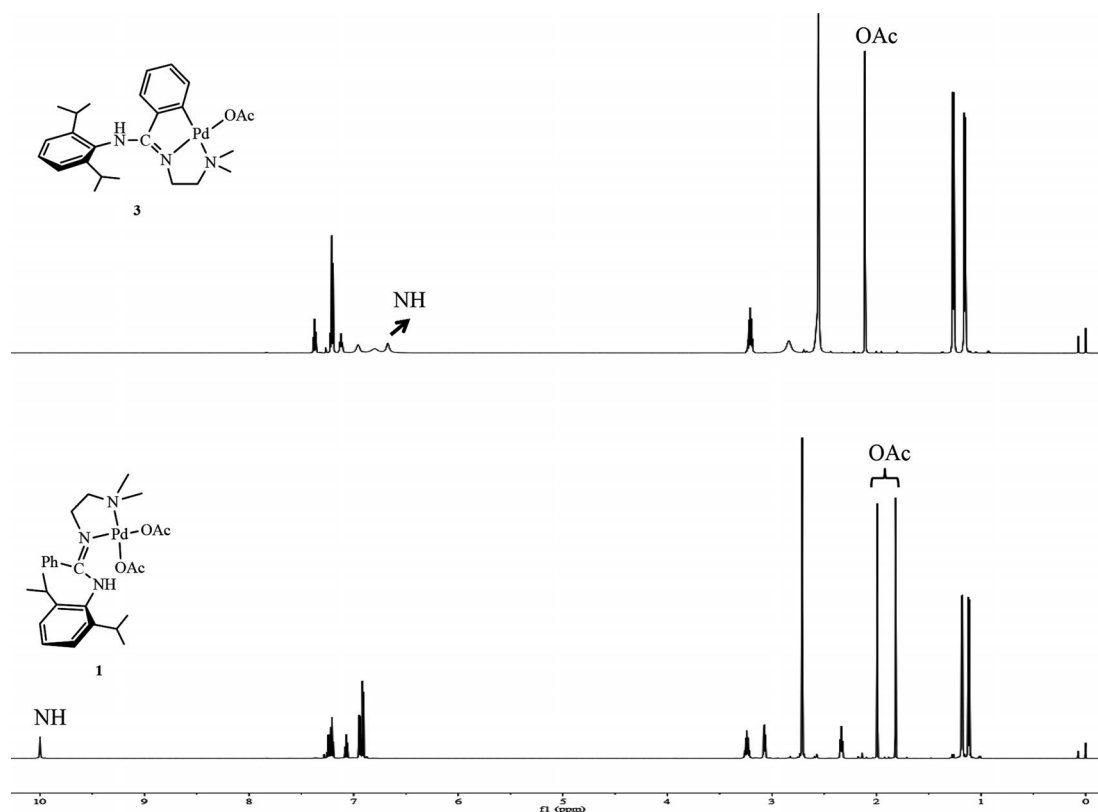

Figure 1. ^{1}H NMR spectra in CDCl$_3$ for **1** (bottom) and **3** (top).
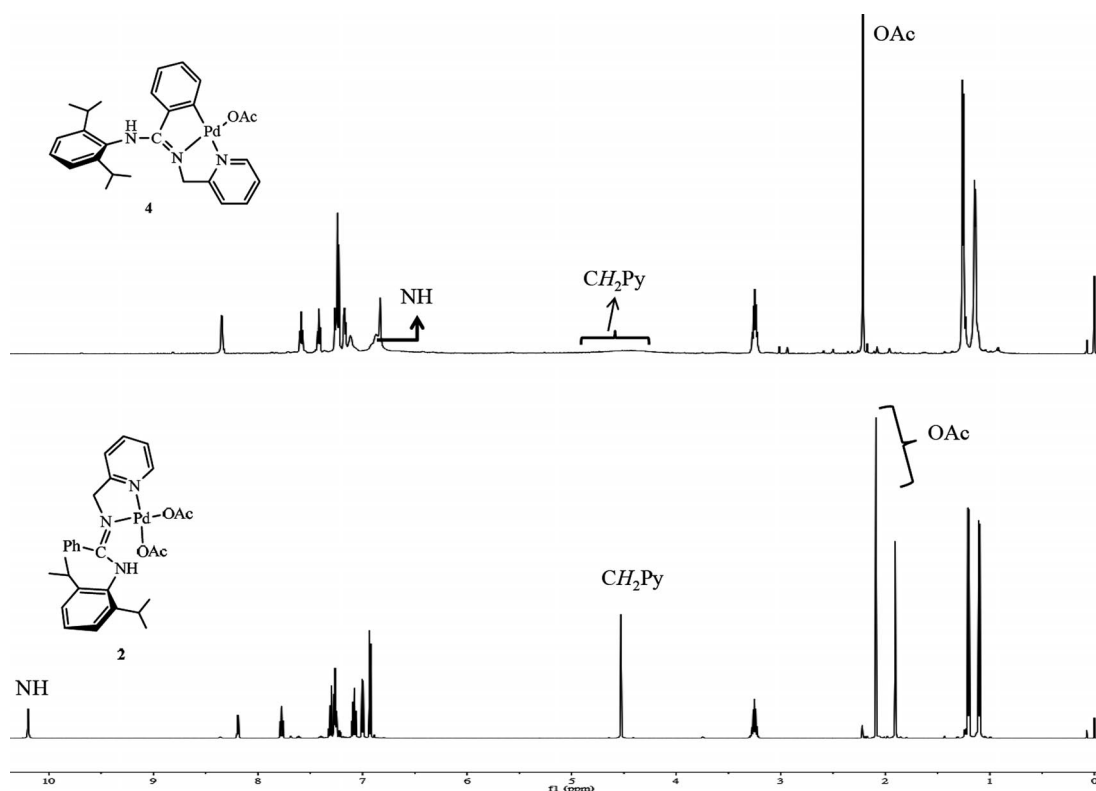
Figure 2. ^{1}H NMR spectra in CDCl$_3$ for **2** (bottom) and **4** (top).

the localized nature of the imine C=N and amine C–N bonds and the 1,3-shift of a proton from the nitrogen atom of the amine group to the nitrogen atom of the imine group on going from the free ligand to the mononuclear CNN cyclopalladated compound. On the basis of the molecular structure of **1**, the *ortho* substituents actually prevent the palladium chelate complexes from taking part in cyclomet-

Figure 3. Molecular structure of **1**. Selected bond lengths [Å] and bond angles [°]: Pd–O(1) 2.032(2), Pd–O(3) 2.021(2), Pd–N(2) 2.042(2), Pd–N(3) 2.042(3), C(1)–N(2) 1.308(4), C(1)–N(1) 1.337(4), N(1)–C(8) 1.439(4); N(2)–Pd–O(1) 96.86(9), N(3)–Pd–O(3) 92.99(11), N(2)–Pd–N(3) 84.14(11), O(3)–Pd–O(1) 84.02(10), O(1)–Pd–N(3) 177.00(11), O(3)–Pd–N(2) 176.67(10). Hydrogen atoms on carbon atoms omitted for clarity.

alation (Scheme 2) to form a six-membered metallacycle and prove the existence of palladacyclic precursors in the previously proposed mechanism.[8]

Suitable crystals of **4** for X-ray refinement were grown from concentrated chloroform solution. The molecular structure is depicted in Figure 4. The bond angles [from 81.54(9) to 99.32(9)°] around the palladium metal centre indicate a complex that has a slightly distorted square-planar geometry, in which the palladium metal centre is co-ordinated with one pyridine nitrogen atom, one imine nitrogen atom, one metalated carbon atom, and one acetate oxygen atom to form two five-membered metallacycles. The bond lengths of Pd–N$_{py}$ [2.113(2) Å] and Pd–C$_{metalated}$ [1.978(3) Å] are within those [1.964(3)–2.150(3) Å for Pd–N$_{py}$; 1.961(4)–2.078(2) Å for Pd–C$_{metalated}$] found in metalated palladacycles.[10,11] The bond length of Pd–O$_{OAc}$ [2.0545(16) Å] are within those [2.036(2)–2.126(3) Å] found in palladacycles.[8,10f,10g,11] The bond length of Pd–N$_{C=N}$ [1.9606(19) Å] is close to those [1.981(3)–2.0321(18) Å] found in palladacycles.[8,10f,10g,11] The C–N bond lengths of the NCN moiety in **4** are not equal [1.304(3) Å for imine C(1)=N(2) and 1.351(3) Å for amine C(1)–N(1)], thereby indicating the localized nature of the imine C=N and amine C–N bonds. On the basis of the molecular structure of **4**, the cyclometalation reaction happens on the *ortho* position of the phenyl ring attached to the carbon atom of the NCN part to form a five-membered metallacycle as mononuclear palladium complex **4** rather than a dinuclear species.[7b] No aliphatic C–H activation product was obtained in this system.[6] Compared with the results reported previously,[8] for-

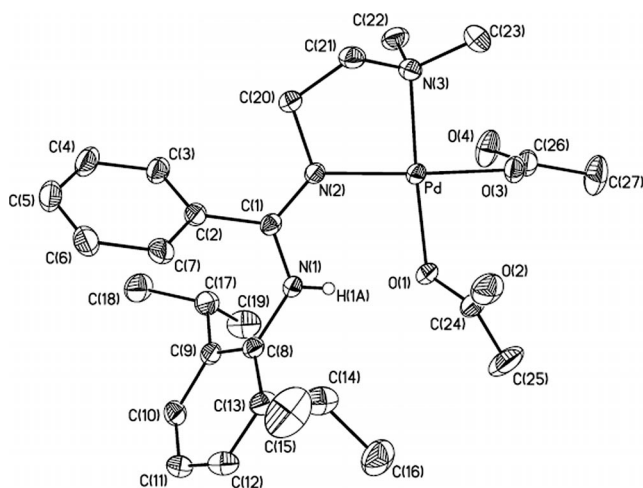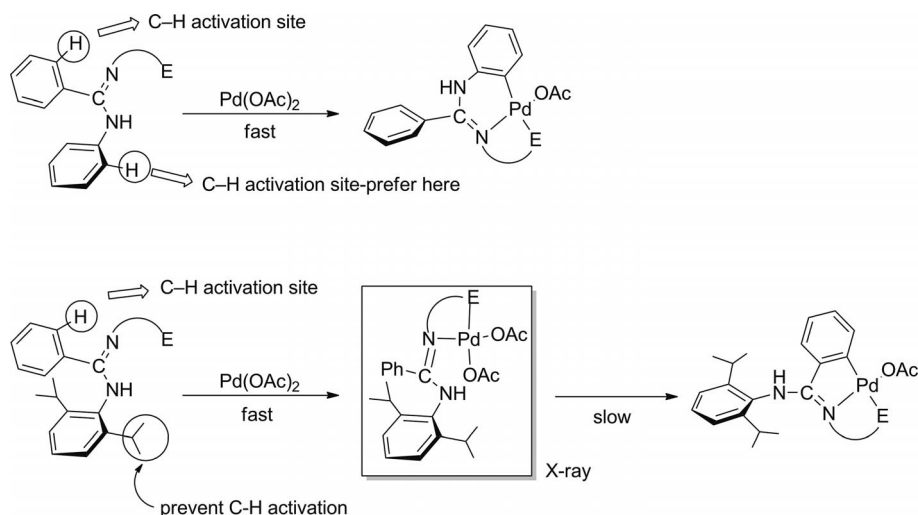Scheme 2. Bulkier group on the *ortho* positions prevent the palladium chelate complexes from cyclometalation.
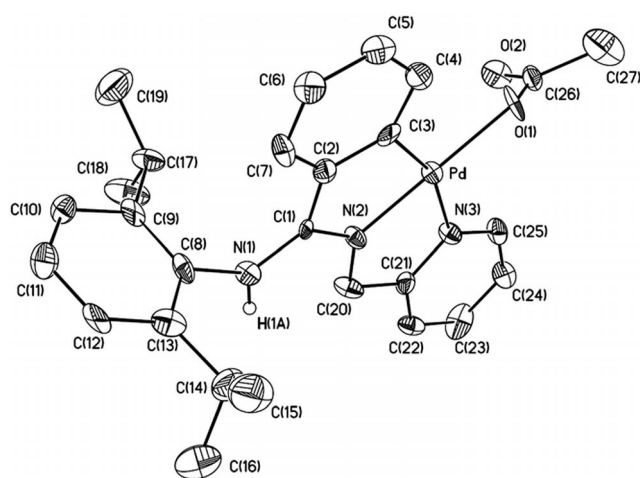
Figure 4. Molecular structure of **4**. Selected bond lengths [Å] and bond angles [°]: Pd–C(3) 1.978(3), Pd–O(1) 2.0545(16), Pd–N(2) 1.9606(19), Pd–N(3) 2.113(2), C(1)–N(1) 1.351(3), C(1)–N(2) 1.304(3), C(8)–N(1) 1.442(3); N(2)–Pd–C(3) 81.54(9), N(2)–Pd–N(3) 81.78(8), N(3)–Pd–O(1) 97.42(7), C(3)–Pd–O(1) 99.32(9), C(3)–Pd–N(3) 163.24(9), N(2)–Pd–O(1) 172.10(8). Hydrogen atoms on carbon atoms omitted for clarity.

mation of six-membered metallacycle through an aromatic C–H activation seems to be faster than that of a five-membered metallacycle. Once the *ortho* position of the phenyl ring is blocked from forming a six-membered metallacycle, an aromatic C–H activation might happen on the *ortho* position of the phenyl ring to form a five-membered metallacycle in this palladium pendant benzamidinate system.

Catalytic Studies for the Suzuki Reaction

With the aim of demonstrating the catalytic activities of palladacycles that contain CNN-type ligands,[8,10f,10g,12] complexes **3** and **4** were introduced into the Suzuki coupling reaction.[13] To examine the catalytic activity, conditions that employ the coupling of 4-bromoanisole with phenylboronic acid (1.5 equiv.) catalyzed by **3** or **4** (1 mol-%) in the presence of base (3 equiv.) at 60 °C within 2 h were conducted. The optimum solvent/base mixture for the reaction was found to be toluene/K$_3$PO$_4$ after several trials with a combination of solvents (dimethylacetamide (DMA), THF and toluene) and base (KF, K$_3$PO$_4$ and Cs$_2$CO$_3$). Selected results are listed in Table 1. Poor conversion exhib-

Table 1. Suzuki coupling reaction catalyzed by palladium complexes (solvent: toluene).[a]

Entry	Catalyst	Aryl halide	Base	[Pd] [mol-%]	T [h]	Conversion [%][b]	Yield [%][c]
1[d]	3	4-bromoanisole	K$_3$PO$_4$	1	2	74	70
2[d]	4	4-bromoanisole	K$_3$PO$_4$	1	2	19	–
3[e]	3	4-bromoanisole	K$_3$PO$_4$	1	2	82	79
4[e]	4	4-bromoanisole	K$_3$PO$_4$	1	2	35	–
5[e]	4	4-bromoanisole	K$_3$PO$_4$	1	3	65	–
6	3	4-bromoanisole	K$_3$PO$_4$	10^{-3}	17	82	80
7	3	4-bromoanisole	K$_3$PO$_4$	10^{-5}	17	58	53
8	3	4-chloroacetophone	K$_3$PO$_4$	1	0.5	63	60
9	3	4-chloroacetophone	K$_3$PO$_4$	2	0.5	81	77
10	3	4-chloroacetophone	K$_3$PO$_4$	2	1	87	84
11	4	4-chloroacetophone	K$_3$PO$_4$	2	1	37	–
12[e]	5	4-bromoanisole	KF	1	3	72	65
13[e]	6	4-bromoanisole	K$_3$PO$_4$	1	3	84	75

[a] Reaction conditions: aryl halide (1.0 mmol), phenylboronic acid (1.5 mmol), base (3 mmol), toluene (3 mL), 100 °C. [b] Determined by ^{1}H NMR spectroscopy. [c] Isolated yield (average of two experiments). [d] T = 60 °C. [e] T = 80 °C.

ited by **4** indicated that the catalytic activity of the complex with pendant amine functionality is better than that with pendant pyridine functionality in this system (Table 1, entries 1 and 2). A similar trend was observed by using less-reactive substrate 4-chloroacetophone with 2 mol-% palladium loading within 1 h at 100 °C (entries 10 and 11). Better conversion was observed by running reactions from 60 to 80 °C (entries 1 and 3). Because of the better activity and solubility of **3**, lower catalyst concentrations were investigated using catalyst/substrate ratios from 10^{-5} to 10^{-7} with 4-bromoanisole as substrate. The reactions gave conversion of 82% within 17 h for the 10^{-5} ratio, and 58% within 17 h for the 10^{-7} ratio at 100 °C (entries 6 and 7). Catalytic activity of **3** was tested by using less-reactive 4-chloroaceto-phenone as substrate with 1 mol-% palladium loading at 100 °C (entry 8). The reaction gave a conversion of 63% within 0.5 h. Better conversions were found by increasing the palladium loading (entry 9) or extending the reaction time (entry 10). To compare the catalytic activity of palladacycles with similar coordination modes in our previous report,[8] palladacycles **5** and **6** (as shown in Scheme 3) were examined by the reaction of 4-bromo-anisole with phenylboronic acid catalyzed by 1 mol-% palladium loading under optimized conditions at 80 °C (entries 3–5, 12 and 13). On the basis of these results, the catalytic activity of the five-membered palladacycle that resulted from cyclometalation at the *ortho* position of the phenyl ring attached to the carbon atom of the NCN amidine function seems to be better than that with the six-membered metallacycle that results from cyclometalation at the *ortho* position of the phenyl ring attached to the nitrogen atom of the NCN amidine function for the palladacycles with the NMe$_2$ pendant functionality (entries 3 and 12). However, a reverse trend was observed for palladium benzamidine complexes with pendant pyridine functionality (entries 5 and 13).
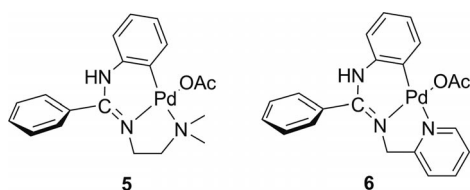
Scheme 3. The palladacycles bearing the benzamidinate ligand precursor.[8]

Conclusion

One new benzamidinate ligand precursor and four palladium complexes were prepared and fully characterized. The catalytic activity of two palladacycles for the Suzuki reaction has been demonstrated. On the basis of the molecular structures of palladium chelates and palladacyclic complexes, thet formation of six-membered palladacycles actually proceeds through a palladium chelate complex as an intermediate followed by a C–H activation process, which was proposed in our previous report. Once the *ortho* posi-

tion for the formation of a six-membered palladacycle had been blocked, the C–H activation process could take place on the other *ortho* position to form a five-membered palladacycle slowly. On the basis of those results demonstrated by palladium benzamidinate complexes, formation of the six-membered palladacycle seems to be faster than that of the five-membered palladacycle. Under optimized conditions, **3** exhibits catalytic activity with lower catalyst loading (10^{-5} to 10^{-7}) and with electronically deactivated aryl bromide in the Suzuki reaction. Complex **3** also demonstrates catalytic activity with a less reactive aryl chloride-containing electron-withdrawing group.

Experimental Section

General: All manipulations were carried out under an atmosphere of dinitrogen by using standard Schlenk line or drybox techniques. Solvents were heated at reflux over the appropriate drying agent and distilled prior to use. Deuterated solvents were dried with molecular sieves.

^{1}H and ^{13}C{^{1}H} NMR spectra were recorded either with Varian Mercury-400 (400 MHz) or Varian Inova-600 (600 MHz) spectrometers in [D]chloroform at ambient temperature unless stated otherwise and referenced internally to the residual solvent peak and reported as parts per million relative to tetramethylsilane. Elemental analyses were performed with an Elementar Vario ELIV instrument.

Pd(OAc)$_2$ (Aldrich), 2,6-diisopropylaniline (Alfa), 2-(aminomethyl)pyridine (Acros) and *N,N*-dimethylethyleneamine (Acros) were used as supplied. NEt$_3$ was dried with CaH$_2$ and distilled before use. *N*-(2,6-Diisopropylphenyl)benzanilide and *N*-(2,6-diisopropylphenyl)benzimidoyl chloride were prepared according to modified literature procedures.[9a]

Preparations

{Ph–C[=N–(2,6-di-*i*Pr–C$_6$H$_3$)][NH(CH$_2$)$_2$NMe$_2$]}: A solution of *N*-(2,6-diisopropylphenyl)benzimidoyl chloride (0.9 g, 3 mmol) and NEt$_3$ (0.70 mL, 4.6 mmol) in toluene (15 mL) was treated with *N,N*-dimethylethyleneamine (0.35 mL, 3.4 mmol) at 0 °C then allowed to warm to room temperature. After 24 h of stirring, the volatile compounds were removed under reduced pressure and the residue was extracted with hexane (50 mL). The extract was pumped to dryness to afford a yellow oily product; yield 0.65 g, 62%. This compound has been reported in the literature.[9b,9c]

{Ph–C[=N–(2,6-di-*i*Pr–C$_6$H$_3$)](NHCH$_2$Py)}: The preparation of {Ph–C[=N–(2,6-di-*i*Pr–C$_6$H$_3$)](NHCH$_2$Py)} was similar to that used for {Ph–C[=N–(2,6-di-*i*Pr–C$_6$H$_3$)][NH(CH$_2$)$_2$NMe$_2$]} but with *N*-(2,6-diisoproyplphenyl)benzimidoyl chloride (1.5 g, 5 mmol), NEt$_3$ (0.84 mL, 6 mmol) and 2-(aminomethyl)pyridine (0.52 mL, 5 mmol). The volatile compounds were removed under reduced pressure and the residue was extracted with toluene (50 mL). The extract was pumped to dryness to afford an orange solid; yield 1.62 g, 87.4%. ^{1}H NMR (600 MHz, 333 K): δ = 0.97 [s, 6 H, *i*Pr–(*CH$_3$*)$_2$], 1.10 [s, 6 H, *i*Pr–(*CH$_3$*)$_2$], 3.03 (s, 2 H, *i*Pr–*H*), 4.64 (s, 2 H, *CH$_2$*Py), 5.64 (s, 1 H, N*H*), 6.91 (s, 1 H), 6.97 (s, 2 H), 7.13 (m, 1 H), 7.26 (br., 4 H), 7.38 (br., 2 H), 7.60 (t, *J* = 7.2 Hz, 1 H), 8.51 (s, 1 H) ppm. ^{13}C{^{1}H} NMR (150 MHz, 333 K): δ = 22.6 (s, *CH$_3$*–*i*Pr), 23.7 (s, *CH$_3$*–*i*Pr), 28.2 (s, *CH*–*i*Pr), 47.9 (s, *CH*–Py), 122.0, 122.3, 122.8, 127.9, 128.2, 129.2, 136.3, 149.2 (*CH*–Ph and *CH*–Py), 135.7, 138.7, 145.1, 154.4, 158.3 (*C$_{ipso}$*–C$_6$H$_5$, *C$_{ipso}$*–Py and one

*C*NN) ppm. $C_{25}H_{29}N_3$ (371.52): calcd. C 80.82, H 7.87, N 11.31; found C 80.74, H 7.53, N 11.27.

Complex 1: CH_2Cl_2 (15 mL) was added at room temperature to a flask that contained {Ph–C[=N–(2,6-di-*i*Pr–C_6H_3)][NH(CH$_2$)$_2$-NMe$_2$]} (0.35 g, 1 mmol) and Pd(OAc)$_2$(0.22 g, 1 mmol). After 1 h of stirring, the volatile compounds were removed under reduced pressure to afford a brown solid. The resulting solid was purified by THF/hexane solution to afford a pale yellow solid; yield 0.44 g, 76%. ^{1}H NMR (600 MHz): δ = 1.12 [d, *J* = 6.6 Hz, 6 H, CH–(CH_3)$_2$], 1.18 [d, *J* = 6.6 Hz, 6 H, CH–(CH_3)$_2$], 1.82 [s, 3 H, O–C(=O)CH_3], 1.99 [s, 3 H, O–C(=O)CH_3], 2.34 [t, *J* = 6.0 Hz, 2 H, CH_2], 2.71 [s, 6 H, N(CH_3)$_2$], 3.07 [t, *J* = 6.0 Hz, 2 H, CH_2], 3.24 [sept, *J* = 6.6 Hz, 2 H, CH–(CH$_3$)$_2$], 6.91 (d, *J* = 7.8 Hz, 2 H, CH–Ar), 6.94 (m, 2 H, CH–Ar), 7.07 (t, *J* = 7.2 Hz, 1 H, CH–Ar), 7.19–7.26 (m, 3 H, CH–Ar), 9.99 (s, 1 H, NH) ppm. ^{13}C{^{1}H} NMR (150 MHz): δ = 21.7 [s, CH–(CH_3)$_2$], 23.5 [s, O–C(=O)CH_3], 23.6 [s, O–C(=O)CH_3], 25.6 [s, CH–(CH_3)$_2$], 28.6 [s, CH–(CH$_3$)$_2$], 50.7 [s, N(CH_3)$_2$], 53.0 (s, CH_2), 65.8 (s, CH_2), 123.0, 127.0, 128.3, 128.4, 130.1 (CH–Ar), 129.9, 131.8, 146.6, 168.6 [two C$_{ipso}$–Ar, one CNN and one C–CH–(CH$_3$)$_2$], 178.1 [s, O–C(=O)CH_3] ppm. $C_{27}H_{39}N_3O_4Pd$ (576.02): calcd. C 56.30, H 6.82, N 7.29; found C 56.36, H 6.71, N 7.25.

Complex 2: The procedure for preparation of **2** was similar to that used for **1** but with {Ph–C(NHCH$_2$Py)[=NH–(2,6-di-*i*Pr–C_6H_3)]} (0.37 g, 1 mmol) and Pd(OAc)$_2$ (0.25 g, 1.1 mmol). A yellow solid was obtained; yield 0.57 g, 96%. ^{1}H NMR (600 MHz): δ = 1.10 [d, *J* = 7.2 Hz, 6 H, CH–(CH_3)$_2$], 1.20 [d, *J* = 6.6 Hz, 6 H, CH–(CH_3)$_2$], 1.91 [s, 3 H, O–C(=O)CH_3], 2.09 [s, 3 H, O–C(=O)CH_3], 3.25 [sept, *J* = 6.6 Hz, 2 H, CH–(CH$_3$)$_2$], 4.53 (s, 2 H, CH_2Py), 6.93 (d, *J* = 7.8 Hz, 2 H, CH–Ar), 7.00 (m, 2 H, CH–Ar), 7.06–7.10 (overlap, 2 H, CH–Ar), 7.25–7.32 (overlap, 4 H, CH–Ar), 7.78 (m, 1 H, CH–Ar), 8.19 (d, *J* = 6 Hz, 1 H, CH–Ar), 10.20 (s, 1 H, NH) ppm. ^{13}C{^{1}H} NMR (150 MHz): δ = 21.6 [s, CH–(CH_3)$_2$], 23.4 [s, O–C(=O)CH_3], 25.6 [s, CH–(CH_3)$_2$], 28.5 [s, CH–(CH$_3$)$_2$], 62.6 (s, CH_2Py), 119.6, 123.06, 123.12, 127.1, 128.46, 128.54, 130.4, 138.8, 148.9 (CH–Ar), 129.1, 131.5, 146.6, 162.1, 168.9 [three C$_{ipso}$–Ar, one NCN and one C–CH–(CH$_3$)$_2$], 178.2, 178.9 [O–C(=O)CH_3] ppm. $C_{27}H_{39}N_3O_4Pd$ (576.02): calcd. C 58.44, H 5.92, N 7.05; found C 58.59, H 5.49, N 6.99.

Complex 3: A solution of **1** (0.58 g, 1 mmol) in toluene (15 mL) was heated at 80 °C for 48 h. The volatile compounds were removed under reduced pressure and the residue was purified by THF/hexane solution to obtain a white precipitate. The crude product was washed hexane (30 mL three times) to afford white solid; yield 0.46 g, 90%. ^{1}H NMR (600 MHz): δ = 1.16 [d, *J* = 6.6 Hz, 6 H, CH–(CH_3)$_2$], 1.27 [d, *J* = 6.6 Hz, 6 H, CH–(CH_3)$_2$], 2.11 [s, 3 H, O–C(=O)CH_3], 2.56 [overlap, 8 H, CH_2 and N(CH_3)$_2$], 2.84 (br., 2 H, CH_2), 3.21 [sept, *J* = 6.6 Hz, 2 H, CH–(CH$_3$)$_2$], 6.67 (br., 1 H, NH), 6.80 (br., 1 H, CH–Ar), 6.96 (br., 1 H, CH–Ar), 7.12 (t, *J* = 7.2 Hz, 1 H, CH–Ar), 7.20 (d, *J* = 7.8 Hz, 2 H, CH–Ar), 7.21 (t, *J* = 8.4 Hz, 1 H, CH–Ar), 7.38 (t, *J* = 7.8 Hz, 1 H, CH–Ar) ppm. ^{13}C{^{1}H} NMR (150 MHz): δ = 22.6 [s, CH–(CH_3)$_2$], 24.15 [s, O–C(=O)CH_3], 24.24 [s, CH–(CH_3)$_2$], 28.6 [s, CH–(CH_3)$_2$], 46.6 (s, CH_2), 47.4 [s, N(CH_3)$_2$], 63.6 (s, CH_2), 123.3, 123.8, 129.4, 130.4, 133.9 (CH–Ar), 122.7, 132.2, 144.9, 146.8, 152.5, 161.8 [two C$_{ipso}$–Ar, one NCN, two C–CH–(CH$_3$)$_2$ and one metalated C–Ph], 177.5 [s, O–C(=O)CH_3] ppm. $C_{25}H_{35}N_3O_2Pd$ (515.97): calcd. C 58.19, H 6.84, N 8.14; found C 57.69, H 6.25, N 8.04.

Complex 4: A solution of **2** (0.57 g, 0.96 mmol) in THF (3 mL) was heated at 80 °C for 3 h. The brown suspension was cooled to room temperature and filtered. The brown residue was washed with THF to afford a pale grey solid; yield 0.57 g, 59%. ^{1}H NMR (600 MHz):

δ = 1.14 [d, *J* = 6.6 Hz, 6 H, CH–(CH_3)$_2$], 1.26 [d, *J* = 6.6 Hz, 6 H, CH–(CH_3)$_2$], 2.21 [s, 3 H, O–C(=O)CH_3], 3.25 [sept, *J* = 6.6 Hz, 2 H, CH–(CH$_3$)$_2$], 4.52 (br., 2 H, CH_2Py), 6.83 (s, 1 H, NH), 6.87 (br., 1 H, CH–Ar), 7.12 (br., 1 H, CH–Ar), 7.17 (m, 2 H, CH–Ar), 7.24 (m, 3 H, CH–Ar), 7.42 (t, *J* = 7.8 Hz, 1 H, CH–Ar), 7.59 (t, *J* = 7.2 Hz, 1 H, CH–Ar), 8.35 (d, *J* = 5.4 Hz, 1 H, CH–Ar) ppm. ^{13}C{^{1}H} NMR (150 MHz): δ = 22.9 [br., CH–(CH_3)$_2$], 24.1 [br., CH–(CH_3)$_2$], 24.4 [s, O–C(=O)CH_3], 28.6 [s, CH–(CH$_3$)$_2$], 55.7 (s, CH_2–Py), 120.9, 122.7, 123.2, 123.9, 124.4, 129.5, 130.7, 133.7, 137.8, 149.0 (CH–Ar), 132.0, 145.1, 147.0, 148.8, 152.9, 162.0 [three C$_{ipso}$–Ar, one metalated C–Ph, one C–CH–(CH$_3$)$_2$ and one NCN], 177.8 [s, O–C(=O)CH_3] ppm. $C_{27}H_{39}N_3O_4Pd$ (576.02): calcd. C 60.50, H 5.83, N 7.84; found C 60.55, H 6.19, N 7.37.

General Procedure for the Suzuki-Type Coupling Reaction: Prescribed amounts of catalyst, aryl halide (1.0 equiv.), phenylboronic acid (1.5 equiv.), base (3.0 equiv.) and a magnetic stir bar were placed in a Schlenk tube under nitrogen. Toluene (3 mL) was added by syringe, and the reaction mixture was heated in an oil bath at the prescribed temperature for the prescribed time. After removal of the volatile compounds, the residue was diluted with ethyl acetate, then filtered through a pad of silica gel. A sample in [D]chloroform was taken for determination of conversion. The crude material was further purified by flash chromatography on silica gel.

Crystal Structure Data: The crystals were grown from a solution of **1** in dichloromethane/hexane or a solution of **4** in concentrated chloroform, then isolated by filtration. Suitable crystals of **1** were sealed in thin-walled glass capillaries under a nitrogen atmosphere at 293 K and mounted on a Bruker AXS SMART 1000 diffractometer. A crystal of **4** was mounted onto a glass fibre by using a perfluoropolyether oil "oil-drop" method and cooled rapidly in a stream of cold nitrogen gas with an Oxford Cryosystems Cryostream unit. Diffraction data were collected at 100 K with an Oxford Gemini S diffractometer. The absorption correction was carried out on the basis of symmetry-equivalent reflections by using SADABS for **1**, and semiempirical absorption correction was based on the spherical harmonics implemented in the SCALE3 ABSPACK scaling algorithm from Crysalis RED, Oxford Diffraction Ltd for **4**.[14]

Table 2. Summary of crystal data for compounds **1** and **4**.

	1·CH$_2$Cl$_2$	**4**·CHCl$_3$·H$_2$O
Formula	$C_{28}H_{39}Cl_2N_3O_4Pd$	$C_{28}H_{34}Cl_3N_3O_3Pd$
M_r	658.92	673.33
T [K]	297(2)	100(2)
Crystal system	monoclinic	monoclinic
Space group	$P2_1/n$	$P2_1/n$
a [Å]	10.3443(14)	9.9600(3)
b [Å]	22.158(3)	18.5872(5)
c [Å]	14.4909(18)	16.5409(5)
a [°]	90	90
β [°]	107.768(2)	101.862(2)
γ [°]	90	90
V [Å^3]	3163.0(7)	2996.80(15)
Z	4	4
$\rho_{calcd.}$ [Mgm^{-3}]	1.384	1.492
μ(Mo-K_α) [mm^{-1}]	0.791	0.920
Reflections collected	17578	28387
Parameters	356	363
Indep. reflections (R_{int})	6182 (0.0269)	7152 (0.0385)
Final R indices R_1[a], wR_2[a]	0.0408, 0.1139	0.0356, 0.0889
R indices (all data)	0.0517, 0.1215	0.0505, 0.0927
GoF[b]	1.041	1.019

[a] $R_1 = [(\Sigma|F_o| - |F_c|)/\Sigma|F_o|]$, $wR_2 = [\Sigma w(F_o^2 - F_c^2)^2/\Sigma w(F_o^2)^2]^{1/2}$, $w = 0.10$. [b] GoF $= [\Sigma w(F_o^2 - F_c^2)^2/(N_{rflns} - N_{params})]^{1/2}$.

The space-group determination was based on a check of the Laue symmetry and systematic absences and was confirmed by using the structure solution. The structure was solved by direct methods using a SHELXTL package.[15] All non-hydrogen atoms were located from successive Fourier maps, and hydrogen atoms were refined using a riding model. Anisotropic thermal parameters were used for all non-hydrogen atoms, and fixed isotropic parameters were used for hydrogen atoms. Some details of the data collection and refinement are given in Table 2.

CCDC-840682 (for **1**) and -840683 (for **4**) contain the supplementary crystallographic data for this paper. These data can be obtained free of charge from The Cambridge Crystallographic Data Centre via www.ccdc.cam.ac.uk/data_request/cif.

[1] A. D. Ryabov, _Chem. Rev._ **1990**, _90_, 403–424.
[2] L. M. Rendina, R. J. Puddephatt, _Chem. Rev._ **1997**, _97_, 1735–1754.
[3] M. L. Tobe, J. Burgess, _Inorganic Reaction Mechanisms_, Addison Wesley Longman, Harlow, **1999**.
[4] M. Crespo, M. Font-Bardia, X. Solans, _Organometallics_ **2004**, _23_, 1708–1713.
[5] L. Xu, Q. Shi, X. Li, X. Jia, X. Huang, R. Wang, Z. Zhou, Z. Lin, A. S. Chan, _Chem. Commun._ **2003**, 1666–1667.
[6] A. Zucca, M. A. Cinellu, M. V. Pinna, S. Stoccoro, G. Minghetti, _Organometallics_ **2000**, _19_, 4295–4304.
[7] a) M. Gómez, J. Granell, M. Martinez, _J. Chem. Soc., Dalton Trans._ **1998**, 37–44; b) I. Favier, M. Gómez, J. Granell, M. Martínez, X. Solans, M. Font-Bardía, _Dalton Trans._ **2005**, 123–132.

[8] K.-M. Wu, C.-A. Huang, K.-F. Peng, C.-T. Chen, _Tetrahedron_ **2005**, _61_, 9679–9687.
[9] a) C. A. Nijhuis, E. Jellema, T. J. J. Sciarone, A. Meetsma, P. H. M. Budzelaar, B. Hessen, _Eur. J. Inorg. Chem._ **2005**, 2089–2099; b) S. Bambirra, E. Otten, D. van Leusen, A. Meetsma, B. Hessen, _Z. Anorg. Allg. Chem._ **2006**, _632_, 1950–1952; c) T. J. J. Sciarone, C. A. Nijhuis, A. Meetsma, B. Hessen, _Organometallics_ **2008**, _27_, 2058–2065.
[10] a) J. Barker, N. D. Cameron, M. Kilner, M. M. Mahmoud, S. C. J. Wallwork, _J. Chem. Soc., Dalton Trans._ **1991**, 3435–3445; b) J. L. Serrano, L. García, J. Pérez, E. Pérez, J. Vives, G. Sánchez, G. López, E. Molins, A. G. Orpen, _Polyhedron_ **2002**, _21_, 1589–1596; c) F. Neve, A. Crispini, C. Di Pietro, S. Campagna, _Organometallics_ **2002**, _21_, 3511–3518; d) B. J. O'Keefe, P. J. Steel, _Organometallics_ **2003**, _22_, 1281–1291; e) M. Ghedini, I. Aiello, A. Crispini, M. L. Deda, _Dalton Trans._ **2004**, 1386–1392; f) C. Seward, W.-T. Jia, R.-Y. Wang, S. Wang, _Inorg. Chem._ **2004**, _43_, 978–985; g) C.-T. Chen, Y.-S. Chan, Y.-R. Tzeng, M.-T. Chen, _Dalton Trans._ **2004**, 2691–2696.
[11] a) M.-T. Chen, C.-A. Huang, C.-T. Chen, _Eur. J. Inorg. Chem._ **2006**, 4642–4648; b) K.-F. Peng, M.-T. Chen, C.-A. Huang, C.-T. Chen, _Eur. J. Inorg. Chem._ **2008**, 2463–2470; c) M.-T. Chen, C.-A. Huang, C.-T. Chen, _Eur. J. Inorg. Chem._ **2008**, 3142–3150.
[12] a) J. Dupont, M. Pfeffer, J. Spencer, _Eur. J. Inorg. Chem._ **2001**, 1917–1927; b) R. B. Bedford, _Chem. Commun._ **2003**, 1787–1796; c) I. P. Beletskaya, A. V. Cheprakov, _J. Organomet. Chem._ **2004**, _689_, 4055–4082; d) J. Dupont, C. S. Consorti, J. Spencer, _Chem. Rev._ **2005**, _105_, 2527–2571.
[13] a) N. Miyaura, A. Suzuki, _Chem. Rev._ **1995**, _95_, 2457–2483; b) A. Suzuki, _J. Organomet. Chem._ **1999**, _576_, 147–168.
[14] G. M. Sheldrick, _SADABS, Program for area detector absorption correction_, Institute for Inorganic Chemistry, University of Göttingen, Germany, **1996**.
[15] G. M. Sheldrick, _SHELXTL-97, Program for refinement of crystal structures_, University of Göttingen, Germany, **1997**.

Superparamagnetic Core-Shell-Type Fe$_3$O$_4$/Ru Nanoparticles as Catalysts for the Selective Hydrogenation of an Unconstrained α,β-Unsaturated Ketone

Farooq-Ahmad Khan[a] and Georg Süss-Fink*[a]

Dedicated to Dr. Christian Bruneau on the occasion of his 60th birthday

Superparamagnetic core-shell-type Fe$_3$O$_4$/Ru nanoparticles (particle size ca. 15 nm) synthesized by co-precipitation, adsorption and reduction methods were found to selectively hydrogenate the carbon-oxygen double bond in *trans*-4-phenyl-3-penten-2-one (conversion 100 %, selectivity > 90 %) with a catalytic turnover of 900 under mild reaction conditions (30 °C, 15 bar H$_2$). The finely dispersed catalyst can be separated from the reaction mixture by using an external magnet, recycled, and reused without significant loss of activity and selectivity.

Introduction

Selective hydrogenation of the carbon-oxygen bond in α,β-unsaturated carbonyl compounds is a synthetic challenge, since C=C bond reduction is thermodynamically more favorable (35 kJ mol^{-1}) than C=O bond reduction.[1] This problem becomes even more complicated by the presence of an aromatic substituent in such systems because of possible ring hydrogenation.[2] Moreover, the transformation of unsaturated ketones into unsaturated alcohols is more difficult than that of unsaturated aldehydes, because ketones are sterically more hindered.[3] In addition, the "promoter effect" to enhance selectivity is also absent in the case of unsaturated ketones.[4]

In a pioneering study, Szöllosi et al. evaluated the potential of different metals such as Pt, Pd, Rh, Ru, Cu, and Ni supported on silica for the selective hydrogenation of α,β-unsaturated ketones.[5] Later, von Arx et al. were able to attain >90 % chemoselectivities for a sterically hindered C=O bond in ketoisophoron over alumina-supported Pt and Pd catalysts.[6] Such a remarkable selectivity might be attributed to steric effects,[1b,3] because the presence of bulky substituents at the olefin double bond presumably hampers its adsorption at catalytic sites.[8] Milone et al. and Mertens et al. showed that unsaturated alcohols can be obtained from different α,β-unsaturated ketones with a selectivity higher than 60 % at a conversion of 90 % by using a gold catalyst.[4,8] Recently, Wang et al. also used gold supported on mesostructured CeO$_2$ to hydrogenate *trans*-4-phenyl-3-penten-2-one at 100 °C with 63 % selectivity for the unsaturated alcohol.[9] However, in spite of extensive studies, efforts to selectively hydrogenate α,β-unsaturated ketones to give the corresponding unsaturated alcohols by molecular hydrogen have not been very successful.[8a,9]

Thus, the synthesis of unsaturated alcohols is mainly achieved with hazardous metal hydrides such as LiAlH$_4$ and NaBH$_4$,[10] with silicon hydrides,[11] or by transfer hydrogenation,[8a,12] as well as by Meerwein–Ponndorf–Verley-type reduction methods.[13] Homogeneous transition-metal catalysts sometimes show high selectivity,[14] but such complexes are often inefficient or have limited reusability.[15] Moreover, the separation of these complexes from the reaction mixture is very difficult.[16] Thus, the development of a highly selective, easily recoverable, and recyclable heterogeneous catalyst for the hydrogenation of unsaturated ketones remains a demanding task,[1a] because unsaturated alcohols are important intermediates used in the production of fine chemicals, pharmaceuticals, perfumery, and food processing industries.[17]

In chemical technology, heterogeneous catalysts are usually preferred, because separation, recovery, and recycling of the catalyst are relatively easy.[18] However, in liquid-phase batch reactions, the separation of the catalyst from the reaction products is still problematic.[19] Therefore, environmentally friendly, cost-effective, robust, easily recoverable, and cleanly reusable catalysts would be highly desirable[16] to ensure minimum loss, enhance their lifetime and minimize the consumption of auxiliary substances used in achieving separations.[19]

Recently, the use of magnetic materials as catalyst supports has attracted much attention,[16] because solid catalysts with magnetic properties can efficiently be separated

[a] Institut de Chimie, Université de Neuchâtel,
Avenue de Bellevaux 51, 2000 Neuchâtel, Switzerland
Fax: +41-32-7182511
E-mail: georg.suess-fink@unine.ch

from the reaction mixture by applying an external magnetic field.[20] This green and sustainable approach has many advantages over traditional time- and solvent-consuming processes, since it provides a fast, economical, and environmentally acceptable way to separate products and recycle catalysts.[19] Thus, ferromagnetic iron–nickel nanoparticles encapsulated in carbon have been prepared by Teunissen et al.; the carbon coating is necessary to overcome the problem of clustering of the nanoparticles.[21]

Superparamagnetic nanoparticles are such materials with high surface area,[22] which can be easily dispersed in solution, because they are intrinsically non-magnetic and therefore show no tendency to aggregate in solution.[18] On the other hand, these nanoparticles can be recovered easily from the reaction mixture by applying an external magnetic field, thus offering better handling properties.[19]

In this paper, we report on superparamagnetic core-shell-type Fe_3O_4/Ru nanoparticles, synthesized by immobilisation of $[(C_6H_6)Ru(H_2O)_3]^{2+}$ cations on freshly prepared magnetite nanoparticles, followed by reduction with molecular hydrogen. They are highly active and selective in the catalytic conversion of *trans*-4-phenyl-3-penten-2-one into 4-phenylbutan-2-ol.

Results and Discussion

Nanosized magnetite (Fe_3O_4) was prepared by the co-precipitation method,[23] by adding an aqueous solution of a 1:2 mixture of $FeCl_2$ and $FeCl_3$ to ammonia (0.7 M), followed by vigorous stirring. The black Fe_3O_4 nanoparticles thus obtained are sensitive to air and must be handled in an inert atmosphere.[24] The NH_4^+ cations adsorbed at the surface of these particles are partially exchanged by Na^+ by adjusting the pH to 10 by using NaOH (2 M).[23b] The Fe_3O_4 nanoparticles containing Na^+ and NH_4^+ at their surface are isolated from the solution by magnetic decantation and further used without washing with water.

$$Fe^{2+}_{(aq)} + 2\,Fe^{3+}_{(aq)} + 8\,OH^-_{(aq)} \longrightarrow Fe_3O_{4(s)} + 4\,H_2O_{(l)}$$
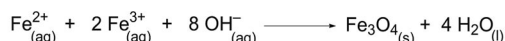
The dinuclear complex, the benzene ruthenium dichloride dimer, dissolves in water with hydrolysis to give, with successive substitution of the chlorido ligands by aqua ligands, a mixture of mononuclear benzene ruthenium complexes in equilibrium.[25] The benzene ^1H NMR signals of the D_2O solution are assigned to $[(C_6H_6)RuCl_2(H_2O)]$ ($\delta = 5.89$ ppm), $[(C_6H_6)RuCl(H_2O)_2]^{2+}$ ($\delta = 5.97$ ppm), and $[(C_6H_6)Ru(H_2O)_3]^{2+}$ ($\delta = 6.06$ ppm).[26] The dication $[(C_6H_6)Ru(H_2O)_3]^{2+}$, which was isolated as the sulfate and structurally characterized,[27] is the major species present in the hydrolytic mixture over the pH range 5–8 according to the NMR spectrum.
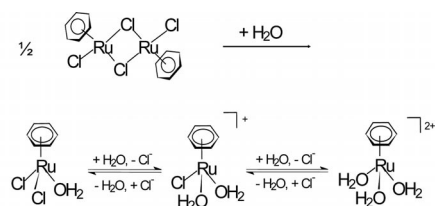
When the yellow solution obtained by dissolving the dinuclear complex $[(C_6H_6)RuCl_2]_2$ in water is added to the magnetite nanoparticles described above, the main hydrolysis product, $[(C_6H_6)Ru(H_2O)_3]^{2+}$, adsorbs on the surface of the nanosized Fe_3O_4 (replacing the appropriate amount of counterions) to give the ruthenium(II)-modified magnetite **1**. This material is isolated by magnetic decantation, washed with deoxygenated water, and dried under vacuum. Inductively coupled plasma optical emission spectroscopy (ICP–OES) analysis of this material shows a ruthenium loading of 0.074 mmol per gram of Fe_3O_4, which is the maximum loading. The Fourier transform infrared (FTIR) spectrum indicates the presence of an absorption band at 576 cm^{-1}, which can be assigned to Fe–O vibrations of bulk Fe_3O_4.[28] Ruthenium(II)-modified magnetite **1** reacts with hydrogen under pressure (50 bar) at 100 °C in *n*BuOH by reduction of the adsorbed $[(C_6H_6)Ru(H_2O)_3]^{2+}$ species to metallic ruthenium to give core-shell-type Fe_3O_4/Ru nanoparticles **2** (Scheme 1), in a manner similar to that for the preparation of hectorite-supported ruthenium nanoparticles.[29]
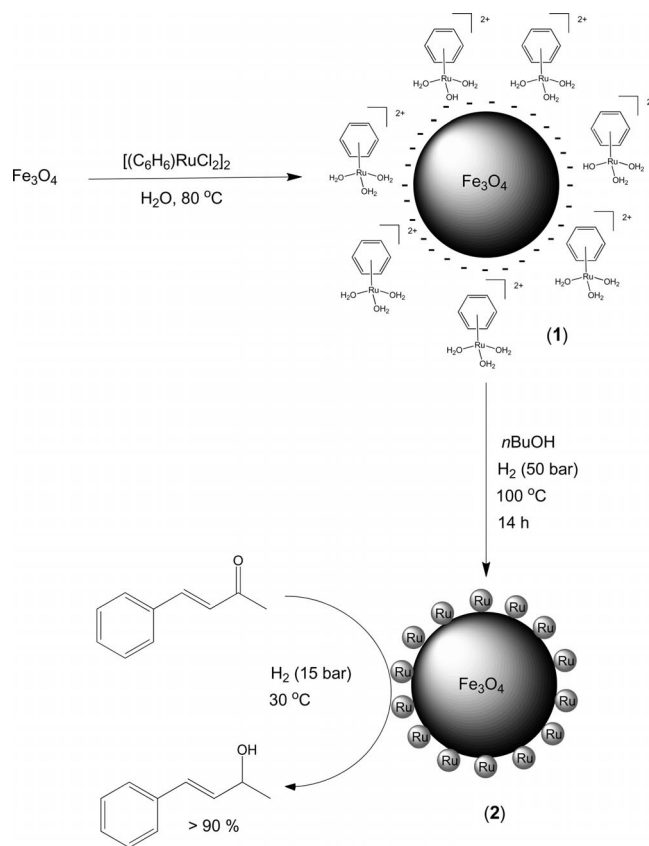
Scheme 1. Synthesis of superparamagnetic core–shell-type Fe_3O_4/Ru nanoparticles and their catalytic action.

Figure 1 shows the TEM micrograph of **2** before the catalytic reaction. The size distribution of these superparamagnetic Fe_3O_4/Ru nanoparticles was studied by transmission electron microscopy (TEM) by using the "ImageJ" software[30] for image processing and analysis. The mean particle size was calculated by using the equation:
$$\bar{d} = \Sigma n_i d_i / n_i.^{[4]}$$

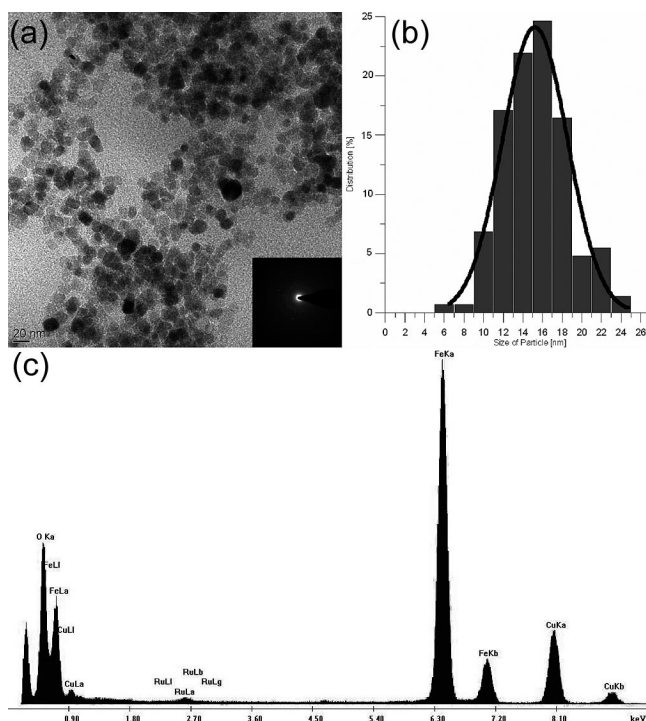Figure 2. X-ray powder diffraction of the Ru^0-modified magnetite **2**.

Figure 1. (a) TEM micrograph with SAED, (b) histogram (the bars show the size distributtion and the solid line the Gaussian fit), and (c) EDAX analysis of core-shell-type Fe$_3$O$_4$/Ru nanoparticles **2**.

Some aggregation of the nanoparticles was observed, presumably because *n*BuOH is not very effective in preventing the aggregation of these particles. However, *n*BuOH favors the accessibility of the substrate to catalytically active sites on the nanoparticles.[31] The micrographs show particles varying from 5 to 25 nm, the average particle size is 15 nm, which is close to the boundary between superparamagnetic and single domains. The mean particle size and standard deviation (σ) were estimated from image analysis of about at least 100 particles. The presence of ruthenium was inferred from energy dispersive X-ray spectroscopic (EDAX) analysis, which was further confirmed by inductively coupled plasma optical emission spectroscopy (ICP-OES). The percent weight loss of **2** as a function of temperature was studied by thermogravimetric analysis (TGA), which shows an overall weight loss of ca. 3% between 180–445 °C. This loss may be attributed to the loss of *n*BuOH molecules adsorbed at the surface of **2**.

The X-ray powder diffraction of Ru^0-modified magnetite **2** nanoparticles is shown in Figure 2. The average crystallite size of 14.4 nm was estimated by applying the Scherrer formula[32] on the full widths at half maximum (0.89) of the strongest (100%) reflection; the value of 2θ is 35.59°.

Figure 3 shows the magnetization curves for ruthenium-(II)-modified magnetite nanoparticles **1** and Ru^0-modified magnetite **2** nanoparticles measured at room temperature. These modified nanoparticles have a saturation magnetization (σ_s) of 62.4 and 69.6 emu/g, respectively. These values are slightly smaller than that of bulk magnetite (92 emu/g),
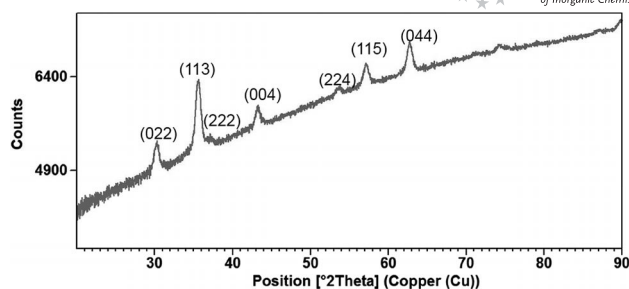
which is consistent with the presence of surface coatings with ruthenium.[22] At low magnetic field, the hysteresis loops of these nanoparticles (insets in Figure 3) indicate low coercivity and almost zero remanence, which suggests that the particles exhibit superparamagnetic behavior. The slightly opened loop can be attributed to particles with grain size larger than ca. 20 nm that still can carry remanent magnetization during the measurement duration of 100 ms.
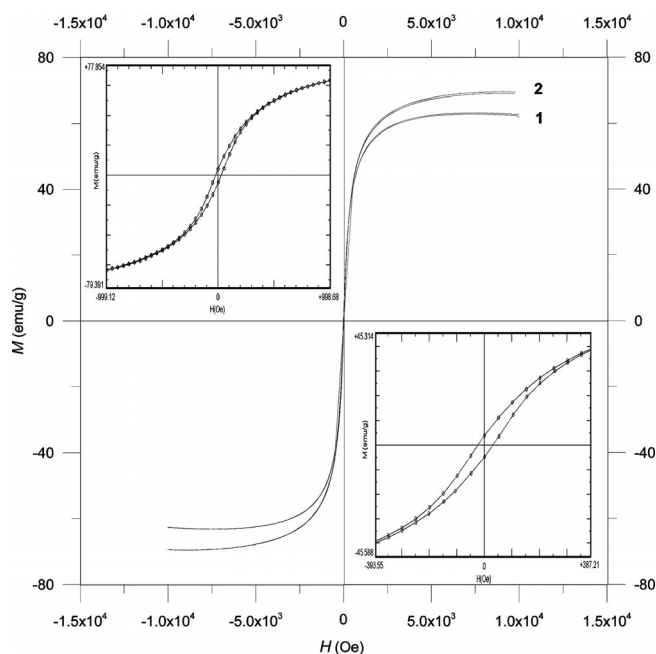
Figure 3. Magnetization curves for **1** and **2** measured at 300 K. The insets show magnified hysteresis loops at low magnetic fields, which highlight the coercivity and remanence of the particles. These particles exhibit predominantly superparamagnetic behavior with some blocked, single-domain particles.

The core-shell-type Fe$_3$O$_4$/Ru nanoparticles **2**, which are intrinsically nonmagnetic can be readily dispersed in *n*BuOH and easily recovered by applying an external magnetic field (Figure 4). They are a highly active and selective hydrogenation catalyst, which convert *trans*-4-phenyl-3-penten-2-one under hydrogen into 4-phenylbutan-2-ol and avoid the formation of saturated products (Scheme 2).

Figure 4. Superparamagnetic core-shell-type Fe$_3$O$_4$/Ru nanoparticles (a) dispersed in *n*BuOH and (b) gathered on the glass wall by an external magnet.

Scheme 2. Selective hydrogenation of *trans*-4-phenyl-3-buten-2-one and possible reaction pathway.

Table 1. Hydrogenation of *trans*-4-phenyl-3-penten-2-one with Fe$_3$O$_4$/Ru nanoparticles in *n*-butanol.

Time (h)	Substrate conversion (%)	Unsaturated alcohol (%)	Unsaturated alcohol selectivity (%)
1	15.2	14.3	94.1
2	32.4	30.9	95.4
3	49.3	46.8	94.9
4	69.0	63.1	91.5
5	88.0	79.5	90.3
6	98.8	89.7	90.8
7	100	92.8	92.8
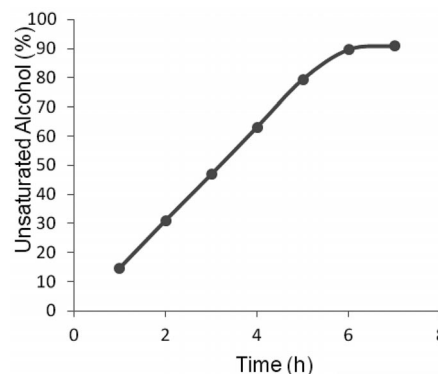
Figure 5. Time dependence of the hydrogenation of *trans*-4-phenyl-3-penten-2-one catalyzed by Ru^0-coated magnetite **2**.

This highly selective reduction of an unconstrained α,β-unsaturated ketone is striking, especially, since no aromatic ring hydrogenation was observed. Thus, the catalyst is capable of reducing the C=O bond selectively. The catalytic reaction was followed by a gas chr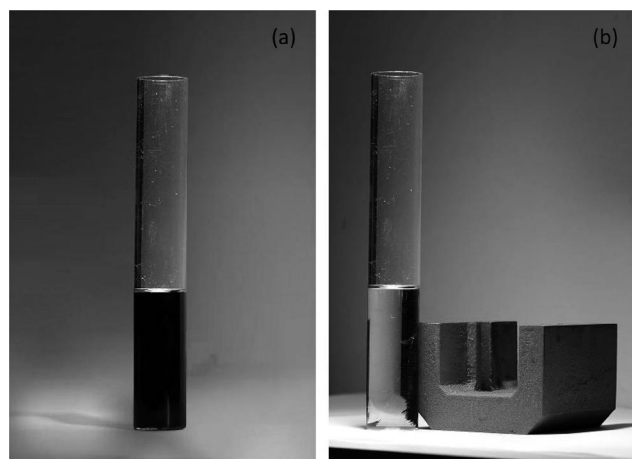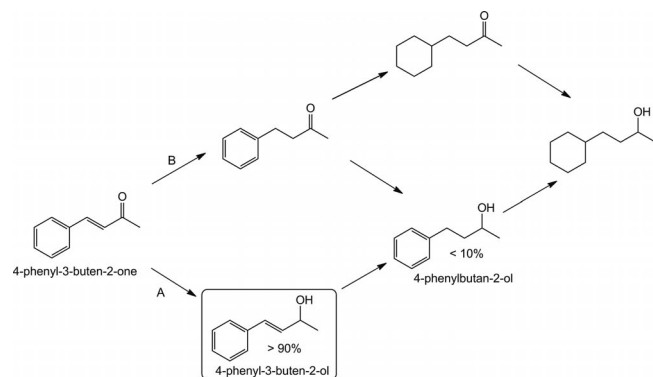omatography coupled to mass spectrometry detector (GC–MS). The products were separated on an apolar column and were identified by their retention time and mass spectrum by using the electron impact (EI) ionization method.

The hydrogenation of *trans*-4-phenyl-3-penten-2-one was carried out by using **2** freshly prepared by the reduction of **1** in *n*BuOH (20 mL) under a pressure of hydrogen (50 bar) at 100 °C for 14 h. GC–MS shows complete conversion of the substrate (100%). The overall selectivity of **2** towards unsaturated alcohols was >90%, presumably because of the mild reaction conditions and the interaction between the catalyst and the support. The turnover number was determined by adding 12.2 mmol (1.78 g) of *trans*-4-phenyl-3-penten-2-one after regular intervals, until the catalyst became almost inactive; the total mass of substrate added was 5.34 g. Table 1 shows the time dependence of the catalytic hydrogenation, which is linear before saturation (Figure 5).

A schematic representation of the reaction pathway (Scheme 2) shows that the reaction undergoes path A and not path B, because no traces of 4-phenylbutan-2-one were observed during GC–MS analysis of the reaction mixtures taken at different reaction times. It may be assumed that the saturated alcohol 4-phenylbutan-2-ol is essentially obtained by further reduction of the unsaturated alcohol 4-phenyl-3-buten-2-ol. Interestingly, no traces of 4-cyclohexylbutan-2-one and 4-cyclohexylbutan-2-ol were observed, which suggests that **2** is unable to catalyze aromatic ring hydrogenation under the reaction conditions.

The high selectivity for hydrogenation of the C=O bond can tentatively be attributed to the activation of the C=O bond by the metal–support interaction. It can be assumed that magnetite probably modifies the electronic properties of ruthenium, which in turn, leads to an increase in the hydrogenation selectivity for the C=O bond. Thus, the specific hydrogenation tendency of *trans*-4-phenyl-3-penten-2-one can be interpreted in terms of an exclusive adsorption of C=O bonds at the surface of the nanoparticles.[7a]

The nanoparticles **2** can be recovered and reused, however, after three catalytic runs, aggregation was observed (Figure 6). In order to determine the amount of ruthenium leaching, the combined washings of three consecutive runs are analyzed by ICP-OES. As there was no iron peak in the spectrum, which could interfere with the ruthenium signals, the ruthenium quantity could be calculated without applying any correction. The leaching observed is around 4.1% with respect to original ruthenium loading after three catalytic runs.

Figure 6. TEM micrograph of **2** after three catalytic runs.

Conclusions

We have prepared novel core-shell-type Fe$_3$O$_4$/Ru nanoparticles, which show a remarkable catalytic activity for the selective hydrogenation of the C=O bond in an unco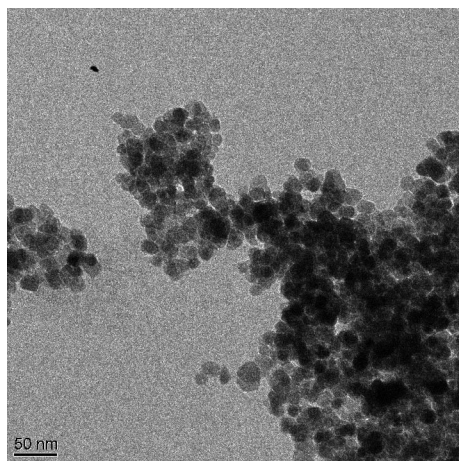nstrained α,β-unsaturated ketone viz. *trans*-4-phenyl-3-penten-2-one. These environmentally friendly superparamagnetic nanoparticles can be easily dispersed because of the intrinsically nonmagnetic nature and can be readily recycled and reused by magnetic decantation.

Experimental Section

Preparation of Fe$_3$O$_4$ Nanoparticles: Fe$_3$O$_4$ nanoparticles were prepared by the co-precipitation method:[23] A freshly prepared aqueous solution of 1 M FeCl$_3$ was mixed with 2 M FeCl$_2$ (2.5 mL) dissolved in 2 M HCl. Both solutions were prepared in deoxygenated water. Immediately after the solutions were mixed under nitrogen, it was added to NH$_3$ (125 mL of a 0.7 M solution) under N$_2$. After 30 min of vigorous stirring, the pH was adjusted to 10 by using a 2 M NaOH. After 1 h, the black Fe$_3$O$_4$ nanoparticles formed were separated magnetically.

Preparation of Fe$_3$O$_4$/[(C$_6$H$_6$)Ru(H$_2$O)$_3$]$^{2+}$ (1): Fe$_3$O$_4$ nanoparticles were redispersed in water (50 mL) containing [(C$_6$H$_6$)$_2$Ru$_2$Cl$_4$] (0.1 g). This mixture was heated at 80 °C overnight. The resulting precipitate was separated magnetically, washed with H$_2$O (3 × 25 mL), and dried in vacuo.

Preparation of Fe$_3$O$_4$/Ru (2): **2** was obtained by reacting a suspension of **1** (0.5 g) in *n*BuOH (20 mL) in a magnetically stirred stainless-steel autoclave (volume 100 mL) under a pressure of H$_2$ (50 bar) at 100 °C for 14 h. After releasing the pressure and cooling, **2** was isolated by magnetic decantation and dried in vacuo.

Hydrogenation of *trans*-4-Phenyl-3-buten-2-one: Freshly prepared **2** (0.5 g) was added to a solution of *trans*-4-phenyl-3-buten-2-one (1.78 g) in *n*BuOH (20 mL). This solution was placed in an autoclave (100 mL), while being rigorously stirred at 30 °C under H$_2$ (15 bar). After every hour, the pressure was released, the sample was taken, and the solution was magnetically decanted from the solid and analyzed. The turnover number was determined by adding 1.78 g of substrate dissolved in *n*BuOH (20 mL) at regular intervals, until the catalyst became inactive; the total volume of substrate added was 5.34 g. The selectivity was checked by GC–MS. For recycling, a permanent magnet was externally applied to isolate **2** on the side wall of reactor. The reaction solution was decanted off, and the catalyst was reused directly for the next run.

[1] a) P. Mäki-Arvela, J. Hájek, T. Salmi, D. Yu. Murzin, *Appl. Catal. A* **2005**, *292*, 1–49; b) S. N. Coman, V. I. Parvulescu, M. De Bruyn, D. E. De Vos, P. Jacobs, *J. Catal.* **2002**, 206–218.

[2] E. Breitner, E. Roginski, P. N. Rylander, *J. Org. Chem.* **1959**, *24*, 1855–1857.

[3] P. Kluson, L. Cerveny, *Appl. Catal. A* **1995**, *128*, 13–31.

[4] C. Milone, R. Ingoglia, A. Pistone, G. Neri, F. Frusteri, S. Galvagno, *J. Catal.* **2004**, *222*, 348–356.

[5] G. Szöllósi, Á. Mastalir, Á. Molnár, M. Bartók, *React. Kinet. Catal. Lett.* **1996**, *57*, 29–36.

[6] M. von Arx, T. Mallat, A. Baiker, *J. Mol. Catal. A* **1999**, *148*, 275–283.

[7] a) F. Delbecq, P. Sautet, *J. Catal.* **1995**, *152*, 217–236; b) F. Delbecq, P. Sautet, *Surf. Sci.* **1993**, *295*, 33–33; c) P. Sautet, J. F. Paul, *Catal. Lett.* **1991**, *9*, 245–260.

[8] a) C. Milone, R. Ingoglia, M. L. Tropeano, G. Neri, S. Galvagno, *Chem. Commun.* **2003**, 868–869; b) C. Milone, R. Ingoglia, L. Schipilliti, C. Crisafulli, G. Neri, S. Galvagno, *J. Catal.* **2005**, *236*, 80–90; c) P. G. N. Mertens, J. Wahlen, X. Ye, H. Poelman, D. E. De Vos, *Catal. Lett.* **2007**, *117*, 15–21; d) C. Milone, R. Ingoglia, S. Galvagno, *Gold Bull.* **2006**, *39*, 54–64.

[9] M.-M. Wang, L. He, Y.-M. Liu, Y. Cao, H.-Y. He, K.-N. Fan, *Green Chem.* **2011**, *13*, 602–607.

[10] a) A. M. Al-Etaibi, N. A. Al-Awadi, M. R. Ibrahim, Y. A. Ibrahim, *Molecules* **2010**, *15*, 407–419; b) N. M. Yoon, T. B. Sim, *Bull. Korean Chem. Soc.* **1993**, *14*, 749–752; c) A. L. Gemal, J. L. Luche, *J. Am. Chem. Soc.* **1981**, *103*, 5454–5459; d) K. E. Wilson, R. T. Seider, S. Masamune, *J. Chem. Soc. C* **1970**, 213; e) L. Mordenti, J. J. Brunet, P. Caubere, *J. Org. Chem.* **1979**, *44*, 2203–2205.

[11] a) H. Ozasa, K. Kondo, T. Aoyama, *Chem. Pharm. Bull.* **2010**, *58*, 989–990; b) T. Inagaki, Y. Yamada, L. T. Phong, A. Furuta, J. Ito, H. Nishiyama, *Synlett* **2009**, 253–256; c) D. Addis, S. Zhou, S. Das, K. Junge, H. Kosslick, J. Harloff, H. Lund, A. Schulz, M. Beller, *Chem. Asian J.* **2010**, *5*, 2341–2345; d) D. Addis, N. Shaikh, S. Zhou, S. Das, K. Junge, M. Beller, *Chem. Asian J.* **2010**, *5*, 1687–1691.

[12] a) N. Erathodiyil, S. Ooi, A. M. Seayad, Y. Han, S. S. Lee, J. Y. Ying, *Chem. Eur. J.* **2008**, *14*, 3118–3125; b) A. J. Blacker, S. M. Brown, C. Bubert, J. M. J. Williams, WO 0244111, **2002**; c) A. J. Blacker, B. V. Mellor, US patent 2002/0156282, **2002**.

[13] a) Y. Ishii, T. Nakano, A. Inada, Y. Kishigami, K. Sakurai, M. Ogawa, *J. Org. Chem.* **1986**, *51*, 240–242; b) M. Gargano, V. D'Orazio, N. Ravasio, M. Rossi, *J. Mol. Catal.* **1990**, *58*, L5; c) J. I. Di Cosimo, A. Acosta, C. R. Apesteguia, *J. Mol. Catal. A* **2004**, *222*, 87–96.

[14] a) K. Junge, B. Wendt, D. Addis, S. Zhou, S. Das, S. Fleischer, M. Beller, *Chem. Eur. J.* **2011**, *17*, 101–105; b) X. Chen, W. Jia, R. Guo, T. W. Graham, M. A. Gullons, K. Abdur-Rashid, *Dalton Trans.* **2009**, 1407–1410; c) I. Warad, Z. Al-Othman, S. Al-Resayes, S. S. Al-Deyab, E.-R. Kenawy, *Molecules* **2010**, *15*, 1028–1040; d) R. Noyori, T. Ohkuma, *Pure Appl. Chem.* **1999**,

71, 1493–1501; e) C. A. Mebi, R. P. Nair, B. J. Frost, *Organometallics* **2007**, *26*, 429–438.

[15] R. A. Sheldon, *Pure Appl. Chem.* **2000**, *72*, 1233–1246.

[16] V. Polshettiwar, R. Luque, A. Fihri, H. Zhu, M. Bouhrara, J.-M. Basset, *Chem. Rev.* **2011**, *111*, 3036–3075.

[17] a) J. Špringerova, P. Kacher, L. Červeny, *Res. Chem. Intermed.* **2005**, *31*, 785–795; b) B. S. Furniss, A. J. Hannaford, P. W. G. Smith, A. R. Tatchell in *Vogel's Textbook of Practical Organic Chemistry* (Ed.: A. Longman), 5th ed., Wiley-VCH, New York, **1989**, pp. 519.

[18] B. Panella, A. Vargas, A. Baiker, *J. Catal.* **2009**, *261*, 88–93.

[19] M. J. Jacinto, P. K. Kiyohara, S. H. Masunaga, R. F. Jardim, L. M. Rossi, *Appl. Catal. A* **2008**, *338*, 52–57.

[20] A. H. Lu, E. L. Salabas, F. Schuth, *Angew. Chem.* **2007**, *119*, 1242; *Angew. Chem. Int. Ed.* **2007**, *46*, 1222–1244.

[21] W. Teunissen, A. A. Bol, J. W. Geus, *Catal. Today* **1999**, *48*, 329–336.

[22] A. Hu, G. T. Yee, W. Lin, *J. Am. Chem. Soc.* **2005**, *127*, 12486–12487.

[23] a) L. M. Rossi, L. L. R. Vono, F. P. Silva, P. K. Kiyohara, E. L. Duarte, J. R. Matos, *Appl. Catal. A* **2007**, *330*, 139–144; b) R. Massart, *IEEE Trans. Magn.* **1981**, *17*, 1247–1248.

[24] W. Wu, Q. He, C. Jiang, *Nanoscale Res. Lett.* **2008**, *3*, 397–415.

[25] A. Meister, G. Süss-Fink, unpublished, see A. Meister, Ph. D. Thesis, University of Neuchâtel, Switzerland, **1994**.

[26] G. Meister, G. Süss-Fink, unpublished, see G. Meister, *Ph. D. Thesis*, University of Neuchâtel, Switzerland, **1994**.

[27] M. Stebler-Röthlisberger, W. Hummel, P.-A. Pittet, H.-B. Bürgi, A. Ludi, A. E. Merbach, *Inorg. Chem.* **1988**, *27*, 1358–1363.

[28] R. M. Cornell, U. Schwertmann in *The Iron Oxides: Structure, Properties, Reactions, Occurences and Uses*, Wiley-VCH, Weinheim, **1996**.

[29] a) F.-A. Khan, A. Vallat, G. Süss-Fink, *Catal. Commun.* **2011**, *12*, 1428–1431; b) A. Meister, G. Meister, G. Süss-Fink, *J. Mol. Catal.* **1994**, *92*, L123–L126; c) G. Süss-Fink, B. Mollwitz, B. Therrien, M. Dadras, G. Laurenczy, A. Meister, G. Meister, *J. Cluster Sci.* **2007**, *18*, 87–95; d) G. Süss-Fink, F.-A. Khan, J. Boudon, V. Spassov, *J. Cluster Sci.* **2009**, *20*, 341–353.

[30] M. D. Abramoff, P. J. Magelhaes, S. J. Ram, *Biophotonics Int.* **2004**, *11*, 36–42.

[31] a) M. Kotani, T. Koike, K. Yamaguchi, N. Mizuno, *Green Chem.* **2006**, *8*, 735–741; b) M. A. Vergés, R. Costo, A. G. Roca, J. F. Marco, G. F. Goya, C. J. Serna, M. P. Morales, *J. Phys. D* **2008**, *41*, 134003–134013.

[32] a) H. P. Klug, L. E. Alexander, *X-ray Diffraction Procedures*, 2nd ed., John Wiley & Sons Inc., **1974**, pp. 687–703; b) A. Patterson, *Phys. Rev.* **1939**, *56*, 978–982.

Proton Sponge Phosphanes: Reversibly Chargeable Ligands for ESI-MS Analysis

Nicola J. Farrer,[a][‡] Krista L. Vikse,[a] Robert McDonald,[b] and J. Scott McIndoe*[a]

Proton sponge phosphanes are unusual ligands in that they possess two basic sites with very different functions: the phosphorus binds to a metal center, while the 1,8-bis(dimethylamino)naphthalene binds protons strongly. Both groups are selective for their target, and the binding of the proton is easily reversible by controlling the pH of the solution. Proton sponge phosphanes therefore make useful chargeable ligands for the purposes of electrospray ionization mass spectrometric analysis of the complexes in which they are bound. However, where the 1,8-bis(dimethylamino)naphthalene is functionalized with the phosphane is critical, and the 1-dimethylamino group can become involved in binding to the

metal when diphenylphosphane is in the 2-position. This behavior is undesirable from the point of view of keeping proton and metal binding segregated, and we introduce an efficient synthesis of the 4-substituted proton sponge phosphane in which the two functional groups are on opposite sides of the naphthalene ring. This precaution solves the problem of the molecule acting as a bidentate ligand, but caution is still needed when using the ligand, because ionization pathways such as halide dissociation to form $[M - X]^+$ ions and oxidation of electron-rich metal complexes to form $[M]^{+}$ can be competitive with protonation.

Introduction

Electrospray ionization mass spectrometry (ESI-MS) has a number of strengths that make it well suited to the study of organometallic catalysis. (1) ESI-MS is a soft technique that operates on solutions and can leave weak bonding interactions intact. (2) Only species that are already charged in solution or contain an easily charged site are detected. Because of this most common solvents are "invisible" and very low detection limits are accessible.[20] (3) Analysis is fast (on the order of seconds), and (4) intermediates at nanomolar concentrations can be detected with ease. Finally, (5) since each species in solution is usually represented by a single peak in the mass spectrum it is often possible to extract information from complex mixtures. A growing body of literature exists in which investigators have taken advantage of these attributes of ESI-MS to study organometallic systems. The first was Berman who used ESI-MS to detect a number of environmentally important organoarsenic ions.[1] Another notable early example comes from Canty in 1993 who reported the positive ESI-MS(/MS)

studies of various palladium and platinum organometallic complexes.[2] Since then, a growing application of ESI-MS in this area has been in the identification of short-lived, low-concentration intermediates. It has been used in the study of catalytic oxidation,[3] hydrogenation,[4] hydrosilylation [5] and carbon–carbon bond-forming reactions.[6] A large amount of the attention has been given to palladium-catalyzed carbon–carbon bond-forming reactions.[7] In order to investigate any catalytic system by ESI-MS all species of interest must be charged; either inherently, adventitiously (e.g., by protonation or loss of a halide), or intentionally by installing a charged or chargeable tag.

Monitoring catalytic reactions that have intrinsically or adventitiously charged intermediates is relatively simple, and analyses of these types of systems constitute the bulk of the literature,[8] but many of the most important catalytic organometallic reactions proceed through neutral intermediates where there are no reliable ionization mechanisms for visualization by ESI-MS. In order to study these systems a charged or chargeable (usually having an acidic or basic site) tag is required. Importantly, the tag must not introduce steric or electronic effects that interfere with the catalysis in any way.

In 1994 Canary et al. purposefully used a substrate with an easily protonated site to study the palladium-catalyzed reactions of pyridyl bromide with three different phenylboronic acids by ESI-MS. Pyridyl bromide was selected as a chargeable tag due to the ability of the ring nitrogen to become protonated. Relying on this ionization mechanism, oxidative addition intermediates and transmetallation inter-

[a] Department of Chemistry, University of Victoria,
P. O. Box 3065, Victoria, BC V8W 3V6, Canada
E-mail: mcindoe@uvic.ca
[b] X-ray Crystallography Laboratory, Department of Chemistry, University of Alberta,
Edmonton, AB, T6G 2G2, Canada
[‡] Current address: Department of Chemistry, University of Warwick,
Coventry CV4 7AL, UK
Supporting information for this article is available on the WWW under http://dx.doi.org/10.1002/ejic.201100820.

mediates were observed.[9] Many of the existing studies using charged ligands focus on ruthenium-catalyzed systems, and they often make use of ligands designed to confer water solubility. The groups of Traeger,[10] Nicholson,[11] and Chen[12] have made significant contributions to this area. However, it is still a somewhat under-appreciated approach.

Chargeable tags are neutral molecules that contain a functional group of interest, and at a secondary site bind either an acid or a base to become charged. Chargeable tags (as opposed to permanently charged tags) are appealing for a number of reasons: (i) Any effect that the charged group may have on reactivity is mitigated since the charged tag is in equilibrium with its neutral counterpart, (ii) the pH of the droplet decreases rapidly as the solvent evaporates,[13] so addition of protons is often not required, and (iii) chargeable ligands have the potential to aid in catalyst recovery since their solubility in organic solvents can be manipulated by changing the pH of the reaction mixture.

We have developed chargeable phosphane ligands derived from the strong base 1,8-bis(dimethylamino)naphthalene also known as "Proton Sponge®" that serve as analogues for commonly used organometallic ligands.[14] First studied by Alder and co-workers, Proton Sponge® (**1**) is a very strong, non-nucleophilic base (pK_a = 12.34 in H_2O) with high thermodynamic basicity but relatively low kinetic basicity.[15] **1** binds H^+ by forming intramolecular hydrogen bonds with both nitrogen centers in the molecule to give the charged $[N\cdots H\cdots N]^+$ moiety. **1** has been used extensively as a non-nucleophilic proton abstractor in organic synthesis,[16] and as a matrix material in MALDI-MS.[17]

The high thermodynamic basicity of **1** is attributed to a combination of factors.[18] The methyl groups bound to each nitrogen sterically clash with each other and force the nitrogen lone pairs to point toward each other adopting an "in-in" conformation.[19] This leads to a high degree of lone pair-lone pair repulsion and causes the naphthalene backbone to be twisted. By protonating the neutral molecule a more optimal geometry is attained, steric strain is relieved, and the naphthalene ring returns to planarity.[20] Additional stabilization is gained through the strong intramolecular hydrogen bonds formed between the proton and both nitrogen lone pairs.[18a] The low kinetic basicity of **1** arises from the steric crowding of the basic site by the four nearby methyl groups. These methyl groups and the proximity of the two nitrogen centers to each other are also responsible for the high selectivity that **1** has for H^+; all other cations are too large to fit in the resulting pocket.[21] The overall effect is that **1** is approximately six orders of magnitude more basic than typical aromatic amines, and can selectively trap adventitious protons and become charged.

Results and Discussion

We expected **1** to be a well-behaved electrospray-active tag based on the properties discussed above. Other potentially interfering cations such as Na^+ or K^+ are too large to

bind to **1**, so mass spectra of **1** display only the $[M + H]^+$ peak even in the presence of competing cations. Its high ionization efficiency in solution leads to signal intensities approaching those of phosphonium ions allowing for detection at very low concentrations and ensuring that all species containing **1** are represented in the spectrum. Di-protonation is extremely unfavorable and the doubly charged ion is never seen, further simplifying the resulting spectra. Appending **1** to common ligands was anticipated to provide a means of reversibly and selectively charging and investigating a variety of organometallic and coordination compounds and their reactivity. Triphenylphosphane was selected as the parent ligand since it is inexpensive, readily available and is used routinely as a ligand in many catalytic reactions. **1** can be substituted for one of the phenyl groups on phosphorus to give the *ortho-* or *para*-electrospray-active ligands 1,8-bis(dimethylamino)-2-(diphenylphosphanyl)-naphthalene (**3a**) or 1,8-bis(dimethylamino)-4-(diphenylphosphanyl)naphthalene (**3b**) (see Scheme 1).
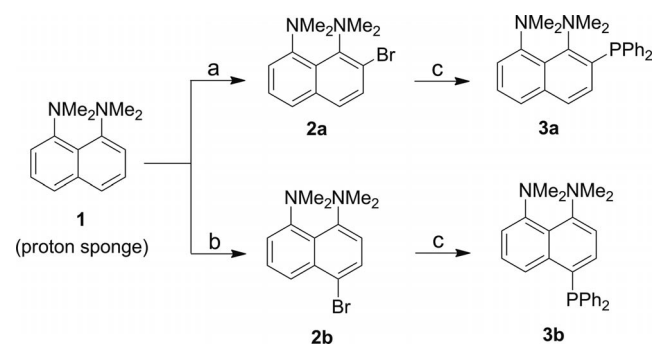
Scheme 1. Synthesis of **3a** and **3b**. a) NBS / THF / –78 °C; 63% yield. b) Br_2 / CCl_4 / 22 °C; 52% yield. c) *n*BuLi / THF / –78 °C, PPh_2Cl / THF / –78 °C.

Initial work on the two isomers revealed that while synthesis of **3a** was straightforward, synthesis of **3b** was not. The problem lies in the first step of the reaction: bromination of **1**, which can be effectively accomplished in the *ortho* (2-) position using the brominating agent *N*-bromosuccinimide, selective for *ortho*-bromination at low temperatures.[22] However, despite attempting the reaction under a variety of brominating conditions that were reported in the literature,[23] selective *para*-bromination at only one of the *para*-sites on Proton Sponge® was elusive. Product mixtures which included *ortho*-substituted and di-substituted compounds were obtained, and purification of **3b** from these mixtures was difficult and low yielding.

3a reacts with a range of metal complexes, including $Fe(CO)_5$, $W(CO)_5(thf)$, $PdCl_2(cod)$ (cod = cyclooctadiene), and {Ru(η⁶-*p*-cymene)Cl_2}$_2$. In the reactions with $Fe(CO)_5$ and $W(CO)_5(thf)$, **3a** coordinated only through the phosphorus atom, and the ESI-MS showed only the expected $[M + H]^+$ ions.[14] Reaction of **3a** with [Ru(η⁶-*p*-cymene)-Cl_2]$_2$ produced Ru(η⁶-*p*-cymene)Cl_2(**3a**) as a crystalline product, but the small orange prisms obtained did not give enough reflections for an X-ray crystallographic structure to be determined. The ESI-MS (in different solvents, in-
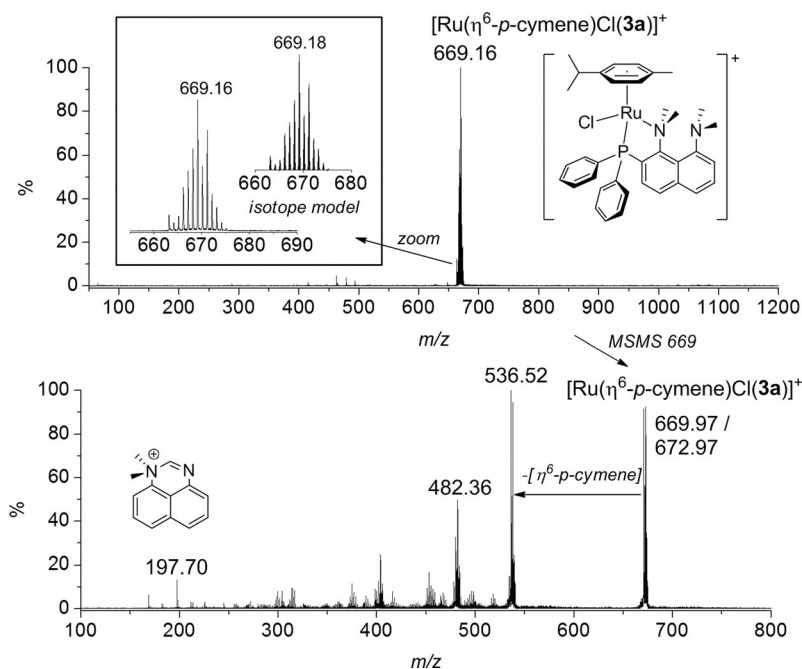
Figure 1. Positive-ion ESI-MS and MS/MS of [Ru(η^6-*p*-cymene)Cl(**3a**)]$^+$ in CH$_2$Cl$_2$. Fragmentation by loss of *p*-cymene rather than loss of **3a** is strong evidence that **3a** is strongly bound and hence not monodentate.

cluding CH$_2$Cl$_2$, MeOH, and MeCN) suggested that a chloride ligand had been displaced, as the product appeared to be [Ru(η^6-*p*-cymene)Cl(**3a**)]$^+$ rather than [Ru(η^6-*p*-cymene)Cl$_2$(**3a**) + H]$^+$. Assessment of NOE interactions (2D ^{1}H NOESY) allowed assignment of the ^{1}H NMR spectrum (see Supporting Information Figure SI2) to give the structure shown in Figure 1. The bulky proton sponge group is seen under the methyl end of the *p*-cymene, rather than the isopropyl end, which is attributed to steric interactions. The protons on the dimethylamino groups nearest to the ruthenium center are deshielded (4.18, 4.02 ppm) and chemically distinct from each other [by way of comparison, in the Fe complex Fe(CO)$_4$(**3a**) the same protons are seen as one signal at $\delta = 2.41$ ppm], indicative of a substantial nitrogen lone pair interaction with the ruthenium.

Evidently the proton sponge functionality was coordinating to the metal in this case and so further complexes were investigated to determine the generality of this behavior. Reaction of PdCl$_2$(cod) with **3a** produced PdCl$_2$(**3a**)$_2$ through displacement of the weakly bound cod ligand by two equivalents of **3a**, and an X-ray crystal structure determination was carried out (Figure 2, CCDC-837948).

The structure shows an essentially conventional triarylphosphane ligand, with some distortion due to the bulk of the proton sponge in the *ortho* position. The considerable bulk of **3a** is evident from the structure, so it is therefore not surprising that the *trans* isomer is favored. The phosphane ligand in *trans*-PdCl$_2$(**3a**)$_2$ is calculated to have a cone angle[24] of 169° with measurements taken directly from the crystal structure. The cone angle of PPh$_3$ in the triphenylphosphane analogue *trans*-PdCl$_2$(PPh$_3$)$_2$ is 146° when calculated by the same method.[25]
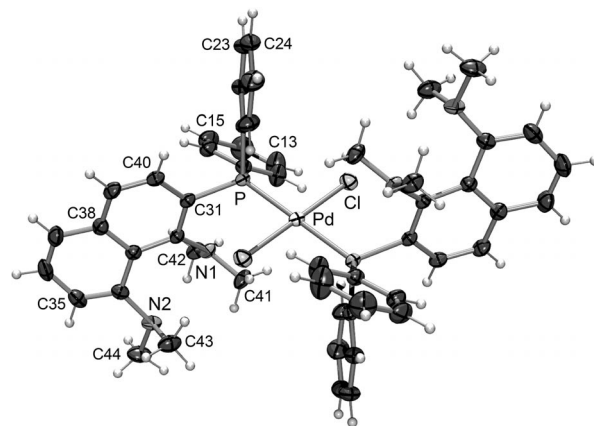
Figure 2. Single-crystal X-ray structure of *trans*-PdCl$_2$(**3a**)$_2$. Key bond lengths: Pd–Cl 2.312 Å; Pd–Cl 2.349 Å; P–C31 1.824 Å; C42–N1 1.427 Å; Me–N (1.45 ± 0.015) Å. Key bond angles: P–Pd–Cl (90 ± 1)°, Pd–P–C31 113.99°, Pd–P–C21 103.12°, Pd–P–C31 125.87°. Key torsion angle: N1–C42–C34–N2 9.00°.

ESI-MS of *trans*-PdCl$_2$(**3a**)$_2$ in CH$_2$Cl$_2$ or MeOH gave no discernible signal, but mixtures of the solvents or addition of a small amount of formic acid enabled detection of charged derivatives of the complex (Figure 3). Free ligand [**3a** + H]$^+$ at *m/z* 399.06 was the most intense signal, less intense (palladium) species were seen at higher values. The parent complex PdCl$_2$(**3a**)$_2$ ionized principally through two different pathways: loss of Cl$^-$ gave [PdCl(**3a**)$_2$]$^+$ at *m/z* 938.91 whereas addition of H$^+$ gave [PdCl$_2$(**3a**)$_2$ + H]$^+$ at *m/z* 974.89.[26] In the presence of formic acid, the intensity of these two peaks was approximately equal despite the large excess of acid available. In CH$_2$Cl$_2$/MeOH with no

N. J. Farrer, K. L. Vikse, R. McDonald, J. S. McIndoe

Figure 3. Top: ESI-MS (CH$_2$Cl$_2$/formic acid) of PdCl$_2$(**3a**)$_2$. Middle: enlargement of *m/z* 920–1000 region. Bottom: MS/MS of [PdCl$_2$-(**3a**)$_2$ + H]$^+$. MS/MS of the species at *m/z* 485.95 and *m/z* 581.89 are shown in the Supporting Information.

added acid the loss of Cl$^-$ was dominant. The intensity of the palladium species in the presence of acid was much lower than in CH$_2$Cl$_2$/MeOH, as the acid causes some decomposition of the original complex to generate a small quantity of free ligand [**3a** + H]$^+$. [PdCl(**3a**)$_2$]$^+$ showed a strong af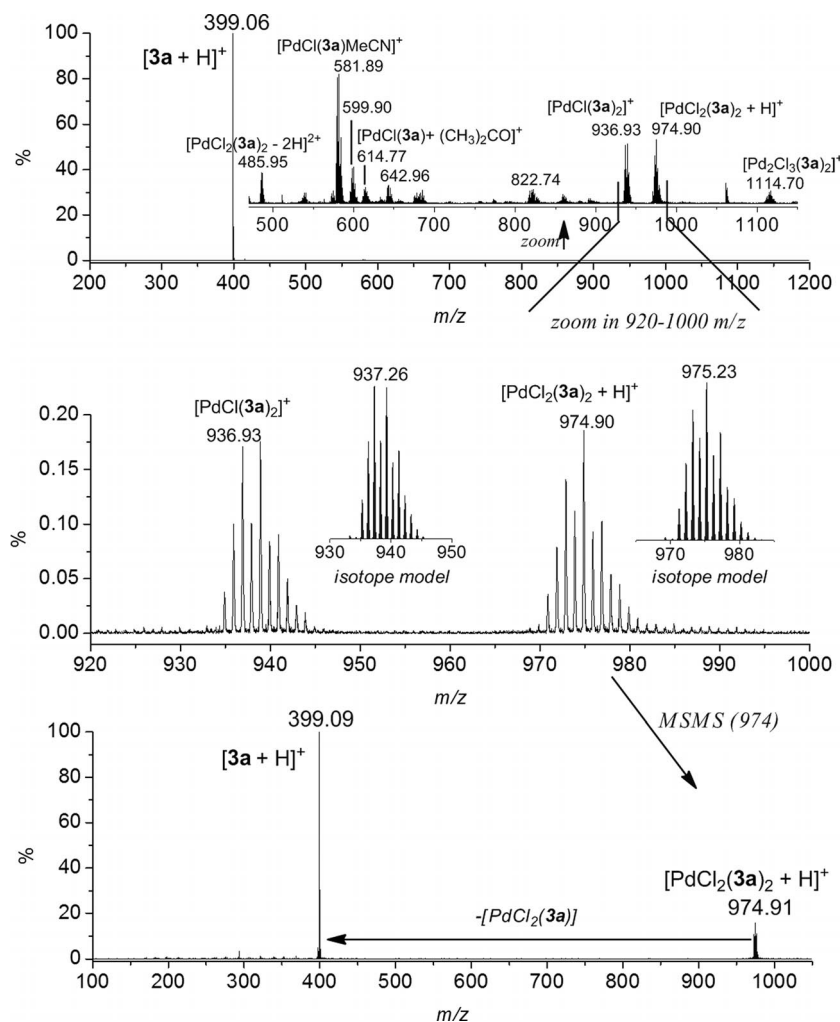finity for CH$_3$CN despite only trace amounts being present in the mass spectrometer; [PdCl(**3a**)(CH$_3$CN)]$^+$ is seen at *m/z* 581.89, and the unsolvated complex [PdCl-(**3a**)]$^+$ is seen at a lower intensity at *m/z* 538.90. Fragmentation of [PdCl(**3a**)(CH$_3$CN)]$^+$ showed facile loss of the CH$_3$CN at low collision energies (Supporting Information, Figure SI2). The acetone adduct [PdCl(**3a**)(Me$_2$CO)]$^+$ was detected at *m/z* 614.77. The complexity of the palladium speciation led us to synthesize the platinum equivalent, PtCl$_2$(**3a**)$_2$, which did ionize predominantly by addition of a proton rather than by chloride loss (see Supporting Information, Figure SI3), though the high abundance of free [**3a** + H]$^+$ confirmed that **3a** was rather labile.

The propensity of the ligand to ionize through chloride displacement was troubling, because ideally the chargeable group should provide a unique ionization pathway that does not involve alteration of the coordination sphere of

the metal. We therefore examined a palladium complex that did not contain chloride, namely Pd(dba)$_2$ (dba = dibenzylideneacetone), which is a useful precursor to Pd^0 phosphane complexes, as the dba ligands are easily displaced. Unfortunately, complicated reactivity ensued and no species of the form [Pd(**3a**)$_n$ + H]$^+$ (*n* = 1, 2, 3) were detected. Instead, the Pd^0 appeared to activate the proton sponge functional group and species of the form [**1** – H]$^+$ were detected, suggesting the ligand had undergone C–P bond activation. The final nail in the coffin for **3a** was that it did *not* promote cross-coupling reactions, including simple Suzuki and Sonogashira couplings that worked well with triphenylphosphane. **3a** was therefore abandoned as a useful ligand, as the proximity of the proton sponge functionality to the metal center compromised the reactivity we hoped to study: it failed the test of a useful chargeable tag for ESI-MS studies.

This nonideal reactivity caused us to revisit **1**, substituted in the *para* position as a charged ligand with the aim of inhibiting unwanted participation of the proton sponge functionality in reactions since the chargeable dimethylamino groups of **3b** are further removed than those of **3a**

and are unable to interfere with reactivity at the metal center. A synthesis was developed under which **3b** could be produced with an overall isolated yield of 19% in two steps (Scheme 1). **2b** was synthesized by dropwise addition of bromine (diluted in carbon tetrachloride) to a carbon tetrachloride solution of **1** at room temperature. This addition must be performed slowly (ca. 2.5 h) to maintain selectivity for **3b**. After addition of aqueous solutions of sodium thiosulfate and sodium hydroxide, ESI-MS showed good selectivity for addition of only one bromine atom to **1** (only small amounts of **1** at *m/z* 215, and the di-brominated side product, *m/z* 457, are observed); although MS could not distinguish between *ortho*- and *para*-brominated isomers (Supporting Information, Figure SI4). After workup, ^{1}H NMR confirmed that the correct isomer was formed (Supporting Information, Figure SI5) in a ratio of 93:7 (*para:ortho*), the reverse of the ratio obtained in the synthesis of **2a** when NBS at –78 °C is used for bromination (9:91). **2b** was used without further purification to form **3b** via lithiation and treatment with PPh$_2$Cl at low temperature in THF. The mixture was warmed to room temperature with stirring and then allowed to settle. After filtration, deep orange crystals of **3b** were formed in the filtrate via solvent evaporation. An X-ray crystal structure determination was performed on a single crystal of **3b** (Figure 4, CCDC-837947).
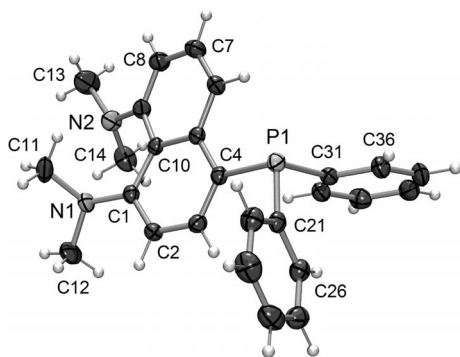

Figure 4. Single-crystal X-ray structure of **3b**. Key bond lengths: P1–C (1.838 ± 0.002) Å; C1–N1 1.402 Å; C9–N2 1.404 Å; N–C$_{Me}$ (1.452 ± 0.002) Å. Key bond angles: C21–P1–C31 101.98°; C21–P1–C4 100.94°; C31–P1–C4 102.28°. Key torsion angle: N1–C1–C9–N2 22.75°.

Comparison of the structure of **3b** to that of **3a**[14] reveals that the torsion angle reflecting the in-and-out of plane bending of the dimethylamino groups is 22.8° in **3b**, significantly less than the 37.4° seen for **3a**. The reduced strain is no doubt due to the –PPh$_2$ group being moved from the proximal 2- to the remote 4-position. The N···N distance is correspondingly reduced, from 2.90 to 2.78 Å. Like **3a**, **3b** displays pH-dependent water solubility[27] – the unprotonated form is soluble in organic solvents only, addition of acid protonates the sponge functionality and allows aqueous dissolution.

The mass spectrum of **3b** gave the expected single, intense [M + H]$^+$ peak (Figure 5). To test the behavior of the tag when coordinated to a metal center, a solution of

PdCl$_2$(cod) in dichloromethane was combined with a solution of **3b** in dichloromethane and an ESI-MS of the mixture was collected. The major signal in the spectrum (*m/z* 975) corresponds to [PdCl$_2$(**3b**)$_2$ + H]$^+$ in which one of the chargeable ligands is protonated. In contrast to **3a**, no signal corresponding to ionization by loss of chloride (*m/z* 940) was observed, and very little of the free ligand is observed (*m/z* 399) suggesting that **3b** performs well as a ligand for palladium.
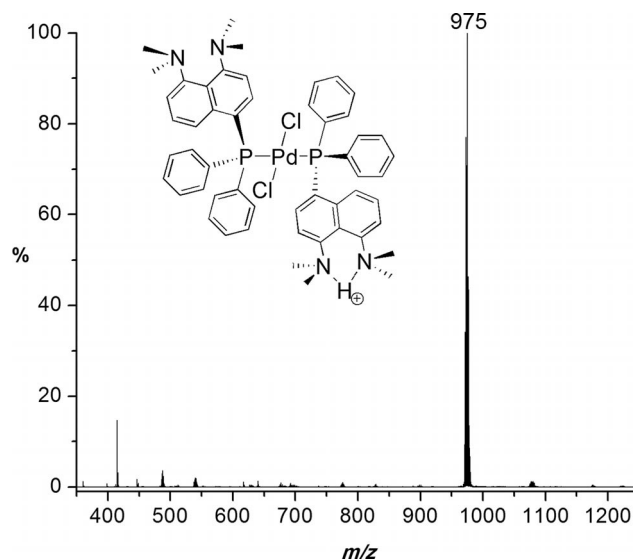

Figure 5. Positive-ion ESI-MS of a dichloromethane solution of PdCl$_2$(cod) and **3b**. Small peaks are observed at: *m/z* 415 for the oxidized ligand [**3b**O + H]$^+$, *m/z* 488 for the doubly charged complex [PdCl$_2$(**3b**)$_2$ + 2H]$^{2+}$, and *m/z* 539 and *m/z* 1077 for the singly and doubly protonated versions of the dimer Pd$_2$Cl$_2$(**3b**)$_2$, respectively.

Given the success of **3b** as a chargeable tag, we next employed **3b** in the study of a catalytic reaction. Our goal was to study palladium-catalyzed systems, and to that end we chose a Stille reaction, which Santos had previously studied by ESI-MS,[28] to test the performance of our chargeable ligand. An acetonitrile solution containing the catalyst Pd(OAc)$_2$ and **3b** was examined by MS, and the result was somewhat disappointing (Figure 6). While species consistent with the ones reported by Santos were detected, more than one ionization pathway was operative; protonation of **3b** was observed, and many of the palladium-containing species were also oxidized to form radical cations. The latter ionization method involves oxidation of Pd^0 at the tip of the electrospray capillary – the very method that Santos relied on in his experiments to obtain positive ions. We had anticipated that protonation of **3b** would be correspondingly more facile, suppressing oxidation of palladium. However, this was not the case.

Why do the radical cations form? ESI-MS owes much of its sensitivity to the creation of an excess of positive (or negative, depending on the ionization mode) charge on the droplets. It does so through electrochemistry – a tiny amount of material is oxidized at the capillary. Typically,
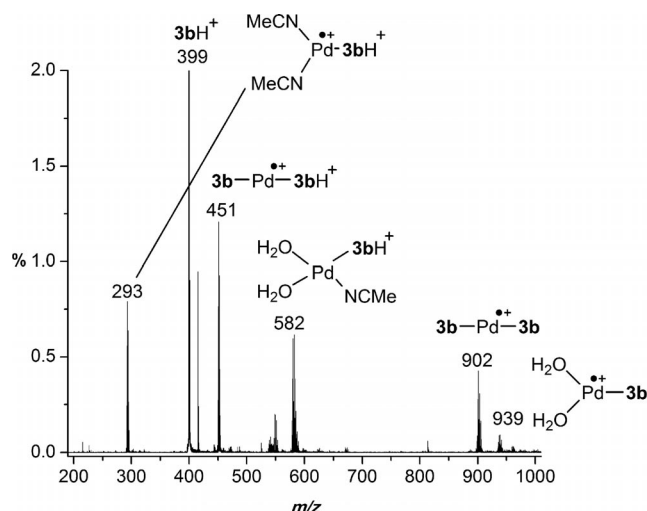
Figure 6. Positive-ion ESI-MS of an acetonitrile solution of Pd(OAc)$_2$ and **3b**.

this process is invisible because the oxidized material, often the iron in the stainless steel capillary, rarely appears in the mass spectrum (its surface activity is low). However, Pd^0 phosphane complexes are both greasy (hydrophobic, surface active) and very easily oxidized, more so than the capillary.

Further investigation of the Stille reaction using **3b** produced spectra containing many peaks that were difficult to assign (Supporting Information, Figure SI6). We attributed these peaks to the products of unknown reactivity involving the radical species formed in the electrospray ionization process and we conclude that while **3b** can perform as an ESI tag, it is not suited to the study of systems for which there are efficient alternative metal-based ionization pathways. It should be noted, however, that Pd^0 is an unusually challenging system, and that for less electron-rich metal complexes, the idea remains valid.

The difficulty in obtaining interpretable MS data on palladium-catalyzed reactions using chargeable ESI tags led us to the investigation of permanently charged ESI tags for the study of these systems.[29] Permanently charged ESI tags have the advantage of (1) being less pH-dependent than chargeable tags, and (2) having fewer potential avenues for reactivity that may interfere with the system of interest. In our experience, the use of a permanently charged tag generally results in simpler spectra.[30] Ammonium or phosphonium groups are most commonly employed as the charged group,[31] and if solubility of the molecule in organic solvents is compromised due to the addition of this polar group, the counterion may be exchanged to obtain more desirable solubility properties.

Conclusions

Proton sponge derivatized phosphane ligands possess – theoretically at least – many of the properties desirable for a chargeable ESI-MS tag. Alone, they are selective for ion-

ization by protons, even in the presence of other cations. Their ionization efficiency is good. They coordinate readily to metal complexes through the phosphorus. However, they have weaknesses that hamper their ability to perform reliably: their ionization is dependent on the acidity of the solution, they are bulkier than the parent triphenylphosphane (especially for **3a**, the *ortho*-substituted sponge), coordination by the sponge functionality can be problematic, and reactivity can be substantially different to the parent triphenylphosphane.

Experimental Section

General: Dry solvents were obtained from an MBraun solvent purification system. All solvents were HPLC grade unless otherwise stated. Reagents were purchased from Aldrich and used without further purification except for **1**, which was recrystallized from hot methanol. Reactions performed under nitrogen were carried out using standard Schlenk techniques. All electrospray ionization mass spectra were collected with a Miromass Q-TOF *micro* instrument. Capillary voltage was set to 2900 V, source temperature was 80 °C and desolvation temperature was 150 °C. Samples were infused via syringe pump at 10 µL min^{-1}. NMR spectra were recorded with a Bruker AC-300 spectrometer. Chemical shifts are quoted in ppm using internal references of CDCl$_3$ (^{1}H δ = 7.26 ppm) or CD$_3$CN (^{1}H δ = 1.94 ppm) where appropriate. Melting points were recorded with a Gallenkamp melting point apparatus and are uncorrected. IR spectra were recorded using a solution cell in a Perkin–Elmer Spectrum 1000 FT-IR spectrometer.

[1,8-Bis(dimethylamino)naphthalene-4-yl] Bromide (2b): A solution of bromine (2.15 mL, 41.7 mmol) in carbon tetrachloride (40 mL) was added dropwise over 2.5 h to a stirring solution of **1** (10.0 g, 46.6 mmol) in carbon tetrachloride (60 mL) under an inert atmosphere, resulting in a dark red solution. To this, aqueous solutions of sodium thiosulfate (1 M, 20 mL) and sodium hydroxide (20% w/v, 20 mL) were added dropwise with stirring. The resultant yellow-brown mixture was filtered and the beige byproduct was washed (CH$_2$Cl$_2$). The organic layer was collected and the volume reduced to give **2b** as a red-brown oil (7.07 g, 52% crude yield). The product was used directly without further purification to synthesize **3b**. ^{1}H NMR (300 MHz, CDCl$_3$): δ_H = 7.80–6.71 (m, 5 H, aromatic protons), 2.81–2.77 [m, 12 H, 2(N*Me*$_2$)] ppm.

[1,8-Bis(dimethylamino)naphthalene-4-yl]diphenylphosphane (3b): A solution of **2b** (1.5 g, 5.1 mmol) in THF (15 mL) was cooled to –78 °C and *n*BuLi (3.3 mL, 1.6 M in hexanes, 5.1 mmol) was added dropwise with stirring, after which the solution was stirred for a further 30 min resulting in an amber-colored solution. Chloro-diphenylphosphane (1 mL, 5.4 mmol) was added dropwise with vigorous stirring, and stirring was continued (–78 °C, 2 h) giving a red-orange solution. The mixture was warmed to room temperature and the yellow-brown precipitate isolated by filtration. Orange crystals of **3b** were collected from the filtrate by solvent evaporation (37% yield). ^{1}H NMR (300 MHz, CDCl$_3$): δ_H = 7.98 (m, 1 H, naphthalene proton), 7.27 (m, 11 H, phenyl protons and one naphthalene proton), 6.90 (d, 1 H, naphthalene proton), 6.78 (m, 2 H, naphthalene proton), 2.804 [s, 6 H, N(C*H*$_3$)], 2.799 [s, 6 H, N(C*H*$_3$)] ppm. ^{31}P NMR (360 MHz, CDCl$_3$): δ_P = –13.41 [s, *P*Ph$_2$(C$_{10}$H$_{17}$N$_2$)] ppm. M.p. 168–169 °C.

Reaction of [Ru(η^6-*p*-cymene)Cl$_2$]$_2$ with 3a in MeOH: Adapted from ref.[32] A methanolic solution of **3a** (2 equiv., 0.131 g, 0.33 mmol)

and [Ru(*p*-cymene)Cl$_2$]$_2$ (0.101 g, 0.165 mmol) was refluxed for 3 h with monitoring (ESI-MS), after which time the reaction was judged to be complete (absence of free **3a**). The solution was left to stand for 2 d, reduced in volume and layered with pentane. Crystallizations were set up, eventually the product decomposed to black oil. ESI-MS (after 2 h reflux, MeOH, selected peaks): *m/z* (%) = 634.94 (40) [Ru(η^6-*p*-cymene)(**3a**) + H]$^+$, isotope model (635.22), 874.53 (3) [Ru$_2$(η^6-*p*-cymene)(MeOH)Cl$_3$(**3a**)]$^+$, isotope model (875.05). MS/MS (635) [Ru(η^6-*p*-cymene)(**3a**) + H]$^+$): *m/z* (%) = 496.41, 457.35, 379.10, 298.81 (major Ru species) and 197.70 ([**M** – CH$_4$]$^+$, model 198.11). MS/MS (874), [Ru$_2$Cl$_3$(η^6-*p*-cymene)(**3a**)MeOH]$^+$: *m/z* (%) = 872.56, general Ru "grass" between 800 and 400, 213.8 ([**M** – H]$^+$, model 213.14).

Reaction of [Ru(*p*-cymene)Cl$_2$]$_2$ with 3a in MeCN/toluene: The compounds **3a** (13 mg, 0.033 mmol) and [Ru(*p*-cymene)Cl$_2$]$_2$ (10 mg, 0.017 mmol) were placed in a flask, which was evacuated and placed under N$_2$. CD$_3$CN (1 mL) was added, the solution mixed and filtered into an NMR tube. The reaction was monitored by ^{31}P and ^{1}H NMR at regular intervals. ^{31}P NMR yield 80%. ^{1}H NMR (360 MHz, CD$_3$CN, [Ru(η^6-*p*-cymene)Cl$_2$]$_2$): δ$_H$ = 5.54 (d, *J* = 6.1 Hz, 4 H, Ar*i*Pr), 5.29 (d, *J* = 6.2 Hz, 4 H, Ar$_{Me}$), 2.90 (septet, *J* = 7.0 Hz, 2 H, H*i*Pr), 2.22 (s, 6 H, Me), 1.29 [d, *J* = 7.0 Hz, 12 H, 2(*i*Pr)Me] ppm. ^{13}C NMR {90 MHz, CD$_3$CN, [Ru(η^6-*p*-cymene)Cl$_2$]$_2$}: δ$_C$ = 103.52 (quat, Ar$_{iPr}$), 99.99 (quat, Ar$_{Me}$), 84.63 (Ar$_{Me}$), 82.21 (Ar$_{iPr}$), 31.79 (secondary *i*Pr), 22.38 (*i*PrMe), 18.96 (Me) ppm. Main product, [Ru(*p*-cymene)(Cl)(**3a**)][Cl]. ^{31}P NMR (red crystals, 146 MHz, CD$_3$CN): δ = 52.69 (s) ppm. ^{1}H NMR (360 MHz, CD$_3$CN): δ$_H$ = 7.85 [ddd, *J* = 11.3, 1.1, 8.3 Hz, 2 H, H$_{12}$, NOE to *p*-cymene (5.07)], 7.71–7.49 (m, 12 H, 1 5-H, 1 4-H, 2 12′-H, 2 13-H & 2 13′-H, 1 14-H & 1 14′-H, 6-H, 7-H) ppm. Within this: 7.54–7.58 (4-H), 7.28–7.16 (m, impurity, 2 H), 7.12 (dd, 1 H, *J* = 8.4, 9.6 Hz, coupling to ^{31}P, H^3), 6.28 (dd, *J* = 7, 1 Hz, 1 H, *p*-cymene ring, NOE to *i*Pr group at 1.22 and 6.07), 6.25 (dd, *J* = 5.2, 1 Hz, 1 H, *p*-cymene ring, NOE to 5.07 and Me at 1.53), 6.07 (dd, *J* = 6.3, 1 Hz, 1 H, *p*-cymene ring, NOE to Me group at 4.02 and Me group at 1.53), 5.07 (dd, *J* = 6.0, 1.5 Hz, 1 H, *p*-cymene ring, NOE to *i*Pr CH group and 6.25, NOE to H$_{12}$ at 7.85), 4.18 [d, *J* = 0.5 Hz, 3 H, NMe group, on C$_{1back}$, NOE to 6.07 (weak) *and* 6.25 *p*-cymene proton], 4.02 (s, 3 H, Me, NMe group, on C$_{1front}$, NOE to 6.07 *p*-cymene, NOE to *p*-cymene Me at 1.53), 2.90 (s, 3 H, NMe group on C8$_{back}$, NOE to NMe at 4.18 and weak NOE to NMe at 4.02), 2.78 (septet, *J* = 6.9 Hz, 1 H, *i*Pr CH, NOE to both 1.22 and 1.18, and 5.07), 2.27 (s, NMe group on C8$_{front}$, 3 H, NOE to Ar-CH$_3$ at 1.53, strong NOE to NMe on C8$_{back}$ at 2.90, very weak NOE to 7-H), 1.53 (s, Ar-CH$_3$ group, NOE to 6.25 and 6.07), 1.22 (d, *J* = 6.7 Hz, 3 H, *i*Pr CH$_3$ group, NOE to 2.78), 1.18 (d, *J* = 6.9 Hz, 3 H, *i*Pr CH$_3$ group, NOE to 2.78) ppm. ESI-MS: *m/z* (%) = 669.16 (100%) ([Ru(η^6-*p*-cymene)Cl-(**3a**)]$^+$ model 669.18). MS/MS (669): *m/z* (%) = 669.97 ([Ru(η^6-*p*-cymene)Cl(**3a**)]$^+$), 536.52 ([RuCl(**3a**)]$^+$ model 535.07), 482.36, 197.70 ([**1a**-CH$_3$]$^+$, model C$_{13}$H$_{13}$N$_2$ 197.11).

Reaction Between [Ru(*p*-cymene)Cl$_2$]$_2$ and Protonated Ligand 3a·HBF$_4$: The reaction was repeated by stirring at room temperature in MeCN with the protonated ligand **3a**·HBF$_4$ overnight. The only new ^{31}P signal detected was due to the intermediate (postulated to be the dimer) not the final product monomer. ^{31}P NMR (121 MHz, CD$_3$CN): δ$_P$ = –18.32 (s, **3a**·HBF$_4$, integral 35), 31.97 (s, integral 1) ppm.

Crystalline *trans*-PdCl$_2$(3a)$_2$ (Orange) with Crystalline Pd$_2$Cl$_4$(3a)$_2$ (Yellow): A yellow solution of **3a** (100 mg, 0.25 mmol) in dry ether (0.5 mL) was layered onto a solution of [Pd(COD)Cl$_2$] (20 mg, 0.07 mmol) in dry CH$_2$Cl$_2$ (0.5 mL) in a narrow glass tube. Orange

crystals of *trans*-[PdCl$_2$(**3a**)$_2$] and a small quantity of yellow crystals of [Pd$_2$Cl$_4$(**3a**)$_2$] slowly formed at the interface. The orange crystals proved to be highly insoluble in most solvents and only sparingly soluble in CH$_2$Cl$_2$. Yellow crystals of [Pd$_2$Cl$_4$(**3a**)$_2$] were completely soluble in CH$_2$Cl$_2$. M.p. ([PdCl$_2$(**3a**)$_2$]) 178–186 °C (decomp.), m.p. ([Pd$_2$Cl$_4$(**3a**)$_2$]): 198 °C (decomp.). PdCl$_2$(**3a**)$_2$·CH$_2$Cl$_2$: C$_{53}$H$_{56}$Cl$_4$N$_4$P$_2$Pd: calcd. C 60.22, H 5.34, N 5.30, P 5.87; found C 59.95, H 5.39, N 5.14, P 5.64. ^{31}P NMR (CDCl$_3$, 202 MHz): δ$_P$ = 42.80 {s, [Pd$_2$Cl$_4$(**3a**)$_2$]}, trace 32.82 (s, *trans*-[PdCl$_2$(**3a**)$_2$]) ppm. ^{1}H NMR (CDCl$_3$, 500 MHz): δ$_H$ = 7.81 (ddd, *J*$_{HP}$ = 13.1, *J*$_{HH}$ = 8.3, 1.0 Hz, 4 H, 12-H), 7.75 (dd, *J* = 7.7, 1.5 Hz, 1 H, 5-H or 7-H) 7.71 (dd, *J* = 8.5, 1.6 Hz, 1 H, 4-H), 7.67 (dd, *J* = 7.5, 1.5 Hz, 1 H, 5-H or 7-H), 7.62 (dd, *J* = 7.7 Hz, 1 H, 6-H), 7.57 (t, 2 H, 14-H), 7.47 (td, *J*$_{HH}$ = 8.8, *J*$_{HP}$ = 3 Hz, 4 H, 13-H), 7.07 (dd, *J*$_{HP}$ = 9.4, *J*$_{HH}$ = 8.5 Hz, 1 H, 3-H), 4.19 (s, 6 H, NMe$_2$), 2.62 (s, 6 H, NMe$_2$) ppm. *Major impurity*: 6.28 (m, cod, 2.5 H), 5.56 (m, cod, 2 H), 2.35 (m, cod, 4 H) ppm. ESI-MS (CH$_2$Cl$_2$/formic acid) selected peaks: *m/z* (%) = 974.89 (0.2%, [PdCl$_2$(**3a**)$_2$ + H]$^+$, model 975.23), 581.88 (0.35%, [MeCN·PdCl(**3a**)]$^+$, model 582.08), 485.95 (0.08%, [PdCl$_2$(**3a**)$_2$ – 2H]$^{2+}$, model 486.94). MS/MS (974): *m/z* (%) = 974.91 ([PdCl$_2$(**3a**)$_2$ + H]$^+$), 399.09 [**3a** +H]$^+$. ESI-MS (yellow crystals) (MeOH/DCM) selected peaks: *m/z* (%) = 1114.84 (100%, [Pd$_2$Cl$_3$(**3a**)$_2$]$^+$, model 1115.10), 1078.89 (2%, [Pd$_2$Cl$_2$(**3a**) – H]$^+$, model 1079.12), 538.94 (100%, [PdCl·**3a**]$^+$, model 539.07).

Synthesis Using 3a·HBr: ESI-MS (orange product): *m/z* (%) = 376.10 (1%, ["Pd"]$^{2+}$), 397.19 [5%, (**3a** – H)]$^+$, 399.20 [1%, (**3a** + H)]$^+$, 486.11 (3%, [PdCl$_2$(**3a** – H)$_2$]$^{2+}$, model C$_{52}$H$_{52}$Cl$_2$N$_4$P$_2$Pd, 486.61), 575.03 (4%, [PdCl$_2$(**3a** – H)]$^+$, model C$_{26}$H$_{26}$Cl$_2$N$_2$PPd, 575.03), 607.05 (2%), [PdCl$_2$(**3a**) + 31]$^+$, 774.12 (0.5%, [Pd$_2$Cl$_4$(**3a** – H)$_3$(**3a**)]$^{2+}$, model C$_{78}$H$_{79}$Cl$_4$N$_6$P$_3$Pd$_2$, 774.62), 791.10 (0.2% ["Pd"]$^{2+}$), 827.05 (0.2% ["Pd$_2$"]$^{2+}$), 844.05 (0.3%, ["Pd$_2$"]$^{2+}$), 863.03 (0.3%, ["Pd$_2$"]$^{2+}$), 880.00 (3%, [Pd$_3$Cl$_7$(**3a** – H)$_3$]$^{2+}$, model 880.52), 933.45 (0.1%, ["Pd$_2$"]$^{2+}$).

Synthesis of PtCl$_2$(3a)$_2$: A solution of **3a** (43 mg, 0.11 mmol) in diethyl ether (1.1 mL) was added to a stirring solution of PtCl$_2$(cod) (20 mg, 0.054 mmol) in CH$_2$Cl$_2$ (0.7 mL). The pale yellow solution intensified in color on stirring for 6 h after which time stirring of the solution was stopped and ether was carefully layered onto the solution which was left overnight. Microcrystalline yellow PtCl$_2$(**3a**)$_2$ was recovered in two successive crops by filtration and washing with ether: yield 23 mg, 41%, m.p. 236–240 °C (decomp). ^{31}P NMR (400 MHz, CDCl$_3$): δ$_P$ = 15.6 (^{1}*J*$_{PPt}$ = 3900 Hz) ppm. ^{1}H NMR (400 MHz, CDCl$_3$): δ$_H$ = 7.79 (m, 10 H, 8 12-H plus 2 4-H), 7.71 (d, *J* = 2, 8 Hz, 2 H, 5-H or 7-H), 7.69 (d, *J* = 8, 2 Hz, 2 H, 5-H or 7-H), 7.62 (t, *J* = 7.6 Hz, 2 H, 2 6-H), 7.54 (m, 4 H, 4 14-H), 7.45 (t with ^{31}P coupling, 8 13-H), 7.20 (dd, *J* = 8, 9 Hz, 2 H, 3-H), 4.40 [s, 6 H, N(CH$_3$)$_2$, 1-H or 8-H], 2.62 [s, 6 H, N(CH$_3$)$_2$, 1-H or 8-H] ppm. ESI-MS (of crude solution, CH$_2$Cl$_2$): *m/z* (%) = 398.89 (100%, [**3a** + H]$^+$), 1062.58 (15%, [PtCl$_2$(**3a**)$_2$ + H]$^+$) and trace amounts (<1%) of: [PtCl(**3a**)$_2$]$^+$ (1026.65, 0.5%), dimer at 1726.23 (model Pt$_2$Cl$_4$(**3a**)$_3$H = 1727.38). MS/MS of [PtCl$_2$(**3a**)$_2$ + H]$^+$ gave exclusively free [**3a** + H]$^+$ at 399.03. MS/MS of the dimer at 1726 gave [PtCl$_2$(**3a**)$_2$ + H]$^+$ and [**3a** + H]$^+$ only.

CCDC-837948 (for **3a**) and CCDC-837947 (for **3b**) contain the supplementary crystallographic data for this paper. These data can be obtained free of charge from The Cambridge Crystallographic Data Centre via www.ccdc.cam.ac.uk/data_request/cif.

Supporting Information (see footnote on the first page of this article): Additional ESI-MS(/MS) and ^{1}H NMR spectra.

Acknowledgments

[1] K. W. M. Siu, R. Guevremont, J. C. Y. Le Blanc, G. J. Gardner, S. S. Berman, *J. Chromatogr. A* **1991**, *554*, 27–38.

[2] A. J. Canty, P. R. Traill, R. Colton, I. M. Thomas, *Inorg. Chim. Acta* **1993**, *210*, 91–97.

[3] a) M. Bonchio, G. Licini, G. Modena, O. Bortolini, S. Moro, W. A. Nugent, *J. Am. Chem. Soc.* **1999**, *121*, 6258–6268; b) Z. Li, Z. H. Tang, X. X. Hu, C. G. Xia, *Chem. Eur. J.* **2005**, *11*, 1210–1216; c) B. C. Gilbert, J. R. L. Smith, A. Mairata i Payeras, J. Oakes, R. Pons i Prats, *J. Mol. Catal. A* **2004**, *219*, 265–272; d) H. Chen, R. Tagore, G. Olack, J. S. Vrettos, T.-C. Weng, J. Penner-Hahn, R. H. Crabtree, G. W. Brudvig, *Inorg. Chem.* **2007**, *46*, 34–43.

[4] a) P. J. Dyson, K. Russell, T. Welton, *Inorg. Chem. Commun.* **2001**, *4*, 571–573; b) P. Pelagatti, M. Carcelli, F. Calbiani, C. Cassi, L. Elviri, C. Pelizzi, U. Rizzotti, D. Rogolino, *Organometallics* **2005**, *24*, 5836–5844; c) C. Daguenet, R. Scopelliti, P. J. Dyson, *Organometallics* **2004**, *23*, 4849–4857.

[5] C. Vicent, M. Viciano, E. Mas-Marza, M. Sanau, E. Peris, *Organometallics* **2006**, *25*, 3713–3720.

[6] a) S. R. Wilson, Y. Wu, *Organometallics* **1993**, *12*, 1478–1480; b) C. Raminelli, M. H. G. Prechtl, L. S. Santos, M. N. Eberlin, J. V. Comasseto, *Organometallics* **2004**, *23*, 3990–3996; c) C. Chevrin, J. Le Bras, F. Henin, J. Muzart, A. Pla-Quintana, A. Roglans, R. Pleixats, *Organometallics* **2004**, *23*, 4796–4799.

[7] a) J. Masllorens, I. Gonzalez, A. Roglans, *Eur. J. Org. Chem.* **2007**, 158–166; b) A. A. Sabino, A. H. L. Machado, C. R. D. Correia, M. N. Eberlin, *Angew. Chem.* **2004**, *116*, 2568; *Angew. Chem. Int. Ed.* **2004**, *43*, 2514–2518; c) P. A. Enquist, P. Nilsson, P. Sjoberg, M. Larhed, *J. Org. Chem.* **2006**, *71*, 8779–8786; d) A. Svennebring, P. J. R. Sjoberg, M. Larhed, P. Nilsson, *Tetrahedron* **2008**, *64*, 1808–1812; e) C. Chevrin, J. Le Bras, A. Roglans, D. Harakat, J. Muzart, *New J. Chem.* **2007**, *31*, 121–126; f) C. Markert, M. Neuburger, K. Kulicke, M. Meuwly, A. Pfaltz, *Angew. Chem.* **2007**, *119*, 5996; *Angew. Chem. Int. Ed.* **2007**, *46*, 5892–5895.

[8] L. S. Santos (Ed.), *Reactive Intermediates: MS Investigations in Solution*, Wiley-VCH, Weinheim, Germany, **2010**.

[9] A. O. Aliprantis, J. W. Canary, *J. Am. Chem. Soc.* **1994**, *116*, 6985–6986.

[10] a) R. Colton, J. C. Traeger, *Inorg. Chim. Acta* **1992**, *201*, 153–155; b) I. Ahmed, A. M. Bond, R. Colton, M. Jurcevic, J. C. Traeger, J. N. Walter, *J. Organomet. Chem.* **1993**, *447*, 59–65.

[11] a) D. J. F. Bryce, P. J. Dyson, B. K. Nicholson, D. G. Parker, *Polyhedron* **1998**, *17*, 2899–2905; b) C. Decker, W. Henderson, B. K. Nicholson, *J. Chem. Soc., Dalton Trans.* **1999**, 3507–3513.

[12] a) C. Hinderling, C. Adlhart, P. Chen, *Angew. Chem.* **1998**, *110*, 2831; *Angew. Chem. Int. Ed.* **1998**, *37*, 2685–2689; b) C. Adlhart, C. Hinderling, H. Baumann, P. Chen, *J. Am. Chem. Soc.* **2000**, *122*, 8204–8214; c) P. Chen, *Angew. Chem.* **2003**, *115*, 2938; *Angew. Chem. Int. Ed.* **2003**, *42*, 2832–2847.

[13] S. Zhou, B. S. Prebyl, K. D. Cook, *Anal. Chem.* **2002**, *74*, 4885–4888.

[14] N. J. Farrer, R. McDonald, J. S. McIndoe, *Dalton Trans.* **2006**, 4570–4579.

[15] R. W. Alder, *Chem. Rev.* **1989**, *89*, 1215–1223.

[16] a) K. Nagasawa, *Related Organocatalysts (1): A Proton Sponge*, in: *Superbases for Organic Synthesis: Guanidines, Amidines, Phosphazenes and Related Organocatalysts* (Ed.: T. Ishikawa), Wiley, Chichester, U.K., **2007**, pp. 931–1139.

[17] a) R. Shroff, A. Svatos, *Anal. Chem.* **2009**, *81*, 7954–7959; b) R. Shroff, A. Svatos, *Rapid Commun. Mass Spectrom.* **2009**, *23*, 2380–2382.

[18] a) H. A. Staab, T. Saupe, *Angew. Chem.* **1988**, *100*, 895–909; b) S. T. Howard, *J. Am. Chem. Soc.* **2000**, *122*, 8238–8244.

[19] A. F. Pozharskii, A. V. Degtyarev, O. V. Ryabtsova, V. A. Ozeryanskii, M. E. Kletskii, Z. A. Starikova, L. Sobczyk, A. Filarowski, *J. Org. Chem.* **2007**, *72*, 3006–3019.

[20] A. L. Llamas-Saiz, C. Foces-Foces, J. Elguero, *J. Mol. Struct.* **1994**, *328*, 297–323.

[21] R. W. Alder, P. S. Bowman, W. R. S. Steele, D. R. Winterman, *Chem. Commun. (London)* **1968**, 723–724.

[22] H. M. Gilow, D. E. Burton, *J. Org. Chem.* **1981**, *46*, 2221–2225.

[23] a) F. Hibbert, J. Emsley, *Adv. Phys. Org. Chem.* **1990**, *26*, 255–279; b) J. P. H. Charmant, G. C. Lloyd-Jones, T. M. Peakman, R. L. Woodward, *Eur. J. Org. Chem.* **1999**, 2501–2510; c) J. Berthelot, C. Guette, M. Essayegh, P. L. Desbene, J. J. Basselier, *Synth. Commun.* **1986**, *16*, 1641–1645; d) N. V. Vistorobskii, A. F. Pozharskii, *Zh. Org. Khim.* **1989**, *25*, 2154–2161.

[24] C. A. Tolman, *Chem. Rev.* **1977**, *77*, 313–348; O. V. Ryabtsova, A. F. Pozharskii, V. A. Ozeryanskii, N. V. Vistorobskii, *Russ. Chem. Bull.* **2001**, *50*, 854–859.

[25] T. E. Müller, D. M. P. Mingos, *Trans. Met. Chem.* **1995**, *20*, 533–539.

[26] W. Henderson, C. Evans, *Inorg. Chim. Acta* **1999**, *294*, 183–192.

[27] A. D. Phillips, L. Gonsalvi, A. Romerosa, F. Vizza, M. Peruzzini, *Coord. Chem. Rev.* **2004**, *248*, 955–993.

[28] L. S. Santos, G. B. Rosso, R. A. Pilli, M. N. Eberlin, *J. Org. Chem.* **2007**, *72*, 5809–5812.

[29] a) K. L. Vikse, M. A. Henderson, A. G. Oliver, J. S. McIndoe, *Chem. Commun.* **2010**, *46*, 7412–7414; b) K. L. Vikse, Z. Ahmadi, C. C. Manning, D. A. Harrington, J. S. McIndoe, *Angew. Chem. Int. Ed.* **2011**, *50*, 8304–8306.

[30] a) D. M. Chisholm, A. G. Oliver, J. S. McIndoe, *Dalton Trans.* **2010**, *39*, 364–373 ; b) S. L. Jackson, D. M. Chisholm, J. S. McIndoe, L. Rosenberg, *Eur. J. Inorg. Chem.* **2010**, 327–330.

[31] D. M. Chisholm, J. S. McIndoe, *Dalton Trans.* **2008**, 3933–3945.

[32] C. S. Allardyce, P. J. Dyson, D. J. Ellis, S. L. Heath, *Chem. Commun.* **2001**, 1396–1397.

TiIV Complexes of Redox-Active Schiff Bases

Alberto Donzelli[a] and Pierre G. Potvin*[a]

Isopropoxy- and *tert*-butoxy-(salicylideneamino-2-thiophen-olato)titanium(IV) complexes from seven different salicyl-aldehydes were prepared and characterized. Two examples, diisopropoxy(4′-methoxysalicylideneamino-2-thiophenolato)-titanium(IV) and di-*tert*-butoxy(salicylideneamino-2-thio-phenolato)titanium(IV), were also characterized crystallo-graphically. Three other examples crystallized as L2Ti spe-cies, one of which was an unusual dinuclear complex in which the ligands had dimerized through S–S interactions and formed amino linkages in an unexpected redox ex-change. In all cases, cyclic voltammetry in CH2Cl2 showed irreversible oxidations at +1.2–1.4 V vs. Ag/AgCl. 2-Propanol induced a cathodic shift of the first oxidation potentials with-out apparent decomposition.

Introduction

Direct methanol fuel cells are a promising, and in many ways more practical, alternative to the better known H_2-driven fuel cells, but the precious metal anodes that ef-ficiently oxidize H_2 work sluggishly with CH_3OH. Poison-ing by the CO intermediate is partly responsible, but this can be remedied with Pt–Ru alloys, for instance. Another problem is mechanistic, as the process is thought to proceed by one-electron steps that involve surface-bound radicals.[1]

We bring to this problem an organic chemist's perspec-tive, whereby laboratory oxidations of alcohols proceed by two-electron steps, which avoids radicals, and would pro-ceed via HCOOH instead of CO (Scheme 1). Our approach calls for redox-active, sulfur-containing molecules coordi-nated to otherwise redox-inert and CO-impervious TiIV alk-oxides, an inexpensive and environmentally benign design that takes advantage of rapid alcohol–alkoxide exchange[2] at TiIV for rapid fuel loading and product unloading. In that vein, our first foray explored the coordination chemis-try of TiIV dithiocarbamate complexes, as dithiocarbamates reversibly oxidize to thiurams.[3] The complexes showed oxi-dation potentials shifted positively to those of the free li-gand by about 1 V, which is too positive to be driven by O_2 reduction (i.e. above +1.24 V vs. SHE) as required at the cathode of a fuel cell. To facilitate the oxidation, we turned to ligands that sport a more delocalized π system.

Schiff bases based on salicylaldehydes are simple to pre-pare, a versatile class of multidentate ligand and they have been widely used in coordination chemistry,[4] especially
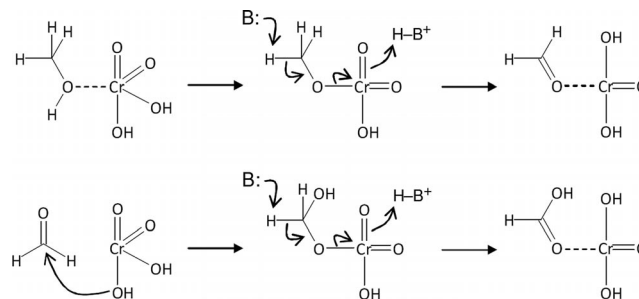
Scheme 1. Mechanism of a laboratory oxidation of CH_3OH to HCOOH.

with early transition metals[5] and for oxidation catalysis.[6] Although their structures have been thoroughly studied,[7] they have been the subjects of relatively few electrochemical investigations, none of which involved TiIV and, with one exception (vide infra), all showed metal-centred redox pro-cesses. Aminophenol–salicylaldehyde Schiff bases are diba-sic tridentates that can be viewed as extended catechols. They are of interest to us because, in the deprotonated form, the catecholate (anil) form can, in principle, be oxid-ized to semiquinonoid and quinonoid forms. Aminothio-phenol-derived analogues, with their larger, softer sulfur atoms, should undergo easier oxidations (Scheme 2). Mixed-ligand complexes of TiIV alkoxides and salicylalde-hyde-2-mercaptoanil were first reported in 1974;[8] they were found to catalyze ethylene polymerization,[9] which was attributed to the soft thiophenolate–Ti interaction and its steric requirements. Their electrochemistry was not ex-amined. Indeed, we uncovered only one report of ligand-centred redox chemistry in Schiff-base complexes of this sort: Wieghardt et al.[10] found that the aminothiophenol–salicylaldehyde Schiff-base ligands in a RuIII dimer under-went two reversible one-electron oxidation processes in an aprotic medium with the initial formation of a radical spe-

[a] Department of Chemistry, York University,
    4700 Keele Street, Toronto, ON M3J 1P3, Canada
    Fax: +1-416-736-5936
    E-mail: pgpotvin@yorku.ca

cies at a potential below +1 V vs. Ag/AgCl. DFT calculations suggested a unique singlet diradical configuration for the doubly oxidized species.
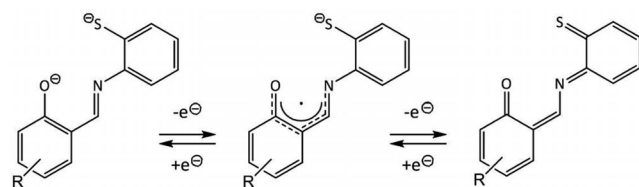
Scheme 2. Oxidation of the catecholate form to semiquinonoid and quinonoid forms.

We present here our investigations of aminothiophenol-derived Schiff bases of a series of salicylaldehydes in mixed-ligand complexes with Ti^{IV} alkoxides, along with a study of their electrochemical properties.

Results and Discussion

Ligands

The seven ligands investigated were prepared according to Scheme 3. Of these seven, five have been described previously, but detailed procedures were available only for H$_2$I,[11] H$_2$II,[12] H$_2$IV[12,13] and H$_2$VII.[14] The synthesis of H$_2$V[15] has been claimed, but no procedure, spectroscopic data or elemental analysis have been reported; yields and NMR spectroscopic data for H$_2$II and H$_2$IV were also lacking. H$_2$III has not hitherto been reported. H$_2$VI is also new, although the methyl analogue has been reported,[16] and it was selected to possibly accommodate two Ti centres. All of the ligands were prepared by the condensation of substituted salicylaldehydes with 2-aminothiophenol, and it has long been recognized[11,12,15,17,18] that these reactions can lead to three products, which depends on the reaction conditions, that have been identified mainly based on IR and elemental analyses as the anil (A), thiazoline (B), or thiazole (C) forms (Scheme 4).
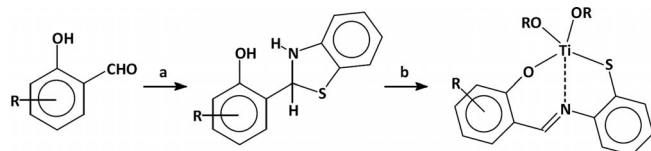
Scheme 3. Synthesis of ligands and complexes. Conditions: (a) 2-aminothiophenol/EtOH/room temperature/18 h; (b) Ti(OR)$_4$/CHCl$_3$/room temperature/10 min.
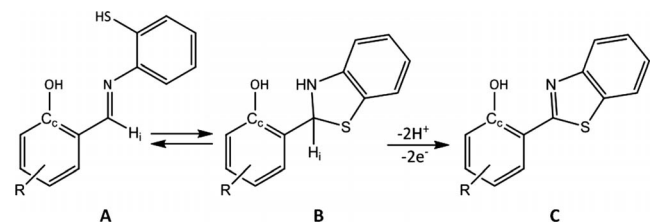
Scheme 4. The anil (A), thiazoline (B) and thiazole (C) forms of the ligands.
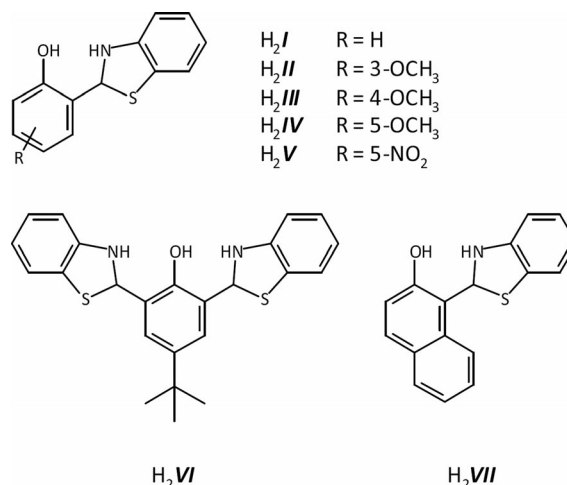
We found ^{1}H NMR spectroscopy (Figure 1) to be an invaluable tool for the rapid differentiation between the A (aldimino H$_i$ singlet near 8 ppm), B (acetal-type H$_i$ singlet near 6 ppm) and C forms (no H$_i$ singlet and increased sharpness of the other signals, indicative of a more rigid structure, probably due to a stronger internal H bond between the phenolic hydrogen and the more dipolar nitrogen atom of the thiazole ring), irrespective of the solvent. The anil form was obtained by the treatment of a solution of the salicylaldehyde in cold ethanol with a precooled solution of 2-aminothiophenol in ethanol under an inert atmosphere. With neat 2-aminothiophenol, the pure thiazoline form was isolated, and conducting these reactions in air led to partial oxidation (formation of disulfides and/or thiazole form). Indeed, ref.[9] reported two products from salicylaldehyde but provided no explanation, whereas in our hands the S–S linked dimer was one of them. The thiazole form was the sole product upon prolonged heating of the reaction mixture in air.

All the ligands in this study were isolated in their thiazoline forms by the procedures described herein. Their ^{1}H and ^{13}C NMR spectra were obtained, for consistency, in [D$_6$]DMSO because of the limited solubility of some (H$_2$I, H$_2$II, H$_2$III and H$_2$VI) in CDCl$_3$. In particular, H$_2$III gave an indistinct room-temperature NMR spectrum in CDCl$_3$ with only very broad signals, which lacked a visible singlet or the sharp peaks typical of thiazole forms. We tentatively ascribed this to an intermediate-rate anil–thiazoline equilibrium made possible by a destabilization of the thiazoline form by the π-donating OCH$_3$ group. This spectrum became sharp and clear upon complexation to Ti (vide infra) to reveal the expected signal pattern. In examples that were soluble in both solvents, the chemical shift of the aldimino proton singlet was found to be minimally affected by the solvent, and its position can be considered diagnostic for the identification of thiazoline forms.

H$_2$VI is unique in that its bis(thiazoline) form contains two stereocentres, and therefore can have *meso* and *d,l* forms. Its ^{1}H NMR spectrum included at least 10 signals, whereas nine are expected for any one diastereomer. It did not show the clean d–dd–dd–d pattern expected for an un-
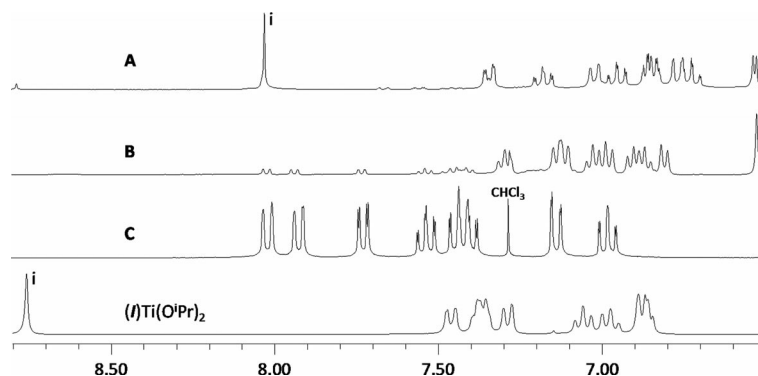
Figure 1. ^{1}H NMR spectra in CDCl$_3$ of the three different forms of H$_2$I (A–C) compared to that of (I)Ti(OiPr)$_2$.

symmetrically *ortho*-substituted benzene, but the possible overlap of two such patterns. Its ^{13}C NMR spectrum showed 22 signals, with clear doubling of the tBu signals and some others, whereas 13 were expected for each diastereomer. This confirms the thiazoline formulation and that both diastereomers were present, with overlap of some ^{1}H signals.

Complexes

The direct reactions of 1:1 ratios of the ligands with Ti(OiPr)$_4$ or Ti(OtBu)$_4$ in anhydrous CHCl$_3$ gave instantaneous color changes and led to the isolation of LTi-(OR)$_2$ species as the only detectable products (Scheme 3). The presence of chelation was supported by 2.2 ppm downfield shifts of the H$_i$ signals, which were consistently found in the 8.6–8.8 ppm range and indicate an opening of the thiazoline ring and reestablishment of the aldimino functionality for metal binding. The doubly deprotonated ligands are designated with primes in the formulas of their complexes. With all ligands, reactions with one equiv. of Ti(OiPr)$_4$ produced one new OiPr methine signal consistently near 4.6 ppm, about 0.2 ppm downfield of that of Ti(OiPr)$_4$.

The structures were confirmed by ^{13}C NMR and, in two cases, by crystallography (vide infra). EI mass spectrometry was uninformative and showed too much fragmentation. These materials are very moisture sensitive. Nine of the complexes gave satisfactory elemental analyses, but the others showed evidence of partial hydrolysis during transit or sampling (loss of alcohol), even after two attempts with handling under N$_2$ in a glovebox and even though the freshly prepared samples had shown clean NMR spectra. Importantly, these elemental analyses were not consistent with any other product formulation, which included oxidized versions or different Ti:L ratios and involved five different ligands. Nevertheless, the evidence of the purities and of correct identities in these five cases therefore relies on their NMR spectra and their close similarities with the other species.

Despite the possibly dinucleating nature of H$_2$VI, it afforded only mononuclear (VI')Ti(OR)$_2$ products (R = iPr or tBu), just as with the other ligands. When a 1:1 ligand-to-Ti ratio was used, only one major product was detected, whose ^{1}H NMR spectrum showed a clear desymmetrized pattern. Both aldimino and thiazoline functionalities were detected, whereas the free ligand showed only one corresponding signal. When using a 1:2 ratio in order to coordinate two metal centres per ligand, as previously reported for other metals,[16] one equivalent of Ti(OR)$_4$ always remained unreacted, irrespective of the reaction conditions. We thereby conclude that stable coordination is only possible for one Ti at only one coordination site, with the other site remaining in the thiazoline form. This was supported by ^{13}C NMR spectroscopy, particularly by the diastereotopicity of the –OCR(CH$_3$)$_2$ (R = H, CH$_3$) groups, for which each complex showed two carbon signals. The selective coordination of one metal can be rationalized as follows: the initial coordination of the ligand to the metal likely occurs at the oxygen atom. The subsequent coordination of the nitrogen atom presumably triggers the opening of the thiazoline ring to reestablish the aldimino functionality and, ultimately, the coordination of the sulfur atom. The phenoxy oxygen is metal bound and possibly hydrogen bonded to the neighbouring thiazoline NH group, which presumably precludes, in combination with steric congestion, any interaction with a second metal centre.

As detailed below, two LTi(OR)$_2$ complexes (from H$_2$I and H$_2$IV) formed diffraction-quality crystals but two LTi(OiPr)$_2$ compounds (from H$_2$III and H$_2$VII) unexpectedly crystallized as L$_2$Ti complexes. In order to clarify this and to obtain bulk samples of these species, reactions at 2:1 L/Ti(OiPr)$_4$ stoichiometric ratios were attempted with several ligands. In all cases, however, only broad and ill-defined signals or multiple sets of signals were seen in the ^{1}H NMR spectra, even after removal of HOiPr. This indicated the formation of mixtures and some exchange, and no further analyses were carried out as bulk L$_2$Ti samples evidently could not form. At least in some cases, L$_2$Ti species seemingly formed the best looking crystal or preferentially crystallized to form either through ligand exchange or partial hydrolysis over the course of months-long crystal growth. With the two-site ligand H$_2$VI (see preceding paragraph), the 2:1 ligand-to-Ti mixture also failed to show a single product but formed a diffraction-quality crystal of a 2:1 ligand/Ti species, which had undergone multiple redox

modifications of the unused sites, a transformation that could not conceivably be replicated in bulk form. Despite the lack of evidence of these three L$_2$Ti species in solution, their crystals nevertheless provide useful points of comparison with the LTi(OR)$_2$ crystals.

Crystallography

Diffraction-quality crystals were obtained for (*I′*)Ti-(O*t*Bu)$_2$ and (*IV′*)Ti(O*i*Pr)$_2$. Table 1 reports the crystallographic data, and Figures 2, 3 and 4 display the structures.
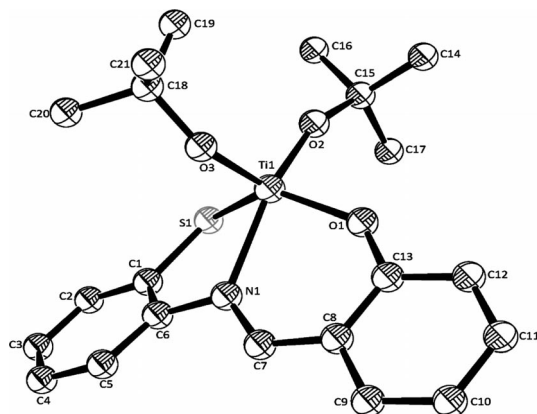

Figure 2. ORTEP diagram of the crystal structure of (*I′*)Ti-(O*t*Bu)$_2$ with H atoms omitted for clarity. Selected bond lengths [Å] and angles [°]: Ti^1–O^1 1.889(2), Ti^1–O^2 1.764(2), Ti^1–O^3 1.777(2), Ti^1–N^1 2.206(2), Ti^1–S^1 2.3867(9), Ti^1–O^2–C^{15} 158.7(2), Ti^1–O^3–C^{18} 149.3(2).

As previously hypothesized,[11a] the coordination geometry and nuclearity seem highly influenced by steric hindrance. Indeed, monomeric structures similar to (*I′*)Ti-(O*t*Bu)$_2$ have previously been reported for CpTi(*I′*)Cl[19] and for CpTi(L)Cl and LTi(O*i*Pr)$_2$ obtained from the 3-*tert*-butyl-5-methylsalicylaldehyde analogue of H$_2$I (H$_2$L).[20] These displayed similarly distorted square pyramidal geometries where three of the four basal positions were occu-
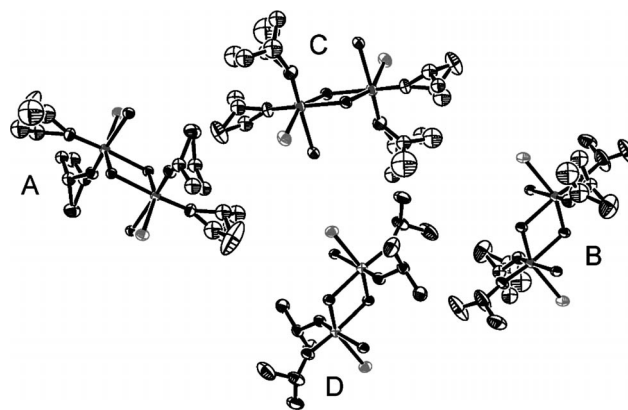

Figure 3. The four crystallographically distinct dimeric molecules A–D of [(*IV′*)Ti(O*i*Pr)$_2$]$_2$ constituted by the unit cell and symmetry equivalents, which shows only the metal-coordinated atoms and the isopropyl groups, includes disordered atoms in A–C and excludes hydrogen atoms.

pied by the ONS ligand, and the OR groups were nonequivalent. As only one set of *t*Bu signals was detected by ^{1}H and ^{13}C NMR spectroscopy of (*I′*)Ti(O*t*Bu)$_2$, the two nonequivalent O*t*Bu groups must undergo rapid exchange in solution. In crystalline (*I′*)Ti(O*t*Bu)$_2$, both O*t*Bu groups show short Ti–O distances and large Ti–O–C angles (1.764 Å and 158° for the basal O*t*Bu vs. 1.777 Å and 149° for the axial position) indicative of π bonding. Compared to LTi(O*i*Pr)$_2$, (*I′*)Ti(O*t*Bu)$_2$ boasts a shorter Ti–O axial bond, which is compatible with the increased electron-donating effect due to the extra CH$_3$ group, and a slightly longer Ti–O basal bond. (*I′*)Ti(O*t*Bu)$_2$ also shows more elongated Ti–S^1 and Ti–O^3 bonds than the literature structures, probably due to the increased steric interaction between the two O*t*Bu groups and the ligand. Moreover, (*I′*)Ti(O*t*Bu)$_2$ showed torsional distortion, with an angle of about 26° between the rings. This distortion seems to be a general phenomenon with ONS ligands − L$_2$Ti species also showed this[20] − but is apparently much reduced or absent in ONO

Table 1. Crystallographic data.[a]

	(*I′*)Ti(O*t*Bu)$_2$	[(*IV′*)Ti(O*i*Pr)$_2$]$_2$	(*III′*)$_2$Ti	(*VII′*)$_2$Ti	[(*VIII*)Ti]$_2$·2CH$_2$Cl$_2$
Formula	C$_{21}$H$_{27}$NO$_3$STi	C$_{40}$H$_{50}$N$_2$O$_8$S$_2$Ti$_2$	C$_{28}$H$_{22}$N$_2$O$_4$S$_2$Ti	C$_{34}$H$_{22}$N$_2$O$_2$S$_2$Ti	C$_{98}$H$_{96}$Cl$_4$N$_8$O$_4$S$_8$Ti$_2$
M_r	421.40	846.74	562.5	602.56	1943.91
Space group	*P*21/*n*	*P*$\bar{1}$	*P*21/*c*	*P*21/*c*	*P*21/*c*
a [Å]	12.9591(8)	14.3442(3)	8.8864(2)	8.9600(3)	13.6494(3)
b [Å]	10.6090(5)	15.7718(3)	15.3542(5)	18.3938(6)	23.6191(7)
c [Å]	15.4891(9)	19.3791(4)	18.2899(6)	16.3184(6)	31.4346(9)
α [°]	90	108.3780(9)	90	90	90
β [°]	94.667(3)	90.209(1)	92.6400(19)	94.6760(19)	91.1220(16)
γ [°]	90	92.2990(12)	90	90	90
V [Å^3]	2122.4(2)	4156.64(15)	2492.89(13)	2680.46(16)	10132.1(5)
Z	4	4	4	4	4
D_{calc} [g cm^{-3}]	1.319	1.353	1.499	1.493	1.274
μ [mm^{-1}]	0.522	0.536	0.55	0.512	0.48
$R(F_o)$[b]	0.0557	0.0625	0.0633	0.0476	0.0942
$R_w(F_o{}^2)$[b][c]	0.1222[d]	0.1592[e]	0.1464[f]	0.1134[g]	0.2433[h]

[a] T = 150(1) K and λ = 0.71073 Å; esd values are expressed as uncertainties in the least significant digits in brackets. [b] For reflections where $I > 2σ(I)$. [c] The weights *w* are given by $w = 1/[σ^2(F_o{}^2) + (aP)^2 + bP]$ where $P = (F_o{}^2 + 2F_c{}^2)/3$ for various values of *a* and *b*. [d] a = 0.0751, b = 0. [e] a = 0.0831, b = 6.523. [f] a = 0.0970, b = 0. [g] a = 0.0616, b = 1.5198. [h] a = 0.1104, b = 40.8862.
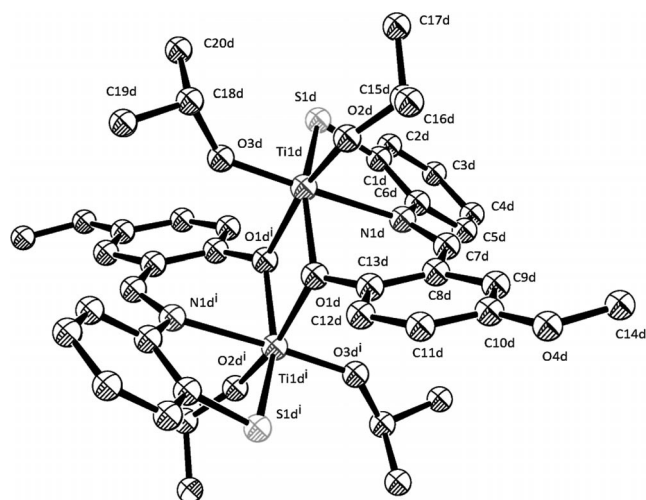
Figure 4. ORTEP diagram of nondisordered D in the crystal structure of $[(IV')\text{Ti}(\text{O}i\text{Pr})_2]_2$ with H atoms omitted for clarity. Selected bond lengths [Å] and angles [°]: Ti^1–O^1 2.006(2), Ti^1–O$^{1'}$ 2.148(2), Ti^1–O^2 1.769(2), Ti^1–O^3 1.796(2), Ti^1–N^1 2.279(3), Ti^1–S^1 2.427(1), Ti^1–O^2–C^{15} 155.2(3), Ti^1–O^3–C^{18} 136.0(2).

analogues.[19,21] Its origin is likely to be the significantly longer Ti–S bond [2.40 Å in CpTi(I')Cl vs. 1.89 Å for the equivalent bond in the ONO analogue],[19] as well as perhaps the greater steric demand of the sulfur atom and its poorer π-overlap with the imino portion.

The crystal structure of $(IV')\text{Ti}(\text{O}i\text{Pr})_2$ was similar to that reported for $(I')\text{Ti}(\text{O}i\text{Pr})_2$.[20] However, this crystal displayed four distinct molecules (labelled A–D) within the same unit cell (Figure 3), which occupy the centre (A), four edges (B), two faces (C) and eight corners (D). Each molecule was dinuclear and locally symmetrical and showed a distorted octahedral environment around the Ti atoms and *meridional* coordination of the tridentate. They all had *cis* OiPr groups and phenoxy O bridges to form trapezoidal Ti$_2$O$_2$ rings, as is normal, with short Ti–O$_{\text{bridging}}$ bonds (average 2.02 Å) within each $(IV')\text{Ti}(\text{O}i\text{Pr})_2$ unit and long bonds (average 2.16 Å) between the units. In B, the axial OiPr groups (*trans* to N) were disordered over two orientations. In A and C, both axial and equatorial OiPr groups were each disordered over two orientations. D (Figure 4) was the only one that did not show disorder. Over all four molecules, the Ti–OiPr distances were always shorter at the equatorial positions (average 1.767 ± 0.005 Å) than the axial ones (average 1.792 ± 0.006 Å). The Ti–O–CHMe$_2$ angles spanned a wide range with larger values at equatorial positions (average $159 \pm 7°$ when occupancies are taken into account) than at axial ones (average $145 \pm 7°$). These shorter Ti–O distances and wider Ti–O–C angles at the equatorial positions indicate stronger π bonding *trans* to the long Ti–O1 bridging bonds. The same was true of (I')-Ti(OiPr)$_2$[20] with essentially the same distances and angles, considering the variability within the crystal of (IV')Ti-(OiPr)$_2$.

All four molecules in the unit cell shared the same configuration, with noncoplanar tridentates. In contrast, the dimeric catecholate[22] and naphthalene-2,3-diolate[23] com-

plexes of Ti(OiPr)$_2$ featured coplanar diolates. The common element of all of these is a strongly π-bonded OiPr in the Ti$_2$O$_2$ plane, which presumably compensates for the weaker Ti–O$_{\text{bridging}}$ bond *trans* to it and would not be possible if the $(IV')^{2-}$ moieties lay coplanar to one another. The π donation by OiPr further reduces steric crowding at the periphery.

As explained earlier, solutions of $(III')\text{Ti}(\text{O}i\text{Pr})_2$ and $(VII')\text{Ti}(\text{O}i\text{Pr})_2$ provided diffraction-quality crystals of $(III')_2\text{Ti}$ (Figure 5) and $(VII')_2\text{Ti}$ (Figure 6). Such ML_2 complexes have been previously reported for Ge^{IV} and Zr^{IV}[18,24] but without crystal structures. Only two examples of crystal structures that show similar salicylidene-2-aminothiophenol Schiff-base ligands coordinated to the same metal centre were reported for Ni^{IV}[25] and Ti^{IV}.[21] These showed a distorted tetrahedral coordination sphere, with the two tridentate ligands arranged in *meridional* fashion. In the examples isolated here, distortion of the ligands was found to be larger than the literature examples with a torsional angle between the aromatic rings of about 48° for $(III')_2\text{Ti}$ and 47° for $(VII')_2\text{Ti}$, which results in *facial* coordination. As a result, the geometry at Ti^{IV} can more appropriately be described as distorted trigonal prismatic, which is typically observed in the presence of three small rigid bidentate ligands[26] where the ON pairs occupy two of the three tetragonal edges and the two sulfur atoms fill the third.

Figure 5. ORTEP diagram of the crystal structure of $(III')_2\text{Ti}$ with H atoms omitted for clarity. Selected bond lengths [Å] and angles [°]: Ti^1–O^1 1.869(2), Ti^1–O^2 1.871(3), Ti^1–N^1 2.176(3), Ti^1–N^2 2.175(3), Ti^1–S^1 2.4067(11), Ti^1–S^2 2.4067(11), S^1–Ti^1–S^2 75.82(4), O^1–Ti^1–O^2 125.44(11), N^1–Ti^1–N^2 148.75(10).

The Ti–O$_1$ and Ti–N$_1$ bond lengths in these L$_2$Ti species were generally shorter than those found in the LTi(OR)$_2$ complexes, probably due to the lack of strongly π-donating alkoxy groups. The Ti–S$_1$ bonds, on the other hand, remained essentially unchanged. Despite using different ligands, these structures and that reported in the literature[21] display bond lengths for analogous bonds within the coordination sphere that fall within 0.01 Å of each other, which suggests a very poor electronic delocalization from the substituents to the metal centre. Because of the particular spatial arrangement in these structures, the more noticeable
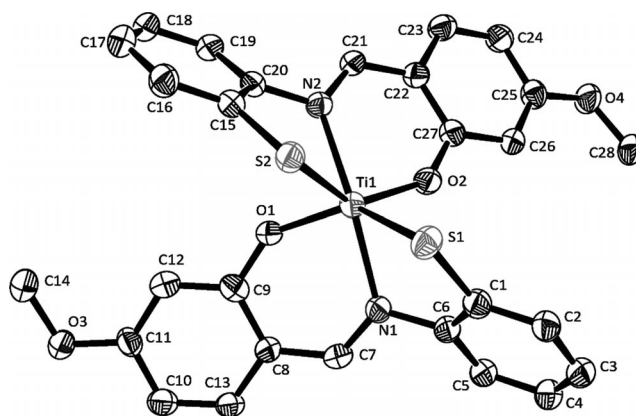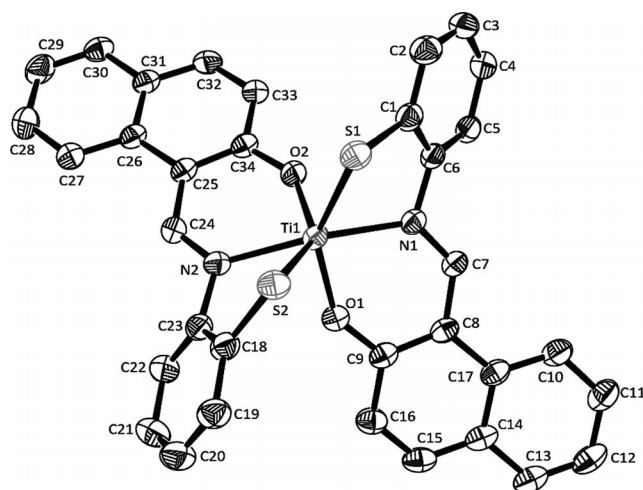
Figure 6. ORTEP diagram of the crystal structure of $(VII')_2$Ti with H atoms omitted for clarity. Selected bond lengths [Å] and angles [°]: Ti^1–O^1 1.8609(16), Ti^1–O^2 1.8722(16), Ti^1–N^1 2.1631(19), Ti^1–N^2 2.1631(19), Ti^1–S^1 2.4239(8), Ti^1–S^2 2.4292(8), S^1–Ti^1–S^2 77.71(2), O^1–Ti^1–O^2 118.88(8), N^1–Ti^1–N^2 151.79(8).

discrepancy between the corresponding bond angles cannot be justified by steric interaction or electronic effects, and we attribute it instead to packing restrictions in the formation of the unit cell: $(VII)_2$Ti, for instance, showed strong π–π stacking between the naphthalene moieties of different molecules in the crystal.

An unexpected complex $[(VIII)Ti]_2\cdot2CH_2Cl_2$ (Figure 7) was obtained from a 2:1 H_2VI/Ti(OiPr)$_4$ solution. As at 1:1 stoichiometry in solution (vide supra), each of the Ti^{IV} centres in this species occupies only one of the two potential coordination sites of each of the subunits of VI' that constitute the modified ligand H_4VIII. The two metals are not crystallographically identical, but both show *meridional* binding with *trans* nitrogen atoms in an overall distorted octahedron (Figure 8).

The modified ligand H_4VIII evidently arose from the coupling of two units of H_2VI but retained the same coordination environment. The mechanism of the formation of this dimeric product is not trivial: after a first reasonable step that involves the formation of two $(VI')_2$Ti units by the use of one of the two binding sites of each ligand, the unreacted thiazoline rings evidently opened, perhaps triggered by strong congestion, which thereby established new aldimino functionalities. The subsequent formation of the S^5–S^6 and S^7–S^8 bonds might be explained by oxidation by adventitious O_2, as thiophenols can undergo facile aerial oxidation to disulfides. Although we cannot exclude that possibility, it is not likely that the complex is actually a product of an overall reduction. Although this is not particularly evident from Figure 7, the noncoordinated nitrogen atoms (N^5, N^6, N^7 and N^8) are actually sp^3 hybridized, in accordance with their bonding to the attached carbon atoms (C–N distances average 1.455 ± 0.003 Å, and C–C–N angles average 108.6 ± 0.4°, compared to the corresponding measurements at the other sp^2-hybridized nitrogen atoms of 1.304 ± 0.006 Å and 126.0 ± 0.4°, respectively). These
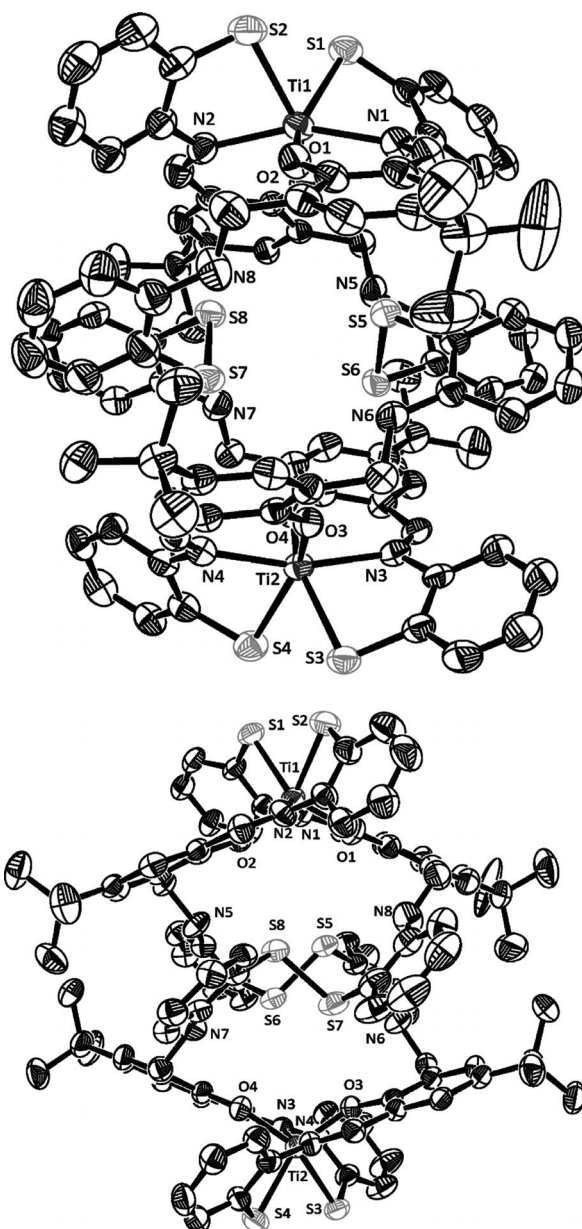

Figure 7. ORTEP diagram of the crystal structure of $[(VIII)Ti]_2$ (two different views) with H atoms omitted for clarity. Selected bond lengths [Å] and angles [°]: S^5–S^6 2.087(3), S^7–S^8 2.085(3), C^{24}–S^7–S^8 101.5(3), C^{25}–S^8–S^7 101.5(2), N^1–C^7 1.302(9), N^2–C^{90} 1.289(9), N^3–C^{42} 1.320(8), N^4–C^{55} 1.302(8), N^5–C^{79} 1.459(8), N^6–C^{66} 1.458(9), N^7–C^{31} 1.454(9), N^8–C^{18} 1.447(10), N^1–C^7–C^8 125.1(7), N^2–C^{90}–C^{84} 126.0(7), N^3–C^{42}–C^{36} 125.7(6), N^4–C^{55}–C^{56} 126.8(6), N^5–C^{79}–C^{80} 108.2(5), N^6–C^{66}–C^{60} 108.0(5), N^7–C^{31}–C^{32} 109.8(6), N^8–C^{18}–C^{10} 109.1(7).

amino (CH$_2$–NH) groups apparently arose by reduction of the noncoordinated aldimino groups (CH=N) after the ring opening of the noncoordinated thiazoline rings. Although an internal redox exchange between four free SH groups oxidizing to two S–S linkages can account for the reduction of two CH=N groups to CH$_2$–NH, the process must have involved external reductants as a total of four CH=N groups were reduced per dimer. The external reducing equivalents may have simply been SH groups from other
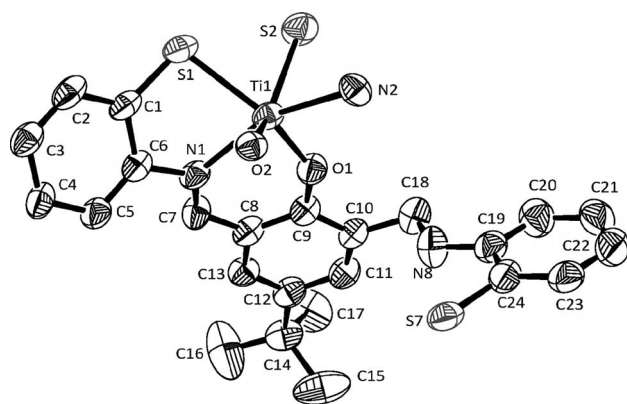
Figure 8. ORTEP diagram of the environment at one metal centre in [(*VIII*)Ti]$_2$ with H atoms omitted for clarity. Selected bond lengths [Å] and angles [°]: Ti^1–O^1 1.862(5), Ti^1 O^2 1.863(5), Ti^1–N^1 2.180(6), Ti^1–N^2 2.173(6), Ti^1–S^1 2.404(2), Ti^1–S^2 2.421(3), S^1–Ti^1–S^2 75.65(8), O^1–Ti^1–O^2 113.7(2), N^1–Ti^1–N^2 157.7(2), Ti^2–O^3 1.860(5), Ti^2–O^4 1.875(5), Ti^2–N^3 2.166(6), Ti^2–N^4 2.168(6), Ti^2–S^3 2.411(2), Ti^2–S^4 2.413(2), O^3–Ti^2–O^4 110.1(2), N^3–Ti^2–N^4 163.5(2), S^3–Ti^2–S^4 77.39(8).

Table 2. Steady-state peak potentials for the oxidations of free ligands and complexes [V] vs. Ag/AgCl in CH$_2$Cl$_2$ (0.1 M *n*Bu$_4$NPF$_6$).

L^{2-}	free H$_2$L	LTi(O*i*Pr)$_2$	LTi(O*t*Bu)$_2$
I	+1.06, + 2.17	+1.37, +1.95	+1.36, +2.05
II	+0.85, +1.59	+1.35, +1.71	+1.34, +1.83
III	+0.97, +1.88	+1.22, +1.46	+1.28, +1.88
IV	+0.95, +1.54	+1.45, +1.79	+1.21, +1.60
V	+1.05	+1.42, +2.10	+1.32, +2.05
VI	+1.37, +1.91	+1.34, +2.01	+1.38, +1.99
VII	+0.89, +1.54	+1.33, +1.47	+1.27, +1.87

molecules that were not part of those forming the crystal. To stabilize the assembly, the NH groups appear to engage in transannular H bonds with sulfur atoms from one of the other ligands, with NH–S distances (3.35–3.55 Å) falling in the usual range.[27]

Despite the steric congestion, the ligands in [(*VIII*)Ti]$_2$ were found to be less distorted than in the other (*L*)$_2$Ti complexes, with a torsional angle of about 38° between the aromatic rings. The bond lengths in the coordination spheres were not significantly different from those in the previous examples, and the bond angles were consistent with those in literature reports.[21] However, the C–S–S–C torsion angles were 80.9° and 74.2°, appreciably smaller than expected (90°).
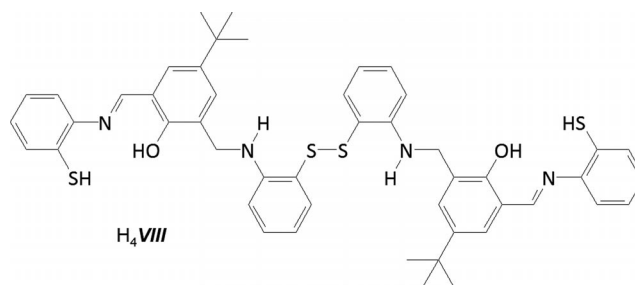
Electrochemistry

To the best of our knowledge, no electrochemical studies have been performed on this class of compound. All of the isolated complexes were tested by standard cyclic voltammetry and compared with the corresponding free ligands under the same conditions (Supporting Information). All of the processes are irreversible, as was the case with the dithiocarbamate complexes,[3] but, because the conditions were identical for all, the steady-state peak anodic potentials (Table 2) can be compared.

The case of H$_2$*VI* will be discussed separately. Scanning in the positive direction, all complexes showed at least two oxidation waves and, in the negative direction, all showed at least one reduction, which was about 200 mV more negative with O*t*Bu than with O*i*Pr ligands. Comparing ligands and complexes, the retardation of the first oxidations owing to coordination amounted to 250–500 mV, considerably less than that found earlier with dithiocarbamates,[3] which is due to the greater electronic delocalization with the Schiff-base ligands. A comparison of the first and second oxi-

dation potentials reveals that the latter were generally less retarded in the O*i*Pr complexes. If, as crystallography suggests, the O*t*Bu complexes are all mononuclear and the O*i*Pr complexes are all dinuclear, then each oxidation in the O*t*Bu complexes (and the free ligands) is a one-electron process that occurs on the same ligand going from catecholate to semiquinonoid to quinonoid forms (Scheme 2), and the second oxidations of the O*i*Pr species represent the second catecholate-to-semiquinonoid process centred on the second ligand in the dinuclear complexes, exactly as previously reported for the Ru^{III} dimer.[10]

The build up of charge during the redox events is affected by solvent polarity. Measurements were also obtained after adding an equal volume of HO*i*Pr to the electrochemical cells. This produced a dramatic shift in the potential of the oxidation peak to less positive values, and the current also increased noticeably despite the attendant dilution. Yet, there was no evidence of extensive decomposition that would liberate the ligand from the metal. We attribute these phenomena to the stabilization of the charged redox products by virtue of the higher dielectric constant as well as by better solvation and, possibly, by proton transfer. With (*I′*)-Ti(O*t*Bu)$_2$ under the same conditions, the same peak potentials were measured, consistent with rapid alkoxide–alcohol exchange to convert this complex to its O*i*Pr analogue in situ. These observations were replicated with the complexes of all ligands, except those of H$_2$*VI*.

H$_2$*VI* presents an exceptional case as it showed an earlier oxidation event at +0.88–0.95 V and the next oxidation was virtually unaffected by complexation. It appears that these oxidation events involved the unused binding site (Scheme 5). The oxidation was unchanged after the addition of HO*i*Pr, which suggests that it does not produce a charged product and likely converted into the half-thiazole form.
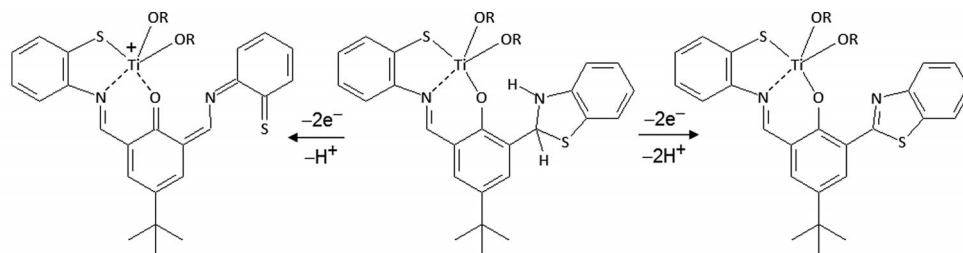
Scheme 5. Possible oxidation processes in $(VI')Ti(OR)_2$ complexes.

We found that $[(I')Ti(OiPr)_2]_2$ can be stably attached to partially oxidized graphite and can catalyze the oxidation of alcohols, details of which will be published elsewhere.

Conclusions

Three new NOS Schiff-base ligands and, with four others previously described, fourteen Ti^{IV} complexes of thiophenol-appended Schiff bases were prepared and characterized. In tandem with literature findings, the crystal structures obtained for two of these revealed that a combination of steric and electronic effects control the coordination geometry. In particular the need for strong π donation appears to dictate the cis disposition of OiPr groups in dinuclear assemblies, whereas steric demands force mononuclearity with bulky substituents in all Ti(OtBu)$_4$-derived complexes. Cyclic voltammograms acquired in homogeneous aprotic solvent showed irreversible oxidations shifted 0.25–0.50 V more positive than those of the free ligands. The addition of iPrOH reduced these shifts without causing decomposition, and these findings bode well for applications in protic environments.

Experimental Section

General: Details on electrochemical and crystallographic data acquisition and processing are presented as Supporting Information. All reactions were carried out under Ar. All reagents were Sigma–Aldrich products. Ti(OiPr)$_4$ was distilled under Ar prior to use. Ti(OtBu)$_4$ was purchased in Sure-Seal bottles and used directly. Deuterated solvents were from Cambridge Isotope Laboratories. CDCl$_3$ was stored over molecular sieves. The other solvents were from Caledon Laboratories (Georgetown, ON, Canada). Prior to use, CHCl$_3$ was dried and kept over MgSO$_4$ and CH$_2$Cl$_2$ was distilled from P$_2$O$_5$. HOiPr was kept over molecular sieves. All NMR spectra were acquired in CDCl$_3$ at 23 °C at 300 MHz with a Bruker ARZ instrument, unless otherwise indicated. Signal assignments were made with the help of COSY, heteronuclear multiple quantum coherence and HMBC spectra. Relative integrations were obtained after careful baseline and phase corrections on spectra acquired with a relaxation delay of 5 s. Assignments and H,H coupling constants (^3J) appear in the Supporting Information. Elemental analyses were performed with weighing under N$_2$ at Guelph Chemical Laboratories (Guelph, ON, Canada) and ANALEST Laboratories (Toronto, ON, Canada). H$_2$I,[11] H$_2$IV[12,13] and H$_2$VII[14] were prepared by published procedures. H$_2$II[12] was prepared by the same procedure used for H$_2$I.[11] NMR spectroscopic data for these are

presented as Supporting Information. H$_2$V has been previously reported without characterization,[15] so was prepared as if new.

Representative Ligand Preparation: Ligand H$_2$III: H$_2$III was prepared in a manner similar to that reported for H$_2$I[11] by dissolving 2-hydroxy-4-methoxybenzaldehyde (0.72 g, 4.6 mmol) in abs. EtOH (10 mL) at room temperature under an Ar atmosphere. The solution was stirred for about 5 min prior to the dropwise addition of 2-aminothiophenol (0.5 mL, 4.6 mmol). The mixture was then stirred for 5 min and left to stand overnight under Ar. The precipitate was collected and washed with a small quantity of abs. EtOH to afford a light yellow crystalline solid in a yield of 89% (1.06 g). ^{1}H NMR ([D$_6$]DMSO): δ = 9.91 (s, 1 H), 7.38 (d, 1 H), 6.96 (d, 1 H), 6.88 (t, 1 H), 6.71 (br. s, 1 H), 6.68 (d, 1 H), 6.58 (t, 1 H), 6.53 (s, 1 H), 6.45, (s, 1 H), 6.41 (d, 1 H), 3.69 (s, 3 H) ppm. ^{13}C NMR ([D$_6$]DMSO): δ = 159.9, 154.7, 147.8, 127.0, 125.4, 125.1, 121.9, 121.3, 118.5, 108.7, 104.2, 101.1, 63.4, 55.0 ppm; m.p. 121–124 °C. C$_{14}$H$_{13}$NO$_2$S (259.32): calcd. C 64.84, H 5.05, N 5.40; found C 64.75, H 5.11, N 5.15.

H$_2$V: After removing the solvent under reduced pressure, the dark orange oil was dissolved in hot CHCl$_3$ and precipitated with petroleum spirits as the pure product as a yellow powder; yield 86%. ^{1}H NMR ([D$_6$]DMSO): δ = 11.64 (s, 1 H), 8.23 (s, 1 H), 8.10 (d, 1 H) 6.96, (m, 4 H), 6.78 (d, 1 H), 6.61 (t, 1 H), 6.44 (s, 1 H) ppm. ^{13}C NMR ([D$_6$]DMSO): δ = 159.9, 147.0, 139.2, 131.1, 125.2, 124.9, 124.7, 121.4, 121.1, 118.9, 115.2, 109.1, 61.9 ppm; m.p. 113–115 °C. C$_{13}$H$_{10}$N$_2$O$_3$S (274.29): calcd. C 56.92, H 3.67, N 10.21; found C 56.70, H 3.77, N 10.05.

H$_2$VI: Prepared in MeOH to give a pale orange solid; yield 73%. ^{1}H NMR ([D$_6$]DMSO): δ = 9.40 (s, 1 H), 7.50 (s, 1 H), 7.48 (s, 1 H), 7.00 (m, 2 H), 6.91 (m, 3 H), 6.73 (m, 2 H), 6.64 (m, 4 H), 1.17 (s, 9 H) ppm. ^{13}C NMR ([D$_6$]DMSO): δ = 148.9, 148.4, 147.6, 147.4, 141.4, 141.3, 128.8, 128.0, 125.8, 125.6, 125.2, 123.2, 122.9, 121.30, 119.2, 119.0, 109.29, 109.04, 65.2, 64.8, 33.9, 31.2 ppm; m.p. 121–123 °C. C$_{24}$H$_{24}$N$_2$O$_2$S$_2$ (420.59): calcd. C 68.54, H 5.75, N 6.66; found C 68.53, H 5.73, N 6.43.

Representative Complex Preparation: [(I')Ti(OiPr)$_2$]$_2$: H$_2$I (0.105 g, 0.46 mmol) was dissolved in anhydrous CHCl$_3$ (1 mL) under Ar and stirred for 1 min before Ti(OiPr)$_4$ (0.135 mL, 0.46 mmol) was added. The resultant dark red solution was stirred in a vortex mixer for a few seconds and placed in a sonicator for approximately 10 min at room temperature. The solvent and reaction byproduct were removed under reduced pressure, and the product was recovered as a red solid in quantitative yield (0.180 g, 99%). The yields of all complex preparations were similarly quantitative. ^{1}H NMR: δ = 8.75 (s, 1 H), 7.46 (d, 1 H), 7.37 (br. m, 2 H), 7.29 (d, 1 H), 7.06 (t, 1 H), 6.98 (t, 1 H), 6.87 (br. m, 2 H), 4.61 (h, 2 H), 1.12 (d, 12 H) ppm. ^{13}C NMR: δ = 164.4, 161.12, 148.2, 142.5, 135.1, 134.0, 129.9, 127.9, 123.8, 121.8, 119.5, 118.6, 116.7, 80.9, 25.4 ppm. C$_{19}$H$_{23}$NO$_3$STi (393.36): calcd. C 58.02, H 5.89, N 3.56; found C 57.48, H 5.35, N 2.90.

(I′)Ti(OtBu)₂: ¹H NMR: δ = 8.78 (s, 1 H), 7.48 (d, 1 H), 7.40 (m, 2 H), 7.31 (d, 1 H), 7.07 (t, 1 H), 6.98 (t, 1 H) 6.88 (br. m, 2 H), 1.21 (s, 18 H) ppm. ¹³C NMR: δ = 164.6, 160.9, 148.5, 142.7, 135.0, 133.9, 123.0, 127.8, 123.7, 121.6, 119.2, 118.6, 116.58, 86.0, 31.2 ppm. C₂₁H₂₇NO₃STi (421.41): calcd. C 59.86, H 6.46, N 3.32; found C 60.15, H 6.21, N 3.04.

(II′)Ti(OiPr)₂: ¹H NMR: δ = 8.79 (s, 1 H), 7.39 (d, 1 H), 7.28 (d, 1 H), 7.07 (m, 2 H), 6.95 (m, 2 H), 6.79 (t, 1 H), 4.62 (h, 2 H), 3.77 (s, 3 H), 1.11 (2d, 12 H ppm.) ppm ¹³C NMR: δ = 161.1, 155.3 (C), 148.4, 148.1, 142.3, 129.8, 127.7, 125.6, 123.8, 122.0, 119.0, 117.0, 116.6, 80.9, 56.4, 25.3 ppm. C₂₀H₂₅NO₄STi (423.38): calcd. C 56.74, H 5.95, N 3.31; found C 57.11, H 6.03, N 2.97.

(II′)Ti(OtBu)₂: ¹H NMR: δ = 8.80 (s, 1 H), 7.40 (d, 1 H), 7.31 (d, 1 H), 7.08 (m, 2 H), 6.99 (m, 2 H), 6.80 (t, 1 H), 3.82 (s, 3 H), 1.20 (s, 18 H) ppm. ¹³C NMR: δ = 160.8, 156.0, 148.8, 148.4, 142.8, 130.0, 127.7, 125.9, 123.7, 122.1, 118.8, 118.1, 116.5, 86.0, 57.0, 31.2 ppm. C₂₂H₂₉NO₄STi (451.44): calcd. C 58.54, H 6.48, N 3.10; found C 57.20, H 5.20, N 2.61.

(III′)Ti(OiPr)₂: ¹H NMR: δ = 8.66 (s, 1 H), 7.33 (m, 2 H), 7.27 (d, 1 H), 7.00 (m, 2 H), 6.48 (d, 1 H), 6.36 (s, 1 H), 4.62 (h, 2 H), 3.72 (s, 3 H), 1.14 (br. d, 12 H) ppm. ¹³C NMR: δ = 166.7, 165.9, 160.0, 148.6, 141.7, 135.1, 129.7, 127.2, 123.8, 116.3, 115.9, 109.4, 101.1, 80.9, 55.5, 25.4 ppm. C₂₀H₂₅NO₄STi (423.38): calcd. C 56.74, H 5.95, N 3.31; found C 56.83, H 5.60, N 3.46.

(III′)Ti(OtBu)₂: ¹H NMR: δ = 8.68 (s, 1 H), 7.35 (m, 2 H), 7.31 (d, 1 H), 7.01 (m, 2 H), 6.50 (d, 1 H), 6.35 (s, 1 H), 3.77 (s, 3 H), 1.22 (s, 18 H) ppm. ¹³C NMR: δ = 166.9, 165.9, 159.8, 148.9, 142.0, 135.1, 129.8, 127.2, 123.7, 116.2, 115.9, 109.1, 101.1, 85.9, 55.5, 31.2 ppm. C₂₂H₂₉NO₄STi (451.44): calcd. C 58.54, H 6.48, N 3.10; found C 48.26, H 5.68, N 2.76.

(IV′)Ti(OiPr)₂: ¹H NMR: δ = 8.73 (s, 1 H), 7.37 (d, 1 H), 7.28 (d, 1 H), 6.98 (m, 4 H), 6.80 (d, 1 H), 4.58 (h, 2 H), 3.69 (s, 3 H), 1.11 (d, 12 H) ppm. ¹³C NMR: δ = 160.6, 160.0, 152.4, 148.1, 142.6, 129.9, 127.8, 123.7, 121.3, 119.4, 116.6, 114.5, 80.7, 55.7, 25.4 ppm. C₂₀H₂₅NO₄STi (423.38): calcd. C 56.74, H 5.95, N 3.31; found C 56.76, H 5.82, N 3.28.

(IV′)Ti(OtBu)₂: ¹H NMR: δ = 8.77 (s, 1 H), 7.40 (d, 1 H), 7.31 (d, 1 H), 7.02 (br. m, 4 H), 6.83 (d, 1 H), 3.73 (s, 3 H), 1.19 (s, 18 H) ppm. ¹³C NMR: δ = 160.4, 159.9, 152.2, 148.4, 142.9, 130.0, 127.7, 123.8, 123.7, 121.0, 119.5, 116.6, 114.4, 85.7, 55.8, 31.2 ppm. C₂₂H₂₉NO₄STi (451.44): calcd. C 58.54, H 6.48, N 3.10; found C 58.82, H 6.64, N 2.99.

(V′)Ti(OiPr)₂: ¹H NMR: δ = 8.85 (s, 1 H), 8.49 (s, 1 H), 8.23 (d, 1 H), 7.43 (d, 1 H), 7.26 (d, 1 H), 7.09 (m, 2 H), 6.94 (d, 1 H), 4.66 (h, 2 H) 1.16 (br. d, 12 H) ppm. ¹³C NMR: δ = 168.7, 159.6, 147.5, 142.5, 139.6, 130.5, 130.2, 129.5, 128.9, 124.5, 120.9, 120.1, 117.0, 82.2, 25.4 ppm. C₁₉H₂₂N₂O₅STi (438.35): calcd. C 52.04, H 5.06, N 6.39; found C 51.85, H 4.95, N 6.53.

(V′)Ti(OtBu)₂: ¹H NMR: δ = 8.85 (s, 1 H), 8.50 (s, 1 H), 8.20 (d, 1 H), 7.46 (d, 1 H), 7.25 (d, 1 H), 7.05 (m, 2 H), 6.91 (d, 1 H), 1.21 (s, 18 H) ppm. ¹³C NMR: δ = 168.7, 159.4, 147.4, 142.6, 139.3, 130.5, 130.0, 129.2, 128.7, 124.3, 120.6, 119.9, 116.9, 87.2, 31.0 ppm. C₂₁H₂₆N₂O₅STi (466.41): calcd. C 54.08, H 5.62, N 6.01; found C 53.81, H 5.38, N 6.22.

(VI′)Ti(OiPr)₂: ¹H NMR: δ = 8.77 (s, 1 H), 7.85 (s, 1 H), 7.37 (m, 2 H), 7.25 (d, 1 H), 7.00 (m, 3 H), 6.81 (t, 1 H), 6.80 (m, 3 H), 4.63 (m, 3 H), 1.21 (s, 9 H), 1.16 (m, 12 H) ppm. ¹³C NMR: δ = 161.2, 159.6, 148.2, 146.5, 142.3, 142.2, 130.1, 129.8, 127.9, 127.1, 125.1, 123.9, 121.8, 121.1, 120.4, 116.7, 110.1, 81.3, 81.0, 64.7, 34.2, 31.3,

25.6 ppm. C₃₀H₃₆N₂O₃S₂Ti (584.65): calcd. C 61.63, H 6.21, N 4.79; found C 60.42, H 6.22, N 4.79.

(VI′)Ti(OtBu)₂: ¹H NMR: δ = 8.84 (s, 1 H), 7.85 (d, 1 H), 7.43 (m, 2 H), 7.31 (d, 1 H), 7.00 (m, 3 H), 6.84 (t, 1 H), 6.64 (m, 3 H), 4.65 (s, 1 H), 1.27 (s, 9 H), 1.23 (s, 9 H), 1.21 (s, 9 H) ppm. ¹³C NMR: δ = 161.0, 159.7, 148.4, 146.5, 142.6, 141.8, 130.2, 130.0, 129.8, 129.6, 127.8, 127.1, 125.1, 123.7, 121.9, 120.9, 120.5, 116.6, 110.1, 86.5, 86.0, 64.8, 34.3, 31.45, 31.42, 31.3 ppm. C₃₂H₄₀N₂O₃S₂Ti (612.70): calcd. C 62.73, H 6.58, N 4.57; found C 62.40, H 6.56, N 4.58.

(VII′)Ti(OiPr)₂: ¹H NMR: δ = 9.69 (s, 1 H), 8.15 (d, 1 H), 7.80 (d, 1 H), 7.67 (d, 1 H), 7.50 (m, 2 H), 7.35 (d, 1 H), 7.28 (t, 1 H), 7.10 (m, 3 H), 4.64 (h, 2 H), 1.16 (d, 12 H) ppm. ¹³C NMR: δ = 166.3, 156.3, 149.5, 142.1, 136.6, 133.3, 130.1, 129.3, 128.21, 128.18, 127.6, 124.1, 124.0, 121.0, 119.6, 117.0, 113.2, 81.0, 25.5 ppm. C₂₃H₂₅NO₃STi (443.42): calcd. C 62.30, H 5.68, N 3.16; found C 62.40, H 6.56, N 4.58.

(VII′)Ti(OtBu)₂: ¹H NMR: δ = 9.51 (s, 1 H), 8.21 (d, 1 H), 7.72 (d, 1 H), 7.56 (d, 1 H), 7.41 (m, 2 H), 7.34 (d, 1 H), 7.18 (t, 1 H), 7.08 (m, 2 H), 6.96 (d, 1 H), 1.23 (s, 18 H) ppm. ¹³C NMR: δ = 166.2, 155.9, 149.7, 142.3, 136.3, 133.2, 130.0, 129.2, 129.97, 127.96, 127.4, 123.9, 123.8, 121.0, 119.4, 116.9, 112.8, 85.8, 31.3 ppm. C₂₅H₂₉NO₃STi (471.47): calcd. C 63.69, H 6.20, N 2.97; found C 63.40, H 6.41, N 3.05.

Supporting Information (see footnote on the first page of this article): General experimental procedures, details of crystallography and electrochemistry, NMR spectra and assignments, Tables of selected bond lengths and angles, Table of electrochemical potentials. CCDC-781098 [for (I)Ti(OtBu)₂], -781099 [for (III)₂Ti], -781100 {for [(IV)Ti(OiPr)₂]₂}, -781101 {for [(VIII)Ti]₂·2CH₂Cl₂} and -781102 [for (VII)₂Ti] contain the supplementary crystallograhic data for this paper. These data can be obtained free of charge from The Cambridge Crystallographic Data Centre via www.ccdc.cam.ac.uk/data_request/cif.

Acknowledgments

[1] H. Liu, J. Zhang (Eds.), *Electrocatalysis of Direct Methanol Fuel Cells: From Fundamentals to Applications*, Wiley-VCH, Weinheim, Germany, **2009**.

[2] A. Pfenninger, *Synthesis* **1986**, 89–116.

[3] A. Donzelli, P. G. Potvin, *Inorg. Chem.* **2009**, *48*, 4171–4178.

[4] R. H. Holm, G. W. Everett, A. Chakravorty, *Prog. Inorg. Chem.* **1966**, *7*, 83–214.

[5] K. C. Gupta, A. K. Sutar, *Coord. Chem. Rev.* **2008**, *252*, 1420–50; A. D. Garnovskii, I. S. Vasilchenko, D. A. Garnovskii, B. I. Kharisov, *J. Coord. Chem.* **2009**, *62*, 151–204.

[6] K. C. Gupta, A. K. Sutar, C. Lin, *Coord. Chem. Rev.* **2009**, *253*, 1926–46.

[7] T. Storr, P. Verma, R. C. Pratt, E. C. Wasinger, Y. Shimazaki, T. D. P. Stack, *J. Am. Chem. Soc.* **2008**, *130*, 15448–59; Y. Shimazaki, T. D. P. Stack, T. Storr, *Inorg. Chem.* **2009**, *48*, 8383–92.

[8] E. C. Alyea, A. Malek, P. H. Merrell, *J. Coord. Chem.* **1974**, *4*, 55–63.

[9] C. Wang, X. Sun, Y. Guo, Y. Gao, B. Liu, Z. Ma, W. Xia, L. Shi, Y. Tang, *Macromol. Rapid Commun.* **2005**, *26*, 1609–14; C. Wang, Z. Ma, X. Sun, Y. Gao, Y. Guo, Y. Tang, L. Shi, *Organometallics* **2006**, *25*, 3259–66; M. Gao, C. Wang, X. Sun, C. Qian, Z. Ma, S. Bu, Y. Tang, Z. Xie, *Macromol. Rapid Com-*

mun. **2007**, *28*, 1511–1516; K. Cui, B. Liu, C. Wang, J. Y. Yu, Z. Ma, *J. Mol. Catal. A* **2007**, *266*, 93–99; M. Gao, X. Sun, Y. Gu, X. Yao, C. Li, J. Bai, C. Wang, Z. Ma, Y. Tang, Z. Xie, S. Bu, C. Qian, *J. Polym. Sci.* **2008**, *46*, 2807–19.

[10] N. Roy, S. Sproules, T. Weyhermüller, K. Wieghardt, *Inorg. Chem.* **2009**, *48*, 3783–91.

[11] a) F. Tisato, F. Refosco, U. Mazzi, G. Bandoli, M. Nicolini, *J. Chem. Soc., Dalton Trans.* **1987**, 1693–1699; b) M. S. Singh, P. Narayan, A. K. Singh, *Phosphorus Sulfur Relat. Elem.* **1999**, *155*, 245–52.

[12] W. W. Fee, J. D. Pulsford, D. Vowles, *Aust. J. Chem.* **1973**, *26*, 675–80.

[13] J. Topich, *Inorg. Chem.* **1981**, *20*, 3704–3707; J. Topich, J. T. Lyon, *Polyhedron* **1984**, *3*, 55–60.

[14] N. Singh, N. Kaur, R. C. Mulrooney, J. F. Callan, *Tetrahedron Lett.* **2008**, *49*, 6690–6692.

[15] C. C. Lee, A. Syamal, L. J. Theriot, *Inorg. Chem.* **1971**, *10*, 1669–73.

[16] W. D. McFadyen, R. Robson, H. Schaap, *Inorg. Chem.* **1972**, *11*, 1777–85.

[17] R. G. Charles, H. Freiser, *J. Org. Chem.* **1953**, *18*, 422–425; W. E. Hill, N. Atabay, C. A. McAuliffe, F. P. McCullough, S. M. Razzoki, *Inorg. Chim. Acta* **1979**, *35*, 35–41; A. W. Addison, T. Nageswara Rao, E. Sinn, *Inorg. Chem.* **1984**, *23*, 1957–67; A. Varshney, J. P. Tandon, *Polyhedron* **1985**, *4*, 1311–1313; C. Zhang, I. A. Guzei, J. H. Espenson, *Inorg. Chem.* **2001**, *40*, 2437–2438; C. Jayabalakrishnan, K. Natarajan, *Trans. Annu.*

Meet. Orthop. Res. Soc. Trans. Met. Chem. **2002**, *27*, 75–79; S. Priyarega, R. Prabhakaran, K. R. Aranganayagam, R. Karvembu, K. Natarajan, *Appl. Organomet. Chem.* **2007**, *21*, 788–93.

[18] R. K. Sharma, R. V. Singh, J. P. Tandon, *J. Inorg. Nucl. Chem.* **1980**, *42*, 1267–70.

[19] J. Zhang, Y. Lin, G. Jin, *Organometallics* **2007**, *26*, 4042–4047.

[20] A. Jia, G. Jin, *Organometallics* **2009**, *28*, 1872–1877.

[21] W. F. Zeng, Y. H. Chen, M. Y. Chiang, C. P. Cheng, *Polyhedron* **2007**, *26*, 1303–1309.

[22] M. G. Davidson, M. D. Jones, M. D. Lunn, M. F. Mahon, *Inorg. Chem.* **2006**, *45*, 2282–2287.

[23] W. A. Wallace, P. G. Potvin, *Inorg. Chem.* **2007**, *46*, 9463–72.

[24] R. V. Singh, J. P. Tandon, *Inorg. Nucl. Chem. Lett.* **1979**, *15*, 429–32.

[25] E. Labisbal, A. De Blas, J. A. Garcia-Vazquez, J. Romero, M. L. Duran, A. Sousa, N. A. Bailey, D. E. Fenton, P. B. Leeson, *Polyhedron* **1992**, *11*, 227–33.

[26] D. Bodie, D. McDaniel, A. John, *Concept and Models of Inorganic Chemistry*, 3rd ed., John Wiley & Sons, New York, **1994**, p. 424.

[27] E. Adman, K. D. Watenpaugh, L. H. Jensen, *Proc. Natl. Acad. Sci. USA* **1975**, *72*, 4854–4858; V. Madhu, S. K. Das, *Eur. J. Inorg. Chem.* **2006**, 1505–14.